



PhD Thesis

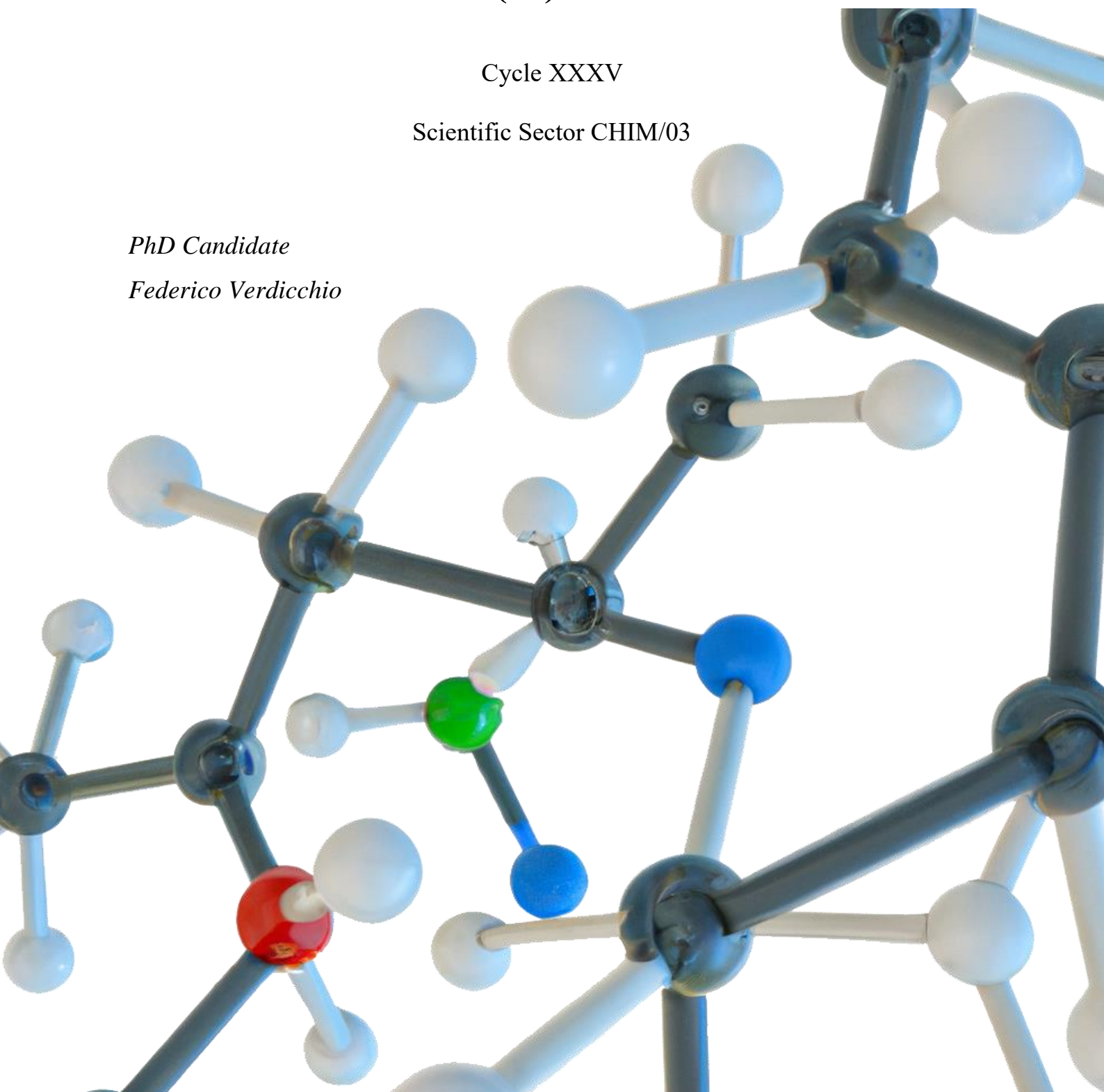
**Pyrazolone-based metal complexes: synthesis,
characterization and theoretical study of Zn(II), Cu(II)
and Mo(IV) derivatives**

Cycle XXXV

Scientific Sector CHIM/03

PhD Candidate

Federico Verdicchio





UNIVERSITY OF CAMERINO

School of Advanced Studies

Chemical and Pharmaceutical Sciences and Biotechnology Area

Ph.D. Curriculum in Chemical Sciences

Pyrazolone-based metal complexes: synthesis, characterization and theoretical study of Zn(II), Cu(II) and Mo(IV) derivatives

PhD Thesis

Cycle XXXV

Scientific Sector CHIM/03

PhD Candidate

Federico Verdicchio

Supervisor

Prof. Riccardo Pettinari

Co-supervisor

Gianfranco Biancini

2020-2022

« And this chaos, it defies imagination »

- Matthew Bellamy

Abstract

4-acyl-5-pyrazolones are a class of compounds that combine the properties of the pyrazolone ring with that of diketones, affording an O,O-chelating ligand with biological features. Since the first synthesis by Jensen in 1959 they have been the subject of a multitude of studies concerning their tautomeric forms, their biological properties, and their coordination chemistry towards a variety of metal centres. Furthermore, the readiness of the structural modifications they can undergo pushed researchers to explore many different variations tailoring the substituents to optimize their coordination with the metals and to vary their properties. In particular, one interesting variant of 4-acyl-5-pyrazolones is obtained by condensation with hydrazine or amine to afford N,O-chelating Schiff base ligands. This class of ligands retains all the characteristics of their synthon and additionally, they show enhanced coordination features due to the presence of one or more nitrogen atoms. In Chapter 1 an introduction to these compounds is reported together with a comprehensive state-of-the-art of their metal complexes, involving zinc, copper, and molybdenum. Chapter 2 deals with the synthesis and characterization of Schiff base ligands and the study of their tautomerism in solid state and solution. The ligands have then been utilized to synthesize the respective zinc(II) complexes of composition $[\text{Zn}(\text{HL}^n)_2]$, they were fully characterized and the structures of two ligands and three complexes were determined by X-ray diffraction, showing that complexes **1** and **2** have a monomeric nature, while complex **4** exists as one-dimensional coordination polymer. DFT calculations on proligands, anions and complexes were exploited to confirm the experimental result and rationalized the polymeric nature of complex **4** and the presence of two water molecules coordinated on complexes **3** and **5**. The antimicrobial activity of the compounds was investigated against *Escherichia coli* and *Staphylococcus aureus*. Complexes **4** and **5** demonstrated good efficiency, the latter probably for its ligand containing aliphatic and fluorinated substituents. Similarly, in Chapter 3 two hydrazone ligands were synthesized, characterized and reacted with Zn(II) and Cu(II) affording four complexes of formula $[\text{Zn}(\text{HL}^1)_2(\text{MeOH})_2]$, $[\text{Cu}(\text{HL}^1)_2]$, and $[\text{M}(\text{HL}^2)_2]$. DFT and XRD studies determined that the free proligands exist in the NH,NH tautomeric form, $[\text{Zn}(\text{HL}^1)_2(\text{MeOH})_2]$ has an octahedral geometry with two apical methanol molecules, $[\text{Cu}(\text{HL}^1)_2]$ adopts a square planar geometry, and the two $[\text{M}(\text{HL}^2)_2]$ are octahedral with the ligands acting as tridentate O,N,N-donors in planar conformation. All the compounds were tested against the parasite *Trypanosoma brucei* and Balb3T3 cells obtaining powerful results, from the ligand H_2L^1 and its Zn complex, showing a high selectivity index. For this reason, the mechanism of action of these two compounds has been

investigated, indicating a strong impact on the CTP (cytidine triphosphate) pools, making it likely that CTP synthetase is the targeted enzyme. Chapter 4 is focused on the theoretical study of the mechanism of molybdenum-catalyzed deoxydehydration (DODH) of vicinal diols to alkenes. The mechanism has been investigated employing DFT calculations and considering $[\text{Mo}(\text{O})_2(\text{Q}^{\text{Me}})_2]$ as a catalyst, where Q^{Me} is an O,O-donor pyrazolone-based ligand, and PMe_3 as a reductant. Two different pathways have been analysed differing in the order of the main steps of the reaction. The lowest energy profiles were calculated for both, and the data obtained suggest that the second pathway is energetically preferred. Finally, In Chapter 5, a list of activities aimed at improving the efficiency of the processes of TechPol srl, a company active in the field of technopolymer molding, is reported. The activities carried out have optimized the use of recycled materials in a circular economy perspective, investigating the nature of the problems encountered and confirming that the main cause was the material used.

Table of Contents

<i>Abstract</i>	I
<i>List of abbreviations</i>	XIII

CHAPTER 1. General introduction and state-of-the-art.

1.1 Pyrazolone fragment and β -diketones	2
1.2 Class of 4-acyl-5-pyrazolone	3
1.2.1 Ligand synthesis	4
1.2.2 Tautomerism	5
1.2.3 Modes of coordination	6
1.2.4 Biological properties	9
1.3 Class of Schiff Bases	9
1.3.1 Classes and synthesis	10
1.3.2 Tautomerism	12
1.4 Nomenclature	13
1.5 Coordination Chemistry of Transition Metals	15
1.5.1 Complexes of Cu	16
1.5.2 Complexes of Zinc	26
1.5.3 Complexes of Molybdenum	34

CHAPTER 2. Synthesis of novel Schiff base ligands and their zinc(II) complexes. Evaluation of their biological activity as antimicrobials.

2.1 Introduction	40
2.2 Experimental section	41
2.2.1 General procedures	41
2.2.2 Synthesis of proligands	41
2.2.2 Synthesis of complexes	43
2.2.3 Crystallographic refinement	46
2.2.4 Computational details	47
2.2.5 Antibacterial activity	47
2.2.6 Reactive oxygen species (ROS) detection assay	48
2.2.7 Propidium iodide (PI) – viability assay	48

2.2.8 Confocal laser scanning microscopy (CLMS) study	49
2.2.9 Scanning electron microscopy (SEM) study	49
2.3 Results and discussion	50
2.3.1 Synthesis and spectroscopic characterization of proligands	50
2.3.2 Synthesis and spectroscopic characterization of complexes	57
2.3.3 X-ray structural characterization	66
2.3.4 Theoretical studies	72
2.3.5 Antibacterial activity	88
2.3.6 Reactive oxygen species (ROS) detection assay	89
2.3.7 Propidium iodide (PI) – viability assay	90
2.3.8 Confocal laser scanning microscopy (CLSM) study	91
2.3.9 Scanning electron microscopy (SEM) study	92
2.3 Conclusions	94

CHAPTER 3. Synthesis of novel Schiff base ligands and their zinc(II) and copper(II) complexes. Evaluation of their antiparasitic activity.

3.1 Introduction	97
3.2 Experimental section	99
3.2.1 General procedures	99
3.2.2 Synthesis of proligands	99
3.2.3 Synthesis of Zn(II) and Cu(II) complexes	101
3.2.4 Crystallographic refinement	103
3.2.5 Computational details	104
3.2.5 Cell culture and Cytotoxicity determinations.	104
3.2.6 Determination of NTP and dNTP pools by HPLC	105
3.3 Results and discussion	107
3.3.1 Synthesis and spectroscopic characterization of proligands and complexes	107
3.3.2 X-ray structural characterization	121
3.3.3 Theoretical DFT analysis	125
3.4 Cytotoxicity studies	135
3.4.1 Mechanism of action	136
3.5 Conclusions	139

CHAPTER 4. DFT studies on the mechanism of the molybdenum-catalyzed deoxydehydration of diols.

4.1 Introduction	142
4.2 Experimental section	146
4.3 Results and discussion	147
4.3.1 Description of pathway A.	149
4.3.2 Description of pathway B	151
4.3.3 Consideration between the two pathways	153
4.4 Conclusions	158

CHAPTER 5. Chemical-physical analyses and studies of non-conformity injection-molded technopolymers.

5.1 The company: TechPol	160
5.2 The materials: Technopolymers	162
5.3 The aim: circular economy	165
5.4 The project: analyses and problem solving	169
5.4.1 Creation of the polymer database	169
5.4.2 Study on the difference between a virgin and regrind material	171
5.4.3 Study of a yellowing phenomenon	173
5.4.4 Study of a product with a burnt surface	174
5.4.5 Study of the heat exchange difference	175
5.4.6 Study of an unknown material	177
5.5 Conclusions	182

Supplementary information

Appendix Chapter 2	183
Appendix Chapter 3	200

<i>Acknowledgments</i>	212
------------------------	-----

<i>Bibliography</i>	213
---------------------	-----

Table of Figures

Figure 1. Number of publication per year using “β-diketone OR acylpyrazolone” as query.....	2
Figure 2. Research areas related to “β-diketone OR acylpyrazolone”.....	3
Figure 3. IR spectrum of proligand H ₂ L ²	52
Figure 4. IR spectrum of proligand H ₂ L ⁴	52
Figure 5. IR spectrum of proligand H ₂ L ⁵	53
Figure 6. ¹ H NMR of proligand H ₂ L ² in CDCl ₃ at 298 K.....	54
Figure 7. { ¹ H, ¹ H}-COSY of proligand H ₂ L ² in CDCl ₃ at 298 K.....	54
Figure 8. ¹³ C{ ¹ H} NMR of proligand H ₂ L ² in CDCl ₃ at 298 K.....	55
Figure 9. { ¹ H, ¹³ C}-HSQC of proligand H ₂ L ² in CDCl ₃ at 298 K.....	55
Figure 10. { ¹ H, ¹³ C}-HMBC of proligand H ₂ L ² in CDCl ₃ at 298 K.....	56
Figure 11. { ¹ H, ¹⁵ N}-HSQC of proligand H ₂ L ² in CDCl ₃ at 298 K.....	56
Figure 12. { ¹ H, ¹⁵ N}-HMBC of proligand H ₂ L ² in CDCl ₃ at 298 K.....	57
Figure 13. IR spectrum of complex 1.....	60
Figure 14. IR spectrum of complex 2.....	61
Figure 15. IR spectrum of complex 3.....	61
Figure 16. IR spectrum of complex 4.....	62
Figure 17. IR spectrum of complex 5.....	62
Figure 18. ¹ H NMR of complex [Zn(HL ²) ₂] (2) in CDCl ₃ at 298 K.....	63
Figure 19. ¹³ C{ ¹ H} NMR of complex [Zn(HL ²) ₂] (2) in CDCl ₃ at 298 K.....	64
Figure 20. { ¹ H, ¹⁵ N}-HSQC of complex [Zn(HL ²) ₂] (2) in CDCl ₃ at 298 K.....	64
Figure 21. { ¹ H, ¹⁵ N}-HMBC of complex [Zn(HL ²) ₂] (2) in CDCl ₃ at 298 K.....	65
Figure 22. Stability study of complex [Zn(HL ²) ₂] (2) in DMSO-d ₆	65
Figure 23. Molecular structures of ligands H ₂ L ² and H ₂ L ⁴	67
Figure 24. Molecular structures of complexes 1, 2 and 4.....	70
Figure 25. Comparison of the calculated (tautomer I) and experimental ¹ H, ¹³ C and ¹⁵ N NMR spectra of H ₂ L ⁵	75
Figure 26. Comparison of selected bond distances of H ₂ L ² and H ₂ L ⁴ : calculated tautomers I and II (italic) and experimental.....	76
Figure 27. Comparison of experimental (black line) and calculated (tautomer I, red line) IR spectrum of H ₂ L ⁵	77
Figure 28. MOs of anionic ligand [HL ¹] ⁻ involved in the coordination to metal centers.....	79
Figure 29. MOs of anionic ligand [HL ²] ⁻ involved in the coordination to metal centers.....	80
Figure 30. MOs of anionic ligand [HL ⁴] ⁻ involved in the coordination to metal centers.....	81
Figure 31. Comparison of experimental (black line) and calculated (octahedral - red line, tetrahedral – blue line) IR spectra of [Zn(H ₂ L ³) ₂].....	85
Figure 32. Comparison of experimental (black line) and calculated (octahedral - red line, tetrahedral – blue line) IR spectra of [Zn(H ₂ L ⁵) ₂].....	85

Figure 33. Comparison of the calculated and experimental ^1H and ^{13}C NMR spectra of complexes 3 (top), 4 (middle) and 5 (bottom).	86
Figure 34. Representation of optimized structures of complexes.....	87
Figure 35. Percentage reduction of viable <i>E. coli</i> cells (top) and <i>S. aureus</i> cells (bottom) exposed to ligands H_2L^1 – H_2L^5 (left) and Zn(II) complexes 1–5 (right) within 24 hours. Blank corresponds to untreated bacterial cells growth.	89
Figure 36. Formation of ROS in <i>E. coli</i> (left) and <i>S. aureus</i> cells (right) exposed to Zn(II) complexes 4 and 5 for 2 and 4 hours. The data are represented as the mean \pm SD of at least three separate experiments.	90
Figure 37. Percentage of PI fluorescent emission for <i>E. coli</i> (left) and <i>S. aureus</i> cells (right) exposed to Zn(II) complexes 4 and 5 for 4, 8, 12 and 24 hours. The data are represented as the mean \pm SD of at least three separate experiments.....	91
Figure 38. Confocal laser scanning microscopy (CLSM) images of (a) <i>E. coli</i> control, (b) <i>E. coli</i> treated with complex 4; (c) <i>S. aureus</i> control; (d) <i>S. aureus</i> treated with complex 5.	92
Figure 39. Scanning electron microscopy (SEM) images of (a) <i>S. aureus</i> control, (b) <i>S. aureus</i> treated with complex 5, both at magnification 100.000; (c) <i>E. coli</i> control at magnification 25.000; (d) <i>E. coli</i> treated with complex 4 at magnification 40.000.....	94
Figure 40. ^1H NMR of proligand H_2L^4 in CDCl_3 at 298 K.	183
Figure 41. $\{^1\text{H}, ^1\text{H}\}$ -COSY of proligand H_2L^4 in CDCl_3 at 298 K.....	183
Figure 42. $^{13}\text{C}\{^1\text{H}\}$ NMR of proligand H_2L^4 in CDCl_3 at 298 K.	184
Figure 43. $\{^1\text{H}, ^{13}\text{C}\}$ -HSQC of proligand H_2L^4 in CDCl_3 at 298 K.	184
Figure 44. $\{^1\text{H}, ^{13}\text{C}\}$ -HMBC of proligand H_2L^4 in CDCl_3 at 298 K.	185
Figure 45. $\{^1\text{H}, ^{15}\text{N}\}$ -HSQC of proligand H_2L^4 in CDCl_3 at 298 K.	185
Figure 46. $\{^1\text{H}, ^{15}\text{N}\}$ -HMBC of proligand H_2L^4 in CDCl_3 at 298 K.....	186
Figure 47. ^1H NMR of proligand H_2L^5 in CDCl_3 at 298 K.	186
Figure 48. $^{13}\text{C}\{^1\text{H}\}$ NMR of proligand H_2L^5 in CDCl_3 at 298 K.	187
Figure 49. Magnification of the $^{13}\text{C}\{^1\text{H}\}$ NMR of proligand H_2L^5 in CDCl_3 at 298 K.....	187
Figure 50. $\{^1\text{H}, ^{15}\text{N}\}$ -HSQC of proligand H_2L^5 in CDCl_3 at 298 K.....	188
Figure 51. $\{^1\text{H}, ^{15}\text{N}\}$ -HMBC of proligand H_2L^5 in CDCl_3 at 298 K.....	188
Figure 52. $^{19}\text{F}\{^1\text{H}\}$ NMR of proligand H_2L^5 in CDCl_3 at 298 K.....	189
Figure 53. ^1H NMR of complex $[\text{Zn}(\text{HL}^1)_2]$ (1) in CDCl_3 at 298 K.	189
Figure 54. $^{13}\text{C}\{^1\text{H}\}$ NMR of complex $[\text{Zn}(\text{HL}^1)_2]$ (1) in CDCl_3 at 298 K.	190
Figure 55. $\{^1\text{H}, ^{15}\text{N}\}$ -HSQC of complex $[\text{Zn}(\text{HL}^1)_2]$ (1) in CDCl_3 at 298 K.....	190
Figure 56. ^1H NMR of complex $[\text{Zn}(\text{HL}^3)_2(\text{H}_2\text{O})_2]$ (3) in CDCl_3 at 298 K.....	191
Figure 57. $^{13}\text{C}\{^1\text{H}\}$ NMR of complex $[\text{Zn}(\text{HL}^3)_2(\text{H}_2\text{O})_2]$ (3) in CDCl_3 at 298 K.....	191
Figure 58. $\{^1\text{H}, ^{13}\text{C}\}$ -HSQC of complex $[\text{Zn}(\text{HL}^3)_2(\text{H}_2\text{O})_2]$ (3) in CDCl_3 at 298 K.	192
Figure 59. $\{^1\text{H}, ^{13}\text{C}\}$ -HMBC of complex $[\text{Zn}(\text{HL}^3)_2(\text{H}_2\text{O})_2]$ (3) in CDCl_3 at 298 K.....	192
Figure 60. $\{^1\text{H}, ^{15}\text{N}\}$ -HSQC of complex $[\text{Zn}(\text{HL}^3)_2(\text{H}_2\text{O})_2]$ (3) in CDCl_3 at 298 K.....	193

Figure 61. $\{^1\text{H}, ^{15}\text{N}\}$ -HMBC of complex $[\text{Zn}(\text{HL}^3)_2(\text{H}_2\text{O})_2]$ (3) in CDCl_3 at 298 K.	193
Figure 62. ^1H NMR of complex $[\text{Zn}(\text{HL}^4)_2]$ (4) in CDCl_3 at 298 K.	194
Figure 63. $^{13}\text{C}\{^1\text{H}\}$ NMR of complex $[\text{Zn}(\text{HL}^4)_2]$ (4) in CDCl_3 at 298 K.	194
Figure 64. $\{^1\text{H}, ^{13}\text{C}\}$ -HSQC of complex $[\text{Zn}(\text{HL}^4)_2]$ (4) in CDCl_3 at 298 K.	195
Figure 65. $\{^1\text{H}, ^{13}\text{C}\}$ -HMBC of complex $[\text{Zn}(\text{HL}^4)_2]$ (4) in CDCl_3 at 298 K.	195
Figure 66. ^1H NMR of complex $[\text{Zn}(\text{HL}^5)_2(\text{H}_2\text{O})_2]$ (5) in CDCl_3 at 298 K.	196
Figure 67. $^{13}\text{C}\{^1\text{H}\}$ NMR of complex $[\text{Zn}(\text{HL}^5)_2(\text{H}_2\text{O})_2]$ (5) in CDCl_3 at 298 K.	196
Figure 68. Magnification of $^{13}\text{C}\{^1\text{H}\}$ NMR of complex $[\text{Zn}(\text{HL}^5)_2(\text{H}_2\text{O})_2]$ (5) in CDCl_3 at 298 K.	197
Figure 69. $\{^1\text{H}, ^{13}\text{C}\}$ -HSQC of complex $[\text{Zn}(\text{HL}^5)_2(\text{H}_2\text{O})_2]$ (5) in CDCl_3 at 298 K.	197
Figure 70. $\{^1\text{H}, ^{13}\text{C}\}$ -HMBC of complex $[\text{Zn}(\text{HL}^5)_2(\text{H}_2\text{O})_2]$ (5) in CDCl_3 at 298 K.	198
Figure 71. $^{19}\text{F}\{^1\text{H}\}$ NMR of complex $[\text{Zn}(\text{HL}^5)_2(\text{H}_2\text{O})_2]$ (5) in CDCl_3 at 298 K.	198
Figure 72. $\{^1\text{H}, ^{15}\text{N}\}$ -HSQC of complex $[\text{Zn}(\text{HL}^5)_2(\text{H}_2\text{O})_2]$ (5) in CDCl_3 at 298 K.	199
Figure 73. $\{^1\text{H}, ^{15}\text{N}\}$ -HMBC of complex $[\text{Zn}(\text{HL}^5)_2(\text{H}_2\text{O})_2]$ (5) in CDCl_3 at 298 K.	199
Figure 74. IR spectrum of H_2L^1	108
Figure 75. IR spectrum of H_2L^2	109
Figure 76. ^1H NMR spectrum CDCl_3 at 298 K of H_2L^1	110
Figure 77. $\{^1\text{H}, ^1\text{H}\}$ -COSY spectrum in CDCl_3 at 298 K of H_2L^1	110
Figure 78. $^{13}\text{C}\{^1\text{H}\}$ NMR spectrum in CDCl_3 at 298 K of H_2L^1	111
Figure 79. Magnification of $^{13}\text{C}\{^1\text{H}\}$ NMR spectrum in CDCl_3 at 298 K of H_2L^1	111
Figure 80. $\{^1\text{H}, ^{13}\text{C}\}$ -HSQC spectrum in CDCl_3 at 298 K of H_2L^1	112
Figure 81. $\{^1\text{H}, ^{13}\text{C}\}$ -HMBC spectrum in CDCl_3 at 298 K of H_2L^1	112
Figure 82. $\{^1\text{H}, ^{15}\text{N}\}$ -HSQC spectrum in CDCl_3 at 298 K of H_2L^1	113
Figure 83. $\{^1\text{H}, ^{15}\text{N}\}$ -HMBC spectrum in CDCl_3 at 298 K of H_2L^1	113
Figure 84. Synthetic procedure and chemical data of complexes 1-4.	115
Figure 85. IR spectrum of $[\text{Zn}(\text{HL}^1)_2(\text{MeOH})_2]$ (1).	115
Figure 86. IR spectrum of $[\text{Zn}(\text{HL}^2)_2]$ (2).	200
Figure 87. IR spectrum of $[\text{Cu}(\text{HL}^1)_2]$ (3).	200
Figure 88. IR spectrum of $[\text{Cu}(\text{HL}^2)_2]$ (4).	201
Figure 89. ^1H NMR spectrum in CDCl_3 at 298 K of $[\text{Zn}(\text{HL}^1)_2(\text{MeOH})_2]$ (1).	116
Figure 90. ^{13}C NMR spectrum in CDCl_3 at 298 K of $[\text{Zn}(\text{HL}^1)_2(\text{MeOH})_2]$ (1).	117
Figure 91. Magnification of ^{13}C NMR spectrum in CDCl_3 at 298 K of $[\text{Zn}(\text{HL}^1)_2(\text{MeOH})_2]$ (1).	117
Figure 92. $\{^1\text{H}, ^{15}\text{N}\}$ -HSQC spectrum in CDCl_3 at 298 K of $[\text{Zn}(\text{HL}^1)_2(\text{MeOH})_2]$ (1).	118
Figure 93. $\{^1\text{H}, ^{15}\text{N}\}$ -HMBC spectrum in CDCl_3 at 298 K of $[\text{Zn}(\text{HL}^1)_2(\text{MeOH})_2]$ (1).	118
Figure 94. UV-Vis spectra of ligand H_2L^1 and Complex (1), (3) in CHCl_3 10^{-5} (a) e 10^{-3} (b).	119
Figure 95. UV-Vis spectra of ligand H_2L^2 and complexes (2), (4) in CHCl_3 10^{-5} M (a) and 10^{-3} M (b).	120
Figure 96. Decomposition pathway of complex 3 to complex 5.	120

Figure 97. Ortep view of the asymmetric unit content H_2L^1 (a) and H_2L^2 (b) with the atomic numbering scheme and intramolecular N-H...O hydrogen bond (ellipsoids at the 40% level).	121
Figure 98. Ortep view of the asymmetric unit content of $[Zn(HL^1)_2(MeOH)_2]$ (1) with the atomic numbering scheme (ellipsoids at the 40% level).	121
Figure 99. Crystal packing view of H_2L^2 showing N-H...O intramolecular and intermolecular hydrogen bonds and π - π interaction between the pyridine rings.	122
Figure 100. Crystal packing view of 1 showing N-H...O hydrogen bonds involving both coordinated and lattice methanol molecules (a) and ortep view of the asymmetric unit content of complex $[Cu(Q^{Bn})_2]$ (5) with the atomic numbering scheme (ellipsoids at the 40% level).	123
Figure 101. Comparison of the calculated (tautomer I) and experimental 1H and ^{13}C NMR spectra of H_2L^1	127
Figure 102. Comparison of selected bond distances of H_2L^1 : calculated tautomers I and II (italic) and experimental.	128
Figure 103. Comparison of the experimental (blue line) and calculated (tautomer II, red line) IR spectrum of H_2L^1 (cm^{-1}).	129
Figure 104. Molecular orbitals of anionic ligands $[HL^1]^-$ involved in the coordination to metal centers.	130
Figure 105. Molecular orbitals of anionic ligands $[HL^1]^-$ involved in the coordination to metal centers.	131
Figure 106. Optimized structures of complexes 1–5	133
Figure 107. Comparison of the calculated and experimental 1H and ^{13}C NMR spectra of complexes 1 (top) and 2 (bottom)	134
Figure 108. Optimized structures of complexes $[Zn(HL^1)_2]$ and $[Zn(HL^3)_2]$	135
Figure 109. (a) Differences in CTP and dCTP pools in non-treated cells and cells treated with H_2L^1 and 1 (both of them at a concentration of 5 μM for 1 hour). (b) Differences in NTP pools in non-treated cells and cells treated with H_2L^1 and 1 (both of them at a concentration of 5 μM for 1 hour).....	138
Figure 110. Increased deoxynucleotide pools in cells treated with 5 μM of H_2L^1 and 1 for 1 h (compared to deoxynucleotide pools in non-treated control cells).....	138
Figure 111. FIR spectrum of H_2L^1	201
Figure 112. FIR spectrum of H_2L^2	202
Figure 113. FIR spectrum of $[Zn(HL^1)_2(MeOH)_2]$ (1).....	202
Figure 114. FIR spectrum of $[Zn(HL^2)_2]$ (2).....	203
Figure 115. FIR spectrum of $[Cu(HL^1)_2]$ (3).	203
Figure 116. FIR spectrum of $[Cu(HL^2)_2]$ (4).	204
Figure 117. $^{19}F\{^1H\}$ NMR spectrum in $CDCl_3$ at 298 K of H_2L^1	204
Figure 118. 1H NMR spectrum in $CDCl_3$ at 298 K of H_2L^2	205
Figure 119. $\{^1H, ^1H\}$ -COSY spectrum in $CDCl_3$ at 298 K of H_2L^2	205
Figure 120. $^{13}C\{^1H\}$ NMR spectrum in $CDCl_3$ at 298 K of H_2L^2	206
Figure 121. $\{^1H, ^{13}C\}$ -HSQC spectrum in $CDCl_3$ at 298 K of H_2L^2	206
Figure 122. $\{^1H, ^{13}C\}$ -HMBC spectrum in $CDCl_3$ at 298 K of H_2L^2	207

Figure 123. $\{^1\text{H}, ^{15}\text{N}\}$ -HMBC spectrum in CDCl_3 at 298 K of H_2L^2	207
Figure 124. $^{19}\text{F}\{^1\text{H}\}$ NMR spectrum in CDCl_3 at 298 K of $[\text{Zn}(\text{HL}^1)_2(\text{MeOH})_2]$ (1).	208
Figure 125. ^1H NMR spectrum in CDCl_3 at 298 K of $[\text{Zn}(\text{HL}^2)_2]$ (2).....	208
Figure 126. ^{13}C NMR spectrum in CDCl_3 at 298 K of $[\text{Zn}(\text{HL}^2)_2]$ (2).....	209
Figure 127. $\{^1\text{H}, ^{13}\text{C}\}$ -HSQC spectrum in CDCl_3 at 298 K of $[\text{Zn}(\text{HL}^2)_2]$ (2).	209
Figure 128. $\{^1\text{H}, ^{15}\text{N}\}$ -HSQC spectrum in CDCl_3 at 298 K of $[\text{Zn}(\text{HL}^2)_2]$ (2).....	210
Figure 129. $\{^1\text{H}, ^{15}\text{N}\}$ -HMBC spectrum in CDCl_3 at 298 K of $[\text{Zn}(\text{HL}^2)_2]$ (2).....	210
Figure 130. Catalytic profiles of pathways A and B for the DODH ethylenediol with PPh_3 catalyzed by $[\text{Mo}(\text{O})_2(\text{Q}^{\text{Me}})_2]$, in vacuo.....	155
Figure 131. Catalytic profiles of pathways A and B for the DODH ethylenediol with PPh_3 catalyzed by $[\text{Mo}(\text{O})_2(\text{Q}^{\text{Me}})_2]$, in toluene.....	155
Figure 132. Structures of the optimized intermediates and transition states of pathway A (1-7b).....	156
Figure 133. Structures of the optimized intermediates and transition states of pathway B (8-14b).	157
Figure 134. Logo and establishment of the company Techpol.....	161
Figure 135. Schematic representation of the molding process; the green arrow indicates the good final product while the red arrow indicates the waste production from non-conformity products and excess materials. .	164
Figure 136. Example of a technopolymer material: in this case the polymer matrix with MMT (montmorillonite) platelets as additive gets furtherly filled with short glass fibers that orientate along the direction of the flow ^[334]	165
Figure 137. Schematic representation of the idea of circular economy: optimizing the recycling of materials and / or energy the waste production is minimized (image credit to snam.it).	167
Figure 138. Example of a TGA analysis of Econamid FL66G30 (nylon 6,6).	170
Figure 139. Example of a DSC analysis of Eplamid G30 (nylon 6,6).	170
Figure 140. DSC scan of sample V (virgin material).	172
Figure 141. DSC scan of sample V+R (reground material).....	172
Figure 142. Photo of a good sample (left) used as standard, and of a yellowed product (right).	173
Figure 143. TGA analysis of the yellowed sample.	174
Figure 144. Recorded temperature vs time for the two samples.....	176
Figure 145. Pictures obtain from the SEM analysis showing the glass fibers at different magnitudes.....	179
Figure 146. EDX analysis of the sample showing the distribution of carbon (blue), oxygen (light blue), and silicon (purple).	180
Figure 147. Molecular structure of polyphenyloxyde (PPO) (left) and polystyrene (PS) (right).....	181

Table of Charts

Chart 1. Structure of Edaravone (3-methyl-1-phenyl-5-pyrazolone).....	3
Chart 2. Generic structure of a 4-acyl-5-pyrazolone (left) and generic structure of an acylpyrazolone starting from edaravone (4-acyl-3-metyl-1-phenyl-5-pyrazolone).....	4
Chart 3. Synthetic procedure of a general 4-acyl-5-pyrazolone starting from 1-phenyl-3-methylpyrazol-5-one.	4
Chart 4. Scheme of the different tautomeric forms that a generic acylpyrazolone can assume.	6
Chart 5. Different possible coordination modes of neutral and deprotonated acylpyrazolone ligands.....	8
Chart 6. Classes of Schiff bases starting from 4-acyl-5-hydrazone synthon.....	11
Chart 7. General synthetic route starting from a substituted pyrazol-5-one leading to the relative 4-acyl-5-pyrazolone and finally to the corresponding Class I or Class IV Schiff base.	11
Chart 8. Tautomeric forms of class I Schiff base (4-aminoalkylidene-5-pyrazolone).....	12
Chart 9. Tautomeric forms of class IV Schiff base (4-hydrazone-5-pyrazolones).	12
Chart 10. Tautomeric forms of class V (4-thiosemicarbazone-5-pyrazolones) and class VI (4-semicarbazone-5-pyrazolones) Schiff bases.....	13
Chart 11. Structure of a generic acylpyrazolone (left); HQ^{Me} where the phenyl and methyl substituent are omitted (center) and $HQ^{Me,Me,Me}$ where every substituent is specified (right).	14
Chart 12. Structure of a generic Schiff base (left), HL^{R^3,R^4} where the phenyl and methyl substituent are omitted (center) and $HL^{Ph,Ph}$ where the methyl and phenyl moieties are omitted while the R3 (phenyl) and R4 (phenyl) substituents are specified.	15
Chart 13. Structure of $[Cu(Q^{Ph})_2]$ (a); $[Cu(Q)(PR_3)_2]$ (b); $[Cu(Q^{nPe})_2(H_2O)]$ (c), the dashed lines represent intermolecular interactions.	17
Chart 14. Left: structure of $CuNCS(Q^{Ph4Me})(N-N)$, where N-N = phen or bipy; Right: Structure of $Cu(Q)(N-N)(NO_3)$ where N-N = phen or bipy, R = H or CH_3 and $R^1 = CH_3$ or Napthayl.	19
Chart 15. Structure of $[Cu(Q^{tBu})(dpephos)]$ (left) and $[Cu(Q^{iPr})(dpephos)]$ (right). The coordination mode of the ligand depends on the different steric hindrance due to the acyl moiety.....	19
Chart 16. Molecular structure of complexes 1-6.....	20
Chart 17. Molecular structure of complexes 7-14.....	21
Chart 18. Molecular structure of complexes 15 and 16. The ligand to metal ratio is different due to the different aromatic spacer.....	22
Chart 19. Molecular structure of complexes 17-20. The coordination mode of complexes 19 and 20 varies only for the different donor atom, respectively O and S.....	23
Chart 20. Molecular structure of complexes 21-23.....	24
Chart 21. Molecular structure of $[Zn(Q^{Hb})_2(H_2O)]$ (left), $[Zn(Q^{Ph})_2(dmf)_2]$ (center) and $[Zn(Q^{Ph})_2]$ (right).	27
Chart 22. Molecular structure of $Zn(Q)_2(H_2O)_2$ (left), $Zn(Q)_2(H_2O)$ (center) and $Zn(Q^{Et})_2(phen)$ (right).	28
Chart 23. Molecular structure of $[Zn(Q^{He})_2(H_2O)]$ (left) and $[Zn(Q^H)(quinoline)]$ (right).	29
Chart 24. Molecular structure of complexes 24-26.....	31

Chart 25. Molecular structure of complexes 27-35.	32
Chart 26. Molecular structure of complexes 36 and 37.	33
Chart 27. Molecular structure of complexes 38-40.	34
Chart 28. Molecular structure of complex 41, [Zn(HMPM) ₄ Cl ₂].	34
Chart 29. Molecular structure of [MoO ₂ (Q ^{Et}) ₂] (left) and [MoO ₂ (Q ^{CCl₃})(Q ^{CCl₃*})] (right).	35
Chart 30. Molecular structure of MoO ₂ (Q ^R) ₂ (left) and [MoO ₂ (8-hq)(H ₂ O)] (right).	36
Chart 31. Molecular structure of complexes 42-48.	37
Chart 32. Molecular structures of complexes 49-60.	38
Chart 33. Synthetic procedure for H ₂ L ¹ – H ₂ L ⁵ proligands. In principle they can exist in two tautomeric forms I or II.	50
Chart 34. Tautomeric forms in the solid state of H ₂ L ¹ – H ₂ L ⁵ proligands with numbered atoms.	51
Chart 35. Synthetic procedure for the preparation of complexes 1-5.	58
Chart 36. Proposed chemical structures of complexes 1-5.	59
Chart 37. Tautomeric forms of proligands considered in the DFT study.	73
Chart 38. Synthesis procedure for proligands H ₂ L ¹ and H ₂ L ² from precursor HQ ^{Bn}	107
Chart 39. Solid-state structure of H ₂ L ¹ and H ₂ L ² with numbered C and N atoms.	108
Chart 40. Representation of tautomeric forms I and II of the two proligands.	125
Chart 41. Example of an overall DODH reaction, using PPh ₃ as reductant and a dioxomolybdenum(VI) complex with acylpyrazolonate ligands as catalyst ^[324]	145
Chart 42. Molecular structure of the two compounds considered for the energy calculations; (1) the simpler model [Mo(O) ₂ (Q ^{H,H,H}) ₂] and (2) the more complex [Mo(O) ₂ (Q ^{Me}) ₂].	147
Chart 43. Pathway A and pathway B of the catalytic cycle theoretically investigated.	148

List of abbreviations

Ac – Acetyl	EDX – Energy dispersive X-ray
ADP – Adenosine diphosphate	En – Ethylenediamine
B. cereus – Bacillus cereus	EPR – Electron paramagnetic resonance
Bipy – 2,2'-bipyridine	ESI-MS – Electron spray ionization mass spectroscopy
Bn – Benzyl	Et – Ethyl
br – Broad	Fur – 2-furyl
CDP – Cytidine diphosphate	GMP – Guanosine monophosphate
CLSM – Confocal laser scanning microscopy	haph – Hydroxyacetophenone
Cp – Cyclopentadienyl	HAT – Human Africa trypanosomiasis
CTP – Cytidine triphosphate	He – Hexyl
CTP – cytidine triphosphate	HL – Schiff base ligand
Cy – Cyclohexyl	Hmimt – 1-methylimidazolin-2-thione
d – Doublet	HMPM – 2-hydroxy-5-methylphenyl(1H-pyrazol-4-yl)methanone
dATP – Deoxyadenosine triphosphate	HOMO – Highest occupied molecular orbital
dCDP – Deoxycytidine diphosphate	HPLC – High performance liquid chromatography
DCF – 2',7'-dichlorofluorescein	HQ – Acyl pyrazolone ligand
DCFDA – 2',7'-dichlorofluorescein diacetate	ICAM-1 – Intercellular adhesion molecule 1
dCTP – Deoxycytidine triphosphate	iPr – iso-propyl
DFT – Density function theory	IR – Infrared spectroscopy
dGTP – Deoxyguanosine triphosphate	LMCT – Ligand-to-metal charge transfer
DMF – Dimethylformamide	m – medium (IR) <i>or</i> multiplet (NMR)
DMSO – Dimethyl sulfoxide	M. luteus – Micrococcus luteus
DNA – Deoxyribonucleic acid	M.p. – Melting point
dNTP – Deoxyribonucleotide triphosphate	MCF-7 – Michigan cancer foundation-7
DODH – Deoxydehydration	Me – Methyl
DON – 6-diazo-5-oxo-L-norleucine	MOs – Molecular orbitals
Dpephos – bis[2-(diphenylphosphino)-phenyl]ether	NADPH – Nicotinamide adenine dinucleotide phosphate
DSC – Differential scanning calorimetry	NDP – Nucleoside diphosphate
DTG – Differential thermogravimetry	NMR – Nuclear magnetic resonance
dTTP – Deoxymethymidine triphosphate	nPe – neo-pentyl
E. coli – Escherichia coli	NTP – Nucleoside triphosphate
EC ₅₀ – Half maximal effective concentration	

OEM – Original equipment manufacturer
Ph – Phenyl
Phen – 1,10-phenanthroline
PI – Propidium iodide
PPA – Polyphthalamide
PPO – Polyphenyloxide
Pr – Propyl
PS – Polystyrene
q – Quartet
ROS – Reactive oxygen species
s – singlet
S. aureus – Staphylococcus aureus
t – Triplet
T. brucei – Trypanosome brucei
tBu – tert-butyl
TD-DFT – Time-dependent DFT
TGA – Thermogravimetric analysis
OOT – Oxidation onset temperature
Thf – Tetrahydrofuran
thi – Thiophene
TLC – Thin layer chromatography
Tmeda – N,N,N',N'-tetramethylethylenediamine
Trime – N,N,N'-trimethylethylenediamine
UTP – Uridine triphosphate
vs – very strong
w – weak
WHO – World health organization

Part 1

CHAPTER 1.

General introduction and state-of-the-art.

1.1 Pyrazolone fragment and β -diketones

β -diketones are a class of molecules that arouse interest since the birth of coordination chemistry. From the first preparation of acetylacetonone by Claisen^[1] this class of molecules have been employed as a ligand for the synthesis of many metal complexes. After many years they are still utilized and much effort has been put into their functionalization in order to achieve ligands and complexes with finely tunable physical-chemical properties, such as thermal stability, luminescence or magnetic and electronic properties. Furtherly transition-metal derivates of these ligands show interesting catalytic features, with the β -diketones behaving as spectator donors.

In the meanwhile, another important scaffold that attracted great attention is pyrazolone. By now pyrazolone has become a well-known synthon for the preparation of a multitude types of molecules in particular for the fields of pharmaceutical chemistry, coordination chemistry and functionalized materials^[2] (but also in other research fields, see Figure 2), in fact, many biological active species in a wide-ranging spectrum of properties, e.g. anticancer, antioxidant, antibacterial etc., bear pyrazolone scaffolds in their structures^{[3]–[8]}. One important feature of the pyrazolone is that the hydrogen on the C4 carbon can be substituted with another moiety to implement another donor atom, thus affording a new class of chelating ligands that can be tailor-made to accomplish efficient coordination of a certain metal ion. One of the most employed precursors bearing a pyrazolone scaffold, also for the purpose of this thesis, is the edaravone (3-methyl-1-phenyl-5-pyrazolone, Chart 1). This molecule itself boasts relevant biological features^{[9]–[12]}. Both compounds are still deeply investigated resulting in a great number of publications issued every year (Figure 1).

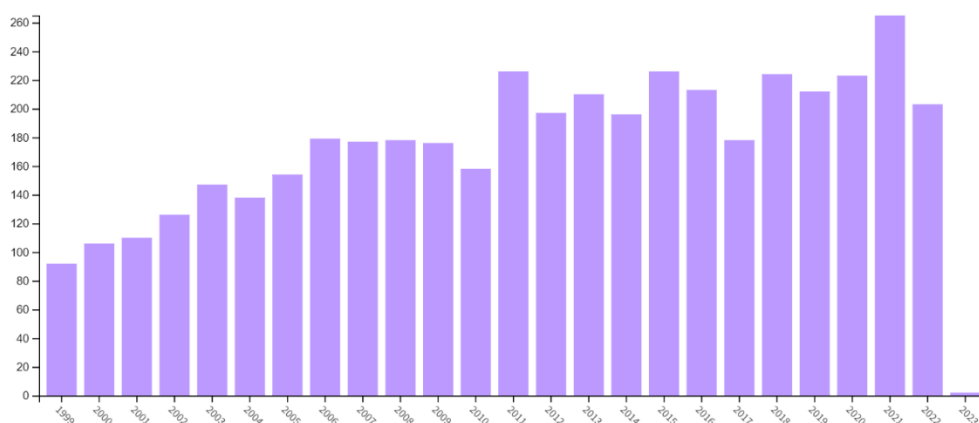


Figure 1. Number of publications per year using “ β -diketone OR acylpyrazolone” as query.



Figure 2. Research areas related to “ β -diketone OR acylpyrazolone”.

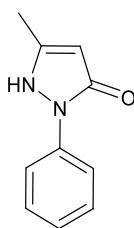


Chart 2. Structure of Edaravone (3-methyl-1-phenyl-5-pyrazolone).

1.2 Class of 4-acyl-5-pyrazolone

When the edaravone is reacted on the C4 carbon with an acyl moiety a novel family of enolizable ligands are obtained, named 4-acyl-5-pyrazolone, that displays the pyrazolone ring fused to another donor arm, thus affording a chelating ligand, first synthesized by Jensen in 1959^[13], combining the coordination properties of the diketones and the biological features due to the presence of the pyrazolone ring. In fact, in the next years, several papers appeared regarding the biological properties of acylpyrazolone^{[14]-[20]}.

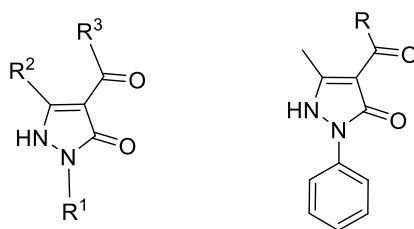


Chart 3. Generic structure of a 4-acyl-5-pyrazolone (left) and generic structure of an acylpyrazolone starting from edaravone (4-acyl-3-methyl-1-phenyl-5-pyrazolone).

1.2.1 Ligand synthesis

The most effortless way to obtain the 4-acyl-5-pyrazolone is through the reaction between the specific acyl chloride and the 1-phenyl-3-methylpyrazol-5-one (Chart 4), the latter obtained easily via condensation of phenylhydrazine and acetoacetate. The reaction proceeds through the acylation of the C4 carbon atom on the pyrazolone ring in basic environment (using calcium hydroxide) and utilizing refluxing thf or dioxane as solvent. Successive treatment with acid water affords the precipitation of the compound generally with high yields^{[13],[21],[22]}.

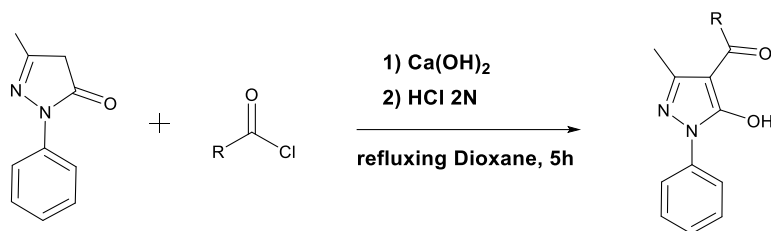


Chart 4. Synthetic procedure of a general 4-acyl-5-pyrazolone starting from 1-phenyl-3-methylpyrazol-5-one.

Different synthetic routes can be followed if the initial pyrazolone is not the 1-phenyl-3-methylpyrazol-5-one, in fact the general substituent R¹, R² and R³ (see Chart 3) can be changed in order to adjust the electronic and steric feature of the molecule. In the literature there are many example of studies where different groups apart from the phenyl moiety are employed in position R¹^{[23]–[26]}. Among them it is noteworthy the introduction of a pyridine ring, offering an additional donor atom and thus allowing a potential O₂,N₂-tetradentate ligand, with two couples of chelating moieties facing in opposite direction^[26]. In the same way and for the same purpose is possible to find acylpyrazolone bearing a different group than the methyl group in position R²^{[27],[28]}. Anyway, the most explored functionalization is the acyl substitution in R³. An enormous group of different

acyl chloride have been applied to provide a large number of acylpyrazolones with different and particular characteristics. The implementation of a heteroatom, aliphatic groups, aryl groups, bridging groups or combination of them can in fact results in ligands with very different structures and coordination features^{[29]-[43]}. Furthermore, another possible functionalization may be the substitution on the N2 atom, that is, the antipyrine. This class of molecules though will not be taken in consideration in this work, however exhaustive information about it can be found on the review by Raman *et al.*^[44].

1.2.2 Tautomerism

One important feature of this class of molecules is their different tautomeric forms. In fact, 4-acylpyrazolones can assume up to six tautomeric forms (Chart 5) and different studies have been reported about the interconversion from one form to another. For example, one paper describes the interconversion in solution between OH and NH forms, through an NMR study in which the molecules give rise to averaged sets of signals^[34]. Usually, the chelating forms A, B, E and F are more stable in non-polar solvents like CDCl₃, while in more polar solvents like DMSO a mixture of the NH and OH tautomers can be found. Single-crystal X-ray studies on the solid state have showed also that most stable tautomer can depend on the solvent of crystallization. For example in various works the ligand crystallizes from chloroform in the enol form B^{[45]-[51]}, while if recrystallized in polar solvent like methanol it assumes the amino diketonic form C, stabilized by a intermolecular N-H...O network^[36]. In some cases, the proligand can also be stable in an uncommon zwitterionic form^[52]. The tautomeric form that a proligand assumes is important because it can influence its mode of coordination and the way it crystallizes.

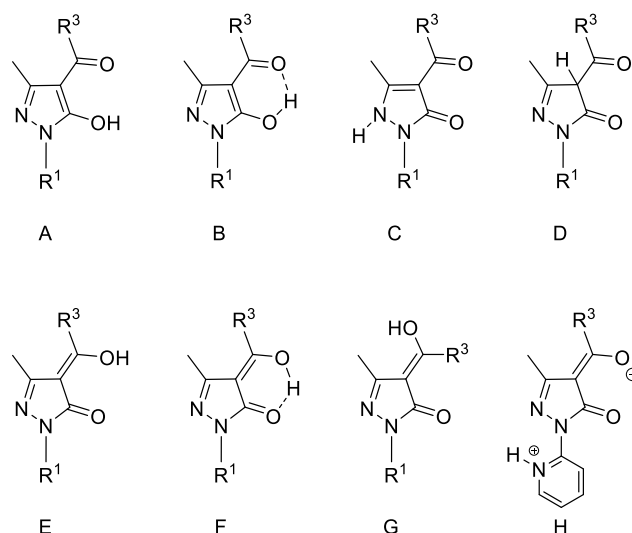


Chart 5. Scheme of the different tautomeric forms that a generic acylpyrazolone can assume.

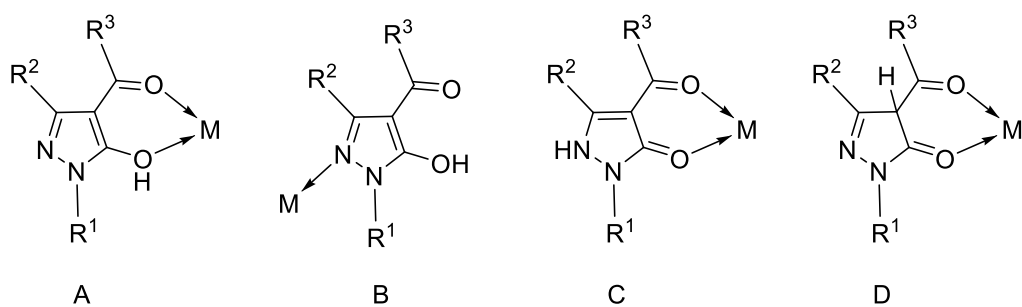
1.2.3 Modes of coordination

Acylpyrazolones display various modes of coordination depending on the most stable tautomeric form and on the ionic state. In the neutral form, the modes of coordination that the ligand can employ are four (Chart 6). The first mode is the O₂-bidentate chelating where the ligand is in its enolic form. The enolic H can be utilized in an intermolecular interaction as found in Uhlemann *et al.*^[53] with an external water molecule. In this tautomeric form the ligand can also coordinate a metal atom with the N2 atom on the pyrazole ring. In this case the enolic H is employed in an intramolecular hydrogen bonding^[54]. Considering the di-keto-amino form the neutral ligand can also use the O₂-chelating moiety to coordinate the metal and placing the proton on the N2 atom. An alternative to the latter mode has been observed in which the proligand in the O₂-diketo form chelates the metal, but the proton is located on the C4 atom of the ring.

When treated with a base like KOH or also reacted directly with M(CH₃COO)_n the proligand can be deprotonated and the number of different modes of coordination increases (Chart 6). In the anionic form the most common mode of coordination is the O₂-bidentate mode, in which the metal is chelated by the two oxygens of the ligand. However, the metal atom is not placed halfway between the oxygen due to the different donating power of the two carbonyl oxygen of the ligand, in fact two different M-O bond distances have been observed (Chart 6, E)^{[55],[56]}. In some derivatives of alkaline earth metal a tetradentate bridging η⁴-coordination mode has also been described (Chart 6, F)^{[57],[58]}. A monodentate O-coordination can also occur as reported by Mahon

et al.^[59] where the other oxygen and the nitrogen are involved in a intermolecular H-bonding network that stabilizes the geometry (Chart 6, G). The acylpyrazolonates can also utilize both the amino and ketonic moieties to act as a bridge between two metal centers, in a tridentate N,O,O-coordination mode (Chart 6, H)^{[60]–[62]}. In some other derivates this can also occur with the coordination of just one oxygen, thus a bridging bidentate N,O-coordination mode (Chart 6, I)^[62]. Another more unusual coordination mode where the ligand acts as a bridge has been reported by Pettinari *et al.*^[63], in which the Pb coordinated with a O₂-coordination mode interacts with the phenyl group of another molecules. When the phenyl in R¹ position is replaced by another substituent with an additional donor group, like the pyridine, further coordination modes become accessible. In fact, the ligand can coordinate the metal center in a N₂-chelating mode or also in a tridentate N,N,O- or tetradentate N,N,O,O- coordination mode bridging two metal atoms (Chart 6, K, L and M)^[64].

Coordination modes of the neutral ligand



Coordination modes of the deprotonated anionic ligand

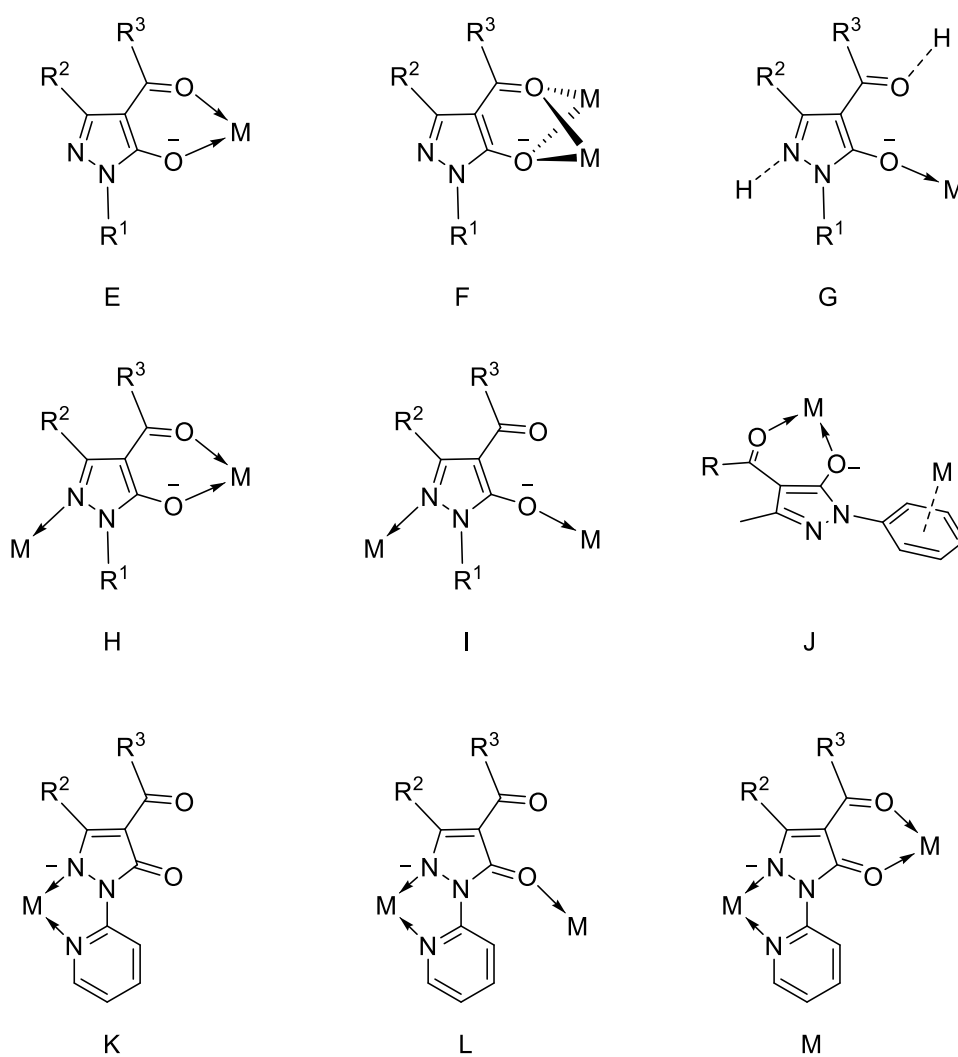


Chart 6. Different possible coordination modes of neutral and deprotonated acylpyrazolone ligands.

1.2.4 Biological properties

As stated before, acylpyrazolones are famous for a variety of applications. However, in the recent years they stand out mostly for their biological properties and pharmaceutical application, therefore here some of the recent works on this field will be reported. Most of the biological features are surely due to the pyrazole ring, in fact the precursor itself of the 4-acyl-5-pyrazolones, edaravone, displays some biological properties, like antipyretic and analgesic activity^{[65]–[70]}. About the 4-acyl-5-pyrazolones, they have been tested in the whole range of biological properties, from anti-inflammatory to antimicrobial and also anticancer. Moreover, some studies demonstrated the importance role of the acyl moiety at C4 through computational analysis^{[71]–[73]}, while another paper investigated the difference in the activity based on the tautomeric form that the molecule assumes^[74]. A different paper reports the anti-inflammatory properties of two ligands, while in a further work different ligands have been essayed as iron chelators, to be used in the treatment of iron excess in hereditary iron overload disease or in acute iron intoxication^[75]. Several works reported the antimicrobial activity of the ligands against different human pathogenic bacteria like *Bacillus subtilis*, *Escherichia coli*, *Staphylococcus epidermis*, *Staphylococcus aureus* and *Pseudomonas aeruginosa*. While some ligands showed potent activity, other resulted totally inactive against all strains^{[76]–[78]}. One more paper essayed the fungicidal and insecticidal activities of some acylpyrazolones showing that they are active against many strains, but ineffective against a few others^[79]. Finally, there are a limited set of works regarding the anticancer activity of the 4-acylpyrazolone, reporting a moderate-to-low or totally ineffective activity^{[80],[81]}.

1.3 Class of Schiff Bases

We have already seen how 4-acyl-5-pyrazolones can be modified by choosing a different acyl chloride to change the acyl moiety. However, any acylpyrazolone can be furtherly modified by a condensation reaction on the carbonyl of the acyl group. One typical reaction consists in the formation of the Schiff bases. By definition Schiff bases are compounds with general structure $R^1R^2C=NR^3$ where R^3 is an alkyl or aryl group. Often this type of compounds bear an extended conjugated system and in fact there are many reports about their optical properties and consequently applications like photochromic materials, optical switches, fluorescent probes for metal ions or doping agent^{[82]–[91]}. In particular, when using the 4-acyl-5-pyrazolone as starting material we obtain pyrazolone-based Schiff bases with a N,O-chelating ability. In this way all the

advantages and properties of the 4-acylpyrazolone are retained in the final compounds. In fact, in the literature it is possible to find many papers regarding the properties of this class of ligands and their relative metal complexes as well as their applications as anticancer^{[92]–[95]}, antimicrobial agents^{[96]–[99]}, catalyst^{[100]–[102]} and optical devices or dyes^{[103]–[111]}.

Following the same line stated before, in this work we will focus on the Schiff bases prepared starting from 1-phenyl-3-methylpyrazol-5-one reacted with the wanted acyl chloride. In this way we will obtain compounds where the azomethine C=N-R fragment is on the position C4 of the pyrazole ring and the N2 atom unsubstituted.

1.3.1 Classes and synthesis

Synthesizing a pyrazolone-based Schiff base it is possible to obtain various types of ligands. To make things clear it is useful to divide the “pyrazolone-based ligand” family into six sub-classes, following the classification proposed by Casas^[112], as illustrated in Chart 7. The general route involves the condensation reaction between the 4-acylpyrazolone with the hydrazine of choice (Chart 8). The nature of the hydrazine determines the sub-class of the final compound.

- Class (I). 4-aminoalkylidene-5-pyrazolones, also called β -ketoamine, are prepared reacting the acylpyrazolone with a substituted amine^{[113],[114]}.
- Class (II). 4-acylhydrazone-5-pyrazolones, prepared using acylhydrazones as reactant^{[115],[116]}.
- Class (III). 4-diazo-5-pyrazolones, obtained using a diazonium salt^[117].
- Class (IV). 4-hydrazone-5-pyrazolones, synthesized using an alkylhydrazone or an arylhydrazone^[118].
- Class (V). 4-thiosemicarbazone-5-pyrazolones, prepared via condensation with an alkylthiosemicarbazide or arylthiosemicarbazide^[97].
- Class (VI). 4-semicarbazone-5-pyrazolones, obtained via condensation with an alkylsemicarbazide or arylsemicarbazide^[119].

As we shall see later, class I and class IV, that is, 4-aminoalkylidenes and 4-hydrazones are the two most investigated classes, with many papers regarding their synthesis and properties. The other classes have been less explored up to now.

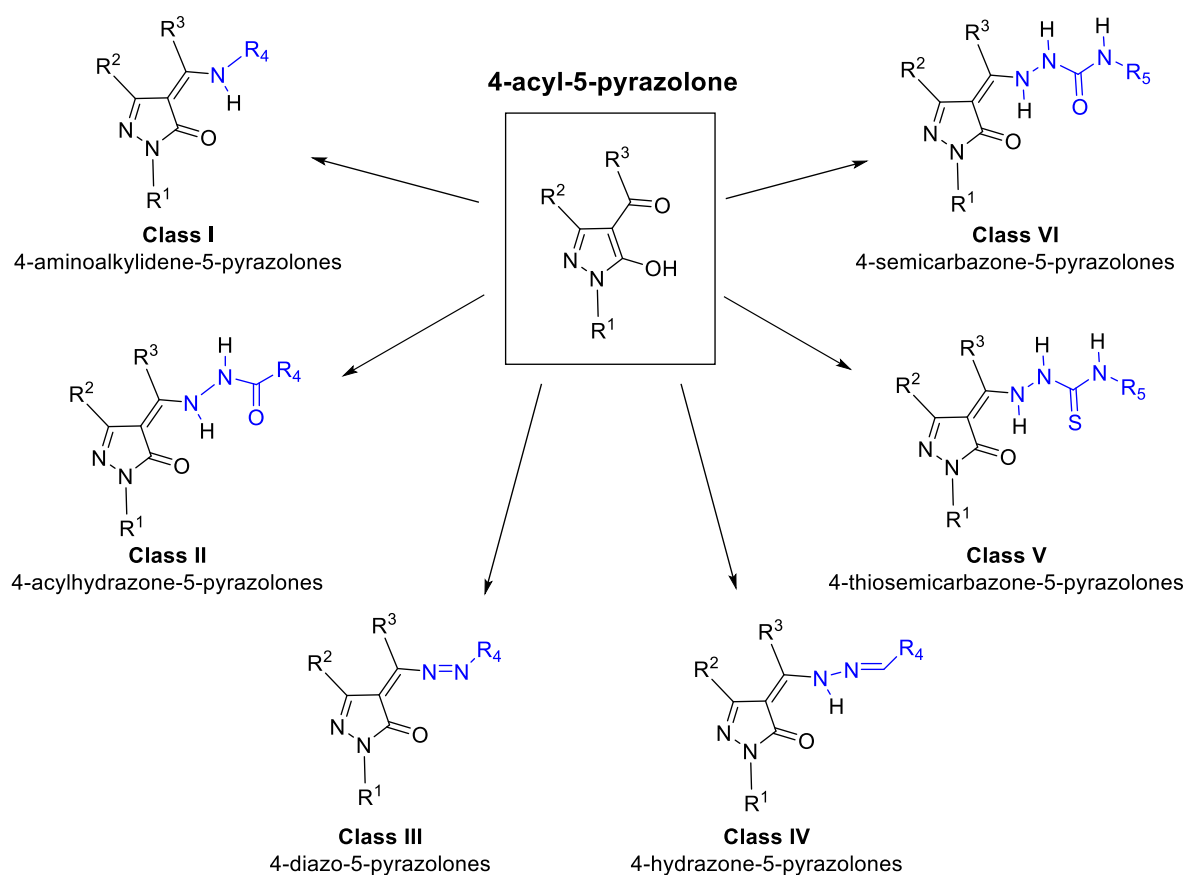


Chart 7. Classes of Schiff bases starting from 4-acyl-5-hydrazone synthon.

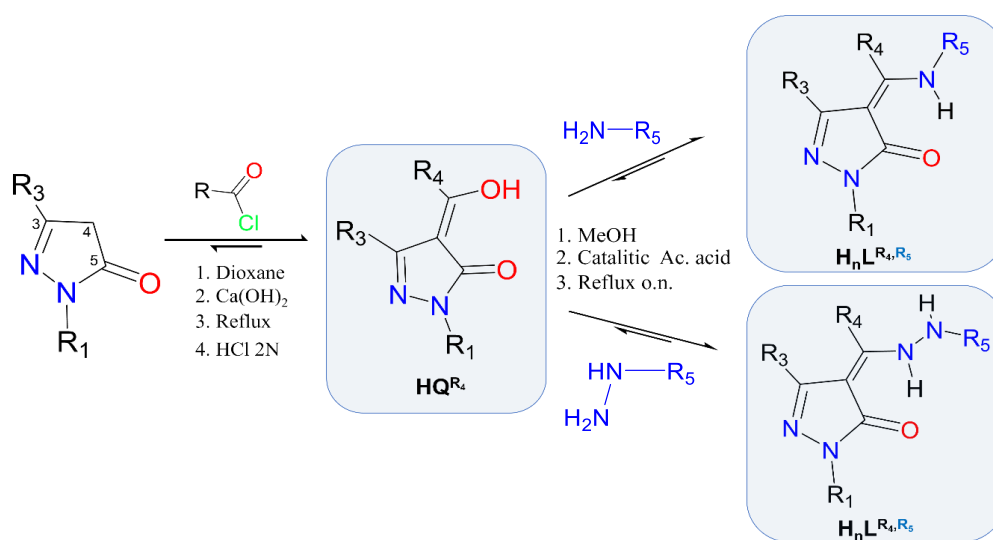


Chart 8. General synthetic route starting from a substituted pyrazol-5-one leading to the relative 4-acyl-5-pyrazolone and finally to the corresponding Class I or Class IV Schiff base.

1.3.2 Tautomerism

It's plain to expect that as implementing an additional moiety to a 4-acylpyrazolone, also the number of possible tautomers will increase. Compounds belonging to class I (4-aminoalkylidene-5-pyrazolones) still present only four tautomeric forms (Chart 9), in detail: imine-ol (A), imine-one (B and C), amine-one (D). The latter form (D) was proved to be the most stable in the solid state by many X-ray diffraction studies^{[93],[94],[98]}. Additional studies demonstrated that this form is also preferred in solution^[120] and in gas phase, thanks to DFT studies that also confirm that the D form is both kinetically and thermodynamically favorable^[121]. Class II and Class III have been much less explored. The few papers that dealt with this two classes reported that the most stable form in the solid state is the keto form^{[122]–[126]}.

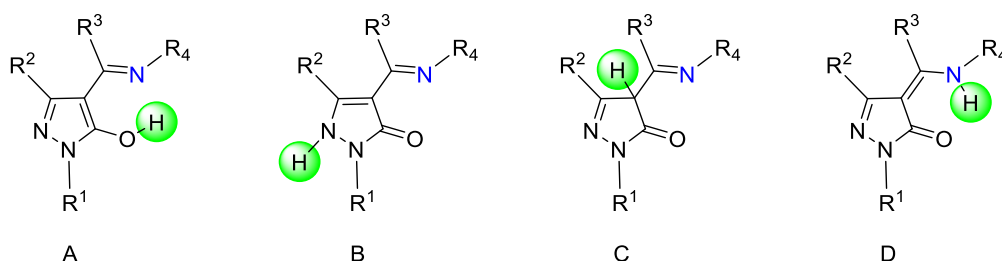


Chart 9. Tautomeric forms of class I Schiff base (4-aminoalkylidene-5-pyrazolone).

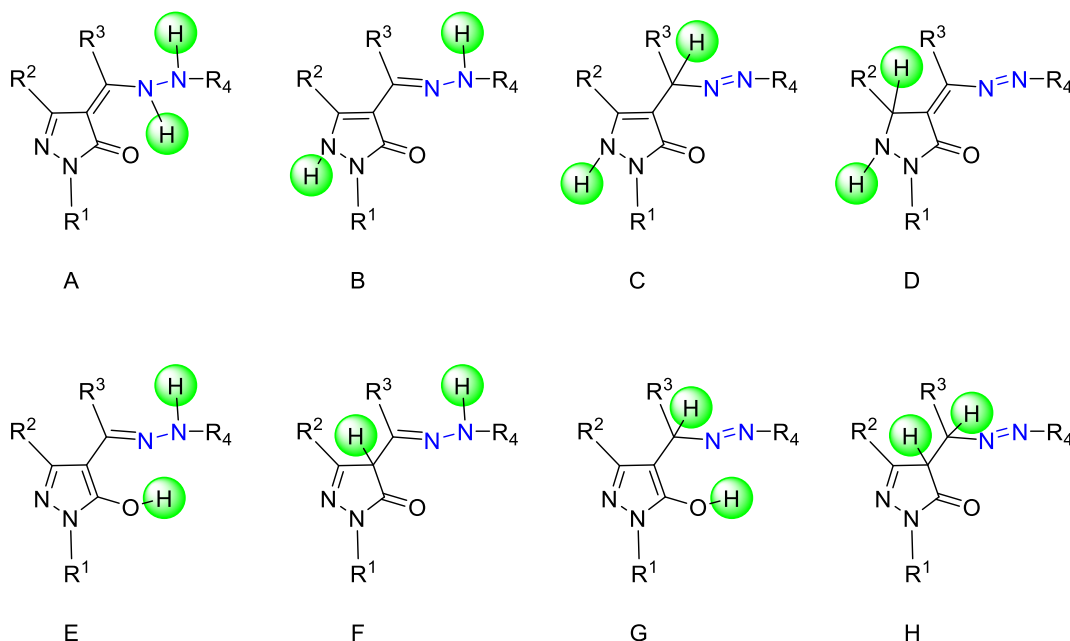


Chart 10. Tautomeric forms of class IV Schiff base (4-hydrazone-5-pyrazolones).

The presence of two acidic hydrogen atoms in class IV, 4-hydrazone-5-pyrazolones, allows these molecules to assume up to eight tautomeric form (Chart 10). Also in this case a general preference for the keto-amine form (A) has been found^{[127]–[131]}, even if sometimes other forms have been found to be preferred, like the keto-imine form^[132]. Curiously, some papers reported also that an uncommon zwitterionic form can be isolated and it is stable in the solid state^{[118],[133]}. In solution, combined studies of DFT calculations and NMR analysis confirmed the imino-ol (E) form to be prevalent. Class V and Class VI also exhibit more than one acidic hydrogens leading to several tautomeric forms (Chart 11). It has been demonstrated that in the solid state the keto form (F) is observed^{[127],[134]–[136]} for Class V, even if examples of structural studies of other forms can be found^{[89],[137],[138]}. About the molecules belonging to Class VI, much less investigation has been carried out regarding their structural features. The few papers present in the literature suggest that they mainly adopt the enol tautomeric form (J)^{[139]–[141]}.

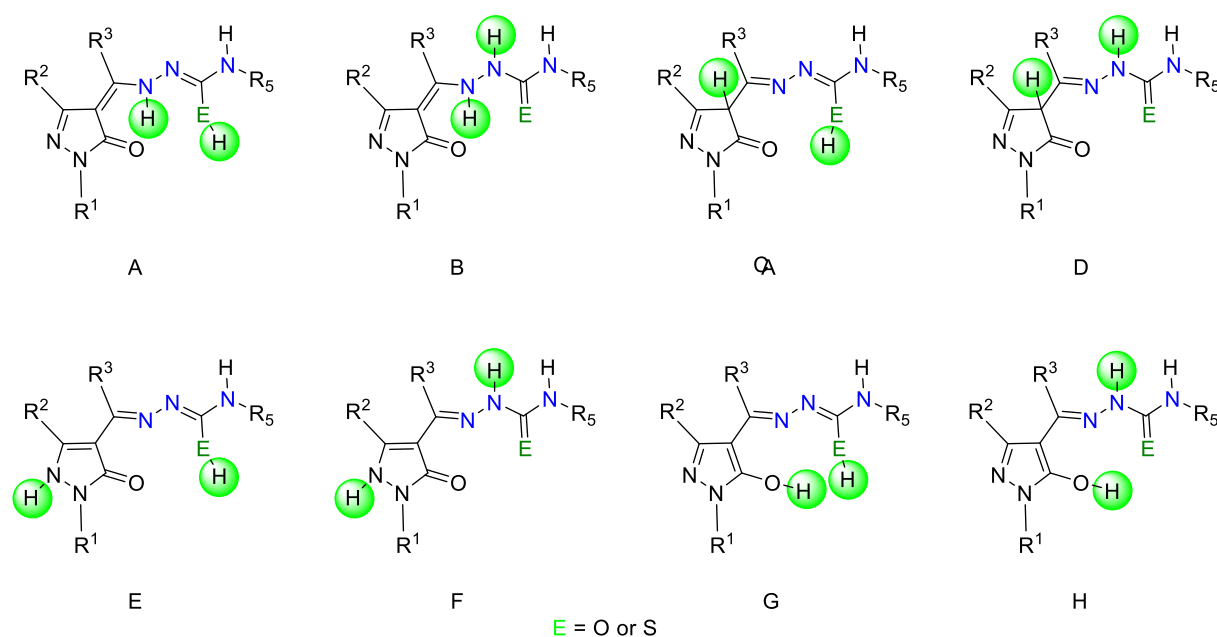


Chart 11. Tautomeric forms of class V (4-thiosemicarbazone-5-pyrazolones) and class VI (4-semicarbazone-5-pyrazolones) Schiff bases.

1.4 Nomenclature

To keep things simple, in the literature a symbolism has caught on for referring to this class of molecules. In this work this same symbolism will be used. HQ^{R^1,R^2,R^3} indicates the most general

acylpyrazolone, where R^1 , R^2 , and R^3 are the three substituents indicated in Chart 12. Usually when $R^1 = \text{phenyl}$ and $R^2 = \text{methyl}$ they are omitted, thus only the substituent on the acyl moiety, R^3 , is specified. For example, HQ^{Me} denotes an acylpyrazolone where $R^1 = \text{Ph}$; $R^2 = \text{Me}$ and $R^3 = \text{Me}$, so *4-acetyl-5-methyl-2-phenyl-3-pyrazolone*. When the acylpyrazolone is deprotonated, the H is removed, like in Q^{Me} . If the R^1 and R^2 groups are not the phenyl and methyl substituents they have to be specified. $\text{HQ}^{\text{Me,Me,Me}}$ for example represents an acylpyrazolone where all the three substituent are methyl groups.

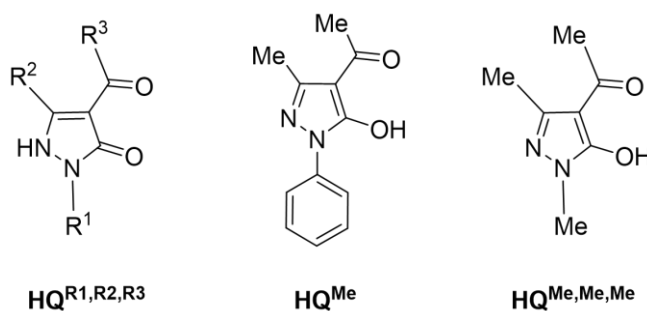


Chart 12. Structure of a generic acylpyrazolone (left); HQ^{Me} where the phenyl and methyl substituent are omitted (center) and $\text{HQ}^{\text{Me,Me,Me}}$ where every substituent is specified (right).

A similar set of rules applies for the symbolism used for Schiff's bases. The general abbreviation is $\text{H}_n\text{L}^{\text{R}1,\text{R}2,\text{R}3,\text{R}4}$ (Chart 13): the letter n indicates the number of acidic hydrogens capable of undergo deprotonation. R^1 and R^2 like for the acylpyrazolone are omitted if they represent the phenyl and methyl substituents on pyrazole ring. R^3 is the substituents on the ex-acyl moiety while R^4 is the substituent due to the new amino moiety. It is important to note that this symbolism does not specify the class of Schiff bases, so that $\text{HL}^{\text{R}4,\text{R}5}$ could represent in the same way a 4-aminoalkylidene-5-pyrazolone or a 4-diazo-5-pyrazolone bearing the same substituents. This should be clarified at the beginning of the work to avoid misunderstanding.

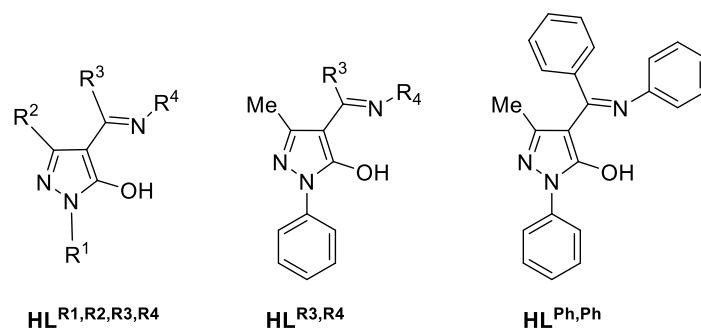


Chart 13. Structure of a generic Schiff base (left), $\text{HL}^{R3,R4}$ where the phenyl and methyl substituent are omitted (center) and $\text{HL}^{\text{Ph,Ph}}$ where the methyl and phenyl moieties are omitted while the R3 (phenyl) and R4 (phenyl) substituents are specified.

1.5 Coordination Chemistry of Transition Metals

Among all the blocks of the periodic table, transition metals are classically the ones on which there is significant and sustained focus in the field of coordination chemistry. In particular, the first row of the d-block is the center of attention because it contains the lighter and usually more abundant and accessible elements of this block. This focus is justified by the fact the d-block elements exhibit stable oxidation states where the nd shell remains partially filled. This characteristic behavior is what confers them their chemical and physical properties. Metal ions that belong to this block readily undergo oxidation or reduction thus offering different chemistry even for the same element as a result of the differing d electrons present in the different oxidation states, which must be considered separately.

Furthermore, d-block elements exhibit a significant distinction among the first row, particularly, the second row and the third row. Lighter d-block elements tend to prefer O-, N- or halide ion donor groups, while heavier atoms lean towards coordination by ligands containing heavier p-block elements such as S- and P-donors. Higher oxidation states are much more stable for 4d and 5d series than for the 3d series. For example, the II and III oxidation states are of a major importance in the 3d series, but they are irrelevant for the 4d and 5d series. In contrast, the 4d and 5d rows are more likely to exhibit metal-metal bonding and, as a result, polynuclear compounds are more prevalent for metals of these two rows.

In this chapter, we will examine the most interesting state of the art of pyrazolone-based complexes of copper, zinc and molybdenum, that are the three metals which the future chapters will concentrate on. The research will primarily focus on the properties of interest. More extensive and inclusive reviews on the argument can be found in the literature^{[142]–[144]}.

1.5.1 Complexes of Cu

Copper is one of the most abundant elements in earth's crust and also an essential trace element nutritionally, being among the most abundant metals in human body, although it can be toxic in large quantities. Copper shows a rich coordination chemistry, primarily in the monovalent (+1) and divalent (+2) oxidation states. Compounds of copper have been used extensively in a wide range of applications, including as catalysts, fungicides, pesticides and also pigments. Copper complexes are known in oxidation states ranging from 0 to +4, although the +2 and +1 oxidation are by far the most common, with the divalent state predominating. The coordination numbers and geometries of copper complexes vary with oxidation state. For the spherically symmetric Cu^{I} d^{10} ion, the common geometries are two-coordinated linear, three-coordinate trigonal planar and four-coordinate tetrahedral, although some distortion from ideal geometries are observed particularly with chelating ligands. Cu^{I} compounds are diamagnetic and colourless. The Cu^{II} ion with d^9 configuration is commonly found in a tetragonal coordination environment although four-coordinate tetrahedral and planar complexes are also known. Additionally, five-coordinate trigonal bipyramidal and square-planar complexes have been reported, as well as a small number of three-, seven-, and eight-coordinate complexes. Most of the Cu^{II} compounds are blue or green in colour because of the d-d absorption in the 600-900nm region, with exception for compounds exhibiting charge-transfer bands. Cu^{I} ion is classified as a soft acid. Its preference for softer ligands is quite apparent in the homoleptic complexes, for instance the halides. The Cu^{II} ion is smaller and harder than the Cu^{I} ion, thus it interacts more strongly with water molecules and it is more stable in aqueous solutions. In fact, Cu^{II} ion is classified as a borderline hard acid, thus its coordination chemistry is dominated by nitrogen- and oxygen-donating ligands, followed by chloride- and sulfur-containing species^[145].

The coordination chemistry of copper with pyrazolone-based ligands are one of the most extended. Since the first report on copper acylpyrazolonate in the compound $[\text{Cu}(\text{Q}^{\text{Ph}})_2]$ (Chart 14) by Caruso *et al.*^[146], many other derivatives have been synthesized and reported, like the compounds $[\text{Cu}(\text{Q})_2(\text{H}_2\text{O})_2]$ where $\text{Q} = \text{Q}^{\text{Me}}, \text{Q}^{\text{Ph}}$ and Q^{CF_3} ^{[147],[148]}. A study by Uzoukwu *et al.*^[149] investigated the effect of the variable chain length on the 4-acyl moiety using $\text{Q}^{\text{Ph}}, \text{Q}^{\text{Me}}, \text{Q}^{\text{Et}}, \text{Q}^{\text{Pr}}, \text{Q}^{\text{Bu}}, \text{Q}^{\text{Hp}}$ as ligands. They showed bathochromic shift of the Q absorption upon coordination. Also the stability of the C=O bond decreases while the Cu-O bond increases as the chain on the substituents in Q grows in length. The compounds $[\text{Cu}(\text{Q}^{\text{Ph}})_2]$ and $[\text{Cu}(\text{Q}^{\text{Ph}})_2(\text{MeOH})_2]$ have been structurally characterized. The first one shows a distorted square-planar geometry, whereas the geometry of

the second one is distorted octahedral with the methanol in the axial positions^[150]. Studies on a large number of complexes of the $[\text{Cu}(\text{Q})_2]$ and $[\text{Cu}(\text{Q})_2(\text{L})]$ type, where $\text{L} = \text{bipy}$ or phen , have been reported and demonstrated that the additional donor atoms present on the heterocycle on the acyl moiety of the ligands Q^{thi} and Q^{fur} has essentially no effect on the structure of the complexes, the coordination happens through always both carbonyl arms of the ligands^{[151]–[153]}. The same studies investigated also the reactivity of the complexes towards an excess of PR_3 , observing the reduction of $\text{Cu}(\text{II})$ to $\text{Cu}(\text{I})$ and obtaining a series of $[\text{Cu}(\text{Q})(\text{PR}_3)_2]$ (Chart 14) compounds. They showed a distorted tetrahedral coordination where the distortion increases as the steric hindrance in 4-acyl moiety of Q and mainly in phosphine substituent increases. A study about the volatility of these compounds showed they are volatile in a narrow range of temperature^[154], while studies on thermal decomposition demonstrated that the melting points decrease linearly by increasing the molecular weight of the complexes. Compound $[\text{Cu}(\text{Q}^{\text{nPe}})_2(\text{H}_2\text{O})]$ (Chart 14) have been investigated showing a square-pyramidal structure with the two hydrogen of the apical water involved in an intermolecular H-bonding network with pyridinic hydrogen atoms of two vicinal complexes^[155]. Dinuclear mixed-ligand complexes of formula $[\text{Cu}(\text{haph})_2(\text{HQ})_2]$ have been obtained by reaction between the metal precursor and ligands $\text{HQ} = \text{HQ}^{\text{Ph}}, \text{HQ}^{\text{Me}}, \text{HQ}^{\text{Et}}, \text{HQ}^{\text{Pr}}$. The geometries proposed are octahedral with the HQ acting as neutral bridging bidentate donor ligands. Tetradentate ligands H_2QnQ have been used to attain different $\text{Cu}(\text{II})$ complexes whose stoichiometry and structure are affected by the polymethylene chain length n . For $n = 1-7$ the complexes are dimeric species, while for greater values the complexes are monomeric^[156].

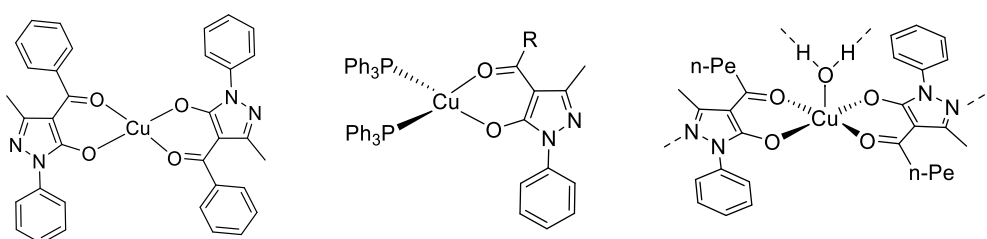


Chart 14. Structure of $[\text{Cu}(\text{Q}^{\text{Ph}})_2]$ (left); $[\text{Cu}(\text{Q})(\text{PR}_3)_2]$ (center); $[\text{Cu}(\text{Q}^{\text{nPe}})_2(\text{H}_2\text{O})]$ (right), the dashed lines represent intermolecular interactions.

Various complexes of formula $\text{Cu}(\text{Q})_2$ have been synthesized and showed the expected square planar geometry with the ligand in anti-configuration. These compounds proved to have an antibacterial activity against a Gram positive strain, but not to the Gram negative^[157]. A series of mixed ligand complexes of type $\text{CuNCS}(\text{Q}^{\text{Ph4Me}})(\text{N-N})$ with $\text{N-N} = \text{phen}$ or bipy (Chart 15) showed

square-pyramidal geometries and the capacity to interact with calf thymus DNA through intercalation. Additionally, they are cytotoxic against human lung cancerous cell line (A549)^[158]. A complex synthesized by Bochkarev *et al.*, [Cu(Q^{iPr})(dpephos)] (Chart 16), revealed a classical tetrahedral structure with O,O-chelating Q^{iPr} and P,P-chelating dpephos, while the complex [Cu(Q^{tBu})(dpephos)] (Chart 16) contains an unexpected three coordinate copper atom with a η^1 -coordination of HQ^{tBu} through the N atom of the pyrazole ring^[159]. The complexes show also a dual emission and they are capable to generate electroluminescence of yellow-orange colours. Complexes of copper(I) Cu(Q)(PPh₃)₂ with different ligands showed a tetrahedral copper environments and fluxionality in chloroform where they dissociate into Cu(Q)(PPh₃) fragments and free PPh₃^[48]. Copper complexes of 4-acetyl-1-aryl-3-methylpyrazole-5-ones have been synthesized and tested as potential antibacterial and antifungal agents. The complexes were found to possess effective antibacterial activity against Gram-positive and Gram-negative bacteria. Also the antifungal activity was very close to the standard antifungal drugs^[160]. A series of pyrazolone based mixed-ligand Cu(II) complexes were synthesized and characterized. The crystallographic data show that the Cu(II) ion is pentacoordinated by three nitrogens (one from a thiocyanate and two from 2,2'-bipyridyl) and two oxygen donors from the chelating ligand. Two complexes exhibited a square-planar geometry while the third one showed a slightly distorted square-planar structure. The free ligands and the three Cu(II) complexes have been tested for their DNA binding, finding out that the compounds bind to CT-DNA via intercalation and the binding affinity increases in Cu(II) complexes. In addition, the synthesized metal complexes exhibit anti-cancer activities altering the Mitochondrial Membrane Potential causing mitochondrial dysfunction^[161]. Another series of transition metal complexes of 4-acetyl-3-methyl-1-phenyl-2-pyrazoline-5-one has been characterized and tested as catalyst for epoxidation of cyclooctene. The highest catalytic activity was found for Cu(II) complex at the optimized condition, also with very high selectivity for epoxide product^[162]. In another research novel bidentate 4-aryl-5-pyrazolone ligands were synthesized and reacted with copper(II) in a 1:2 metal to ligand ratio. The resulting complexes are mononuclear and the proposed geometry distorted square-planar, even if no crystallographic data were obtained^[163]. In a different study a mixed-ligand Cu(II) complex of formula [Cu(Q)(bipy)(OH₂)]ClO₄ was synthesized and its battery-like behavior tested. The complex demonstrated excellent activity and a high capacity for three-electrode construction^[164]. Four Cu(II) mixed ligand complexes of formula [Cu(Q)(N-N)(NO₃)], where N-N = phen or bipy (Chart 15), have been reported by Jadeja *et al.* The ligands are coordinated in a bidentate manner and Cu ion in the complexes is penta-coordinated by two nitrogen atoms and the oxygen donors. The

compounds were screened for anti-cancer activities towards human lung carcinoma (A549) and human lung epithelial cells (L132) obtaining encouraging results^[165]. Lastly, a study reported the synthesis of a pyrazolone-based ligand, isolated in the NH amino diketone form. The relative Cu(II) complex was crystallized and the structure observed via XRD, presenting a distorted square planar coordination geometry with two chelating ligand molecules^[166].

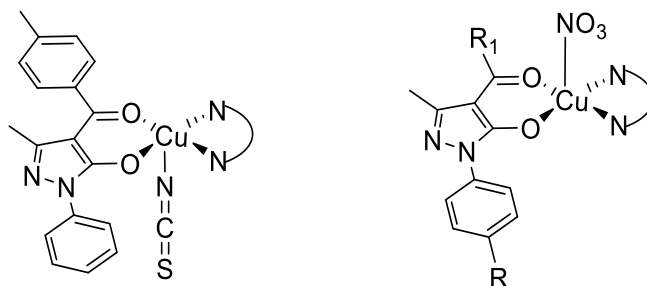


Chart 15. Left: structure of $\text{CuNCS}(Q^{\text{PhMe}})(N-N)$, where $N-N = \text{phen or bipy}$; Right: Structure of $\text{Cu}(Q)(N-N)(\text{NO}_3)$ where $N-N = \text{phen or bipy}$, $R = \text{H or CH}_3$ and $R^1 = \text{CH}_3 \text{ or Naphthyl}$.

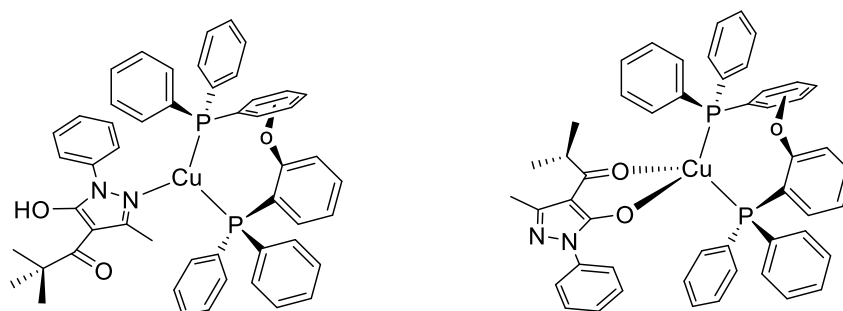


Chart 16. Structure of $[\text{Cu}(Q^{\text{Bu}})(\text{dpephos})]$ (left) and $[\text{Cu}(Q^{\text{Pr}})(\text{dpephos})]$ (right). The coordination mode of the ligand depends on the different steric hindrance due to the acyl moiety.

Also for what concern the Schiff bases, copper is one of the most explored metals. Several complexes with generic formula of $\text{CuL}\cdot n\text{H}_2\text{O}$ and $\text{Cu}_2\text{L}\cdot 6\text{H}_2\text{O}$ have been prepared and the suggested geometry is tetrahedral^[167], while other complexes (**1-4**, Chart 17) showed square planar environments. The structure of complex **5** was resolved revealing a pseudo-tetrahedral geometry. This compound showed an intense absorption in the red region of the spectrum due to ligand-to-metal charge transfer transition^[168]. Complexes prepared using ligands with bulky substituents display distorted tetrahedral geometries due to Jahn-Teller effect^[169]. Complex of Cu(II) and 4-aminoalkylidene-5-pyrazolone, **6**, has been reacted with excess of triphenylphosphine affording a

reduction of the copper center to Cu(I) in a tetrahedral environment with the chelating Schiff base and two PPh_3 ^[152]. The hydrate complex **7** shows a square pyramidal geometry^[170]. Octahedral dihydrate complexes have also been reported with two molecules of water at the axial position^[171]. A complex of Cu(II) with a Schiff base bearing a long aliphatic chain on N1 atom of pyrazole was synthesized and characterized showing it exists in square planar structure^{[172]–[174]}. Complex **8** instead has been shown to exist in a distorted square planar geometry and displayed a moderate catalytic activity. The same group reported the synthesis of other complexes, **9–12**, and the study on the relationship between their structure and the catalytic efficiency: the presence of bulky and/or electron withdrawing substituents in N-R position favor higher activities^{[175],[176]}.

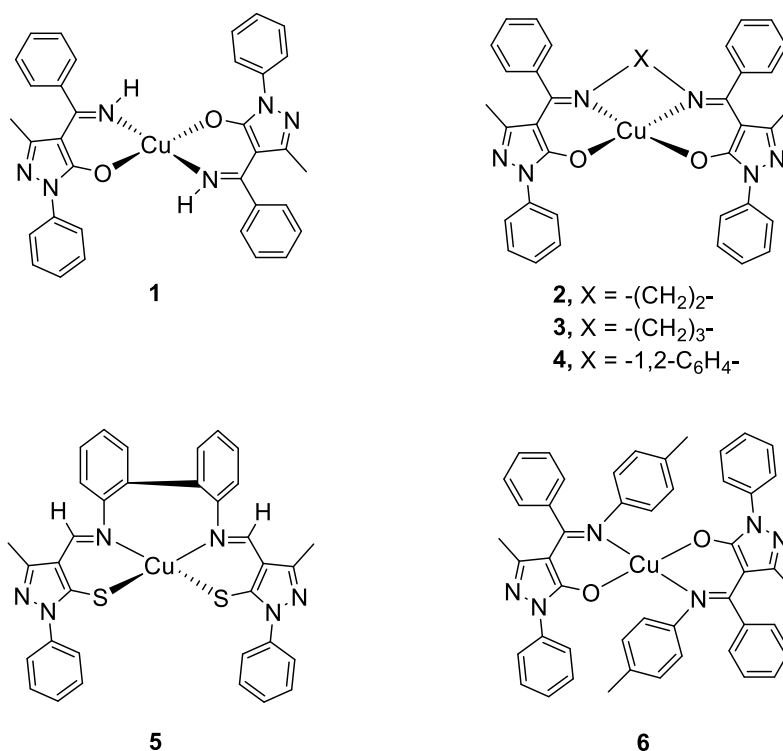


Chart 17. Molecular structure of complexes 1-6.

Other octahedral dihydrate complexes synthesized by Thakar *et al.* show moderate antibacterial activity^[177]. Also octahedral complexes **13** and **14** with tridentate Schiff base donors showed a moderate antibacterial activity and antifungal activity^[99]. In the same way other complexes reported by Sunitha *et al.* proved an antibacterial and antifungal activity, but only the complexes showed the antibacterial behavior, the free ligands being not active at all^[178]. Two complexes, **15** and **16**, were synthesized with different metal-to-ligand ratio, respectively 1:1 and 1:2, due to a

different aromatic spacer in the ligand. The complexes have then been tested as copper extractors from an aqueous phase to non-aqueous phase with the ligands^[179]. The complex prepared by Cheng *et al.* displays a octahedral environment bearing a tridentate Schiff base ligand, a bidentate nitrate and a molecule of water. It showed scavenging activity against hydroxyl radical and cytotoxicity^[180]. A series of complexes prepared using neutral ligands displays a octahedral geometry with the chloride in trans position and the chelating ligands in the equatorial plane^[181].

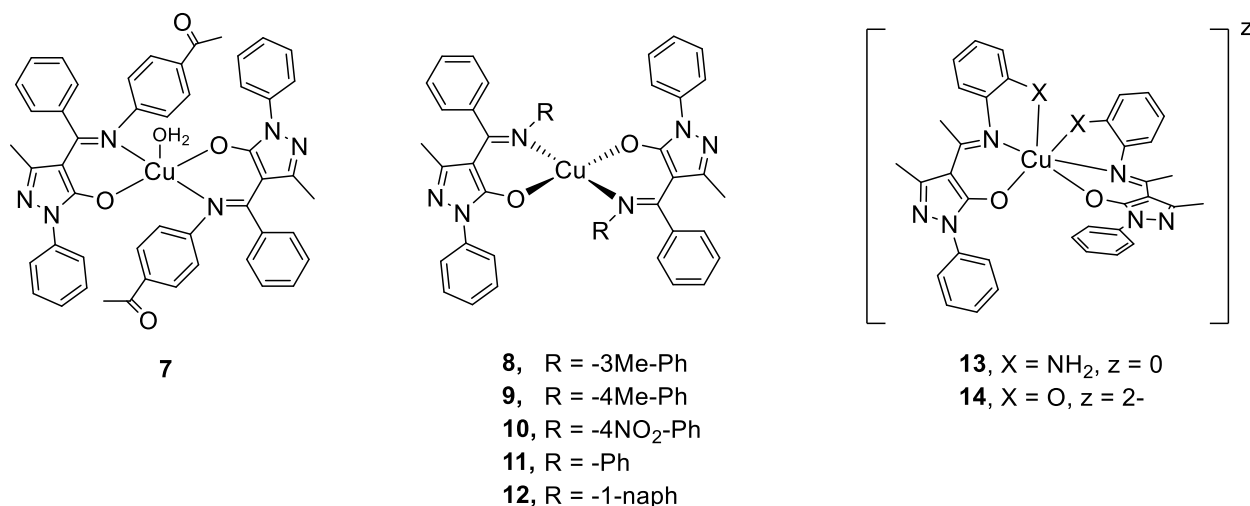


Chart 18. Molecular structure of complexes 7-14.

A series of different complexes of copper are reported to possess antibacterial activity^[182]. A mixed-ligand complex bearing a tridentate 4-acylhydrazone-5-pyrazolone and a bidentate bipy was shown to exist in a trigonal bipyramidal geometry^[183]. Complex **17** has shown antimicrobial activity inhibiting the growth of gram-positive *B. cereus*, *M. luteus* and *S. aureus*. It also displayed cytotoxic activity^[184]. Other Cu(II) 4-acylhydrazone-5-pyrazolone complexes have also shown a cytotoxicity against cervical cancer HeLa cell. They are reported to exist in square pyramidal geometry^[116]. The thermal behavior of the square planar complex **18** have been investigated: the decomposition occurs through the loss of pyridine molecule followed by the decomposition of the anionic ligand and formation of copper(II) oxide residue^[185]. A series of diaquo copper(II) complexes was synthesized by Kandil, containing Schiff bases bearing an azidosulfo substituent. They were characterized analytically and spectrally and showed octahedral structures^[186]. Complexes of copper(II) were synthesized using 4-diazo-5-pyrazolone ligands containing a pyridine or antipyrine moiety. The first was found to have a polynuclear nature where each ligand

act as bridge between two six-coordinated Cu atoms in a distorted octahedral environment. The latter instead are mononuclear with a square planar geometry completed by a chloride^[187].

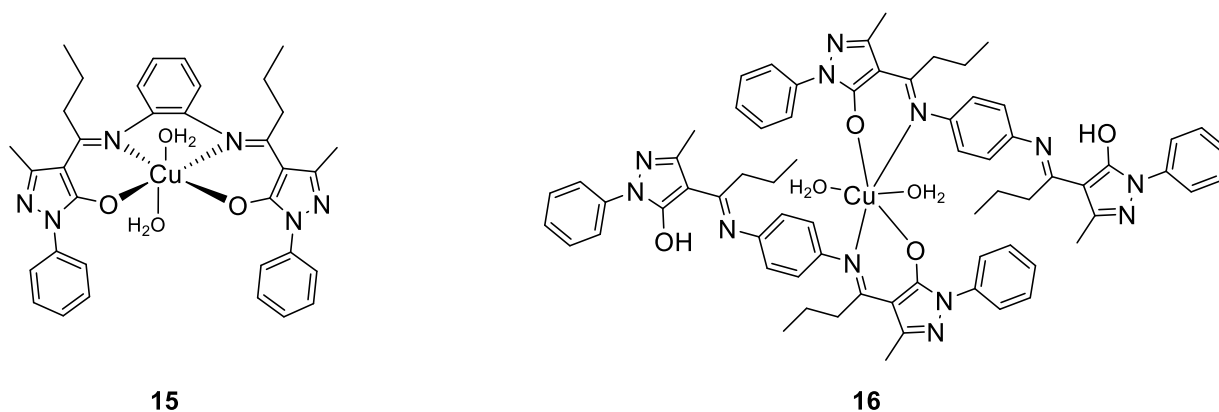


Chart 19. Molecular structure of complexes 15 and 16. The ligand to metal ratio is different due to the different aromatic spacer.

Two complexes, **19** and **20**, of copper(II) were synthesized by Koval'chukova *et al.* using two similar 4-diazo-5-pyrazolone ligands, one bearing a oxygen whereas the other a sulfur atom on the C3 position. Despite the similarity they show different coordination environments: the O,N-bidentate displays a pseudo-octahedral CuN_4O_2 core while the S,N-bidentate complex exists in a square pyramidal CuN_3S_2 geometry^[188]. Abdel-Latif's research group studied the electronic structure and nonlinear optical parameter of two complexes using DFT. They showed trigonal bipyramidal and square pyramidal structures^[189]. Two series of 4-diazo-5-pyrazolone copper(II) complexes were synthesized using 1:1 and 1:2 metal to ligand ratio. The first series showed a square planar geometry while the second a trans octahedral geometry^[190]. Complex **21** was synthesized and assayed for its antifungal and antimicrobial activity, showing only a moderate efficiency against *E. coli* and a weak antitumor activity^[191]. Complex **22** synthesized with a 4-hydrazone-5-pyrazolone ligand showed an antiferromagnetic coupling due to weak intermolecular exchange interaction between copper(II) ions of molecules connected via a H-bonding through uncoordinated acetate ion oxygen atom and hydrazone NH group^[192]. Three other complexes of the same family have been synthesized and found to build zigzag polymer chains linked by intermolecular H-bonds^[193]. Different thiosemicarbazone-5-pyrazolone ligands have been used to prepare monohydrate square planar complexes where the ligand coordinated the metal center in a O,N,S-tridentate way^[194]. Two ligands of the same class have been reacted in their neutral form to afford the relative complexes as polymeric chains with a bridging chlorine atom and a square

pyramidal geometry on copper. Moreover they show a significant cytotoxic activity against several tumor cell lines^[195]. An unusual coordination mode has been found for a pyrazolone-based ligand bearing a thiosemicarbazone moiety on the N1 of the pyrazole, affording the trigonal bipyramidal hydrate Cu(II) complex **23** capable to interact with DNA through an intercalative binding mode^[196].

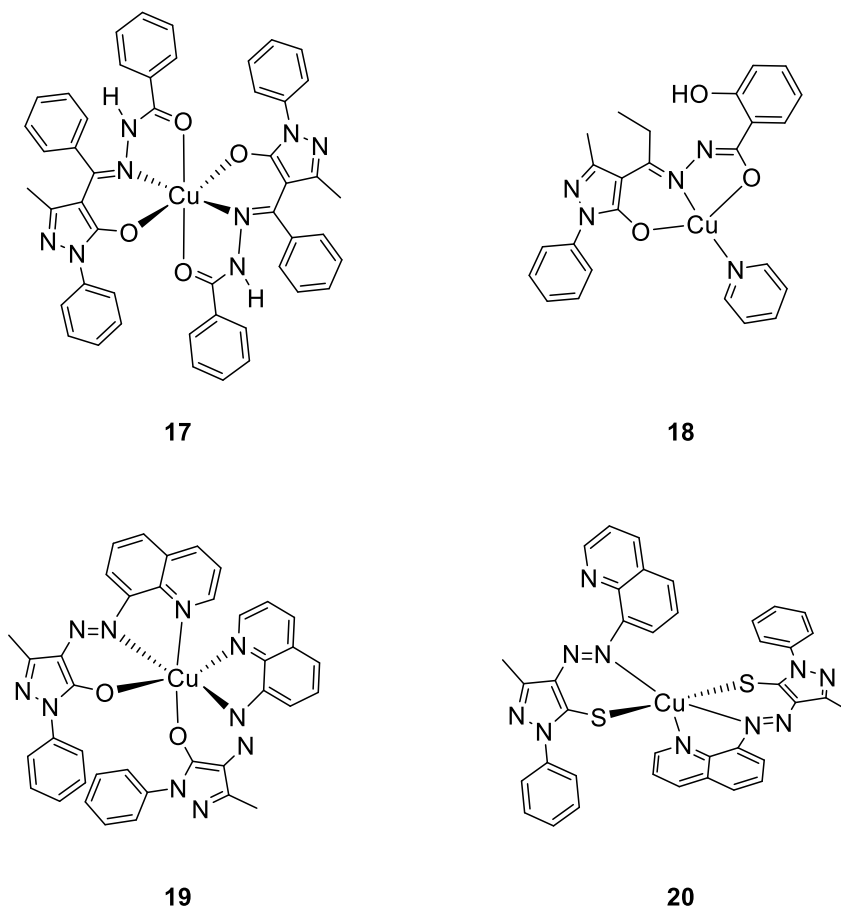


Chart 20. Molecular structure of complexes 17-20. The coordination mode of complexes 19 and 20 varies only for the different donor atom, respectively O and S.

A metal complex of Cu(II) with Schiff base derived from amino-antipyrene was synthesized. The crystal structure showed the complex is mononuclear with the Cu ion 4-coordinated in a square planar environment. The anticancer effect of ligands and complexes were investigated and the biological activity results illustrate that both compounds are active^[197]. Two Schiff base ligands prepared by a condensation reaction between sulfanilamide and the respective acylpyrazolone were used to synthesized two Cu(II) complexes. According to experimental data obtained the

proposed geometry by the author is octahedral with two molecules of the bidentate keto-imine ligand and two molecules of water. A moderate to low antibacterial and antioxidant activity have been exhibited by the compounds^[198]. A novel ligand, hetarylhydrazone, has been synthesized by condensation of 2-hydrazino-4,6-dimethylpyrimidine with 1-phenyl-3-methyl-4-formylpyrazol-5-one and reacted with CuCl_2 and $\text{Cu}(\text{ClO}_4)_2$ obtaining two different complexes. In both compounds the coordination unit is a trigonal bipyramid, but copper chloride gives mono-nuclear complex $[\text{Cu}(\text{H}_2\text{L})\text{Cl}_2]\cdot\text{H}_2\text{O}$ while the copper perchlorate yields the polymeric structure $([\text{Cu}(\text{HL})(\text{CH}_3\text{OH})]\text{ClO}_4)_n$ ^[199]. An additional study reported the synthesis of three new Schiff base ligands obtained by the condensation reaction of phenylhydrazine and dinitrophenylhydrazine with 4-acetyl and 4-benzoyl pyrazole isolated in their keto imine form. The relative $\text{Cu}(\text{II})$ complexes are shown to be octahedral with two molecules of ligands coordinating the metal ion through the azomethine nitrogen $\text{C}=\text{N}$ and the keto oxygen $\text{C}=\text{O}$, plus two molecules of water. The compounds have shown low antibacterial activity, but good antioxidant activity, with the metal complexes having a better bioactivity overall^[131]. In another research a series of mixed-ligand complexes were prepared from 9-anthraldehyde, 4-aminoantipyrina and 1,10-phenanthroline and metal chlorides. The experimental analysis revealed that the compounds possess octahedral geometry with monomeric nature. The biological potential of the compounds was screened by biological evaluation studies: the compounds are bound to the DNA through an intercalated pathway. The antimicrobial screening remarked the complexes as excellent antipathogenic screeners. Also the compounds shown an admirable anticancer skill. Among them, the copper complexes are more efficient than the other metal complexes^[200].

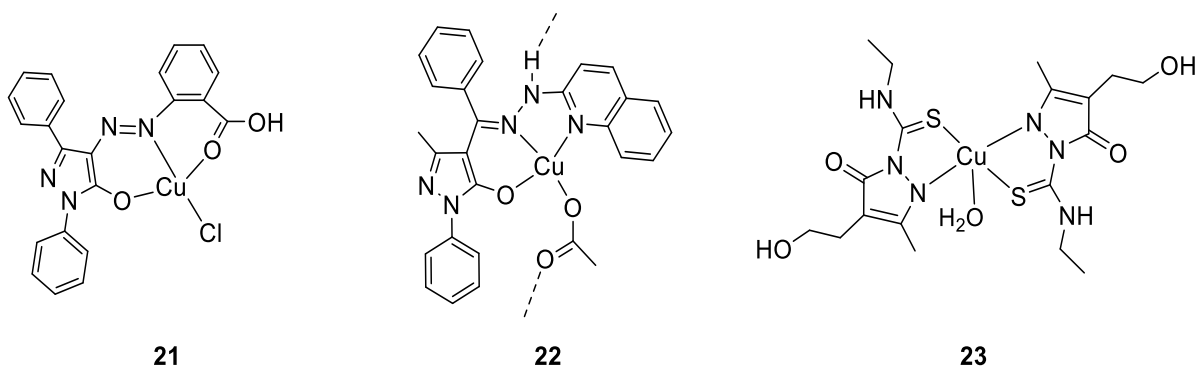


Chart 21. Molecular structure of complexes 21-23.

Two new Cu(II) Schiff base complexes were synthesized by Poormohammadi *et al.* from the condensation of 2,5-dimethylaniline or 3,5-dimethylaniline with 4-acetyl-3-methyl-1-phenyl-5-pyrazolone. The crystal structure of one of the complexes was determined revealing a distorted square planar or distorted tetrahedral geometry. The ligands and complexes show considerable antibacterial activity against the studied bacteria even if the ligands demonstrated a higher antibacterial activity than the relative complexes. This could be rationalized based on their steric effects^[201]. A new tetradentate N₂O₂ type Schiff bases ligand and its related copper complex is reported in an additional paper. The crystal structure of the complex CuL was obtained showing that copper has a slightly distorted square planar coordination geometry. Additionally, since the ligand can exist in different tautomeric forms, the conformational and geometrical aspects were investigated computationally by DFT methods and suggest that the amine-one is the more thermodynamically stable tautomeric form in the gas and solvent phase^[202]. Xi et al. reported a new 4-acylpyrazolone derivative ligand and two related complexes fully characterized. Reaction of the ligand HL with CuCl₂ resulted in a mononuclear compound with tetra-coordinated quadrilateral plane [Cu(HL)Cl]. When reacted with Cu(OAc₂) instead, a dinuclear Cu(II) compound with chemical formula [Cu₂L₂(CH₃OH)]·CH₃OH was obtained and the coordination geometry of Cu(II) is a square pyramid with the units bridged via the salicylhydrazide hydroxyl group of the ligand by replacing the chloride anion with acetate. The compounds were tested for their biological activity and they demonstrated how the steric hindrance of the compound plays pivotal role in DNA binding^[203]. The azo-coupling reaction of phloroglucinol with a 5-pyrazolone amino-derivative led to the isolation of a H₃L¹ ligand, presented in the hydroxy-azo tautomeric form. Nitrosation of this ligand afforded a second ligand described as trioxo di-hydroxylamino hydrazone. The authors claim that according to EPR spectra, the Cu-complex of the first ligand exhibited distorted tetragonal symmetry associated with the d_{x²-y²} ground state, and the corresponding complex of the second ligand was described by a cubic symmetry of the coordination medium. All the compounds showed coloristic activity towards wool, polyamide and polyacetate fibers^[204]. Lastly, Burlov et al. synthesized a Schiff base ligand by condensation of 5-hydroxy-3-methyl-1-phenylpyrazole-4-carbaldehyde with N,N-diethylethylenediamine. The ligand coordinate the Cu(II) ion in a bis(chelate) way and the pentacoordinated complex assumes a distorted tetragonal pyramidal structure^[205].

In conclusion, the coordination chemistry of copper(II) with pyrazolone-based ligands is very rich in terms of number of compounds synthesized and of potential applications, while copper(I) remains poorly investigated.

1.5.2 Complexes of Zinc

Zinc is a relatively recent arrival among the common metals even if it plays a vital role in both industry, mainly extracted as sulfide ZnS and carbonate ZnCO₃, and biological spheres. In fact it has been shown to be essential for all life forms where it generally plays either a catalytic or a structural role. Even for the human body zinc is essential under many aspects like strong immune system, bone metabolism and proper wound healing. More than 30 clinical disorders have been documented to be related to a zinc deficiency in the diet, however also an excess of zinc could have a negative impact on the system. For this reason many zinc compounds and complexes have been developed with therapeutic purposes. The coordination chemistry of zinc is undoubtedly dominated by the +II oxidation state, while under the point of view of the coordination numbers in its compounds zinc is very versatile and it can range from 2 to 8. The filled d shell confers no crystal field stabilization on Zn²⁺ thus the coordination number and stereochemistry are determined by the size of the Zn²⁺ cation and the steric hindrance of the ligands. Generally tetrahedral and octahedral geometries are commonly found in complexes, the former in particular are readily formed with halides and O-donors ligands. When chelating ligands are involved, distortions from regular geometries are widespread. Lately, zinc complexes assumed considerable importance in the generation and self-assembly of 1-, 2- and 3-D infinite structures. Zinc complexes of amino acid, peptide, nucleotide and nucleoside ligands are instead of obvious biological significance. N,O-donors Schiff bases are powerful ligand and many examples of their zinc complexes are known. An interesting feature is that these ligands readily exert a stereochemical control over the complex and thereby provide many examples of unusual geometry about the central ion, illustrating once more the coordination flexibility of zinc^[206].

The first compounds found in literature regarding the synthesis on Zn(II) complexes with acylpyrazolone ligands are studies reported in 1981 about complexes of the type [Zn(Q)₂(H₂O)₂] with Q = Q^{Me}, Q^{Ph}, Q^{CF₃}. They were hypothesized to be six-coordinate with the two O₂-chelating ligands and two molecules of water in the coordination sphere^{[21],[22],[207]}. The complex [Zn(Q^{Hp})₂(H₂O)] (Chart 22) reported by Mickler *et al.* presents instead a five-coordinate Zn in a square pyramidal environment with the two O₂-chelating Q ligands in the equatorial plane and the water molecule in the apical position^[208]. In the same way the compound [Zn(Q^{Ph})₂(dmf)₂] (Chart 22) has been synthesized and characterized. The ligand coordinates the zinc through the two oxygens and it presents a octahedral geometry^[209]. Removing the solvent molecules, i.e. [Zn(Q^{Ph})₂], makes the geometry distorted square-planar^[210]. Other derivatives of the same type

have been reacted with N-donors L (L = phen, bipy, trime, tmeda) yielding an exchange reaction with the solvent molecule affording $[Zn(Q)_2(L)]$ with a six-coordinated zinc in a distorted octahedral environment^[211]. A similar study with different ligands has also been reported by Marchetti in which the reactivity of the compounds has been tested towards N_2 -donor ligands. In this case the compounds have been shown to exist in square-pyramidal structures due to the steric hindrances of the N-donor ligands^[212]. Compounds of the type $[M(Q)_2(solvent)]$ were synthesized reacting $Zn(OAc)_2$ with HQ and then subsequently subjected to a condensation reaction with diamines to afford Schiff bases metal derivatives $[M(L)(H_2O)_2]$, where the zinc has a six coordinate environment. This compound reacts with $CuCl_2$ and $Cu(ClO_4)_2$ breaking the C=N bond in the Schiff base donor affording $[Cu(Q)_2]$ and $[Cu(en)_2](ClO_4)$. Moreover, $[Zn(L)(H_2O)_2]$ reacts with phen and Hmimt substituting the water molecules with phen, whereas reaction with $CdCl_2$ affords the exchange of the metal center^[213].

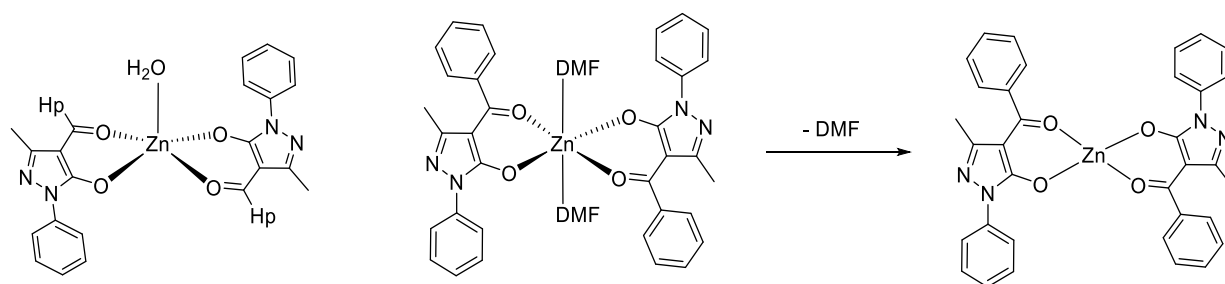


Chart 22. Molecular structure of $[Zn(Q^{Hp})_2(H_2O)]$ (left), $[Zn(Q^{Ph})_2(dmff)_2]$ (center) and $[Zn(Q^{Ph})_2]$ (right).

A work submitted about the complexes $Zn(Q^{fur})_2(ROH)_2$ where R = Me or Et described the complexes as distorted octahedral structures with the solvent molecules in trans position^[214]. Other derivatives in which Q = Q^{tBu} or Q^{nPe} displayed ICAM-1 inhibitory activities^[74]. Other zinc heteroleptic complexes of formula $Zn(Q)_2(N-N)$ where N-N is 4,4'-dinonyl-2,2'-bipyridine are active against three different human cancer cells. An additional study proved that complexes $Zn(Q)_2(H_2O)_2$ where Q = $Q^{Ph_4NO_2}$, Q^{Me} , Q^{Et} or Q^{Pr} have the same octahedral structure while complexes $Zn(Q)_2(H_2O)$ where Q = Q^{Et} or $Q^{Ph_3Cl,Et}$ exist as five-coordinated structures with water in axial position and Q ligands in anti-configuration. $Zn(Q^{Et})_2(phen)$ instead is octahedral with the chelating phen ligand (Chart 23). All of these compounds form adducts with DNA^[215]. The complex $Zn(Q^{Hc})_2(H_2O)$ (Chart 24) reported by Xu *et al.* adopts a square pyramidal geometry with apical water molecule, but unexpectedly the Q ligands are in a syn-configuration. It exhibits

antibacterial activity and a purple emission as result of fluorescence from the intraligand emission excited state^[216]. Metal complexes of 4-acyl-5-pyrazolones, both homoleptic and heteroleptic with 1,10-phenanthroline were prepared and screened for their biological activity. Zn complexes showed powerful antifungal activity close to the standard drugs^[217]. In a different study novel 4-acyl-5-pyrazolones ligands have been prepared by acylation of pyrazolone derivatives with 4-chloro benzoyl chloride.

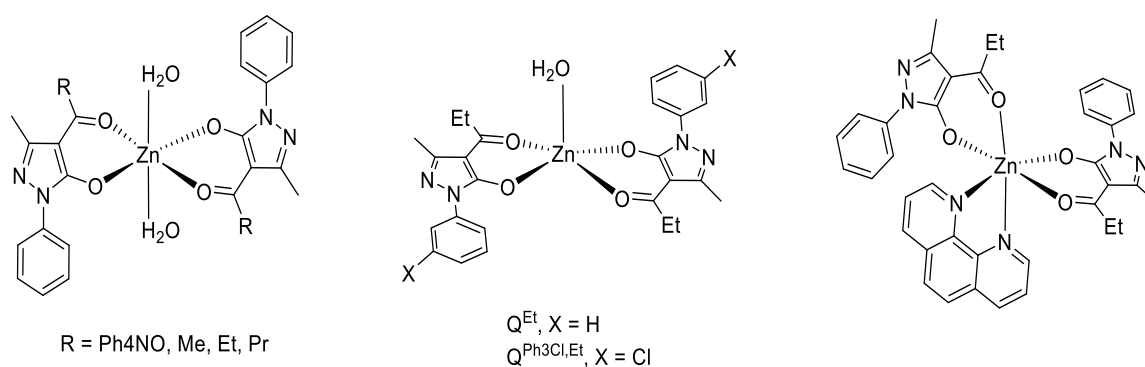


Chart 23. Molecular structure of $\text{Zn}(\text{Q})_2(\text{H}_2\text{O})_2$ (left), $\text{Zn}(\text{Q})_2(\text{H}_2\text{O})$ (center) and $\text{Zn}(\text{Q}^{\text{Et}})_2(\text{phen})$ (right).

The relative Zn(II) complexes have been synthesized and characterized showing a mononuclear six-coordinated Zn ion center with a classical octahedral geometry. Both the ligands and complexes exhibited antimalarial activity^[218]. In another paper a series of zinc(II) complexes bearing aliphatic groups in the acyl moiety of the ligands were prepared to evaluate the influence of a long alkyl chain and cyclohexyl substituent on their anticancer activity. Two complexes exhibited penta- and hexa-coordination with the coordination sphere completed by solvent molecules. Other two complexes instead proved to exist in the expected hexa-coordination form, with two nitrogen atoms of the chelated N_2 -donor ligand and the oxygens of two HQ^{R} ligands. The complexes were tested in vitro toward the human breast cancers cell line MCF-7, displaying an inhibitory activity with high anti-proliferative and pro-apoptotic effects. In particular the complex bearing bipyridine as chelating N,N-donor ligand gave the most interesting results^[219]. Three novel heteroleptic Zn(II) complexes containing 8-hydroxy quinoline and different pyrazolone base derivatives, $[\text{Zn}(\text{Q}^{\text{H}})(\text{quinoline})]$, have been studied for their photoluminescence ability (Chart 24). The complexes showed good photoluminescence properties with the maximum emission range from 475 to 490 nm with a quantum yield of 0.45 to 0.51, an absorption range of 272-281 nm and

high thermal stability. With these characteristics they are suitable for cheap light emitter for organic light-emitting diodes^[220]. A similar study describes the synthesis of other three Zn(II) heteroleptic metal complexes with 8-hydroxyquinoline and pyrazolone-derivates ligands. The complexes showed a photoluminescence in the range of 540-549 nm. Moreover, via theoretical studies, the authors proved the significant contribution of ligands to tune the emission in the case of Zn(II) complexes^[221].

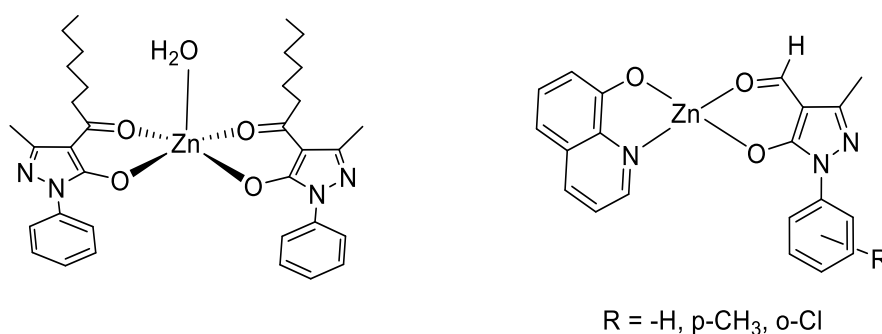


Chart 24. Molecular structure of $[Zn(Q^{He})_2(H_2O)]$ (left) and $[Zn(Q^H)(quinoline)]$ (right).

Two acyl pyrazolones have been synthesized and used to prepare three different zinc(II) complexes with other N,N-donor ligands like bipy and phen. All the complexes showed a distorted octahedral coordination geometry with four coordination sites being occupied by the two acyl pyrazolones and two coordination sites by the N,N-donor. The complexes have been screened for antimalarial activity, one complex in particular showed encouraging results^[222].

The zinc coordination chemistry has been largely explored also in relation to Schiff bases. Compounds reported with 4-aminoalkylidene-5-pyrazolone possess a tetrahedral geometry^[223]. Marchetti *et al.* reported the synthesis of a series of complexes prepared by reacting the zinc bis(acylpyrazolone) with the appropriate diamine. The reactivity of one of these compounds towards metal acceptor was investigated: with $CdCl_2$ in hot DMF, zinc is replaced by cadmium, while using $CuCl_2$ in hot DMF leads to the breaking of the C=N bonds in the tetradentate N_2,O_2 -ligand, with the formation and precipitation of the parent $Cu(acylpyrazolonate)_2$. Additionally, a similar phenomenon occurs when the compound reacts with phen affording $[Zn(acylpyrazolonate)(phen)]$ after the breaking of the same bond C=N^[213]. Complex **24** assumes a octahedral geometry and shows low florescence in solution, increased upon complexation with Ag^+ through the available nitrogen atoms of the pyrazole ring^[224]. Similarly a complex based on a

tetradentate Schiff base with an uncoordinated NH group displays a fluorescent enhancement when complexed with zinc, respect to the free ligand, suggesting a potential fluorescent sensor^[104]. Complexes **25** and **26** involve a five-coordinated zinc center, but the former is mononuclear while the latter is a dinuclear compound with intermolecular Zn-O interactions. Complex **25** shows a strong fluorescence in solid state and aqueous solution, complex **26**, instead, only a moderate emission in solid state^[225]. Complex **27** has been structurally characterized and shown to interact with DNA. Moreover, it displayed antioxidant and cytotoxic activity against lung cancer A549 cells^[226]. Complex **28** have been synthesized in both anhydrous or solvated (acetonitrile or ethanol) forms. It exhibits tunable luminescence from blue to yellow by varying the excitation wavelength. Additionally, the intensity of the emission in solid state can be changed modifying the crystal solvent molecules. This effect has been rationalized by TD-DFT studies demonstrating the decisive role of intermolecular interactions^[227]. Additional photoluminescence studies have been performed on complexes based on analogous 4-formylpyrazolone Schiff base, complexes **29-35** (Chart 26), exhibiting high photoluminescence activity in the blue range^[107]. A Zn(II) mixed-ligand complex containing a bipyridine and a O,N,O-tridentate 4-acyllhydrazone-5-pyrazolone ligand have been synthesized and proved to be octahedral with a molecule of methanol completing the coordination sphere^[228]. Another complex has been found to be polynuclear in the solid state thanks to Zn-N interaction of nicotinic moiety in the Schiff base pyrazolone, with water and DMF completing the octahedral surroundings of the metal centers^[105]. The study reported Zhang *et al.* describes the synthesis of two compounds, complexes **36** and **37** (Chart 27), with the same synthetic procedure, but affording a mononuclear and a polynuclear compounds. The first contains a mono-deprotonated tridentate 4-acylhydrazone-5-pyrazolone ligand plus an acetate group and an ethanol coordinated. In the second one instead the tridentate pyrazolone is doubly deprotonated and the coordination environment in completed by an ethanol molecule and the N atom from a pyrazolone ring of a neighbour unit, affording a 1D network^[229]. Two tetracoordinate zinc(II) complexes containing deprotonated 4-diazo-5-pyrazolone ligands with a diastereotopic isopropyl substituent were demonstrated to display a slow $R \rightleftharpoons S$ inversion of the tetrahedral configuration due to steric overcrowding^[230].

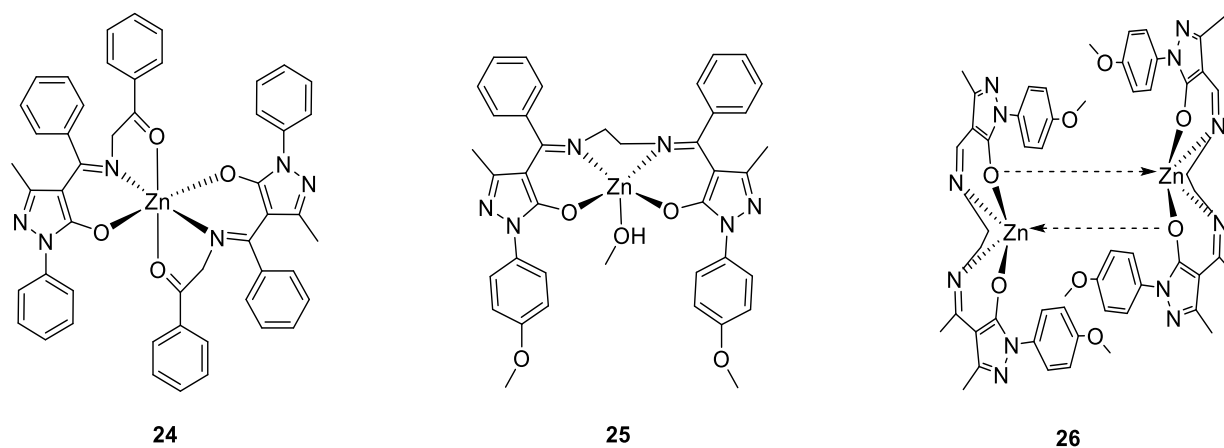


Chart 25. Molecular structure of complexes 24-26

Another complex structurally characterized was proved to exist in a pseudo-tetrahedral geometry^[117], while a series of complexes containing azo ligands displayed both octahedral and tetrahedral geometries^[231]. Two other complexes, **38** and **39** (Chart 28), bearing a O,N,O-tridentate 4-diazo-5-pyrazolone monoanionic ligands are reported to possess a tetrahedral geometry, with a chloride completing the fourth coordination site^[187]. The same result has been obtained for complex **40** with a tridentate dianionic ligand and a molecule of ethanol^[188]. Two series of complexes with metal to ligand ratio of 1:2 and 1:1 respectively, were investigated theoretically by DFT analysis. The first series is reported to possess five-coordinated zinc centers with water molecules in apical position. In the second series the zinc is six-coordinated by a N,O-chelating ligand, three water molecules and a hydroxyl group^[232]. Another series of nine Zn(II) complex was synthesized by Gusev *et al.* based on Salen-type tetradentate N₂O₂ ligands derived from 1-phenyl-3-methyl-4-formyl-5-pyrazolone. They studied the photoluminescence properties of the compounds and found out that the electronic states of the diamine moieties can effectively modulate the photophysical properties^[233]. Two novel ligands were synthesized by association of acylpyrazolones and benzhydrazide. On complexation with Zn(II) acetate dihydrate complexes with distorted octahedron framework are afforded. The structural analysis of the compounds showed that the ligands are stable in the diketo form, while intramolecular hydrogen bonds in the complexes give rise to dimers. The complexes also exhibit excellent antimalarial activity and their MIC values are found higher than the standard drug Quinine^[234].

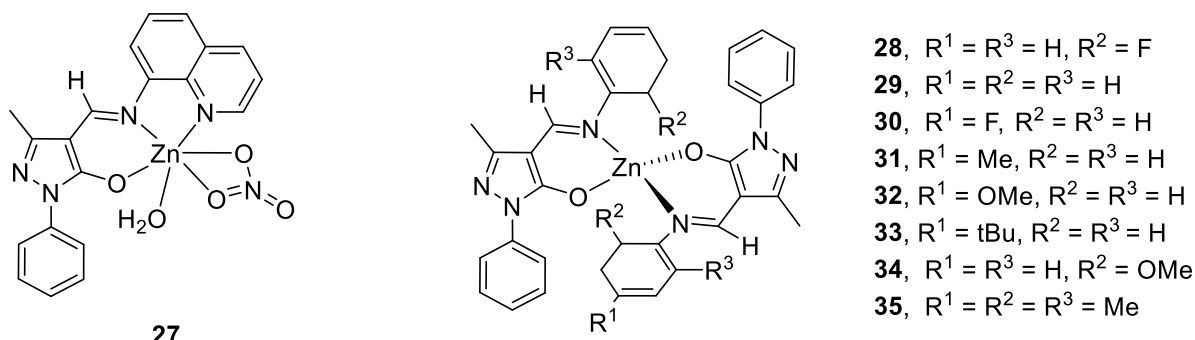


Chart 26. Molecular structure of complexes 27-35.

In another study a Schiff base ligand has been used to prepare the zinc coordination compound in an attempt to determine the vibrational properties using infrared and Raman spectroscopy combined with density functional theory methods. The comparison of experimental and theoretical spectra allowed to assign most of the normal modes of the crystal^[235]. Two new 4-acylpyrazolone derivatives were synthesized by Shaik *et al.* affording one homoleptic zinc complex $[\text{Zn}(\text{L}^1)_2] \cdot \text{DMF}$ and two mixed ligands complexes $[\text{Zn}(\text{L}^2)(\text{bpy})(\text{OAc})] \cdot \text{EtOH}$ and $[\text{Zn}(\text{L}^2)(\text{phen})(\text{DMF})]$. X-ray diffraction studies suggested a distorted octahedral environment around the zinc through coordination of O,N,O-chelating 4-acylhydrazone-5-pyrazolone ligands for two complexes, while a distorted square pyramidal geometry was found for the third complex. All compounds exhibited decent outcomes in *in vitro* antimalarial activity^[236]. A novel ligand prepared by the condensation of 3-formyl-6-methyl chromone and thiosemicarbazide (HMPM) has been used to synthesized the zinc complex **41** of formula $[\text{Zn}(\text{HMPM})_4\text{Cl}_2]$. Single crystal XRD permitted to reveal that the complex possesses a hexadentate slightly distorted octahedral coordination geometry with four HMPM ligand molecules serving as four independent monodentate ligands through their pyrazoles' sp^2 nitrogens along with two chloride ions in a near trans disposition. *In vitro* and *in silico* studies suggested a potential antimicrobial and antidiabetic activity for both the ligand and the complex^[237].

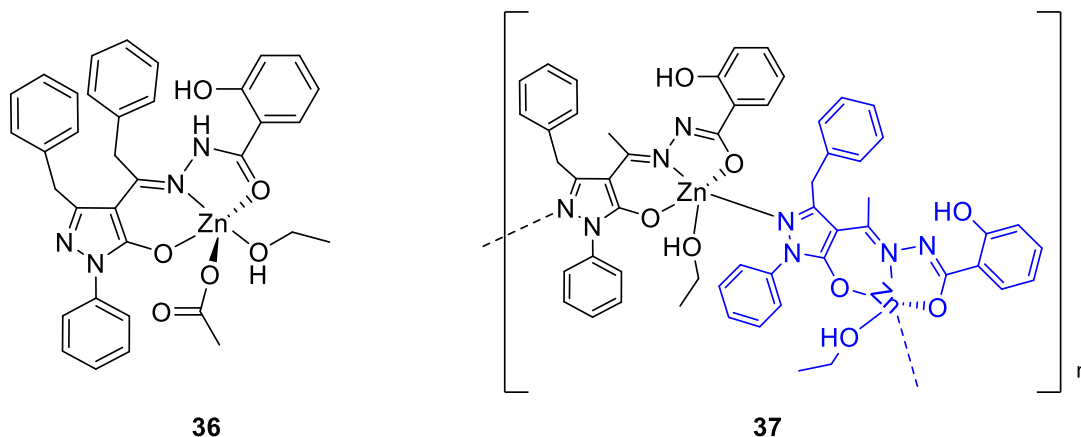


Chart 27. Molecular structure of complexes 36 and 37.

A novel mononuclear complex of Zn(II) using a pyrazolone-derived Schiff base ligand has been reported. The complex adopts an octahedral arrangement around the central metal ion. The study reveals also that the complex binds with CT-DNA via an intercalation mode. Moreover the antimicrobial activity against a set of bacterial and fungal strains reveals that the compound exhibits better activity than the free ligand^[238]. Refluxing equimolar amounts of 2,2'-bipyridine and a N,N,S-tridentate basic form of a Schiff base ligand L with the adequate metal acetate, Garnovskii *et al.* reports the synthesis of the corresponding mononuclear mixed ligand zinc complex of formula $[M(L)bipy](CH_3CN)$. The X-ray diffraction data of the compound shows that it adopts a trigonal bipyramidal geometry with $\{MN_4S\}$ coordination mode^[239]. Lastly, in a recent study quinolyl-3-pyrazole and quonolyl-6-pyrazole azomethines were synthesized as precursor for zinc complexes, and their atomic structure was determined by DFT calculation. Theoretical and experimental data on the bond lengths within the metal coordination sites are in good agreement. Additionally photo- and electroluminescent properties of the complexes have been investigated: the maximum occurs around $\lambda = 478$ nm for both compounds^[240].

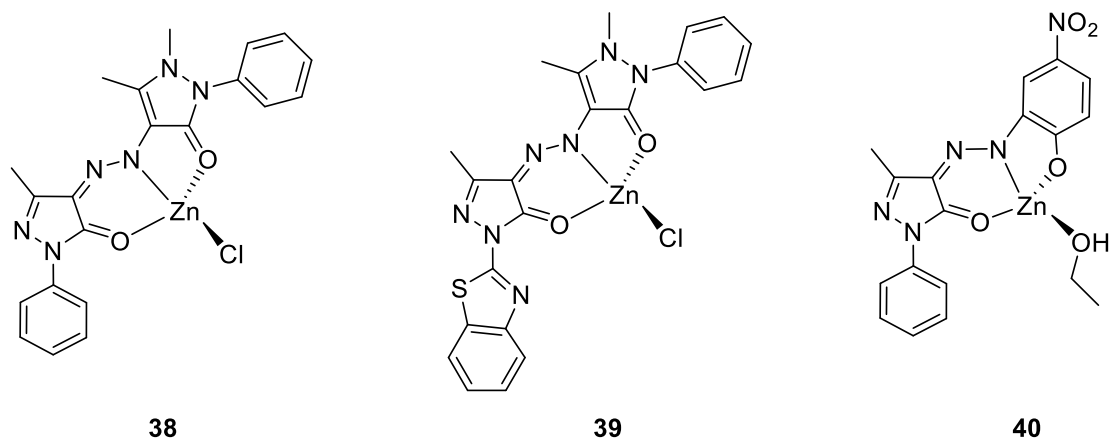


Chart 28. Molecular structure of complexes 38-40.

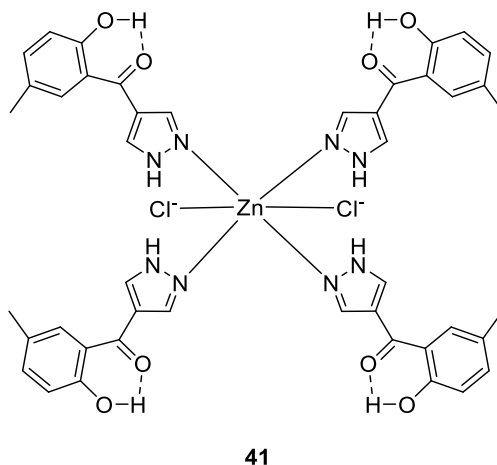


Chart 29. Molecular structure of complex 41, $[Zn(HMPM)_4Cl_2]$.

1.5.3 Complexes of Molybdenum

Molybdenum compounds play a significant role in industry catalysis. During the last decade the inorganic and coordination chemistry of molybdenum has expanded substantially mostly thanks to the introduction of a versatile range of polydentate ligands and the development of the chemistry and catalytic applications of a range of complexes. Molybdenum is a truly versatile element and the full measure of its coordination chemistry is matched by few other elements. While dioxo-Mo(IV) complexes are very rare and almost invariably adopt trans-octahedral structures, the molybdate(IV) ion, $[MoO_4]^{2-}$ is tetrahedral, stable and inert under basic conditions, but it is readily protonated on acidification. Many dioxo complexes of Mo(VI) are used in oxidation catalysis as enzymes, and in metal oxide surface modes as sensor and drugs, prepared by ligand addition,

exchange, and/or metathesis using $\text{cis-[MoO}_2\text{]}^{2+}$ precursors such as $[\text{MoO}_2\text{X}_2]$, where X = halide. The oxo groups are invariably cis in order to maximize donation into empty metal orbitals and usually have four- or six-coordination. The four-coordinate species $[\text{MoO}_2\text{X}_2]$ are tetrahedral and X is almost always a π -donor ligand. Five-coordination in dioxomolybdenum(VI) chemistry is rare, but examples included trigonal bipyramidal and square-pyramidal geometries. The majority of dioxo-Mo(VI) complexes have distorted octahedral geometries, with the weakest π -donor ligands being trans to the oxo ligands, whereas stronger π -donor ligands are mutually trans and cis to the oxo groups, due to the strong trans influence of the π -donor oxo ligands^[241].

An octahedral molybdenum(II) derivate has been synthesized by Maurya *et al.* of formula $[\text{Mo}(\text{NO})(\text{CN})_3(\text{HQ}^{\text{Ph}})(\text{H}_2\text{O})]$. Two different $\nu(\text{C}=\text{O})$ absorption bands have been detected in the IR spectrum, the lower one for the cyclic and the higher one for exocyclic carbonyl groups^[242]. Two other complexes of structure $[\text{MoO}_2(\text{Q}^{\text{Et}})_2]$ and $[\text{MoO}_2(\text{Q}^{\text{CCl}_3})(\text{Q}^{\text{CCl}_3*})]$ (Chart 30) have been studied. The X-ray analysis showed the two oxo groups in cis position and a distorted octahedral geometry for both. The peculiarity of the latter is the presence of the Q^{CCl_3*} ligand, in which an ethoxy moiety is introduced in the acyl moiety due to a deprotonation reaction between the complex and the solvent^[243].

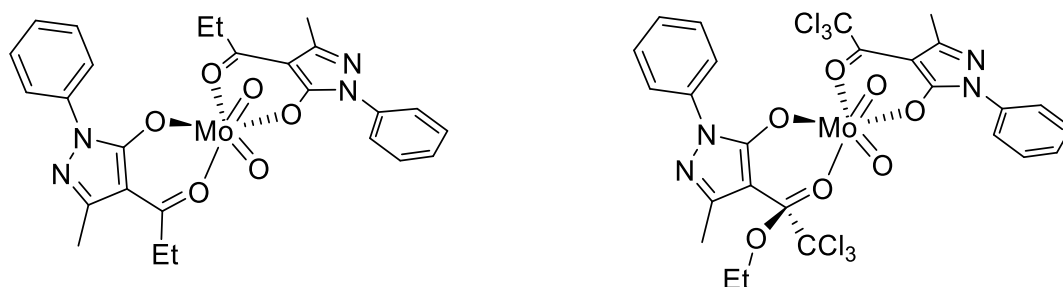


Chart 30. Molecular structure of $[\text{MoO}_2(\text{Q}^{\text{Et}})_2]$ (left) and $[\text{MoO}_2(\text{Q}^{\text{CCl}_3})(\text{Q}^{\text{CCl}_3*})]$ (right).

A series of complexes of type $\text{MoO}_2(\text{Q})_2$ where $\text{Q} = \text{Q}^{\text{Cy}}, \text{Q}^{\text{EtCp}}, \text{Q}^{\text{He}}$ and Q^{nPe} (Chart 31) have been synthesized and showed catalytic activity on deoxygenation of epoxide substrates to alkene in toluene, employing PPh_3 as oxygen acceptor. The possible isomers, due to asymmetric ligands, have also been studied by DFT calculation founding the isomer with the two acylpyrazolones in cis position to be the most stable from an energetic point of view^[244]. In a recent paper, oxidoperoxido-molybdenum(VI) complexes containing acylpyrazolonate ligands were obtained.

A series of complexes of general formula $\text{Ph}_4\text{P}(\text{Mo}(\text{O})(\text{O}_2)_2(\text{Q}^{\text{R}})]$ were obtained with one equivalent of the ligand in the presence of Ph_4PCl . Instead, neutral complexes $[\text{Mo}(\text{O})(\text{O}_2)(\text{Q}^{\text{R}})_2]$ were formed using two equivalents of HQ^{R} . Some of the complexes were selected to investigate their catalytic activity in epoxidation of selected alkenes and oxidation of selected sulphides. Other complexes were tested as catalyst precursors in the deoxygenation of selected epoxide substrates to alkenes. Complexes $\text{Ph}_4\text{P}(\text{Mo}(\text{O})(\text{O}_2)_2(\text{Q}^{\text{R}})]$ were shown to be poor catalyst precursors while the homoleptic complexes $[\text{Mo}(\text{O})(\text{O}_2)(\text{Q}^{\text{R}})_2]$ showed good activity in all the studied reactions^[245]. Finally, a novel series of mixed-ligand complexes of dioxomolybdenum(VI) of the general formula $[\text{MoO}_2(8\text{-hq})(\text{H}_2\text{O})]$ (Chart 31) has been synthesized starting from $[\text{MoO}_2(\text{acac})_2]$. Based on experimental and theoretical data pseudo-pentagonal bipyramidal structures have been proposed by the authors for the complexes. Biological studies have been carried out proving the complexes as potent antibacterial agents^[246].

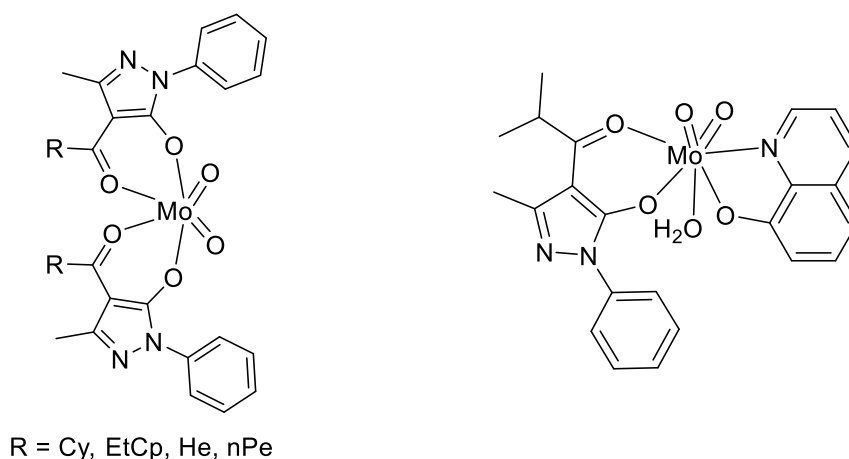


Chart 31. Molecular structure of $\text{MoO}_2(\text{Q}^{\text{R}})_2$ (left) and $[\text{MoO}_2(8\text{-hq})(\text{H}_2\text{O})]$ (right).

A series of Schiff bases complexes have been reported by Maurya *et al.* using dioxomolybdenum(IV) and 4-aminoalkylidene-5-pyrazolone ligands. Based on the ligand they obtain mononuclear compounds **42-44** and **45-46** (Chart 32) with four-, five- and six-coordinated Mo centers. Additionally, ligands bearing a bridging group large enough not to hinder the bis-chelating possibility afforded dinuclear complexes **47** and **48**^[247]. The same ligands have also been used to synthesized dinitrosyl molybdenum(II) complexes. The two nitrosyl groups have been demonstrated to be in trans position to each other in all complexes^[248].

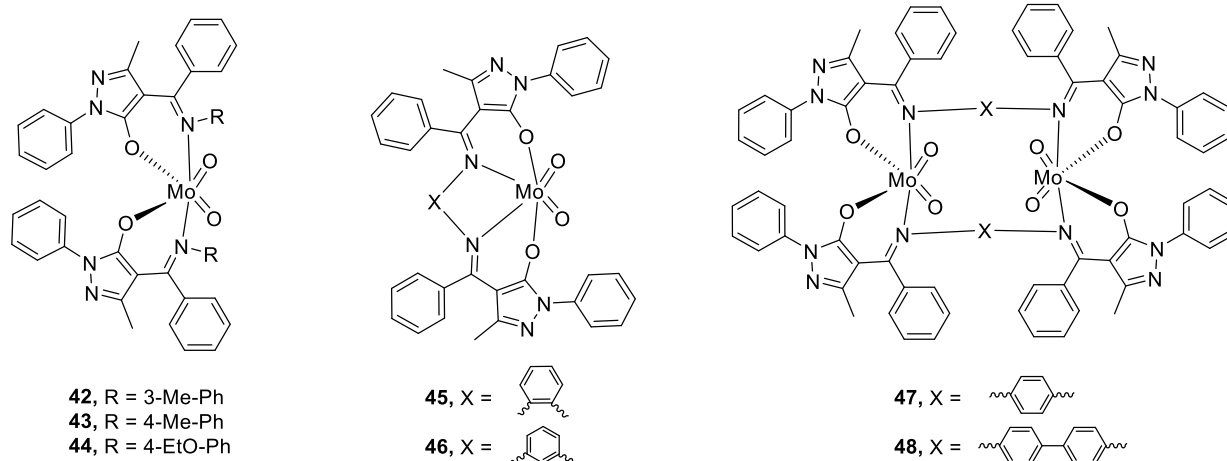
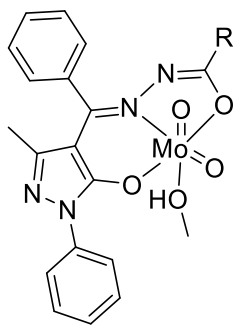


Chart 32. Molecular structure of complexes 42-48

Another series of similar complexes has been obtained using dioxomolybdenum(VI) and Schiff base ligands where the phenyl group in the imino moiety is replaced with a methyl or a propyl group^{[249],[250]}. Complexes of cis-dinitrosylmolybdenum(II) were reported with a N,O,N-tridentate ligand created by condensation of antipyrine to the imino nitrogen atom. The complexes are octahedral with the sixth position occupied by a water molecule^[250]. Oxomolybdenum(V) complexes were reported and shown to have a distorted octahedral geometry with the ligands acting as N,O-bidentate donors, despite the additional and potential donor group -OH^[251]. An additional series of dioxomolybdenum(IV) complexes have been reported and demonstrated to display the typical octahedral geometry with the oxo ligands in cis position^[252]. Complexes **49-52** have been synthesized using dioxomolybdenum(VI) and 4-acylhydrazone-5-pyrazolone ligands. They have been tested as catalysts in the oxidation of secondary alcohols with H₂O₂ as oxidant, in liquid phase conditions and microwave irradiation^[252]. Another series of dioxomolybdenum(VI) complexes **53-56** and of oxoperoxomolybdenum(VI) **57-60** with the same kind of ligands have been reported and investigated also with X-ray diffraction techniques. Also their catalytic potential have been examined in Hantzsch reaction using H₂O₂ as oxidant in solvent free conditions^[253].

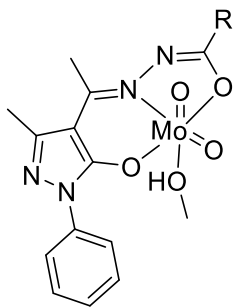


49, R = Ph

50, R = 4-pyridyl

51, R = 3-pyridyl

52, R = 2-furyl

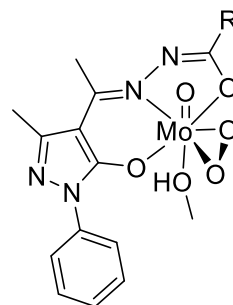


53, R = Ph

54, R = 4-pyridyl

55, R = 3-pyridyl

56, R = 2-furyl



57, R = Ph

58, R = 4-pyridyl

59, R = 3-pyridyl

60, R = 2-furyl

Chart 33. Molecular structures of complexes 49-60.

CHAPTER 2.

Synthesis of novel Schiff base ligands and their zinc(II) complexes. Evaluation of their biological activity as antimicrobials.

2.1 Introduction

It has been previously pointed out in the general introduction that the pyrazolone fragment plays a crucial role as a structural element in a variety of compounds that display a wide range of biological activity. As a result, pyrazolone-based ligands, such as acylpyrazolones or Schiff base compounds, maintain and potentially enhance this important characteristic. The coordination chemistry between these ligands and metals is a field of ever-increasing interest^{[112],[142],[143]}. The complexation process alters the steric and electronic properties of the ligands, leading to novel or improved characteristics. Numerous metal complexes containing elements such as titanium^{[146],[254],[255]}, ruthenium^{[15],[93],[94],[256]–[259]}, platinum^[260], tin^{[261]–[263]} and silver^{[52],[264],[265]} have been observed to exhibit promising anticancer and antibacterial activity. The purpose of the work described in this chapter is aimed to examine and rationalize the role of different hydrazone substituents in determining the nuclearity and antibacterial activity of the ligands and the corresponding zinc(II) complexes.

The discussion reported in this Chapter is adapted from the corresponding work: Marchetti, F., Pettinari, R., **Verdicchio, F.**, Tombesi, A., Scuri, S., Xhafa, S., Olivieri, L., Pettinari, C., Choquesillo-Lazarte, D., García-García, A., Rodríguez-Diéguez, A., & Galindo, A. (2022). Role of hydrazone substituents in determining the nuclearity and antibacterial activity of Zn(ii) complexes with pyrazolone-based hydrazones. *Dalton Transactions*, 2022, Volume 51, Issue 37, Pages 14165 – 14181.

2.2 Experimental section

2.2.1 General procedures

All reagents were purchased (Aldrich) and used without further purification. All solvents were purified by conventional methods and stored under nitrogen. All reactions and manipulations for the syntheses of proligands H_2L^n and their interactions with zinc acetate dihydrate were carried out in the air. The samples for microanalyses were dried in vacuo to constant weight (20 °C, ca. 0.1 Torr). Elemental analyses (C, H, N) were performed in-house with a Fisons Instruments 1108 CHNS-O Elemental Analyser. Melting points are uncorrected and were recorded on a STMP3 Stuart scientific instrument and on a capillary apparatus. IR spectra were recorded from 4000 to 200 cm^{-1} with a PerkinElmer Spectrum 100 FT-IR instrument. 1H , ^{19}F , and ^{13}C NMR spectra were recorded with a 500 Bruker Ascend™ (500 MHz for 1H , 470.6 for ^{19}F , 125 MHz for ^{13}C) instrument operating at room temperature relative to TMS. Positive ESI-Mass Spectra were obtained with a Series 1100 MSI detector HP spectrometer, using acetonitrile as mobile phase. Solutions for electrospray ionization mass spectrometry (ESI-MS) were prepared using reagent grade methanol and obtained data (masses and intensities) were compared to those calculated by using the IsoPro isotopic abundance simulator version 2.1. Peaks containing zinc(II) ions were identified as the highest peak of an isotopic cluster.

2.2.2 Synthesis of proligands

The proligands H_2L^1 and H_2L^3 were synthesized and characterized as previously reported^[118] whereas H_2L^2 , H_2L^4 and H_2L^5 are new and their synthesis and characterization is reported below.

H_2L^2 . The proligand H_2L^2 was synthesized by mixing (5-hydroxy-3-methyl-1-phenyl-1H-pyrazol-4-yl)(phenyl)methanone (m.w. 278.3, 278 mg, 1 mmol) and 4-methylbenzenesulfonohydrazide (m.w. 186.2, 186 mg, 1 mmol) in ethanol at reflux and stirring the reaction mixture for 4 h. The product precipitated out from the hot solution as the reaction proceeded. After cooling, the product was filtered off and recrystallized from ethanol to give a brown solid (325 mg, 78%). H_2L^2 is soluble in DMSO, DMF, acetone, acetonitrile, chlorinated solvents and slightly soluble in hot methanol. M. p.: 230–232 °C. Anal. Calculated for $C_{24}H_{22}N_4O_3S$ (m.w. 446.5): C, 64.56; H, 4.97; N, 12.55; S, 7.18%. Found: C, 64.38; H, 5.01; N, 12.38; S, 7.09%. IR (cm^{-1}): 3496w br $\nu(N-H\cdots O)$, 3160w br $\nu(N-H)$, 3080w br $\nu(C-H\text{ aromatics})$, 1632 $\nu(C=O)$, 1611, 1582 $\nu(C=C)$, 1538

$\nu(\text{C}=\text{N})$, 1535 $\nu(\text{C}-\text{N})$, 1301 $\nu_{\text{as}}(\text{SO}_2)$, 1165 $\nu_{\text{s}}(\text{SO}_2)$, 1089 $\nu(\text{N}-\text{N})$. ^1H NMR (CDCl_3 with 0.05% v/v TMS, 500 MHz, 298 K): δ_{H} 1.61 (s, 3H, H_2O), 2.19 (s, 3H, H_{19}), 6.82 (d, 2H, $\text{H}_{17,17'}$), 7.20 (sbr, 1H, $\text{N}_4 - \text{H}$), 7.25 (t, 1H, H_9), 7.36 (d, 2H, $\text{H}_{12,12'}$), 7.45 (t, 2H, $\text{H}_{8,8'}$), 7.58 (m, 3H, $\text{H}_{13,13'}$, H_{14}), 7.90 (d, 2H, $\text{H}_{7,7'}$), 8.15 (d, 2H, $\text{H}_{16,16'}$). ^{13}C NMR (CDCl_3 , 125 MHz, 298 K): δ_{C} 14.5 (C_{20}), 30.9 (C_{19}), 99.6 (C_4), 111.6 ($\text{C}_{17,17'}$), 120.4 ($\text{C}_{7,7'}$), 126.1 (C_9), 126.2 ($\text{C}_{16,16'}$), 127.7 ($\text{C}_{12,12'}$), 129.1 ($\text{C}_{8,8'}$), 129.6 ($\text{C}_{13,13'}$), 131.9 (C_{14}), 137.5 (C_6), 141.0 (C_{15}), 147.5 (C_3), 150.1 (C_{18}), 158.7 (C_{10}), 159.3 (C_5), C_{11} not observed. $\{^1\text{H}, ^{15}\text{N}\}$ gs-HSQC NMR (CDCl_3 , 51 MHz, $^3\text{J}(\text{N}-\text{H}) = 3$ Hz, 298 K): δ_{N} 117.3 (N_4). $\{^1\text{H}, ^{15}\text{N}\}$ gs-HMBC NMR (CDCl_3 , 51 MHz, $^3\text{J}(\text{N}-\text{H}) = 3$ Hz, 298 K): δ_{N} 189.8 (N_1), 217.7 (N_2), N_3 not observed. ESI-MS (+) CH_3CN (m/z, relative intensity %): 447 [35] $[\text{H}_3\text{L}^2]^+$; 469 [100] $[\text{H}_2\text{L}^2 + \text{Na}]^+$; 485 [30] $[\text{H}_2\text{L}^2 + \text{K}]^+$; 916 [15] $[2\text{H}_2\text{L}^2 + \text{Na}]^+$.

H_2L^4 . The proligand H_2L^4 was synthesized from 1-(5-hydroxy-3-methyl-1-phenyl-1H-pyrazol-4-yl)-2-phenylethan-1-one (m.w. 292.3, 292 mg, 1 mmol) and (4-nitrophenyl)hydrazine (m.w. 153.4, 153 mg, 1 mmol) following the same procedure used for H_2L^2 (80 °C, reaction time 4 h). The product precipitated out from the hot solution as the reaction proceeded. After cooling, the product was filtered off and recrystallized from ethanol to give a brown solid (308 mg, 72%). H_2L^4 is soluble in DMSO, DMF, acetone, acetonitrile, chlorinated solvents and slightly soluble in hot methanol. M.p.: 229–231 °C. Anal. Calculated for $\text{C}_{24}\text{H}_{21}\text{N}_5\text{O}_3$ (m.w. 427.5): C, 67.44; H, 4.95; N, 16.38%. Found: C, 67.23; H, 4.83; N, 16.11%. IR (cm^{-1}): 3184 w br $\nu(\text{O}-\text{H}\cdots\text{N})$, 3135 br $\nu(\text{N}-\text{H})$, 3062 w br $\nu(\text{C}-\text{H}$ aromatics), 1615 m $\nu(\text{C}=\text{O})$, 1593 s, 1584 s $\nu(\text{C}=\text{C})$, 1530 m $\nu(\text{C}=\text{N})$ and $\nu_{\text{as}}(\text{NO}_2)$, 1376 m $\nu(\text{C}-\text{N})$, 1325 s $\nu_{\text{s}}(\text{NO}_2)$, 1108 s $\nu(\text{N}-\text{N})$. ^1H NMR (CDCl_3 with 0.05% v/v TMS, 500 MHz, 298 K): δ_{H} 2.41 (s, 3H, C_3-CH_3), 4.11 (s, 2H, H_{11}), 6.49 (s, 1H, N_4-H), 6.63 (d, 2H, $\text{H}_{17,17}$), 7.14 (d, 2H, $\text{H}_{13,13}$), 7.24 (m, 4H, $\text{H}_{14,14}$, H_{15} , H_9), 7.43 (t, 2H, $\text{H}_{8,8}$), 7.98 (d, 2H, $\text{H}_{7,7}$), 8.04 (d, 2H, $\text{H}_{18,18}$), 12.40 (sbr, 1H, $\text{O}-\text{H}$). ^{13}C NMR (CDCl_3 , 125 MHz, 298 K): δ_{C} 16.9 (C_3-CH_3), 33.8 (C_{11}), 100.9 (C_4), 112.0 ($\text{C}_{17,17}$), 119.7 ($\text{C}_{7,7}$), 125.2 (C_9), 126.0 ($\text{C}_{18,18}$), 127.8 (C_{15}), 128.1 ($\text{C}_{13,13}$), 129.1 ($\text{C}_{8,8}$), 129.5 ($\text{C}_{14,14}$), 134.3 (C_{12}), 138.7 (C_6), 141.9 (C_{19}), 147.2 (C_3), 151.5 (C_{16}), 165.4 (C_{10}), 167.1 (C_5). $\{^1\text{H}, ^{15}\text{N}\}$ gs-HSQC NMR (CDCl_3 , 51 MHz, $^3\text{J}(\text{N}-\text{H}) = 3$ Hz, 298 K): δ_{N} 98.9 (N_4), 140.6 (N_3). $\{^1\text{H}, ^{15}\text{N}\}$ gs-HMBC NMR (CDCl_3 , 51 MHz, $^3\text{J}(\text{N}-\text{H}) = 3$ Hz, 298 K): δ_{N} 288.9 (N_2), 98.9 (N_4), 140.6 (N_3), 379.4 (NO_2), N_1 not observed. ESI-MS (+) CH_3CN (m/z, relative intensity %): 428 [100] $[\text{H}_3\text{L}^4]^+$; 450 [30] $[\text{H}_2\text{L}^4 + \text{Na}]^+$; 491 [15] $[\text{H}_2\text{L}^4 + \text{MeCN} + \text{Na}]^+$; 878 [10] $[2\text{H}_2\text{L}^4 + \text{Na}]^+$.

H₂L⁵. The proligand H₂L⁵ was synthesized from 1-(5-hydroxy-3-methyl-1-phenyl-1H-pyrazol-4-yl)-3,3-dimethylbutan-1-one (m.w. 272.3, 272 mg, 1 mmol) and 4-(trifluoromethyl)phenylhydrazine (m.w. 176.1, 176 mg, 1 mmol) following the same procedure used for H₂L² (80 °C, reaction time 4 h). The product precipitated out from the hot solution as the reaction proceeded. After cooling, the product was filtered off and recrystallized from ethanol to give a white solid (323 mg, 75%). H₂L⁵ is soluble in DMSO, DMF, acetone, acetonitrile, chlorinated solvents, diethyl ether and slightly soluble in hot methanol. M.p.: 213–214 °C. Anal. Calculated for C₂₃H₂₅F₃N₄O (m.w. 430.5): C, 64.17; H, 5.85; N, 13.02%. Found: C, 64.01; H, 5.68; N, 12.87%. IR (cm⁻¹): 3239 m br ν(O–H···N), 3068w br ν(N–H), 1615s ν(C=O), 1577s ν(C=C), 1524 m ν(C=N), 1312vs ν_s(CF₃), 1163, 1112 ν_{as}(CF₃), 1120vs ν(N–N), 1065vs ν_s(CF₃). ¹H NMR (CDCl₃ with 0.05% v/v TMS, 500 MHz, 298 K): δ_H 1.11 (s, 9H, H13,13,13), 2.49 (s, 3H, H19), 2.83 (s, 2H, H11), 6.58 (s br, 1H, N4–H), 6.79 (d, 2H, H15,15), 7.22 (t, 1H, H9), 7.45 (t, 2H, H8,8), 7.50 (d, 2H, H16,16), 8.01 (d, 2H, H7,7), 12.83 (s br, 1H, O–H). ¹³C NMR (CDCl₃, 125 MHz, 298 K): δ_C 17.6 (C19), 30.6 (C13,13,13), 34.7 (C12), 39.0 (C11), 100.4 (C4), 113.0 (C15,15), 119.6 (C7,7'), 124.0q (¹J_{C–F} = 271.3 Hz, C17), 124.2q (¹J_{C–F} = 271.3 Hz, C18), 125.2 (C9), 126.9q (³J_{C–F} = 3.9 Hz, C16,16'), 128.9 (C8,8'), 138.0 (C6), 147.0 (C3), 148.9 (C14), 164.9 (C10), 169.6 (C5). ¹⁹F NMR (CDCl₃): δ, –61.77. {¹H,¹⁵N} gs-HSQC NMR (CDCl₃, 51 MHz, ³J(N–H) = 3 Hz, 298 K): δ_N 143.8 (N3), 99.7 (N4). {¹H,¹⁵N} gs-HMBC NMR (CDCl₃, 51 MHz, ³J(N–H) = 3 Hz, 298 K): δ_N 191.4 (N1), 285.8 (N2), 143.8 (N3), 99.7 (N4). ESI-MS (+) CH₃CN (m/z, relative intensity %): 431 [95] [H₃L⁵]⁺; 453 [100] [H₂L⁵ + Na]⁺; 469 [15] [H₂L⁵ + K]⁺; 494 [15] [H₂L⁵ + MeCN + Na]⁺; 884 [20] [2H₂L⁵ + Na]⁺.

2.2.2 Synthesis of complexes

[Zn(HL¹)₂], (1). Complex 1 was synthesized by mixing Zn(O₂CCH₃)₂·2H₂O (0.022 g, 0.1 mmol) and the proligand H₂L¹ (0.074 g, 0.2 mmol) in 30 ml of methanol. A yellow solid slowly precipitated from the solution. After 24 h the suspension was filtered off, the precipitate was washed with Et₂O and dried to constant weight under reduced pressure. It was recrystallized from dichloromethane/n-hexane. It is soluble in DMSO, DMF, acetonitrile, acetone, and chlorinated solvents. Yield 86%. M.p. 320 °C decomposes. Elemental Analyses Calculated for C₄₄H₃₆N₁₀O₂Zn (m.w. 802.2): C, 65.88; H, 4.52; N, 17.46. Found: C, 66.06; H, 6.42; N, 17.13%. Λ_M (in acetonitrile) = 4.0 Ω⁻¹ cm² mol⁻¹. IR (cm⁻¹): 3351 m ν(N–H), 1612s ν(C=N), 1595vs ν(C=N), 1567s ν(C=C), 1536s ν(C=C), 1509 m ν(C=O), 1092 m ν(N–N), 410 m ν(Zn–N), 364s

$\nu(\text{Zn-N})$, 321s $\nu(\text{Zn-O})$. $^1\text{H NMR}$ (CDCl_3): δ_{H} , 1.50 (s, 6H, H_2O), 6.31 (d, 2H, H16), 6.58 (t, 2H, H18), 7.01 (t, 2H, H17), 7.21 (t, 4H, H8,8'), 7.34 (t, 2H, H14), 7.49 (s, 2H, N4 - H), 7.58 (d, 4H, H12,12'), 7.70 (t, 4H, H13,13'), 7.80 (d, 4H, H7,7'), 7.90 (d, 2H, H19). $^{13}\text{C NMR}$ (CDCl_3): δ_{C} , 15.3 (C20), 96.6 (C4), 108.7 (C16), 114.9 (C17), 120.6 (C7,7'), 123.7 (C9), 128.2 m (C8,8',12,12'), 129.8 m (C13,13',14), 133.3 (C11), 134.6 (C6), 138.5 (C18), 139.8 (C3), 144.9 (C19), 152.0 (C15), 154.6 (C10), 162.2 (C5). $\{^1\text{H},^{15}\text{N}\}_{\text{gs-HSQC}}$ NMR (CDCl_3 , 51 MHz, $^3\text{J}(\text{N-H}) = 3$ Hz, 298 K): δ_{N} 132.9 (N4). $\{^1\text{H},^{15}\text{N}\}_{\text{gs-HMBC}}$ NMR (CDCl_3 , 51 MHz, $^3\text{J}(\text{N-H}) = 3$ Hz, 298 K): δ_{N} N1, N2, N3 and N5 not observed. ESI-MS (+) CH_3CN (m/z, relative intensity %): 432 [20] $[\text{Zn}(\text{HL}^1)]^+$; 801 [80] $[\text{Zn}(\text{HL}^1)(\text{H}_2\text{L}^1)]^+$; 823 [70] $[\text{Zn}(\text{HL}^1)_2 + \text{Na}^+]$.

$[\text{Zn}(\text{HL}^2)_2]$, (2). Complex 2 was synthesized by mixing $\text{Zn}(\text{O}_2\text{CCH}_3)_2 \cdot 2\text{H}_2\text{O}$ (0.022 g, 0.1 mmol) with the proligand H_2L^2 (0.089 g, 0.2 mmol) in 30 ml of methanol, with a procedure similar to that of 1. It is soluble in DMSO, DMF, acetonitrile, acetone, chlorinated solvents, and methanol. Yield 76%. M.p. 241–242 °C. Elemental Analyses Calculated for $\text{C}_{48}\text{H}_{42}\text{N}_8\text{O}_6\text{S}_2\text{Zn}$ (m.w. 956.4): C, 60.28; H, 4.43; N, 11.72; S, 6.71. Found: C, 60.53; H, 4.40; N, 11.57; S, 6.73%. Λ_{M} (in acetonitrile) = $6.0 \Omega^{-1} \text{ cm}^2 \text{ mol}^{-1}$. IR (cm^{-1}): 3062w br $\nu(\text{N-H})$, 1592 m $\nu(\text{C=N})$, 1562s $\nu(\text{C=O})$, 1528 m $\nu(\text{C=C})$, 1522 $\nu(\text{C=N})$, 1481vs $\nu_{\text{as}}(\text{SO}_2)$, 1475 $\nu(\text{C-N})$, 1164vs $\nu_{\text{s}}(\text{SO}_2)$, 1079 m $\nu(\text{N-N})$, 551s $\nu(\text{Zn-N})$, 430 m $\nu(\text{Zn-O})$. $^1\text{H NMR}$ (CDCl_3 with 0.05% v/v TMS, 500 MHz, 298 K): δ_{H} 1.22 (s, 3H, H_2O), 2.45 (s, 3H, H19), 6.61 (sbr, 1H, N4 - H), 6.78 (d, 2H, H17,17'), 7.19 (d, 2H, H12,12'), 7.24 (t, 1H, H9), 7.42 (t, 2H, H8,8'), 7.45 (m, 3H, H13,13', H14), 7.83 (d, 2H, H7,7'), 7.98 (d, 2H, H16,16'). $^{13}\text{C NMR}$ (CDCl_3 , 125 MHz, 298 K): δ_{C} 15.4 (C20), 21.7 (C19), 98.3 (C4), 121.3 (C11), 125.0 (C17,17'), 127.2 (C9), 128.6 (C7,7'), 128.7 (C16,16'), 129.4 (C12,12'), 129.9 (C8,8'), 130.2 (C13,13'), 132.1 (C6), 133.5 (C14), 139.0 (C15), 145.0 (C3), 149.0 (C18), 162.8 (C10), 167.6 (C5). $\{^1\text{H},^{15}\text{N}\}_{\text{gs-HSQC}}$ NMR (CDCl_3 , 51 MHz, $^3\text{J}(\text{N-H}) = 3$ Hz, 298 K): δ_{N} 151.1 (N4). $\{^1\text{H},^{15}\text{N}\}_{\text{gs-HMBC}}$ NMR (CDCl_3 , 51 MHz, $^3\text{J}(\text{N-H}) = 3$ Hz, 298 K): δ_{N} 192.9 (N1), 276.4 (N2), N3 not observed. Stability Test: compound 2 was dissolved in DMSO-d_6 and its $^1\text{H NMR}$ spectrum immediately recorded. After 5 days the spectrum was unchanged. ESI-MS (+) CH_3CN (m/z, relative intensity %): 957 [30] $[\text{Zn}(\text{HL}^2)(\text{H}_2\text{L}^2)]^+$; 979 [30] $[\text{Zn}(\text{HL}^2)_2 + \text{Na}^+]$; 1467 [30] $[\text{Zn}_2(\text{HL}^2)_3]$.

$[\text{Zn}(\text{HL}^3)_2(\text{H}_2\text{O})_2]$, (3). Complex 3 was synthesized by mixing $\text{Zn}(\text{O}_2\text{CCH}_3)_2 \cdot 2\text{H}_2\text{O}$ (0.022 g, 0.1 mmol) with the proligand H_2L^3 (0.083 g, 0.2 mmol) in 30 ml of methanol, with a procedure similar to that of 1. It is soluble in DMSO, DMF, acetone, acetonitrile, chlorinated solvents and slightly soluble in methanol. Yield 83%. M.p. 232–236 °C. Elemental Analyses Calculated for

$C_{46}H_{40}N_{10}O_8Zn$ (m.w. 924.2): C, 59.65; H, 4.35; N, 15.12. Found: C, 59.40; H, 4.23; N, 14.89%. Λ_M (in acetonitrile) = $9.0 \Omega^{-1} \text{ cm}^2 \text{ mol}^{-1}$. IR (cm^{-1}): 3314 m $\nu(\text{H}_2\text{O})$, 3190w br $\nu(\text{N-H})$, 3062w br $\nu(\text{N-H})$, 1598s $\nu(\text{C=N})$, 1575 m $\nu(\text{C=O})$, 1558 m $\nu(\text{C=C})$, 1526 m $\nu(\text{C=C})$, 1480vs $\nu_{\text{as}}(\text{NO}_2)$, 1319s, 1300vs $\nu_{\text{s}}(\text{NO}_2)$, 1110 m $\nu(\text{C-N})$, 961 m $\nu(\text{N-N})$, 511 m $\nu(\text{Zn-N})$, 475s $\nu(\text{Zn-O})$. ^1H NMR (CDCl_3): δ_{H} , 1.57s (4H, H_2O); 1.27s (6H, H_{19}); 6.31 (sbr, 1H, $\text{N}_4 - \text{H}$), 6.68 (d, 2H, $\text{H}_{17,17'}$), 7.14 (d, 2H, $\text{H}_{12,12'}$), 7.25 (t, 1H, H_9), 7.41 (t, 2H, $\text{H}_{8,8'}$), 7.45 (m, 3H, $\text{H}_{13,13'}$, H_{14}), 7.77 (d, 2H, $\text{H}_{7,7'}$), 7.97 (d, 2H, $\text{H}_{16,16'}$). ^{13}C NMR (CDCl_3): δ_{C} , 15.2 (C_{19}), 98.5 (C_4), 112.6 ($\text{C}_{17,17'}$), 125.7 ($\text{C}_{7,7'}$), 126.2 (C_9), 126.7 ($\text{C}_{16,16'}$), 127.7 (C_{14}), 128.8 ($\text{C}_{12,12'}$), 129.2 ($\text{C}_{8,8'}$), 130.6 ($\text{C}_{13,13'}$), 133.0 (C_6), 140.9 (C_{15}), 150.8 (C_{18}), 162.2 (C_{11}), C_3 , C_5 and C_{10} not observed. $\{^1\text{H}, ^{15}\text{N}\}_{\text{gs-HSQC}}$ NMR (CDCl_3 , 51 MHz, $^3\text{J}(\text{N-H}) = 3 \text{ Hz}$, 298 K): δ_{N} 125.2 (N_4). $\{^1\text{H}, ^{15}\text{N}\}_{\text{gs-HMBC}}$ NMR (CDCl_3 , 51 MHz, $^3\text{J}(\text{N-H}) = 3 \text{ Hz}$, 298 K): δ_{N} 197.4 (N_1), N_2 and N_3 not observed. ESI-MS (+) CH_3CN (m/z, relative intensity %): 478 [25] $[\text{Zn}(\text{HL}^3)]^+$; 891 [50] $[\text{Zn}(\text{HL}^3)(\text{H}_2\text{L}^3)]^+$; 913 [20] $[\text{Zn}(\text{HL}^3)_2 + \text{Na}^+]$.

$[\text{Zn}(\text{HL}^4)_2]_n$, (4). Complex 4 was synthesized by mixing $\text{Zn}(\text{O}_2\text{CCH}_3)_2 \cdot 2\text{H}_2\text{O}$ (0.022 g, 0.1 mmol) with the proligand H_2L^4 (0.085 g, 0.2 mmol) in 30 ml of methanol, with a procedure similar to that of 1, however it immediately precipitates from the solution. It is soluble in DMSO, DMF, acetone, acetonitrile, and chlorinated solvents. Yield 85%. M.p. 251–253 °C. Elemental Analyses Calculated for $C_{48}H_{40}N_{10}O_6Zn$ (m.w. 918.2): C, 62.78; H, 4.39; N, 15.25%. Found: C, 62.44; H, 4.20; N, 15.06%. Λ_M (in acetonitrile) = $6.0 \Omega^{-1} \text{ cm}^2 \text{ mol}^{-1}$. IR (cm^{-1}): 3275 m $\nu(\text{N-H})$, 3075w br $\nu(\text{N-H})$, 1593s $\nu(\text{C=N})$, 1566s $\nu(\text{C=O})$, 1520 m $\nu(\text{C=C})$, 1478vs $\nu_{\text{as}}(\text{NO}_2)$, 1321vs, 1303s $\nu_{\text{s}}(\text{NO}_2)$, 1100 m $\nu(\text{N-N})$, 548 m $\nu(\text{Zn-N})$, 430 m $\nu(\text{Zn-O})$. ^1H NMR (CDCl_3): δ_{H} , 2.29s (s, 3H, H_2O), 4.15 (s, 2H, H_{11}) 6.14 (sbr, 1H, $\text{N}_4 - \text{H}$), 6.44 (d, 2H, $\text{H}_{17,17'}$), 7.02 (d, 2H, $\text{H}_{13,13'}$), 7.25 (m, 3H, H_9 , $\text{H}_{8,8'}$), 7.41 (m, 3H, $\text{H}_{14,14'}$, H_{15}), 7.77 (d, 2H, $\text{H}_{7,7'}$), 7.93 (d, 2H, $\text{H}_{16,16'}$). ^{13}C NMR (CDCl_3): δ_{C} , 17.3 (C_{20}), 35.9 (C_{11}), 98.6 (C_4), 112.4 ($\text{C}_{17,17'}$), 121.2 ($\text{C}_{7,7'}$), 125.6 ($\text{C}_{13,13'}$), 125.9 (C_{16}), 127.4 (C_9), 127.8 ($\text{C}_{8,8'}$), 127.9 (C_{12}), 128.8 ($\text{C}_{14,14'}$), 128.9 (C_{15}), 129.3 ($\text{C}_{18,18'}$), 134.8 (C_6), 141.0 (C_3), 151.2 (C_{19}), 162.5 (C_{10}), 178.3 (C_5). $\{^1\text{H}, ^{15}\text{N}\}_{\text{gs-HSQC}}$ NMR (CDCl_3 , 51 MHz, $^3\text{J}(\text{N-H}) = 3 \text{ Hz}$, 298 K): δ_{N} N_4 not observed. $\{^1\text{H}, ^{15}\text{N}\}_{\text{gs-HMBC}}$ NMR (CDCl_3 , 51 MHz, $^3\text{J}(\text{N-H}) = 3 \text{ Hz}$, 298 K): δ_{N} N_1 , N_2 and N_3 not observed. ESI-MS (+) CH_3CN (m/z, relative intensity %): 492 [20] $[\text{Zn}(\text{HL}^4)]^+$; 919 [40] $[\text{Zn}(\text{HL}^4)(\text{H}_2\text{L}^4)]^+$; 941 [30] $[\text{Zn}(\text{HL}^4)_2 + \text{Na}^+]$.

$[\text{Zn}(\text{HL}^5)_2(\text{H}_2\text{O})_2]$ (5). Complex 5 was synthesized by mixing $\text{Zn}(\text{O}_2\text{CCH}_3)_2 \cdot 2\text{H}_2\text{O}$ (0.022 g, 0.1 mmol) with the proligand H_2L^5 (0.086 g, 0.2 mmol) in 30 ml of methanol, with a procedure similar

to that of 1. It is soluble in DMSO, DMF, acetone, acetonitrile, chlorinated solvents, and methanol. Yield 92%. M.p. 154–156 °C. Elemental Analyses Calculated for $C_{46}H_{52}F_6N_8O_4Zn$ (m.w. 960.0): C, 57.53; H, 5.46; N, 11.67%. Found: C, 57.15; H, 5.42; N, 11.38%. Λ_M (in acetonitrile) = 11.0 $\Omega^{-1} \text{ cm}^2 \text{ mol}^{-1}$. IR (cm^{-1}): 3540w br $\nu(\text{H}_2\text{O})$, 3304w $\nu(\text{N-H})$, 1593s $\nu(\text{C=N})$, 1565s $\nu(\text{C=O})$, 1525 m $\nu(\text{C-N})$, 1321vs $\nu_s(\text{CF}_3)$, 1100s $\nu_{\text{as}}(\text{CF}_3)$, 1064s $\nu_s(\text{CF}_3)$, 981 $\nu(\text{N-N})$, 549 m $\nu(\text{Zn-N})$, 425 m $\nu(\text{Zn-O})$. $^1\text{H NMR}$ (CDCl_3 with 0.05% v/v TMS, 500 MHz, 298 K): δ_{H} 0.97 (s, 9H, H13,13',13''), 1.60s (s, 2H, H₂O), 2.33 (s, 3H, H19), 2.82 (s br, 2H, H11), 5.98 (s br, 1H, N4 - H), 6.43 (d, 2H, H15,15'), 7.24 (t, 1H, H9), 7.35 (d, 2H, H16,16'), 7.46 (t, 2H, H8,8'), 8.01 (d, 2H, H7,7'). $^{13}\text{C NMR}$ (CDCl_3 , 125 MHz, 298 K): δ_{C} 18.0 (C19), 30.4 (C13,13',13''), 34.7 (C12), 40.6 (C11), 99.2 (C4), 114.3 (C15,15'), 120.4 (C7,7'), 123.5q ($^2J_{\text{C-F}} = 33.0 \text{ Hz}$, C17), 124.2q ($^1J_{\text{C-F}} = 271.3 \text{ Hz}$, C18), 125.2 (C9), 126.4q ($^3J_{\text{C-F}} = 3.9 \text{ Hz}$, C16,16'), 128.7 (C8,8'), 139.0 (C6), 147.8 (C3), 149.1 (C14), 161.9 (C10), 180.1 (C5). $^{19}\text{F NMR}$ (CDCl_3): δ_{F} , -61.45. $\{^1\text{H}, ^{15}\text{N}\}$ gs-HSQC NMR (CDCl_3 , 51 MHz, $^3J(\text{N-H}) = 3 \text{ Hz}$, 298 K): δ_{N} 120.0 (N4). $\{^1\text{H}, ^{15}\text{N}\}$ gs-HMBC NMR (CDCl_3 , 51 MHz, $^3J(\text{N-H}) = 3 \text{ Hz}$, 298 K): δ_{N} 274.1 (N2), N1 and N3 not observed. ESI-MS (+) CH_3CN (m/z, relative intensity %): 925 [20] $[\text{Zn}(\text{HL}^5)(\text{H}_2\text{L}^5)]^+$.

2.2.3 Structural characterization by X-ray diffraction

X-ray data collection of suitable single crystals was done on a Bruker D8 VENTURE area detector equipped with graphite monochromated Mo-K α radiation ($\lambda = 0.71073 \text{ \AA}$) by applying the ω -scan method. The data reduction was performed with the APEX3 suite^[266] and corrected for absorption using SADABS^[267]. The final structures were solved using SHELXT^[268] and refined on F2 by a full-matrix least-square technique using anisotropic displacement parameters^[269] by means of the Olex2 v1.3 crystallographic package and the SHELXL-2018 program^[268]. All hydrogen atoms were included as fixed contributions riding on attached atoms with isotropic thermal displacement parameters 1.2 or 1.5 times those of the respective atom. In complex **2**, due to the disorder within the voids, the SQUEEZE procedure implemented in PLATON program was used during the refinement and two crystallization methanol molecules were removed from the structure. In addition, in this structure, one phenyl ring is disordered over two alternate positions, so it was refined with occupancies of 40% and 60% for all atoms and anisotropic displacement parameters of the ring.

2.2.4 Theoretical calculations

The electronic structure and geometries of the proligands H_2L^2 , H_2L^4 and H_2L^5 , their tautomers and anions, $[HL^n]^-$, and their zinc complexes were investigated by using density functional theory at the B3LYP level^{[270],[271]}. For the proligands and their corresponding anions the 6-311G** basis set was used for the optimization, while for the Zn complexes the optimization was carried out using 6-311G*. Molecular geometries were optimized without symmetry restrictions. Frequency calculations were carried out at the same level of theory to identify all stationary points as minima (zero imaginary frequencies) and to provide the thermal correction to free energies at 298.15 K and 1 atm. Solution-phase SCF energies were calculated by a single-point calculation on the in vacuum optimized structure using the CPCM solvation model in chloroform^[266]. Gibbs free energies in chloroform solution were estimated from the equation $G_{\text{solv}} = E_{\text{solv}} + (G_{\text{gas}} - E_{\text{gas}})$. The GIAO method was used for the NMR calculations (1H , ^{13}C and ^{15}N NMR isotropic shielding tensors), which were carried out at the 6-311 + G(2d,p) level of theory. The computed IR spectra were scaled by a factor of 0.96^{[267],[268]}. The DFT calculations were executed using the Gaussian 09 program package^[269].

2.2.5 Antibacterial activity

The antibacterial activity of the ligands H_2L^1 – H_2L^5 and of the Zn(II) complexes 1–5 was investigated against Gram-positive bacteria, *Staphylococcus aureus* (*S. aureus*) ATCC 25923 and Gram-negative, *Escherichia coli* (*E. coli*) ATCC 25922. Bacteria were grown aerobically at 37 °C overnight using Tryptone Soya Broth (OXOID) as the growth medium. Bacteria proliferation was monitored by measuring the increase of optical density in the culture suspension at 600 nm (OD600). The enriched culture (log phase) obtained was further diluted to 10⁶ CFU mL⁻¹ concentration. A preliminary bacterial growth inhibition (BGI) analysis was carried out by using the Agar diffusion method with a fixed concentration of 2 mg mL⁻¹ of the ligands and 4 mg mL⁻¹ of the Zn(II) complexes (both corresponding to ~5 μmol mL⁻¹). A loop full of the given test strain (*E. coli* and *S. aureus*) was inoculated in 10 mL of N-broth (nutrient broth) and incubated for 24 h in an incubator at 37 °C in order to activate the bacterial strain. The various compounds were weighed into Eppendorf content and suspended in autoclaved physiological solution, to which 1 mL of the enriched culture was then added (reaching the concentration of 10⁶ CFU mL⁻¹) and kept on an IKA KS 130 BASIC platform shaker for 24 hours at slow speed. The final solution was

included uniformly into Petri dishes containing Plate Count Agar (OXOID). Adopting the same procedure, a strain without treatment were used as negative control. The tests were carried out at different time intervals (0, 2, 4, 8, 12, 24 hours) for viability measurements over time. The bacterial viability was reported as Growth Rate (%) using the following formula: Percentage of cell viability (%) = $(\text{CFU } t_x / \text{CFU } t_0) \times 100$ (where t_0 is the time zero at the beginning of the experiment and t_x is a specific time in hours of the experiment). The growth curves of *E. coli* and *S. aureus* without antibacterial agents were also measured as blanks^[272]. All tests were done in triplicate^[273].

2.2.6 Reactive oxygen species (ROS) detection assay

To better evaluate the antibacterial activity of such compounds, the test for ROS measurement was carried out against the compounds **4** and **5**, that showed better bacterial inhibition. To quantify the ROS generated in our system, the 2',7'-dichlorofluorescein diacetate (DCFDA) assay was performed. The test protocol is based on the spread of 20 μL of DCFDA in the bacterial cultures in the range of $1-3 \times 10^6 \text{ CFU mL}^{-1}$ for 30 minutes at 37 °C. Then 10 μL are added to the Eppendorf containing 4 mg of **4** and **5** respectively, suspended in 1 mL of physiological solution. 100 μL of each Eppendorf were transferred to a 96-well plate in triplicate in the dark and ROS generation was assessed for the first two and four hours. Maintaining the same procedure, an untreated sample strain was used as a control (blank). Fluorescence from each sample well was read using the FLUOstar Omega fluorescence cytometer from BMG LABTECH at 485/20 nm and 528/20 nm wavelengths for excitation and emission respectively. The average of the triplicate was calculated and reported as the intensity of fluorescence in arbitrary unit (a.u.).

2.2.7 Propidium iodide (PI) – viability assay

To assess the viability of bacteria treated with compounds **4** and **5**, the fluorescent PI staining assay was carried out, since it allows to evaluate the level of damage related to membrane permeability. A suspension (10^6 CFU mL^{-1}) of *E. coli* and *S. aureus*, treated with 4 mg of compounds **4** and **5**, were incubated for a period of 24 h at 37 °C. After 4 h, 8 h, 12 h, and 24 h, 100 μL of the content was transferred in triplicate into 96-well plate in the dark and 1,5 μL of Propidium Iodide (PI) was added in each well. Maintaining the same procedure, an untreated sample strain was used as a control (blank). Fluorescence emitted by the cells was read using the FLUOstar Omega fluorescence cytometer from BMG LABTECH at 485/20 nm and 528/20 nm wavelengths for

excitation and emission respectively. The average of the triplicate was calculated and reported as the intensity of fluorescence in arbitrary unit (a. u.).

2.2.8 Confocal laser scanning microscopy (CLMS) study

To determine the damaging effect of **4** and **5** on the cell membranes of *S. aureus* and *E. coli*, CM analysis was carried out with LIVE/DEAD® BacLight™ Bacterial Viability Kits (Invitrogen), which utilize mixtures of SYTO®9 green-fluorescent nucleic acid stain and propidium iodide (PI) red-fluorescent nucleic acid stain. Briefly, a bacterial suspension in the range of 1×10^8 CFU mL⁻¹ (~0.03 OD₆₇₀) for *E. coli* and 1×10^7 CFU mL⁻¹ (~0.15 OD₆₇₀) for *S. aureus* were treated with 4 mg of **4** and **5** during the logarithmic growth phase for 4 h. After the incubation period, suspensions were concentrated by centrifugation at 10000g for 10–15 minutes, then the supernatant was removed, and the pellet resuspended in 0.85% NaCl solution. Afterwards, equal volumes of Syto-9 and Propidium iodide were added to all samples and incubated for 15 min in the absence of light. Samples were then fixed between a slide and an 18 mm square coverslip to observe the fluorescence under confocal microscope (Nikon ECLIPSE Ti). The control assay was conducted without treatment. The excitation/emission maxima for these dyes are about 480/500 nm for SYTO 9 stain and 490/635 nm for PI.

2.2.9 Scanning electron microscopy (SEM) study

The morphology of the bacterial cells after treating with **4** and **5** was determined by SEM (Sigma 300, Zeiss) operating at 15.0 kV, Bruker. For SEM sample preparation, log phase cells of *E. coli* and *S. aureus* (10⁶ CFUs) were incubated with 4 mg of complexes **4** and **5** for 4 hours at 37 °C. After incubation period, bacterial strains were centrifugated (2000g × 5 min), washed thrice with physiological solution and fixed with 200 µL of 2.5% (v/v) glutaraldehyde solution for 2 hours on glass slide. The fixed pellets were washed twice with physiological solution, then were immersed in a solution with increasing concentrations of ethanol (10, 30, 50, 70, 90 and 100%), 5 min for each concentration. After drying, samples were placed on aluminium stubs using self-adhesive carbon conductive tab and chrome-coated. The untreated bacterial cells were taken as control.

2.3 Results and discussion

2.3.1 Synthesis and spectroscopic characterization of proligands

Proligands H_2L^n ($n = 1-5$) have been prepared following the general procedure described in the introduction by reaction of 4-acyl-5-pyrazolones and monosubstituted hydrazones in ethanol at reflux and stirring for 4 h, illustrated in Chart 34. Proligands H_2L^1 and H_2L^3 were previously reported by our research group and fully characterized in combination with (arene)Ru(II) acceptors^[274]. Proligands H_2L^2 , H_2L^4 and H_2L^5 instead are new. All the compounds have been characterized by means of 1H -NMR, ^{13}C -NMR, ^{15}N -NMR, $\{^1H,^1H\}$ -COSY, $\{^1H,^{13}C\}$ -HSQC, $\{^1H,^{13}C\}$ -HMBC, IR spectroscopy and ESI-MS spectroscopy.

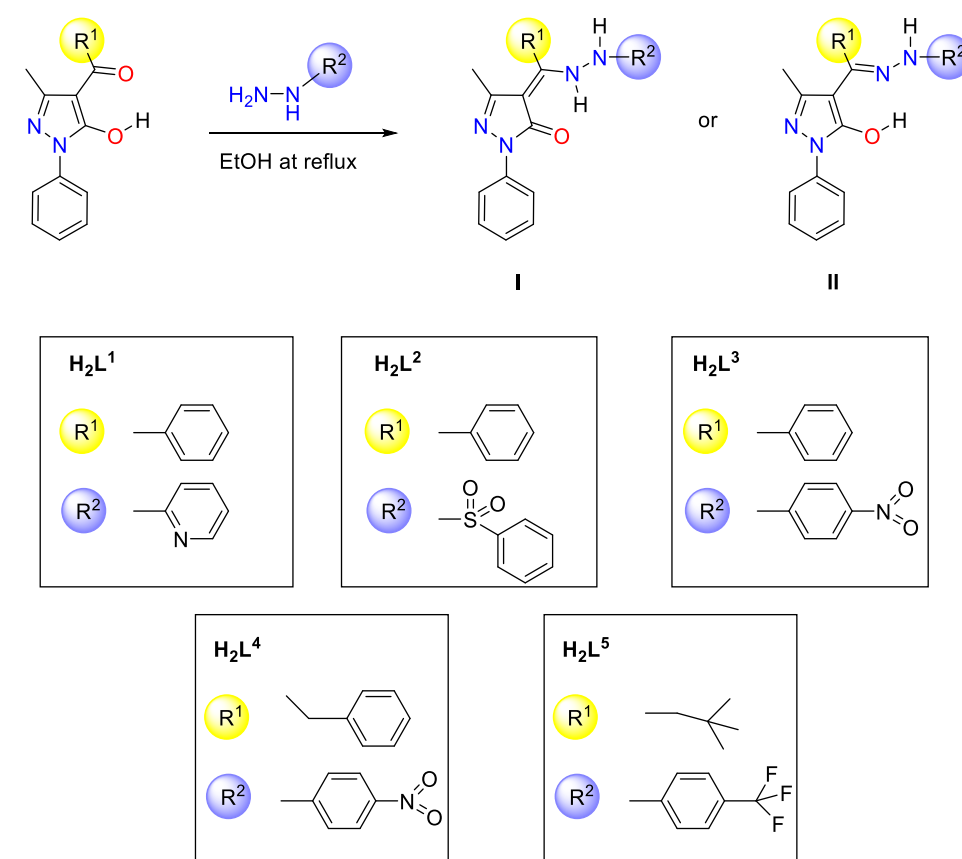


Chart 34. Synthetic procedure for $H_2L^1 - H_2L^5$ proligands. In principle they can exist in two tautomeric forms I or II.

The compounds form as sharp melting solid, soluble in DMSO, DMF, chlorinated solvents, acetone, acetonitrile, and alcohols and only slightly soluble in diethyl ether. In principle the compounds can exist in two different tautomeric forms (I and II in Chart 34) depending on the

electronic features of the two substituents R^1 and R^2 and on the solvent of crystallization^[144]. In particular, H_2L^1 is reported to exist in the solid state as uncommon zwitterionic form, whereas H_2L^3 adopts a N-H,O-H tautomeric form in both solid state and chlorinated solution^[274].

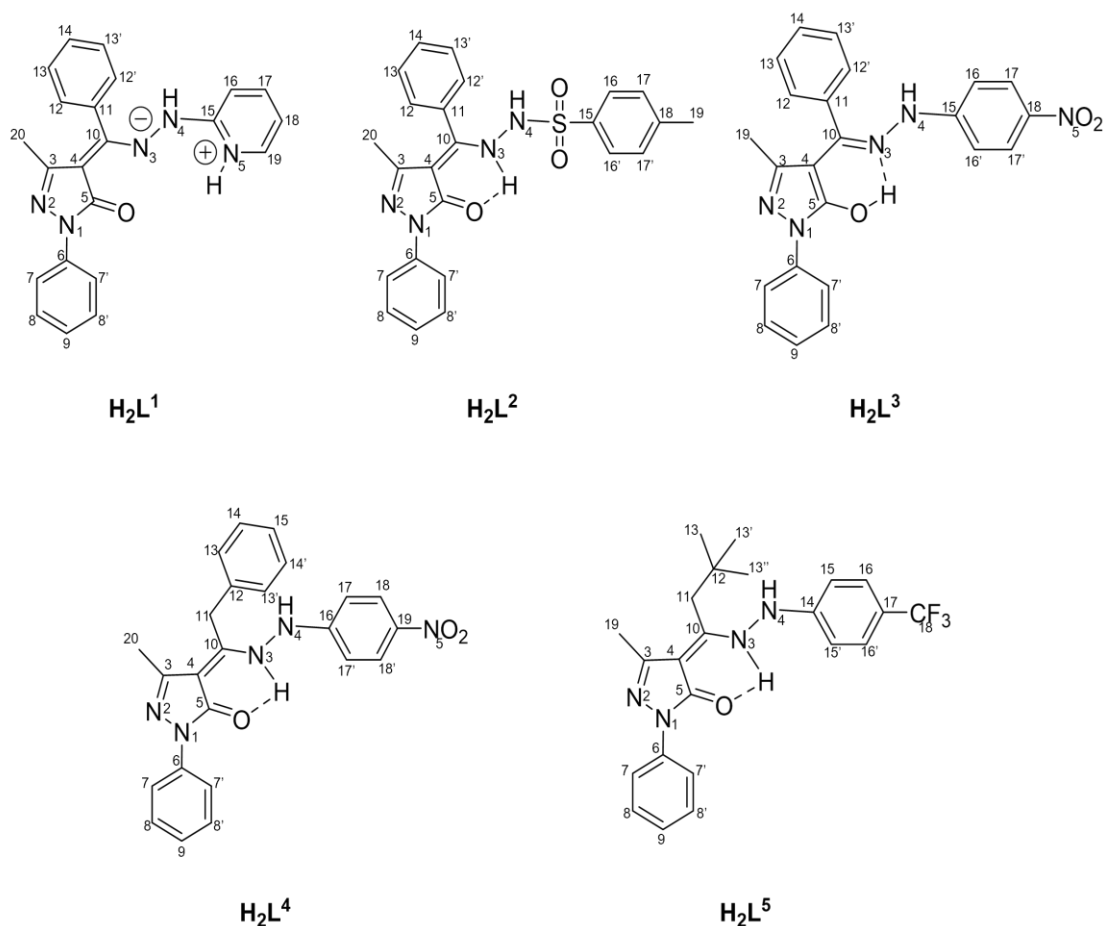


Chart 35. Tautomeric forms in the solid state of $H_2L^1 - H_2L^5$ proligands with numbered atoms.

The novel proligands H_2L^2 , H_2L^4 and H_2L^5 were proved to exist in the N-H,N-H tautomeric form (tautomer I in Chart 34). For the solid state, this is confirmed by the X-ray structures of H_2L^2 and H_2L^4 (that will be discussed in the X-ray diffraction section) and by the IR spectrum of H_2L^5 . From the infrared spectra of the proligands characteristic bands were identified and assigned to the relative mode of vibration also by comparison with computed IR spectra (discussed in the DFT study section). In particular, asymmetric and symmetric stretching modes of the sulfonyl SO_2 group of H_2L^2 were assigned to the bands at 1301 and 1165 cm^{-1} ^{[275],[276]} (Figure 3), the asymmetric and symmetric stretching modes of nitro group NO_2 of H_2L^3 and H_2L^4 ^{[277],[278]} were assigned to the bands in the range of $1490\text{-}1530\text{ cm}^{-1}$ and $1325\text{-}1331\text{ cm}^{-1}$ (Figure 4) and the asymmetric and

symmetric vibration modes of CF_3 group of H_2L^5 were assigned to bands at 1312, 1163, 1112 and 1065 cm^{-1} [279],[280] (Figure 5). Finally the typical $\nu(\text{N-N})$ mode for all proligands was identified in the range $1040\text{-}1120\text{ cm}^{-1}$ [118],[236].

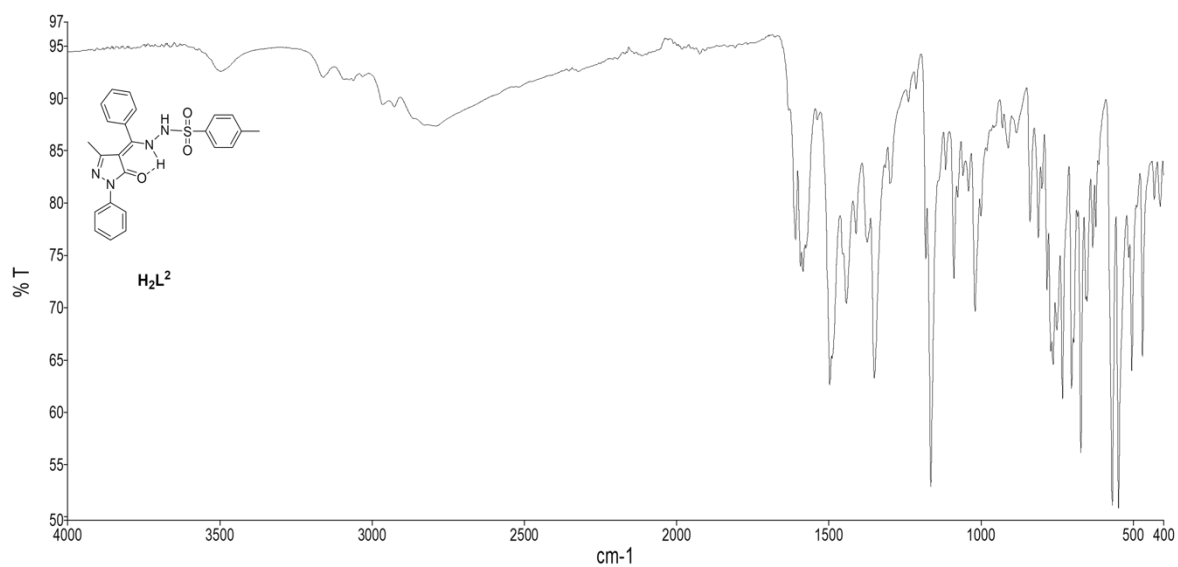


Figure 3. IR spectrum of proligand H_2L^2 .

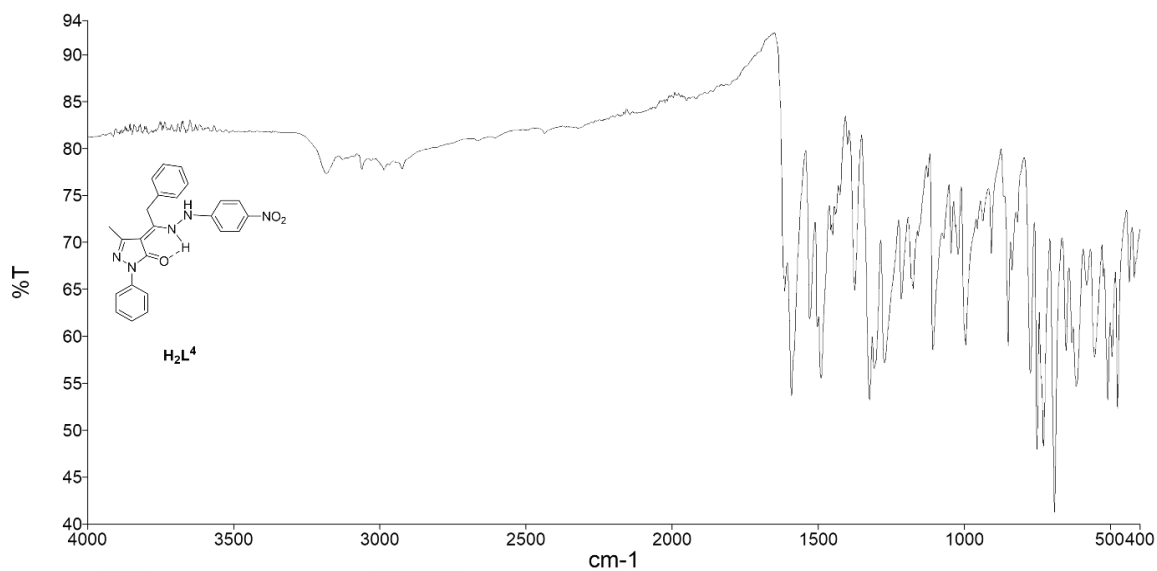


Figure 4. IR spectrum of proligand H_2L^4 .

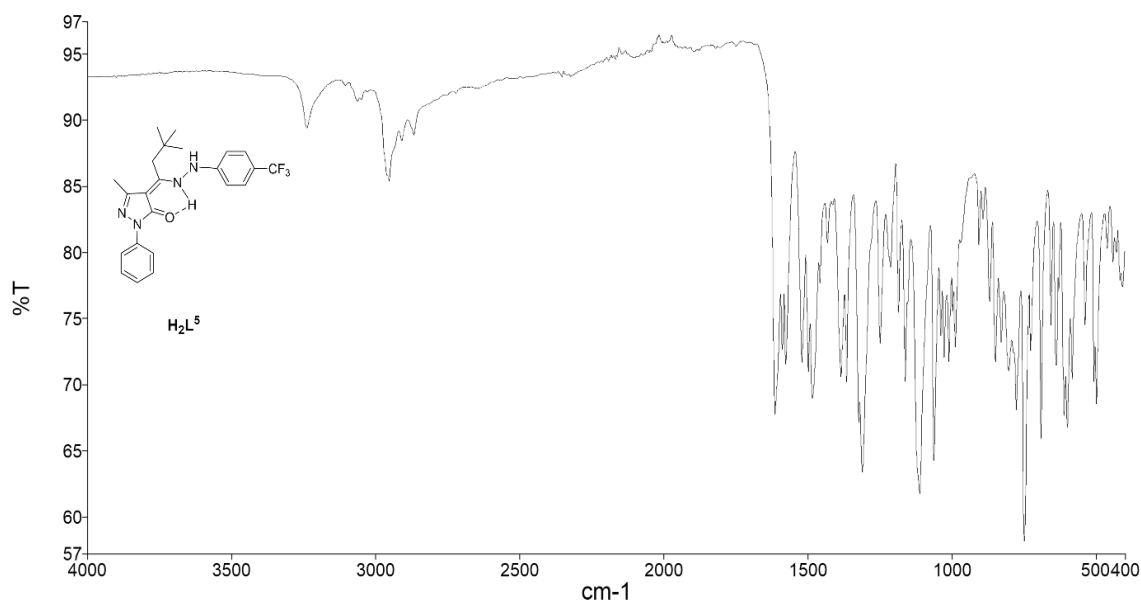


Figure 5. IR spectrum of proligand H_2L^5 .

1H and ^{13}C NMR were assigned based on the 1H - 1H , and one-bond and long-range 1H - ^{13}C couplings, seen in the $\{^1H, ^1H\}$ -COSY, $\{^1H, ^{13}C\}$ -HSQC, and $\{^1H, ^{13}C\}$ -HMBC. Additionally, indirect ^{15}N NMR chemical shifts were assigned based on the $\{^1H, ^{15}N\}$ -HSQC and $\{^1H, ^{15}N\}$ -HMBC for both proligands and complexes **1-5** (see Chart 35 for atoms numeration). Figures 6-12 report all the NMR characterization for the ligand H_2L^2 with assigned resonances as example. Although for H_2L^2 only one NH resonance was observed at 7.20 ppm, the N-H,N-H tautomeric form observed in the X-ray is assumed to be preserved also in solution (see DFT studies), even if in the $\{^1H, ^{15}N\}$ -HSQC NMR only the N4-H direct coupling was displayed. The $\{^1H, ^{15}N\}$ -HMBC spectrum instead allowed to assign the signals of N1, N2 and N4, but also in this case not that of N3. The proton NMR spectra of proligands H_2L^4 and H_2L^5 in deuteriochloroform display broad resonances at 12.40-12.83 and 6.50-6.80 ppm, due to the two types of NH groups, in accordance with the prevalence in solution of N-H,N-H tautomer I. Additionally, in this case the $\{^1H, ^{15}N\}$ -HSQC spectra show the direct coupling signal of both N3-H and N4-H furtherly confirming the hypothesis about the tautomeric form. In the $\{^1H, ^{15}N\}$ -HMBC spectrum, for H_2L^4 , as for H_2L^2 , all the nitrogen atoms could be assigned but the N3, that it is not observed. For H_2L^5 instead also the N3 can be observed in the spectrum. About H_2L^5 it is also possible to see one single resonance in the ^{19}F -NMR suggesting the absence of any other non-reacted species. Furtherly, its ^{13}C -NMR spectrum shows the effect of the coupling between the F atom with the adjacent C atoms: in fact

it is possible to find three quartets with a gradually larger J value from the farther C16 to the closer C18 atoms (see Figure 100 and Figure 101 Supplementary Information).

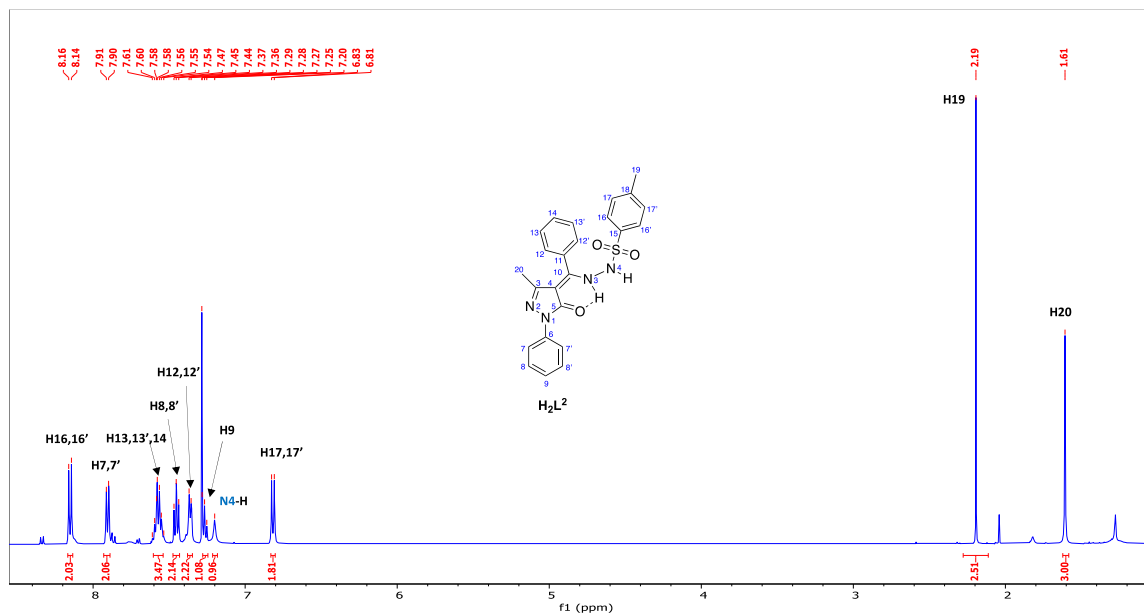


Figure 6. ^1H NMR of proligand H_2L^2 in CDCl_3 at 298 K.

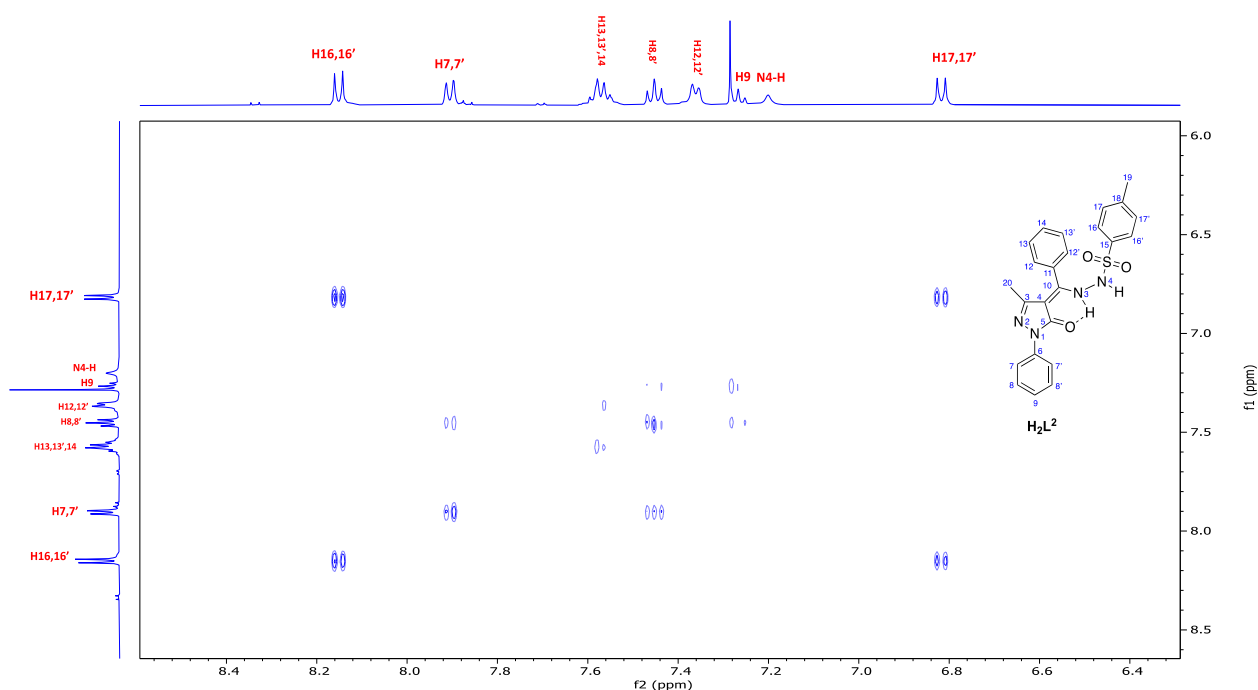


Figure 7. $\{^1\text{H},^1\text{H}\}$ -COSY of proligand H_2L^2 in CDCl_3 at 298 K.

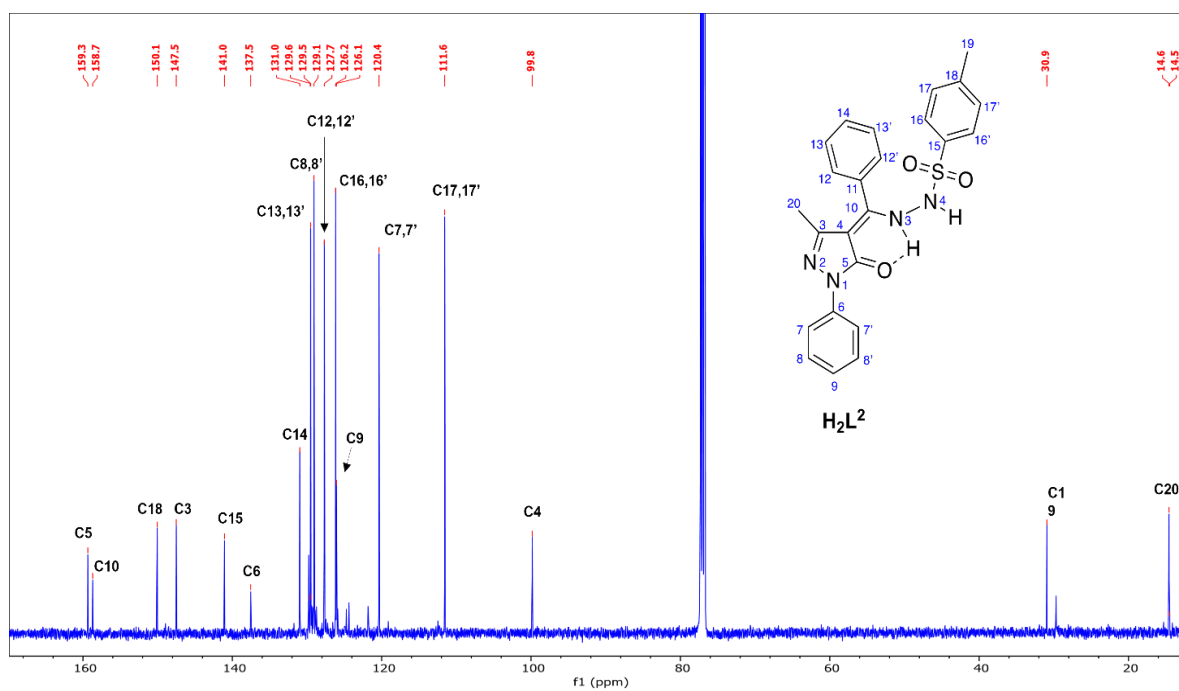


Figure 8. $^{13}\text{C}\{^1\text{H}\}$ NMR of proligand H_2L^2 in CDCl_3 at 298 K.

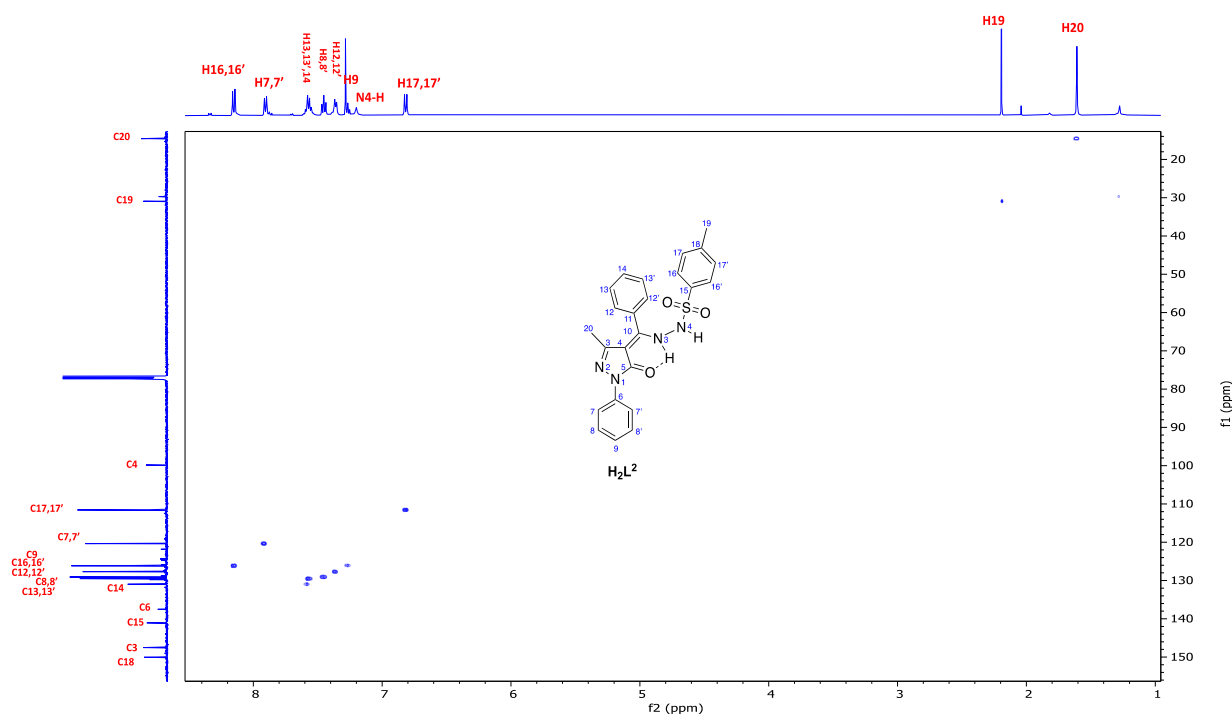


Figure 9. $\{^1\text{H},^{13}\text{C}\}$ -HSQC of proligand H_2L^2 in CDCl_3 at 298 K.

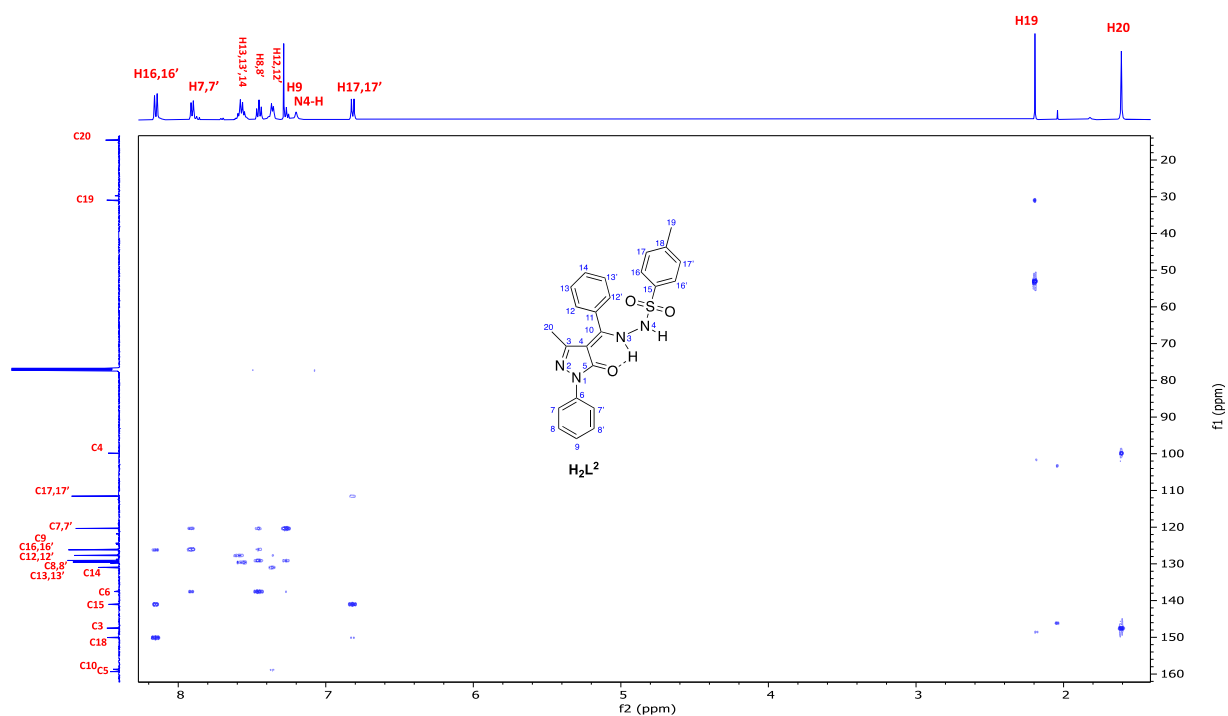


Figure 10. $\{^1\text{H}, ^{13}\text{C}\}$ -HMBC of proligand H_2L^2 in CDCl_3 at 298 K.

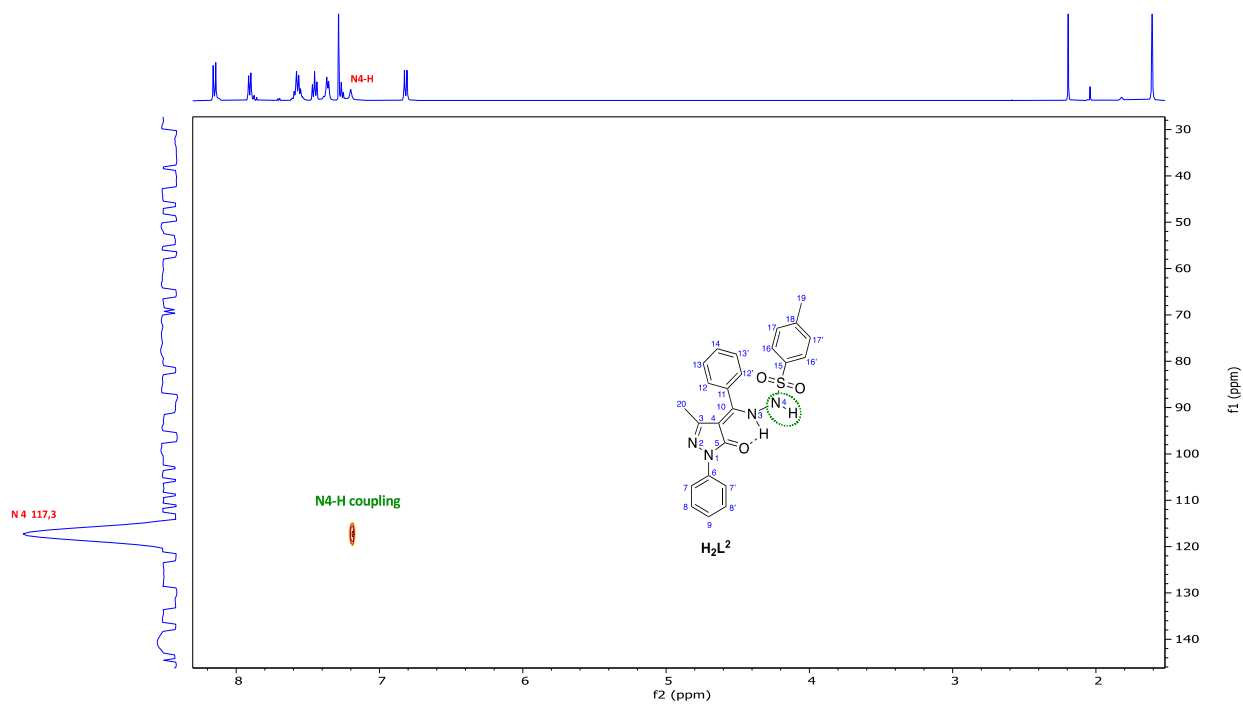


Figure 11. $\{^1\text{H}, ^{15}\text{N}\}$ -HSQC of proligand H_2L^2 in CDCl_3 at 298 K.

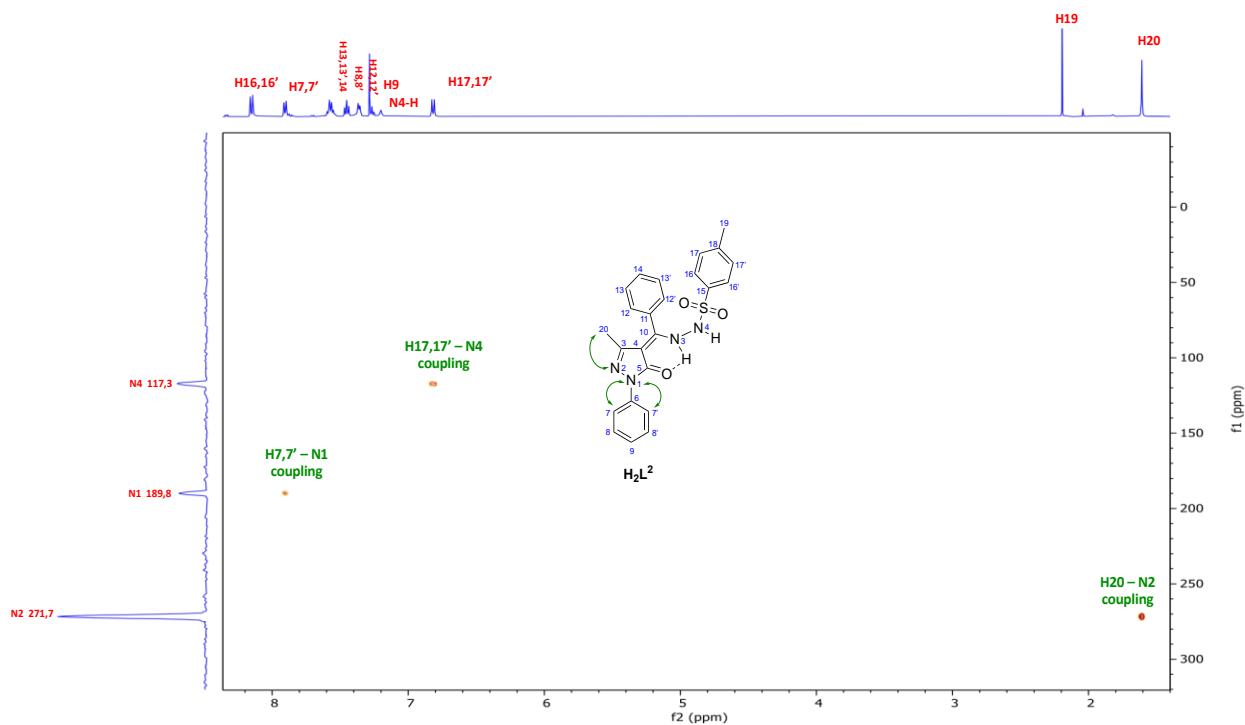


Figure 12. $\{^1\text{H}, ^{15}\text{N}\}$ -HMBC of proligand H_2L^2 in CDCl_3 at 298 K.

2.3.2 Synthesis and spectroscopic characterization of complexes

Complexes **1-5** were synthesized by interaction of $\text{Zn}(\text{O}_2\text{CCH}_3)_2 \cdot 2\text{H}_2\text{O}$ with the proligands H_2L^n , in methanol at room temperature, affording a precipitate that after 24 hours was filtered, washed with Et_2O and dried. The product was then recrystallized from dichloromethane/n-hexane. The compounds are sharp melting solids soluble in most organic solvents, and in the case of **2**, **3** and **5** also quite soluble in methanol, while not soluble at all in water and ethers. All the compounds have been characterized by means of ${}^1\text{H}$ -NMR, ${}^{13}\text{C}$ -NMR, ${}^{15}\text{N}$ -NMR, $\{^1\text{H}, ^1\text{H}\}$ -COSY, $\{^1\text{H}, {}^{13}\text{C}\}$ -HSQC, $\{^1\text{H}, {}^{13}\text{C}\}$ -HMBC, IR spectroscopy and ESI-MS spectroscopy.

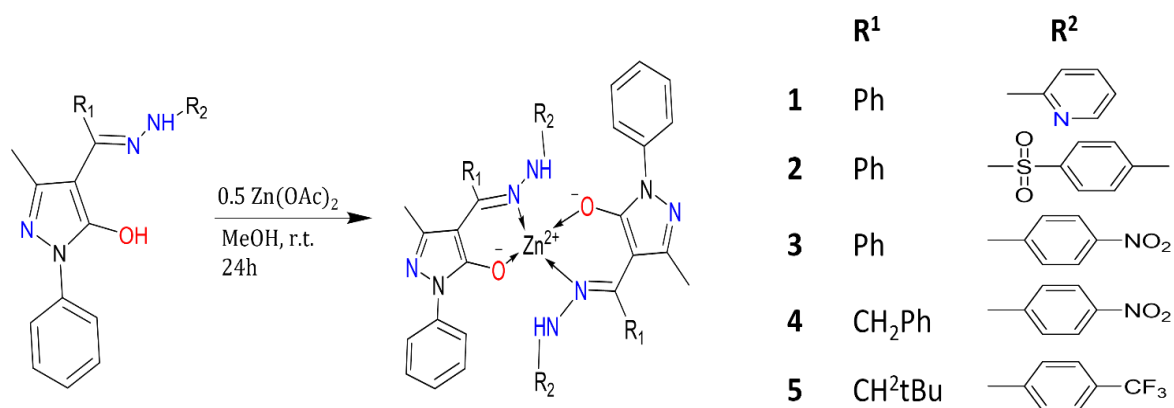


Chart 36. Synthetic procedure for the preparation of complexes 1-5.

All analytical and spectral data are in accordance with the formulation of complexes proposed in Chart 37: while **1** and **2** are mononuclear anhydrous $[\text{Zn}(\text{HL}^1)_2]$ and $[\text{Zn}(\text{HL}^2)_2]$ species, complex **3** and **5** were isolated as diaqua $[\text{Zn}(\text{HL}^n)_2(\text{H}_2\text{O})_2]$ compounds, with two water molecules in the zinc coordination sphere. Unexpectedly, complex **4** is a monodimensional coordination polymer with formula $[\text{Zn}(\text{HL}^4)_2]_n$. While complex **3**, structurally similar to **4**, is quite soluble in methanol and is isolated as a precipitate from methanol only after few hours of reaction, **4** is not soluble at all in methanol, from which it immediately precipitates. The recorded melting point of **4** is higher than that of **3** of about 20 °C, in accordance with a different solid-state structure. Conductivity measurements in acetonitrile indicated that complexes **1-5** are stable and do not dissociate in solution at room temperature.

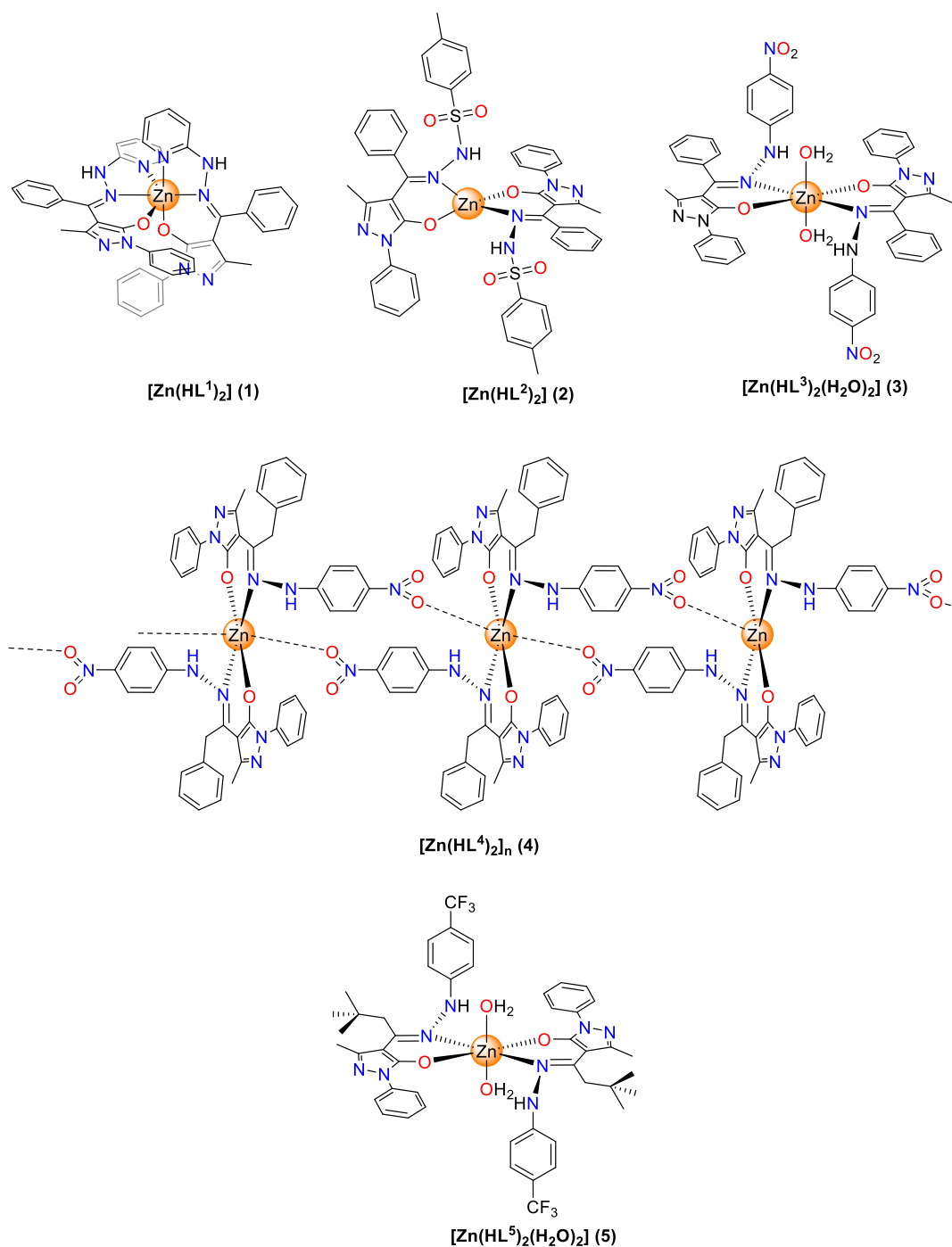


Chart 37. Proposed chemical structures of complexes 1-5.

The IR spectra of **1-5** provide valuable information about the nature of the functional group coordinated to the zinc atom. However, the spectra of proligands are quite complex, especially in the 1500-1650 cm^{-1} region for the presence of C=O, C=C, and more than one C=N in their structure, thus definitive assignment are not straightforward. An attempt to assign some bands has been made on the basis of previous literature on similar chemical systems and DFT calculations.

The $\nu(\text{C}=\text{O})$ band at 1641 cm^{-1} for the free proligand H_2L^1 is shifted upon coordination, which suggests involvement of the keto group of a pyrazolone ring in coordination^[274] (Figure 13). The strong bands falling between 1626 and 1600 cm^{-1} in the spectra of the other free proligands, which are characteristic of the $\nu(\text{C}=\text{N})$ azomethine group, are shifted to lower wavenumbers in the spectra of complexes, implying the coordination of the ligand through azomethine nitrogen^{[281]–[283]}. Additionally, a medium and broad band at circa $3300\text{--}3400\text{ cm}^{-1}$ in the spectra of dihydrate complexes **3** and **5** confirms the presence of water in the zinc environment (Figure 15 and Figure 17). By contrast, in the IR of **4** a medium and sharp band was found at 3275 cm^{-1} , assigned to $\nu(\text{N-H})$ (Figure 16). Finally, the formation of a new band in the low frequencies regions $520\text{--}580\text{ cm}^{-1}$ and $430\text{--}470\text{ cm}^{-1}$ is attributed to $\nu(\text{M-N})$ and $\nu(\text{M-O})$, respectively.

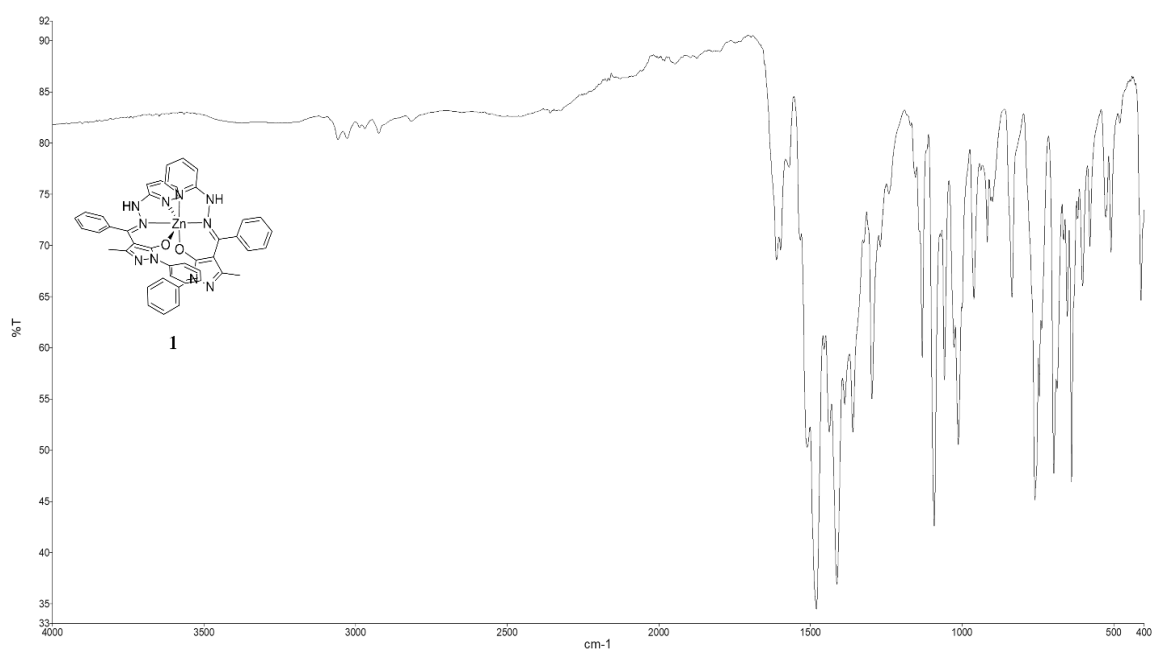


Figure 13. IR spectrum of complex 1.

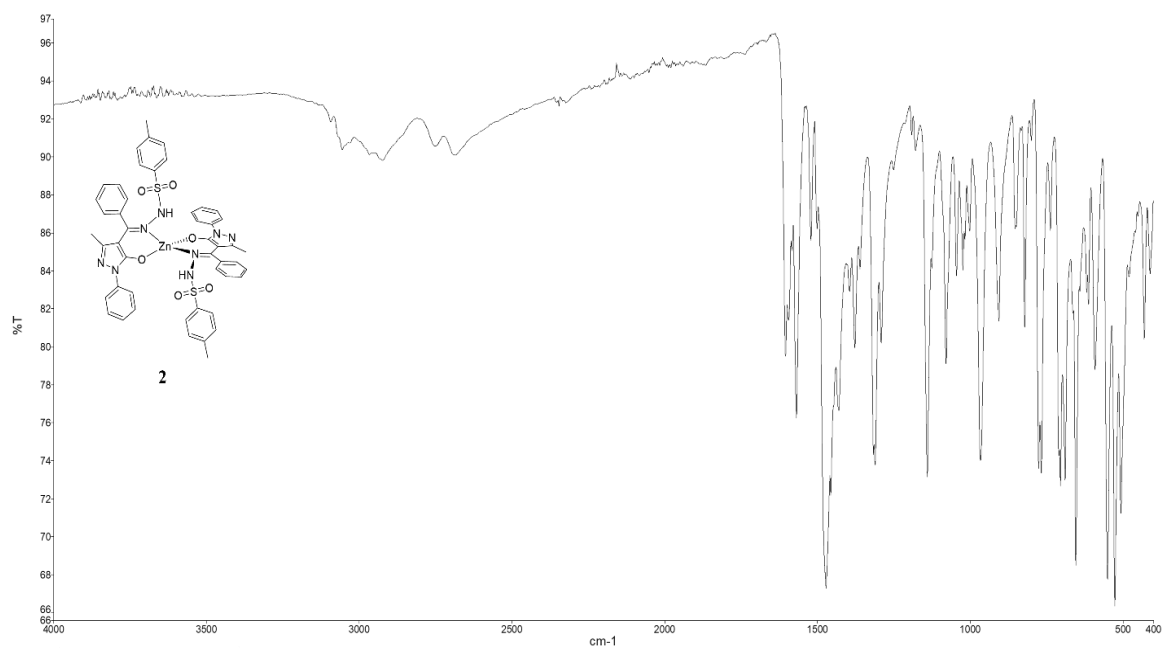


Figure 14. IR spectrum of complex 2.

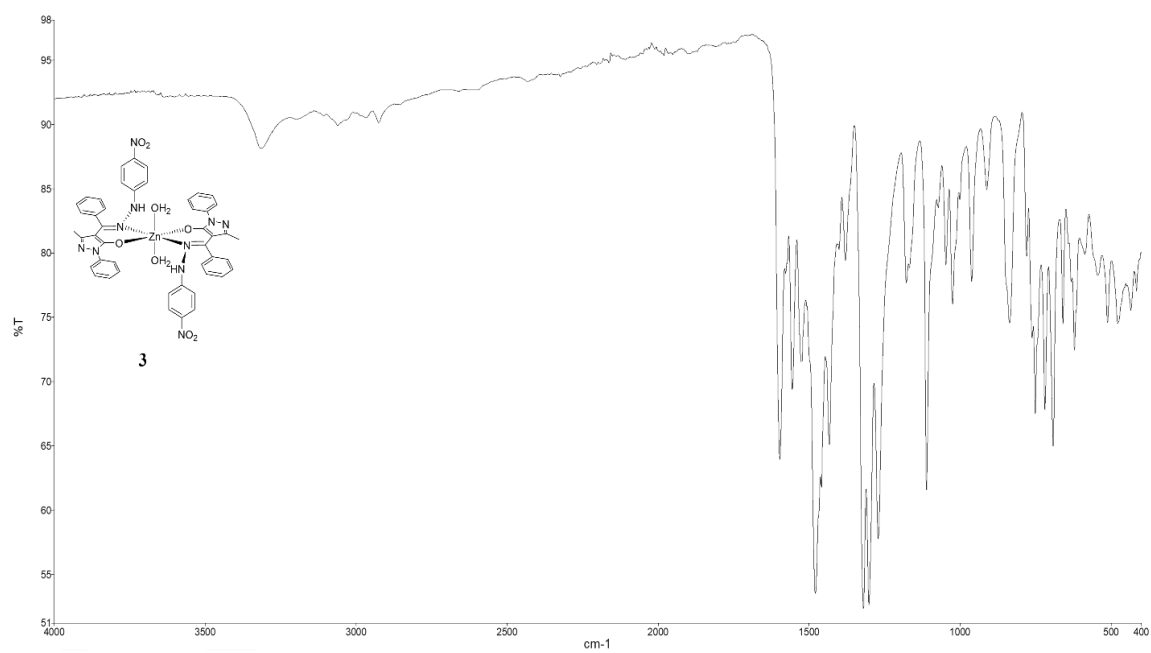


Figure 15. IR spectrum of complex 3.

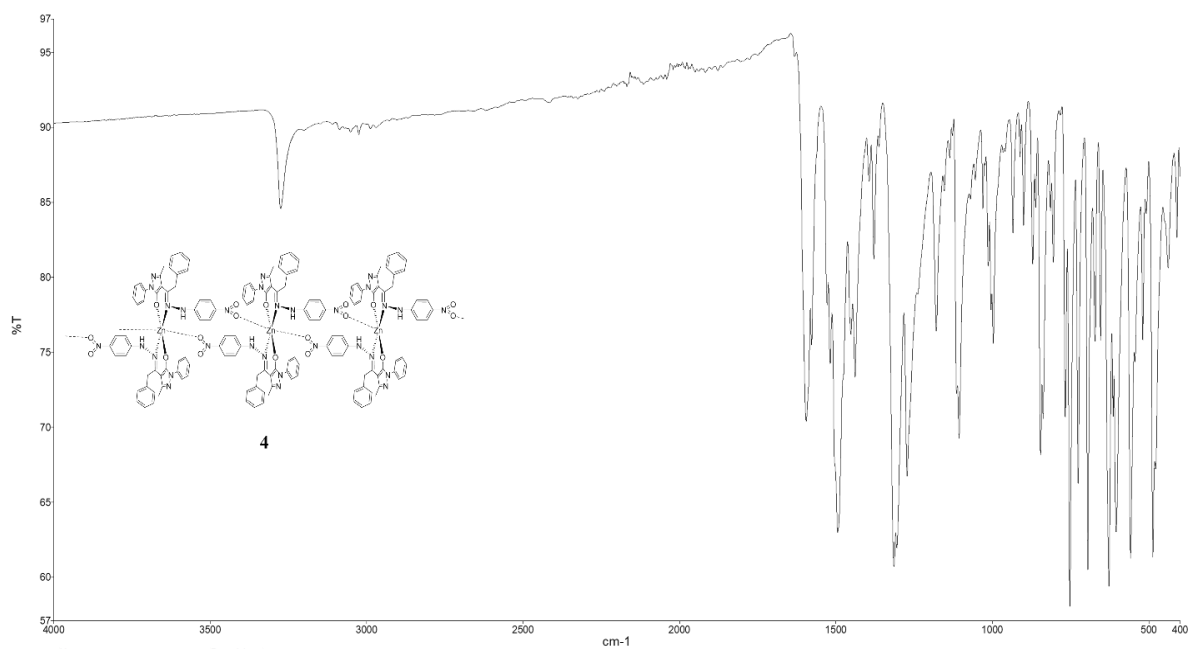


Figure 16. IR spectrum of complex 4.

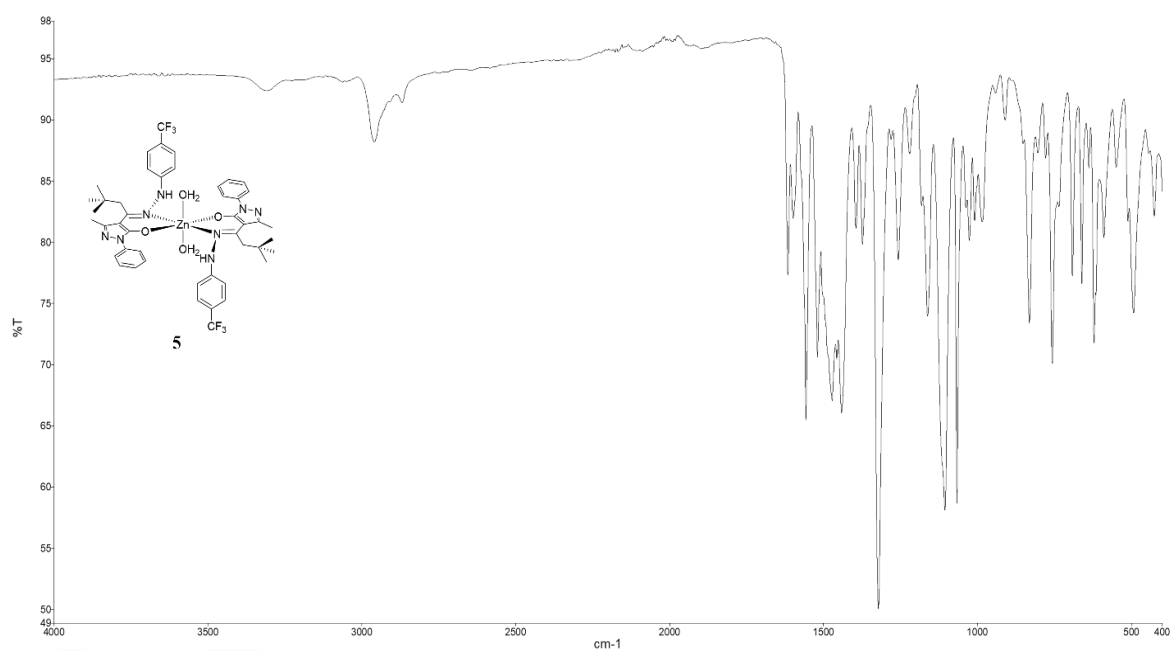


Figure 17. IR spectrum of complex 5.

The electrospray ionization (ESI) mass spectra of **1-5** in positive ion mode, recorded in acetonitrile, show the typical isotopic patterns expected for Zn and display main peaks that corresponds to the

species $[\text{Zn}(\text{HL}^n)]^+$ arising from dissociation of one ligand and/or $[\text{Zn}(\text{HL}^n)(\text{H}_2\text{L}^n)]^+$ due to protonation of one ligand in the zinc complex or also to $[\text{Zn}(\text{HL}^n)_2 + \text{Na}]^+$.

^1H and ^{13}C chemical shifts in the NMR spectra of complexes **1-5** display the expected shift of those resonances due to proton and carbon atoms close to N and O donor atoms involved in bonding to zinc, as showed in NMR spectra of **2** reported as example in Figures 18-21. In the case of polynuclear complex **4**, it can be assumed that in chloroform the weak intermolecular $\text{Zn}-\text{O}_{(\text{nitro})}$ interactions are easily broken and mononuclear species are present in solution. The disappearance of resonances at 12.60-12.89 ppm, but the persistence of those at 6.50-6.80 ppm confirms deprotonation of proligands and presence of hydrazide N-H upon coordination of the ligands to zinc. Unfortunately, no ^{15}N NMR chemical shift was observed for complex **4** and only some indirect ^{15}N NMR chemical shifts of **1-3** and **5** were detected (see Table 1), but not those of N3 atoms directly coordinated to zinc (and also N5 for complex **1**). However, those of vicinal N4 were clearly identified to lower fields for complexes **2, 3** and **5**, in accordance with deshielding upon coordination. Complexes **1-5** are stable in $\text{DMSO}-d_6$ and do not undergo any dissociation, as established by NMR studies and demonstrated in Figure 22.

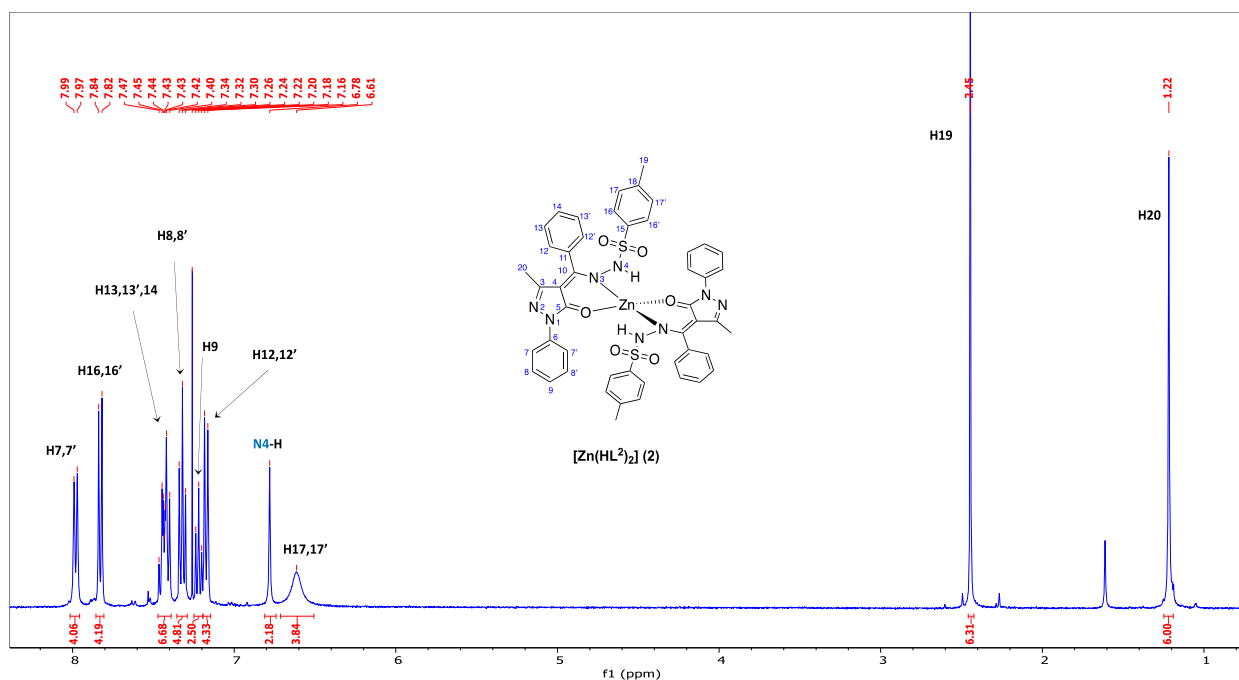


Figure 18. ^1H NMR of complex $[\text{Zn}(\text{HL}^2)_2]$ (**2**) in CDCl_3 at 298 K.

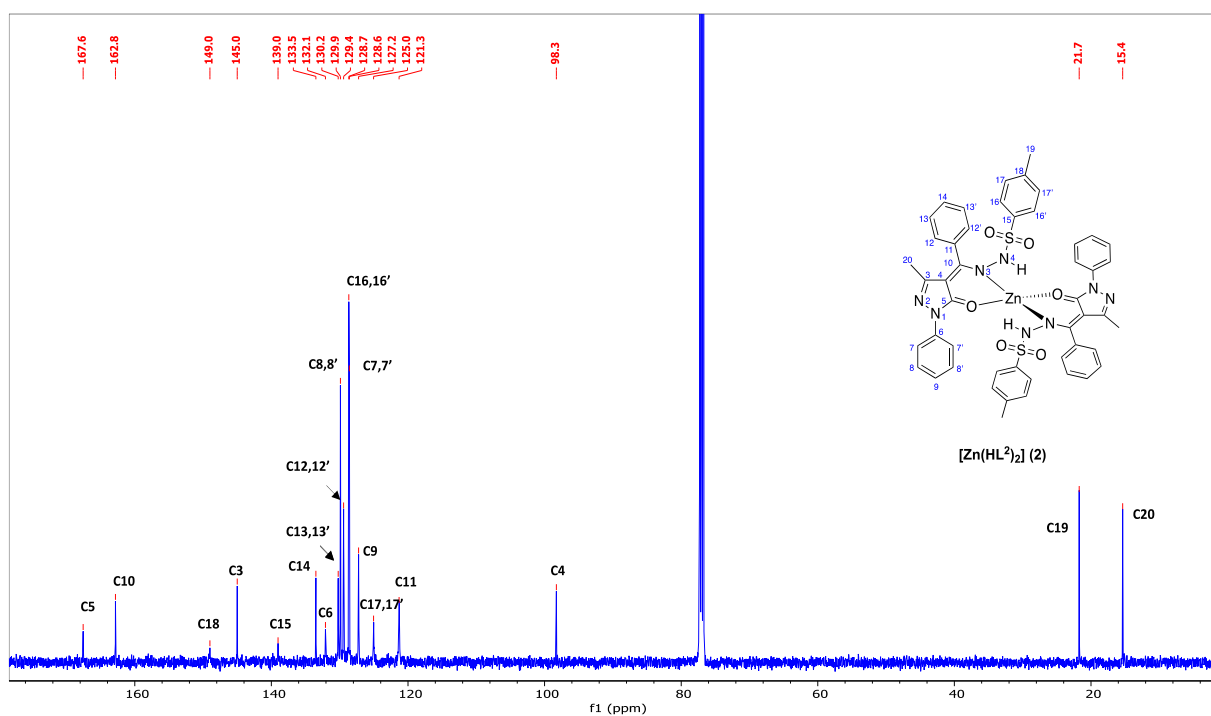


Figure 19. $^{13}\text{C}\{^1\text{H}\}$ NMR of complex $[\text{Zn}(\text{HL}^2)_2]$ (2) in CDCl_3 at 298 K.

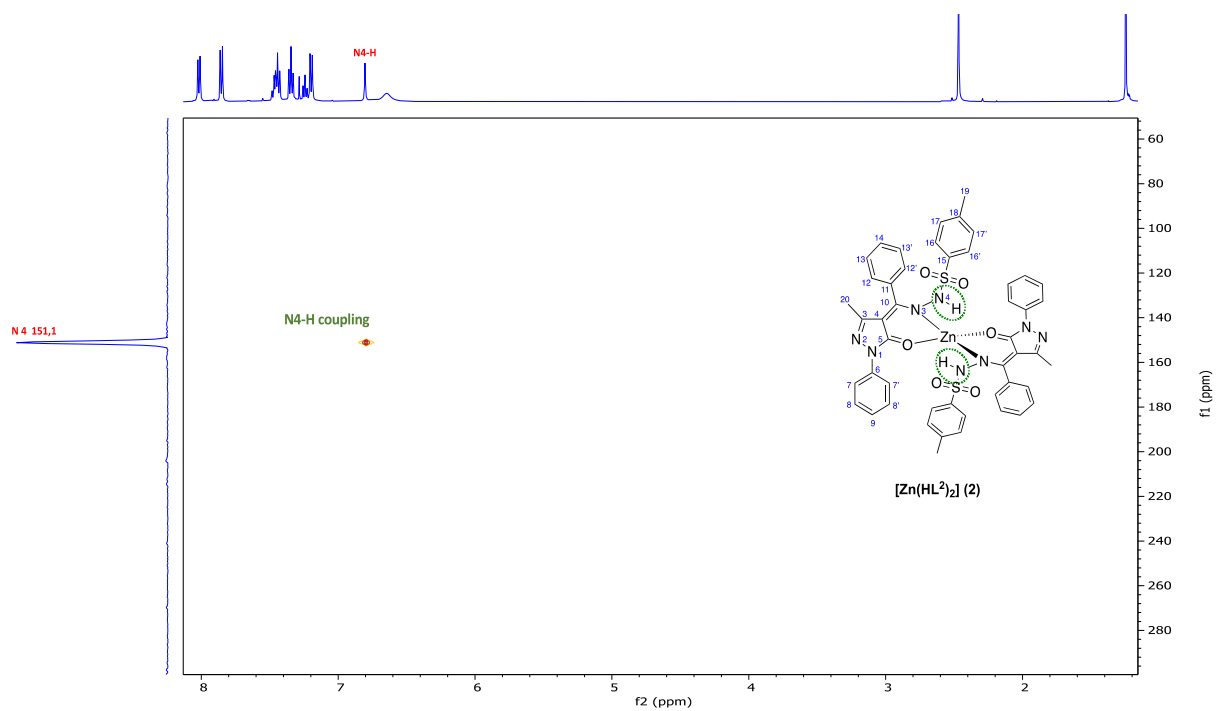


Figure 20. $\{^1\text{H}, ^{15}\text{N}\}$ -HSQC of complex $[\text{Zn}(\text{HL}^2)_2]$ (2) in CDCl_3 at 298 K.

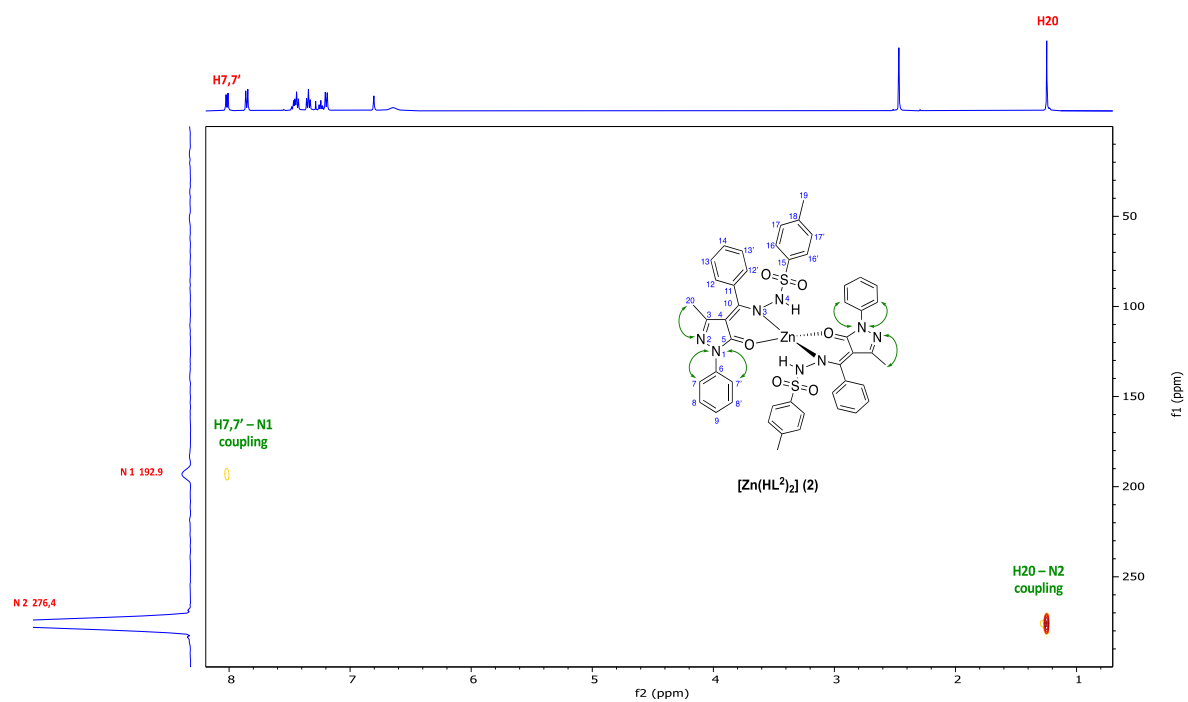


Figure 21. $\{^1\text{H}, ^{15}\text{N}\}$ -HMBC of complex $[\text{Zn}(\text{HL}^2)_2]$ (2) in CDCl_3 at 298 K.

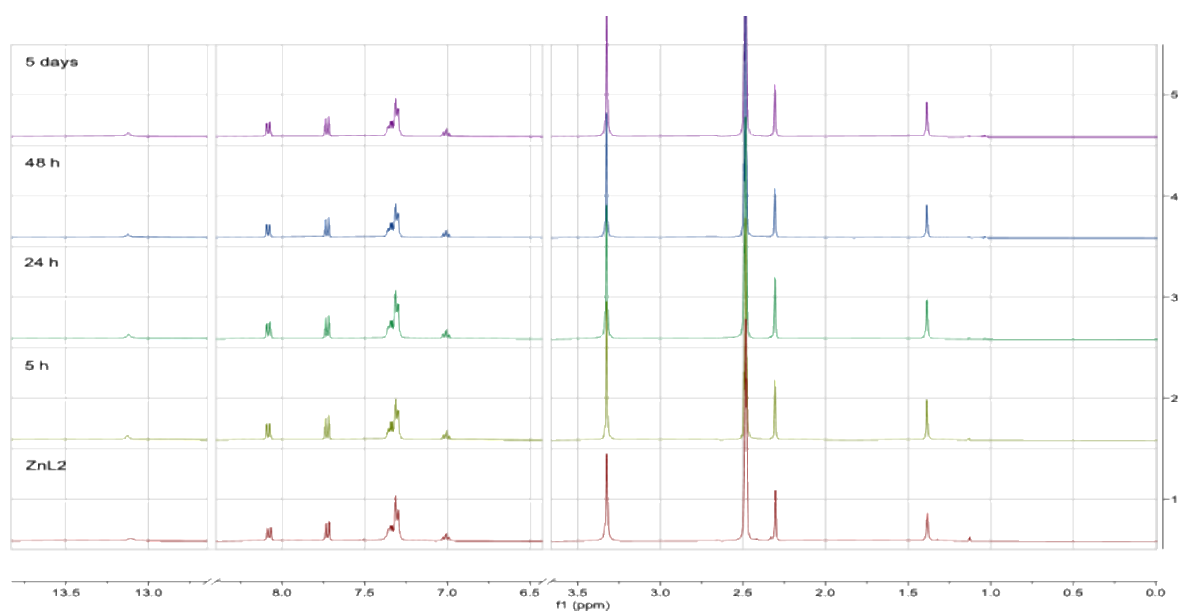


Figure 22. Stability study of complex $[\text{Zn}(\text{HL}^2)_2]$ (2) in $\text{DMSO}-d_6$.

Table 1. ^{15}N chemical shifts (ppm) in free proligands and complexes 1-5 obtained with $\{^1\text{H},^{15}\text{N}\}$ HSQC and HMBC NMR experiments as numbered in Chart 35.

Ligands	N1	N2	N3	N4	N5
H₂L¹	n.o.	n.o.	n.o.	n.o.	n.o.
H₂L²	189.8	271.7	n.o.	117.3	-
H₂L³	190.1	271.6	n.o.	117.0	369.9
H₂L⁴	n.o.	288.9	140.6	98.9	379.4
H₂L⁵	191.4	285.8	143.8	99.7	-
Complexes					
1	n.o.	n.o.	n.o.	132.9	n.o.
2	192.9	276.4	n.o.	151.1	-
3	197.5	n.o.	n.o.	125.2	n.o.
4	n.o.	n.o.	n.o.	n.o.	n.o.
5	n.o.	274.1	n.o.	120.0	-

2.3.3 X-ray structural characterization

The structures of proligand H₂L² and H₂L⁴, together with complexes **1**, **2** and **4**, were determined by single-crystal X-ray diffraction. Selected bond distances and angles are shown in Table 2 and Table 4. The crystallographic data are given in Table 5. Although both proligands show a similar scaffold based on pyrazolone, hydrazone and phenyl fragments, their molecular structure are different since H₂L² crystallizes in monoclinic *C2/c* space group and H₂L⁴ does in *P*-1 (Figure 23). The structures of proligands are nonplanar since the phenyl ring is turned with respect to the pyrazolone plane by 26.5(3)° and 17.8(3)° in H₂L² and H₂L⁴, respectively. The torsion angles in hydrazone group are -92.6° for H₂L² (S-N-N-C) and -126.9° for H₂L⁴ (C-N-N-C). The hydrazone N-N bond distances for all measured compounds are in the range of 1.397(3)-1.432(4) Å, being slightly higher for metal complexes. Proligand molecules are stabilized within the crystal through hydrogen bonds between two molecules. In both proligands the intermolecular interaction occurs between the hydrogens of hydrazone (N3 and N4) and the oxygen of the pyrazolone (O1) (see Table 3).

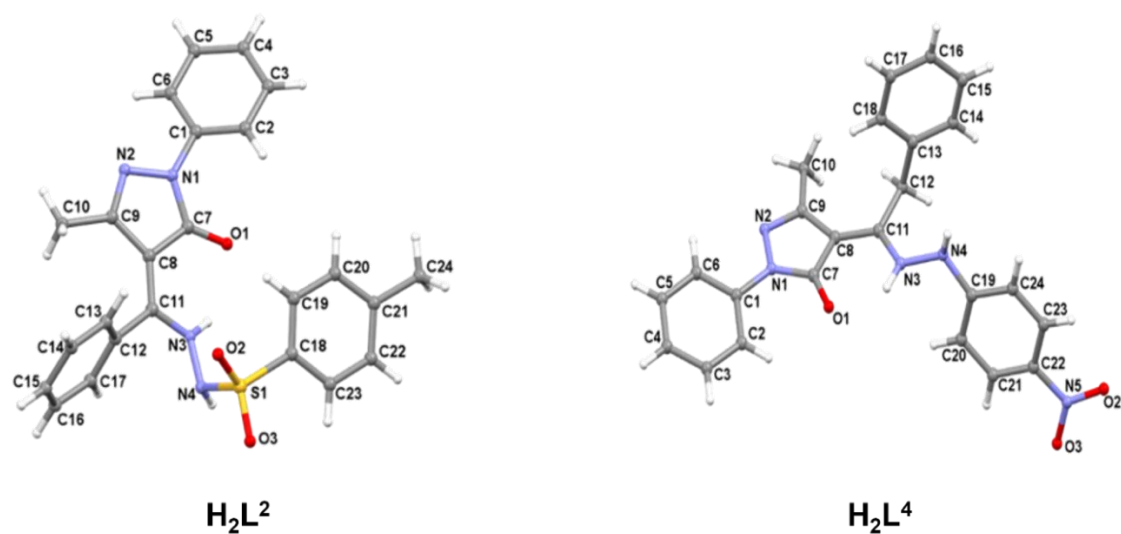


Figure 23. Molecular structures of ligands H_2L^2 and H_2L^4 .

Table 2. Selected bond distances (Å) and angles (°) of proligands H_2L^2 and H_2L^4 .

Bond	Distance (Å)	Bond	Angle (°)
H_2L^2			
C1-N1	1.418 (3)	C2-C1-N1	119.4 (2)
C7-N1	1.369 (3)	O1-C7-N1	125.5 (2)
C7-O1	1.254 (4)	C8-C11-C12	123.1 (2)
C8-C11	1.382 (4)	N3-C11-C8	117.6 (2)
C9-N2	1.307 (3)	C7-N1-N2	112.07 (19)
N1-N2	1.403 (3)	C11-N3-N4	122.3 (2)
C11-N3	1.332 (3)	N3-N4-S1	113.66 (17)
N3-N4	1.397 (3)	C19-C18-S1	119.7 (2)
N4-S1	1.677 (2)	N4-S1-C18	108.10 (12)
C18-S1	1.755 (3)		
H_2L^4			
C1-N1	1.424 (2)	C2-C1-N1	120.52 (15)
C7-N1	1.371 (2)	O1-C7-N1	125.90 (15)
C7-O1	1.258 (2)	C8-C11-C12	124.43 (15)
C8-C11	1.397 (2)	N3-C11-C8	117.81 (16)
C9-N2	1.313 (2)	C7-N1-N2	112.09 (13)
N1-N2	1.4007 (19)	C11-N3-N4	120.83 (15)
C11-N3	1.332 (2)		
N3-N4	1.389 (2)		
C22-N5	1.456 (2)		

Table 3. Hydrogen bonds distances (Å) and angles (°) for proligands H_2L^2 and H_2L^4 .

D-H...A	D-H	H...A	D...A	Angle
H_2L^2				
N3-H3A...O1	0.88	2.05	2.706 (3)	130.4
N3-H3A...O1	0.88	2.24	2.833 (3)	124.1
N4-H4A...O1	0.81 (3)	2.38 (3)	2.925 (3)	125 (3)
H_2L^4				
C2-H2...O1	0.93	2.32	2.913 (2)	121.4
N4-H4A...O1	0.87 (2)	2.01 (2)	2.8564 (19)	162 (2)
N3-H3A...O1	0.89 (2)	1.94 (2)	2.6662 (19)	138.0 (19)

Regarding the coordination compounds, complex **1** is based on ligand $(HL^1)^-$, **2** is based on $(HL^2)^-$ and crystallization methanol molecules, and **4** is formed by the coordination of $(HL^4)^-$ ligand (Figure 24). **1**, with general formula $[Zn(HL^1)_2]$, crystallizes in the triclinic space group P-1. The asymmetric units consist in one Zn(II) ion and two monoanionic $(HL^1)^-$ ligands. The metal center exhibits a distorted octahedral coordination environment, ZnO_2N_4 . Zn-O bond distances are in the 2.049(2)-2.051(2) Å range, while Zn-N bond distances range from 2.132(2) Å to 2.151(2) Å. Each ligand is coordinated by the oxygen of pyrazolone, one nitrogen of hydrazone and the nitrogen of pyridine rings. The structures of **1** consists of a monomer where neither hydrogen bonds nor van der Waals interactions exist.

Complex **2** consists of a monomer as well that crystallizes in the monoclinic $C2/c$ space group with general formula $[Zn(HL^2)_2] \cdot 2MeOH$. The asymmetric unit contains half of a Zn(II) ion and one $(HL^2)^-$ molecule. Each Zn(II) ion shows a tetrahedral ZnO_2N_2 geometry formed by two oxygen atoms from pyrazolone and two nitrogen atoms from hydrazone of two different monoanionic $(HL^2)^-$ ligands. The Zn-O bond distance is 1.958(3) Å whereas the Zn-N bond length is 1.998(4) Å. Due to the disorder within the voids, the crystallization methanol molecules were removed from the structure.

Table 4. Selected bond distances (Å) and angles (°) of complexes 1, 2 and 4.

Bond	Distance (Å)	Bond	Angle (°)
Complex 1			
Zn1-N3A	2.151 (2)	N3B-Zn1-N3A	171.98 (9)
Zn1-N3B	2.143 (2)	N5A-Zn1-N3A	76.33 (9)
Zn1-N5A	2.132 (2)	N5A-Zn1-N3B	97.47 (9)
Zn1-N5B	2.142 (2)	N5A-Zn1-N5B	92.74 (9)
Zn1-O1A	2.051 (2)	N5B-Zn1-N3A	98.99 (9)
Zn1-O1B	2.049 (2)	N5B-Zn1-N3B	76.00 (9)
		O1A-Zn1-N3A	87.22 (8)
		O1A-Zn1-N3B	98.96 (9)
		O1A-Zn1-N5A	163.54 (8)
		O1A-Zn1-N5B	90.30 (9)
		O1B-Zn1-N3A	98.05 (9)
		O1B-Zn1-N3B	87.25 (9)
		O1B-Zn1-N5A	92.94 (9)
		O1B-Zn1-N5B	162.88 (8)
		O1B-Zn1-O1A	88.80 (8)
Complex 2			
Zn1-O1	1.958 (3)	O1-Zn1-O1	97.6 (2)
Zn1-N1	1.998 (4)	O1-Zn1-N1	119.19 (11)
		O1-Zn1-N1	96.95 (12)
		O1-Zn1-N1	96.94 (12)
		O1-Zn1-N1	119.19 (11)
		N1-Zn1-N1	125.0 (2)
Complex 4			
Zn1-N3	2.069 (3)	N3-Zn1-N3	180.0
Zn1-O1	2.004 (3)	N3-Zn1-O2	89.09 (12)
Zn1-O2	2.342 (3)	N3-Zn1-O2	90.91 (12)
		O1-Zn1-N3	88.44 (12)
		O1-Zn1-N3	91.56 (12)
		O1-Zn1-O1	180.0
		O1-Zn1-O2	84.67 (11)
		O1-Zn1-O2	95.33 (11)
		O2-Zn1-O2	180.0

Finally, complex 4 crystallizes in the triclinic $P-1$ space group and the structure consists of a monodimensional coordination polymer with general formula $[\text{Zn}(\text{HL}^4)]_n$. The asymmetric unit shows half of zinc(II) ion and one monoanionic $(\text{HL}^4)^-$ ligand. Each central atom is coordinated to four different ligand molecules by showing an octahedral ZnO_4N_2 geometry formed by two oxygen atoms of pyrazolone ring, two oxygen atoms from nitro group and two nitrogen atoms pertaining to hydrazone moiety. The oxygens of pyrazolone occupy the basal plane of the octahedron together

with nitrogen bonds, with Zn-O_{basal} bond distances of 2.004(3) Å and Zn-N bond length of 2.069(3) Å. On the other hand, the oxygen atoms pertaining to nitro groups are situated at the apical position with a Zn-O_{apical} bond distance value of 2.342(3) Å. Each proligand molecule coordinates to two Zn(II) ions. This disposition of the ligands creates chains that propagate along *b* axis. Within chains, stacking interaction between nitrophenyl moieties occurs, with a centroid-to-centroid distance of 4.155 Å. Only one intramolecular hydrogen bond helps to stabilize the structure between the nitrogen of the hydrazone (N4) and the oxygen from pyrazolone (O1) of two different ligand molecules, with a N4-H4A...O1 distances of 2.786(4) Å.

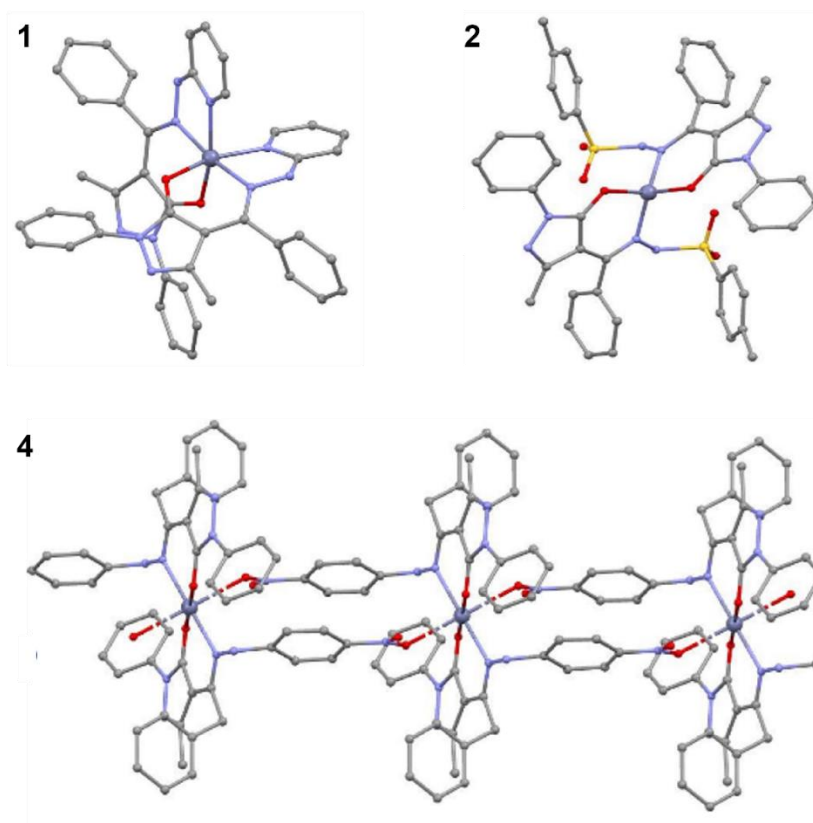


Figure 24. Molecular structures of complexes 1, 2 and 4.

Table 5. Crystallographic data and structure refinement details of proligands H_2L^2 and H_2L^4 and complexes 1, 2 and 4.

Compound	H_2L^2	H_2L^4
Formula	$C_{24}H_{24.4}N_4O_{4.2}S$	$C_{24}H_{21}N_5O_3$
CCDC	2158177	2158178
M_r (g mol ⁻¹)	468.13	427.46
Crystal system	Monoclinic	Triclinic
Space group	$C2/c$	$P-1$
a (Å)	24.3936(19)	8.8530(8)
b (Å)	10.9327(7)	9.6590(8)
c (Å)	17.3895(12)	12.8829(12)
α (°)	90	85.651(3)
β (°)	92.135(4)	74.757(3)
γ (°)	90	78.819(3)
V (Å ³)	4634.3(6)	1042.34(16)
Z	8	2
T (K)	120(2)	293(2)
ρ_{calc} (g cm ⁻³)	1.342	1.362
F (000)	1968	448
μ (Mo K α) (mm ⁻¹)	0.179	0.093
GoF on F ²	1.007	1.068
Final R indexes [I > 2 σ (I)]	$R_1 = 0.0500$; $wR_2 = 0.1102$	$R_1 = 0.0451$; $wR_2 = 0.1020$
Final R indexes [all data]	$R_1 = 0.0820$; $wR_2 = 0.1249$	$R_1 = 0.0674$; $wR_2 = 0.1116$

Compound	Complex 1	Complex 2	Complex 4
Formula	C ₄₄ H ₃₈ N ₁₀ O ₂ Zn	C ₅₀ H ₅₂ N ₈ O ₈ S ₂ Zn	C ₄₈ H ₄₀ N ₁₀ O ₆ Zn
CCDC	2158179	2158180	2158176
M _r (g mol ⁻¹)	804.21	1022.48	918.27
Crystal system	Triclinic	Monoclinic	Triclinic
Space group	<i>P</i> -1	<i>C</i> 2/ <i>c</i>	<i>P</i> -1
a (Å)	9.8944(6)	17.44(3)	9.8009(8)
b (Å)	11.3405(6)	13.34(2)	9.9718(9)
c (Å)	18.1843(10)	22.28(4)	12.2060(12)
α (°)	89.300(2)	90	88.090(3)
β (°)	86.246(2)	105.95(3)	70.399(3)
γ (°)	67.2918(18)	90	73.834(3)
V (Å ³)	1878.02(18)	4987(16)	1076.97(17)
Z	2	4	1
T (K)	100(2)	273.15	298(2)
ρ _{calc} (g cm ⁻³)	1.422	1.362	1.416
F (000)	836	2136	476
μ (Mo Kα) (mm ⁻¹)	0.708	0.637	0.634
GoF on F ²	1.060	1.048	1.017
Final R indexes [I ≥ 2σ]	R ₁ = 0.0561; wR ₂ = 0.1450	R ₁ = 0.0561; wR ₂ = 0.1367	R ₁ = 0.0739; wR ₂ = 0.1476
Final R indexes [all data]	R ₁ = 0.0731; wR ₂ = 0.1538	R ₁ = 0.0773; wR ₂ = 0.1585	R ₁ = 0.1479; wR ₂ = 0.1765

2.3.4 Theoretical studies

Tautomers I and II of proligands H₂L², H₂L⁴ and H₂L⁵ (Chart 38) have been investigated using density functional theory (DFT) at the B3LYP/6-311G** level of theory, while theoretical studies on proligands H₂L¹ and H₂L³ have already been reported in the past^[274]. For all the ligands tautomer I showed to be the most stable in gas phase and in chloroform solution, even if the energy differences are small and comprised in the range of *ca.* 0.6 – 5.7 kcal/mol (see Table 6 for more precise data). The comparison between the computed and experimental ¹H, ¹³C and ¹⁵N NMR spectral data showed a better fit for tautomer I, proving to be the observed species. In particular, the values for ¹H and ¹³C are very similar for both tautomers (R² = 0.98-0.99), while R² values from ¹³N-NMR are entirely different, in favor of tautomer NH,NH, as shown in Figure 25.

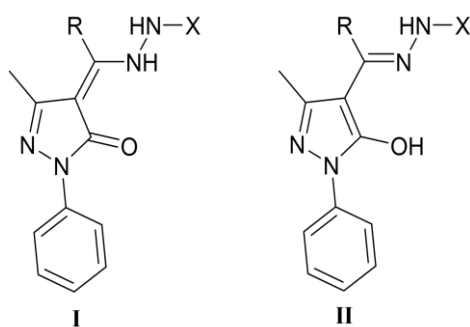
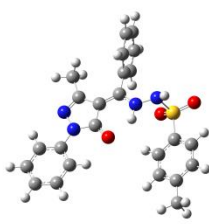
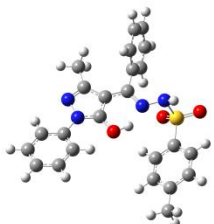
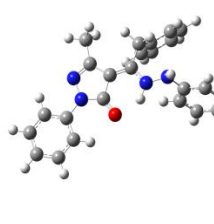
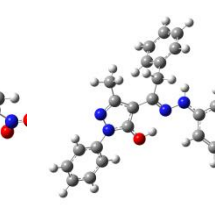
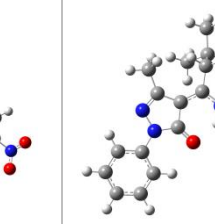
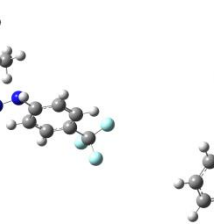


Chart 38. Tautomeric forms of proligands considered in the DFT study.

The calculated structural parameter of tautomer I for proligands H_2L^2 and H_2L^4 are in agreement with those observed from the X-ray diffraction on the crystals (see Figure 26). In particular the experimental C=O bond distance of 1.254 Å (for H_2L^2) is well reproduced by the calculation with a value of 1.242 Å for tautomer I vs 1.321 for tautomer II, confirming the proposed assignment. Finally, the calculated infrared spectra of I fit well with the experimental ones (see Figure 27 and Table 7), further supporting the discussed assignment.

Table 6. Energies (Hartree) and relative energy differences (kcal/mol) for the tautomers of proligands H_2L^2 , H_2L^4 and H_2L^5 .

	H_2L^2		H_2L^4		H_2L^5	
	Tautomer I	Tautomer II	Tautomer I	Tautomer II	Tautomer I	Tautomer II
						
E	-1770.946848	-1770.937687	-1426.865589	-1426.864598	-1485.635608	-1485.630883
E₀	-1770.526114	-1770.517408	-1426.450842	-1426.450241	-1485.187451	-1485.183379
E_t	-1770.497523	-1770.48903	-1426.423841	-1426.423223	-1485.158598	-1485.154414
H	-1770.496579	-1770.488085	-1426.422897	-1426.422279	-1485.157654	-1485.153470
G	-1770.590327	-1770.58033	-1426.513320	-1426.512049	-1485.250309	-1485.245797
ΔE	0.0	5.7	0.0	0.6	0	3.0
ΔG	0.0	6.3	0.0	0.8	0	2.8
ΔE_(CHCl₃)	0.0	6.6	0.0	2.8	0	4.3
ΔG_(CHCl₃)	0.0	7.1	0.0	2.9	0	4.2

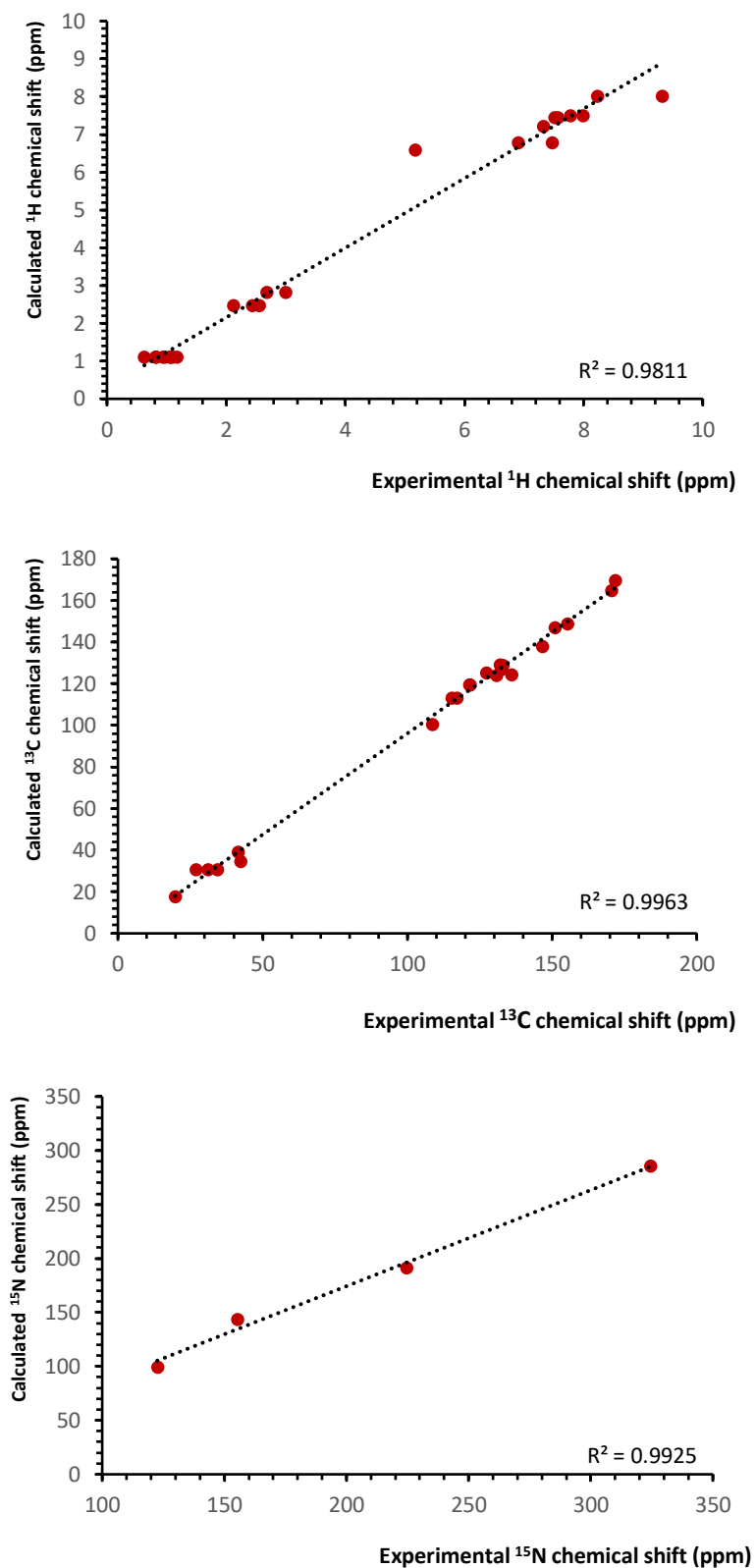


Figure 25. Comparison of the calculated (tautomer I) and experimental 1H , ^{13}C and ^{15}N NMR spectra of H_2L^5 .

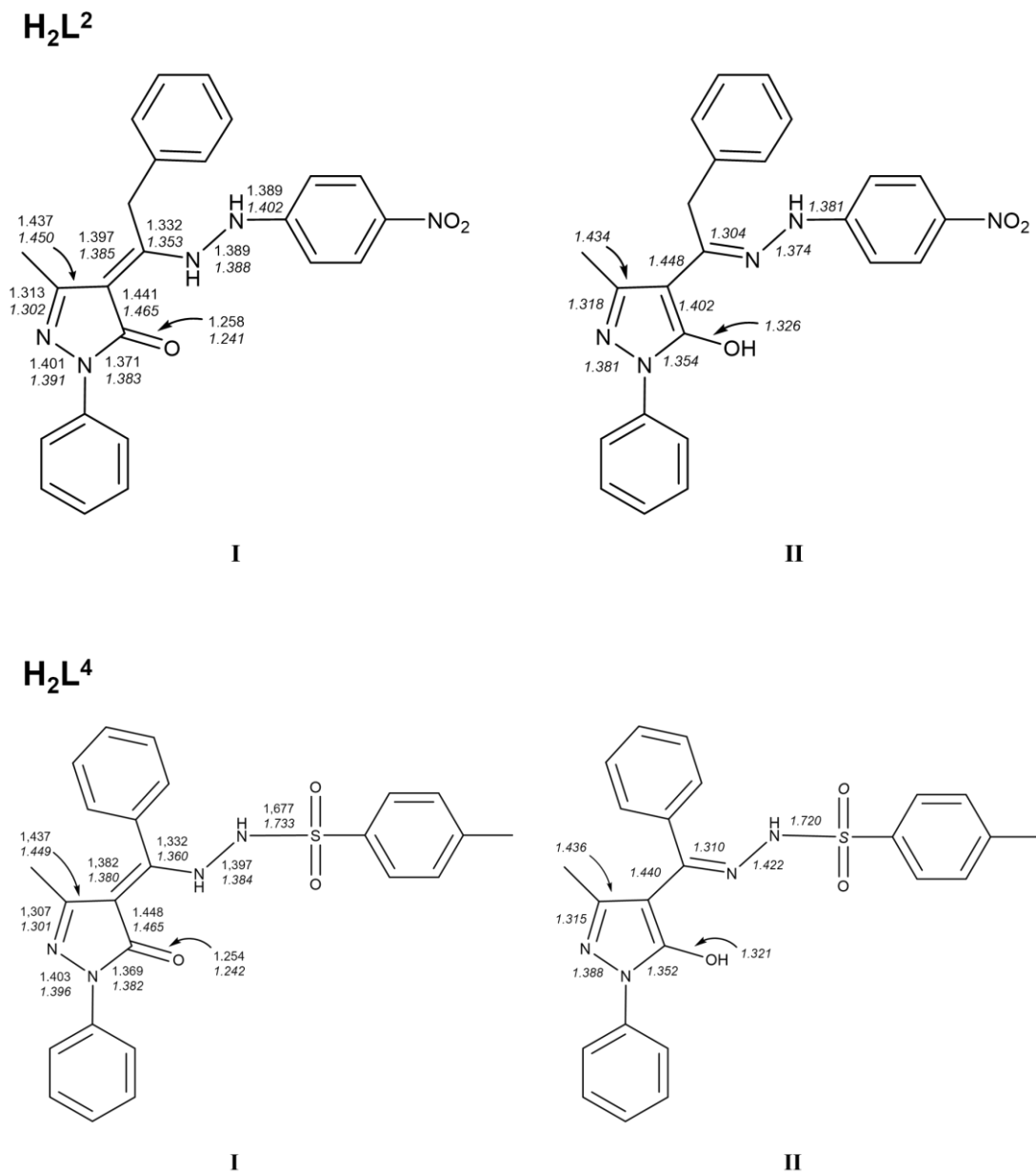


Figure 26. Comparison of selected bond distances of H₂L² and H₂L⁴: calculated tautomers I and II (*italic*) and experimental.

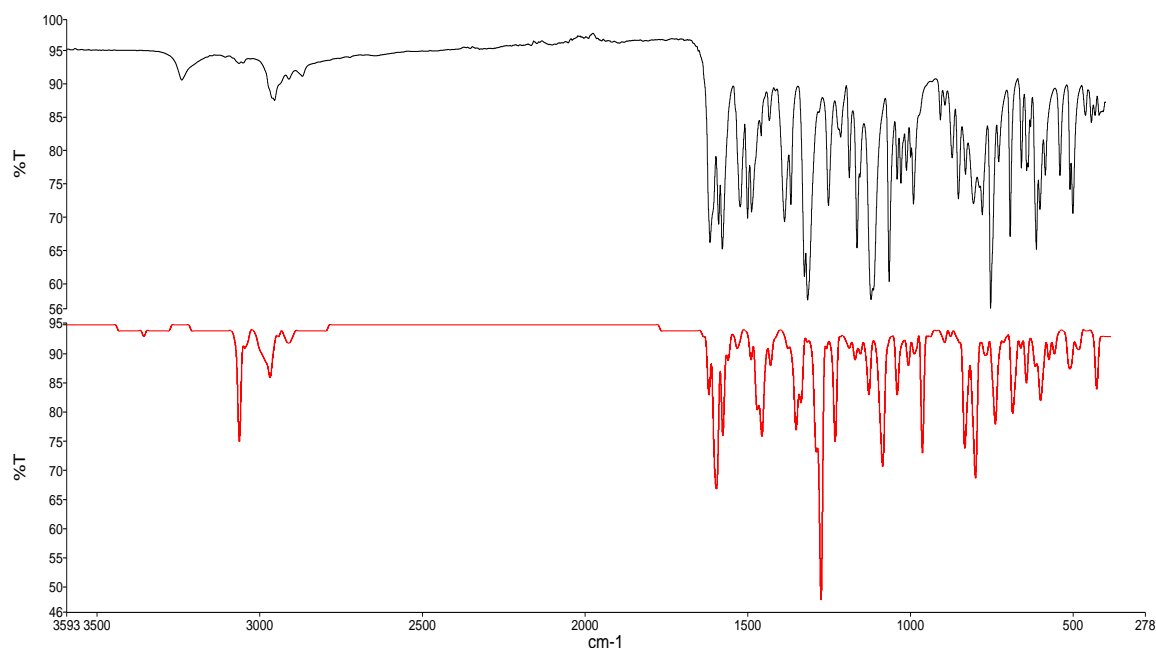


Figure 27. Comparison of experimental (black line) and calculated (tautomer I, red line) IR spectrum of H_2L^5 .

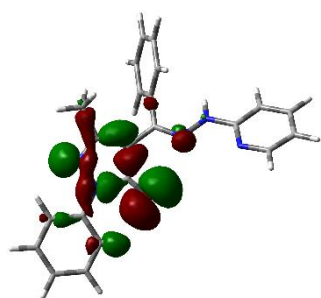
Table 7. Selected stretching assignments of the IR spectrum of H_2L^5 .

IR band (cm^{-1})	Experimental	Calculated
$\nu(N3-H)$	3064	3062
$\nu(C=N2)$	1524	1530
$\nu(C=O)$	1615	1618
$\nu_{as}(C-F)$	1315, 1065	1274, 1084
$\nu_s(C-F)$	1163	1127

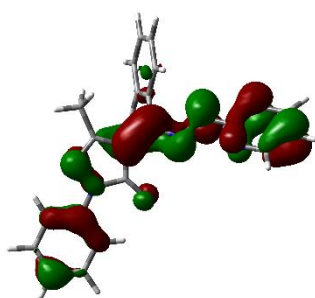
In order to study the coordination capabilities of the proligands, their anionic forms have been optimized as well. For all $[HL^n]^-$ anions the charge localization reflects the deprotonation of tautomer I, showing a shorter C=O bond than C-N bond ($\sim 1.23 \text{ \AA}$ vs $\sim 1.30 \text{ \AA}$). The molecular orbitals (MOs) mostly involved in the coordination to the metal center for anions $[HL^2]^-$, $[HL^3]^-$, $[HL^4]^-$ and $[HL^5]^-$ are shown to be HOMO-2 and HOMO-8/-9/-10 (depending on the species), these being respectively the *in-phase* and *out-of-phase* contributions of σ type. Other minor contributions are present with orbitals localized on the N or O atom. Concerning $[HL^1]^-$ many different contributions have been found due to its O,N,N-tridentate hapticity (Figures 28-30). The optimized structures of the anions show some differences with the structure they assume upon coordination, as we will see later in the discussion. The most noticeable difference is the conformation of the phenyl moiety (X group on Chart 38): in the optimized anion the phenyl ring

is positioned on the same plane of O and N atoms, while in the complex it orientates perpendicularly. Secondly, in the complex, ligand HL² directs its SO₂ group towards the metal center and in a similar fashion ligand HL⁴ directs its NO₂ group to perform an intermolecular interaction. For these reasons single-point calculations have been carried out on the ligands with the geometries found in the optimization of their respective complexes. In this case the MOs involved are more clearly identified in HOMO-2, HOMO-4, HOMO-6 and HOMO-8 for [HL¹]⁻, HOMO-1 and HOMO-4 for [HL⁴]⁻. For [HL²]⁻ instead, the designation of the orbitals becomes more blurred as more combinations of contributions arise. Finally, the weak interactions of [HL²]⁻ and [HL⁴]⁻ are probably performed respectively through the HOMO-13 and HOMO-12 molecular orbitals.

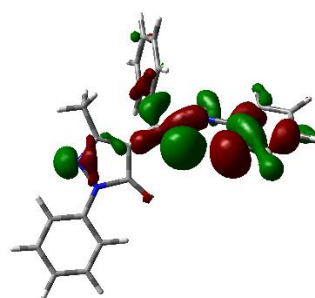
Optimized [HL¹]



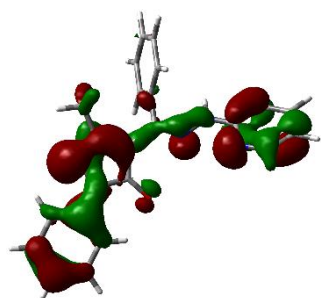
HOMO-2



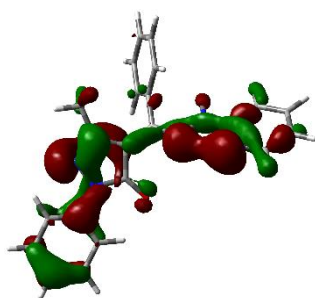
HOMO-3



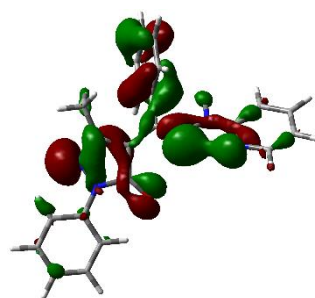
HOMO-5



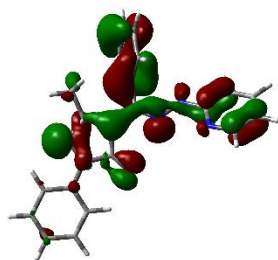
HOMO-6



HOMO-7

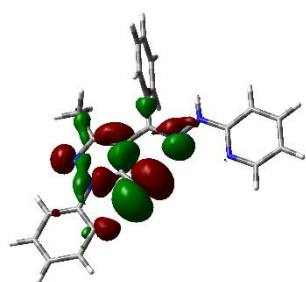


HOMO-8

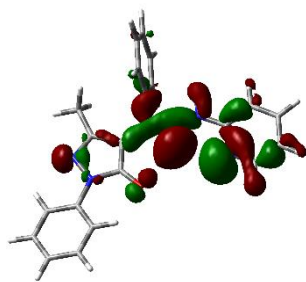


HOMO-9

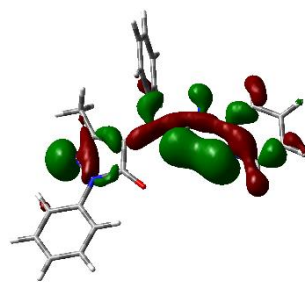
Single point calculation of [HL¹]⁻ from the optimization of 1.



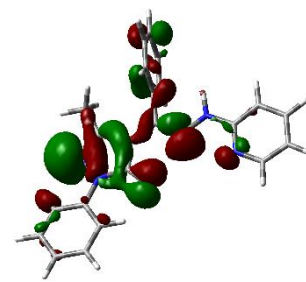
HOMO-2



HOMO-4



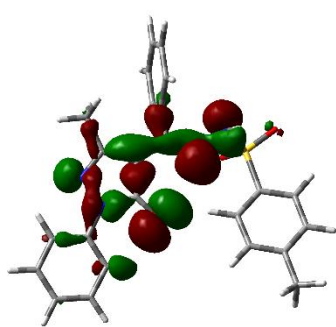
HOMO-6



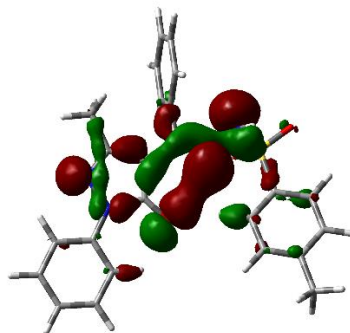
HOMO-8

Figure 28. MOs of anionic ligand [HL¹]⁻ involved in the coordination to metal centers.

Optimized [HL²⁻]

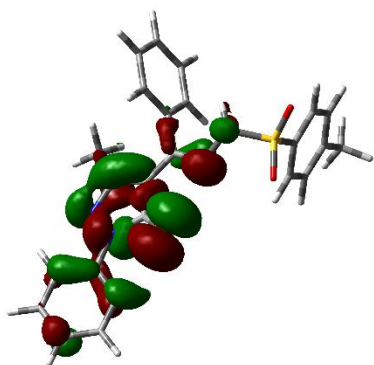


HOMO-2

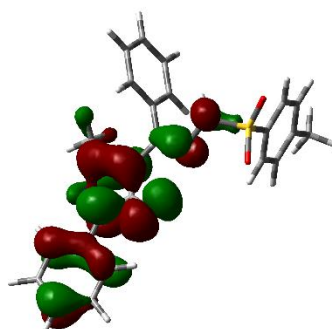


HOMO-3

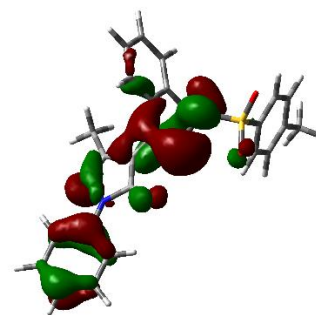
Single point calculation of [HL²⁻] from the optimization of 2.



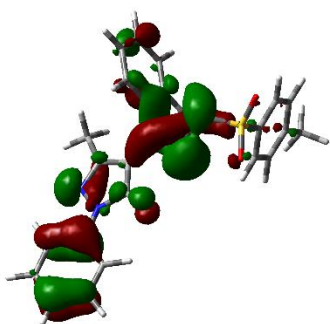
HOMO-1



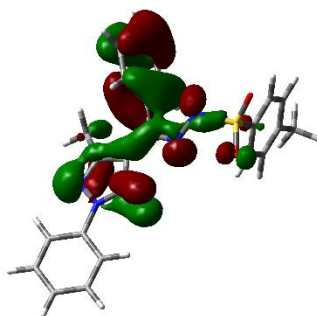
HOMO-2



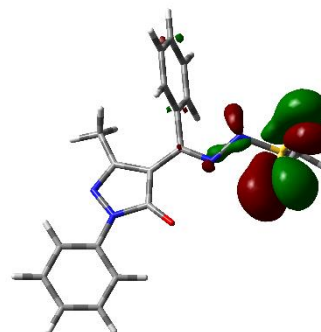
HOMO-3



HOMO-5



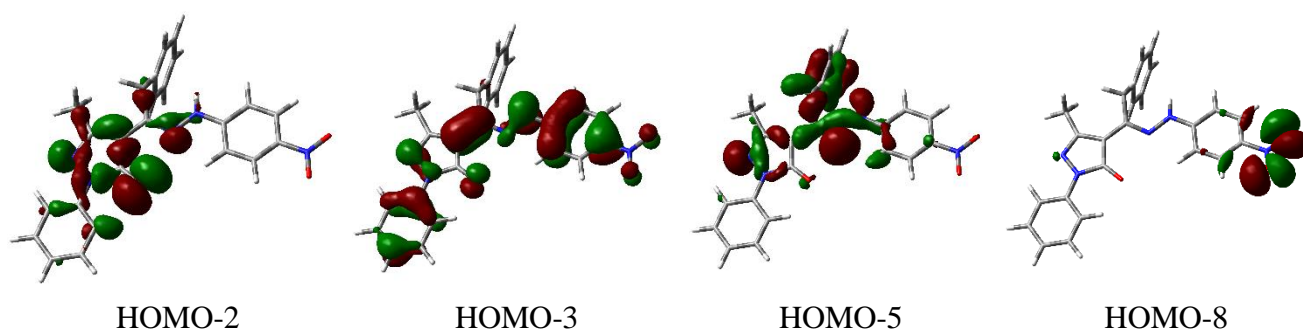
HOMO-8



HOMO-13

Figure 29. MOs of anionic ligand [HL²⁻] involved in the coordination to metal centers.

Optimized $[HL^4]^-$



Single point calculation of $[HL^4]^-$ from the optimization of 4.

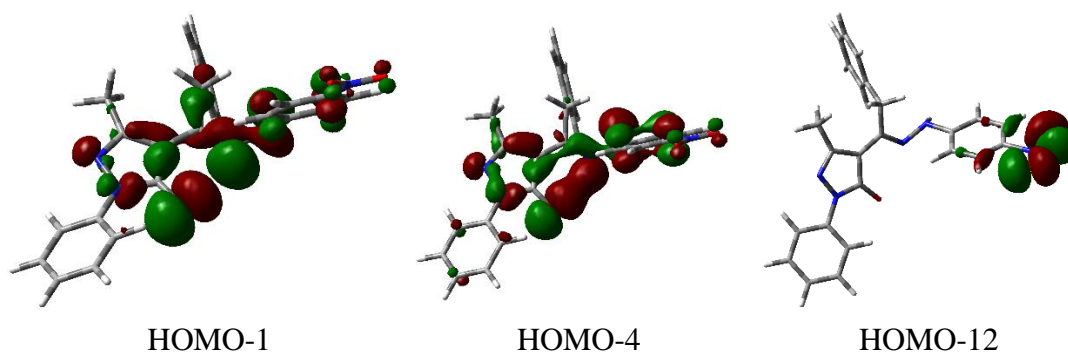


Figure 30. MOs of anionic ligand $[HL^4]^-$ involved in the coordination to metal centers.

Complexes **1-5** were also analyzed by DFT using the 6-311G* basis set. Complex $[Zn(HL^1)_2]$ is reproduced well by the calculations, showing an excellent match between calculated and experimental data obtained from the XRD analysis as reported in Table 8. The optimized structure is also consistent with the experimental infrared and NMR data (R^2 correlation value = 0.9908).

The geometry optimized for complex **2**, $[Zn(HL^2)_2]$, slightly differs from the experimental crystallographic data at this level of theory. In fact, the calculation tends to overestimate the interaction between Zn and O of the SO_2 group, resulting in a Zn- O_{SO_2} distance of 2.277 Å against the experimental value of 2.770 Å. This could be addressed to some reticular interactions not taken into account by the optimization method. Due to this difference the optimized structure resembles more a distorted octahedral geometry than the tetrahedral geometry reported experimentally. Nonetheless, other structural parameters (also reported in Table 8) and NMR spectra correlation ($R^2 = 0.9904$) demonstrate a good match between the two structures.

Table 8. Comparison of selected experimental and calculated structural parameters of complexes $[\text{Zn}(\text{HL}^1)_2]$ and $[\text{Zn}(\text{HL}^2)_2]$.

$[\text{Zn}(\text{HL}^1)_2]$		
Bond distances (Å) and angles (°)	Experimental	Calculated
N3_A-Zn	2.151	2.178
N5_A-Zn	2.132	2.183
O_A-Zn	2.051	2.053
N3_B-Zn	2.144	2.176
N5_B-Zn	2.142	2.183
O_B-Zn	2.049	2.053
C-O	1.270	1.262
C-N3	1.310	1.318
N3_A-Zn-N5_A	76.34	75.98
N3_A-Zn-N5_B	98.99	100.32
N3_A-Zn-O_A	87.21	86.67
O_A-Zn-O_B	88.80	94.47
O_A-Zn-N5_B	90.3	88.71
O_A-Zn-N5_A	162.5	162.62
$[\text{Zn}(\text{HL}^2)_2]$		
Bond distances (Å) and angles (°)	Experimental	Calculated
N-Zn	1.998	2.109
O-Zn	1.958	2.032
O_{SO2}-Zn	2.770	2.277
C-O	1.275	1.270
C-N	1.330	1.317
N3-N4	1.432	1.403
C4=C10	1.425	1.425
O-Zn-N	96.94	90.12
O-Zn-O_{SO2}	163.26	167.74

As already discussed in the X-ray structural characterization, complex **4**, $[\text{Zn}(\text{HL}^4)_2]$ arranges in a monodimensional polymeric structure. In order to investigate its structure, we optimized the geometries of the monomer $[\text{Zn}(\text{HL}^4)_2]$ and of the dimer $[\text{Zn}(\text{HL}^4)_2]_2$, both with coordinated water and without, and of the trimer $[\text{Zn}(\text{HL}^4)_2]_3$. The optimized monomer structure presents a quite perfect square planar geometry with bond distances of 2.017 Å (Zn-N) and 2.021 Å (Zn-O) and the two nitrophenyl groups placed pointing out the metal coordination plane with an angle of 116.05° (N-N-Ph) In the dimer and in the trimer the complex arranges in a moderately distorted square planar geometry with longer Zn-N and shorter Zn-O bonds. Considering the intermolecular

interaction in trans position of the metal with the NO₂ groups, the metal environment is octahedral with Zn-O_{NO₂} distances of 2.367 Å and 2.3860 Å. In the dimer and in the two terminal molecules of the trimer the distortion is accentuated and the Zn-O_{H₂O} bond distance is 2.247 Å. The energies of the optimized structures were then used to investigate the readiness of the polymerization process. The results suggest that, without considering the water molecules, the dimerization process is favored with $\Delta E_{\text{reaz}} = -29.2$ kcal/mol and $\Delta G_{\text{reaz}} = -7.9$ kcal/mol. This gives a further proof that the polymerization process is accessible. Instead, if we consider the coordinated water the process becomes a little disadvantaged with $\Delta E_{\text{reaz}} = 12.5$ kcal/mol and $\Delta G_{\text{reaz}} = 4.8$ kcal/mol. However, the comparison of the experimental NMR spectrum with the computed one obtained from the optimized monomer with coordinated water provides an optimal correlation (R^2 value of 0.9991). Given the presence of the water signal in the experimental NMR and that it integrates perfectly 4, one could reckon that the complex is formed bearing the coordinated water which gets then removed during the crystallization process while the polymer is formed.

The optimized structure proposed for complex **3**, [Zn(HL³)₂] presents a octahedral geometry with two water molecules coordinated in trans position. The geometry is similar to the monomer of complex [Zn(HL⁴)₂] with bond distances of 2.076 Å (Zn-O), 2.073 Å (Zn-N) and 2.236 Å (Zn-O_{H₂O}) and angles of 87.81° (N1-Zn-O1) and 92.19° (N1-Zn-O2). The negative charge on the ligands is more localized on the oxygen reflecting the different bond lengths of C=O (1.269 Å) and C=N (1.320 Å). To rationalize the octahedral geometry it has been decided to also optimized the structure without the coordinated water and the tetrahedral arrangement of the complex as well. The energy evaluation between the structures reveal that the proposed structure is the most stable with an energy difference of 32.2 kcal/mol (ΔE) for the structure without water and of 28.1 kcal/mol (ΔE) for the tetrahedral structure. This suggests that a certain amount of steric hindrance is responsible for the octahedral geometry. Nevertheless, the experimental infrared spectrum displays a good correlation with the one calculated, but in the fingerprint region some similarities can be found with the calculated spectrum for the tetrahedral structure (Figure 31). Therefore it might be possible to have a small percentage of the Td structure while most of the molecules assume the Oh geometry with water coordination. The calculated NMR spectrum instead is very well correlated to the experimental NMR with a R2 value of 0.995.

Also for complex [Zn(HL⁵)₂], **5**, the proposed structure has a octahedral geometry with two molecules of water coordinated in trans position. Like for the previous complex, the structure has been optimized both with and without coordinated water. In this case the computation of the

structure with no water converges spontaneously toward a distorted tetrahedral geometry without finding other local minima. The two structures have an energy difference of 30.9 kcal/mol (ΔE) and 6.8 kcal/mol (ΔG), the octahedral one being the most stable. The structural parameters of the ligand remain almost unaltered with C=O bond distances of 1.279 Å and C=N bond distances of 1.331 Å. Ligand-to-metal bond distances instead differ: 1.986 Å - 2.001 Å (Th, Zn-N); 1.943 Å - 1.975 Å (Th, Zn-O) and 2.084 Å (Oh, Zn-N); 2.048 Å (Oh, Zn-O). Comparing the experimental infrared spectrum with the calculated ones, similarities can be found for both geometries and to the same extent (Figure 32). In the same way, the experimental NMR data fit well with both the computed spectra, exhibiting satisfying correlation values of $R_{2\text{Oh}} = 0.9945$ and $R_{2\text{Th}} = 0.9942$ (Figure 33). As before, the data suggest that a partial formation of the Th species could occur during the synthesis of the complex.

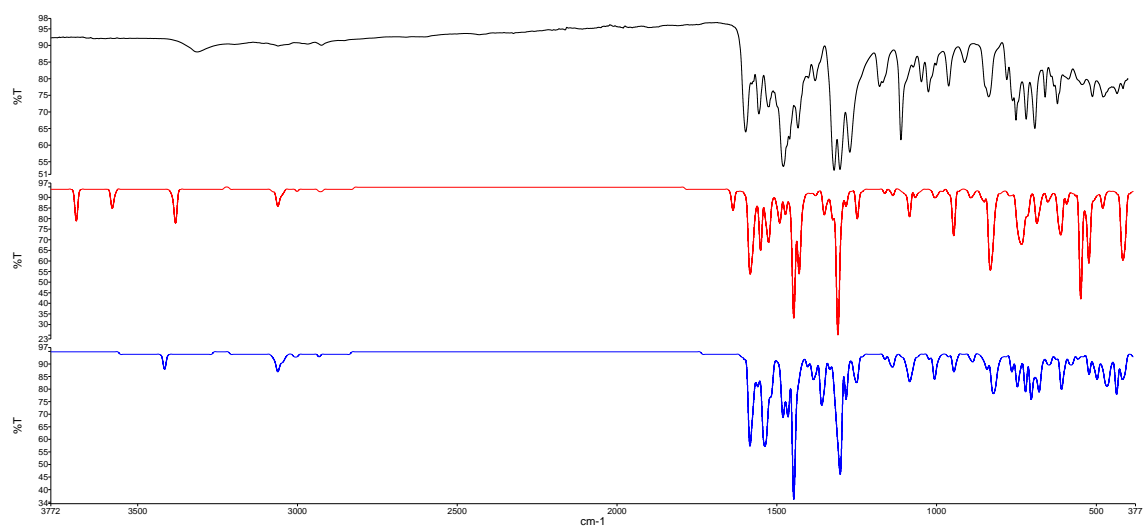


Figure 31. Comparison of experimental (black line) and calculated (octahedral - red line, tetrahedral – blue line) IR spectra of $[Zn(H_2L^3)_2]$.

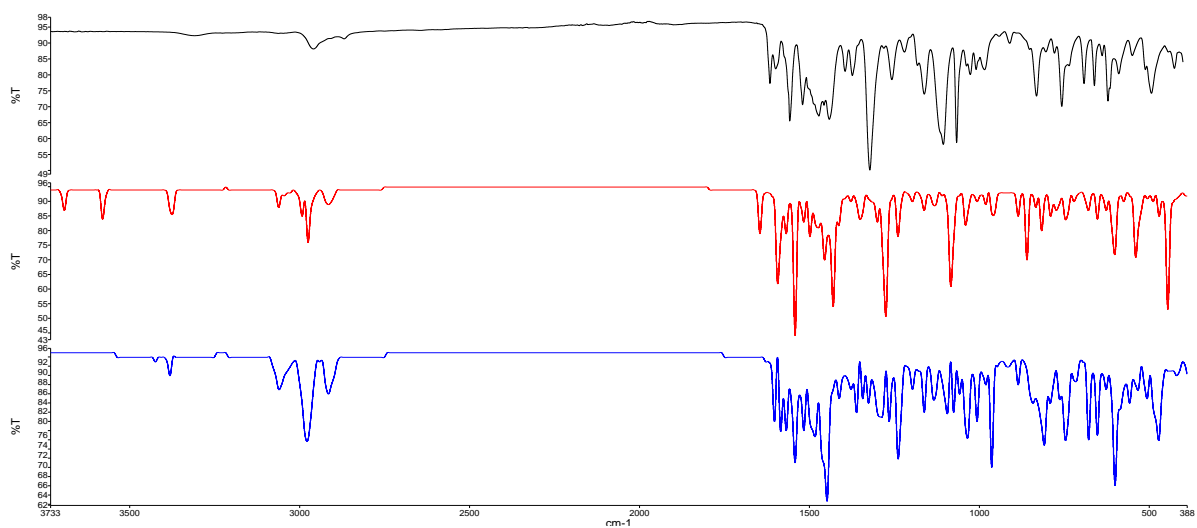


Figure 32. Comparison of experimental (black line) and calculated (octahedral - red line, tetrahedral – blue line) IR spectra of $[Zn(H_2L^5)_2]$.

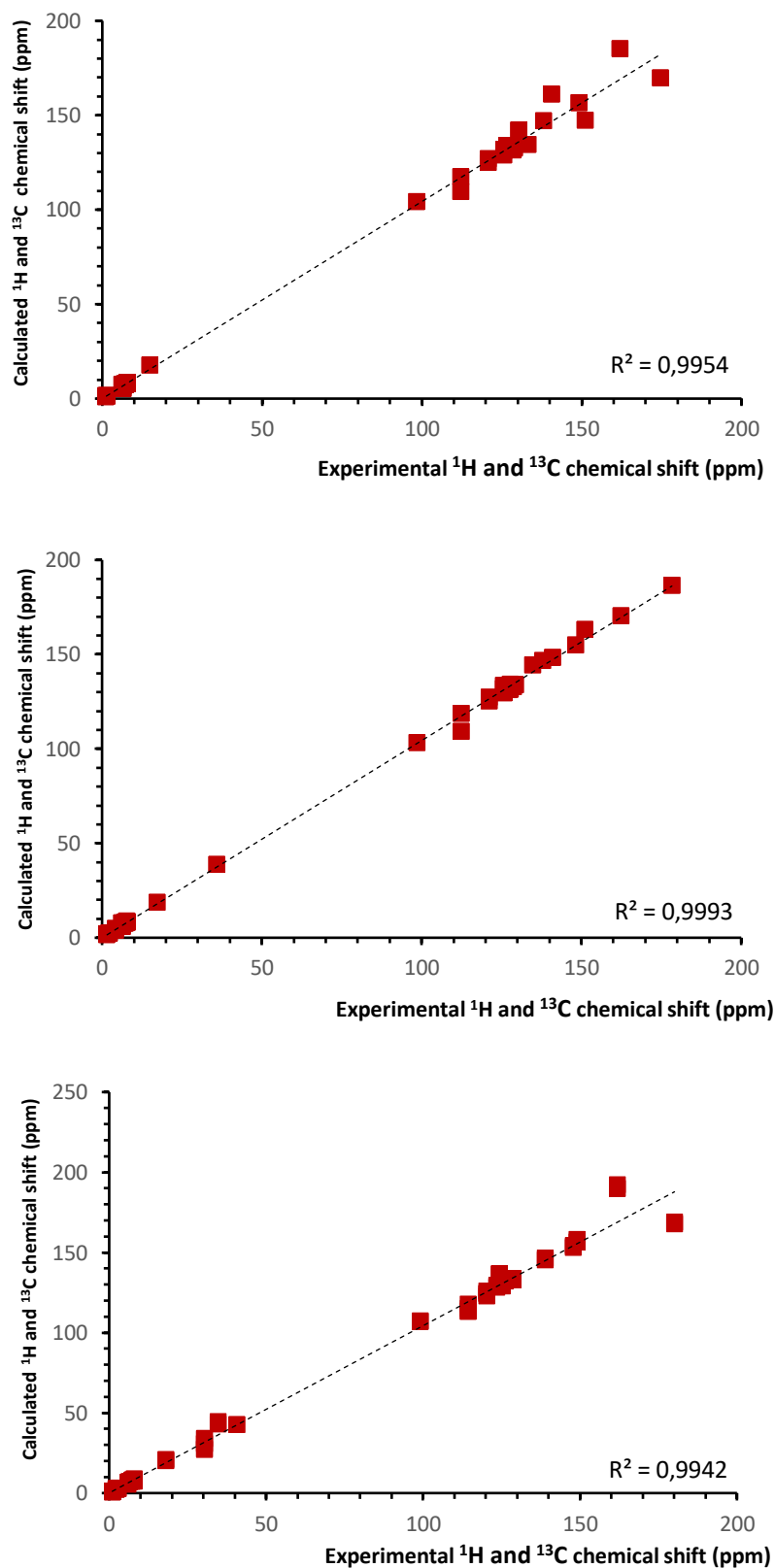
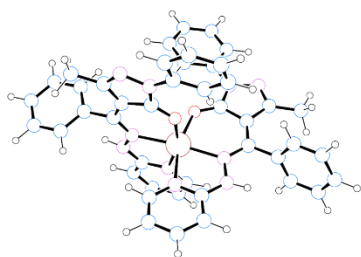
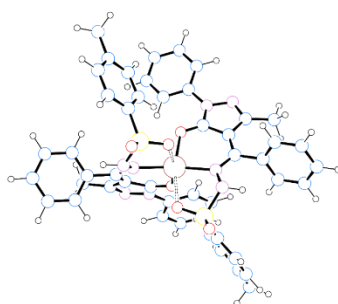


Figure 33. Comparison of the calculated and experimental ^1H and ^{13}C NMR spectra of complexes 3 (top), 4 (middle) and 5 (bottom).

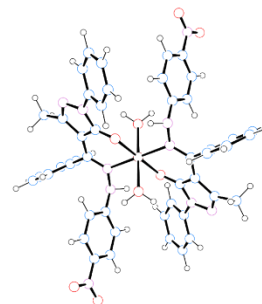
Complex 1 - $[\text{Zn}(\text{HL}^1)]_2$



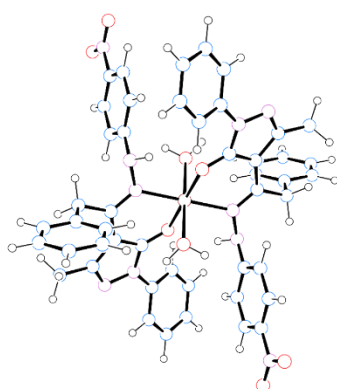
Complex 2 - $[\text{Zn}(\text{HL}^2)]_2$



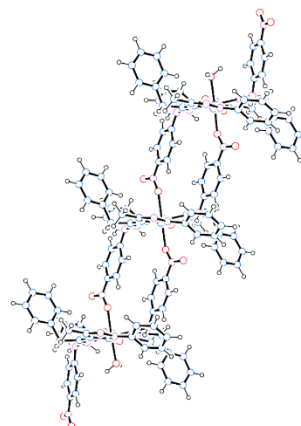
Complex 3 - $[\text{Zn}(\text{HL}^3)]_2 \cdot 2\text{H}_2\text{O}$



Complex 4 - $[\text{Zn}(\text{HL}^4)]_2 \cdot 2\text{H}_2\text{O}$

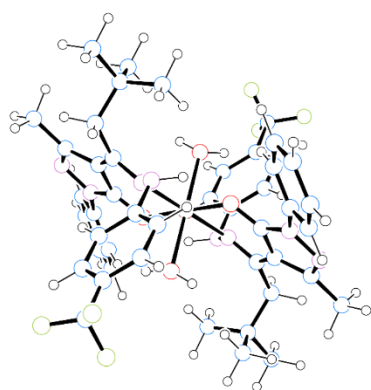


Mononuclear

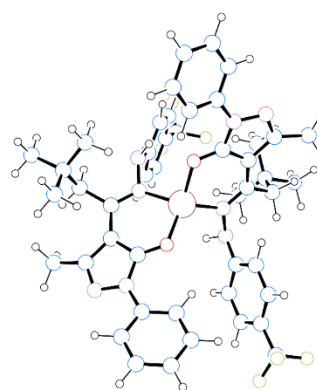


Trinuclear representation

Complex 5a - $[\text{Zn}(\text{HL}^5)]_2 \cdot 2\text{H}_2\text{O}$ and Complex 5b - $[\text{Zn}(\text{HL}^5)]_2$



a



b

Figure 34. Representation of optimized structures of complexes.

2.3.5 Antibacterial activity

To evaluate the antibacterial activity of the ligands $H_2L^1 - H_2L^5$ and of the Zn(II) complexes **1-5**, Gram-positive *S. aureus* and Gram-negative *E. coli* were selected as models. In the following discussion, bactericidal activity is defined as the reduction of bacterial growth $\geq 99.9\%$ within 18-24 hours of inoculation, while bacteriostatic activity is associated with a reduction of bacterial growth maintained stable between 90% and 99%, within 18 and 24 hours of inoculation^[284]. The number of viable cells was used to calculate the growth rate which numerically corresponds to the inverse of the killing rate, a parameter used to define whether a substance exhibits a bactericidal or bacteriostatic action^[264].

The results illustrated in Figure 35 showed that all tested ligands and complexes did not achieve stable antibacterial activity against *E. coli* within 24 h, except **4** and **5**. In particular, complex **4** needs 24 hours to achieve good performance, while **5** achieves 93% reduction of viable cells within the first 2 hours of exposure, then increasing to 99.99% after 24 hours. By contrast, all tested ligands and complexes showed good bacterial killing properties against *S. aureus*. In detail, ligands are able to inhibit the growth of bacterial cells within 24 hours while compounds **1-5** showed good performance with over 80% of bacterial death in the first 4 hours. Going deeper into the analysis of the results, it can be seen that the ligands H_2L^3 and H_2L^4 , whose structures differ only in the acyl fragment, with a phenyl and a benzyl respectively, show a different efficiency as antibacterial agents, with H_2L^4 more active than H_2L^3 against both bacterial strains tested. Consistent with these results, complex **4**, which differs from **3** being polynuclear rather than mononuclear, is more powerful than **3**, especially against *E. coli*. Furthermore, **5** showed a bactericidal performance after the first two hours of inoculation and it was able to maintain the performance achieved during all treatment periods. In general, the performances of all compounds are more homogeneous towards *S. aureus*, both in terms of efficiency and time. A growth inhibition between 95% and 99% of *S. aureus* was achieved by compounds **1-5** within the first 8 hours of treatment, showing clear bacteriostatic activity, Furthermore, **1** and **2** showed bactericidal activity within 12 hours of treatment, **3** and **4** within the first 8 hours, and **5** within the first 2 hours, with 99.99% growth inhibition which remains stable even 24 hours after the test. Significantly, a different behavior was observed towards *E. coli*, since 99.9% inhibition of bacterial growth was observed only by complex **5** after 8 hours, which was maintained even 24 hours after treatment, showing both bacteriostatic and bactericidal activity. Generally, other Schiff base complexes reported in the

literature^{[285]–[287]} display an enhanced bactericidal effect than the free ligands, according to the Overton's concept^[288] and the chelation theory^[289].

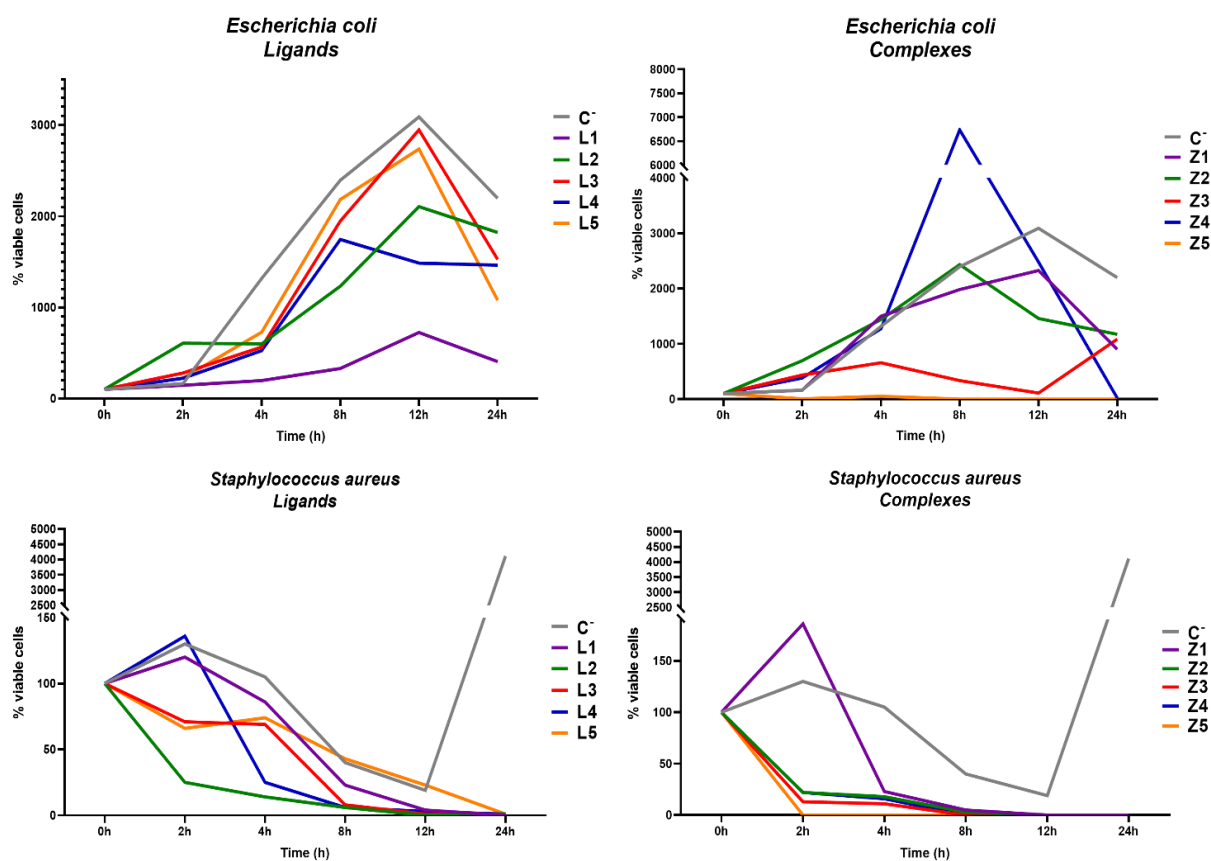


Figure 35. Percentage reduction of viable *E. coli* cells (top) and *S. aureus* cells (bottom) exposed to ligands H_2L^1 – H_2L^5 (left) and Zn(II) complexes 1–5 (right) within 24 hours. Blank corresponds to untreated bacterial cells growth (C = blank).

2.3.6 Reactive oxygen species (ROS) detection assay

To comprehend the possible mechanism of action of the Zn(II) complexes, the most effective compounds **4** and **5** were subject to further investigation through the ROS assay against *E. coli* and *S. aureus*. To detect the amount of reactive oxygen species (ROS) generated, the 2',7'-dichlorofluorescein diacetate (DCFDA) was used as a reagent. This reagent is deacetylated by cellular esterase to a non-fluorescent compound, which is subsequently oxidized by ROS to 2',7'-dichlorofluorescein (DCF). The resulting compound, DCF, is highly fluorescent and is detected by excitation / emission fluorescence spectroscopy at 485 nm / 535 nm. The increased generation of free radicals leads to greater stress for the bacterial cell and the increase in the fluorescence intensity in the first hours (2 h, 4 h) of treatment (as depicted in Figure 36) confirmed the

generation of ROS in both bacterial strains after incubation with compounds **4** and **5**. The fluorescence signal of the untreated bacterial suspension (the blank) was negligible, in agreement with a generation of free radicals in both *E. coli* and *S. aureus* cells.

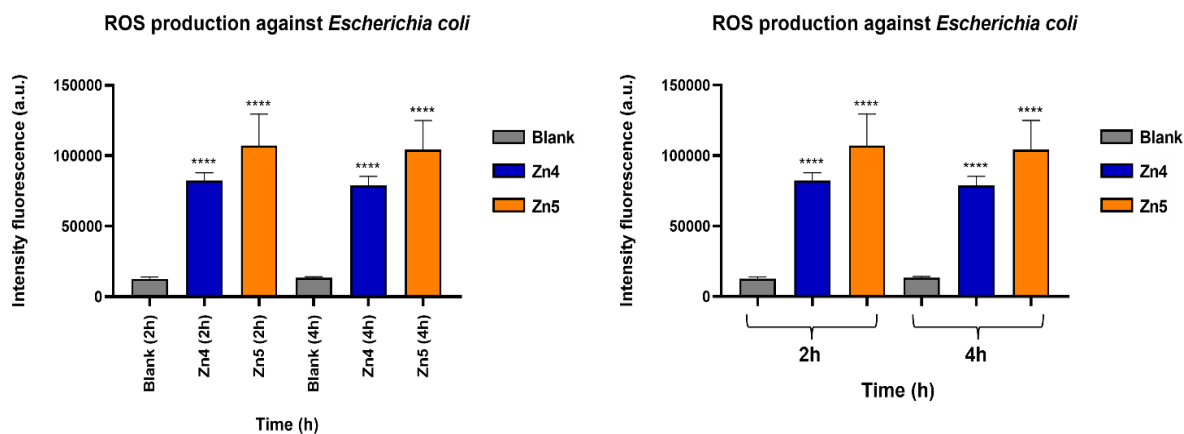


Figure 36. Formation of ROS in *E. coli* (left) and *S. aureus* cells (right) exposed to Zn(II) complexes **4** and **5** for 2 and 4 hours. The data are represented as the mean \pm SD of at least three separate experiments.

2.3.7 Propidium iodide (PI) – viability assay

The viability test was conducted to assess the membrane damage of *E. coli* and *S. aureus* bacterial cells caused by compounds **4** and **5**, using the fluorescent PI dye. PI binds DNA and freely penetrates the cell membranes of dead or dying cells, but not the membranes of viable cells, allowing for the evaluation of the damage in terms of permeabilization. The quantification of the damage on the bacterial cell, following treatment with compounds **4** and **5**, was performed at various time intervals (4 h, 8 h, 12 h, 24 h) as reported in Figure 37. The red fluorescence emission was determined with respect to the untreated bacterial suspension (the blank). In general, it is possible to observe a moderate increase in fluorescence intensity within the first 12 hours, which remains higher compared to the blank even after 24 hours of treatment by both compounds against both bacterial strains, with a superior efficiency of complex **5** with respect to complex **4**, thus demonstrating the ability of Zn(II) complexes to alter the permeability of the cell membrane by disrupting it and leading to the death of the bacterium.

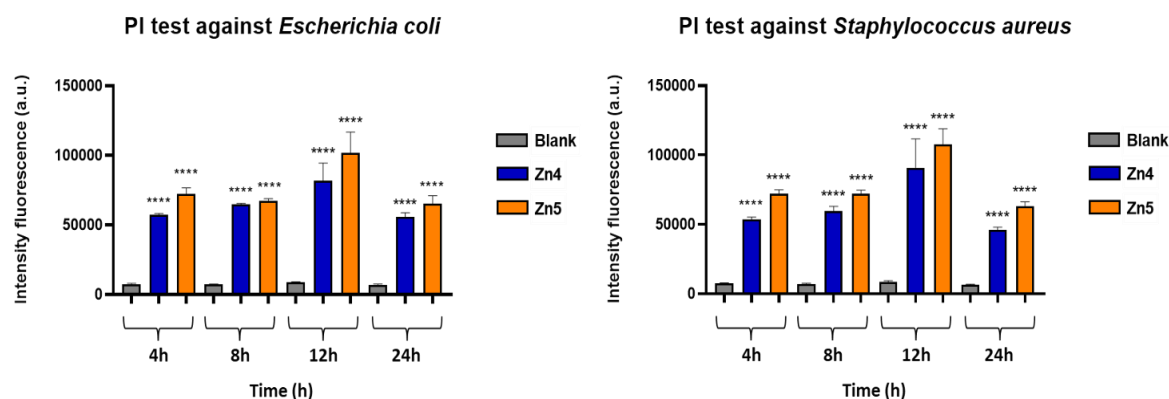


Figure 37. Percentage of PI fluorescent emission for *E. coli* (left) and *S. aureus* cells (right) exposed to Zn(II) complexes **4** and **5** for 4, 8, 12 and 24 hours. The data are represented as the mean \pm SD of at least three separate experiments.

2.3.8 Confocal laser scanning microscopy (CLSM) study

To further determine the overall viability of the bacterial cells the CLSM was performed. According to the LIVE/DEAD BacLight Bacterial Viability Kits, the SYTO 9 stain generally labels all bacteria in a population, while propidium iodide penetrates only bacteria with damaged membranes, causing a reduction in the SYTO 9 stain fluorescence when both dyes are present. Thus, with an appropriate mixture of both strains, bacteria with intact cell membranes stain fluorescent green, whereas bacteria with damaged membranes stain fluorescent red. The images obtained under the confocal microscope show in Fig 38a and c, respectively, the untreated *E. coli* and *S. aureus* cells, which clearly appear to produce green fluorescence. In Figure 38b and d, corresponding respectively to the *E. coli* cells treated with complex **4** and the *S. aureus* cells treated with complex **5**, it is possible to observe a large number of bacterial cells marked with red fluorescent material. These results revealed that after treatment with complexes **4** and **5**, the cell membrane of both bacterial strains is severely damaged, thus confirming the results obtained from previous assay.

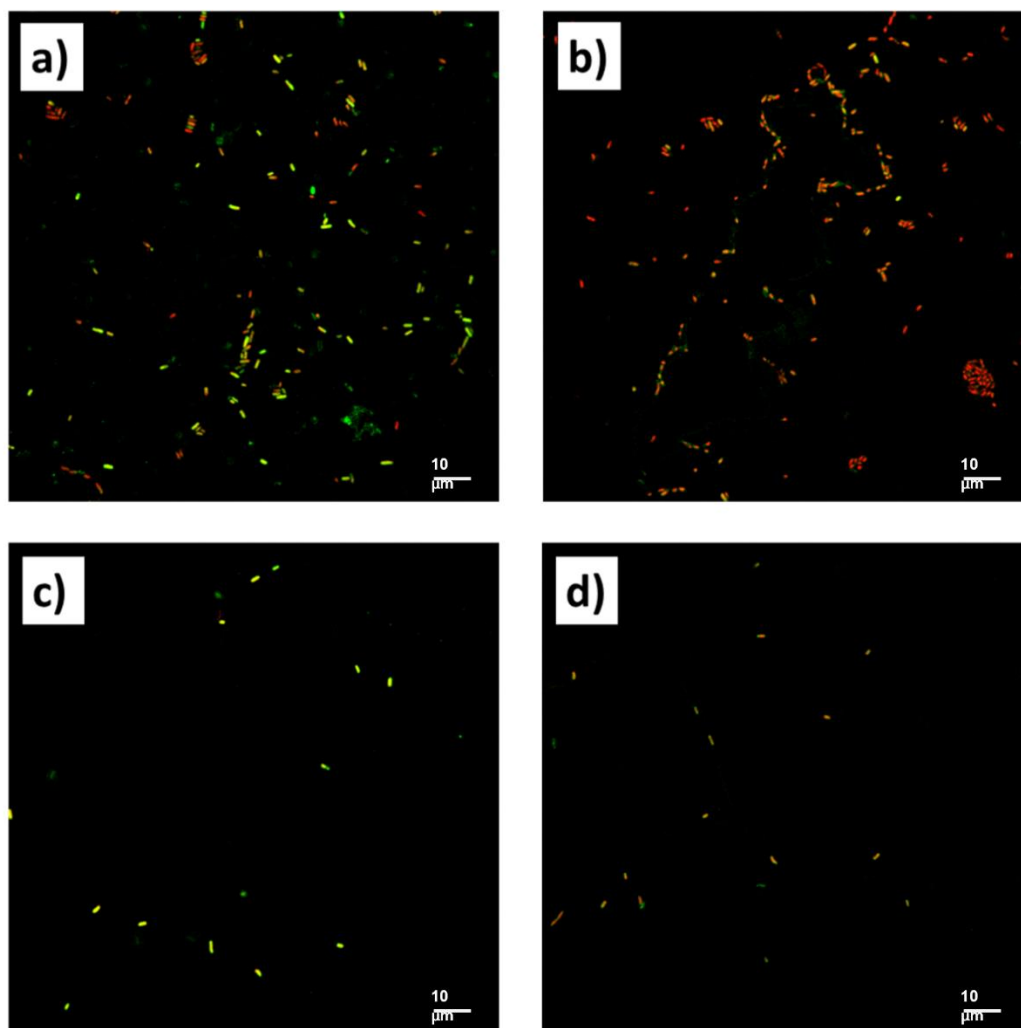


Figure 38. Confocal laser scanning microscopy (CLSM) images of (a) *E. coli* control, (b) *E. coli* treated with complex 4; (c) *S. aureus* control; (d) *S. aureus* treated with complex 5.

2.3.9 Scanning electron microscopy (SEM) study

The images obtained from scanning electron microscopy (SEM) analysis reveal the morphological alterations of the bacterial cells following the treatments with complexes 4 and 5. In Figure 39a it is possible to observe the control sample of the *S. aureus*, having a round appearance with a rigid cell wall. After treatment with complex 5 (Figure 39b), the cells appear significantly smaller and have vesicular structures. In Figure 39c instead is reported the control sample of *E. coli*, having a classic morphology with a rod shape and smooth surface, following treatment with complex 4 (Figure 39d), the cells appear to have lost their regular surface layer and exhibit deformation and

clustering. The SEM results clearly reveal the damage of the membrane permeability of bacterial cells thus confirming the results of the previous tests carried out.

In conclusion, all zinc(II) complexes have been found to significantly enhance the antimicrobial activity against both *E. coli* and *S. aureus*. Complexes **4** and **5** were found to exhibit the most notable performance, with the latter being able to completely inhibit the growth of both bacterial strains within just two hours after contact. One possible explanation for the greater efficacy of Zn(II) complexes against *S. aureus* compared to *E. coli* is attributed to the different cell wall structures of these bacteria, with the cell wall of Gram-negative bacteria being thicker and more resistant. Additionally, the different nuclearity of the zinc complexes and the structures of the ligands may also play a role in the distinctive activities observed. For instance, complex **4** is a polynuclear compound, where the nitro groups of the ligand (HL⁴) interact with zinc atoms of vicinal units, as evidenced by the structural characterization. On the other hand, complex **5**, which is the only compound with an aliphatic neopentyl group instead of an aromatic one on the R¹ position and a trifluoromethyl on the hydrazone fragment, is believed to have improved lipophilic behavior, which contributes to its excellent bacterial killing ability by facilitating the crossing and disruption of the bacterial cell membrane. The results of the viability assay appear to support this hypothesis, and the results of the ROS detection tests provide evidence of the formation of highly reactive radicals associated with membrane dysfunction and cellular destruction. These findings are further confirmed by CLSM and SEM studies.

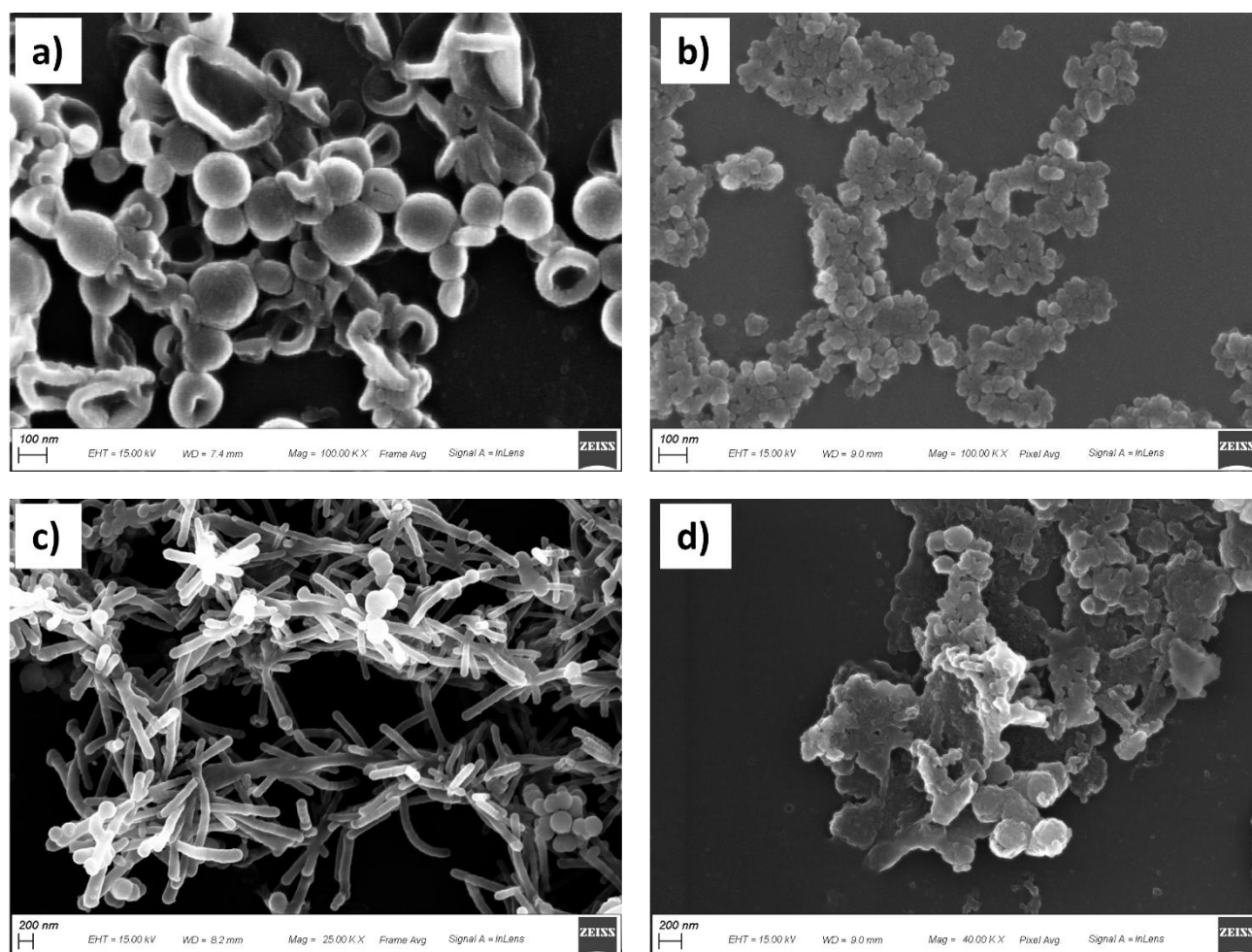


Figure 39. Scanning electron microscopy (SEM) images of (a) *S. aureus* control, (b) *S. aureus* treated with complex 5, both at magnification 100.000; (c) *E. coli* control at magnification 25.000; (d) *E. coli* treated with complex 4 at magnification 40.000.

2.3 Conclusions

In this chapter, a detailed examination of the synthesis and characterization of new hydrazone-pyrazolone ligands was performed. The X-ray studies on the free ligands H_2L^2 and H_2L^4 showed that they existed in the NH,NH tautomeric form, which was a significant finding. Based on this discovery, five new zinc(II) complexes were synthesized and characterized both in the solid state and in solution. Complexes 1 and 2 were found to be mononuclear anhydrous compounds, while complexes 3 and 5 were determined to exist as mononuclear diaqua compounds. One particularly interesting result was obtained from the X-ray studies on complex 4, which showed that it was a polynuclear species assembled through involvement of nitro groups of the ligand (HL^4) in interactions with zinc atoms of vicinal units. However, these interactions were found to be very weak and long, with a Zn-O distance of 2.342(3) Å, as compared to the Zn-O distance of the

carbonyl oxygen of the pyrazolone moiety, which was equal to 2.004(3) Å. This evidence provided insight into how such weak interactions of nitro groups can be easily broken even in chlorinated solutions, where complex **4** is soluble, or how they can be replaced by molecules of water or alcohols during synthesis in methanol, as in the case of complex **3**, which was isolated as a molecular diaqua compound.

To further understand the behaviour of pyrazolone-based hydrazones as ligands in coordination chemistry, a theoretical DFT study was conducted. This study was used to rationalize the structures experimentally found, such as the polymeric nature of complex **4**, as well as to support the spectrochemical assignments, such as IR and NMR spectroscopy. Finally, exploration of the antibacterial potential of both free ligands and zinc(II) complexes revealed that coordination to zinc(II) significantly improved the efficiency against both Gram-negative and Gram-positive bacteria. Among all the complexes studied, the polynuclear Zn(II) complex **4** and the mononuclear dihydrate Zn(II) complex **5** with the hydrophobic-substituted ligand displayed exceptional activity against both bacterial cell lines.

In conclusion, the results of this study not only shed light on the synthesis, characterization and behaviour of hydrazone-pyrazolone ligands and zinc(II) complexes, but also provided new insight into their potential for use as antimicrobial agents.

CHAPTER 3.

Synthesis of novel Schiff base ligands and their zinc(II) and copper(II) complexes. Evaluation of their antiparasitic activity.

3.1 Introduction

Parasitic protozoal diseases, including trypanosomiasis, are listed by the World Health Organization (WHO) as part of 17 neglected tropical diseases which are defined as “a diverse group of communicable diseases that prevail in tropical and subtropical conditions”^[290]. These diseases are referred to as “neglected” primarily because there is little financial incentive to develop drugs for a patient population that cannot afford them. Consequently, there few or no reason for “for-profit” companies to invest in research and development of drugs that will not result in high financial returns. Therefore, much of the drug discovery and hit-to-lead optimization for these diseases is performed in academic laboratories without the financial, personnel, and technical resources of a pharmaceutical company. To make matters worse, the absence of vaccines and, in some cases, the emergence of resistant parasite strains underlines the importance of the successful track record of antiprotozoal drug discovery. The disease is characterized first by a hemolymphatic stage (also known as early stage or stage 1), in which parasite is present in the blood and in the lymphatic system and patients present general flu-like symptoms. In the second or late stage (also known as meningo-encephalic stage or stage 2), parasites will penetrate the blood-brain barrier, invade the perivascular areas, and subsequently infiltrate the white and gray matter of the brain.

Only a few drugs are effective and registered so far for the treatment of human African trypanosomiasis (HAT), such as suramin and pentamidine, and all of them have a certain level of toxicity^{[291]–[293]}. More recently, another drug, named fexinidazole, has been discovered as effective against HAT and listed as essential medicine by WHO^[291]. It is effective both in early and late stage of the disease, unlike suramin, which is used only in the early stage of HAT^{[294],[295]}. Although it delivers all these advantages, fexinidazole shows a significant toxicity profile: neutropenia, body weight loss, reduction in food intake, psychotic disorders, tremors, and dizziness. Therefore, novel scaffolds or new drug entities are urgently needed.

Hydrazones and their metal complexes have been thoroughly investigated over decades for their antioxidant, anti-inflammatory, anticonvulsant, analgesic, antimicrobial antiparasitic, antitubercular, anti-HIV, and anticancer behaviour, raising great interest in the field of medicinal chemistry^[296]. It is known that pyrazolone is also a structural motif with a broad-spectrum of pharmacological feature, including antimicrobial, antitumor, anti-inflammatory, antioxidant, antitubercular, antiviral, lipid-lowering, antihyperglycemic, and protein inhibitory activities^[297].

Previous studies underlined the wide biological activities of a series of Zn(II) complexes with acylpyrazolones, displaying antiproliferative activity against human breast cancer cells^[298], and of pyrazolone-based hydrazones as anticancer multitarget agents^{[274],[299]}. Moreover, some Cu(II) and Zn(II) complexes with acylpyrazolones and acylhydrazone-5-pyrazolones were reported in literature and found to display *in vitro* antimalarial activity with considerable inhibitory effects against *Plasmodium falciparum*^{[218],[236]}. Based on these findings, two new pyrazolone-based hydrazones and their corresponding Zn(II) and Cu(II) complexes have been synthesized and screened against *T. brucei* and mammalian Balb/3T3 cells. The most active and selective metal complex containing a Zn(II) center was further investigated to identify the mechanism of action and the possible target, focusing the study on the peculiar nucleotide metabolism of *T. brucei*. In particular, it is not able to synthesize purines and must recover them from the host^[300], while concerning pyrimidine synthesis and metabolism^[301], the parasites behave normally for uridine nucleotides and in a similar way for cytidine nucleotides since they are produced through a unique *de novo* pathway involving the CTP synthetase (CTPS) enzyme inside the parasite. The complete dependence on CTPS for the production of CTP makes trypanosomes vulnerable to inhibitors of this enzyme^[302].

The discussion reported in this Chapter is adapted from the corresponding work: Marchetti, F., Tombesi, A., di Nicola, C., Pettinari, R., **Verdicchio, F.**, Crispini, A., Scarpelli, F., Baldassarri, C., Marangoni, E., Hofer, A., Galindo, A., & Petrelli, R. (2022). Zinc(II) Complex with Pyrazolone-Based Hydrazones is Strongly Effective against *Trypanosoma brucei* Which Causes African Sleeping Sickness. *Inorganic Chemistry*, 2022, Volume 61, Issue 34, Pages 13561–13575.

3.2 Experimental section

3.2.1 General procedures

All reagents and solvents were purchased from Sigma-Aldrich Chemical Co and were of analytical grade and used as received. Thin-layer chromatography (TLC) was run on silica gel 60 F254 plates. The final compounds were characterized by ^1H NMR, ^{19}F NMR, ^{13}C NMR, MS, and elemental analyses. ^1H NMR and ^{13}C NMR spectra were recorded with the 500 Bruker Ascend (500 MHz for ^1H , 470.6 for ^{19}F , and 125 MHz for ^{13}C) instrument operating at room temperature. The chemical shift values are expressed in δ values (ppm), and coupling constants (J) are in Hertz; tetramethyl silane (TMS) was used as an internal standard. Proton chemical data are reported as follows: chemical shift, multiplicity (s = singlet, d = doublet, dd = doublet of doublets, t = triplet, dt = doublet of triplets, q = quartet, dq = doublet of quartets, and m = multiplet, brs = broad singlet) coupling constant (s), and integration. The presence of all exchangeable protons was confirmed by addition of D_2O . ^1H NMR and ^{13}C NMR spectra were assigned with the aid of $\{^1\text{H}-^1\text{H}\}$ COSY, $\{^1\text{H}-^{13}\text{C}\}$ -HSQC, and $\{^1\text{H}-^{13}\text{C}\}$ -HMBC NMR techniques. Indirect ^{15}N NMR chemical shifts were assigned based on the $\{^1\text{H}-^{15}\text{N}\}$ -HSQC and $\{^1\text{H}-^{15}\text{N}\}$ -HMBC NMR techniques. Mass spectra were recorded on an HP 1100 series instrument. All measurements were performed in the positive ion mode using atmospheric pressure electrospray ionization (API-ESI). Elemental analyses (C, H, and N) were determined on the Thermo Fisher Scientific FLASH2000CHNS analyzer and are within 0.4% of theoretical values. Melting points are uncorrected and were recorded on the STMP3 Stuart scientific instrument and on a capillary apparatus.

3.2.2 Synthesis of proligands

General Procedure for the Synthesis of H_2L^1 and H_2L^2 . The acylpyrazolone ligand 5-hydroxy-3-methyl-1-phenyl-1H-pyrazol-4-yl(phenyl)methanone (HQ^{Bn}) was synthesized following a procedure previously reported in literature^[143]. A mixture of HQ^{Bn} (1.0 equiv) and the appropriate hydrazine (1.0 equiv) in methanol (10 mL) containing 5–10 drops of glacial acetic acid was heated to 80°C , and the reaction was monitored by TLC ($\text{CH}_3\text{Cl}/\text{MeOH}$ 96:4 v/v). A precipitate slowly formed from the hot solution, and after completion, the reaction mixture was placed at 4°C overnight. The obtained precipitate was filtered, redissolved in ethanol (10 mL) and recrystallized from slow evaporation of the solution, to give a light yellow solid which was collected by filtration and dried to a constant weight.

H₂L¹. The proligand H₂L¹ was synthesized from 5-hydroxy-3-methyl-1-phenyl-1H-pyrazol-4-yl(phenyl)methanone (HQ^{Bn}) (500 mg, 1.710 mmol) and 4-trifluoromethylphenylhydrazine (301 mg, 1.710 mmol), following the general procedure previously described (80°C, reaction time 2 h). Yield: 68%, 531 mg, 1.18 mmol. H₂L¹ is a yellow powder soluble in DMSO, acetone, acetonitrile, alcohols, diethyl ether, and chlorinated solvents. Melting point: 195–196°C. Analysis calculated for C₂₅H₂₁F₃N₄O; C, 66.66; H, 4.70; N, 12.65%. Found: C, 66.20; H, 4.60; N, 12.77%. IR (cm⁻¹): 3214w ν(N–H), 3063w ν(C–H aromatic), 3130-2700wbr ν(O–H), 1619vs ν(C=N), 1590vs ν(C=N), 1534s ν(C=C), 1495s ν(C=C), 1488vs ν(C=C), 1327vs ν(C–F), 1317vs ν(C–F), 1112vs ν(C–F), 1064s ν(N–N). ¹H NMR (CDCl₃, 500 MHz, with 0.05% v/v TMS, 298 K): δ_H 12.39s (1H, O–H), 7.97d (2H, ³J = 8.7 Hz, H7 and H7'), 7.50–7.35m (4H, H8, H8', H18 and H18'), 7.27–7.22m (3H, H14, H14' and H15), 7.22–7.17m (1H, ³J = 8.7 Hz, H9), 7.16–7.10m (2H, H13 and H13'), 6.66d (2H, ³J = 8.2, Hz, H17 and H17'), 6.36s (1H, N–H), 4.13s (2H, H11), 2.38s (3H, H21). ¹³C{¹H} NMR (CDCl₃, 125 MHz, with 0.05% v/v TMS, 298 K): δ_C 164.2 (C5), 161.8 (C10), 145.2 (C3), 143.4 (C16), 138.5 (C6), 134.4 (C12), 129.19 (C14 and C14'), 128.9 (C8 and C8'), 127.9 (C13 and C13'), 127.4 (C15), 126.7q (³J_{C–F} = 3.9 Hz, C18 and C18'), 125.0 (C9), 123.7q (²J_{C–F} = 32.9 Hz, C19), 124.2q (¹J_{C–F} = 270.6 Hz, C20), 119.5 (C7 and C7'), 112.6 (C17 and C17'), 100.1 (C4), 33.5 (C11), 16.7 (C21). ¹⁹F{¹H} NMR (CDCl₃, 125 MHz, with 0.05% v/v TMS, 298 K): δ_F 61.7. {¹H,¹⁵N} gs-HSQC NMR (CDCl₃, 51 MHz, ³J_{(N–H)} = 3 Hz, 298 K): δ_N 96.2 (N4). {¹H,¹⁵N} gs-HMBC NMR (CDCl₃, 51 MHz, ³J_{(N–H)} = 3 Hz, 298 K): δ_N 284.9 (N2), 140.6 (N3), 96.2 (N4), N1 not observed. ESI-MS(–) CH₃CN (m/z, relative intensity %): 449 [100] [HL¹][–]. UV–visible (CH₃CN, 10⁻⁵ M): 248 nm (π–π*), 299nm (n–π*).}}

H₂L². The proligand H₂L² was synthesized from (5-hydroxy-3-methyl-1-phenyl-1H-pyrazol-4-yl(phenyl)methanone HQ^{Bn}) (385mg, 1.374mmol) and 2-hydrazinopyridine (150mg, 1.374 mmol), following the general procedure previously described (80°C, reaction time 2 h). Yield: 65%, 333 mg, 0.85 mmol). H₂L² is a brown powder soluble in DMSO, acetone, acetonitrile, alcohols, diethyl ether, and chlorinated solvents. Melting point: 240–241°C. Analysis calculated for C₂₃H₂₁N₅O; C, 72.04; H, 5.52; N, 18.26%. Found: C, 71.96; H, 5.41; N, 18.33%. IR (cm⁻¹): 3301wbr ν(N–H), 3057w ν(C–H_{aromatic}), 3027w ν(C–H_{aromatic}), 1615s ν(C=N), 1592vs ν(C=N), 1538m ν(C=C), 1488m ν(C=C), 1472m ν(C=C), 1009m ν(N–N). ¹H NMR (CDCl₃, with 0.05% v/v TMS, 500 MHz, 298 K): δ_H 12.54s (1H, O–H), 8.10d (1H, ³J = 5.0 Hz, H20), 8.04d (2H, ³J = 7.8 Hz, H7,7'), 7.49t (1H, ³J = 7.4 Hz, H18), 7.42t (2H, ³J = 7.8 Hz, H8,8'), 7.31t (2H, ³J = 7.6 Hz, H13,13'), 7.26–7.21m (3H, H14,14',15), 7.19t (1H, H9), 6.82t (1H, ³J = 7.3 Hz, H19), 6.56d (1H,

$^3J = 8.3$ Hz, H17), 4.22s (2H, H11), 2.42s (3H, H21). ^{13}C NMR(CDCl_3 , 125 MHz with 0.05% v/v TMS, 298 K): δ_{C} 167.1 (C5), 165.7 (C10), 157.9 (C16), 148.2 (C20), 147.0 (C3), 138.9 (C6), 138.5 (C18), 134.6 (C12), 129.2 (C14,14'), 128.8 (C13,13'), 128.1 (C8,8'), 127.3 (C15), 124.6 (C9), 119.3 (C7,7'), 117.2 (C19), 106.8 (C17), 100.2 (C4), 33.6 (C11), 16.8 (C21). $\{^1\text{H}, ^{15}\text{N}\}$ gs-HSQC NMR (CDCl_3 , 51 MHz, $^3J_{(\text{N-H})} = 3$ Hz, 298 K): δ_{N} N4 not observed. $\{^1\text{H}, ^{15}\text{N}\}$ gs-HMBC NMR (CDCl_3 , 51 MHz, $^3J_{(\text{N-H})} = 3$ Hz, 298 K): δ_{N} 286.9 (N2), 139.4 (N3), N4, N1 not observed. ESI-MS(-) CH_3CN (m/z, relative intensity %): 382 [100] $[\text{HL}^2]^-$. UV-visible (CH_3CN , 10^{-5} M): 260 nm ($\pi-\pi^*$), 304 nm ($n-\pi^*$, $>\text{C}=\text{N}-$), 372 nm ($n-\pi^*$, py).

3.2.3 Synthesis of Zn(II) and Cu(II) complexes

[Zn-(HL¹)₂(MeOH)₂] (1). A solution of $\text{Zn}(\text{OOCCH}_3)_2 \cdot 2\text{H}_2\text{O}$ (29 mg, 0.133 mmol) in water (5 mL) was added to a solution of H_2L^1 (120 mg, 0.166 mmol) dissolved in methanol (15 mL). The mixture was stirred at reflux, and within an hour, a light yellow precipitate formed, which was removed by filtration, washed with a EtOH/H₂O (60:40 v/v) solution and shown to be complex **1**. It is soluble in DMSO, DMF, acetonitrile, acetone, diethyl ether and chlorinated solvents. Yield = 86%, 118mg, 0.114 mmol. Melting point: 139–140°C. Analysis calculated for $\text{C}_{52}\text{H}_{48}\text{F}_6\text{N}_8\text{O}_4\text{Zn}$; C, 60.73; H, 4.70; N, 10.90%. Found: C, 60.68; H, 4.67; N, 10.81%. IR (cm^{-1}): 3299m $\nu(\text{N-H})$, 3.134wbr $\nu(\text{O-H} \cdots \text{N})$, 3060w $\nu(\text{C-H}_{\text{aromatic}})$, 1603s $\nu(\text{C}=\text{N})$, 1576s $\nu(\text{C}=\text{N})$, 1532w $\nu(\text{C}=\text{C})$, 1506s $\nu(\text{C}=\text{C})$, 1479m $\nu(\text{C}=\text{C})$, 1322vs $\nu(\text{C-F})$, 1103vs $\nu(\text{C-F})$, 1065s $\nu(\text{N-N})$, 550m $\nu(\text{Zn-N})$, 472s $\nu(\text{Zn-O})$. ^1H NMR (CDCl_3 with 0.05% v/v TMS, 500 MHz, 298 K): δ_{H} 7.84d (4H, $^3J = 8.0$ Hz, H7 and H7'), 7.43t (4H, $^3J = 7.8$ Hz, H8 and H8'), 7.34–7.23m (12H, H14, H14', H15, H18, H18', H19), 7.03d (4H, $^3J = 6.6$ Hz, H13 and H13'), 6.46d (4H, $^3J = 8.3$ Hz, H17 and H17'), 5.98s (2H, N-H), 4.17s (4H, H11), 3.44s (6H, MeOH), 2.28s (6H, H21), 1.30s (4H, MeOH). $^{13}\text{C}\{^1\text{H}\}$ NMR (CDCl_3 with 0.05% v/v TMS, 125 MHz, 298 K): δ_{C} 177.7 (C5), 162.6 (C10), 149.1 (C3), 148.1 (C16), 138.5 (C6), 135.3 (C12), 129.1 (C14 and C14'), 128.7 (C8 and C8'), 127.9 (C13 and C13'), 127.0 (C15), 126.3q ($^3J_{\text{C-F}} = 3.4$ Hz, C18 and C18'), 125.6 (C9), 124.3q ($^1J_{\text{C-F}} = 271.3$ Hz, C20), 123.1q ($^2J_{\text{C-F}} = 32.3$ Hz, C19), 119.5 (C7 and C7'), 114.1 (C17 and C7'), 98.3 (C4), 35.7 (C11), 17.3 (C21). $^{19}\text{F}\{^1\text{H}\}$ NMR (CDCl_3 , 125 MHz, with 0.05% v/v TMS, 298 K): δ_{F} 61.4. $\{^1\text{H}, ^{15}\text{N}\}$ gs-HSQC NMR (CDCl_3 , 51 MHz, $^3J_{(\text{N-H})} = 3$ Hz, 298 K): δ_{N} 117.3 (N4). $\{^1\text{H}, ^{15}\text{N}\}$ gs-HMBC NMR (CDCl_3 , 51 MHz, $^3J_{(\text{N-H})} = 3$ Hz, 298K): δ_{N} 276.4 (N2), N3, N4, N1 not observed. ESI-MS(+) CH_3CN (m/z, relative intensity %): 965 [100]

$[\text{Zn}(\text{HL}^1)(\text{H}_2\text{L}^1)]^+$; 987 [40] $[\text{Zn}(\text{HL}^1)_2 + \text{Na}]^+$; 1479 [30] $[\text{Zn}_2(\text{HL}^1)_3]^+$. UV-visible (CH_3CN , 10^{-5} M): 249 nm ($\pi-\pi^*$), 299 nm ($n-\pi^*$), 388 nm sh (LMCT).

$[\text{Zn}(\text{HL}^2)_2]$ (2). A solution of $\text{Zn}(\text{OOCCH}_3)_2 \cdot 2\text{H}_2\text{O}$ (29 mg, 0.133 mmol) in water (5 mL) was added to a solution of H_2L^2 (120 mg, 0.313 mmol) dissolved in methanol (15 mL). The mixture was stirred at room temperature and within an hour a light yellow precipitate formed, which was removed by filtration, washed with a EtOH/ H_2O (60:40 v/v) solution, and shown to be complex **2**. Yield: 78%, 102mg, 0.122 mmol. It is soluble in DMSO, DMF, acetone, acetonitrile, and chlorinated solvents. Melting point: 172–174 °C. Analysis Calculated for $\text{C}_{46}\text{H}_{40}\text{N}_{10}\text{O}_2\text{Zn}$; C, 66.55; H, 4.86; N, 16.87 %. Found: C, 63.65; H, 4.72; N, 15.64%. IR (cm^{-1}): 3316w $\nu(\text{N-H})$, 3187wbr $\nu(\text{N-H})$, 3056w $\nu(\text{C-H}_{\text{aromatic}})$, 1614s $\nu(\text{C=N})$, 1593 $\nu(\text{C=N})$, 1570s $\nu(\text{C=N})$, 1055m $\nu(\text{N-N})$, 540m $\nu(\text{Zn-N})$, 444s $\nu(\text{Zn-O})$. ^1H NMR (CDCl_3 with 0.05% v/v TMS, 500 MHz, 298 K): δ_{H} 8.05d (1H, $^3\text{J} = 8.0$ Hz, H_2O), 7.73 (2H, d, $^3\text{J} = 8.0$ Hz, H7 and H7'), 7.55 (1H, s, N-H), 7.50 (2H, d, $^3\text{J} = 7.8$ Hz, H13 and H13'), 7.44 (3H, m, H15, H14 and H14'), 7.38 (2H, d, $^3\text{J} = 7.6$ Hz, H18), 7.15 (2H, t, $^3\text{J} = 8.0$ Hz, H8 and H8'), 6.99 (1H, t, $^3\text{J} = 8.0$ Hz, H9), 6.52 (1H, t, $^3\text{J} = 7.6$ Hz, H19), 6.33 (1H, d, $^3\text{J} = 8.0$ Hz, H17), 4.41 (2H, dbr, H11), 2.42 (3H, s, H21). ^{13}C NMR (CDCl_3 with 0.05% v/v TMS, 125 MHz, 298 K): δ_{C} 165.5 (C5), 162.2 (C10), 152.6 (C16), 146.7 (C20), 144.6 (C3), 139.0 (C6), 138.5 (C18), 134.6 (C12), 129.8 (C15), 128.8 (C14,14'), 128.2 (C8,8'), 128.0 (C13,13'), 124.6 (C9), 119.3 (C7,7'), 115.4 (C19), 109.3 (C17), 97.6 (C4), 35.4 (C11), 17.2 (C21). $\{^1\text{H}, ^{15}\text{N}\}$ gs-HSQC NMR (CDCl_3 , 51 MHz, $^3\text{J}_{(\text{N-H})} = 3\text{Hz}$, 298 K): δ_{N} 130.2 (N4). $\{^1\text{H}, ^{15}\text{N}\}$ gs-HMBC NMR (CDCl_3 , 51 MHz, $^3\text{J}_{(\text{N-H})} = 3$ Hz, 298 K): δ_{N} 51.2 (N5), N3, N2, and N1 not observed. ESI-MS(+) CH_3CN (m/z, relative intensity %): 829 [70] $[\text{Zn}(\text{HL}^2)(\text{H}_2\text{L}^2)]^+$; 851 [100] $[\text{Zn}(\text{HL}^2)_2 + \text{Na}]^+$; 1276 [55] $[\text{Zn}_2(\text{HL}^2)_3]^+$. UV-visible (CH_3CN , 10^{-5} M): 266 nm ($\pi-\pi^*$), 305 nm ($n-\pi^*$, $>\text{C=N-}$), 371 nm ($n-\pi^*$, py), 406 nm sh (LMCT).

$[\text{Cu}(\text{HL}^1)_2]$ (3). A solution of $\text{Cu}(\text{OOCCH}_3)_2 \cdot 2\text{H}_2\text{O}$ (26 mg, 0.133 mmol) in water (5 mL) was added to a solution of H_2L^1 (120 mg, 0.166 mmol) dissolved in methanol (15 mL). The mixture was stirred at room temperature, and immediately a red precipitate formed, which was removed by filtration, washed with a EtOH/ H_2O (60:40v/v) solution, and shown to be complex **3**. It is soluble in DMSO, DMF, acetone, and chlorinated solvents. Yield: 63%, 80 mg, 0.084 mmol. Melting point: 205–208°C. Analysis calculated for $\text{C}_{50}\text{H}_{40}\text{CuF}_6\text{N}_8\text{O}_2$; C, 62.40; H, 4.19; N, 11.64%. Found: C, 62.19; H, 4.24; N, 11.32%. IR (cm^{-1}): 3294m $\nu(\text{N-H})$, 3026w $\nu(\text{C}_{\text{arom}}-\text{H})$, 3028w $\nu(\text{C}_{\text{arom}}-\text{H})$, 1614m $\nu(\text{C=N})$, 1601m $\nu(\text{C=N})$, 1588m $\nu(\text{C=N})$, 1575m $\nu(\text{C=C})$, 1516vs $\nu(\text{C=C})$, 1489vs $\nu(\text{C=C})$, 1327vs $\nu(\text{C-F})$, 1103vs $\nu(\text{C-F})$, 1065s $\nu(\text{N-N})$, 540m $\nu(\text{Cu-N})$, 510s

$\nu(\text{Cu-O})$. ESI-MS(+) CH_3CN (m/z, relative intensity %): 963 [15] $[\text{Cu}(\text{HL}^1)(\text{H}_2\text{L}^1)]^+$; 1067 [20] $[\text{Cu}(\text{HL}^1)(\text{H}_2\text{L}^1)(\text{MeOH})_2(\text{MeCN})]^+$. UV-visible (CH_3CN , 10^{-5} M): 259 nm ($\pi-\pi^*$), 278 nm ($n-\pi^*$), 392 nm sh (LMCT).

[Cu(HL²)₂] (4). A solution of $\text{Cu}(\text{OOCCH}_3)_2 \cdot 2\text{H}_2\text{O}$ (31 mg, 0.157 mmol) in water (5 mL) was added to a solution of H_2L^2 (120 mg, 0.313 mmol) dissolved in methanol (15 mL). The mixture was stirred at room temperature, and immediately a brown green precipitate formed, which was removed by filtration, washed with a $\text{EtOH}/\text{H}_2\text{O}$ (60:40 v/v) solution, and shown to be complex **4**. It is soluble in DMSO, DMF, acetone, acetonitrile, and chlorinated solvents. Melting point: 181–182°C. Analysis calculated for $\text{C}_{46}\text{H}_{40}\text{CuN}_{10}\text{O}_2$; C, 66.69; H, 4.87; N, 16.91%. Found: C, 66.23; H, 4.75; N, 16.86%. IR (cm^{-1}): 3297wbr $\nu(\text{N-H})$, 3062w $\nu(\text{N-H})$, 3030w $\nu(\text{C-H}_{\text{aromatic}})$, 1617m $\nu(\text{C=N})$, 1588m $\nu(\text{C=N})$, 1572v $\nu(\text{C=N})$, 1528m, 1508m $\nu(\text{C=C})$, 1071m $\nu(\text{N-N})$, 546m $\nu(\text{Cu-N})$, 508s $\nu(\text{Cu-O})$. ESI-MS(+) CH_3CN (m/z, relative intensity %): 828 [100] $[\text{Cu}(\text{HL}^2)(\text{H}_2\text{L}^2)]^+$; 1274 [75] $[\text{Cu}_2(\text{HL}^2)_3]^+$. UV-visible (CH_3CN , 10^{-5} M): 256 nm ($\pi-\pi^*$), 305 nm ($n-\pi^*$, $>\text{C}=\text{N}-$), 378 nm ($n-\pi^*$, py), 414 nm sh (LMCT).

[Cu(Q^{Bn})₂] (5). Complex **5** is obtained with a procedure similar to that of **3** but leaving the reaction mixture under stirring for 24 h, during which the red precipitate slowly converts to dark green. It is soluble in DMSO, DMF, acetone, and chlorinated solvents. Yield: 86%, 74 mg, 0.114 mmol. Melting point: 264–266°C. Analysis calculated for $\text{C}_{36}\text{H}_{30}\text{CuN}_4\text{O}_4$; C, 66.91; H, 4.68; N, 8.67%. Found: C, 66.55; H, 4.57; N, 8.71%. IR (cm^{-1}): 3065w $\nu(\text{C}_{\text{arom}}-\text{H})$, 3037w $\nu(\text{C}_{\text{arom}}-\text{H})$, 1604s $\nu(\text{C=O})$, 1590s $\nu(\text{C=N})$, 1575vs $\nu(\text{C=C})$, 1532m $\nu(\text{C=C})$, 1486vs $\nu(\text{C=C})$, 510s, 400m $\nu(\text{Cu-O})$. ESI-MS(+) CH_3CN (m/z, relative intensity %): 647 [100] $[\text{Cu}(\text{Q}^{\text{Bn}})(\text{HQ}^{\text{Bn}})]^+$.

3.2.4 Structural characterization by X-ray diffraction

Single-crystal X-ray diffraction data of proligands H_2L^1 and H_2L^2 and complexes **1** and **5** were collected at room temperature with the Bruker-Nonius X8APEXII CCD area detector system equipped with a graphite monochromator with radiation $\text{Mo K}\alpha$ ($\lambda = 0.71073 \text{ \AA}$). Data were processed through the SAINT reduction and SADABS absorption software^{[303],[304]}. Structures were solved by direct methods and refined by full-matrix least-squares based on F^2 through the SHELX and SHELXTL structure determination package^[303]. All non-hydrogen atoms were refined anisotropically. Fluorine atoms F(2) and F(3) of the $-\text{CF}_3$ group in complex **1** are found to be disordered in two positions and refined with an occupancy factor of 0.80 and 0.20, respectively.

Both sets of atoms were refined anisotropically. Hydrogen atoms were included as idealized atoms riding on the respective carbon, nitrogen, and oxygen atoms with bond lengths appropriate to the hybridization. H(1a) and H(4a) hydrogen atoms in H₂L² were located in the best difference map and refined isotropically. Constrains and restrains have been applied on the N5/C(23) pyridine ring (refinement with idealized geometry and thermal motion restrains) in order to fix a slight disorder. All graphical representations have been obtained by using the Olex2 software package^[305].

3.2.5 Theoretical calculations

The electronic structure and geometries of the proligands H₂L¹ and H₂L², their tautomers and anions, [HL¹]⁻ and [HL²]⁻, and zinc and copper complexes were investigated by using DFT at the B3LYP level^{[270],[271]}. For the proligands and their corresponding anions, the 6-311G** basis set was used for the optimization, while for the Zn and Cu complexes, the optimization was carried out using 6-311G*. Molecular geometries were optimized without symmetry restrictions. Frequency calculations were carried out at the same level of theory to identify all of the stationary points as minima (zero imaginary frequencies) and to provide the thermal correction to free energies at 298.15K and 1 atm. Solution-phase SCF energies were calculated by a single-point calculation on the *in vacuo* optimized structure using the CPCM solvation model in chloroform^[266]. Gibbs free energies in chloroform solution were estimated from the equation $G_{\text{solv}} = E_{\text{solv}} + (G_{\text{gas}} - E_{\text{gas}})$. The GIAO method was used for the NMR calculations (¹H-, ¹³C-, and ¹⁵N NMR isotropic shielding tensors) which were carried out at the 6-311++G** level of theory. The computed IR spectra were scaled by a factor of 0.96^{[267],[268]}. The DFT calculations were executed using the Gaussian09 program package^[269].

3.2.5 Cell culture and Cytotoxicity determinations.

The biological assays have been conducted in collaboration with Prof. Anders Hofer, Department of Medical Biochemistry and Biophysics, Umeå University, Umeå, Sweden. *T. brucei* TC221 bloodstream forms and mouse embryonic fibroblast Balb/3T3 cells (ATCC no CCL-163) were cultivated in a vented plastic flask at 37°C with 5% CO₂. For *T. brucei*, the growth medium was Hirumi's modified Iscoves medium (HMI)-9 supplemented with 10% (v/v) fetal bovine serum (Thermo Fischer Scientific Gibco, Waltham, MA, USA), whereas the Balb/3T3 cells were grown in Dulbecco's modified Eagle's medium (Sigma-Aldrich) supplemented with 10% (v/v) heat-

inactivated fetal bovine serum, glutamine (0.584 g/L), and 10 mL/L 100 × penicillin–streptomycin (Gibco)^{[306],[307]}. The synthetic compounds tested were dissolved in DMSO and serially diluted with growth medium in white 96-well microtiter plates. 20,000 bloodstream forms of *T. brucei* cells were added to each well in the final volume of 200 μL. In the case of mammalian cells (Balb3T3), 2000 cells/well was added, with similar results. To avoid any damage to the cells, the concentration of DMSO in the solution was never higher than 1% (no cell growth inhibition was observed with this concentration of DMSO). Cell viability was verified by a drug-free control for each compound. The plates were incubated for 48 h in the 5% CO₂ incubator; then, 20 μL of 0.5 mM resazurine (Sigma-Aldrich) was added to each well, and the plates were incubated for an additional 24 hours before the fluorescence was measured with the Synergy H4 microplate reader (excitation wavelength 530 or 540 nm and emission wavelength 590 nm). The half-maximal efficacious concentration (EC₅₀) values were calculated on the log inhibitor versus the response curves by non-linear regression using the GraphPad prism 5.2 software (GraphPad Software, Inc., La Jolla, CA, USA). The procedure was repeated three times to make data reliable.

3.2.6 Determination of NTP and dNTP pools by HPLC

The bloodstream form of *T. brucei* (strain 221) was maintained at 37 °C and 5% CO₂ in Hirumi's modified Iscove's medium (HMI)-9 medium and Serum Plus containing 10% fetal bovine serum. Trypanosomes (50 mL), harvested in the late logarithmic phase, were chilled on ice for 5 min before being collected and centrifuged at 4000 rpm for 5 min at 4°C. Subsequently, the pellet was resuspended in 1 mL of culture medium, transferred to an Eppendorf tube, and centrifuged at 14000 rpm for 1 min at 4°C. The NTP, NDP, dNDP, and dNTP pools were not affected by the time on ice (5 min), the centrifugation time (varied between 5 and 15 min), the centrifugation speed (varied between 4000 and 14000 rpm), or how many washings in culture medium were made (3 times). After the medium wash, the collected trypanosomes were disintegrated by pipetting them up and down in 720 μL of ice-cold 0.6 M trichloroacetic acid containing 15 mM MgCl₂. The resultant solution was centrifuged at 14,000 rpm for 1 min at 4°C, and the supernatant was extracted twice with 1.13 the volume of Freon (78% v/v)-trioctylamine (22% v/v) or chloroform–trioctylamine. 400 μL of the resulting solution was transferred and centrifuged in a pre-washed Eppendorf tube with a 5 kDa filter (Nanosep 3k Omega, Pall Life Sciences). The sample was purified on a WAX cartridge properly prewashed, and the collected solution was evaporated to dryness in a Speedvac (Savant) and dissolved in 200 μL of water. This fraction was

used for quantification of nucleotides and deoxynucleotide diphosphates and triphosphates by a 150×3 mm C18-WP HPLC column (Chromanik Sunshell)^[308]. The analyses were performed on a 150×2.1 mm Sunshell C18-WP 2.6 μm column (ChromaNik Technologies Inc), at 30 °C using a mobile phase of 43% solution A and 57% solution B. Solution A contained 5.8% (v/v) acetonitrile, 23 g/L KH_2PO_4 , and 0.7 g/L tetrabutylammonium bromide (TBA-Br) adjusted to pH 5.6 with KOH, while solution B contained 5.8% (v/v) acetonitrile and 0.7 g/L TBA-Br. All reagents and solvents were of HPLC grade. The size of the sample loop was 100 μL , and the flow rate was 1.2 mL/min. The peaks were detected by their absorption at 270nm with a UV-2075 Plus detector. Nucleotides were quantified by measuring peak heights and areas and comparing them to a standard curve.

3.3 Results and discussion

3.3.1 Synthesis and spectroscopic characterization of proligands and complexes

The precursor used to synthesize the proligands described in this chapter is 1-(5-hydroxy-3-methyl-1-phenyl-1*H*-pyrazol-4-yl)-2-phenylethanone, HQ^{Bn} , and it was prepared following a procedure previously reported in literature^[143]. The proligands H_2L^n were synthesized by reacting an equimolar amount of HQ^{Bn} and the appropriate hydrazine, in detail 1-(4-trifluoromethylphenyl)-hydrazine for the preparation of the proligand H_2L^1 and 2-hydrazinopyridine to afford the proligand H_2L^2 , in methanol with the addition in traces of glacial acetic acid, as illustrated in Chart 39^[144]. All the compounds have been characterized by means of 1H -NMR, ^{13}C -NMR, ^{15}N -NMR, $\{^1H,^1H\}$ -COSY, $\{^1H,^{13}C\}$ -HSQC, $\{^1H,^{13}C\}$ -HMBC, IR spectroscopy and ESI-MS spectroscopy.

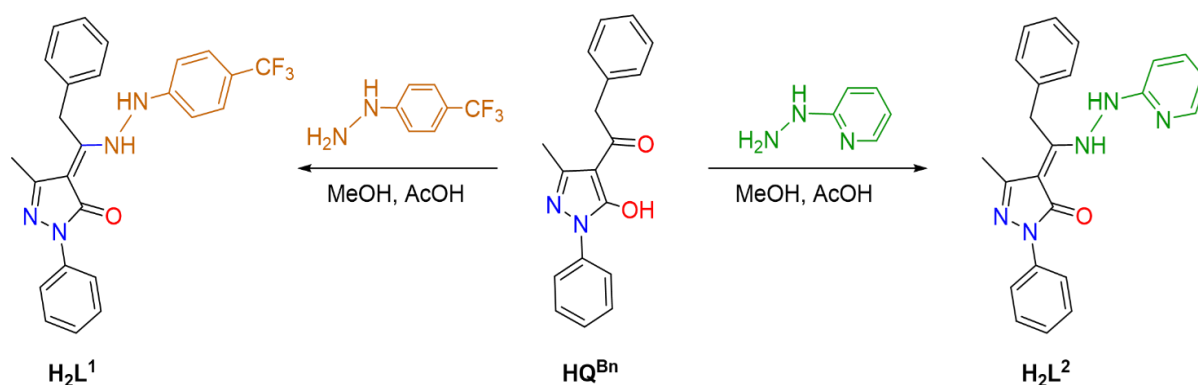


Chart 39. Synthesis procedure for proligands H_2L^1 and H_2L^2 from precursor HQ^{Bn} .

The two proligands are air-stable in the solid-state and soluble in most organic solvents. In their solid state IR spectra shown in Figures 40-41, it was possible to assign the strong bands in the range of 1618 - 1614 cm^{-1} to $\nu(>C=N-)$ of the azomethine fragment, while those in the range of 1593 - 1532 cm^{-1} were assigned to the vibrational mode $\nu(C=N)$ of the pyrazolone ring and, for H_2L^2 , also of the pyridine ring^{[283],[309]-[311]}. Additional strong bands at around 1320 cm^{-1} and 1100 cm^{-1} in the IR spectra of H_2L^1 were assigned to the asymmetric and symmetric stretching vibrations of CF_3 group^[280], while those falling in the range of 1009 - 1064 cm^{-1} are typical of the stretching $\nu(N-N)$ ^{[118],[274]}. The band found at 3211 cm^{-1} , due to the vibration mode $\nu(N-H)$, and the broad absorption in the range of 3130 - 2700 cm^{-1} , which is typical of $\nu(N-H\cdots O)$ involved in

intramolecular H-bonding, led to the conclusion that proligand H_2L^1 exists in the N-H,N-H tautomeric form, as shown in Chart 40 as further confirmed by the X-ray diffraction study discussed later in this chapter. In a similar manner, the broad band centered at 3301 cm^{-1} in the infrared spectrum of H_2L^2 is in accordance with a N-H,N-H tautomeric form, also shown in Chart 40, and contrarily to an analogous pyridine-containing proligand, differing only in the C10 substituent bearing a phenyl moiety as a replacement for the benzyl moiety in H_2L^2 , that was isolated in a N5-H,N4-H zwitterionic form^[118].

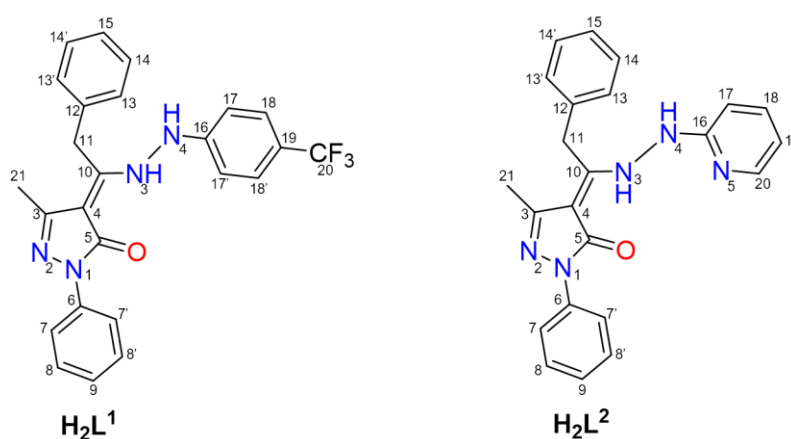


Chart 40. Solid-state structure of H_2L^1 and H_2L^2 with numbered C and N atoms.

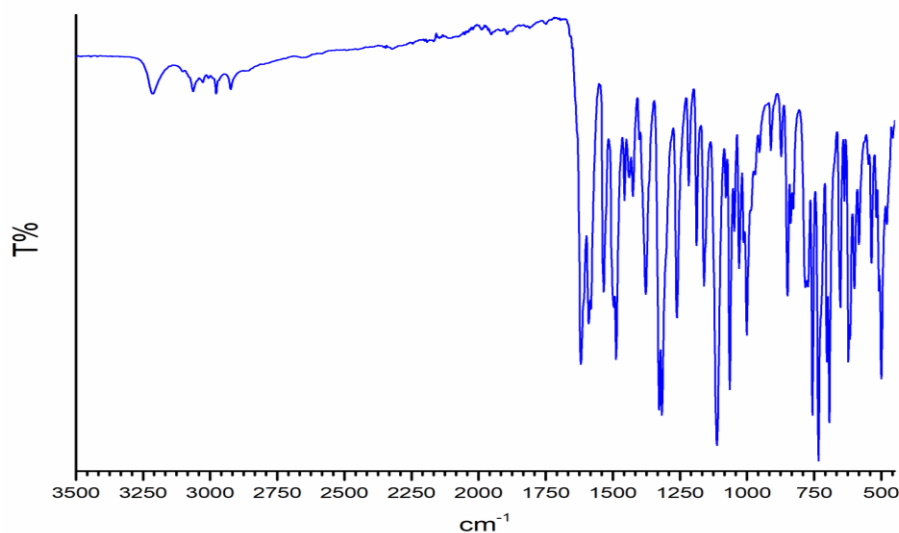


Figure 40. IR spectrum of H_2L^1 .

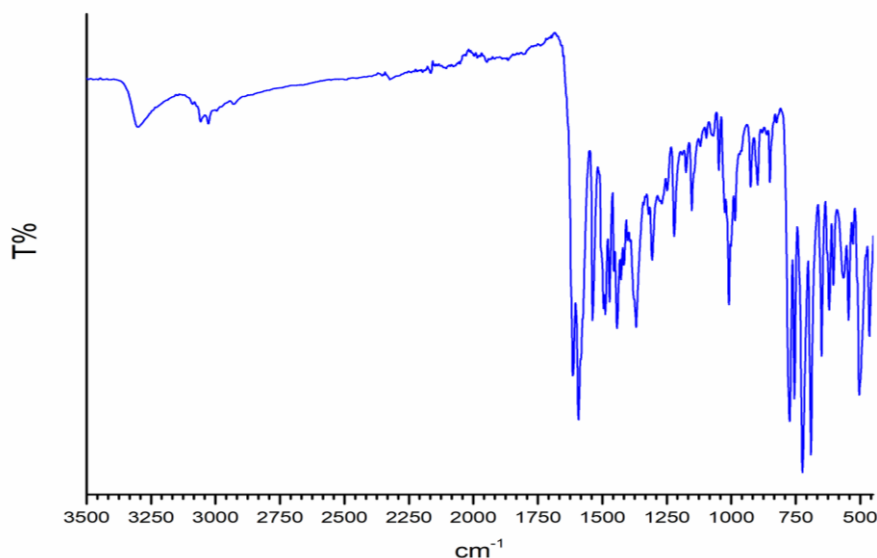


Figure 41. IR spectrum of H_2L^2 .

The 1H and ^{13}C NMR chemical shifts were assigned based on 1H - 1H and one-bond and long range 1H - ^{13}C couplings, observed in $\{^1H$ - 1H }-COSY, $\{^1H$ - ^{13}C }-HQSC and $\{^1H$ - ^{13}C }-HMBC. Moreover, indirect ^{15}N chemical shifts were assigned based on $\{^1H$ - ^{15}N }-HSQC and $\{^1H$ - ^{15}N }-HMBC for the free proligands H_2L^1 and H_2L^2 , giving support to the hypothesis that in solution the two proligands appear mostly in the N-H,O-H tautomeric forms. In Figures 42-49 the full NMR characterization is shown with the labelled resonances as example. In fact, for both proligands it is possible to observe only one resonance in the $\{^1H$ - ^{15}N }-HSQC corresponding to the N4-H coupling. The other N atoms were assigned based on the resonance of the $\{^1H$ - ^{15}N }-HMBC spectrum, expect for N1 that remains not observed. For H_2L^1 , similarly to the case of H_2L^5 in the previous chapter, it is possible to observe a single resonance in the ^{19}F NMR spectrum, as well as the ^{13}C - ^{19}F coupling resonances in the ^{13}C NMR spectrum, affording the set of the three characteristic quartets corresponding to C18, C19 and C20.

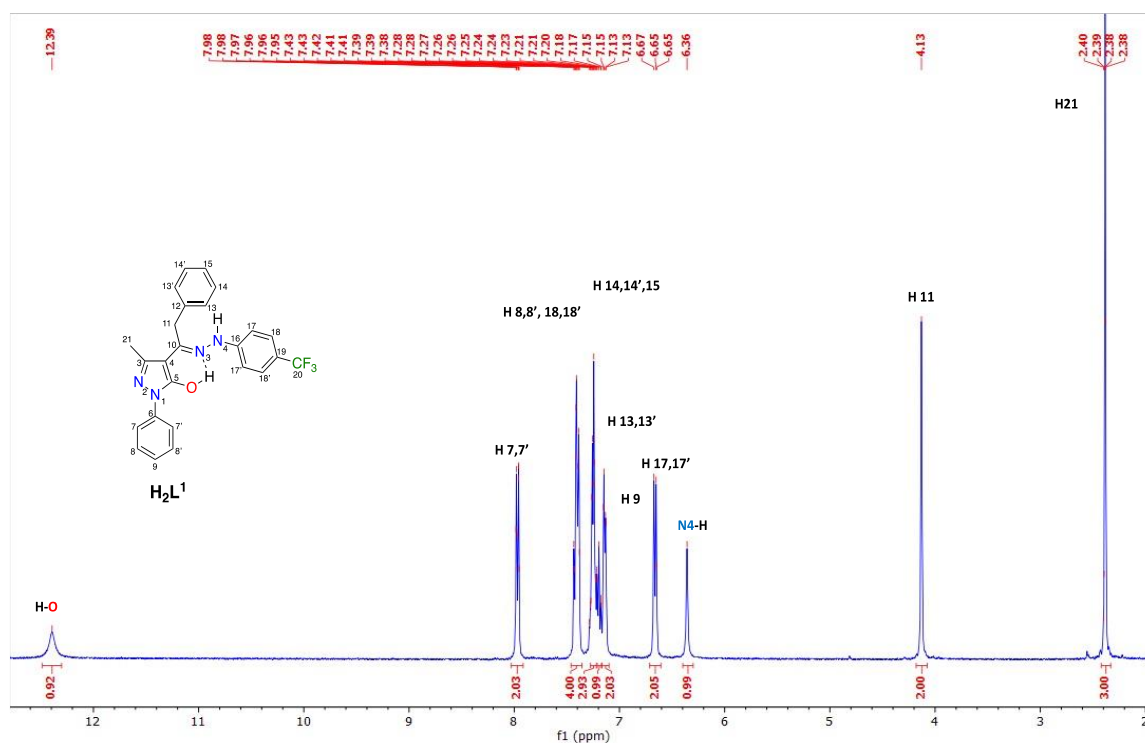


Figure 42. ^1H NMR spectrum CDCl_3 at 298 K of H_2L^1 .

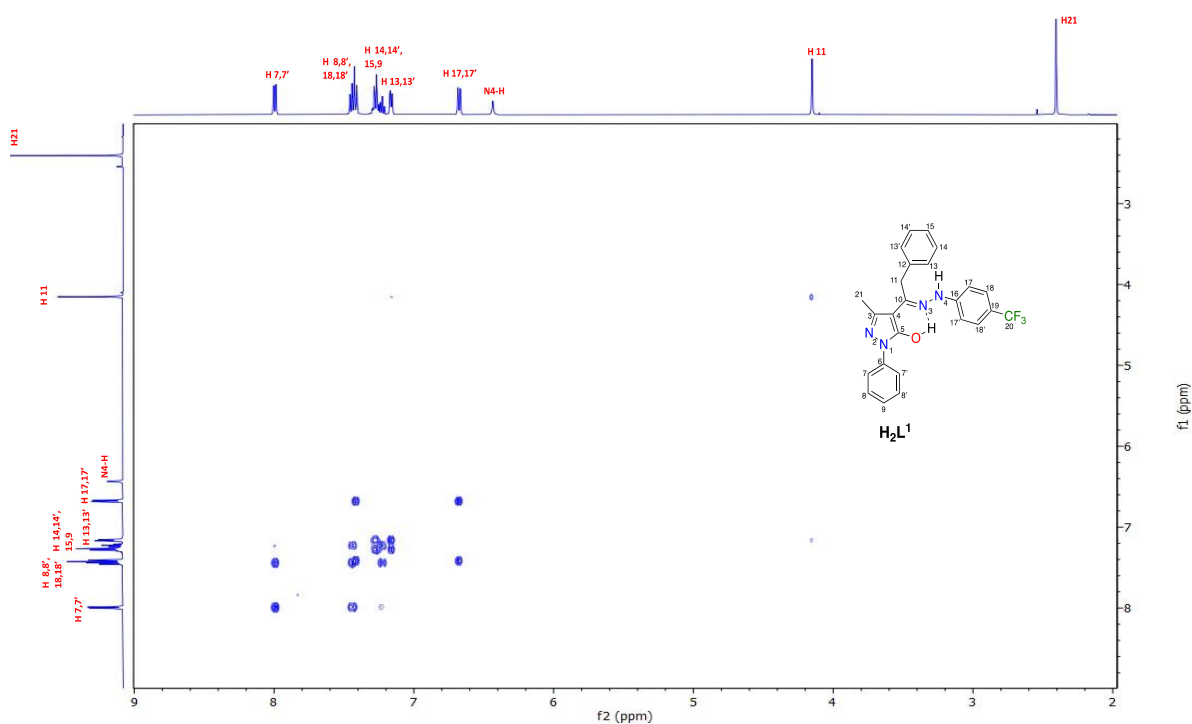


Figure 43. $\{^1\text{H}, ^1\text{H}\}$ -COSY spectrum in CDCl_3 at 298 K of H_2L^1 .

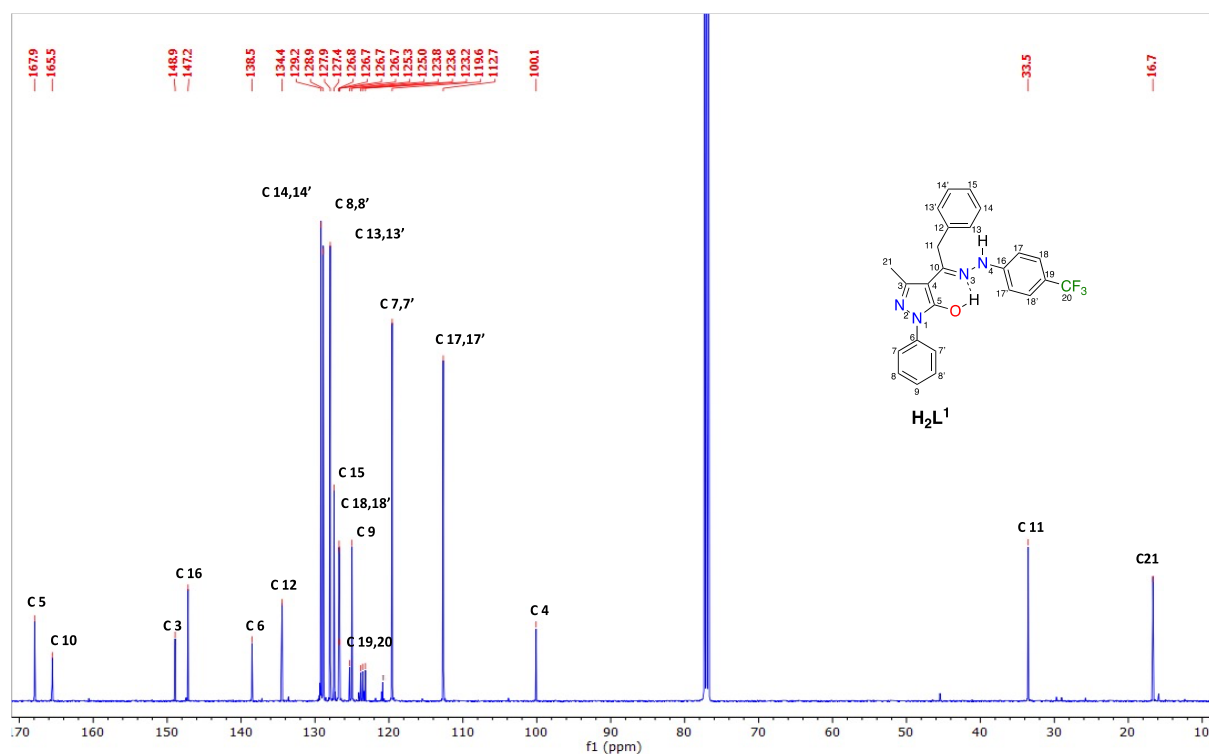


Figure 44. $^{13}\text{C}\{^1\text{H}\}$ NMR spectrum in CDCl_3 at 298 K of H_2L^1 .

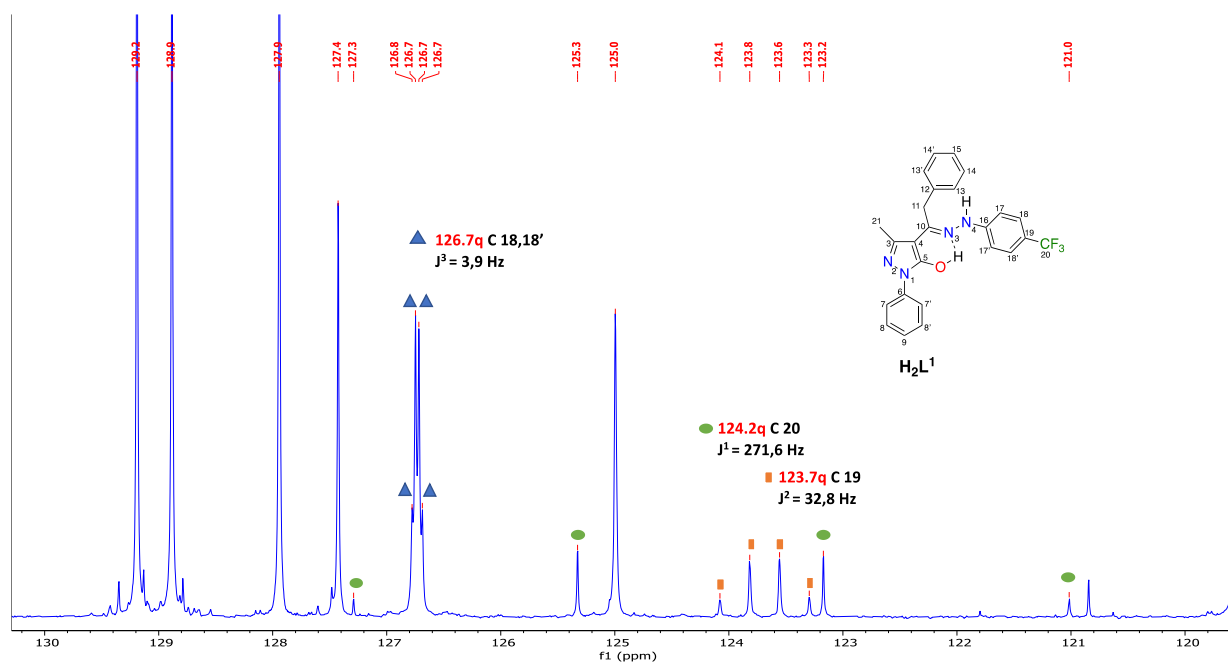


Figure 45. Magnification of $^{13}\text{C}\{^1\text{H}\}$ NMR spectrum in CDCl_3 at 298 K of H_2L^1 .

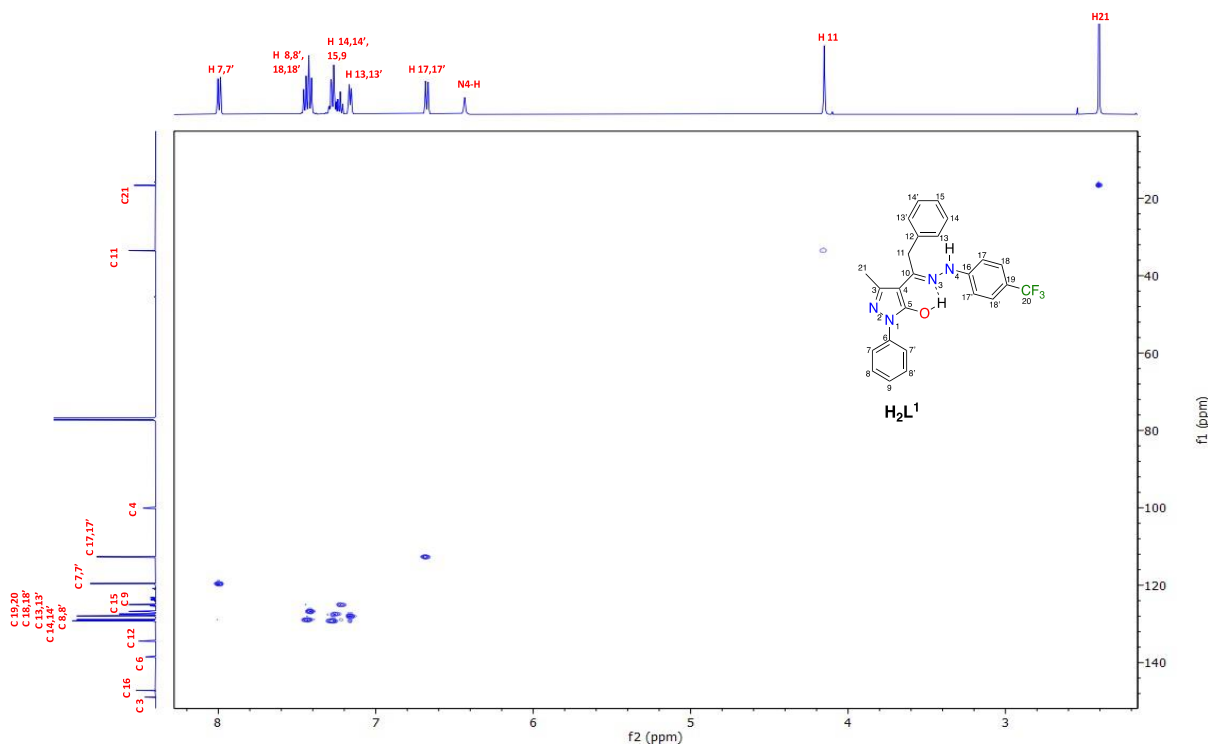


Figure 46. $\{^1\text{H}, ^{13}\text{C}\}$ -HSQC spectrum in CDCl_3 at 298 K of H_2L^1 .

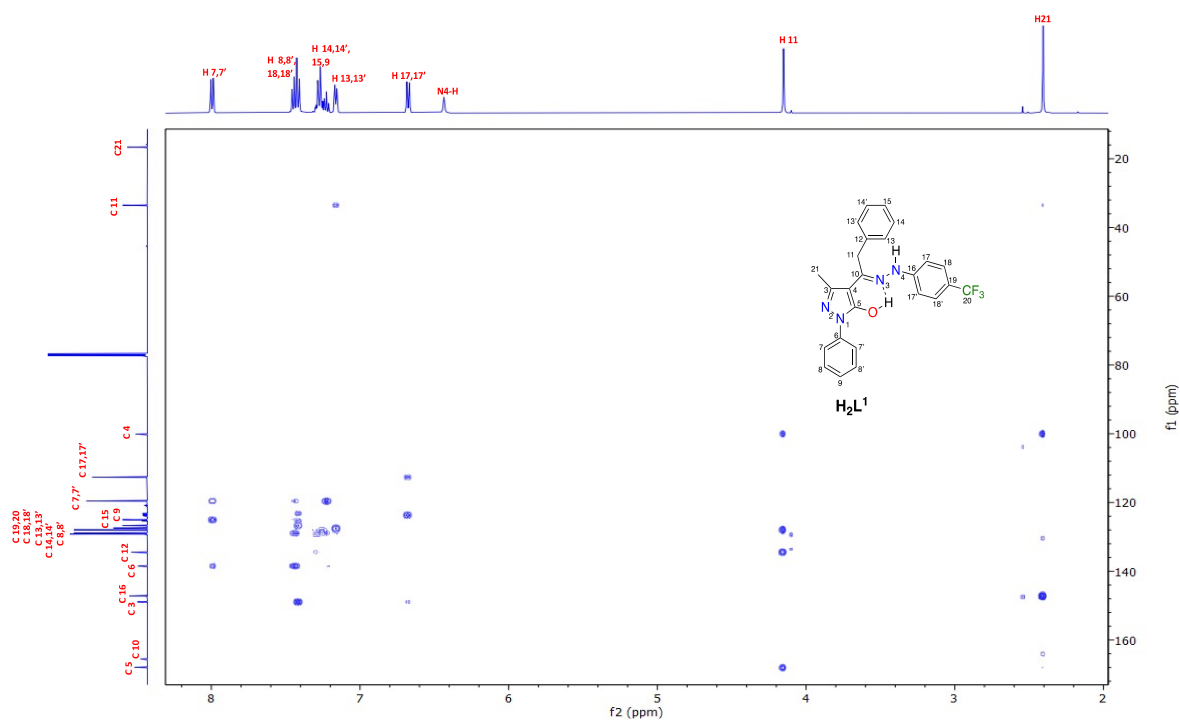


Figure 47. $\{^1\text{H}, ^{13}\text{C}\}$ -HMBC spectrum in CDCl_3 at 298 K of H_2L^1 .

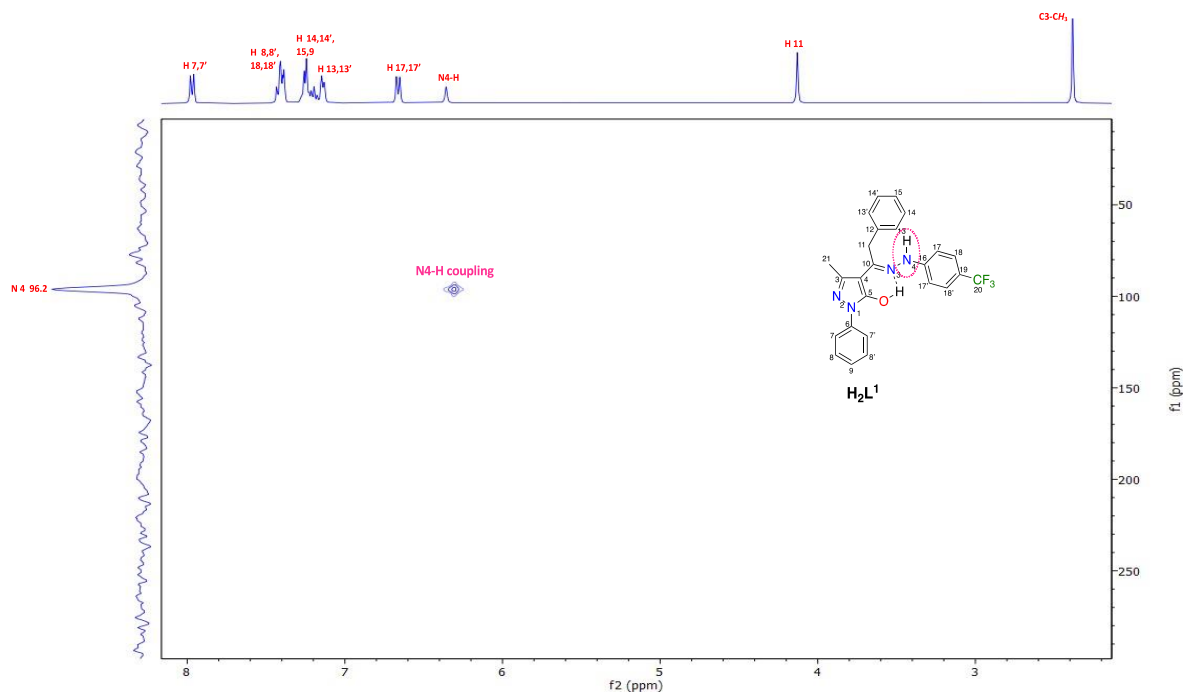


Figure 48. $\{^1\text{H}, ^{15}\text{N}\}$ -HSQC spectrum in CDCl_3 at 298 K of H_2L^1 .

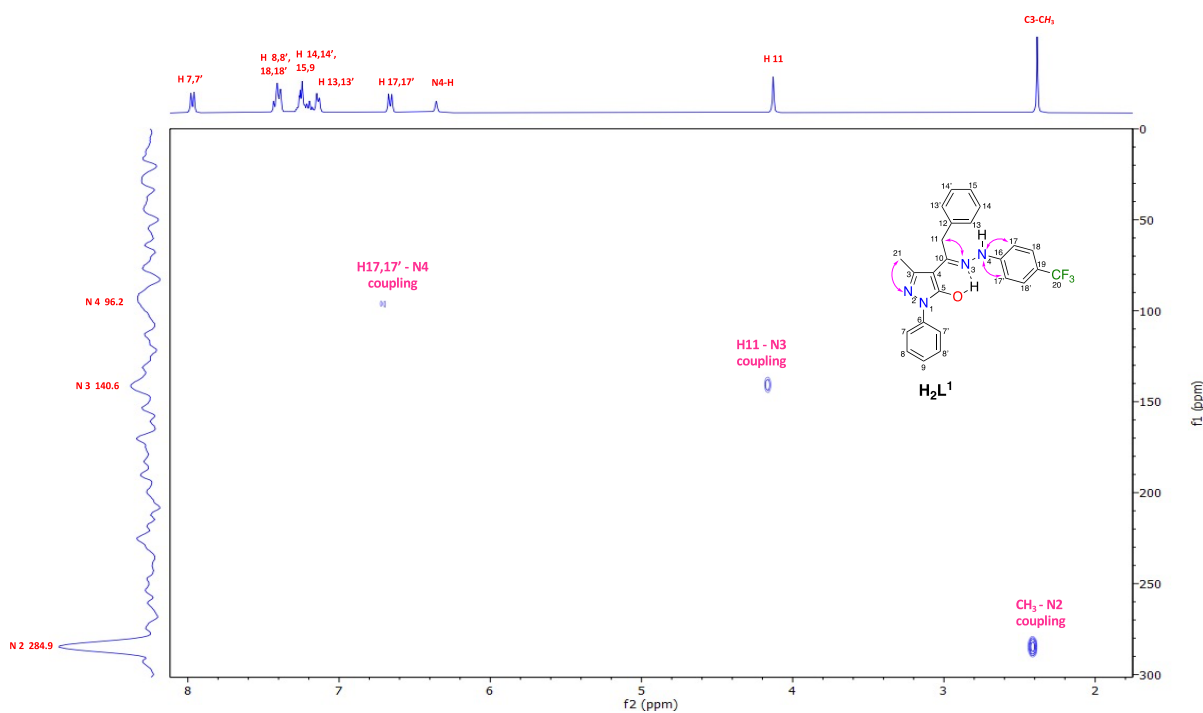


Figure 49. $\{^1\text{H}, ^{15}\text{N}\}$ -HMBC spectrum in CDCl_3 at 298 K of H_2L^1 .

The metal complexes **1-4** were prepared by reacting metal acetate hydrate and the appropriate proligand using methanol as solvent and stirring the mixture for 1-2 hours at room temperature, affording a solid precipitate that get filtrated and dried (Figure 50). The basic anionic form of the ligand $[\text{HL}^1]^-$ coordinate Zn(II) and Cu(II) in a chelating $\kappa\text{-N,O}$ bidentate fashion, affording complexes $[\text{Zn}(\text{HL}^1)_2(\text{MeOH})_2]$ (**1**) and $[\text{Cu}(\text{HL}^1)_2]$ (**3**), whereas the basic anionic form of the ligand $[\text{HL}^2]^-$ coordinates the Zn(II) and Cu(II) atom in a chelating $\kappa\text{-O,N,N}$ tridentate fashion, affording complexes $[\text{Zn}(\text{HL}^2)_2]$ (**2**) and $[\text{Cu}(\text{HL}^2)_2]$ (**4**). The structures of **1** and **3**, with the two N,O-chelating ligands in the anti-configuration, have been proposed on the basis of analogous zinc(II) and copper(II) complexes previously reported in the literature with other non-symmetric pyrazolone-based hydrazones^[144]. Complexes **1-4** are air-stable in the solid state and are soluble in most organic solvents, but not in alcohols and water. The solid-state infrared spectra of **1-4** display a shift of the band relative to the $\nu(\text{C}=\text{N})$ stretching for the azomethine fragment and for HL^2 also of the pyridine ring, to lower wavelengths with respect to those observed for the free proligands, in accordance with coordination to the metal center of the N atom of hydrazide fragments and for **2** and **4**, also N of the pyridine. The $\nu(\text{N-H})$ stretching produce a sharp band at circa 3300 cm^{-1} in the IR spectra of complexes **1-4** at higher wavelengths than in the free proligands. Moreover, the IR spectrum of **1** produces a broad band at 3134 cm^{-1} due to the $\nu(\text{O-H}\cdots\text{N})$ of extensive intermolecular H-bonding involving coordinated methanol molecules and pyrazolone N2 atom of neighboring molecules, which is a structural feature observed also in many other pyrazolone-based metal complexes^{[142]-[144]} (Figure 51). In the IR spectra of **1** and **3**, the stretching modes of the CF_3 group in the chelating HL^1 were identified at circa 1320 cm^{-1} , 1100 cm^{-1} and 1065 cm^{-1} , unchanged from the free proligand. In the far-IR region of **1-4**, some medium absorptions in the range of $550\text{-}400\text{ cm}^{-1}$ were tentatively assigned to $\nu(\text{M-N})$ and $\nu(\text{M-O})$ ^{[229],[236],[312]}.

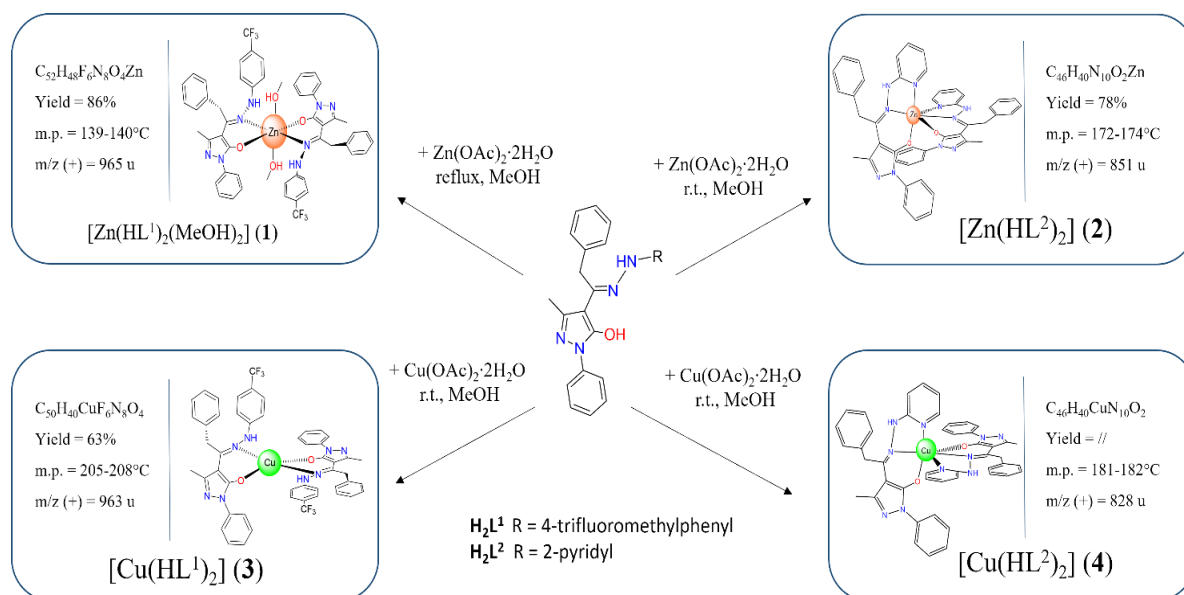


Figure 50. Synthetic procedure and chemical data of complexes **1-4**.

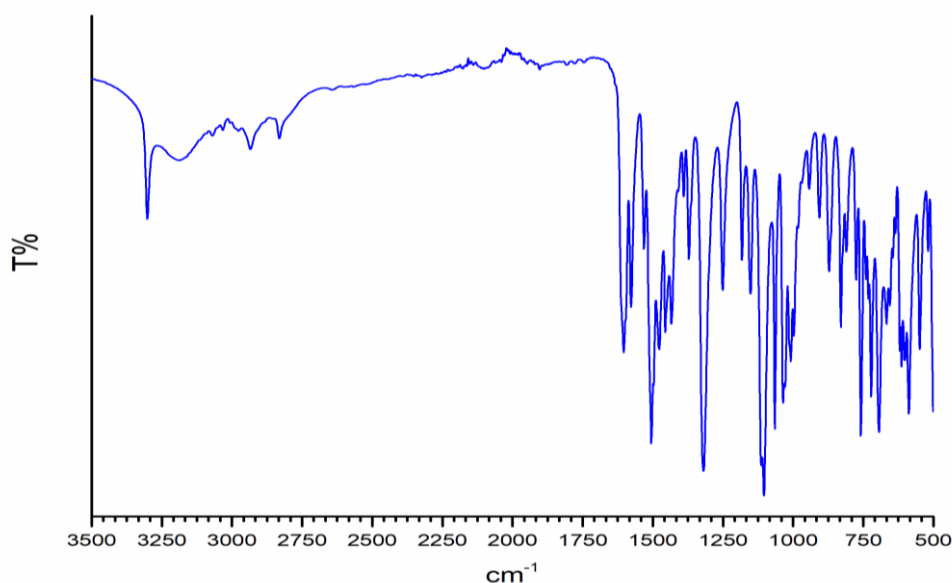


Figure 51. IR spectrum of $[Zn(HL^1)_2(MeOH)_2]$ (1).

The 1H and ^{13}C NMR spectra in deuterated chloroform of Zn(II) complexes **1** and **2** are in accordance with the expected structures containing the N,O-chelating (for **1**, Figures 52-56) and N,N,O-dichelating (for **2**, Figures 143-147 in Supporting Information) ligands, confirming the existence of complexes in solution with the ligand signals downfield-shifted with respect to the

corresponding signals in the free ligand spectrum. In principle, the geminal methylene protons of the benzyl moiety in proligand H_2L^2 (H11 in Chart 40) should undergo diastereotopic splitting in complex **2** due to the stereochemistry of the zinc center. In fact, the broad resonance of the CH_2 group appears as two overlapped signals in the 1H NMR spectrum of **2** (Figure 143 in Supporting Information). In addition, by recording the 1H NMR spectrum of **2** in dimethylsulfoxide (DMSO), the expected AB quartet of the geminal methylene protons is clearly observed. The $\{^1H,^{15}N\}$ -HSQC and $\{^1H,^{15}N\}$ -HMBC of H_2L^1 and complex **1** in chlorinated solvents are quite interesting: in fact, even if the N3 resonance at 140.6 ppm in the free H_2L^1 is not observed for the complex **1**, the N4-H resonance shifts from 96.2 ppm to 117.3 ppm and that of N2 from 284.9 ppm to 276.4 ppm upon coordination to zinc.

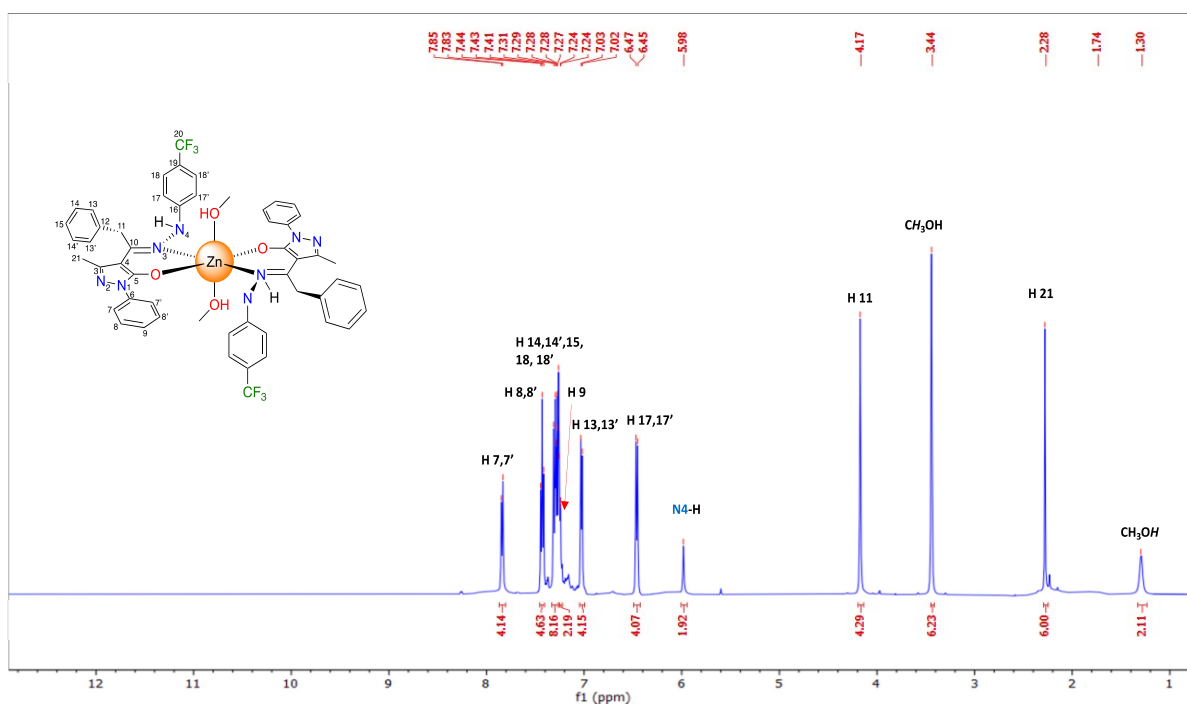


Figure 52. 1H NMR spectrum in $CDCl_3$ at 298 K of $[Zn(HL^1)_2(MeOH)_2]$ (**1**).

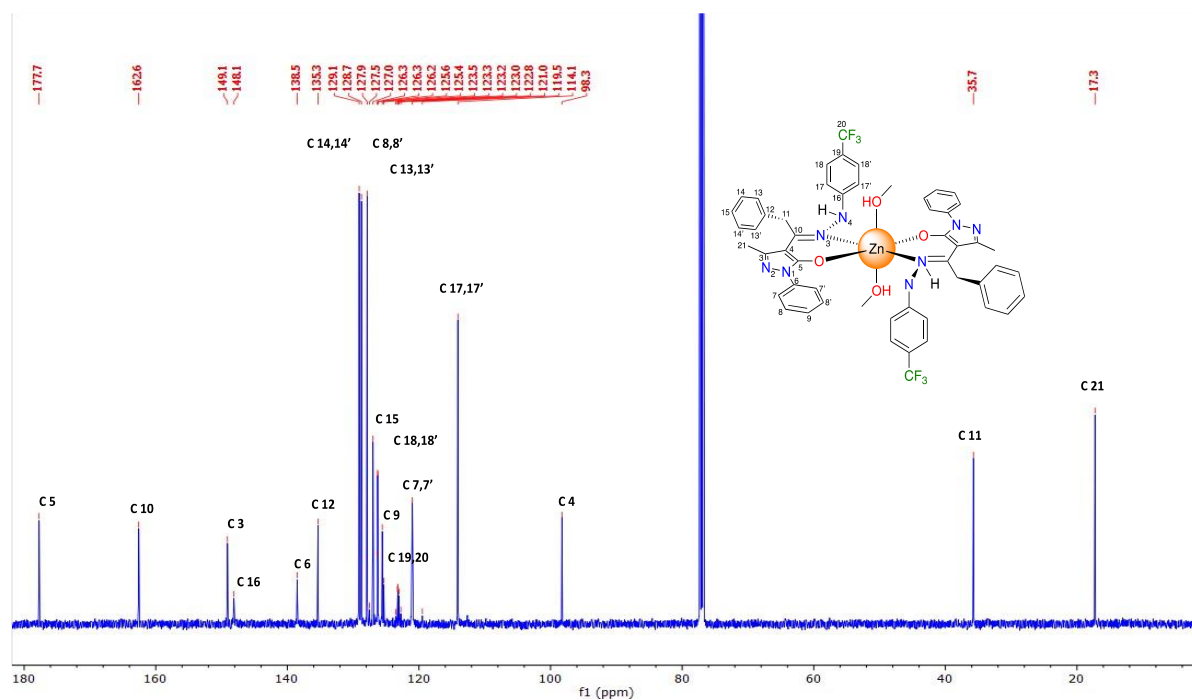


Figure 53. ^{13}C NMR spectrum in CDCl_3 at 298 K of $[\text{Zn}(\text{HL}^1)_2(\text{MeOH})_2]$ (**1**).

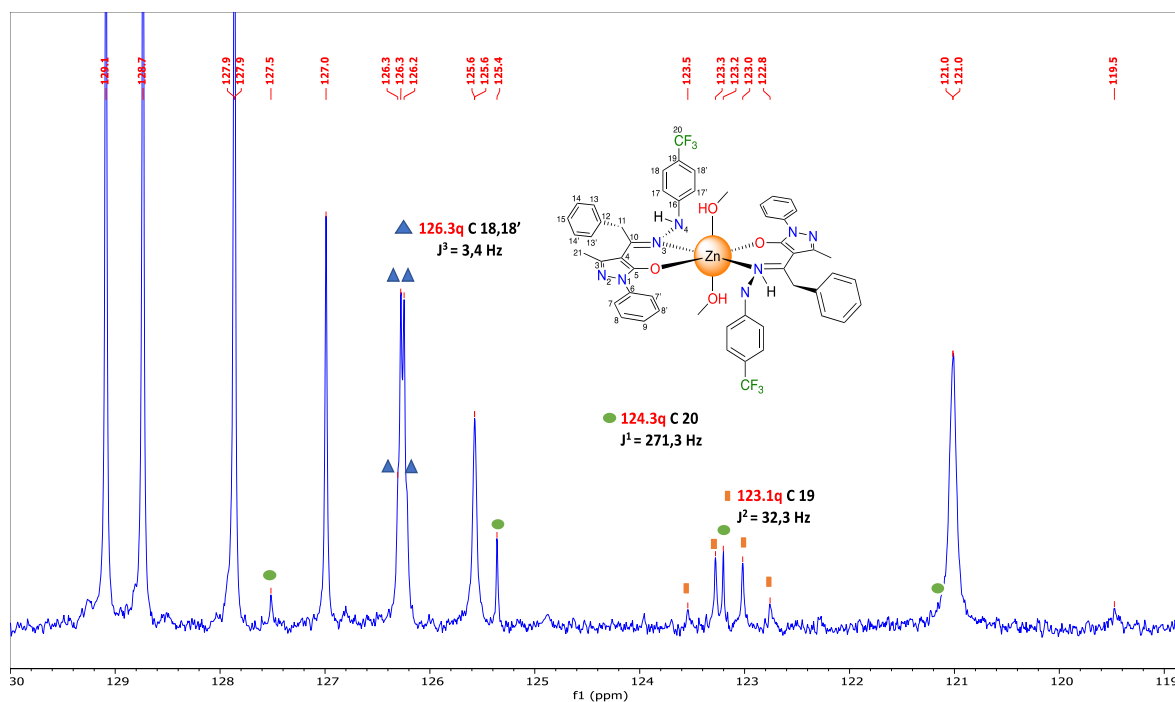


Figure 54. Magnification of ^{13}C NMR spectrum in CDCl_3 at 298 K of $[\text{Zn}(\text{HL}^1)_2(\text{MeOH})_2]$ (**1**).

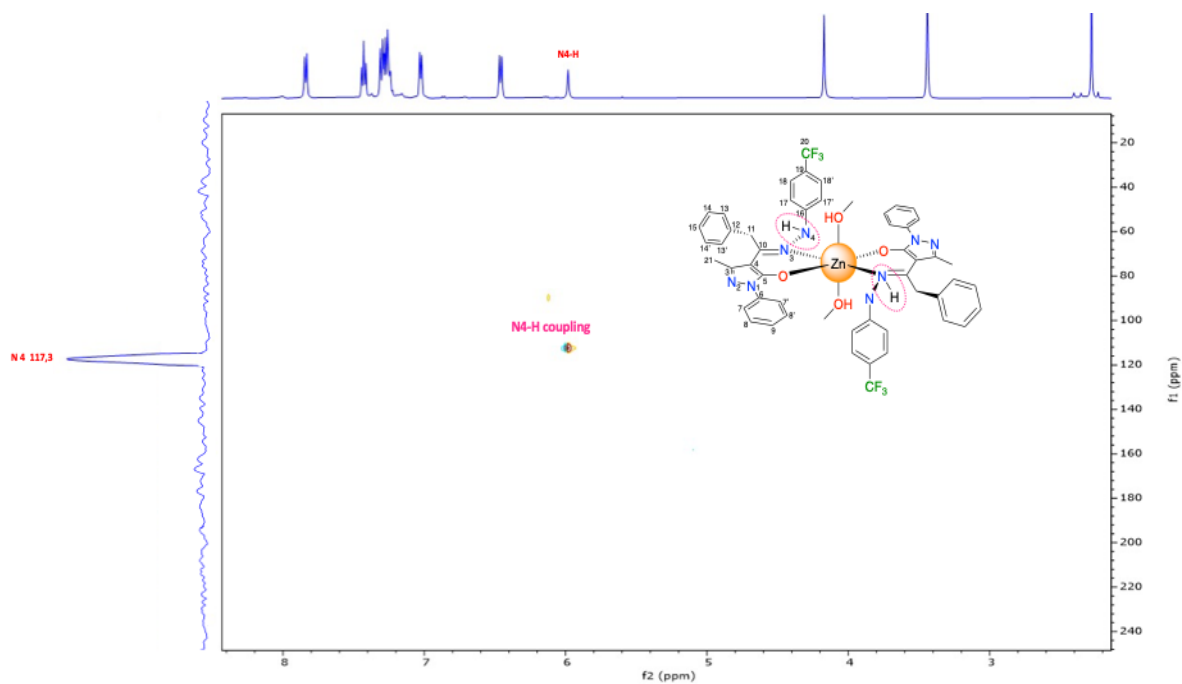


Figure 55. $\{^1\text{H},^{15}\text{N}\}$ -HSQC spectrum in CDCl_3 at 298 K of $[\text{Zn}(\text{HL}^1)_2(\text{MeOH})_2]$ (**1**).

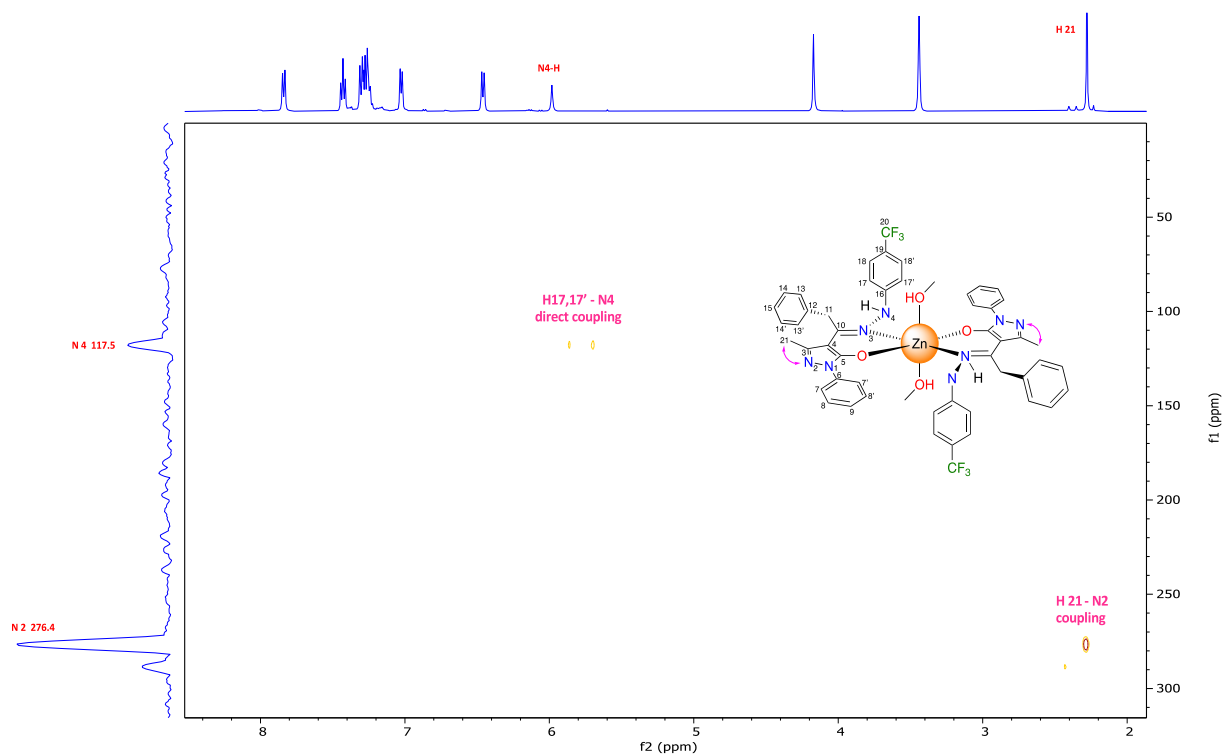


Figure 56. $\{^1\text{H},^{15}\text{N}\}$ -HMBC spectrum in CDCl_3 at 298 K of $[\text{Zn}(\text{HL}^1)_2(\text{MeOH})_2]$ (**1**).

Positive ESI-MS spectra recorded in acetonitrile show similar patterns for all complexes **1-4**, with main peaks due to $[M(HL^n)(H_2L^n)]^+$ arising from protonation of one ligand, or $[M(HL^n)_2 + Na]^+$, as well as to clusters $[M_2(HL^n)_3]^+$.

The UV-visible spectra of the ligands and complexes **1-4** were obtained in chloroform solution at concentrations of 10^{-3} and 10^{-5} M, in the range of 200-700 nm at room temperature. The spectra of the two ligands H_2L^1 and H_2L^2 exhibit two bands between 245 nm and 304 nm due to a ligand-centered $\pi-\pi^*$ transition localized on the aromatic rings and the $n-\pi^*$ transitions within the $>C=N-N$ chromophore^{[118],[313]}. In addition, the band observed at 370 nm in the H_2L^2 spectrum can be ascribed to $\pi\rightarrow\pi^*$ transition of pyridine rings present in the ligand structure (Figure 58)^[314]. In the spectra of metal complexes, the bands due to $\pi\rightarrow\pi^*$ and $n\rightarrow\pi^*$ transitions are almost unchanged, with the exception of Cu(II) complex **3**; however, the band due to the pyridine ring undergoes a bathochromic shift upon coordination in the spectrum of Cu(II) complex **4**. Shoulders around 406-414 nm are present attributed to ligand to metal charge transfer (LMCT) transitions. In the spectra of complexes **1** and **3** (Figure 57) the bands due to LMCT transition appear as shoulders at 388 nm and 392 nm, respectively. As expected there are no d-d transitions in complex **1** and **2** due to the d^{10} configuration of Zn(II). However, no absorption attributable to d-d transition has been observed also for Cu(II) complexes **3** and **4**, even upon increasing the solution concentration to 10^{-3} M.

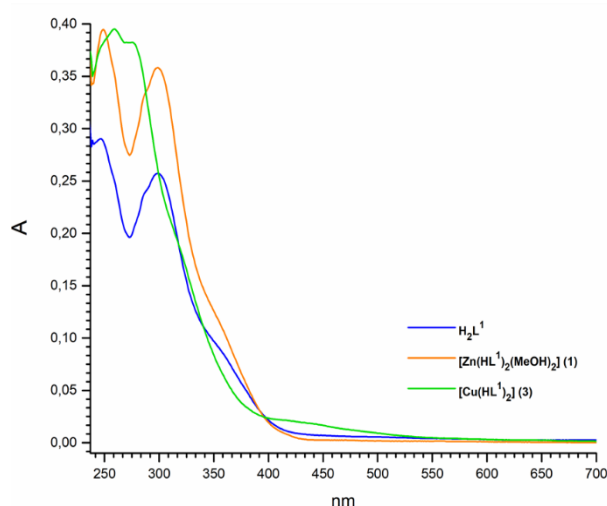


Figure 57. UV-Vis spectra of ligand H_2L^1 and Complex (**1**), (**3**) in $CHCl_3$ 10^{-5} (a) e 10^{-3} (b).

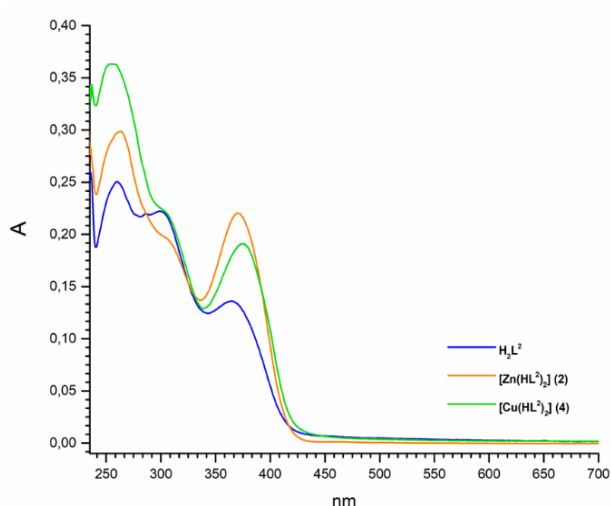


Figure 58. UV-Vis spectra of ligand H_2L^2 and complexes (2), (4) in $CHCl_3$ 10.5 M (a) and $10^{-3}M$ (b).

Finally, when the synthesis of complex **3** is performed at room temperature, leaving the reaction mixture under stirring for 24 hours, or under reflux, the red precipitate that corresponds to complex **3** slowly converts to a dark green color precipitate (Figure 59). This green substance was investigated spectroscopically and with single crystal X-ray analysis which confirmed the degradation of the coordinated HL^1 to the corresponding precursor acylpyrazolonate Q^{Bn} ligands, by loss of the (4-(trifluoromethyl)phenyl)hydrazine moiety. The new complex obtained is indicated as $[Cu(Q^{Bn})_2]$ (**5**). The infrared spectrum of **5** displays strong absorptions at 1604 cm^{-1} , 1590 cm^{-1} and 1574 cm^{-1} due to $\nu(C=O)$, $\nu(C=N)$ and $\nu(C=C)$. In the far region of the spectrum the bands at 510 cm^{-1} and 401 cm^{-1} were assigned to the stretching of the bond $\nu(Cu-O)$.

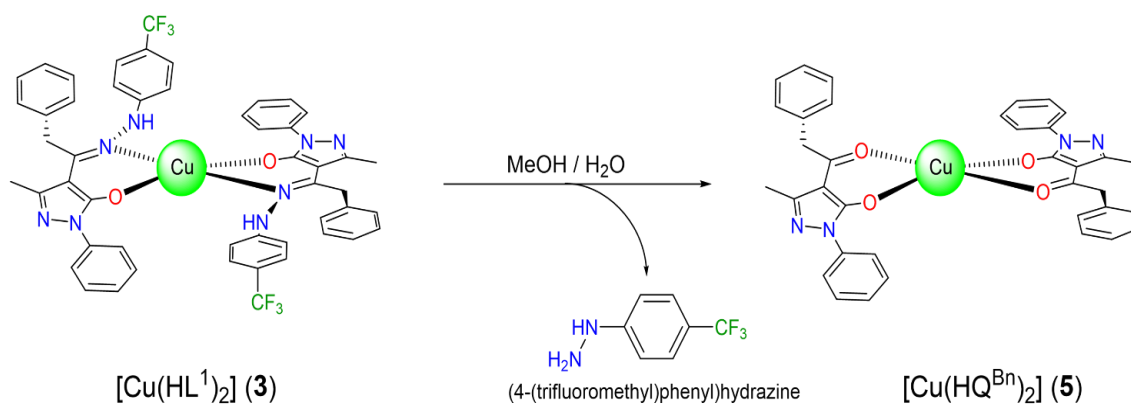


Figure 59. Decomposition pathway of complex **3** to complex **5**.

3.3.2 X-ray structural characterization

The X-ray single crystal molecular structures of proligands H_2L^1 and H_2L^2 and of complex **1**, with the atomic numbering scheme are reported in Figures 60a,b and Figure 61. Selected bond distances and angles are reported in Table 9, while details of data and structural refinements are reported in Table 15 and Table 16 in Appendix. Both proligands H_2L^1 and H_2L^2 are found in the solid crystalline state, in the N–H, N–H, C=O tautomeric form, crystallizing, in the case of H_2L^2 in the triclinic space group, differently from the monoclinic phase already reported originating from the unexpected zwitterionic form^{[218],[315]}.

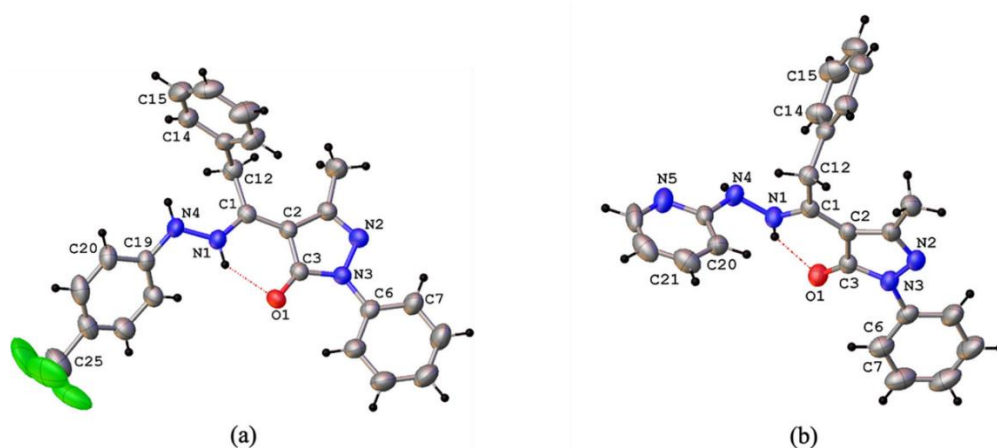


Figure 60. Ortep view of the asymmetric unit content H_2L^1 (a) and H_2L^2 (b) with the atomic numbering scheme and intramolecular N–H...O hydrogen bond (ellipsoids at the 40% level).

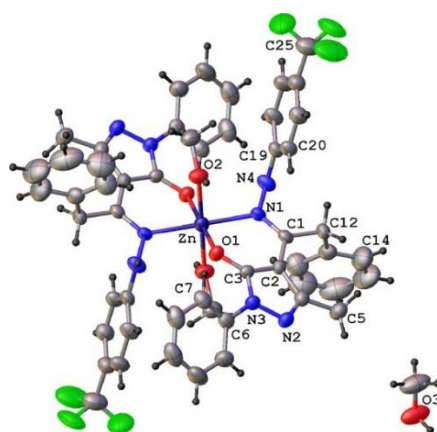


Figure 61. Ortep view of the asymmetric unit content of $[Zn(HL^1)_2(MeOH)_2]$ (**1**) with the atomic numbering scheme (ellipsoids at the 40% level).

Within both ligands, the C(3)–O(1) bond distances of 1.264(3) and 1.253(2) Å, respectively, are similar to the C=O double bond found in similar pyrazolone-based hydrazones in the same tautomeric form^[301]. Confirming this, the bond distances N(1)–C(1) and N(2)–C(4) are very near to the C=N double bond. The hydrazone N–N bond distances are similar in the two proligands H₂L¹ and H₂L² (Table 9). In both cases, the overall structure is not planar, with the major distinctive difference related to the orientation of the hydrazone fragment, with a C–N–N–C torsion angle of 149.5(2) and –94.7(3)° in H₂L¹ and H₂L², respectively. The intramolecular hydrogen bond between the N–H and C=O carbonyl groups are observed [N(1)···O(1) and N(1)–H(1a)∠O(1) of 2.670(3) and 2.703(3) Å, 139 and 137(3)° in H₂L¹ and H₂L²], as typically formed in these types of ligands. In the case of H₂L², the oxygen atom of the C=O group is also involved in intermolecular hydrogen bonding involving the second N atom of the –NH group of benzylhydrazone (N(4)–H(4a)···O(1)). Moreover, π – π interactions between pyridine rings are a further structural feature in the 3D crystal packing of the H₂L² proligand (Figure 62).

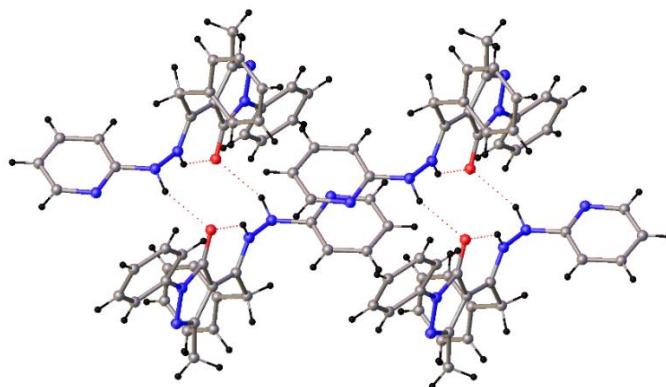


Figure 62. Crystal packing view of H₂L² showing N–H···O intramolecular and intermolecular hydrogen bonds and π – π interaction between the pyridine rings.

The X-ray crystal structure analysis of complex **1** confirmed its neutral nature and therefore the general formula [Zn(HL¹)₂(MeOH)₂]. Complex **1** co-crystallized with one methanol molecule in the asymmetric unit (Figure 61). Additionally, in complex **1**, the zinc ion, located on the symmetry inversion center, is hexa-coordinated with two N,O bis-chelated H₂L¹ ligands and two oxygen atoms belonging to methanol molecules. The oxygen and nitrogen atoms of the chelated H₂L¹ ligands lie in the same plane with bond distances at the zinc ion comparable with those found in analogous complexes. The distances between the zinc ion and the oxygen atoms of the methanol

molecules are relatively elongated with respect to the other Zn–O distances (Table 9). Most of the intermolecular interactions are attributable to methanol molecules both coordinated and co-crystallized (Figure 63a). In particular, the co-crystallized methanol molecules act as both hydrogen bond donors and acceptors, with the formation of O–H–N and O–H–O interactions with the nitrogen atom N(3) of the pyrazole ring and the hydrogen atom of the coordinated methanol molecule [O(3)⋯N(2)ⁱ 2.828(4) Å, O(3)–H(3)∠N(2) 161°, *i* = –*x* + 1, –*y* + 1, –*z* + 2; O(2)⋯O(3)ⁱⁱ 2.698(4) Å, O(2)–H(2)∠O(3) 157°, *ii* = *x*, *y* – 1, *z*]. The X-ray single crystal molecular structure of complex [Cu(Q^{Bn})₂] (**5**) confirmed the degradation of the coordinated H₂L¹ ligands to acylpyrazolones and their O₂-chelation to the Cu(II) ion. As reported in Figure 63b, the four-coordinated Cu(II) ion, sitting on the symmetry inversion center, is found in a distorted square planar geometry, with the two chelated ligands arranged in anti-conformation. As reported in Table 9, bond distances and angles are similar to those reported for analogous four-coordinated Cu(II) complexes containing two bidentate pyrazolonates^{[157],[166]}. The overall planar central metal core is characterized by a dihedral angle between the best mean planes passing through the chelated six-membered and pyrazole rings of 3.7(1)°, while the rotationally free phenyl rings C(6)–C(11) and C(14)–C(18) show dihedral angles with respect to the chelated six-membered ring of 16.1(1) and 71.4(1)°, respectively.

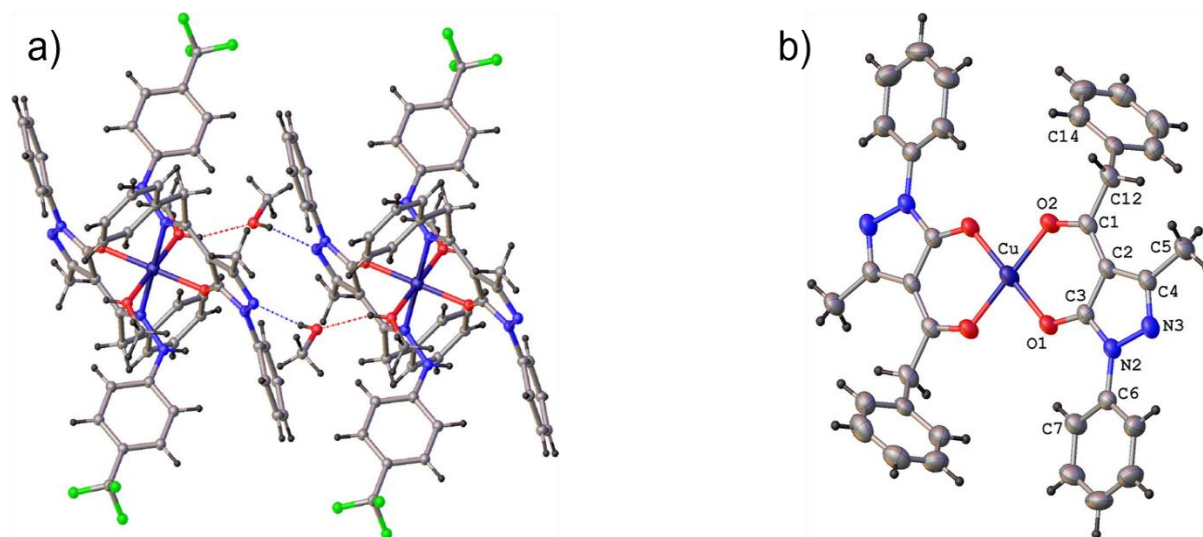


Figure 63. Crystal packing view of **1** showing N–H⋯O hydrogen bonds involving both coordinated and lattice methanol molecules (a) and ortep view of the asymmetric unit content of complex [Cu(Q^{Bn})₂] (**5**) with the atomic numbering scheme (ellipsoids at the 40% level).

Table 9. Selected bond distances (Å) and angles (deg) in proligands H_2L^1 and H_2L^2 and complexes **1** and **5**; $i = -x + 2, -y, -z + 2$; $ii = -x, -y + 2, -z + 2$.

LIGANDS	H_2L^1	H_2L^2
N(1)–N(4)	1.401 (3)	1.400 (3)
N(1)–C(1)	1.335 (3)	1.318 (3)
C(1)–C(2)	1.401 (3)	1.400 (3)
C(2)–C(3)	1.438 (3)	1.436 (4)
C(2)–C(4)	1.451 (3)	1.435 (4)
C(3)–N(3)	1.390 (3)	1.371 (3)
C(3)–O(1)	1.264 (3)	1.256 (3)
N(2)–N(3)	1.412 (3)	1.399 (3)
N(2)–C(4)	1.309 (3)	1.304 (3)
N(3)–C(6)	1.416 (3)	1.418 (3)
COMPLEXES	1	5
M–O(1)	2.008 (2)	1.893 (1)
Zn–N(1)	2.100 (3)	
Cu–O(2)		1.931 (1)
Zn–O(2) _{solv}	2.223 (2)	
N(1)–N(4)	1.420 (4)	
N(1)–C(1)	1.302 (4)	
O(2)–C(1)		1.268 (2)
C(1)–C(2)	1.435 (4)	1.420 (3)
C(2)–C(3)	1.417 (4)	1.404 (3)
C(2)–C(4)	1.425 (4)	1.438 (3)
C(3)–N(3)	1.359 (4)	
C(3)–O(1)	1.281 (4)	1.276 (2)
O(1)–Zn–N(1)	87.9 (1)	
O(1)–Zn–O(2)	85.7 (1)	
O(1)–Zn–N(1) ⁱ	92.1 (1)	
N(1)–Zn–O(2) ⁱ	89.0 (1)	
O(1)–Cu–O(2)		94.0 (1)
O(1)–Cu–O(2) ⁱⁱ		86.0 (1)
O(2)–Cu–O(1) ⁱⁱ		86.0 (1)

3.3.3 Theoretical DFT analysis

Tautomers I and II of proligands H_2L^n (Chart 41) were examined using density functional theory (DFT) at the B3LYP/6-311G** level of theory. In both cases, the energy differences between them are small (for example, *ca.* 2 kcal/mol for H_2L^1 in gas phase; see Table 10 for other data). In solution, tautomer I is the predominant species according to experimental NMR data (see the discussion in the section “Results and discussion” of the present Chapter). This is corroborated by the calculation of the NMR for tautomer I of H_2L^1 . The comparison of the computed 1H and ^{13}C NMR spectra with the experimental data is good, while a poorer fit for these spectra was found for tautomer II of H_2L^1 (see Figure 64). However, in the solid-state the observed species is tautomer II. The comparison of selected structural parameters of the tautomer II of H_2L^1 with those from X-ray data is good (see Figure 65), which confirms the proposed assignment. In particular, the experimental C=O bond distance of 1.264 Å is well reproduced by calculations (1.241 Å for II *versus* 1.327 Å for tautomer I). Furthermore, the calculated IR spectrum of tautomer II of H_2L^1 fits well with the experimental solid-state IR and confirms the assignments previously discussed as illustrated in Figure 66 and Table 11.

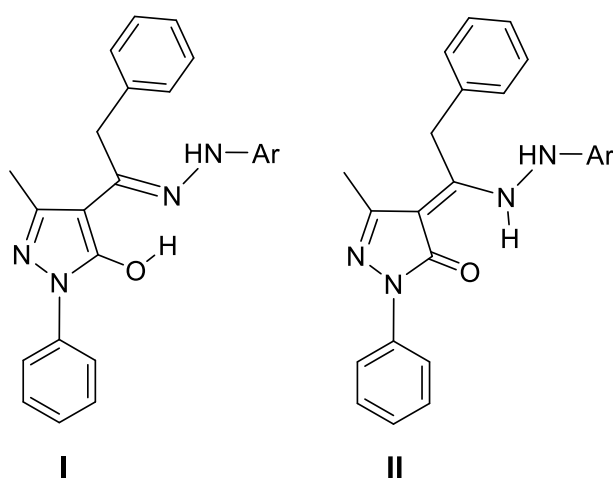
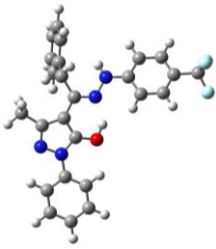
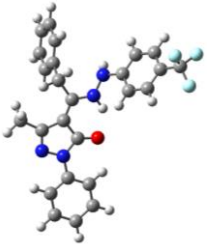
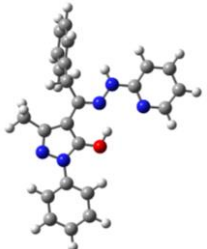
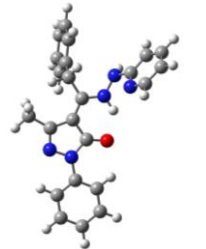


Chart 41. Representation of tautomeric forms I and II of the two proligands.

Table 10. Energies (Hartree) and relative energy differences (kcal/mol) for the tautomers of proligands H_2L^1 and H_2L^2 .

	H_2L^1		H_2L^2	
	Tautomer I	Tautomer II	Tautomer I	Tautomer II
				
E	-1559,445250	-1559,449708	-1238,350939	-1238,354998
E₀	-1559,028991	-1559,032877	-1237,951191	-1237,954410
E_t	-1559,000852	-1559,004778	-1237,926833	-1237,930083
H	-1558,999908	-1559,003833	-1237,925889	-1237,929139
G	-1559,093531	-1559,097074	-1238,00875	-1238,012944
ΔE	0,0	-2,8	0,0	-2,5
ΔG	0,0	-2,2	0,0	-2,6
ΔE(CHCl₃)	0,0	-4,4	0,0	-4,2
ΔG(CHCl₃)	0,0	-3,8	0,0	-4,3

To gain information on the coordination capabilities of the ligands in metal complexes **1-4**, the anions $[HL^1]^-$ and $[HL^2]^-$ were also optimized. The bonding localization of $[HL^1]^-$ agrees with the deprotonation of tautomer II showing a shorter C=O bond (1.232 Å) than the C-N bond (1.303 Å). Evidently, these distances change upon coordination, as we will discuss later in this section. The molecular orbitals involved in the coordination to the metal atom for the HL^1 ligand are HOMO-2 and HOMO-3, with a minor contribution of HOMO-9 (Figure 67), these being MOs in which the lone pairs of the N and O donor atoms take part in the *in-phase* and *out-of-phase* contributions of σ type that afford the M-O and M-N bonds. These MOs were compared with those obtained from the single-point calculation of the HL^1 ligand with the geometry found in the optimization of complex **1**. In this case, the *in-phase* and *out-of-phase* combinations are clearly detected in HOMO-1 and HOMO-3 (also shown in Figure 67 for an appropriate comparison).

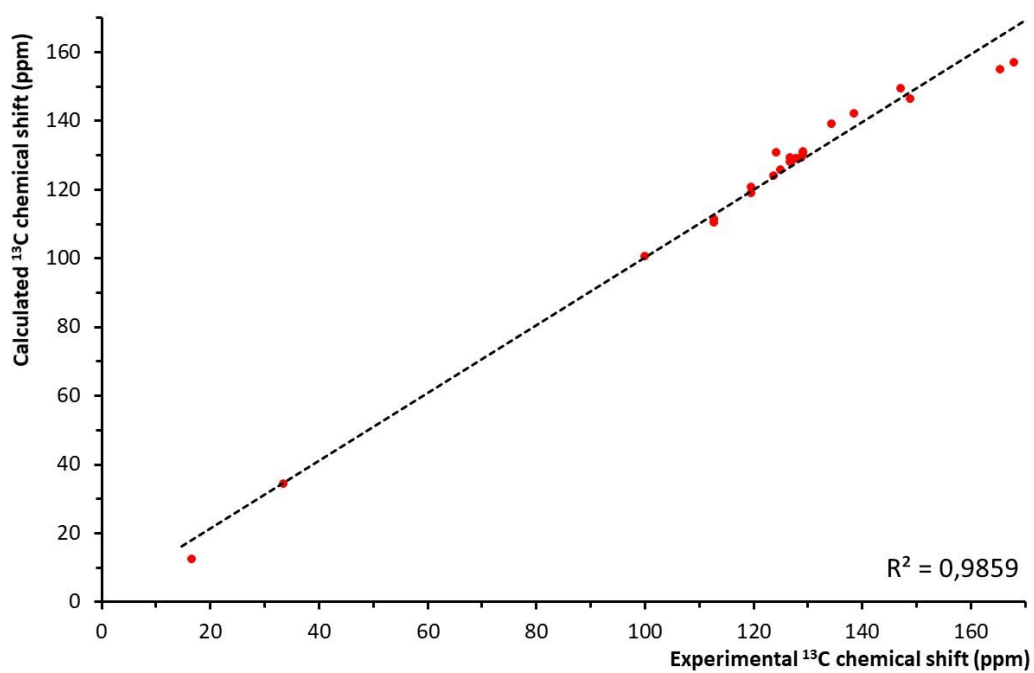
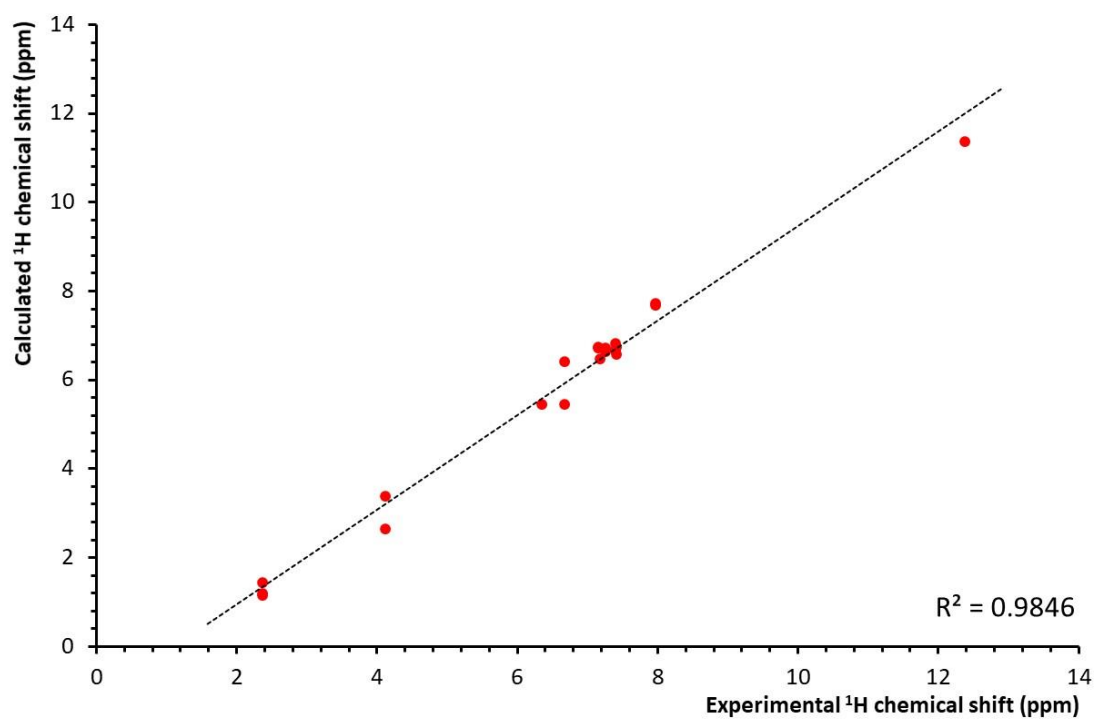


Figure 64. Comparison of the calculated (tautomer I) and experimental ^1H and ^{13}C NMR spectra of H_2L^1 .

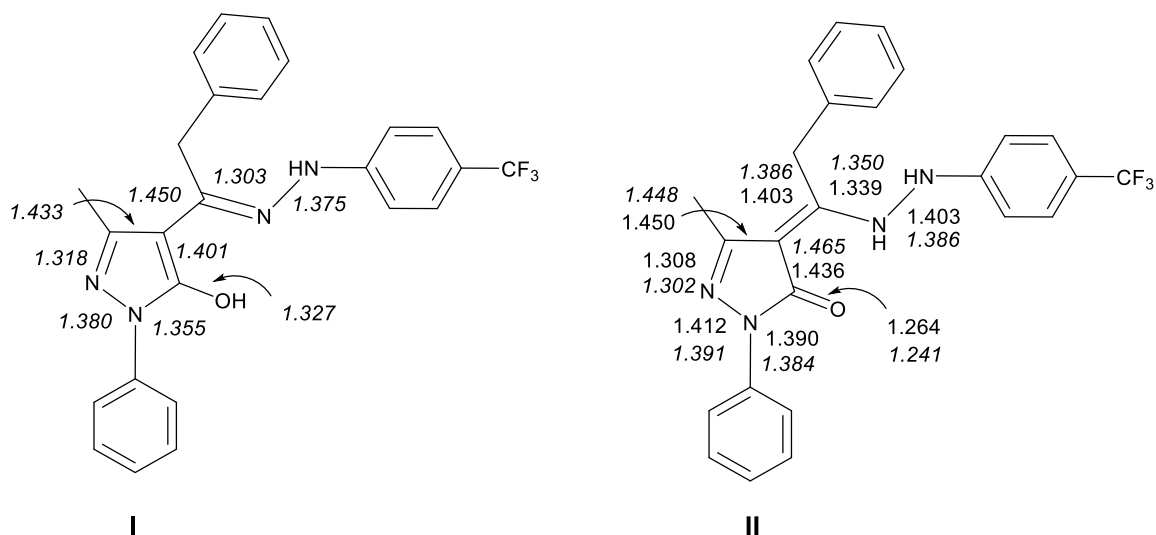


Figure 65. Comparison of selected bond distances of H_2L^1 : calculated tautomers I and II (*italic*) and experimental.

Concerning the $[HL^2]^-$ anion, its structure is again consistent with the deprotonation of tautomer II with a shorter C=O bond (1.242 Å) than the C-N bond (1.296 Å). The anion does not show the planar conformation expected in complexes **2** and **4** and, for this reason, their molecular orbitals from the single-point calculation of the HL^2 ligand were analyzed with the geometry found in the optimization of complex **2**. The MOs involved in the coordination to the metal are HOMO-1, HOMO-2, HOMO-3, HOMO-4 and HOMO-6 (Figure 68). The lone pair of the oxygen atom is distributed between HOMO-1 and HOMO-2, the *out-of-phase* combinations of both N lone pairs appear at the HOMO-3 and HOMO-4, while the HOMO-6 is clearly the *in-phase* combination of both N lone pairs.

Complexes **1–5** were also analyzed by DFT. The resulting optimized structures of these complexes are shown in Figure 69. The selected combination of the method and basis sets provides a good structural description of these complexes according to the good comparison of the calculated and experimental structural parameters of complex **1** (Table 12). The HL^1 ligands exhibit delocalized C-O and C-N bonds (1.279 and 1.315 Å, respectively) in agreement with experimental values and the two six-membered metallacycles $[Zn(HL^1)]$ show an envelope conformation with an angle between the ligand and molecular planes of 30.3° (experimental 30.9°).

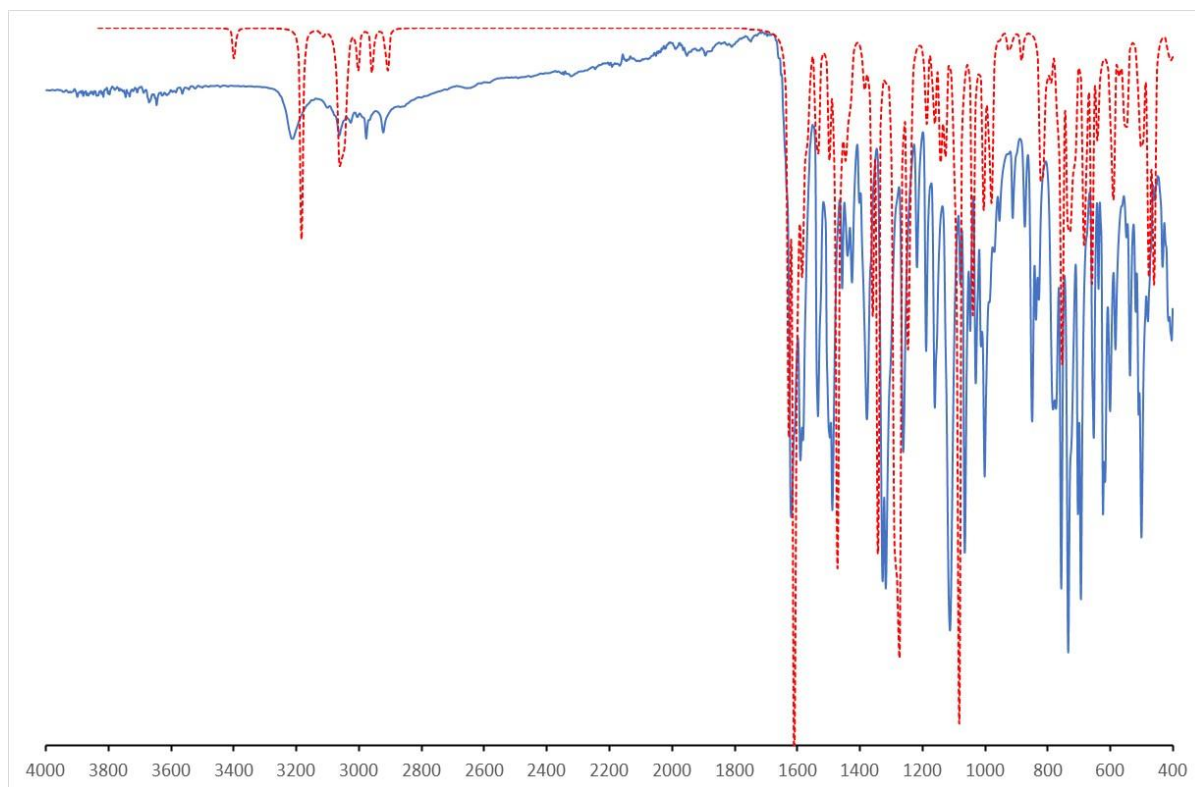
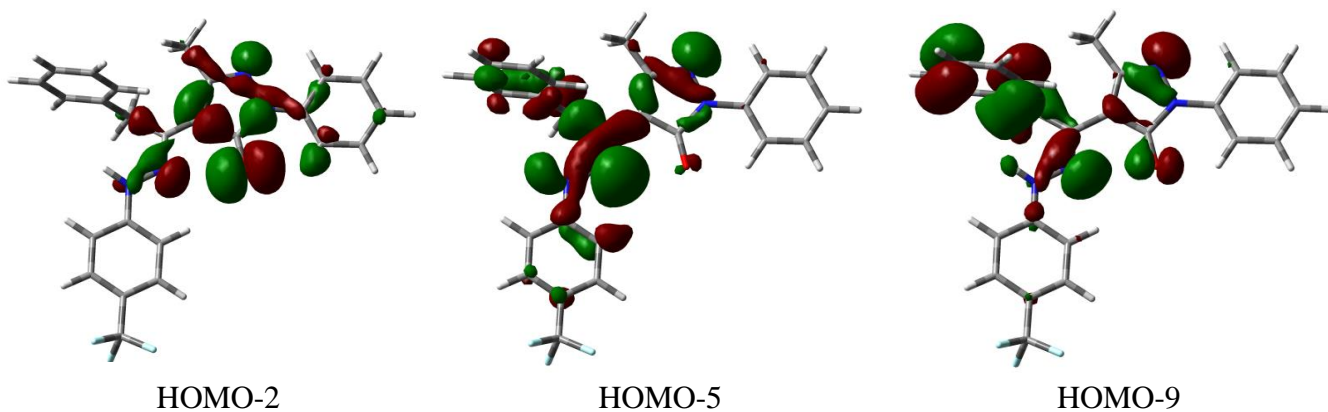


Figure 66. Comparison of the experimental (blue line) and calculated (tautomer II, red line) IR spectrum of H_2L^1 (cm^{-1}).

Table 11. Selected stretching assignments of the IR spectrum of H_2L^1 .

IR band (cm^{-1})	Experimental	Calculated
$\nu(N-H)$	3211	3181
$\nu(C=O)$	1620	1626
$\nu(C=N)_{\text{pyrazole}}$	1534	1537
$\nu_s(C-F)$	1320	1278
$\nu(N-N)$	1064	1141, 1128
$\nu_{as}(C-F)$	1100	1086

Optimized [HL¹]



Single point calculation of [HL¹] from the optimization of 1.

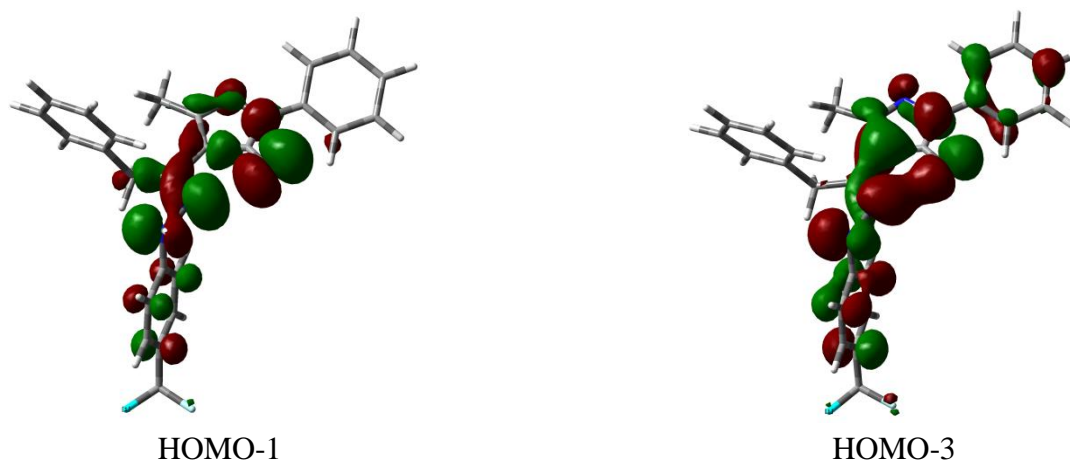


Figure 67. Molecular orbitals of anionic ligands [HL¹] involved in the coordination to metal centers.

Single point calculation of $[HL^2]^-$ from the optimization of **2**.

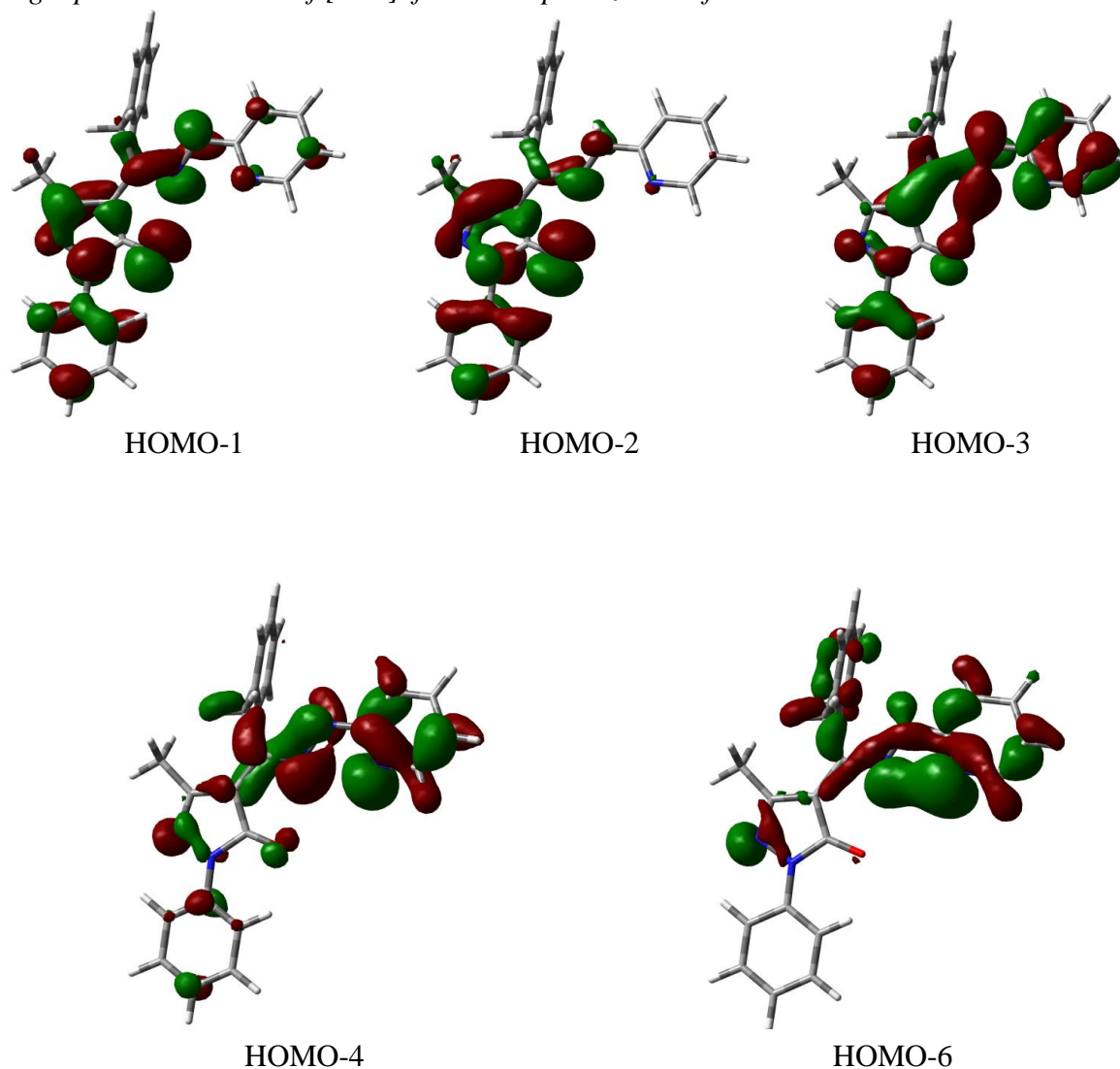


Figure 68. Molecular orbitals of anionic ligands $[HL^1]^-$ involved in the coordination to metal centers.

The proposed optimized structure of **1** also gives a calculated NMR that matches well with experimental ^1H and ^{13}C NMR spectra (R^2 value of 0.9971 in the correlation shown in Figure 70). To rationalize the observed *trans* disposition of methanol molecules in **1**, also the hypothetical complex $[\text{Zn}(\text{HL}^1)_2]$ without these solvent ligands has been optimized. The resulting structure is square planar (Figure 71), which is unexpected for a four-coordinated d^{10} complex. This fact suggests that the adoption of such a geometry is mainly due to steric reasons. This is confirmed by optimizing the related complex $[\text{Zn}(\text{HL}^3)_2]$, where the HL^3 ligand is like HL^1 , but the *p*-trifluoromethylphenyl substituent is replaced by a methyl group. Optimized $[\text{Zn}(\text{HL}^3)_2]$ is tetrahedral and is 5.8 kcal/mol (ΔG) more stable than the square planar structure (Figure 71).

Consequently, the presence of the *p*-trifluoromethylphenyl group in HL¹ causes enough steric pressure to impede the adoption of the expected d¹⁰-tetrahedral arrangement of [Zn(HL¹)₂], explaining the *trans*-(MeOH)₂ geometrical configuration observed in **1**. A square planar structure closely related to that found for [Zn(HL¹)₂] was optimized for complex [Cu(HL¹)₂], **3**. The six-membered metallacycles within the [M(HL¹)] moiety display an envelope conformation in both cases and the angle between the ligand and molecular planes is quite similar in both complexes (29.5° and 28.8° for Cu and Zn, respectively). A minor difference found is the M-O and M-N bond distances, which are slightly longer for zinc (2.029 and 2.013 Å, respectively) than those for copper (1.950 and 1.987 Å, respectively), in agreement with its higher ionic radius^[316].

Complexes **2** and **4** have an analogous formulation, [M(HL²)₂], but their optimized structures showed some differences. In **4** it is clearly appreciable the Jahn-Teller effect with two distances, Cu-O and Cu-N_{py} of 2.204 and 2.399 Å, respectively, which are longer than the other Cu-O and Cu-N_{py} (2.045 and 2.000 Å, respectively) and longer than those observed for Zn complex **2** (Zn-O: 2.045 and 2.053 Å; Zn-N_{py}: 2.183 and 2.191 Å). Furthermore, the planes defined for the HL² ligand formed different angles in both complexes. This angle between the two planes is 83.9° for the Zn derivative, close to the regular angle of 90° for an ideal octahedral geometry, while for the Cu complex is more distorted with respect to such a geometry, 72.9°. As occurred with complex **1**, the proposed calculated structure of **2** provides an excellent NMR prediction for this complex, according to the correlation of experimental and calculated ¹H and ¹³C NMR parameters (R² value of 0.9991 in the correlation shown in Figure 70). Complex **5** was also optimized and shows a square planar structure, which is typical for related four-coordinated copper-acylpyrazolonate complexes^[143]. Again, a good comparison of the calculated and experimental structural parameters of this complex was found (Table 13), which is common for these [Cu(Q^R)₂] complexes^[142].

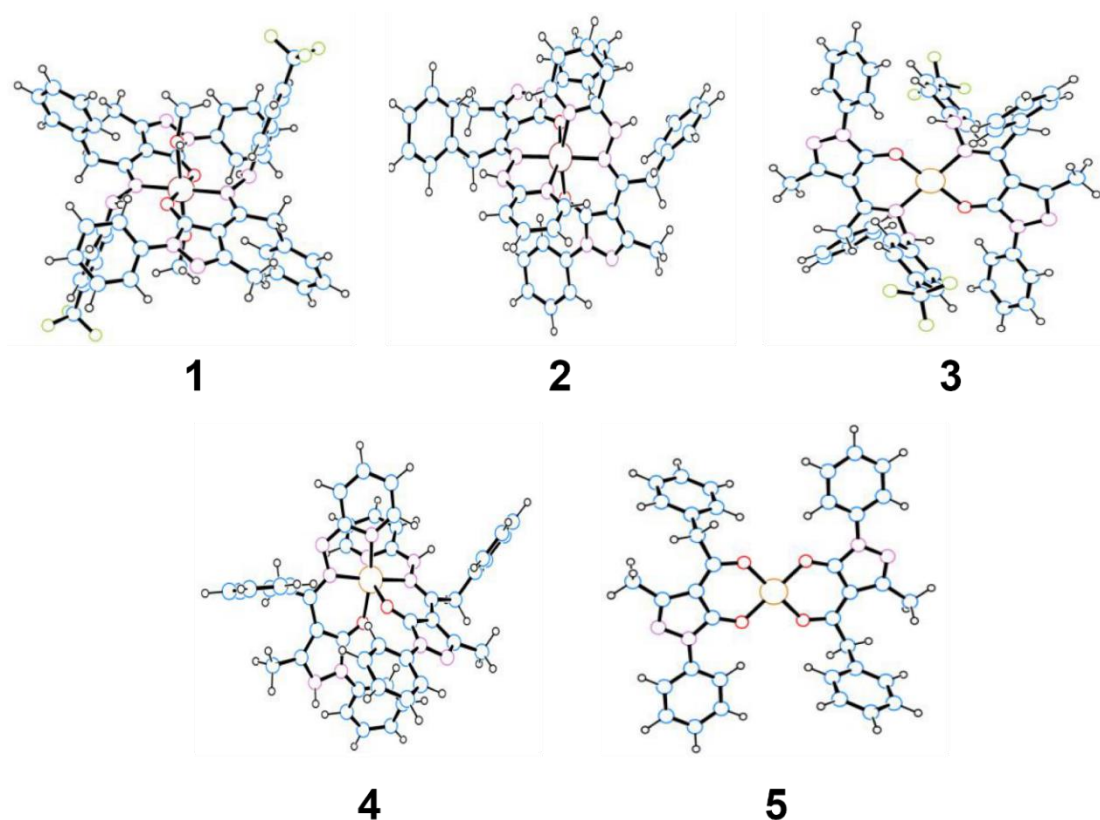


Figure 69. Optimized structures of complexes 1–5

Table 12. Comparison of selected experimental and calculated structural parameters of complex 1.

Bond distances (Å) and angles (°)	Experimental	Calculated
Zn-O	1.989	2.050
Zn-N	2.116	2.088
Zn-O _{MeOH}	2.285	2.270
C=O	1.277	1.279
C-N	1.303	1.315
N-N	1.444	1.424
C-C	1.445	1.432
C-C _{pyrazol}	1.430	1.430
O-Zn-O	180.0	180.0
N-Zn-N	180.0	180.0
O _{MeOH} -Zn-O _{MeOH}	180.0	180.0

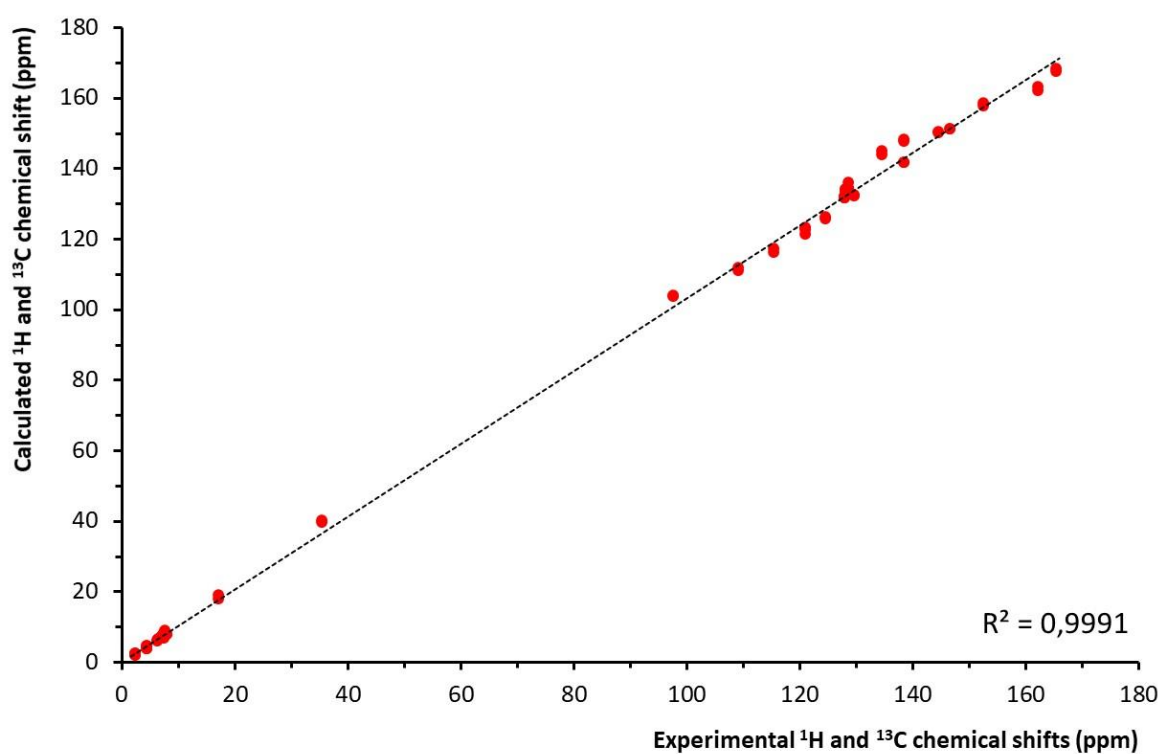
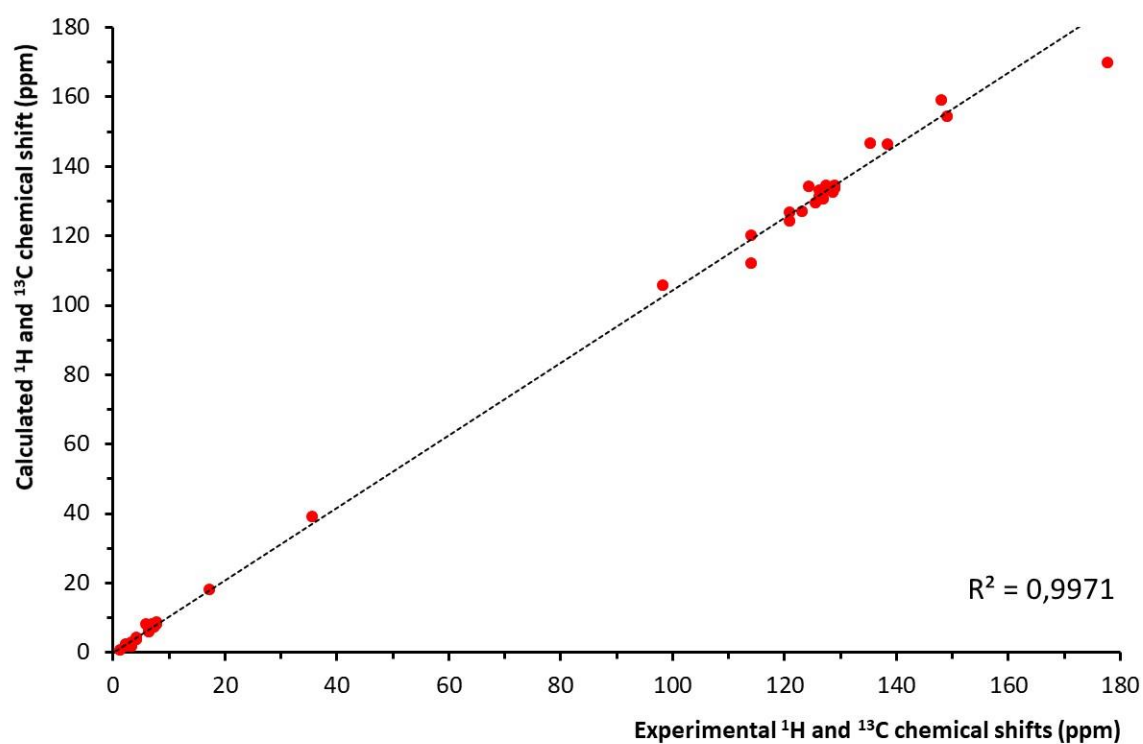


Figure 70. Comparison of the calculated and experimental ^1H and ^{13}C NMR spectra of complexes 1 (top) and 2 (bottom)

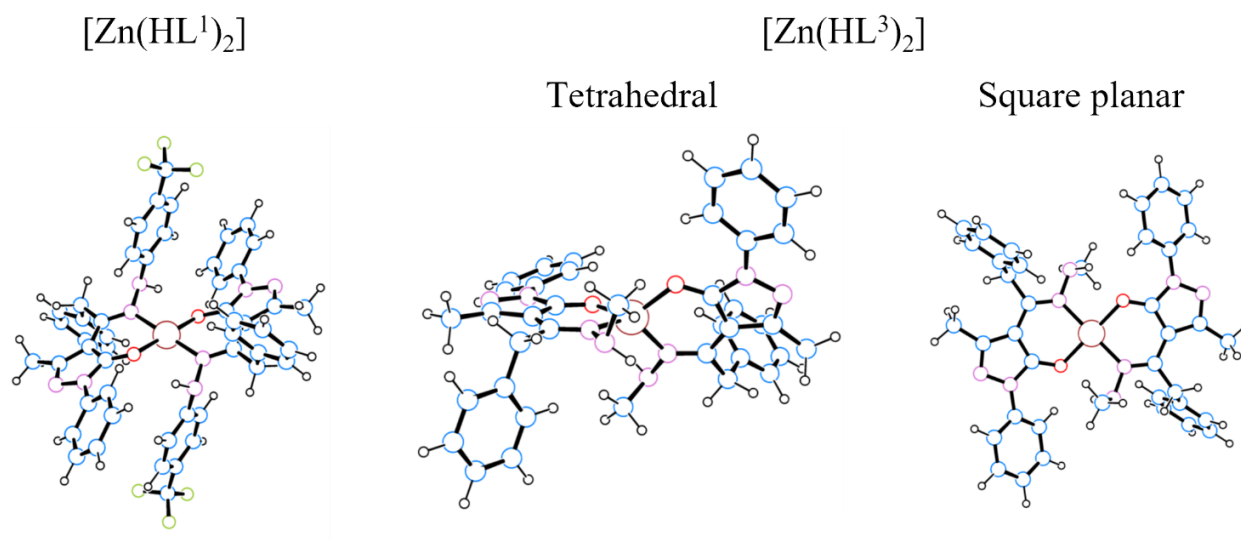


Figure 71. Optimized structures of complexes $[Zn(HL^1)_2]$ and $[Zn(HL^3)_2]$.

Table 13. Comparison of selected experimental and calculated structural parameters of complex 5.

Bond distances (Å) and angles (°)	Experimental	Calculated
<i>Cu-O</i>	1.931	1.936
	1.893	1.919
<i>C=O</i>	1.268	1.271
	1.276	1.272
<i>C-N</i>	1.354	1.367
<i>N-N</i>	1.401	1.392
<i>C-C</i>	1.404	1.406
<i>C-C_{pyrazol}</i>	1.420	1.435
<i>O-Cu-O</i>	180.0	180.0

3.4 Cytotoxicity studies

Both the free ligands H_2L^1 and H_2L^2 and the metal complexes **1-4** were assayed *in vitro* on *T. brucei* and Balb/3T3 cells (mammalian cells), and interesting results were obtained, schematized in Table 14. EC_{50} values were calculated with the GraphPad Prism 5.2 software and the selectivity index was calculated by the correlation of the obtained values for *T. brucei* versus the mammalian reference cells. First of all, H_2L^2 was slightly more active against *T. brucei* than H_2L^1 ($EC_{50} =$

0.189 vs 0.213 μM), but also more cytotoxic, having an EC_{50} value of 0.4665 μM against mammalian cell, compared to 12.51 μM for H_2L^1 . From the SI, it is clear that the safety profile of H_2L^1 is much better than the H_2L^2 profile, and the latter seems to strongly affect both parasitic and mammalian cells. As evident from the data reported in Table 14, also Zn and Cu complexes of the proligand H_2L^1 (**1** and **3**) are less toxic than Zn and Cu complexes of the proligand H_2L^2 (**2** and **4**). Therefore, the selectivity index is very low for **2** and **4** ($\text{SI} = 2.065$ and 1.345 , respectively) and much higher for **1** and **3** ($\text{SI} > 100$ and 7.586 , respectively). This is in line with the results above which H_2L^1 is always much more specific than H_2L^2 , regardless of whether it is complex or not. The interesting results obtained for H_2L^1 and its complexes **1** and **3** pushed the research to furtherly focus on these compounds. In particular, **1** seems to be more active than H_2L^1 , and it also maintains a good safety level since SI is greater than 100. Because of the derivation of complex **1** from H_2L^1 , it is logical to suppose that the type of action of these two compounds against *T. brucei* could be the same.

Table 14. Activity of tested compounds on *T. brucei* TC221.

COMPOUND	EC_{50} <i>T. BRUCEI</i> TC221	(MM) BALB/3T3	SI
H_2L^1	0.231 ± 0.008	12.51 ± 1.354	55
H_2L^2	0.189 ± 0.038	0.465 ± 0.013	2.460
1	0.084 ± 0.005	12.322 ± 0.346	>100
2	0.169 ± 0.038	0.349 ± 0.109	2.065
3	4.347 ± 2.610	32.977 ± 0.347	7.586
4	12.763 ± 4.060	17.163 ± 3.448	1.345
SURAMIN	0.023 ± 0.0008	43.912 ± 1.438	>100

3.4.1 Mechanism of action

Among the complexes tested, **1** is the most convincing, thus, for this reason, a detailed investigation about the mechanism of action of compound **1** and its precursor H_2L^1 sparked interest. The study was conducted by measuring the cellular nucleotide pools, which gives information of nucleotide-metabolizing enzymes and energy metabolism and redox status (NADPH is required by ribonucleotide reductase). Untreated *T. brucei* NTP, dNTP, and ADP pools were measured by HPLC and compared to the pools of parasites treated with H_2L^1 and complex **1**. For the analysis, the method by Ranjbarian *et al* was applied^[308]. The procedure started

by adding 5 μM of the drug tested to 50 mL of a *T. brucei* culture (10^6 logarithmically growing cells per mL) and incubating the parasites for 1 hour before extracting the NTPs, dNTPs, NDPs, and dNDPs from them with trichloroacetic acid and quantifying the nucleotides with HPLC. From these experiments, it was possible to evaluate changes in nucleotide pools between non-treated trypanosomes and those treated with H_2L^1 and **1**. A striking difference between the drug-treated and non-treated cells was the levels of CTP and dCTP. In fact, although CTP and dCTP are low also in *T. brucei* cells without treatment ($\sim 2\%$ of the total NTP pool), they are much lower in parasites treated with H_2L^1 and especially with the Zn complex **1** (Figure 72a). The CTP pools were decreased to 25% in the cells treated with H_2L^1 and 6% in the cells treated with complex **1**, as compared to control cells. This result is in accordance with the results obtained in Table 14; complex **1** is more active than H_2L^1 (EC_{50} value is lower), and it is therefore logical that if CTP is affected by the treatment with H_2L^1 , this effect is much stronger with complex **1**. No obvious effect was observed on the other NTPs or ADP (Figure 72b). From this results, it can be assumed that the target of these compounds could be CTPS. Indeed, CTPS is the enzyme responsible for the *de novo* synthesis of CTP from UTP, which is the only pathway of synthesis of CTP in *T. brucei*^[302]. The low CTP level could also be a reason why less dCTP is produced. CTP and other NTPs in the cell are in equilibrium with the corresponding diphosphates. Consequently, it will be less CDP substrate for ribonucleotide reductase to make dCDP from dATP, dGTP and dTTP levels increased in trypanosomes treated with **1** (Figure 73). This could be a consequence of the low dCTP pools, leading to that the other deoxynucleotides accumulate in the cell as the DNA polymerase is not able to synthesize DNA because of the lack of dCTP. The inhibition of DNA synthesis lead to growth inhibition.

To further investigate the different activities between Zn(II) complexes **1** and **2**, their stability in DMSO-d_6 was evaluated through an NMR study within 48 hours. While the ^1H NMR of complex **2** remains unchanged after 48 hours, confirming its stability in DMSO, in the case of complex **1**, some modifications have been immediately observed after dissolution. In fact, the appearance of a resonance due to free MeOH at 3.16 ppm confirms its replacement in the zinc coordination environment by deuterated DMSO molecules. Moreover, the geminal CH_2 of the benzyl group in (HL^1) affords three different signals, two of them undergoing diastereotopic splitting, in accordance with the presence of a trans and two cis isomers, containing a chiral zinc center, in equilibrium with each other. Furthermore, by comparison with the spectrum of the free H_2L^1 ligand in DMSO-d_6 , no ligand release was observed. In conclusion, complex **1** in DMSO replaces

methanol with DMSO molecules in the zinc environment and it undergoes trans-cis interconversion without any decomposition.

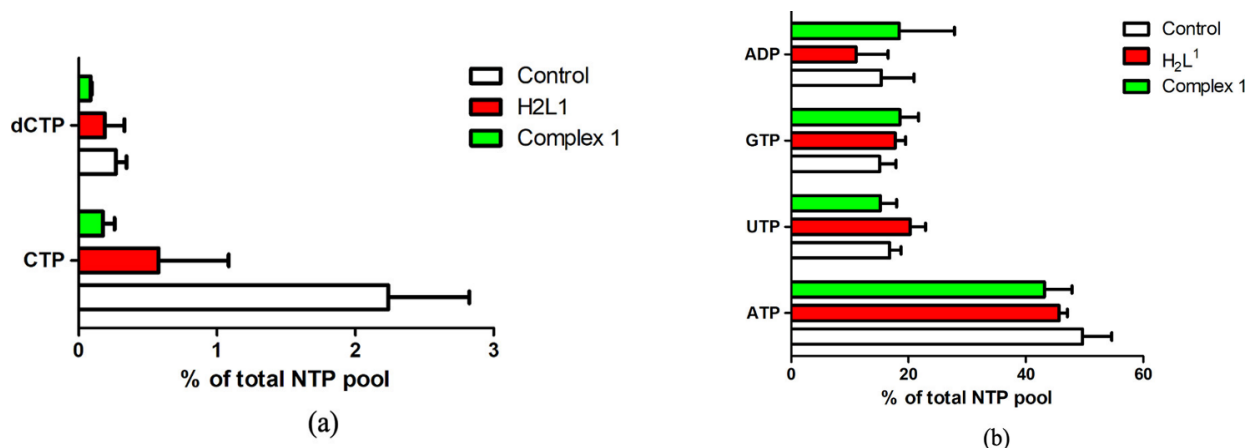


Figure 72. (a) Differences in CTP and dCTP pools in non-treated cells and cells treated with H₂L¹ and **1** (both of them at a concentration of 5 μ M for 1 hour). (b) Differences in NTP pools in non-treated cells and cells treated with H₂L¹ and **1** (both of them at a concentration of 5 μ M for 1 hour).

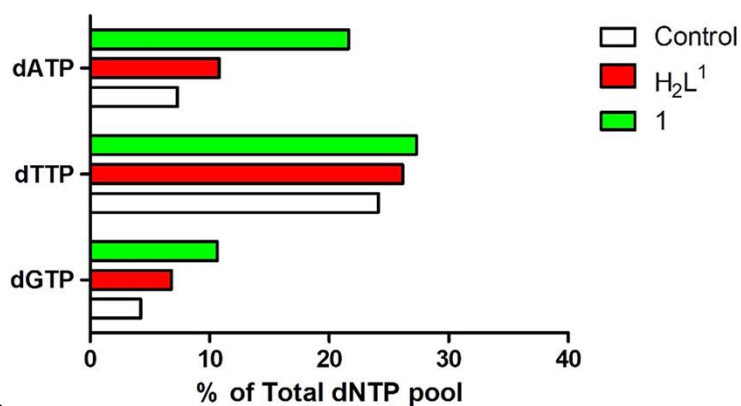


Figure 73. Increased deoxynucleotide pools in cells treated with 5 μ M of H₂L¹ and **1** for 1 h (compared to deoxynucleotide pools in non-treated control cells).

3.5 Conclusions

To summarize, in this chapter two novel pyrazolone-based hydrazones H_2L^1 and H_2L^2 and their Zn(II) and Cu(II) complexes **1-4** have been described. The compounds were fully characterized both in the solid state and solution, together with a bis(acylpyrazolonate)copper(II) species (**5**) arising from the decomposition of the complex $[Cu(HL^1)_2]$ (**3**). All ligands and metal complexes were structurally characterized both in solid state and solution and investigated as potential antitrypanosomal agents, and the overall results of this study shed light on the biological properties of this new series of compounds as a relevant source of bioactive substances, which can serve as possible lead candidates for further antiprotozoal drug development. The exhibited antitrypanosomal activity of H_2L^1 and its Zn(II) complex **1**, revealed through biological *in vitro* assays, is an important result also because a very low cytotoxicity has been detected. An important outcome is the finding of mechanism of action. The analysis of NTP and dNTP pools clearly revealed that CTP is severely affected by H_2L^1 and its Zn(II) complex **1**. *T. brucei* lacks salvage pathways for CTP synthesis, and the preliminary results on the purified *T. brucei* CTPS indicate that it is the targeted enzyme of the Zn(II) complex **1**, whereas H_2L^1 seems inactive by itself. The effect of H_2L^1 on the CTP/dCTP pools may possibly come from that it is chelated by naturally occurring metals in the trypanosomes or the growth medium. Accordingly, the Zn(II) chelated complex **1** had a stronger effect on the CTP and dCTP pools than H_2L^1 . CTPS was previously found to be a good target in *T. brucei* because, in contrast to the situation in mammalian cells, the inhibition of this enzyme cannot be rescued by cytidine (or cytosine) in the surrounding medium. The parasite was therefore sensitive to the CTPS inhibitors 6-diazo-5-oxo-L-norleucine (DON) and α -amino-3-chloro-4,5-dihydro-5-isoxazoleacetic acid (acivicin)^[302]. However, DON and acivicin are both glutamine analogues, and in mammalian cell, they also affect other glutamine-requiring enzymes / pathways such as *de novo* purine biosynthesis (DON) and GMP synthase (acivicin). Indeed, they were originally tried out as anticancer drugs, and the selectivity against the trypanosomes is dependent on nucleosides / nucleobases in the growth medium that selectively rescues the mammalian cells. In contrast, the drugs investigated here are from another class of compounds and have a high selectivity against the trypanosomes with almost no effect on the mammalian reference cells. Since then, improved version of acivicin have been produced with higher selectivity against *T. brucei* CTPS^[317]. Experience from studies on mammalian cells has shown that it is possible to achieve much higher selectivity against CTPS over other cellular

enzyme by using cytidine / uridine analogues such as cyclopentenyl cytosine. However, these analogues need to be phosphorylated in the cell to achieve their function as CTPS inhibitors, and *T. brucei* lacks uridine-cytidine kinase. All drugs developed against the *T. brucei* CTPS have therefore so far been glutamine analogues. In contrast, the drugs investigated here are from another class of compounds. Furthermore, they have a high selectivity against the trypanosome with almost no effect on the mammalian reference cells.

CHAPTER 4.

DFT studies on the mechanism of the molybdenum-catalyzed deoxydehydration of diols.

4.1 Introduction

Biomass conversion is the process of converting plant-based materials into useful chemicals and fuels. The process typically begins with the pretreatment of the biomass, which involves breaking down the complex structures of the plant material to make the sugars and other molecules inside more accessible. This can be done through a variety of methods, such as mechanical grinding, chemical treatment, or exposure to heat and pressure. Next, the pretreated biomass is fermented to produce a variety of intermediates, such as ethanol, butanediol, and acetic acid. These intermediates can then be converted into added-value chemicals through further chemical processing and distillation. For example, ethanol can be converted into ethylene and propylene, which are used to make plastics and other industrial materials. Finally, the remaining biomass can be used as a source of energy through direct combustion or gasification to produce heat and electricity. Overall, the goal of biomass conversion is to produce high-value chemicals and fuels while minimizing waste and maximizing the use of renewable resources.

Biomass conversion is important because it allows us to utilize such plant-based materials, which are abundant and renewable, as a source of chemicals and fuels. The importance of this process resides in the possibility to reduce our dependence on fossil fuels, which are non-renewable and contribute to climate change. Additionally, using biomass as a feedstock for chemicals and fuels can help create new economic opportunities in rural areas, where many plants are grown. The impact of biomass conversion on society can be significant. For example, it can lead to the development of new, sustainable technologies that can create jobs, reduce the cost of chemicals and fuels, and decrease greenhouse gas emissions. It can also help to improve the energy security of countries by reducing their dependence on imported fossil fuels. Moreover, using biomass conversion to produce biofuels can lead to a reduction of air pollution and greenhouse gas emissions, which is important for the public health and the environment. Overall, the development and implementation of biomass conversion technologies have the potential to have a positive impact on society by creating new economic opportunities, improving energy security, and reducing environmental impacts.

With this premise, chemical reactions capable of reducing the oxygen content from biomass-derived compounds such as glycerol and sugar alcohols are in increasing demand^[318]. In particular, the metal-catalyzed deoxydehydration (DODH) of vicinal diols into alkenes is one of most promising research field^[319]. Metal-catalyzed diol dehydration is a widely studied chemical process in which a diol (a molecule containing two hydroxyl groups) is converted into a carbonyl

compound, such as a ketone or an aldehyde, and ultimately in the corresponding alkene, through the removal of water. This process has been widely utilized in the synthesis of various organic compounds, including fine chemicals and pharmaceuticals. Transition metal catalysts, such as titanium, zirconium, and vanadium, have been shown to be highly effective in promoting the diol dehydration reaction. The mechanism of the metal-catalyzed diol dehydration process typically involves the formation of a metal-alcoholate intermediate, which then loses water to form the carbonyl product. The mechanism can be further divided into two pathways, namely the direct and the indirect pathways. The direct pathway involves the formation of the metal-alcoholate intermediate through the coordination of the diol to the metal catalyst, followed by water elimination to form the carbonyl product. The indirect pathway, on the other hand, involves the formation of the metal-alcoholate intermediate through the coordination of one of the hydroxyl groups of the diol to the metal catalyst, followed by the nucleophilic attack of the other hydroxyl group on the metal-coordinated alkoxide to form the carbonyl product. The choice of the transition metal catalyst, reaction conditions, and the nature of the diol substrate greatly influence the outcome of the diol dehydration reaction. For instance, titanium catalysts have been shown to be highly effective in promoting the diol dehydration reaction, particularly for the conversion of 1,2-diols to aldehydes. Zirconium catalysts, on the other hand, have been shown to be highly effective in promoting the diol dehydration reaction, particularly for the conversion of 1,2-diols to ketones. Vanadium catalysts have been shown to be effective in promoting the diol dehydration reaction of both 1,2-diols and 1,3-diols. The first report of this type of overall transformation is to be found more than a century ago when Sabatier and Gaudion reported allyl alcohol as one of the products from conversion of glycerol on copper^[320]. The factors of the recently heightened interest in this field is due to the introduction of catalytic deoxydehydration of diols and polyols to alkene found to be stereospecific, and the increased availability of glycerol as a byproduct of biodiesel, thus routes were sought to convert glycerol to chemicals. Additionally, more recently another motivation stems from the attempt to use the carbohydrate fraction of lignocellulosic biomass, meaning transforming the large number of OH groups present in sugar into other functionalities.

Although different transition metals like molybdenum^{[244],[321]} and vanadium^[322] complexes have been reported as catalysts, rhenium derivatives are the most investigated catalysts for DODH. Given the fact that the final extrusion of the olefin from a diolate leads to oxidation of the metal with an increase of valence by two and formation of a dioxide complex many compounds used as starters of the catalytic cycle are characterized by the dioxido structural motif, for example perrhenate ReO_4^- or the Cp^*ReO_3 , the first rhenium compound used for DODH reported by Cook

and Andrews, using PPh_3 as reductant^[323]. By now, a large number of substrates has been tested like, for example, “model” diols used to demonstrate characteristic of the DODH mechanism. Similarly, many reductants have been successfully tested and employed: target properties of the reductants are effectivity, sustainable sourcing and recyclability, large scale availability, and separability from the reaction mixture. Triphenylphosphane remains a commonly used strong reductant. Speaking about the mechanism of the reaction, it is not yet completely clear, but there is some consensus on the fact that the steps of the catalytic cycle are principally similar for the three most reported metals (rhenium, molybdenum and vanadium) and that the product forming step of deoxydehydration is extrusion of the olefin from a glycolate with increase of the metal oxidation state by +2. The other steps leading to this intermediate are still under debate and may depend on the nature of reductant and catalyst. From a thermodynamical point of view, one can subdivide the reaction into three thermodynamic contributions: the transformation of the substrate, the elimination of a molecule of water, and the oxidation of the reductant. The transition from diol to olefin requires a great step up in terms of Gibbs energy of formation, implying a large endergonic contribution to the overall reaction. The elimination of water slightly alleviates this issue, but a big contribution is needed by the reductant to provide a thermodynamic driving force. As a consequence the reductant must be strong and easily accept oxygen.

As previously mentioned, rhenium is the most investigated metal in this field, but given its rarity and resulting high price, alternatives are being sought. Some promising results have been obtained with molybdenum and vanadium. In particular, the choice of molybdenum resides on the similarities between oxorhenium(VII) and oxomolybdenum(VI) complexes, thus one can expect that molybdenum's ability to cycle between the two oxidation states +IV and +VI could make it a viable substitute. In addition, over-hydrogenation of alkene to alkane when using H_2 as reductant could probably be avoided as molybdenum is expected to be a poorer hydrogenation catalyst than rhenium. Amongst the molybdenum complexes viable for this application, acylpyrazolone-based complexes have aroused interest for their ability to chelate and stabilize the metal by creating a π -conjugated system, obtaining stable complexes compatible with high oxidation states and harsh reaction conditions^[244].

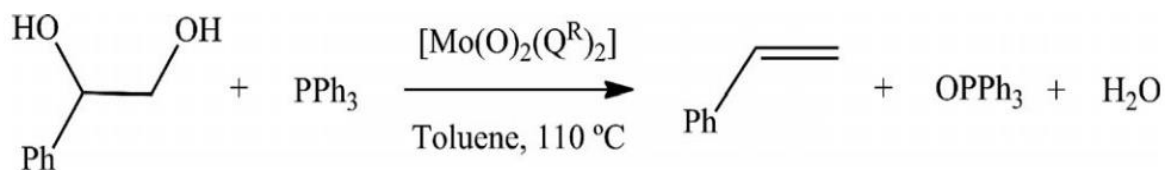


Chart 42. Example of an overall DODH reaction, using PPh_3 as reductant and a dioxomolybdenum(VI) complex with acylpyrazolonate ligands as catalyst^[324].

A considerable amount of publication on molecular DODH catalysis include computational chemistry with the aim to better understand the mechanism lying behind every single step. DODH catalysis by molybdenum compounds was computationally investigated by Fristrup *et al.*^[321] using one molecule of MoO_3 or MoO_2Cl_2 as the model, methanol as solvent, and B3LYP and implicit solvation model as methods. Luppet *et al.* computed the free energy profile for alkene extrusion from a monodiolate and from a bisdiolate complex formed from MoO_3 and 1,2-propanediol, finding the activation energies to be comparable. Moreover, they investigated the effect of the temperature on the entire cycle with propanediol as substrate and as reductant^[325]. Dethlefsen *et al.* compared the free energies of the reduction of molybdenum(VI) to molybdenum(IV) starting from MoO_3 and found that 1,2-propanediol and isopropyl alcohol were more effective if the diolate had already formed^[321].

From such studies on the reaction mechanism, three main stages of the process have been generally identified:

1. The activation of the diol by condensation to the metal complex.
2. The reduction of the metal center by and oxygen atom transfer to the reductant.
3. The extrusion of the alkene from diolate.

In this Chapter, a computational study on the mechanism of a Mo-catalyzed deoxydehydration of vicinal diols is reported, based on the work of Hills *et al.*^[244] in which they synthesized and tested the catalytic activity of a series of novel acylpyrazolonate $[\text{Mo}(\text{O})_2(\text{Q}^{\text{R}})_2]$ compounds towards the deoxygenation of selected epoxide and deoxydehydration of selected vicinal diols to alkenes, employing PPh_3 as oxygen acceptor. Their compounds showed moderate catalytic activity with a yield up to 55% for the DODH of vicinal diols.

4.2 Experimental section

The electronic structure and geometries of the model compounds were computed using density functional theory at the B3LYP level^{[270],[326]}, using the effective core potential LANL2DZ basis set for Mo and 6-31G** basis set for the other atoms. Molecular geometries of all model complexes were optimized without symmetry constraints. Frequency calculations were carried out at the same level of theory to identify all of the stationary points as transition states (one imaginary frequency) or as minima (zero imaginary frequencies) and to provide the thermal correction to free energies at 298.15 K and 1 atm. In some cases, a structure was considered a minimum in spite of a very low imaginary frequency ($< 10 \text{ cm}^{-1}$), possibly due to the use of an insufficiently large integration grid^[327]. Solution-phase SCF energies of intermediates and transition states were calculated by a single point calculation of the vacuo optimized structure using the CPCM solvation mode in toluene^[266]. Gibbs free energies in toluene were estimated from the equation $G_{\text{solv}} = E_{\text{solv}} + (G_{\text{gas}} - E_{\text{gas}})$. The energy profile are presented in terms of relative free energies, derived from thermochemical analysis. The DFT calculations were performed using the Gaussian 09 suite of programs^[269].

4.3 Results and discussion

In order to efficiently compute the energies of the intermediates, a series of exemplification were made. First, the substrate was considered to be a simpler ethanediol, the PPh_3 reductant was substituted by a PMe_3 , the reaction conditions were considered to be at 298 K, and as catalyst two model compounds were used, first a molybdenum complex with a simple acylpyrazolone ligand where all the substituents are hydrogens, namely $[\text{Mo}(\text{O})_2(\text{Q}^{\text{H,H,H}})_2]$ (where $\text{Q}^{\text{H,H,H}} = 4\text{-formyl-1H-pyrazol-5-olate}$), and then the calculations were repeated employing a more computational demanding complex $[\text{Mo}(\text{O})_2(\text{Q}^{\text{Me}})_2]$ (where $\text{Q}^{\text{Me}} = 4\text{-acetyl-3-methyl-1-phenyl-1H-pyrazol-5-olate}$), illustrated in Chart 43.

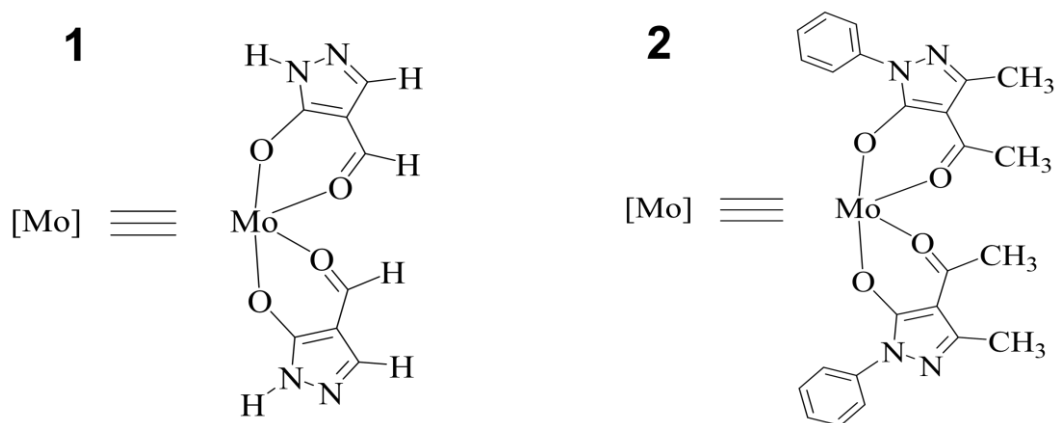


Chart 43. Molecular structure of the two compounds considered for the energy calculations; (1) the simpler model $[\text{Mo}(\text{O})_2(\text{Q}^{\text{H,H,H}})_2]$ and (2) the more complex $[\text{Mo}(\text{O})_2(\text{Q}^{\text{Me}})_2]$.

Taking in consideration the three stages of the process mentioned earlier (activation of the diol, reduction of the metal center, and alkene extrusion), two different pathways have been proposed and investigated by DFT calculation and their respective lower energy profile were found. The two pathways differ for the order of the steps involving the diol activation and the oxygen atom transfer: in pathway **A** (Chart 44), the diol activation by condensation takes place before the oxygen atom transfer to the phosphane reductant, while the opposite situation occurs in pathway **B** (Chart 44), where the reduction of the metal center by the phosphane from molybdenum(VI) to

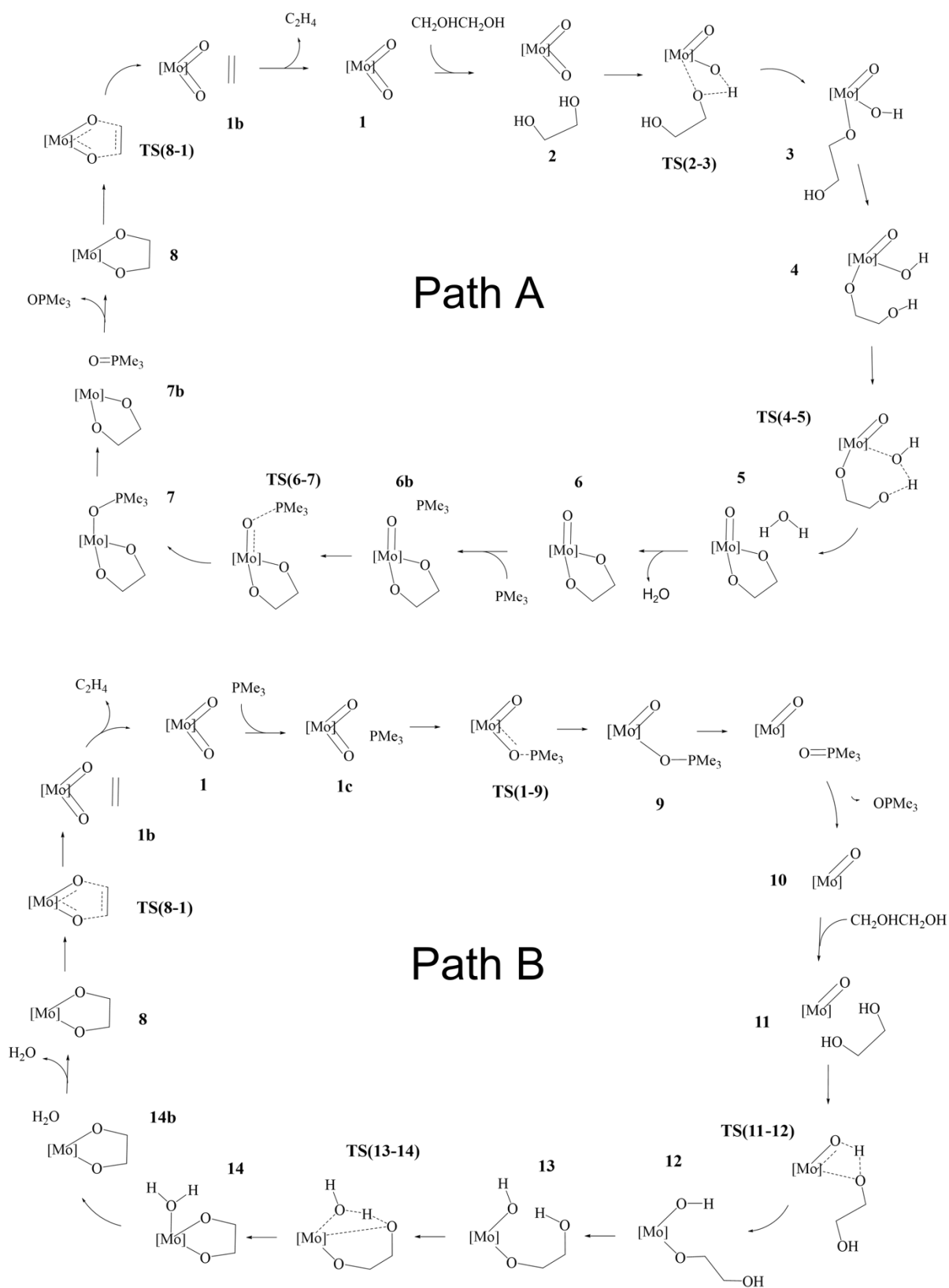


Chart 44. Pathway A and pathway B of the catalytic cycle theoretically investigated.

molybdenum(IV) species occurs before the diol condensation. Both pathways have in common the final step corresponding to the ethylene extrusion from the molybdenum glycolate species.

Energetically speaking, the profiles of the two models of the catalyst (Chart 43) are pretty similar, although in the second model the energies of the intermediates are averagely higher, especially those of the transition states, even if certain intermediates are stabilized. This can be rationalized considering the additional steric hindrance of the catalyst in the second model, particularly in the transition states where the metal center is even more crowded. The only difference that could be worth mentioning is an issue found in the simpler model at the transition state **TS(2-3)**. Optimizing the structure with a positive displacement along the reaction coordinates should result in the intermediate **3**, however the initial optimization resulted in a reaction path in which the diol reacts with the ligand rather than coordinating the metal. This problem was resolved adjusting the structure of the transition state, but it could represent a possible alternative reaction path leading to the formation of by-products. Nevertheless, with the second model of the catalyst this phenomenon didn't arise, probably due to the more hindered ligand that prevents the approach of the diol molecule. For these reasons, here the discussion will be focused on the second model. Other possible routes in the DODH such as the oxidative cleavage of the diolate ligand or an alternative radical mechanism were not investigated. In the same way the disproportionation reaction between Mo(IV) and Mo(VI) that yields the catalytical inactive species Mo(V) has not been taken in consideration; although this reaction can cause a lower efficiency of the catalysis, it is not of interest for the purposes of the analysis of the catalytic mechanism.

4.3.1 Description of pathway A.

The schematic representation of pathway **A** is illustrated in Chart 44, while the relative Gibbs free energy profile is reported in Figure 74 and 75 together with that of pathway **B** for comparison. The optimized structures of the intermediates are illustrated in Figure 76. The zero energy reference was taken as the energy of the reagents before the reaction takes place ($\text{OHCH}_2\text{CH}_2\text{OH} + [\text{Mo}(\text{O})_2(\text{Q}^{\text{Me}})_2] + \text{PMe}_3$). The first step of the cycle (intermediate **2**) consists in the approaching and interaction of the ethylene glycol towards the catalyst, **1**. The condensation occurs through the subsequent transition state **TS(2-3)**: the H atom is transferred from the diol to one of the oxo group of the Mo complex, while the same oxygen of the diol moves towards the metal center. As a consequence, the acceptor oxo group elongates to 1.832 Å (vs 1.705 Å of the other double-bonded

oxo group) and at the same time it moves aside increasing the $O_Q\text{-Mo-O}_{\text{oxo}}$ angle from 99.88° in of the distorted SBP geometry in **1** to 135.45° in **TS(2-3)**, in order to accommodate the diol. The proton is placed halfway the O_{oxo} and the O of the diol with $O_{\text{oxo}}\text{-H}$ distances of 1.170 \AA and $O_{\text{diol}}\text{-H}$ of 1.241 \AA . This step requires to overrun an energy barrier of $\Delta G = 31.68 \text{ kcal/mol}$ and it is the highest barrier of the cycle. The condensation terminates in **3** with the complex assuming a pentagonal bipyramidal geometry. The newly formed coordination bond displays a length of 1.981 \AA while the Mo-OH bond length reaches 1.931 \AA . The acyl-pyrazolone opposed to the reaction site tilts out of the plane, probably due to an energetic and/or overlapping factor. The compound then rearranges to the lower energetic ($\Delta G = -3.12 \text{ kcal/mol}$) conformer **4**: the diol assumes the *anti*-conformation pointing the terminal OH group toward the hydroxy ligand. Also the complex as a whole alters its geometry toward a highly distorted capped octahedron, thus causing a shortening of the $\text{Mo-O}_{\text{diol}}$ bond to 1.903 \AA . The stabilization is also due to a partial formation of an intramolecular hydrogen bond between the terminal hydroxyl group of the glycol ($O_{\text{diol}}\text{-H} = 0.976 \text{ \AA}$) and the hydroxo group ($O_{\text{oxo}}\text{-H} = 0.972 \text{ \AA}$); at this stage the hydrogen bond length $\text{-O-H}\cdots\text{O}$ is of 1.828 \AA . This interaction drives the cycle through the next transition state **TS(4-5)** with a small energetic barrier of $\Delta G = 17.16 \text{ kcal/mol}$, where the terminal oxygen of the glycol draws in the metal center ($\text{Mo-O}_{\text{diol}} = 2.383 \text{ \AA}$) and simultaneously it transfers the proton to the hydroxo ligand, also pushing it down and away from the molybdenum ($\text{Mo-OH} = 2.242 \text{ \AA}$). The proton is located quite halfway the two oxygens (1.201 \AA and 1.999 \AA). This proton transfer results in the complete removal of the water molecule from the coordination sphere of the intermediate **5**, repristinating the pentagonal bipyramidal geometry. The coordination of the second oxygen of the 1,2-ethanediol affords the formation of a diolate ligand with a dihedral angle Mo-O-C1-C2 of 30.50° and $\text{Mo-O}_{\text{diol}}$ bond distances of 1.960 \AA and 1.964 \AA . We weren't able to locate a transition state with the water still coordinated to the metal center. The structure then keeps rearranging making minor adjustments in order to furtherly lower the energy, settling in intermediate **6**. The cycle continues with the reductive oxygen atom transfer: firstly the phosphane places itself around the site of reaction, in the opposite direction of the diolate. One acylpyrazolone leans downward to allow the drawing in of the PMe_3 (**6b**). The actual oxygen atom transfer begins after surpassing the energy barrier of $\Delta G = 30.63 \text{ kcal/mol}$ in the transition state **TS(6-7)**: the phosphane moves toward the remaining oxo group with the phosphorous 2.052 \AA distant from the oxygen and at the same time the Mo-O_{oxo} double bond elongates to 1.793 \AA . The oxygen atom transfer involving a Mo complex and a phosphine as reductant has already been studied both computationally^[328] and experimentally^{[329],[330]}. The formation of the P=O bond is completed in **7**, with a bond length of

1.540 Å, that results in a huge energy gain of $\Delta G = 32.50$ kcal/mol. The phosphine oxide remains still coordinated to the metal via the oxygen with metal-oxygen distance of 2.129 Å, consequently the molybdenum reduces to Mo(IV). The structure then starts rearranging in **7b** shifting from the pentagonal bipyramidal geometry to a capped trigonal prismatic partially relieving the steric pressure: the phosphine oxide recedes with the oxygen at 2.309 Å from the metal center while diol rotates by about 90° positioning itself perpendicularly to the plane it was lying. The complete removal of the phosphine oxide in **8** allows the complex to achieve an octahedral geometry, gaining a great energy decrease from the reduction of the previously crowded environment ($\Delta G = -6.67$ kcal/mol). All the ligands move closer to the metal center. The last step of the cycle involves the ethene extrusion through **TS(8-1)**. The transition state passes through a concerted mechanism^[331] characterized by the weakening of the C–O bonds of the diol (1.846 Å vs 1.426 Å in **8**) and the strengthening of Mo–O and C–C bonds, respectively 1.787 Å vs 1.928–1.933 Å and 1.416 Å vs 1.530 Å. Additionally the hydrogens on the forming ethene lay out on the C=C plane, reflecting the adoption of the sp^2 hybridization by the carbon atoms. Finally the completed removal of the ethene affords the regeneration of catalyst **1**, passing through an energy barrier of 24.75 kcal/mol

4.3.2 Description of pathway B

The schematic representation of pathway **B** is reported in Chart 44, while the relative Gibbs free energy profile is reported in Figure 74 and 75. The optimized structures of the intermediates are illustrated in Figure 77. The zero energy reference was taken as the energy of the separate reagents. In pathway **B** the first step of the mechanism involves the oxygen atom transfer from the catalyst **1** to the reductant agent, PMe_3 . Initially, PMe_3 approaches the catalyst passing by the local minima **1c** to finally reach the **TS(1-9)**, where the P–O bond starts forming with a length of 2.042 Å and a bond angle P–O–Mo of 128.16°. The transition state is also characterized by an elongated Mo=O (1.819 Å) compared to the other (1.701 Å). The energy required to overcome this barrier, in toluene, is equal to 15.27 kcal/mol, smaller than the barrier present in pathway **A** for the same process. Moreover the addition of the PMe_3 group implies a great gain in energy of -37.02 kcal/mol in intermediate **9**. As said, the transition state results in the intermediate **9** where the P–O bond is completely formed. The compounds preserve the octahedral structure with an elongated O–Mo bond (2.225 Å). The P–O bond distance is 1.531 Å and the PMe_3 is placed at angle P–O–Mo of 125.36°, almost above the remaining oxo group. The subsequent dissociation of the phosphine

oxide push the compounds into a ligand rearrangement that yields firstly to intermediate **9b**, where the OPMe_3 group stands still in the whereabouts of the metal center and finally to intermediate **10**, where it assumes a distorted square based pyramidal structure with the Mo atom slightly elevated from the square plane. The two acylpyrazolone ligands are placed parallelly in opposed directions and their oxygen form the four points of the base of the pyramid, while the oxo group is the vertex. Additionally all the ligands move closer to the metal center. The process goes on with the approaching of the diol to the oxo group in the intermediate **11** to achieve the transition state **TS(11-12)**, surpassing the energetic barrier of 31.28 kcal/mol, the greatest barrier involved in this pathway. In this transition intermediate the diol is in its chair conformation with the hydrogen of one of the OH group positioned closer to the oxo group on the metal ($\text{O}_{\text{oxo}}\text{-H}$ 1.045 Å and 1.534 Å $\text{O}_{\text{diol}}\text{-H}$). At the same time one of the two acylpyrazolone ligands tilts placing itself vertically with respect to the previous square planar plane. This rearrangement is due to the simultaneous coordination of the diol, Mo-O 2.183 Å, that affords a distorted octahedral structure, with the oxo group leaning towards the diol. This transition state ends with the reaching of intermediate **12** in which the diol is fully coordinated to the metal center (Mo-O 1.941 Å) and the hydrogen completely transferred to the oxo group (O-H 0.972 Å). This intermediate shows a standard octahedral geometry that quickly shifts to the energetically favored intermediate **13** where the diol rotates pointing the hydroxy group towards the Mo-OH, positioning the diol hydrogen at a distance of 1.840 Å ($\text{HO}_{\text{Mo}}\text{-O}_{\text{diol}}$). This positioning leads to the transition state **TS(13-14)**: the hydrogen of the diol approaches the hydroxy group on the metal center positioning halfway, while the second oxygen of the diol starts advancing closer to the molybdenum Mo-O_{diol} 2.224 Å compared to the distance of 1.951 Å of the other already coordinated oxygen. One of the ligands rotates a little to make room for the approaching oxygen, moving towards a pentagonal bipyramidal structure. The rearrangement leads to intermediate **14**, that assumes a capped octahedral geometry with the diol coordinated with both oxygens (Mo-O of 1.935 Å and 1.981 Å). The hydrogen transfer affords a coordinated water molecule with a distance from the metal center Mo-OH₂ of 2.291 Å. In the intermediate **14b** the water molecule moves further away Mo-OH₂ = 2.466 Å and it finally gets removed in intermediate **8** where the compound resumes a more favorable octahedral geometry. From intermediate **8** the catalyst is regenerated passing through the transition state **TS(8-1)**, that is, the extrusion of the ethylene with the same mechanism as described in pathway **A**.

4.3.3 Comparison between the two pathways

To propose a valid mechanism for the molybdenum catalyzed reaction we have compared the energies of both pathways. In Table 17 are reported the energies related to the three main stages of the reaction (diol activation, oxo-transfer and alkene extrusion) and that of the water formation process, both in gas phase and toluene solution. Additionally other energies have been taken in consideration in order to reach a more detailed discrimination between the pathways^{[332],[333]}. The alkene extrusion step is the same in both pathways, thus it has the same energy barrier of 24.75 kcal/mol. The diol activation also has comparable energy barriers, 31.68 kcal/mol for **A** and 31.28 kcal/mol for **B**, even if it takes place in a less hindered environment in pathway **B**. However, the major differences that discern the two pathways are given by the processes of oxo-transfer and water formation, both having a lower energy barrier in **B**. In particular the oxo-transfer process takes place in **TS(6-7)** in **A** with a barrier of 18.1 kcal/mol in toluene and **TS(1-9)** in **B** with a barrier of 15.3 kcal/mol in toluene. The higher barrier for the pathway **A** can be due to the presence of the diolate ligand in **TS(6-7)** while the molybdenum in **TS(1-9)** is coordinatively unsaturated. In the same way, the water formation requires to overcome a barrier of 17.16 kcal/mol in toluene in **A**, **TS(4-5)**, while a barrier of 14.01 kcal/mol in toluene in **B**, **TS(13-14)**. Also in this case the reason may be found in the steric hindrance, the presence of the oxo group in **TS(4-5)** forces the compound to pass through an octa-coordinated transition state, while in **TS(13-14)** the compound is a hepta-coordinated system. Further considering also the other parameters we can see that the relative energy of the highest transition state is 49.36 kcal/mol in toluene for **A**, **TS(6-7)**, while just 26.85 kcal/mol in toluene for **B**, **TS(1-9)**. The highest barrier instead is related to the activation of the diol, a step with comparable energy for both pathways, as stated before. Finally, the differences between the system in gas phase and in toluene phase are not so marked. Most of the intermediates are slightly stabilized in toluene, like **TS(11-12)** that is lowered from 26.85 kcal/mol in gas phase to 24.66 kcal/mol in toluene solution, although some are very slightly destabilized like **TS(1-9)** that moves from 25.48 kcal/mol in gas phase to 25.67 kcal/mol in toluene solution. Taking into account these information we can support the hypothesis that the molybdenum catalyzed DODH mechanism proceeded along pathway **B**, that is, with the oxo transfer process preceding the diol activation.

Table 15. Comparison of computed barriers and selected energies for pathways A and B in the DODH of ethylene glycol with PPh₃ catalyzed by [Mo(O)₂(Q^{Me})₂].

Path A				Path B		
	Transition state	Gas phase	Toluene solution	Transition state	Gas phase	Toluene solution
ΔG (kcal/mol)				ΔG (kcal/mol)		
Diol activation	TS (2-3)	31.29	31.68	TS (11-12)	30.69	31.28
Water formation	TS (4-5)	17.02	17.16	TS (13-14)	13.99	14.01
Oxo-transfer	TS (6-7)	19.6	18.1	TS (1-9)	16.5	15.3
Alkene extrusion	TS (8-1)	24.62	24.75	TS (8-1)	24.62	24.75
Energies				Energies		
Highest TS relative energy	TS (6-7)	49.83	49.36	TS (11-12) gas TS (1-9) tol	25.68	26.85
Highest barrier	TS (2-3)	31.29	31.68	TS (11-12)	30.69	31.28
Maximum relative ΔG between intermediates		48.2	52.8		28.9	30.3

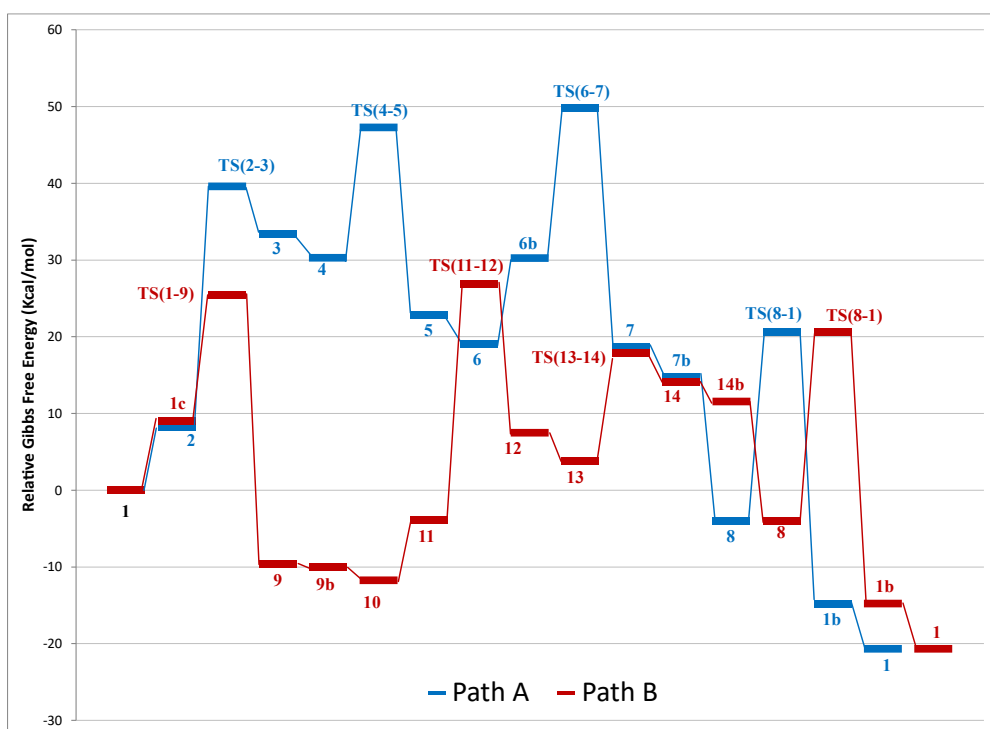


Figure 74. Catalytic profiles of pathways A and B for the DODH ethylenediol with PPh_3 catalyzed by $[Mo(O)_2(Q^{Me})_2]$, in vacuo.

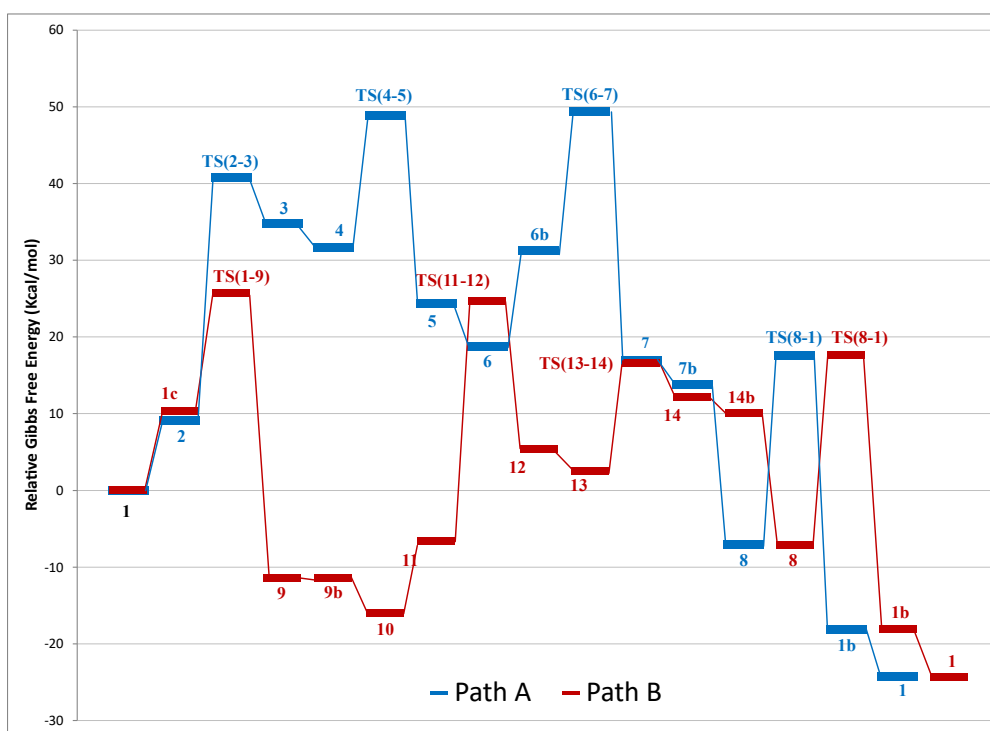


Figure 75. Catalytic profiles of pathways A and B for the DODH ethylenediol with PPh_3 catalyzed by $[Mo(O)_2(Q^{Me})_2]$, in toluene.

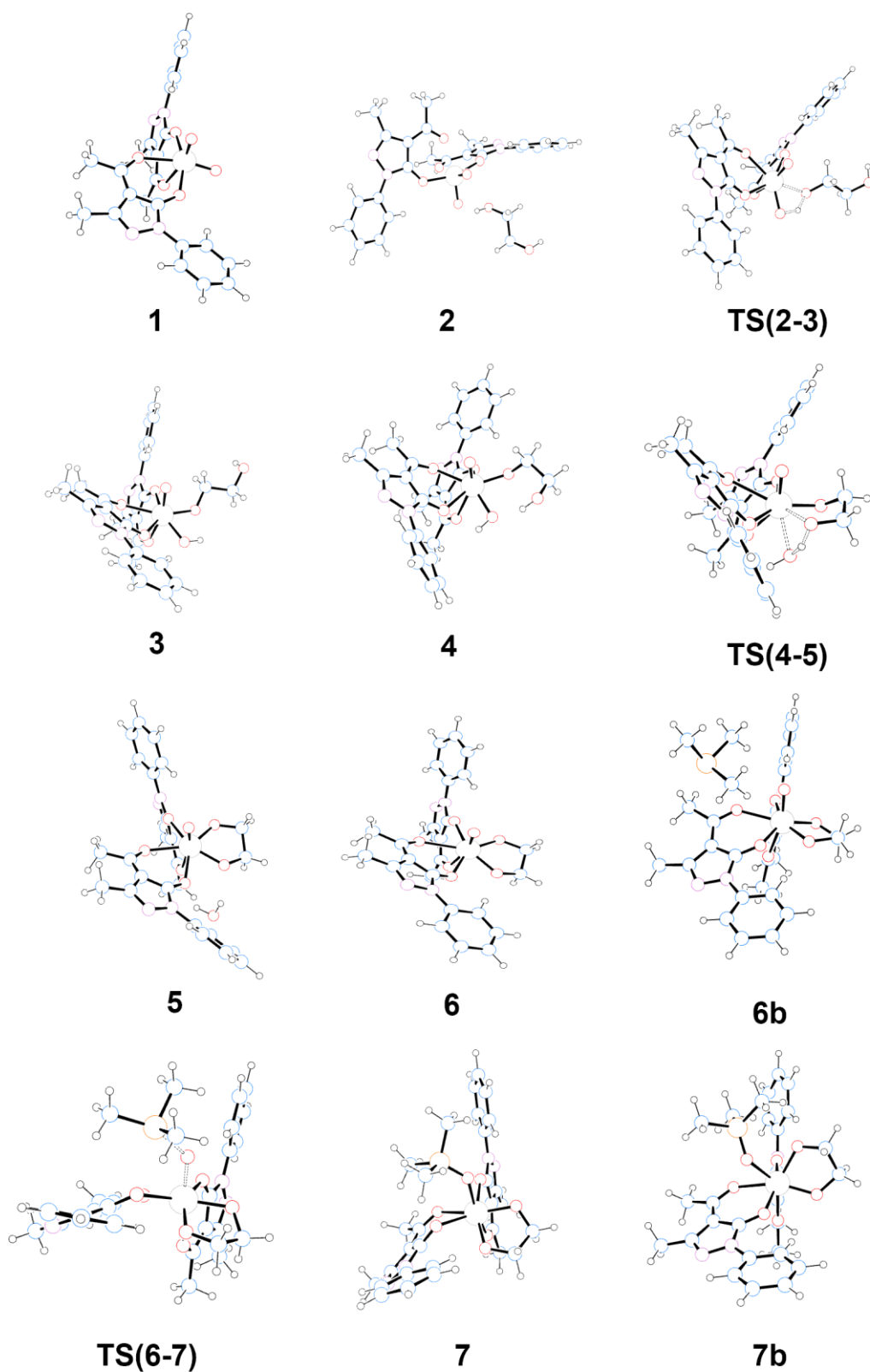


Figure 76. Structures of the optimized intermediates and transition states of pathway A (1-7b).

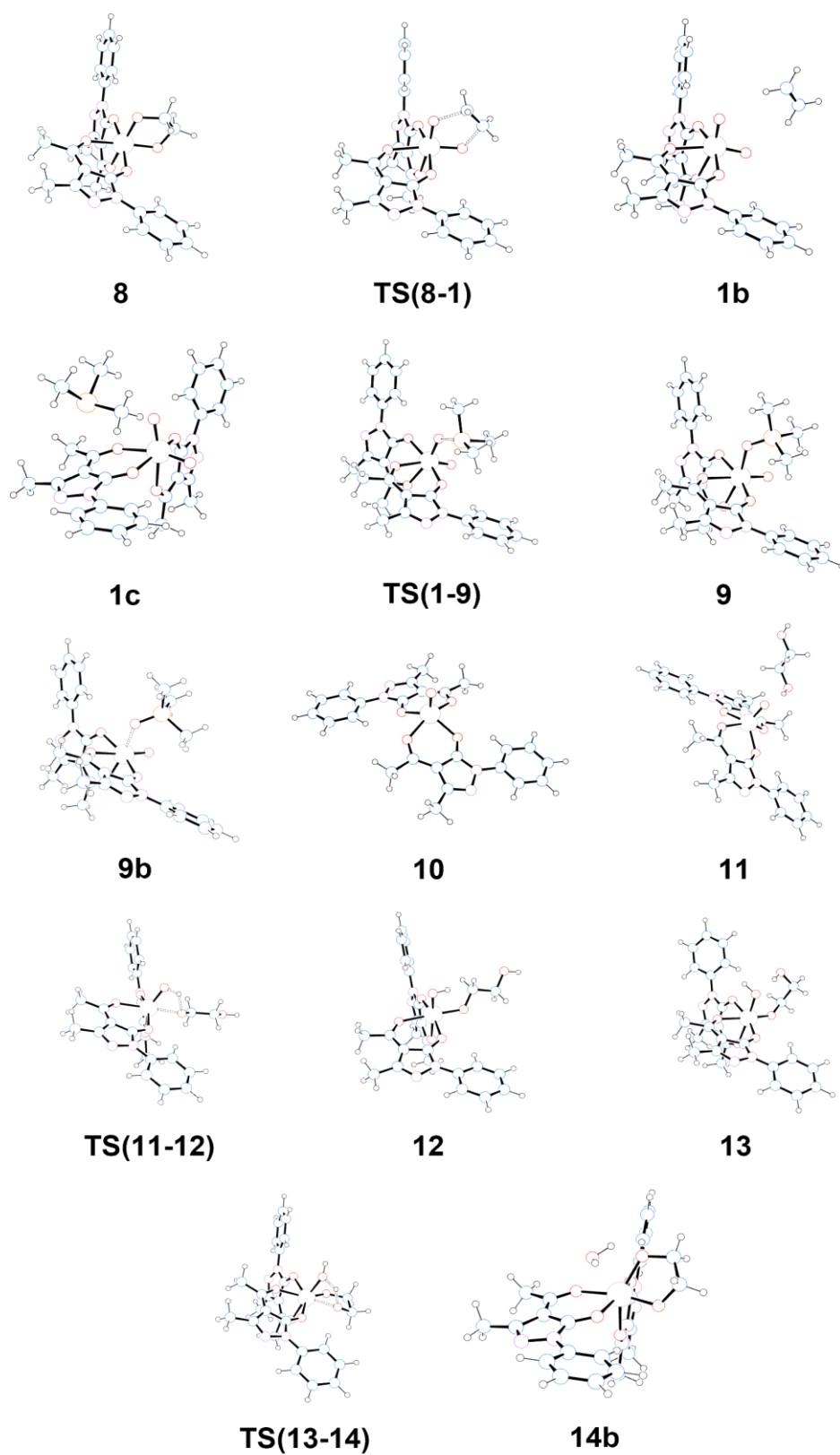


Figure 77. Structures of the optimized intermediates and transition states of pathway B (8-14b).

4.4 Conclusions

In summary, a DFT investigation of the mechanism of the molybdenum-catalyzed deoxydehydration of vicinal diols has been carried out, using PMe_3 as reductant and an acylpyrazolone-based molybdenum complex as catalyst, in gas phase and toluene solution. Two different pathways of the catalytic cycle have been explored: in pathway **A** the diol activation by condensation on the catalyst take place before the oxygen atom transfer to the phosphane, whereas in pathways **B** the opposite situation happens, that is, the reduction of molybdenum(VI) to molybdenum(IV) by the phosphane reductant and only then the condensation of the diol occurs. The two pathways have in common the final step involving the alkene extrusion, that occurs with a energy barrier of 24.75 kcal/mol. Surprisingly, the two pathways share also the same energy barrier of ~ 31 kcal/mol for the diol activation. In fact, even if in pathway **A** the diol condensation takes place in the **TS(2-3)**, where the molybdenum(IV) is sterically more hindered, while in pathway **B** it occurs in the more optimal environment of **TS(11-12)**, the energy required for this step appears to be unrelated to the coordination environment and oxidation state of the metal. The steps that discern the two hypothetical catalytic cycles in favor of pathway **B** are the oxo-transfer process and the water formation. These data, together with the other energy values, in particular the highest transition state relative energy, support the hypothesis that pathway **B** is the preferred mechanism for the Mo-catalyzed DODH reaction. The current investigation has the potential to serve as a foundation for additional experimental studies to verify the obtained results, as well as computational efforts aimed at expanding the array of substrates, reductants, and catalysts utilized as models.

Part 2

CHAPTER 5.

Chemical-physical analyses and studies of non-conformity injection-molded technopolymers.

5.1 The company: TechPol

Techpol srl is a company founded over 40 years ago with its main headquarters located in Morro d'Alba, Marche, Italy. Throughout its growth journey, the company has specialized in the production of thermoplastic materials through injection molding, particularly technopolymers. The company's motto is "metal replacement technology" and indeed its flagship sector is the automotive industry where their designed and printed products replace under-the-hood parts, thanks to the use of specific technopolymers with high chemical-physical characteristics resulting in several advantages such as lower production costs and reduced product weight compared to the corresponding metal product. The know-how gained over the years has allowed the company to stand out in the market, maintaining the highest quality and technological standards and becoming in 1996 an OEM supplier for the Audi-Volkswagen group. Today the company produces about 80 million pieces annually using a total of 2,100 tons of polymer material and generating 15,000 kg of waste annually.

The production process begins with the design, in collaboration with the customer who requests the order, of the mold and the injection parameters to be applied based on the geometry of the piece and the material used. In this phase, simulations are also carried out using specific software of the molding process in order to predict critical steps and optimize production values and times. The next step is the actual molding, in which the designed mold is installed in one of the fifty presses available and the chosen polymer material is conveyed inside the press. One of the company's strengths is the molding of bi-component parts thanks to the use of bi-material machines capable of printing two different materials simultaneously. In addition, the entire molding process, from the insertion of the material to the removal of the piece, is fully automated allowing to always comply with the required quality standards. The process continues with the assembly or processing of the pieces, also in this case completely automated thanks to robots designed over time, in fact the company has an internal robotics and automation department that creates ad hoc assembly and control equipment for each product using state-of-the-art technologies. The instruments, equipped with collaborative robots for the handling of the pieces, allows for dimensional and accessory presence checks through the use of vision systems, control sensors and other error-proof technologies. Finally, the pieces are packaged and shipped to the customer. An additional confirmation of the quality of the products is provided by the quality system that according to the company's vision defines policies, business functions, customer

relations and the continuous improvement of processes, guaranteeing compliance with the highest quality standards and customer satisfaction.

Finally, the company has developed and is characterized by an increasingly greater sensitivity towards the environmental sustainability of its processes and products. The plants and machines are managed with particular attention to energy efficiency, aiming for maximum containment of consumption and reducing the environmental impact of the entire production process to a minimum. The theme of the circular economy is also the subject of attention from the design of new products, considering the life cycle analysis (LCA), from production to disposal, an integral part of the project context, for the selection of materials and technologies. In this way, the company intends to contribute to the reduction of pollution due to the accumulation of waste plastics, determined by incorrect design and management of the disposal phase in the product life cycle, which today has become one of the main issues for the preservation of the sea and the quality of water in general. The culture of recycling, where grinding is allowed, is a fundamental principle established by contract, a responsibility that concerns the entire life cycle of the product, a design culture that is applied to each project. The sustainability supply chain is completed with a constant replacement of the machinery and the progressive transition from hydraulic to hybrid to electric: an upgrade that takes place on a constant basis, an investment in terms of energy savings, optimization of consumption with a significant improvement for the quality and safety of the working environment.



Figure 78. Logo and establishment of the company Techpol.

5.2 The materials: Technopolymers

Technopolymers are a class of advanced engineering polymers that are known for their exceptional mechanical and chemical-physical properties. These properties make them suitable for a wide range of industrial applications, particularly in the automotive, aerospace, and medical industries. Technopolymers are formed through the polymerization process of monomers. The polymerization process can be done through various methods, such as condensation, addition, and ring-opening polymerization. In condensation polymerization, monomers are linked together through the removal of small molecules such as water, alcohol, or ammonia. This process results in the formation of long chains of polymer molecules and the production of by-products such as water or alcohol. Examples of technopolymers produced through condensation polymerization include polyamide (nylon) and polyester. In addition polymerization, monomers are linked together through the addition of chemical groups to the monomers, without the production of by-products. This process results in the formation of long chains of polymer molecules. Examples of technopolymers produced through addition polymerization include polyethylene and polypropylene. Ring-opening polymerization, monomers containing ring-like structures are opened up to form long chains of polymer molecules. This process is usually initiated by a catalyst, and the resulting polymer has a different chemical composition than the monomer. An example of technopolymer produced through ring-opening polymerization is polyoxymethylene (POM). After the polymerization process, the technopolymers are usually shaped into pellets or granules, which are then used in the manufacturing process. The polymerization process can be done in batch or continuous, and it can be done using various types of reactors, such as stirred tank, tubular, or gas-phase reactors. The final properties of the technopolymer depend on the type and composition of the monomers used in the polymerization process and the conditions of the polymerization process, such as temperature, pressure, and catalysts used. Therefore, the chemical and mechanical properties of technopolymers can be tailored to specific industrial applications.

One of the main characteristics of technopolymers is their high resistance to mechanical stress. This is due to their high tensile strength and modulus of elasticity, which are significantly higher than those of traditional polymers such as polyethylene and polypropylene. Technopolymers also have a high resistance to thermal degradation, making them suitable for use in high-temperature applications and a wide range of chemical environments. They are resistant to a wide range of chemicals, including acids, bases, and organic solvents, making them ideal for use in harsh environments. They are also resistant to UV radiation, making them suitable for outdoor

applications. The reason behind their great mechanic and chemical-physical properties is the heavy addition of different types of additives. Additives are substances that are added to technopolymers during the manufacturing process in order to improve certain properties or to impart specific characteristics. Common additives used in technopolymers include:

1. **Fillers:** Fillers are substances that are added to technopolymers to improve their mechanical properties, such as stiffness, strength, and thermal stability. Common fillers used in technopolymers include glass fibers, carbon fibers, talc, and clay. These fillers are typically added in the form of powders and are mixed with the polymer melt before the injection molding process.
2. **Lubricants:** Lubricants are added to technopolymers to reduce friction and improve the flow of the polymer melt during the injection molding process. This improves the surface finish of the finished parts and reduces the wear on the injection molding machine. Common lubricants used in technopolymers include stearates, waxes, and fatty acids.
3. **Stabilizers:** Stabilizers are added to technopolymers to protect them from degradation caused by heat, light, and other environmental factors. These additives help to improve the thermal stability and UV resistance of the technopolymers. Common stabilizers used in technopolymers include antioxidants, UV absorbers, and heat stabilizers.
4. **Colorants:** Colorants are added to technopolymers to provide a specific color or appearance to the finished parts. Colorants can be added in the form of pigments or dyes and can be mixed with the polymer melt before the injection molding process or can be added to the surface of the finished parts through painting or coating.
5. **Flame Retardants:** Flame retardants are added to technopolymers to improve their fire resistance properties. Common flame retardants used in technopolymers include halogenated compounds, phosphorus compounds, nitrogen compounds and some minerals.

The additives are typically added to the polymer melt before the injection molding process, and the amount of additive used can range from less than 5% to more than 35% of the total weight of the polymer. The additives are mixed with the polymer melt using specialized equipment such as a mixing machine, or a blender. The mixing process is carefully controlled to ensure that the additives are evenly distributed throughout the polymer melt. Once the additives are mixed with the polymer melt, it is then fed into the injection molding machine where it is shaped into the desired form. It's important to note that not all additives are compatible with all types of technopolymers, and care must be taken when selecting the appropriate additive for a specific

application. Additionally, the use of certain additives may have an impact on the environmental and health safety, so it's important to consider the potential risks and benefits of using specific additives in technopolymers. The process of injection molding is widely used for the production of technopolymer parts. Injection molding is a manufacturing process in which a thermoplastic material is heated, mixed, and then injected into a mold where it cools and solidifies to take the shape of the mold. This process allows for the production of parts with complex geometries and high precision, making it particularly suitable for the production of technopolymer parts.

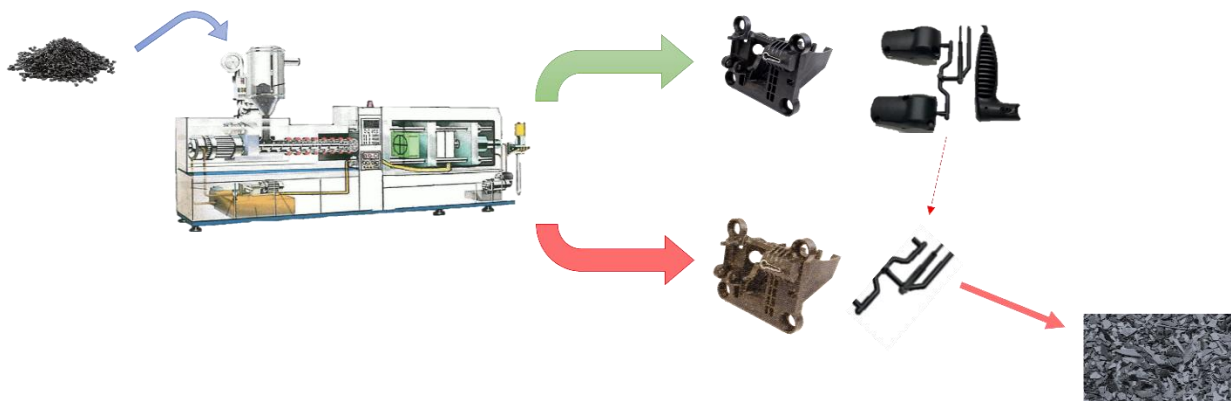


Figure 79. Schematic representation of the molding process; the green arrow indicates the good final product while the red arrow indicates the waste production from non-conformity products and excess materials.

When it comes to disposal, technopolymers can be recycled through mechanical recycling process, where the material is ground, cleaned, and then remolded into new products. However, it should be noted that not all technopolymers are recyclable and it depends on the specific polymer and its composition. Other technopolymers should be disposed of as hazardous waste due to their chemical and physical properties. It's important to note that recycling and disposal of technopolymers can be challenging as they may not be compatible with traditional recycling methods and may require specialized techniques and facilities. In addition to recycling, technopolymers can also be disposed of through energy recovery, where they are burned in controlled conditions to generate heat or electricity. This method is considered to be the most environmentally friendly way to dispose of technopolymers as it reduces the amount of waste sent to landfills and produces energy in the process.

In conclusion, technopolymers are a class of advanced engineering polymers that have exceptional mechanical and chemical-physical properties. They are formed through the polymerization process of monomers and are suitable for a wide range of industrial applications. The process of injection

molding is widely used for the production of technopolymer parts. However, when it comes to disposal, it's important to consider the specific polymer and its composition and various options such as recycling, energy recovery and disposal as hazardous waste. This thesis aims to provide a detailed study on technopolymers, their characteristics, applications, production process, disposal options and the sustainability of their usage.

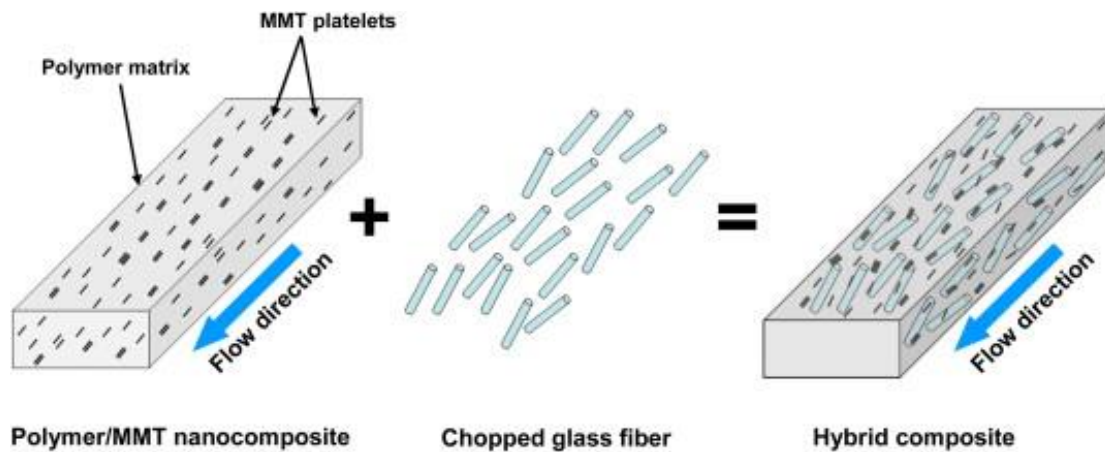


Figure 80. Example of a technopolymer material: in this case the polymer matrix with MMT (montmorillonite) platelets as additive gets furtherly filled with short glass fibers that orientate along the direction of the flow^[334].

5.3 The aim: circular economy

The circular economy is an innovative economic model that aims to redefine traditional economic growth and development by prioritizing the sustainable use of resources. This model is based on the idea that instead of the traditional linear economy, in which resources are extracted, used, and discarded, the circular economy aims to keep resources circulating in the economy for as long as possible. This is achieved through a combination of design, production, and consumption strategies that prioritize the reuse, repair, refurbishment, and recycling of materials and products. The circular economy is a regenerative economic model that promotes the use of closed-loop systems, in which waste products from one process are used as inputs for another. This approach allows for the efficient use of resources and minimizes waste and pollution. For example, in a circular economy, waste heat from industrial processes could be captured and used to heat buildings, and organic waste could be used to generate energy and fertilizer. This not only reduces the reliance on virgin materials but also reduces the amount of waste that goes to landfill. In addition, the circular economy prioritizes the use of renewable energy sources and the application

of digital technologies to optimize resource use and improve efficiency. This can lead to significant environmental and economic benefits, including reduced greenhouse gas emissions, improved resource efficiency, and increased economic competitiveness. The circular economy has the potential to create new business opportunities and jobs, particularly in the areas of design, manufacturing, and recycling. This can lead to the development of new products and services, as well as the creation of new jobs and industries. The circular economy also promotes the concept of circular design, which is the process of designing products and services that can be easily disassembled, repaired, refurbished, and recycled. This approach encourages the use of durable and long-lasting products, which can reduce the need for frequent replacements and repairs. This can lead to cost savings for consumers and businesses, as well as reduced environmental impacts from the extraction and disposal of raw materials. Furthermore, the circular economy also promotes the concept of circular procurement, which is the process of sourcing materials, products, and services that are consistent with the principles of the circular economy. This approach encourages the use of sustainable and environmentally friendly products and services, which can reduce the environmental impact of business operations and improve the reputation of businesses.

In conclusion, the circular economy represents a fundamentally different approach to economic growth and development, one that prioritizes the long-term sustainability of both the economy and the environment. By promoting the efficient use of resources, reducing waste and pollution, and creating new business opportunities and jobs, the circular economy can provide significant economic and environmental benefits. It is an approach that is gaining increasing attention and support, as governments, businesses, and individuals recognize the need for a more sustainable and resilient economic system.



Figure 81. Schematic representation of the idea of circular economy: optimizing the recycling of materials and / or energy the waste production is minimized (image credit to snam.it).

One example of the application of the circular economy in the field of polymer molding is the use of recycled plastics in the production process. This approach reduces the need for virgin materials and minimizes the environmental impacts associated with the extraction and disposal of raw materials. In the traditional linear economy, plastic waste is often treated as a waste product and sent to landfills or incinerated. However, in a circular economy, plastic waste is viewed as a valuable resource that can be used to produce new products. This is achieved through the process of plastic recycling, which involves the collection, sorting, and processing of plastic waste to produce recycled plastic pellets that can be used as raw materials in the production of new products. The use of recycled plastics in the production of new products not only reduces the demand for virgin materials but also reduces the environmental impacts associated with the extraction and disposal of raw materials. Additionally, it also helps to reduce the amount of plastic waste that ends up in landfills or the environment, which can have negative impacts on ecosystems and human health. In the polymer molding industry, the use of recycled plastics can lead to significant cost savings for manufacturers, as well as improved environmental performance. For example, manufacturers can use recycled plastic pellets as raw materials in the production of products such as plastic bottles, containers, and automotive parts. In addition, manufacturers can also use digital technologies such as traceability software and lifecycle assessments to optimize the use of resources and improve the environmental performance of their operations. This can lead to improved efficiency and reduced environmental impacts throughout the entire life cycle of the

product. Overall, the use of recycled plastics in the polymer molding industry is a clear example of how the circular economy can be applied in practice to promote the efficient use of resources, and reduce waste and pollution. It is an approach that has the potential to provide significant economic and environmental benefits, and it is an approach that is gaining increasing attention and support in the industry.

However, although the use of recycled plastics in the polymer molding industry have many benefits, it also comes with some disadvantages. One potential drawback of using recycled plastics in the polymer molding industry is the lower quality of the recycled materials compared to virgin materials. Recycled plastics may contain impurities, such as additives and contaminants, that can affect the properties of the final product. This can lead to reduced performance and quality of the final product, which may not meet the standards required by customers. Another potential drawback is the higher cost of processing and cleaning recycled plastics compared to virgin materials. The recycling process can be more complex and time-consuming, which can increase the cost of production. Additionally, the cost of cleaning and purifying recycled plastics to remove impurities may also be higher than the cost of using virgin materials. This can make the use of recycled plastics less cost-effective for manufacturers. Furthermore, the availability and consistency of recycled materials can also be a challenge, as the quality and quantity of recycled materials can vary depending on the source and collection methods. This can make it difficult for manufacturers to secure a reliable supply of recycled materials, which can affect their production schedule. Hence, it is of grave importance for manufacturers to carefully consider the quality of the recycled materials, the percentage to add, and the effects it can lead to the properties of the final product.

5.4 The project: analyses and problem solving

In order to allow the company to operate in accordance with the principles of the circular economy, a database of the mechanical and chemical-physical properties of the materials used and their recycled counterpart was created in order to compare the characteristics, allowing for optimization of the percentage of reground material that can be incorporated into the polymer mix through targeted research lines, separate from the ordinary production line. The mechanical tests were then carried out by the company on the final printed product. Similarly, analyses were conducted following non-conformities or specific requirements of the company, to determine that the cause was not related to the material itself, but to other factors like the molding process or the geometry of the product. These analyses aimed to ensure a better understanding of the pure and recycled material, its properties and its limitations.

5.4.1 Creation of the polymer database

To create a viable database of the properties of the materials utilized by the company, a pareto diagram has been designed concerning the costs and the materials. It appears that 70 % of the total cost incurred by the company comes from 17 commercial polymers. Thus, a series of analyses were carried out on these 17 materials and the results stored in the database, namely:

- Thermogravimetric Analysis (TGA), to analyze the degradation profile, both in N₂ or O₂ atmosphere (examples in Figures 82 and 83);
- Differential Scanning Calorimetry (DSC), to analyze various parameters of great importance to describe the behavior of the material such as glass transition temperature (T_g), melting temperature (T_m), crystallization temperature (T_c), and the relative enthalpies;
- Onset Oxidation Temperature (OOT), to estimate the temperature required to start the oxidation of the material;
- Infrared Spectroscopy (IR), to know the chemical nature of the material;
- Rheometric analysis, to obtain mechanical information on the material, for example viscosity or the elastic module.

The database obtained has a great value because it allows to compare from time to time the properties of a recycled or novel material to the respective standard. In this way one could guess the behavior of such material before utilizing it.

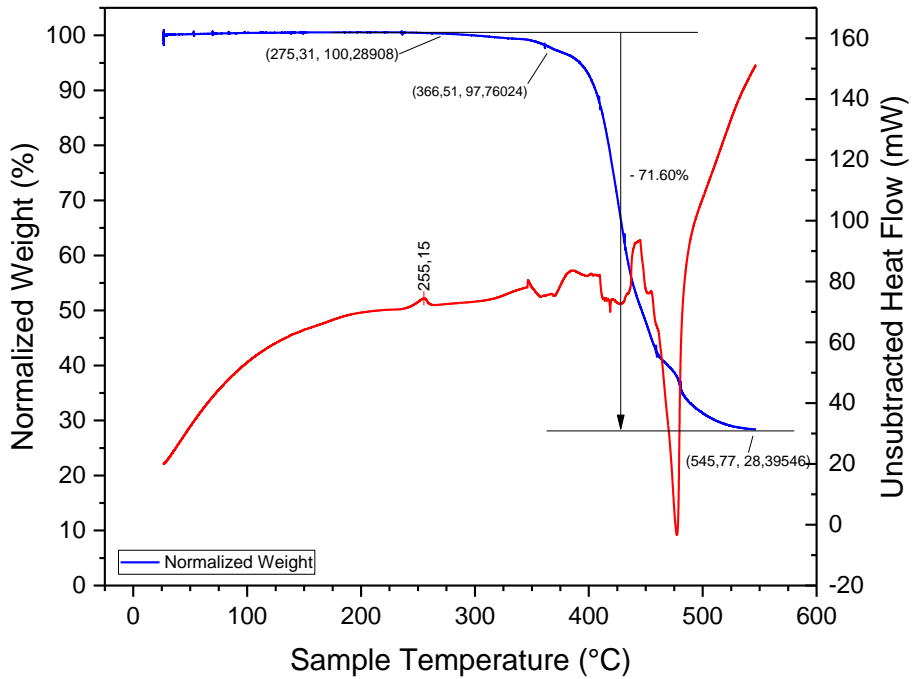


Figure 82. Example of a TGA analysis of Econamid FL66G30 (nylon 6,6).

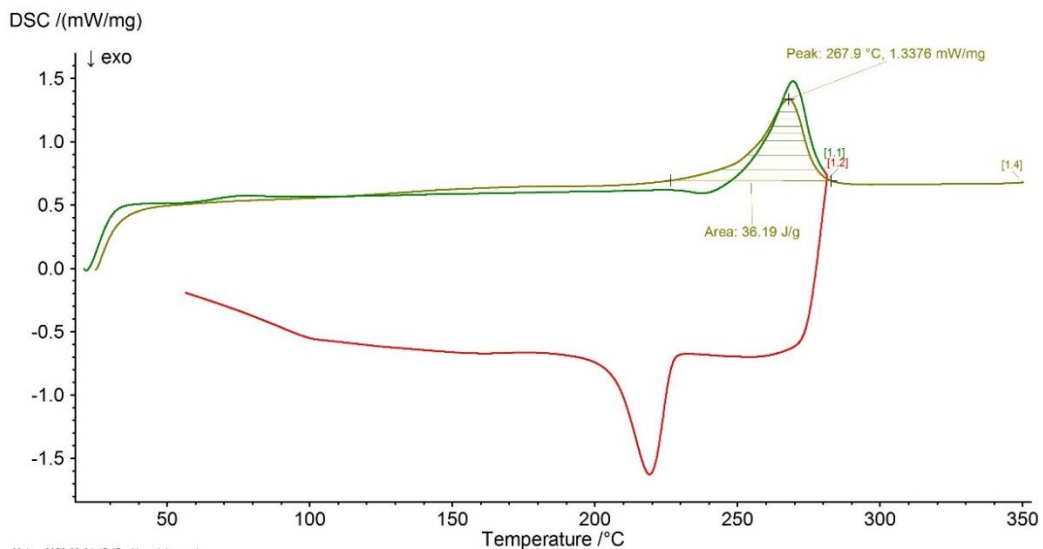


Figure 83. Example of a DSC analysis of Eplamid G30 (nylon 6,6).

5.4.2 Study on the difference between a virgin and regrind material

The study aimed to analyze the difference between two products: the first molded using a virgin polyphthalamide (PPA) filled at 35% with glass fiber (sample V) and the second one molded using the same material with a 70% of it already being molded and regrind (sample V+R).

As expected from the IR analysis no difference are found between the two product, as the regrind process does not modify the chemical nature of the material. From the TGA analysis it is possible to see that the two-degradation profile are very similar, but with slight differences:

- The initial part of the graph ranging from 30°C to 350°C shows slightly more pronounced weight loss for sample. This part of the graph corresponds to the release of volatile species such as moisture and low molecular weight additives such as lubricants. In sample V+R, the regrind material may have already lost some of these components in the first molding process, unlike sample V, which therefore shows greater release here. However, the difference is less than 1%, so it could be insignificant in the process.
- The degradation process of sample V ends at 483°C (but continues to lose weight slowly), while the degradation of sample V+R ends at 496°C and stops completely. The representation of the first derivative (DTG) shows, however, in both cases a single peak (i.e. a single degradation step) with the same shape, it can be excluded that the regrind material portion degrades at different temperatures than the virgin material.

The DSC analysis was carried out in three scans: the first heating scan to nullify the thermal history of the material, the controlled cooling and the second heating scan for analysis, as reported in Figures 84 and 85. Considering the second scan (green lines), the material does not exhibit thermal differences due to degradation as both the T_g and T_m are the same for both samples. However, it should be noted that on the first scan (blue line), sample V+R shows much more pronounced relaxation processes compared to sample V (region 30 - 175 °C). This is because the regrind material portion has more stored stress from two molding processes, while sample V has undergone only one molding process.

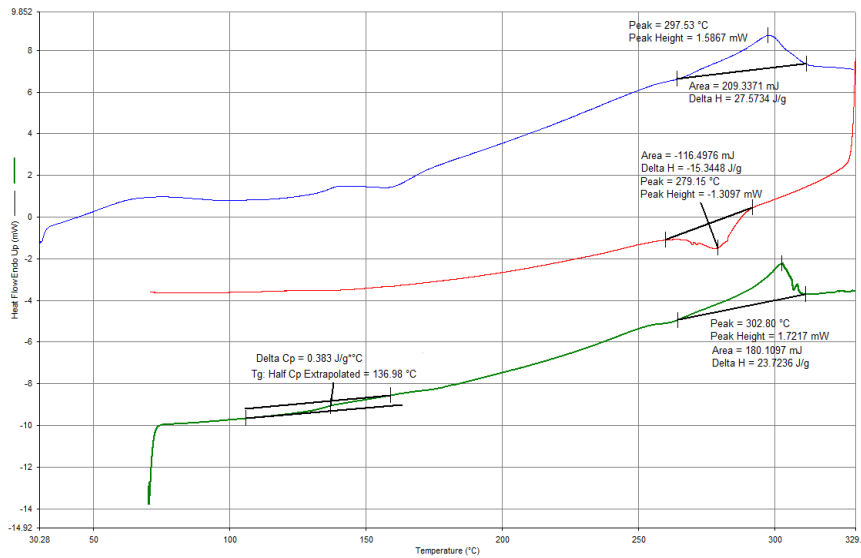


Figure 84. DSC scan of sample V (virgin material).

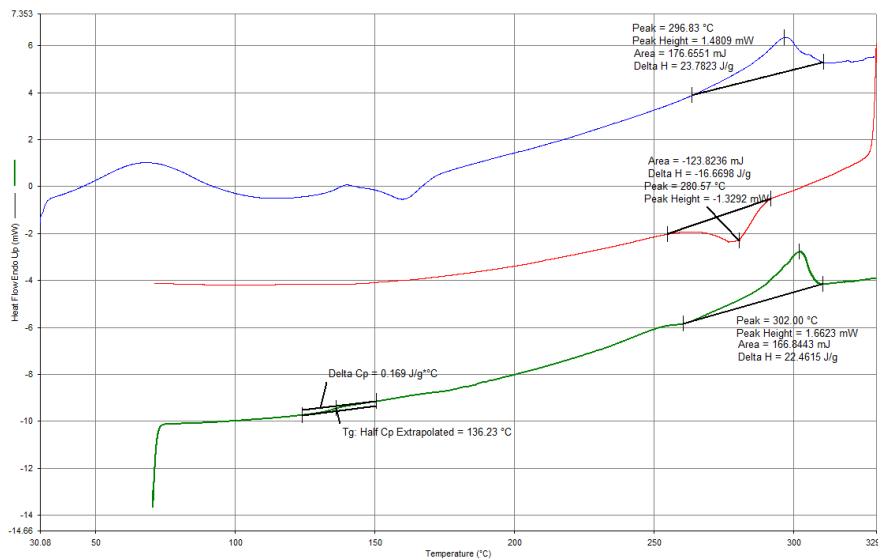


Figure 85. DSC scan of sample V+R (reground material).

In conclusion, from a chemical point of view, the two samples do not show any differences, while some small differences can be found in thermal analyses. Based on the results of the DSC, a mechanical type analysis could be useful. In case of substantial differences or problems in molding, it might be worth trying to treat the reground material before molding, keeping it at temperatures higher than its T_g ($> 136^\circ\text{C}$) to relax the stress accumulated in the previous molding.

5.4.3 Study of a yellowing phenomenon

Some products following the molding process show yellowing, likely due to temperature fluctuations during molding or prolonged exposure to high temperatures, resulting in slight material oxidation. In order to ensure the absence of excessive degradation, infrared spectroscopy, thermogravimetry (TGA) and differential scanning calorimetry (DSC) analyses were carried out on two samples, one good and one yellowed, comparing their results. The samples chosen for analysis are shown in Figure 86.



Figure 86. Photo of a good sample (left) used as standard, and of a yellowed product (right).

From the IR analysis it can be clearly seen that the two spectra are completely identical, all the peaks fall at the same wavelength and there are no additional peaks on the spectrum of the yellowed sample that can be correlated to the formation of any degradation compounds. The thermogravimetric analysis conducted in an inert atmosphere at 10°C/min shows that the degradation profile of the samples is essentially identical, consisting of an initial weight loss due to the release of volatile species (water, plasticizers, lubricants, etc.) followed by the degradation of the polymer matrix that occurs within the range of 350-500°C in a single step. Both samples show a post-degradation residue equal to 31.9% of the initial weight (Figure 87). The DSC analyses were conducted in an inert atmosphere by initially heating the sample above the T_m to nullify its thermal history, cooling it and then performing a second heating scan. The rate is 10°C/min for both heating and cooling. Again in this case, the graphs of the two samples are very similar. Considering the second heating scan, the two samples have the peak of melting very close (261.16 vs 259.75 °C) and the heat of fusion is the same (31.6 J/g). Therefore, there are no differences in thermal behavior.

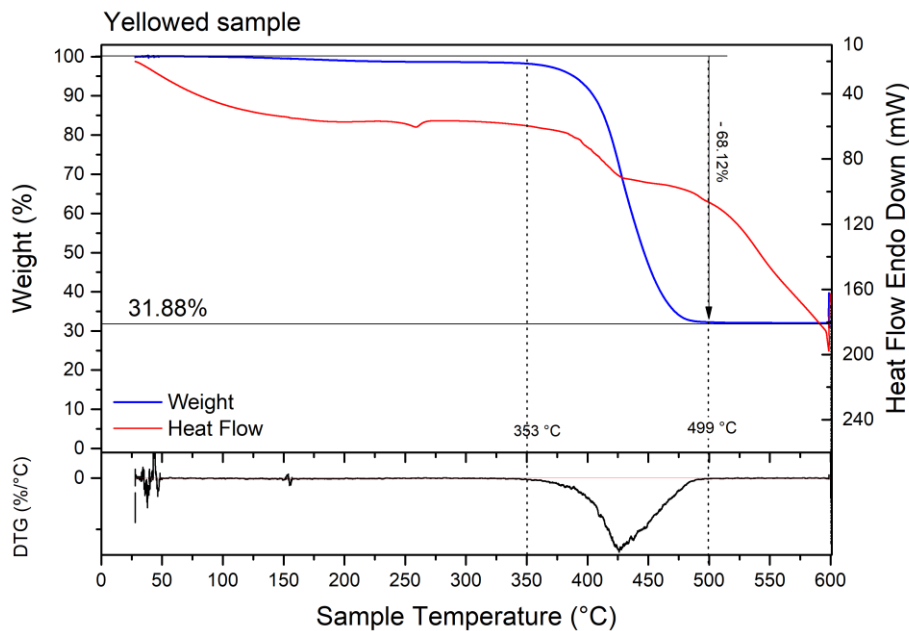


Figure 87. TGA analysis of the yellowed sample.

Analyzing the obtained results, variations in the chemical composition and thermal behavior of the discolored sample can be excluded. Presumably, given the transparent coloration of the piece, a minimal material oxidation results in a significant color change. However, the amount of oxidized species is so low that it does not affect the chemical characteristics of the material.

5.4.4 Study of a product with a burnt surface

The study aims to investigate the thermal-structural properties of a product printed with Polyphenylene sulfide with 40% glass fiber, which presents slight burns in localized areas, through a comparison with the results obtained from a reference sample of the same piece. The IR analysis was carried out directly on the surface of the piece. The graph shows a complete overlap of the spectra of the sample and the reference. The chemical structure of the two samples is therefore the same, the sample is not degraded. To perform the thermal analysis with DSC, the two samples were mechanically ground to obtain a fine powder to maximize the contact surface and therefore the thermal conductivity. About 9 mg of sample were used, in N₂ flow (20 ml/min) and performing three scans (heating, cooling, heating) from 30°C to 330°C with a T rate of 10°C/min. For each sample, the glass transition temperatures, the heat of fusion, and the degree of crystallinity were calculated. In particular, the degree of crystallinity was calculated by applying the equation:

$$x_c(\%) = \frac{\Delta H_m}{\Delta H_m^0(1-x)} \times 100$$

Where:

- ΔH_m is the heat of fusion calculated by integrating the area of the fusion peak;
- x is the weight percentage of glass fiber (0.4);
- ΔH_m^0 is the theoretical heat of fusion of 100% crystalline material, equal to 80 J/g.

The degree of crystallinity is important because it has a great influence on the chemical and mechanical properties of thermoplastics, the crystalline phase increases the stiffness and tensile strength of the piece, while the amorphous phase increases the ability to absorb impacts. Changes in crystallinity can result in significant alterations in the mechanical properties of the material. Considering the second heating run, i.e. once the thermal history of the sample has been nullified, the two samples have the same T_g and the same degree of crystallinity. Therefore, the burned material has not undergone structural degradation. The IR analysis and especially the thermal analysis with DSC do not reveal any difference between the two samples, as they show exactly the same IR spectrum, same T_g and same degree of crystallinity. From the results obtained, it is understood that the burned part does not have any appreciable degradation.

5.4.5 Study of the heat exchange difference

The aim of the investigation is that to confirm that a product printed with a commercial polymer “Xydar” has an higher thermal conductivity than the same products printed using the commercial polymer “Durethan”. For each of the two materials, a piece of identical dimensions has been printed. Given the size of the piece, only a portion of the body was considered for the analysis. This portion was cut from the main body and drilled on the upper face to allow the insertion of the sensor. The hole was made in the same position for both samples and with a depth of 12 mm, equal to half the total thickness of the piece. The experimental setup involves the sample placed on the preheated plate at 100°C. The sensor for temperature detection is inserted into the upper hole. To improve contact with the sample, thermal paste was applied both on the bottom surface and inside the hole. To further increase adhesion above the sample, a weight of 1 kg was placed. As soon as the sample comes into contact with the plate, a 15-minute timer is started and the temperature is recorded every 30 seconds. Plotting the recorded temperature against the elapsed time, it can be

seen that the Xydar sample heats up more quickly and reaches an equilibrium temperature of 60°C against the 46°C of Durethan (Figure 88).

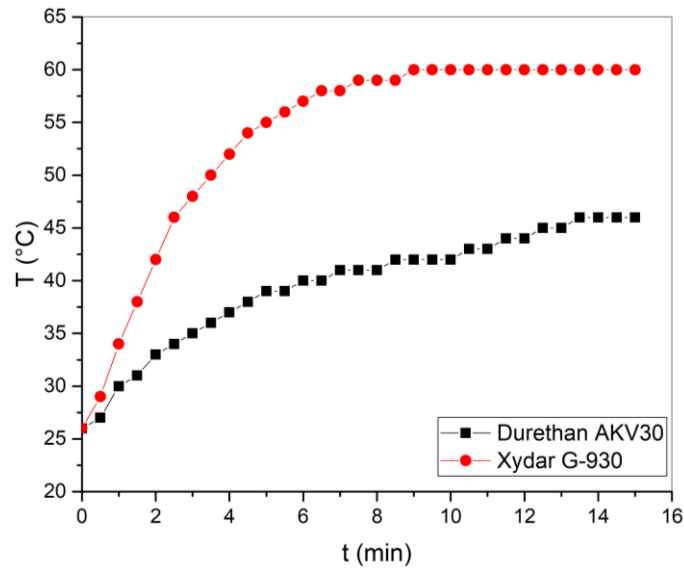


Figure 88. Recorded temperature vs time for the two samples.

The equation that describes the heat flow through a material is:

$$\frac{Q}{t} = \lambda S \frac{\Delta T}{d}$$

With:

- Q = quantity of heat (J);
- t = time (s);
- λ = coefficient of thermal conductivity (W / m*K);
- ΔT = temperature difference between the two faces (K);
- d = distance between the two faces (m) (that is between the contact surface and the hole).

With the type of analysis adopted, it is not possible to quantify the amount of heat exchanged (Q), but it is possible to calculate the ratio between the conductivity of Durethan (λ_D) and that of Xydar (λ_X). Considering the equilibrium situation, it can be assumed that the amount of heat exchanged is the same for both materials ($Q_D = Q_X$), therefore:

$$\lambda_D \frac{S_D \Delta T_D}{d_D} t = \lambda_X \frac{S_X \Delta T_X}{d_X} t$$

Considering that the time is the same for both the samples and approximating the surface and the distance between the two faces identical for both the samples, the equation simplifies in:

$$\lambda_D \Delta T_D = \lambda_X \Delta T_X$$

Thus:

$$\frac{\lambda_X}{\lambda_D} = \frac{\Delta T_D}{\Delta T_X}$$

From the previous graph it is possible to calculate the ΔT :

- $\Delta T_D = 100 - 46 = 54 \text{ }^\circ\text{C}$
- $\Delta T_X = 100 - 60 = 40 \text{ }^\circ\text{C}$

$$\frac{\lambda_X}{\lambda_D} = \frac{54}{40} = 1.35$$

$$\lambda_X = \lambda_D \times 1.35$$

From the test performed, it is found that the sample of Xydar material is actually a better thermal conductor, with the relative value of the thermal conductivity coefficient (λ) equal to 1.35 times the coefficient of Durethan.

5.4.6 Study of an unknown material

The aim of the study is that to identify the chemical natural of two unknow materials. The thermogravimetric analysis of both samples shows that there is an initial loss of volatile substances (likely plasticizers) starting at 280°C , while the actual degradation begins at around 350°C . Burning the sample in an inert atmosphere results in a loss of 58% of the initial weight, which makes up the polymer matrix. Moving to an oxidative atmosphere results in an additional 11% weight loss, which is composed of the organic residue (degradation products and organic additives), leaving a final residue of 30% in weight, composed of glass fibers. In the thermogram of the second material, it can be seen that the degradation curve is composed of two phases, this suggests the presence of two different components. In the first sample, this phenomenon is not noticed, but being slightly marked it could be a consequence of differences in variables in the two

analyses (amount of sample, heating rate, etc.). The DSC analysis shows a flat profile with the glass transition at 140°C for both samples, indicating a completely amorphous structure.

The IR analysis of the two samples initially gave a 70% match with PPO/PS for one sample and a match with a silicone polymer for the other. However, upon repeating the test a second time, it was noted that the signal varied slightly depending on how the piece was positioned. Therefore, several tests were carried out for both samples, observing that for both samples at least one spectrum highlighted the characteristic Si-O signals. However, on average, the spectra always show the same peaks and especially, comparing the two materials, the recorded signal is the same for both materials. Although the match is only 70%, the most likely hypothesis is that of PPO/PS, in fact, even interpreting the spectrum, the peak frequencies are in agreement with those expected by the PPO and PS molecules superimposed. The IR analysis of the inorganic residues instead showed the presence of glass fibers. Elemental analysis allows determining the weight percentage of hydrogen, carbon, nitrogen and sulfur through the combustion of the sample. The analysis was carried out on both samples showing that the percentage of carbon and hydrogen are the same in both and equal respectively to 60% and 5%. The rest is due to oxygen and inorganic fillers. The data obtained therefore confirm that both materials were printed with the same polymer.

By using the electron microscope, it was possible to both observe the surface morphology of the sample (Figure 89) and investigate the chemical nature of the matrix and fillers (EDX analysis, Figure 90). Both samples were subjected to analysis and in addition, a granule of a glass fiber-reinforced polyamide 6,6 was used as a reference to compare the morphologies. In this case as well, no differences were found between the two materials. From the photographs obtained, it is clearly visible that the glass fibers are well embedded in the polymer matrix, but in the points where the sample was cut or scratched, the broken fibers emerge overlapping the surface of the resin. This would explain why in some points the IR signals related to the Si-O bond were more intense.



Figure 89. Pictures obtain from the SEM analysis showing the glass fibers at different magnitudes.

The EDX analysis was performed on different points of the surface of the samples. The results show that the atomic composition percentage is the same in the two samples and is composed of carbon (~86%) and oxygen (14%), in line with what one might expect following the PPO/PS hypothesis, as the PPO monomer contains an oxygen atom. Analyzing a more homogeneous point, the presence of other elements such as sodium, magnesium, aluminum, silicon, and calcium was found. The presence of these metals is due to various filler minerals, in addition to the treatment of glass fibers. In fact, E-glass fibers, the most common, include the addition of an alkali metal (such as sodium) and minerals such as CaO and MgO. In addition, inorganic fillers used to improve the properties of polymer materials include various minerals such as CaSiO_3 , CaCO_3 , Al_2O_3 , $\text{Al}_2\text{Si}_2\text{O}_5(\text{OH})_4$, MgOH, and various types of mica. In fact, focusing the signal on a filler particle, the values of C, O and Ca increase, suggesting the presence of calcium carbonate among other fillers.

The analysis of the elements on the surface reveals important information about their distribution. As expected, carbon (blue) is present in a homogeneous manner throughout the sample except on the fibers. Oxygen (light blue) is more intense on the glass fibers, as the Si/O ratio is 1/1 in the fibers, but it is also present throughout the rest of the sample, both in fillers and in the polymer structure. Finally, silicon (purple) is only present on the fibers.

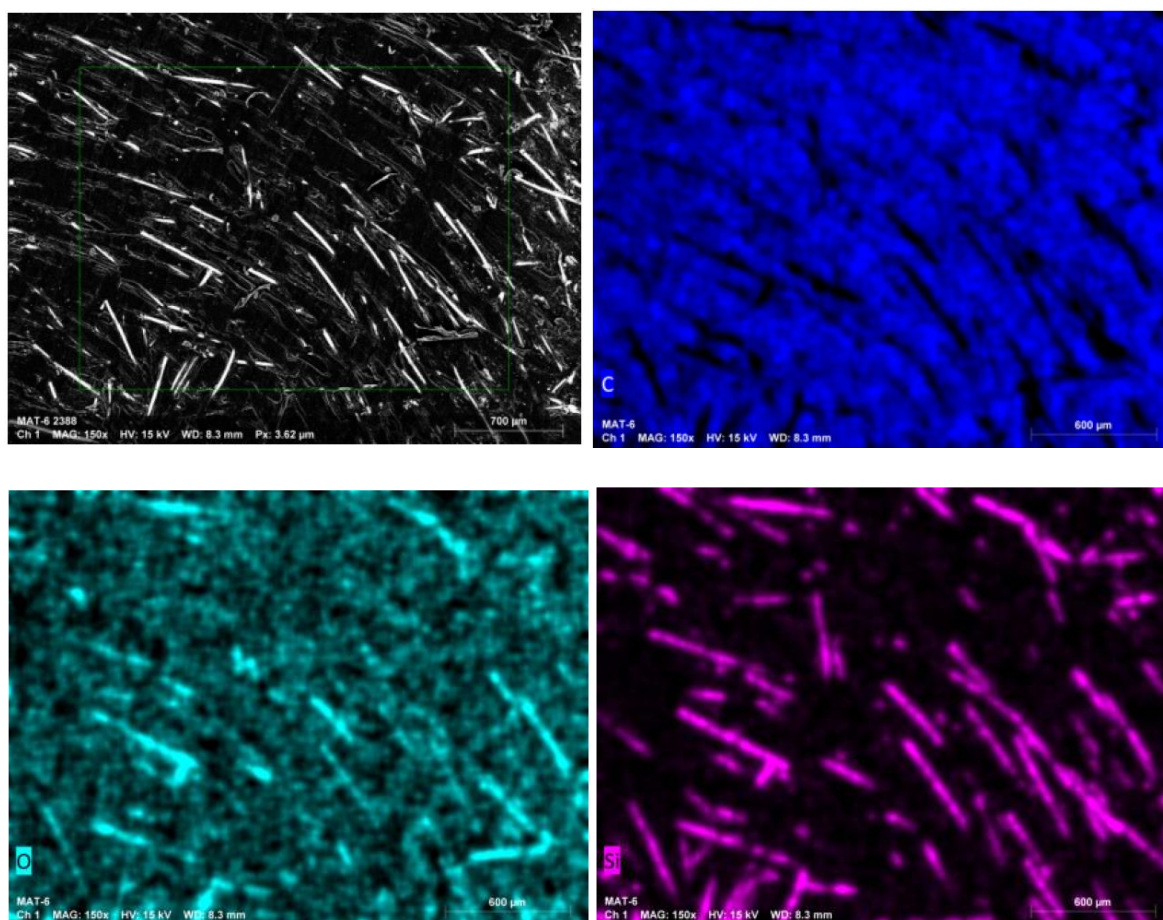


Figure 90. EDX analysis of the sample showing the distribution of carbon (blue), oxygen (light blue), and silicon (purple).

Assuming that the two materials were made of the same polymer and based on the PPO/PS hypothesis, an attempt was made to solubilize the sample in chloroform, which is a solvent capable of solubilizing both PPO and PS. The sample was cut into small pieces to facilitate dissolution and, in fact, the sample completely dissolved. The solution thus prepared was filtered and used for proton NMR analysis. The resulting spectrum was interpreted based on the spectra of the two pure polymers found in literature and on the simulated spectra of the respective monomers (styrene for PS and 2,6-dimethylphenol for PPO). In this way, it was possible to attribute all signals to the two

molecular structures, thereby confidently confirming the chemical nature of the polymer: a blend of PPO and PS where PPO is the major component. As reported in literature, in fact, PPO is hardly used alone due to its high glass transition temperature (210 °C), high viscosity and low oxidative stability. For this reason, it is often sold in the form of a blend with another polymer in order to make it more workable, almost always with PS because it is completely compatible^{[335]–[338]}. The most well-known blend commercially is the NORYL family from Sabic, which also includes the resin loaded with 30% glass fibers.

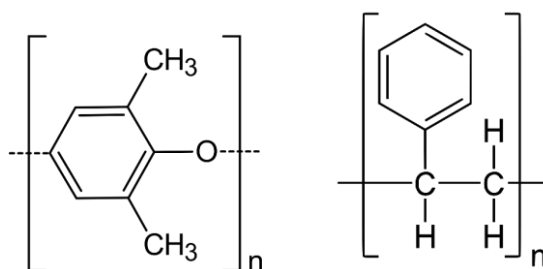


Figure 91. Molecular structure of polyphenyleneoxide (PPO) (left) and polystyrene (PS) (right).

The set of analyses carried out, especially the NMR and SEM analyses, have proved that the two samples are composed of the same type of polymer, a blend of PPO/PS reinforced with 30% glass fiber, where PPO is the main component.

5.5 Conclusions

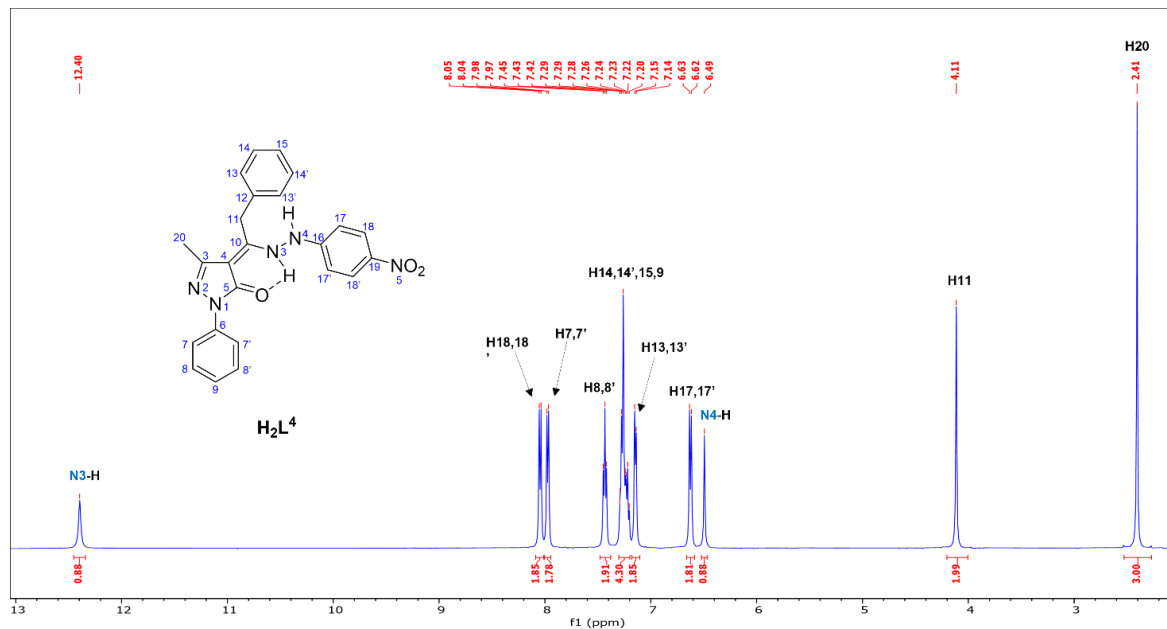
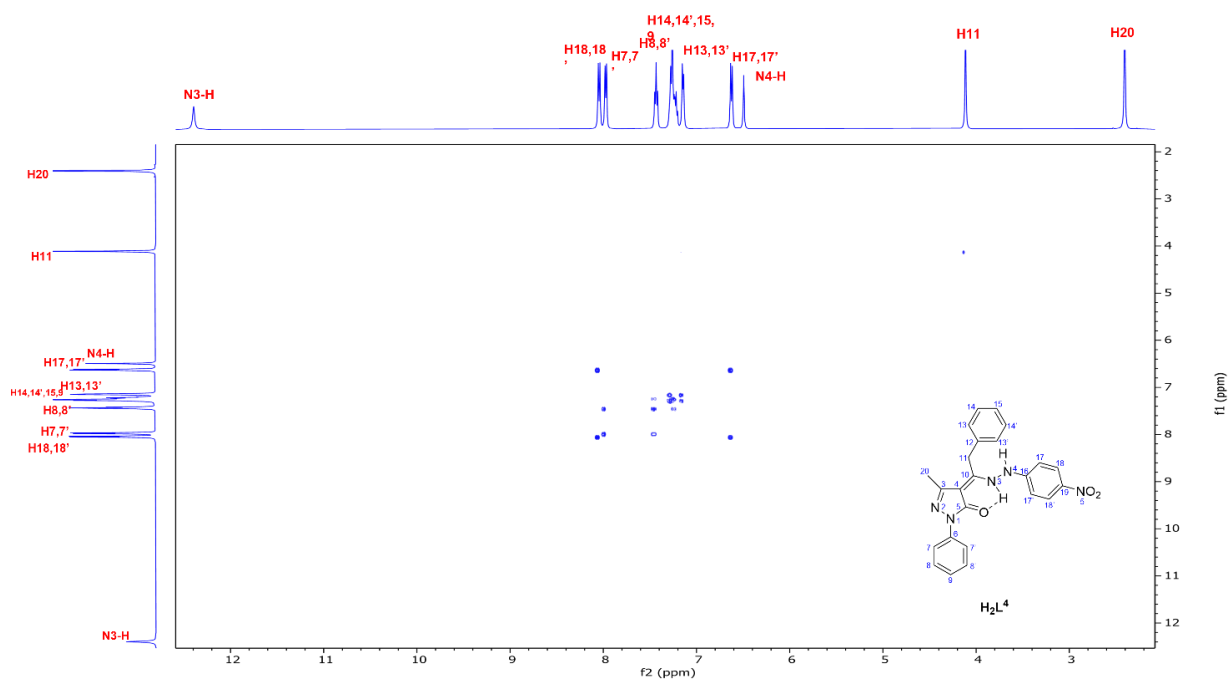
The analyses conducted on the materials allowed to resolve occasional problems encountered during the molding process, verifying the conformity of the final piece and suggesting the nature of the problem.

- It has been proved that using a certain percentage of regrind material, the performances of the product are not altered, even though additional mechanical analysis would be useful.
- In case of yellowing phenomena, variation in the chemical composition and thermal behavior of the discolored sample have been excluded, the amount of oxidized species is too low to affect the chemical characteristics of the material.
- The analysis conducted on a burn surface demonstrated that the burned material has not undergone structural degradation, thermal analysis do not reveal any difference between the samples: the burnt part does not present any appreciable degradation such as to invalidate the structural properties.
- Probing the heat exchange of two different materials it has been proved that one polymer is actually a better thermal conductor than the second, by a value of 1.35.
- The set of analyses led on a unknown material permitted to expose the chemical nature of the polymer, being a PPO/PS blend with 30% glass fibers.

Additionally, the creation of the database including information about the properties of the polymers employed by the company allowed to compare new materials with the one in stock or even the recycled materials with virgin ones. In this way it is possible to reduce potential problems arising during the molding process, making sure the polymer used meet the defined standards.

Supplementary information

Appendix Chapter 2

Figure 92. ^1H NMR of proligand H_2L^4 in CDCl_3 at 298 K.Figure 93. $[\text{H}, \text{H}]$ -COSY of proligand H_2L^4 in CDCl_3 at 298 K.

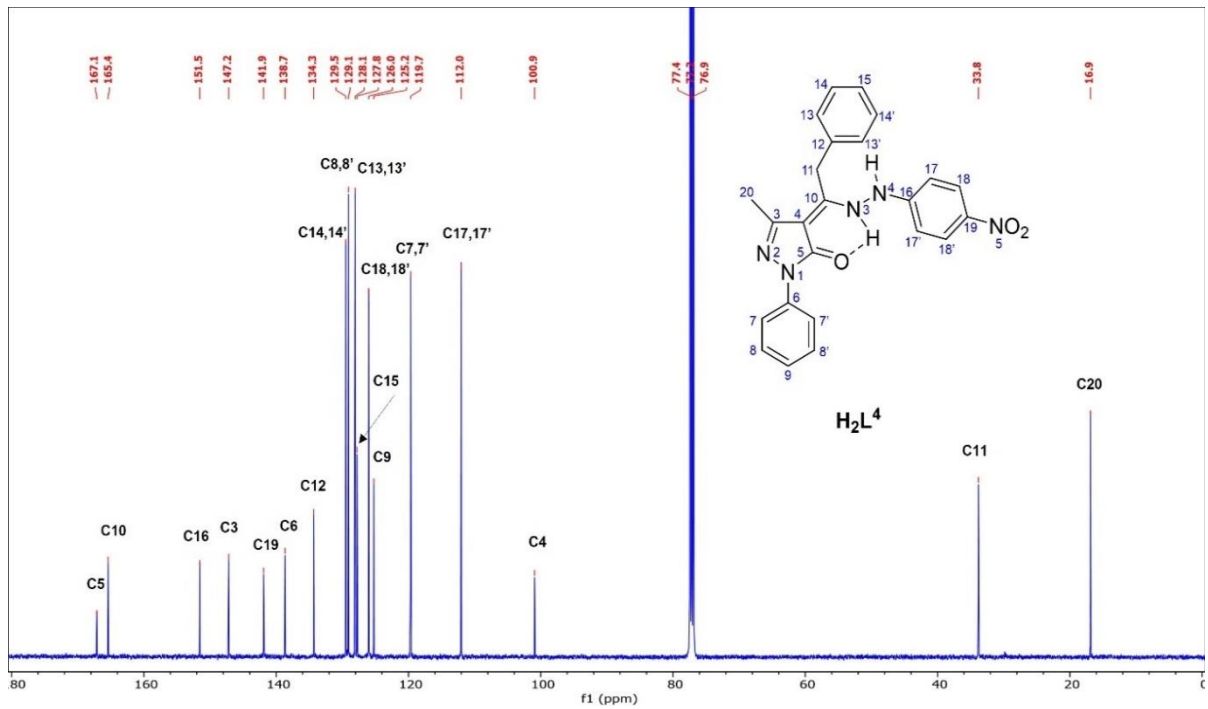


Figure 94. $^{13}\text{C}\{^1\text{H}\}$ NMR of proligand H_2L^4 in CDCl_3 at 298 K.

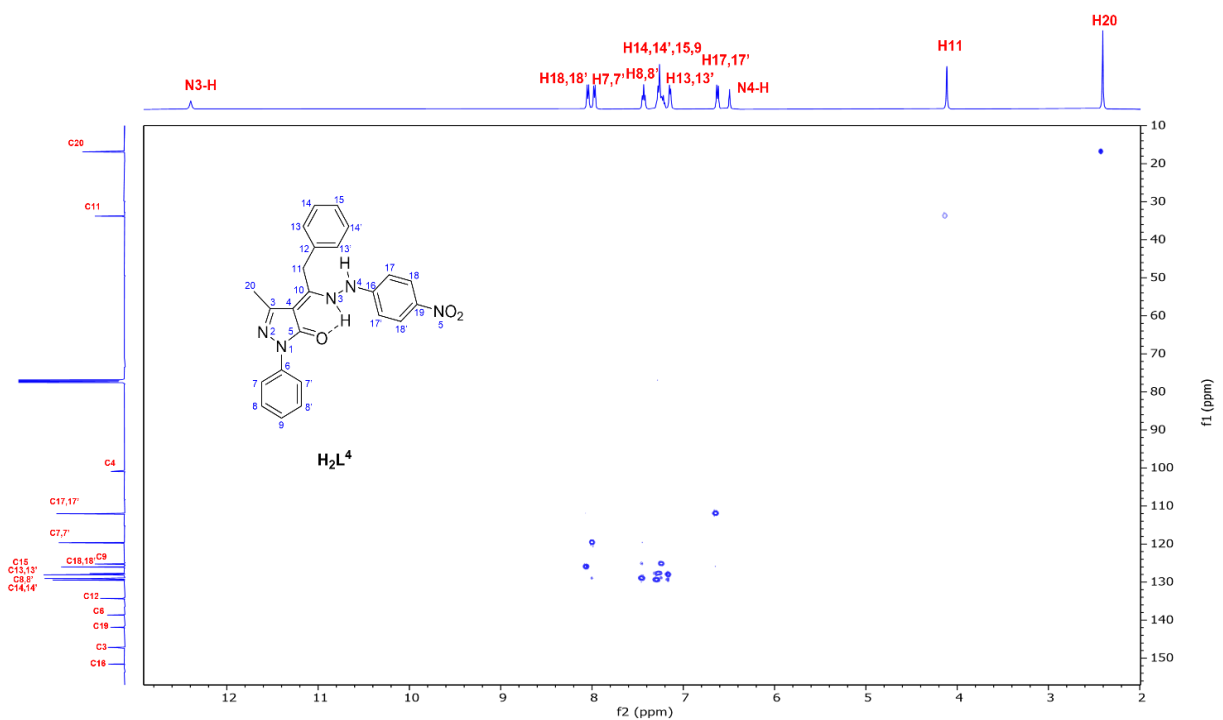


Figure 95. $\{^1\text{H},^{13}\text{C}\}$ -HSQC of proligand H_2L^4 in CDCl_3 at 298 K.

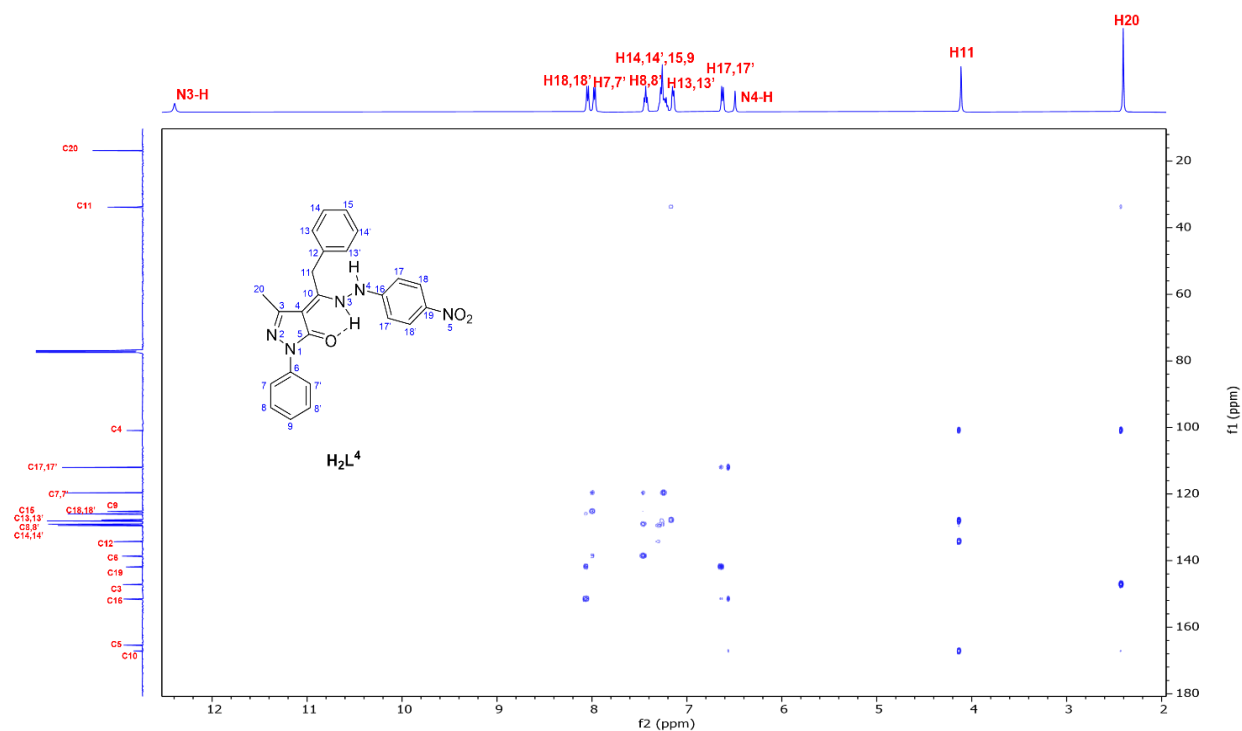


Figure 96. $\{^1\text{H},^{13}\text{C}\}$ -HMBC of proligand H_2L^4 in CDCl_3 at 298 K.

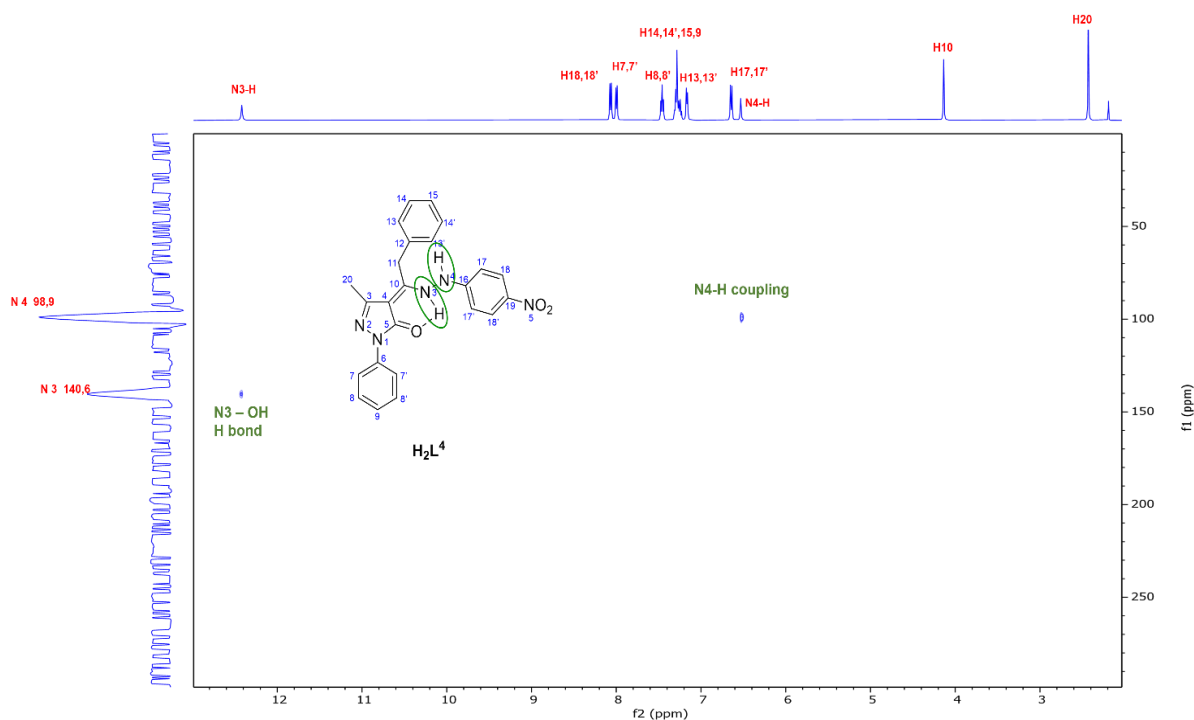


Figure 97. $\{^1\text{H},^{15}\text{N}\}$ -HSQC of proligand H_2L^4 in CDCl_3 at 298 K.

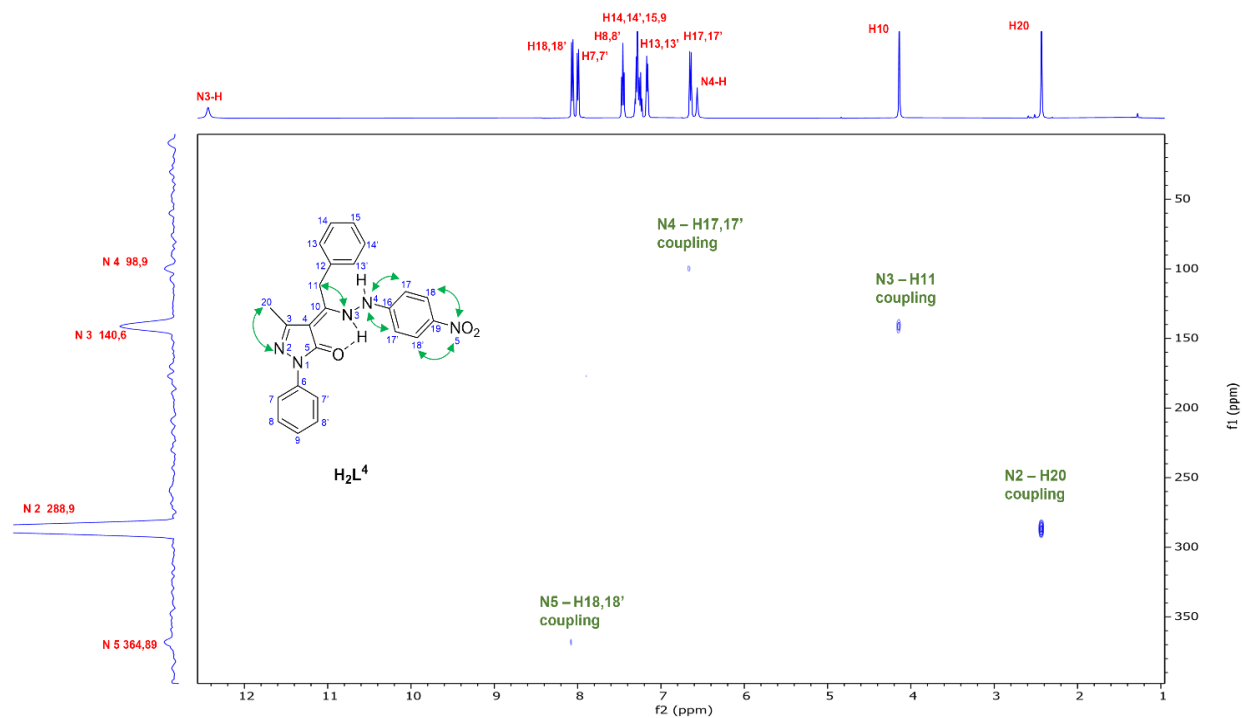


Figure 98. $\{^1\text{H},^{15}\text{N}\}$ -HMBC of proligand H_2L^4 in CDCl_3 at 298 K.

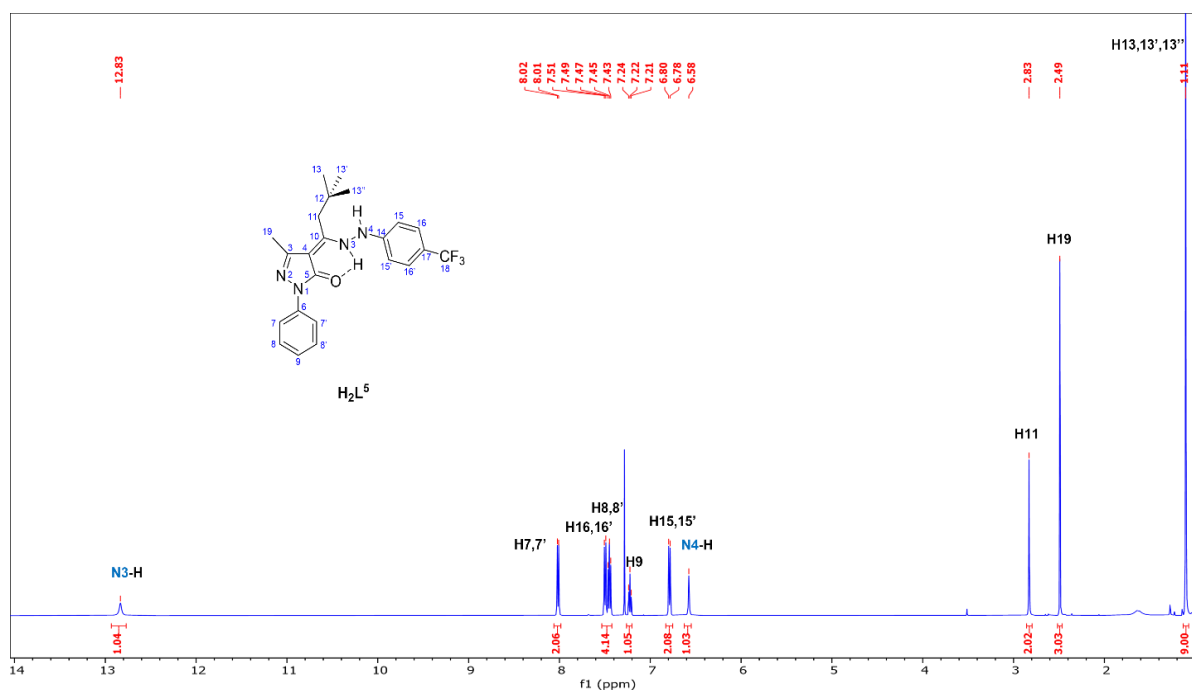


Figure 99. ^1H NMR of proligand H_2L^5 in CDCl_3 at 298 K.

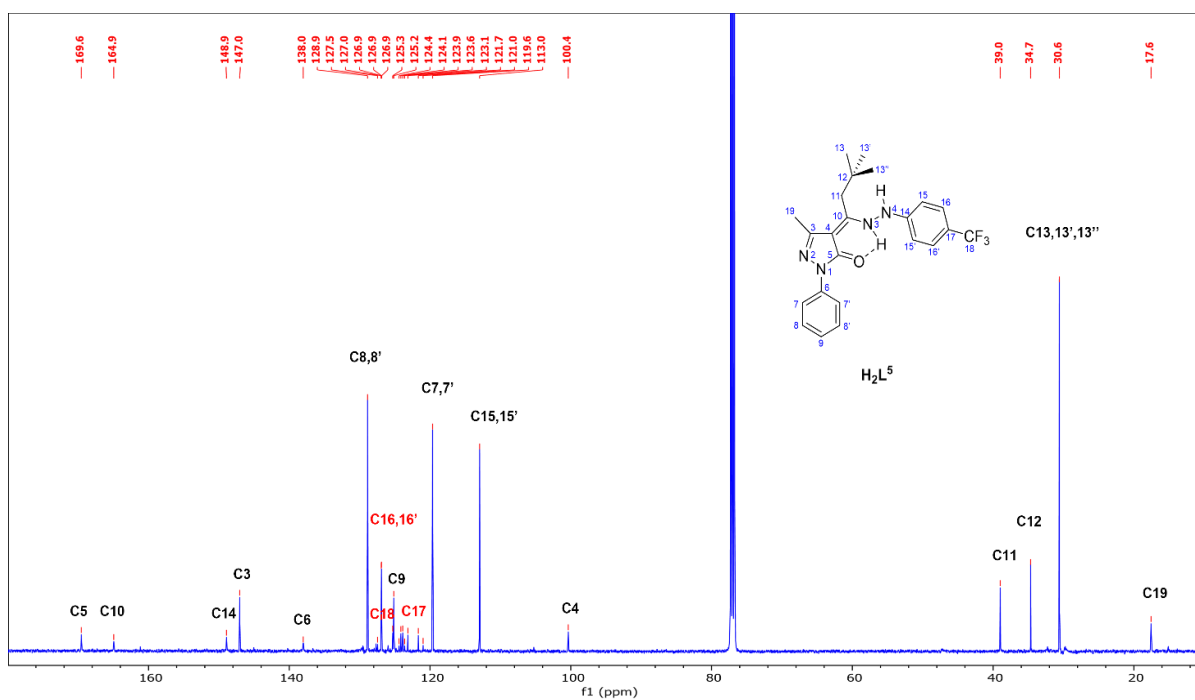


Figure 100. $^{13}\text{C}\{^1\text{H}\}$ NMR of proligand H_2L^5 in CDCl_3 at 298 K.

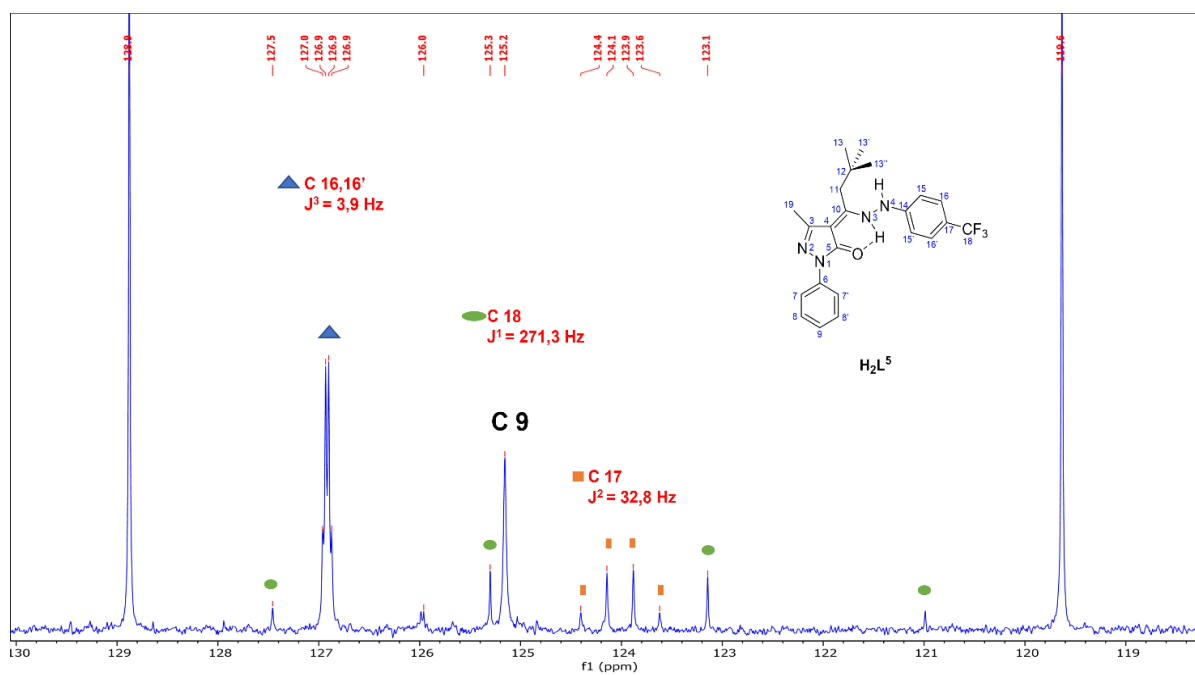


Figure 101. Magnification of the $^{13}\text{C}\{^1\text{H}\}$ NMR of proligand H_2L^5 in CDCl_3 at 298 K.

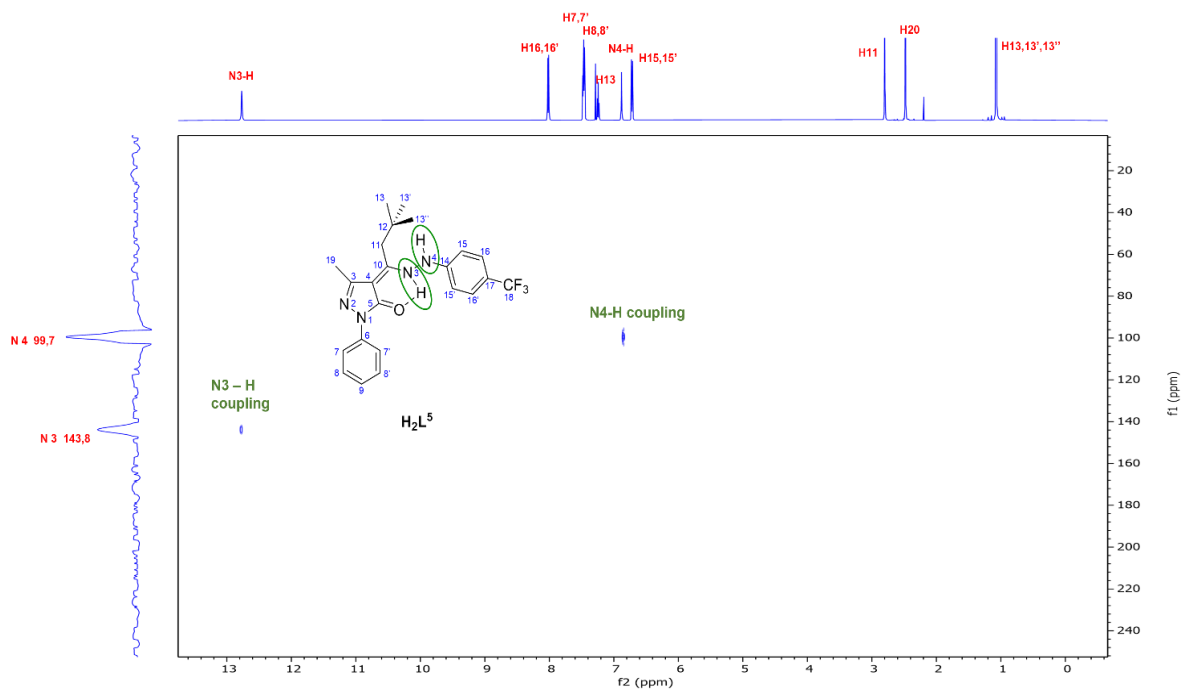


Figure 102. $\{^1\text{H},^{15}\text{N}\}$ -HSQC of proligand H_2L^5 in CDCl_3 at 298 K.

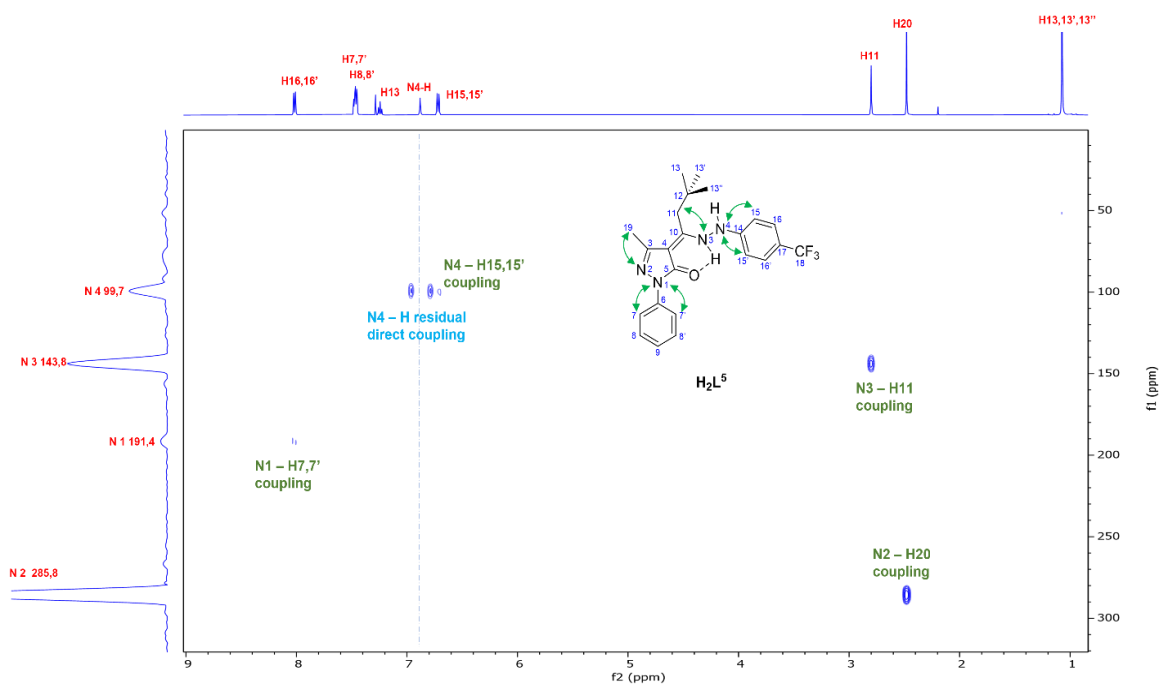


Figure 103. $\{^1\text{H},^{15}\text{N}\}$ -HMBC of proligand H_2L^5 in CDCl_3 at 298 K.

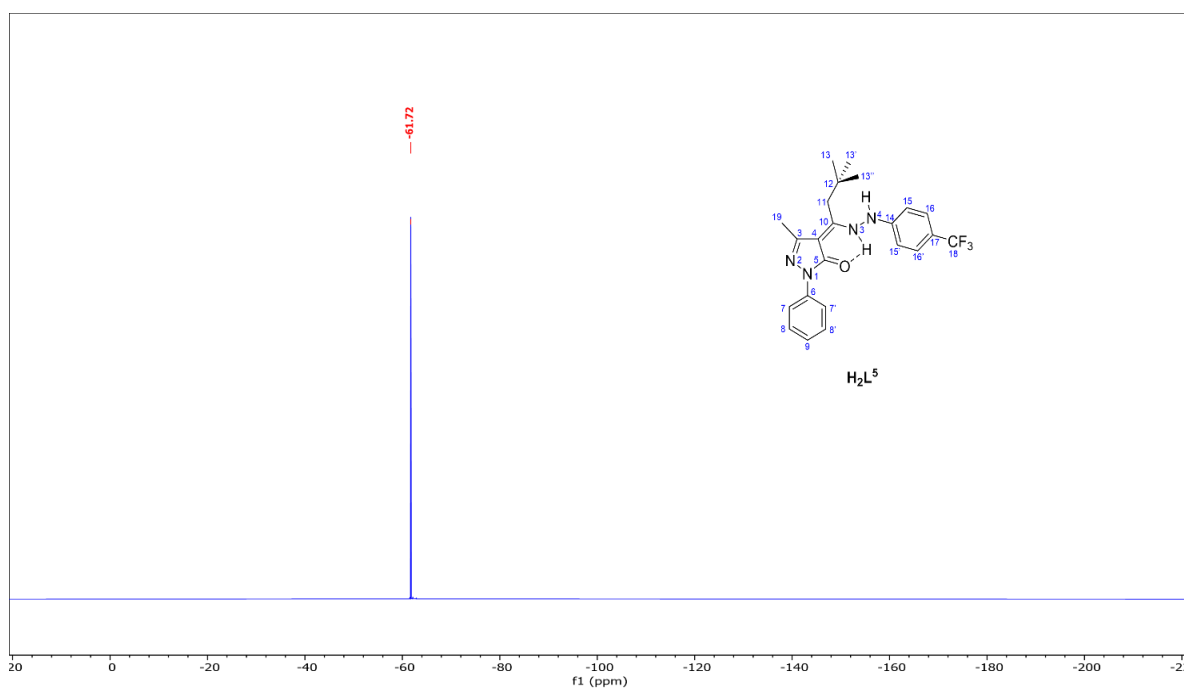


Figure 104. $^{19}\text{F}\{^1\text{H}\}$ NMR of proligand H_2L^5 in CDCl_3 at 298 K.

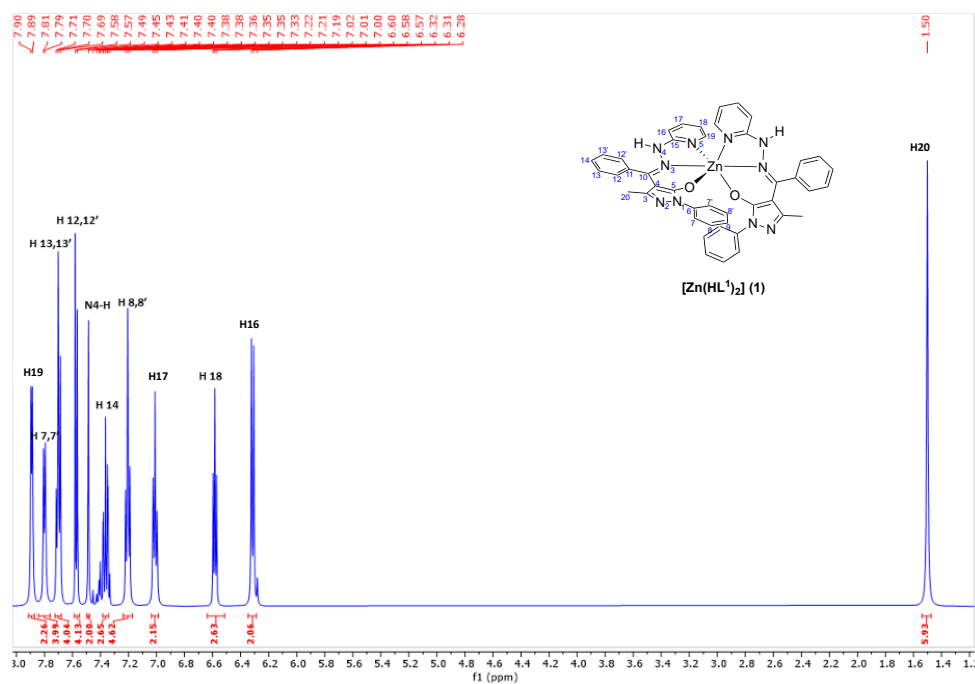


Figure 105. ^1H NMR of complex $[\text{Zn}(\text{HL}^1)_2] (1)$ in CDCl_3 at 298 K.

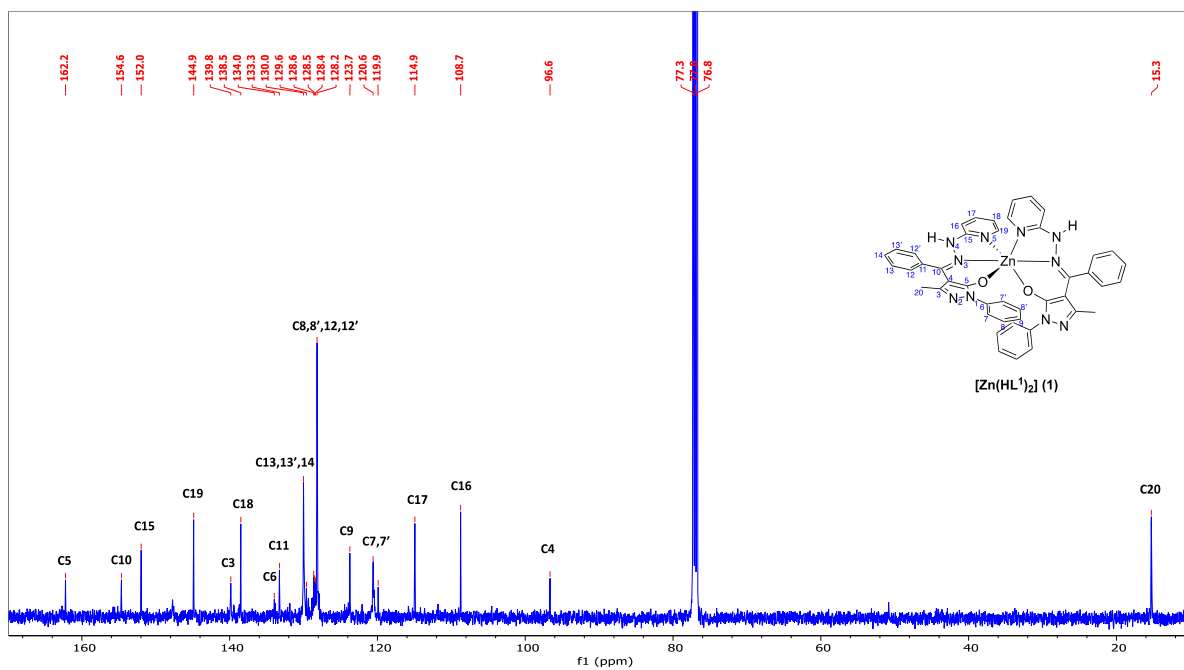


Figure 106. $^{13}\text{C}\{^1\text{H}\}$ NMR of complex $[\text{Zn}(\text{HL}^1)_2]$ (1) in CDCl_3 at 298 K.

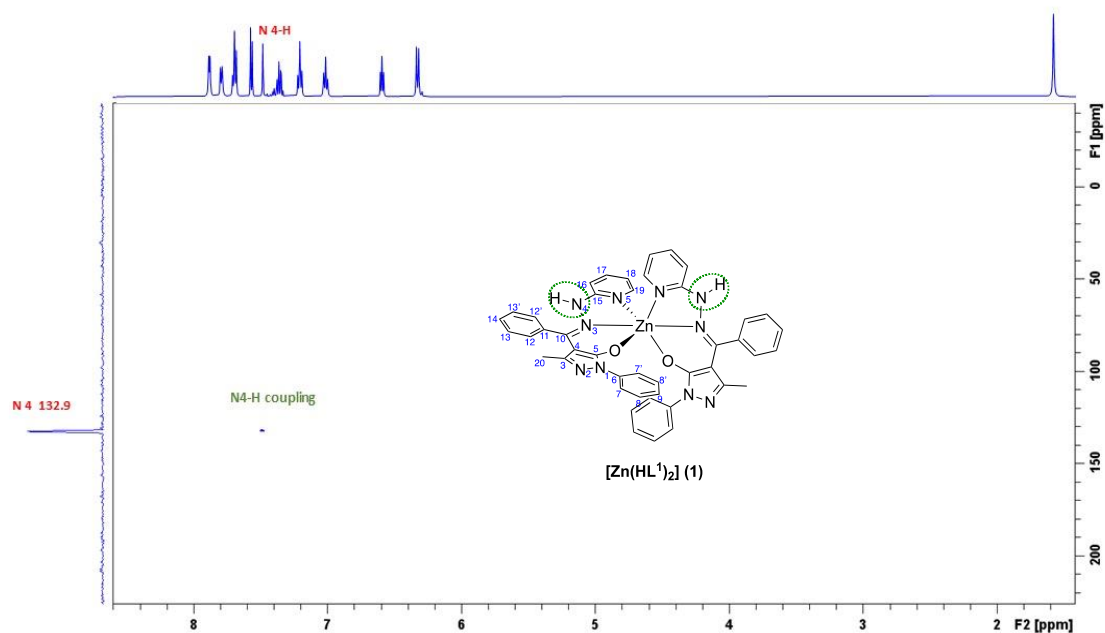


Figure 107. $\{^1\text{H},^{15}\text{N}\}$ -HSQC of complex $[\text{Zn}(\text{HL}^1)_2]$ (1) in CDCl_3 at 298 K.

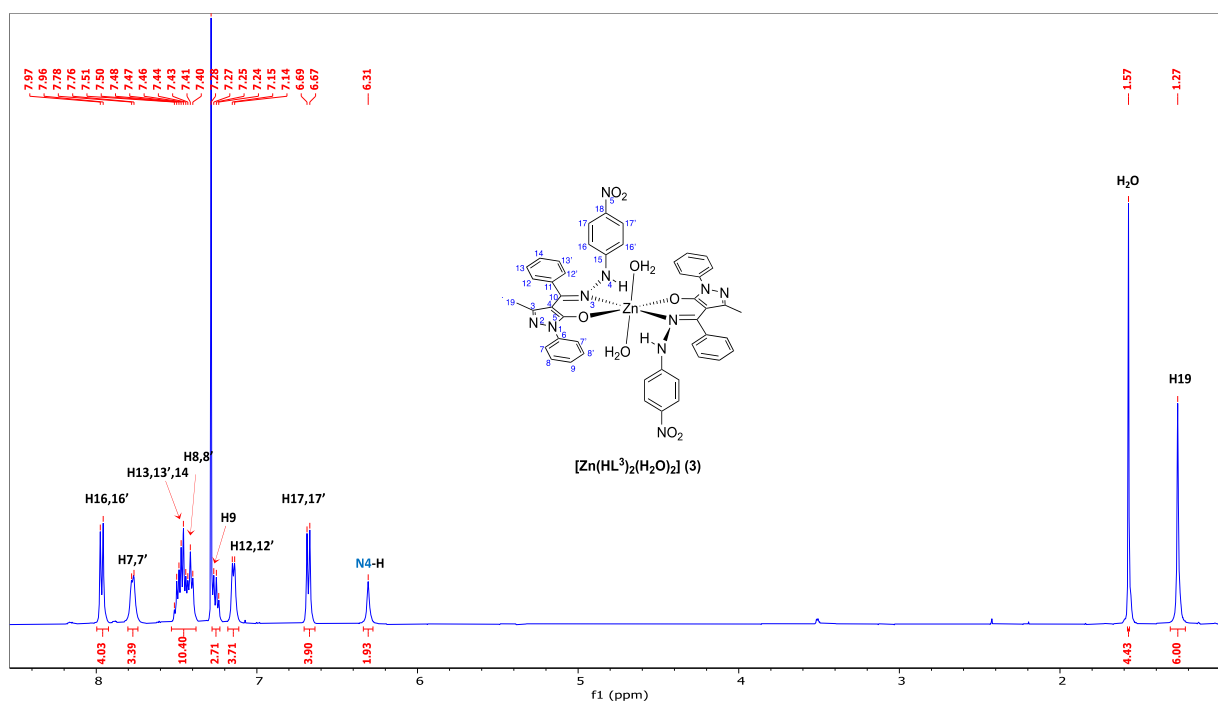


Figure 108. ^1H NMR of complex $[\text{Zn}(\text{HL}^3)_2(\text{H}_2\text{O})_2]$ (3) in CDCl_3 at 298 K.

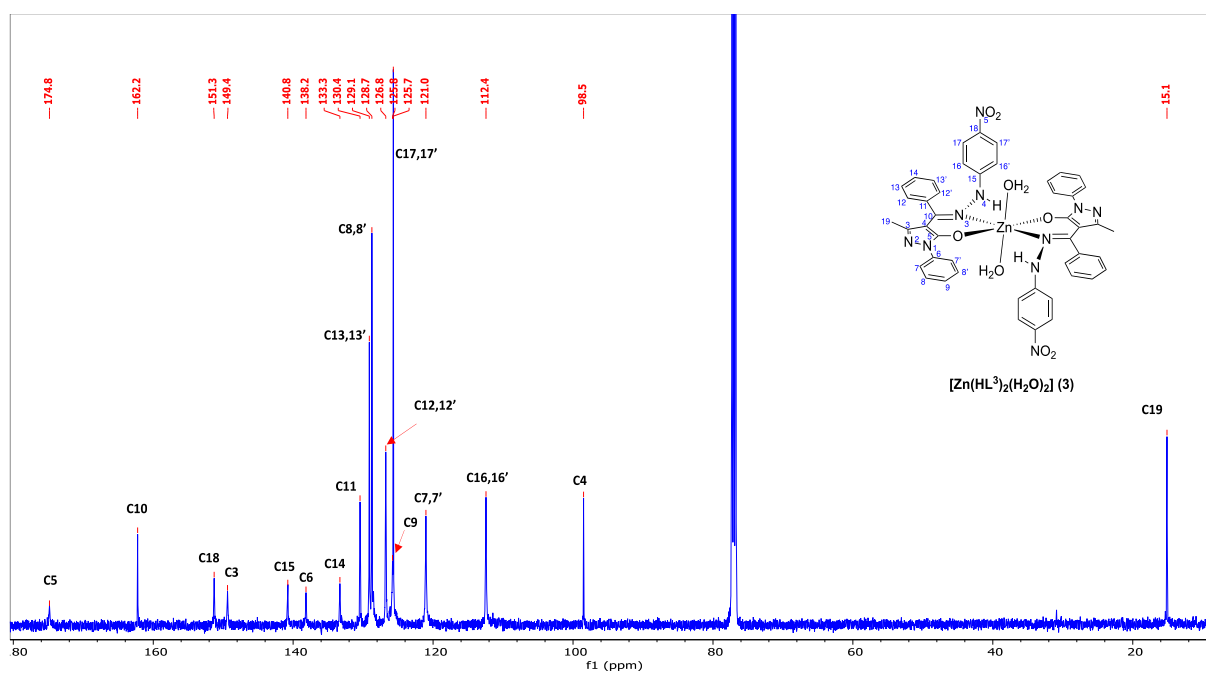


Figure 109. $^{13}\text{C}\{^1\text{H}\}$ NMR of complex $[\text{Zn}(\text{HL}^3)_2(\text{H}_2\text{O})_2]$ (3) in CDCl_3 at 298 K.

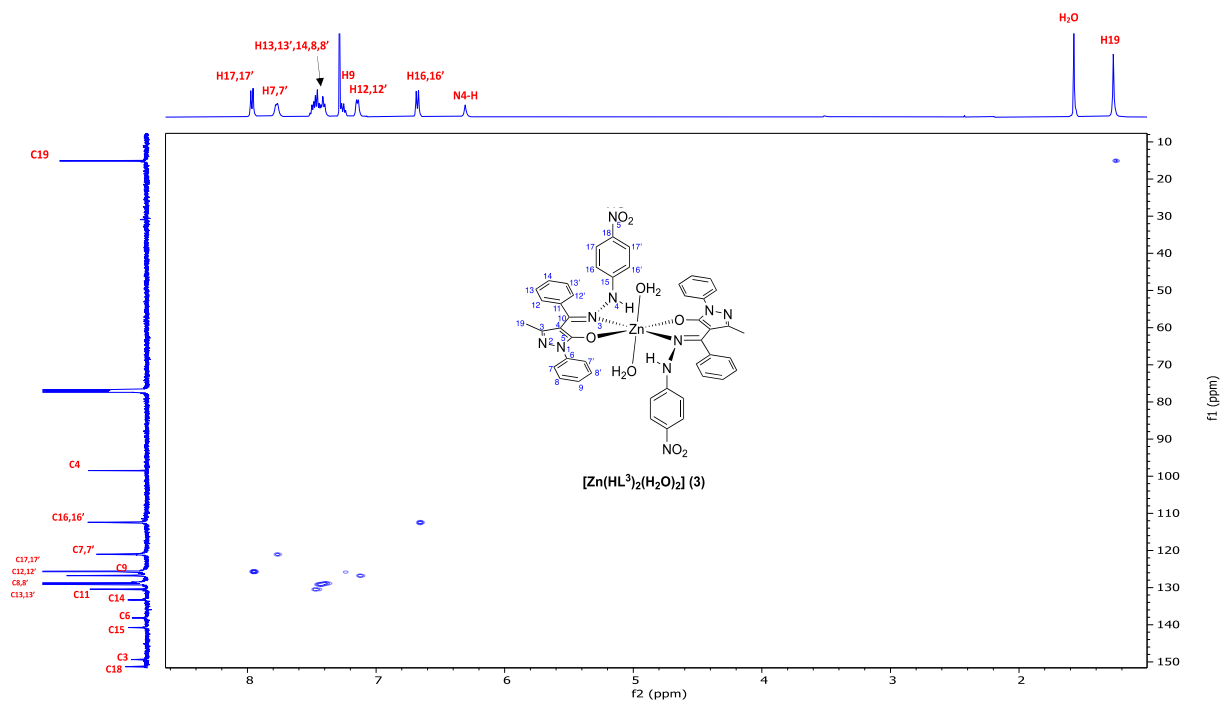


Figure 110. $^1\text{H}, ^{13}\text{C}$ -HSQC of complex $[\text{Zn}(\text{HL}^3)_2(\text{H}_2\text{O})_2]$ (3) in CDCl_3 at 298 K.

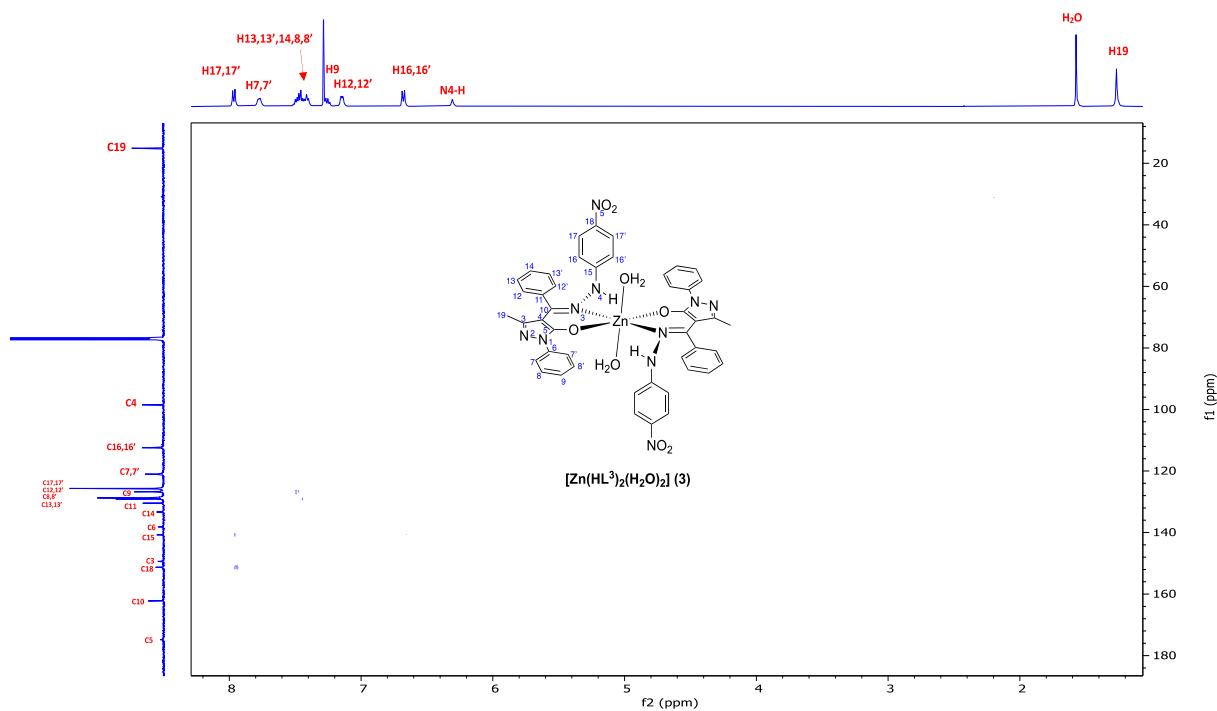


Figure 111. $^1\text{H}, ^{13}\text{C}$ -HMBC of complex $[\text{Zn}(\text{HL}^3)_2(\text{H}_2\text{O})_2]$ (3) in CDCl_3 at 298 K.

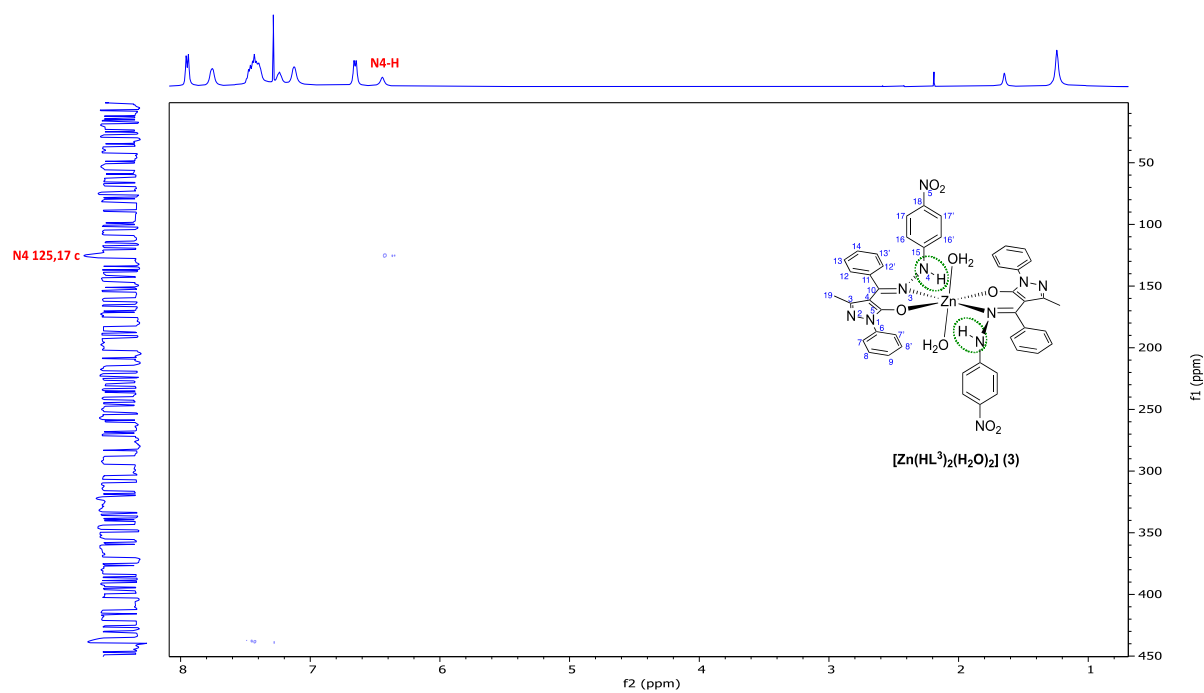


Figure 112. ^1H , ^{15}N -HSQC of complex $[\text{Zn}(\text{HL}^3)_2(\text{H}_2\text{O})_2]$ (3) in CDCl_3 at 298 K.

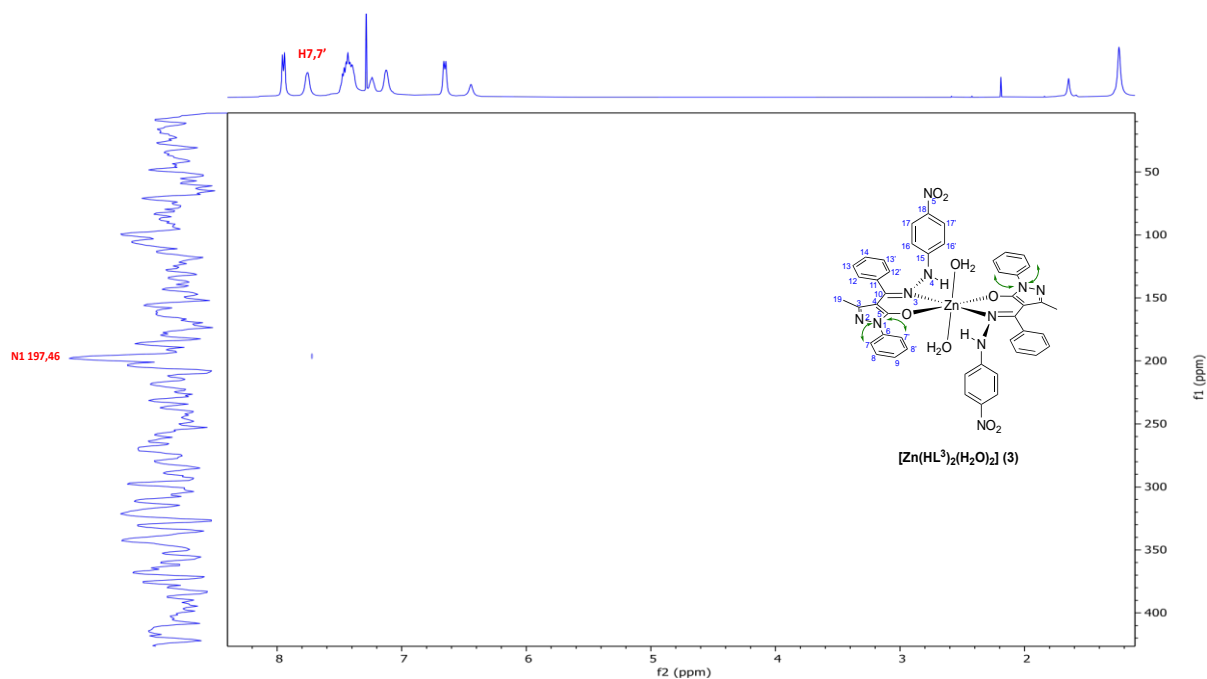


Figure 113. ^1H , ^{15}N -HMBC of complex $[\text{Zn}(\text{HL}^3)_2(\text{H}_2\text{O})_2]$ (3) in CDCl_3 at 298 K.

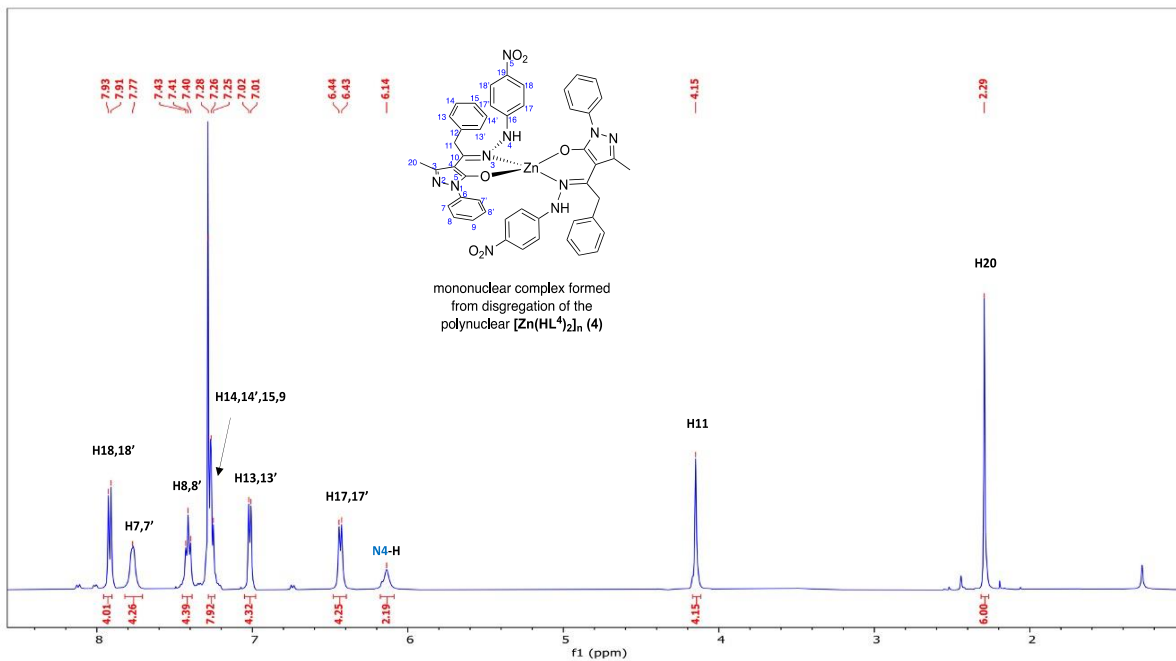


Figure 114. 1H NMR of complex $[Zn(HL^4)_2]$ (4) in $CDCl_3$ at 298 K.

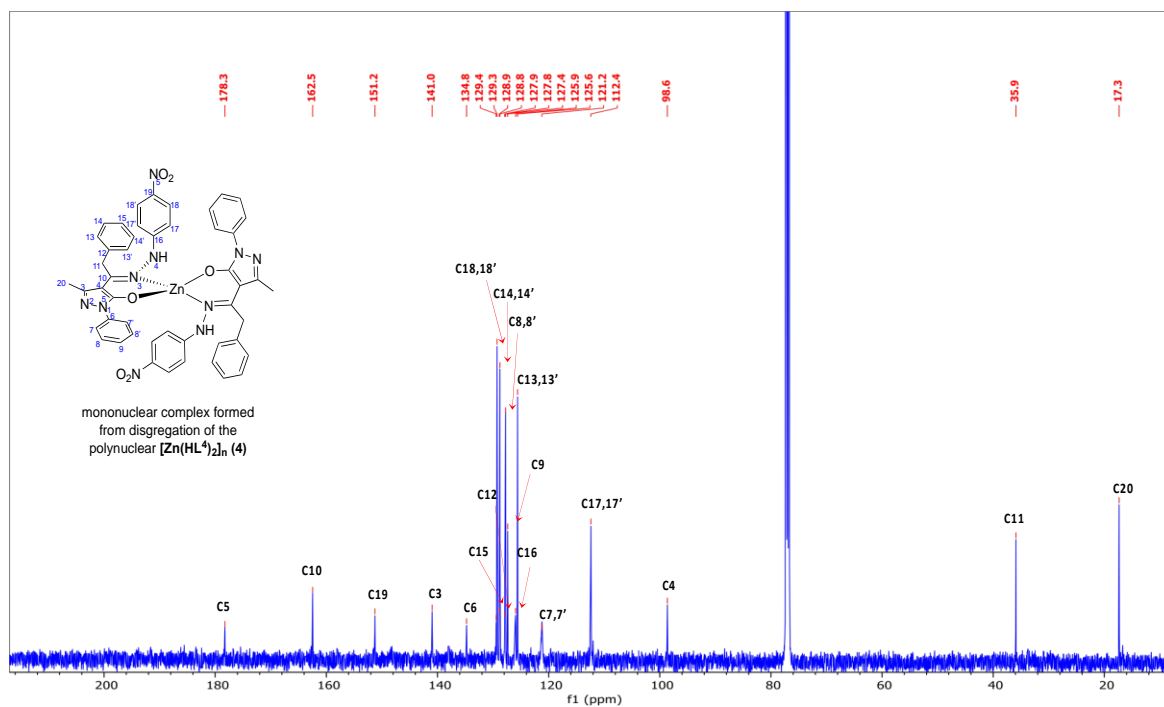


Figure 115. $^{13}C\{^1H\}$ NMR of complex $[Zn(HL^4)_2]$ (4) in $CDCl_3$ at 298 K.

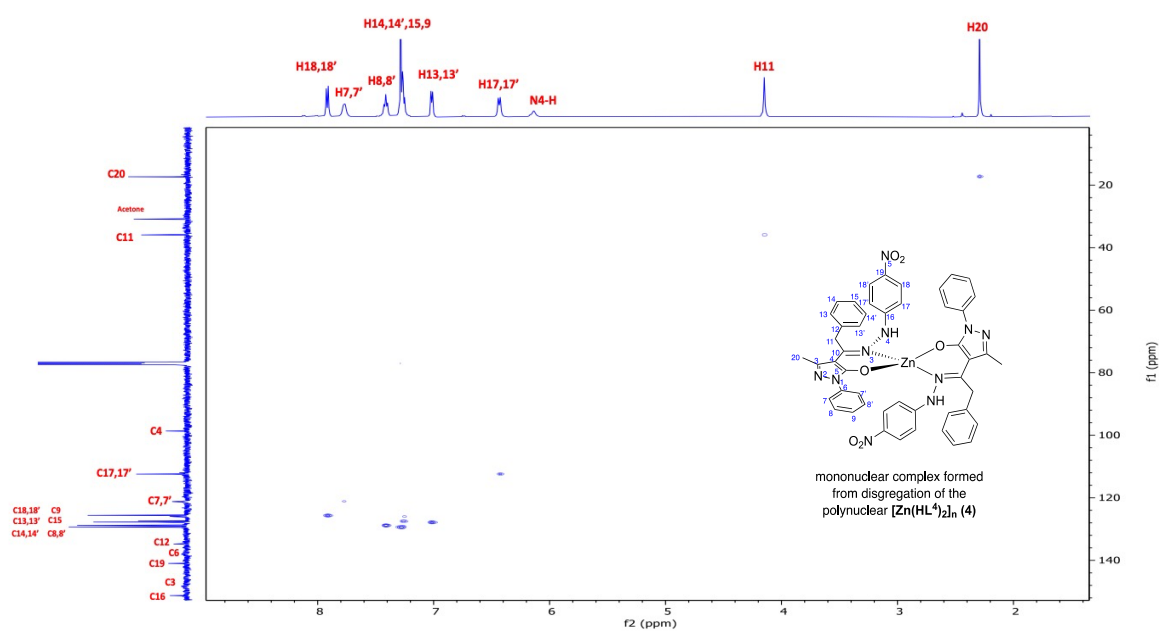


Figure 116. $\{^1H,^{13}C\}$ -HSQC of complex $[Zn(HL^4)_2]$ (4) in $CDCl_3$ at 298 K.

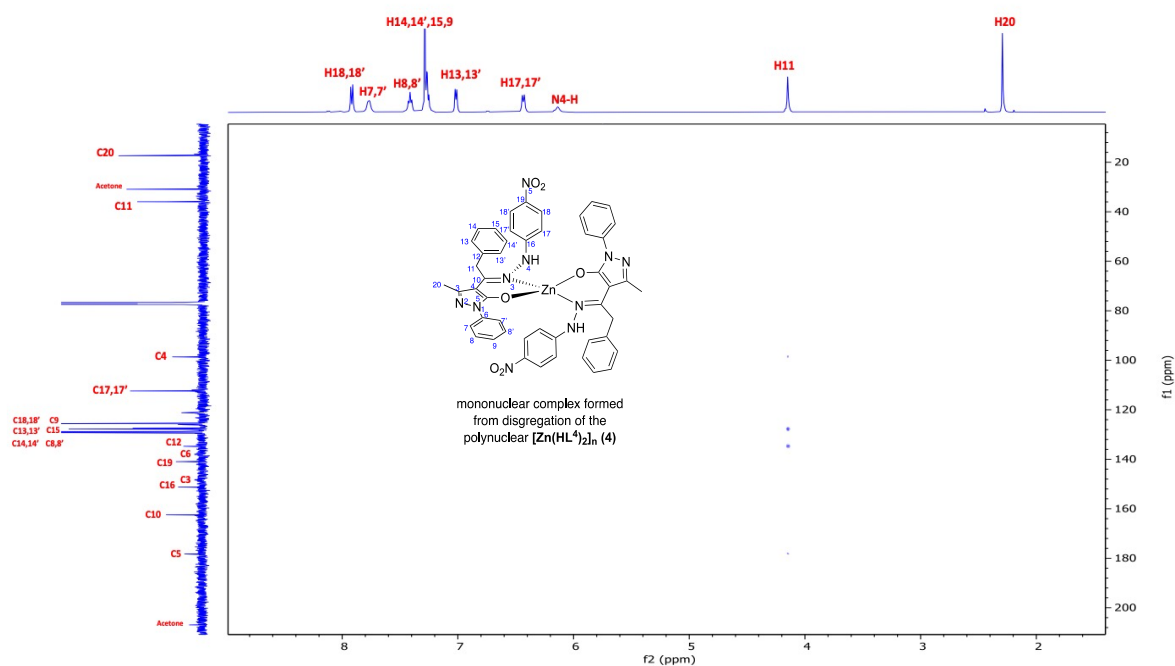


Figure 117. $\{^1H,^{13}C\}$ -HMBC of complex $[Zn(HL^4)_2]$ (4) in $CDCl_3$ at 298 K.

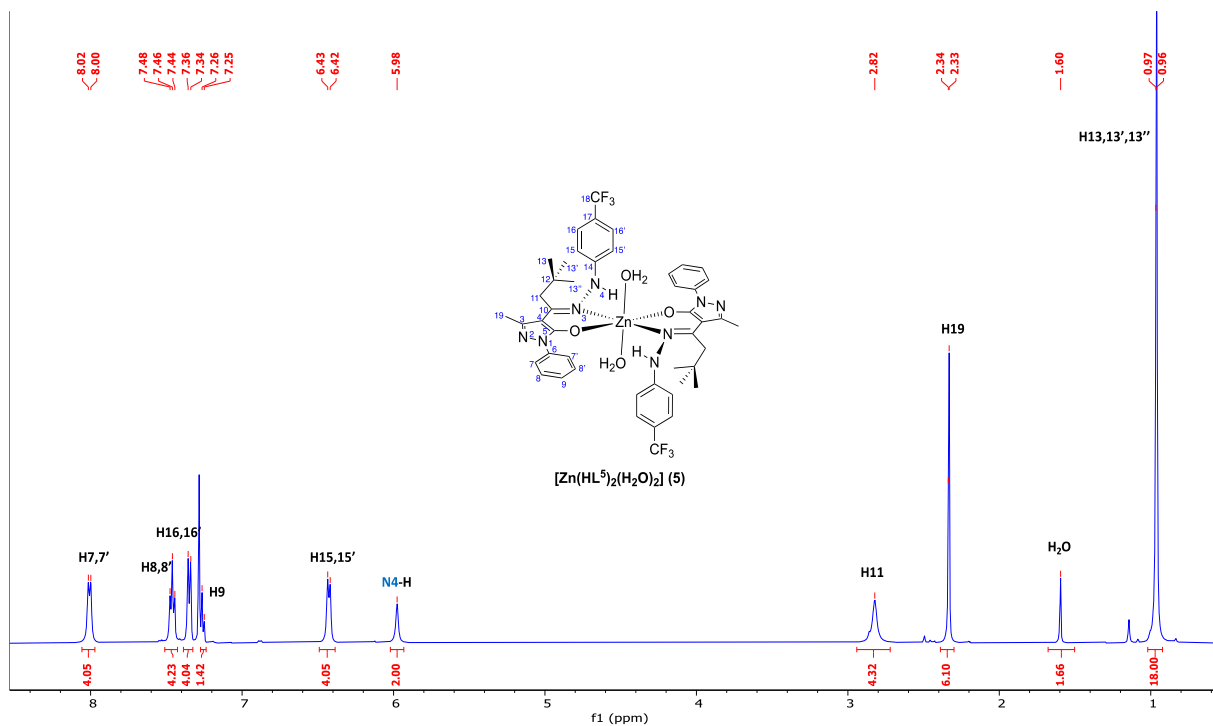


Figure 118. ^1H NMR of complex $[\text{Zn}(\text{HL}^5)_2(\text{H}_2\text{O})_2]$ (5) in CDCl_3 at 298 K.

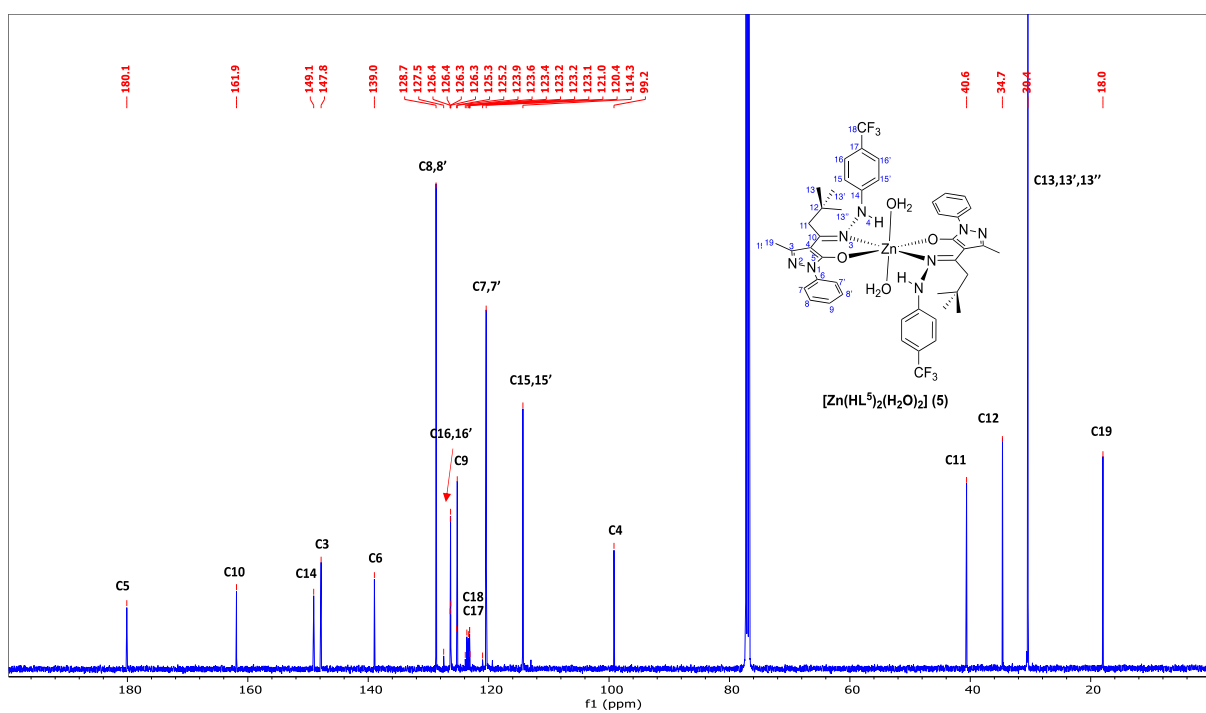


Figure 119. $^{13}\text{C}\{^1\text{H}\}$ NMR of complex $[\text{Zn}(\text{HL}^5)_2(\text{H}_2\text{O})_2]$ (5) in CDCl_3 at 298 K.

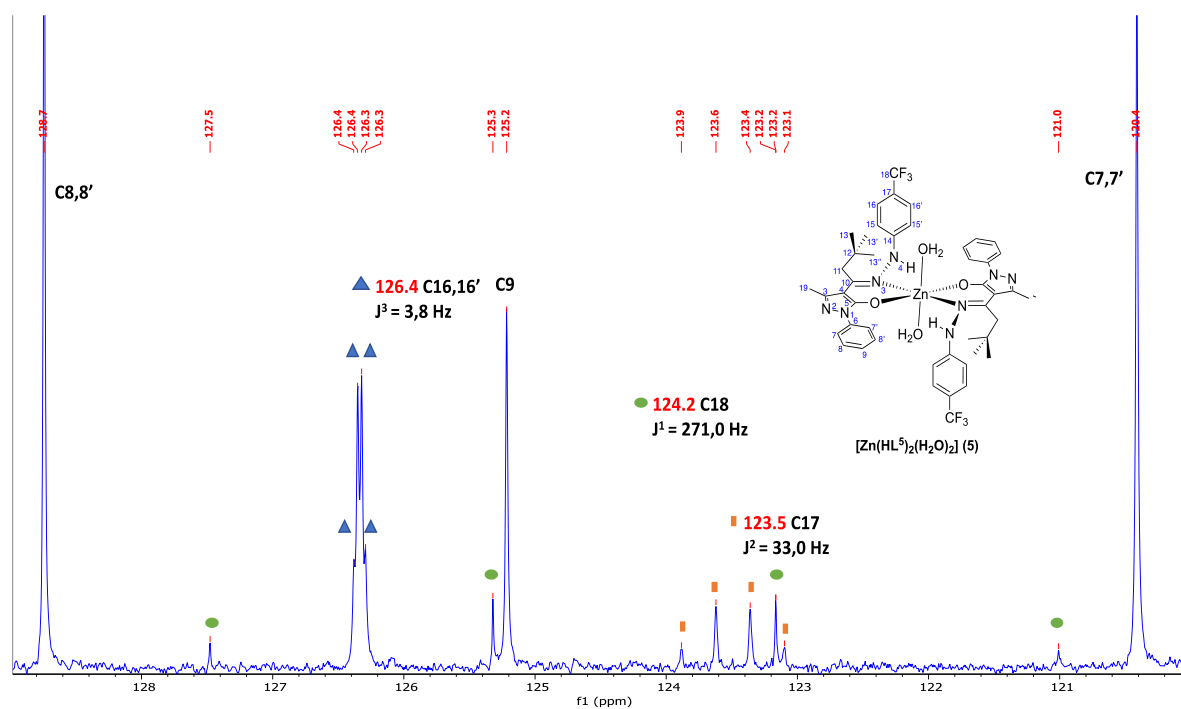


Figure 120. Magnification of $^{13}\text{C}\{^1\text{H}\}$ NMR of complex $[\text{Zn}(\text{HL}^5)_2(\text{H}_2\text{O})_2]$ (5) in CDCl_3 at 298 K.

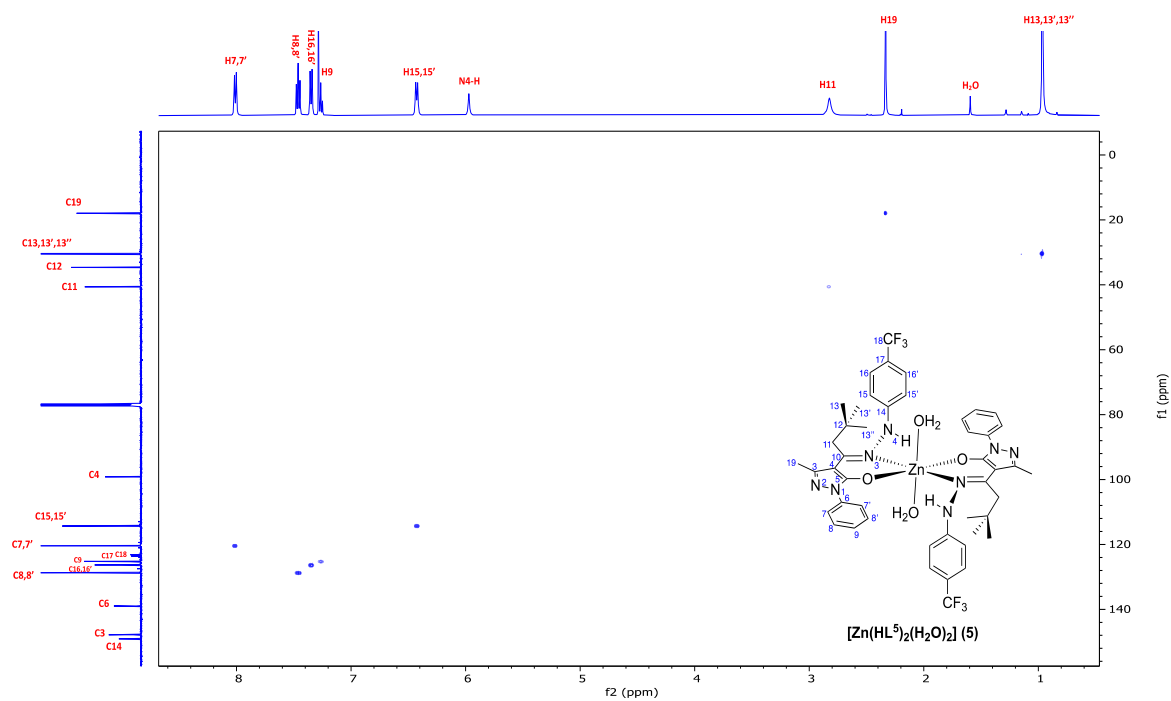


Figure 121. $^1\text{H},^{13}\text{C}$ -HSQC of complex $[\text{Zn}(\text{HL}^5)_2(\text{H}_2\text{O})_2]$ (5) in CDCl_3 at 298 K.

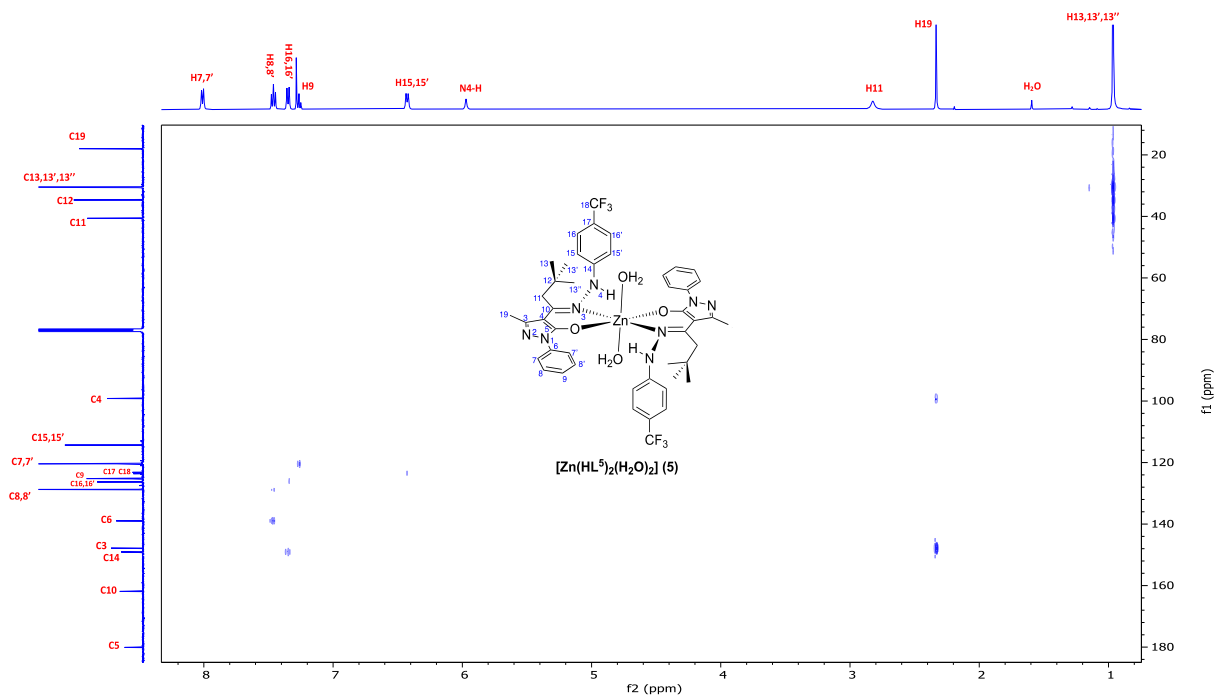


Figure 122. ${}^1\text{H}$, ${}^{13}\text{C}$ -HMBC of complex $[\text{Zn}(\text{HL}^5)_2(\text{H}_2\text{O})_2]$ (5) in CDCl_3 at 298 K.

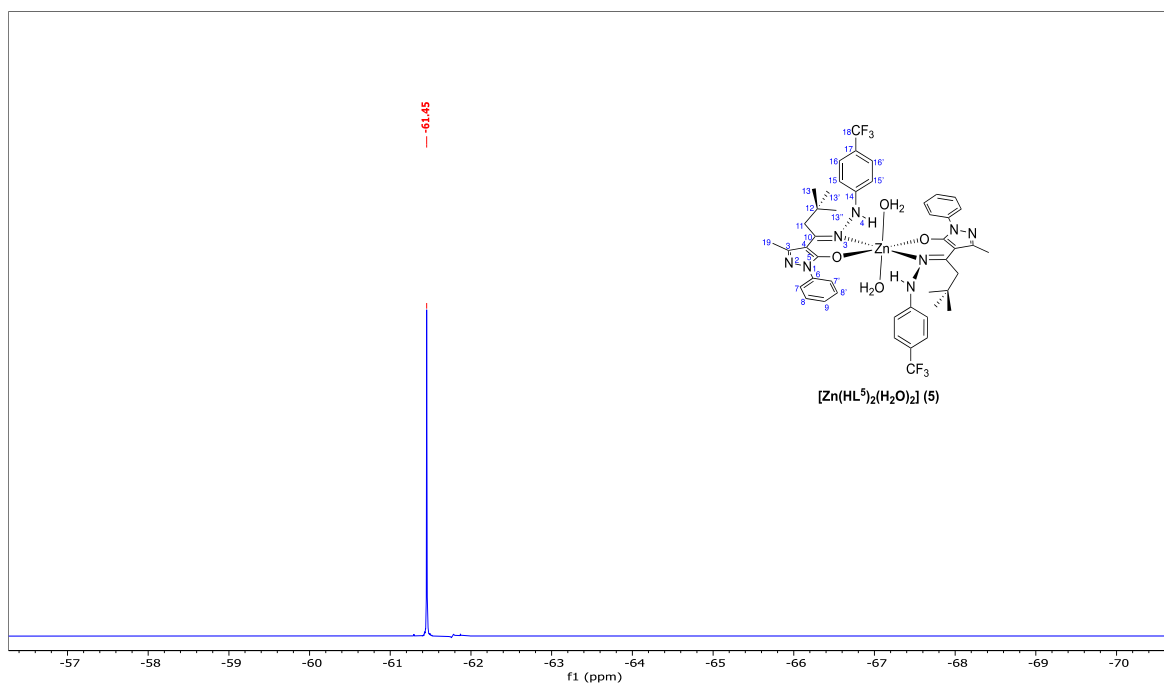


Figure 123. ${}^{19}\text{F}\{{}^1\text{H}\}$ NMR of complex $[\text{Zn}(\text{HL}^5)_2(\text{H}_2\text{O})_2]$ (5) in CDCl_3 at 298 K.

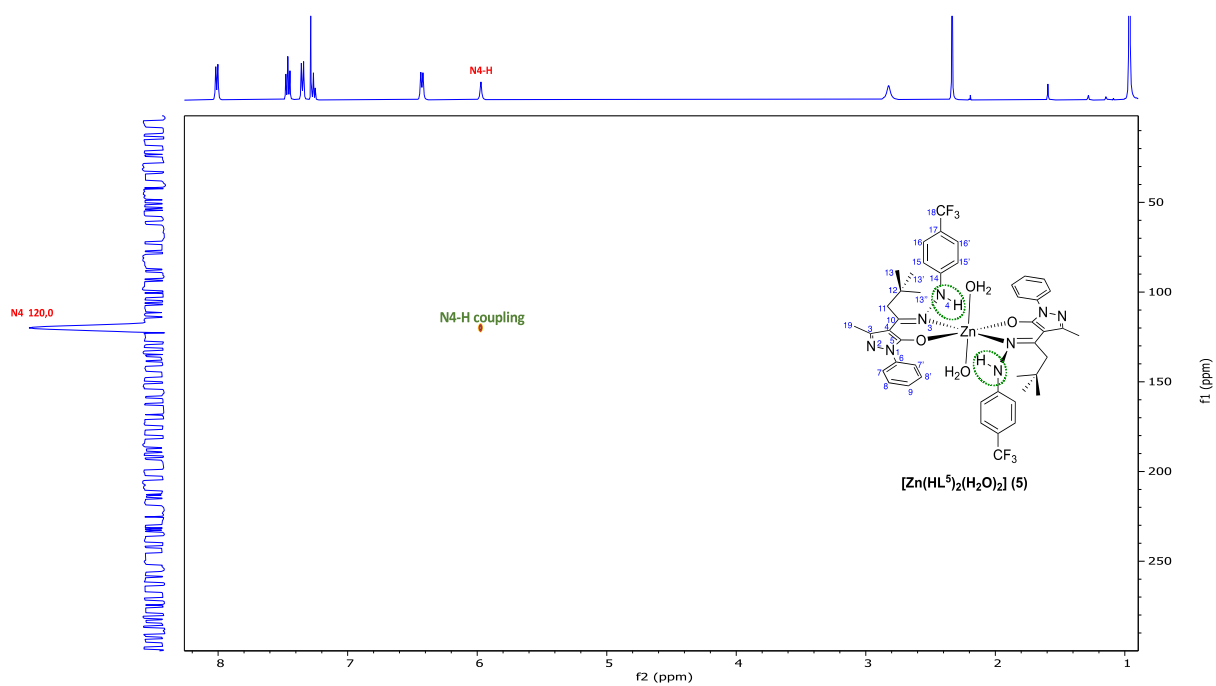


Figure 124. $[\text{H}, ^{15}\text{N}]$ -HSQC of complex $[\text{Zn}(\text{HL}^5)_2(\text{H}_2\text{O})_2]$ (5) in CDCl_3 at 298 K.

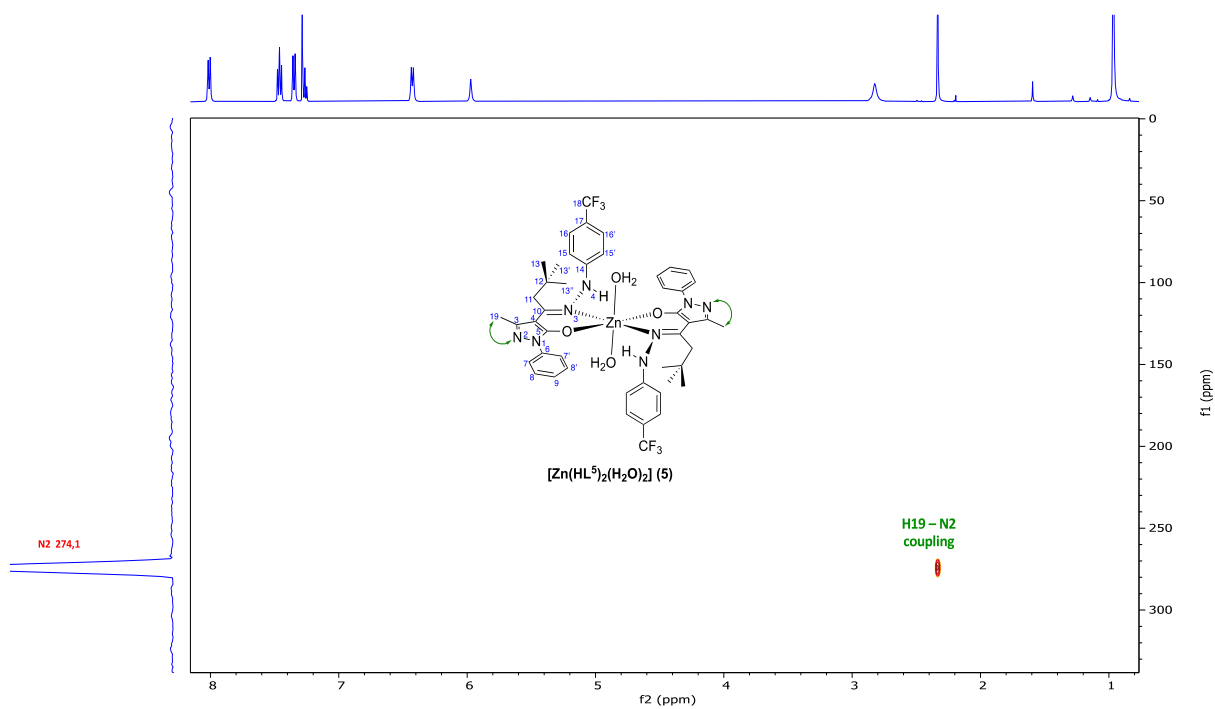


Figure 125. $[\text{H}, ^{15}\text{N}]$ -HMBC of complex $[\text{Zn}(\text{HL}^5)_2(\text{H}_2\text{O})_2]$ (5) in CDCl_3 at 298 K.

Appendix Chapter 3

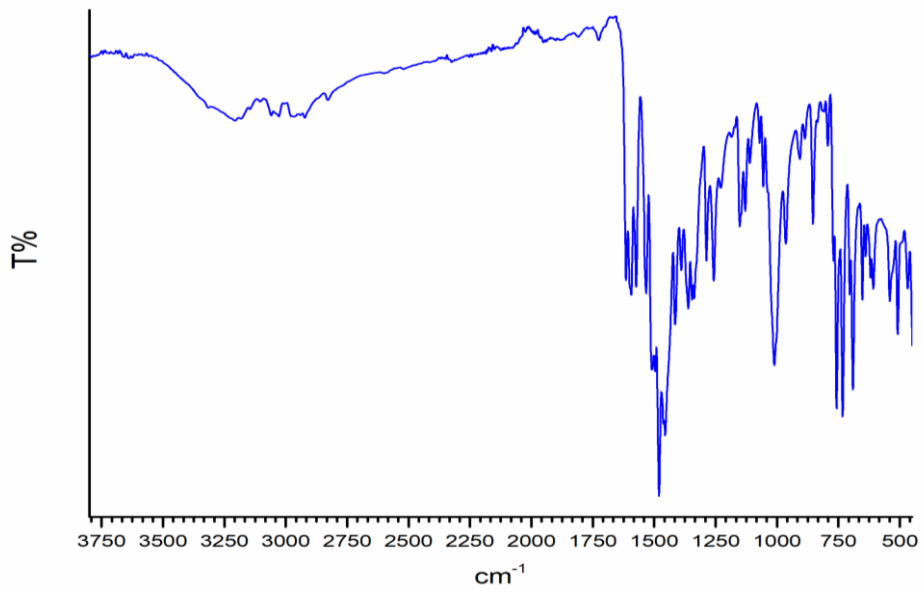


Figure 126. IR spectrum of $[Zn(HL^2)_2]$ (2).

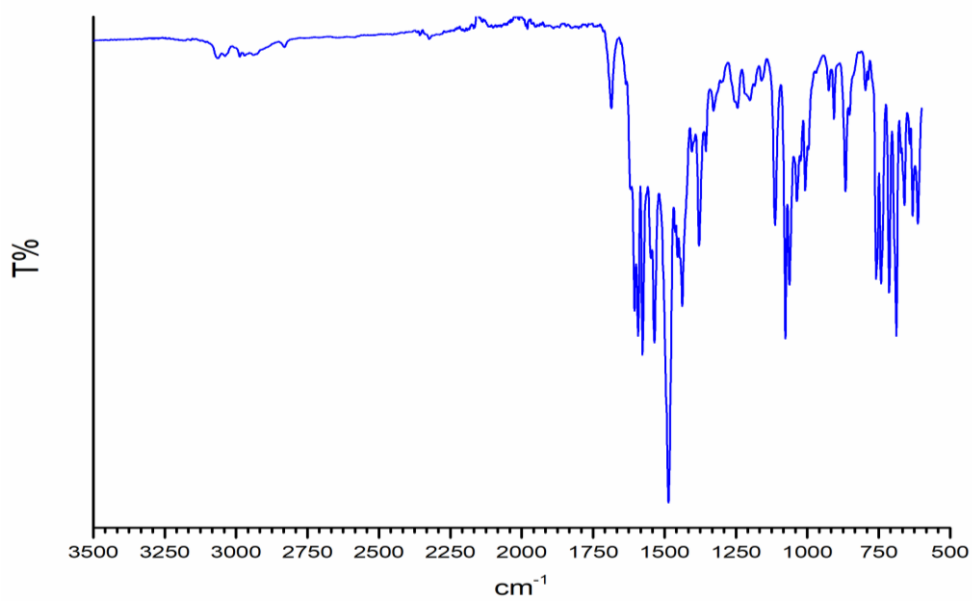


Figure 127. IR spectrum of $[Cu(HL^1)_2]$ (3).

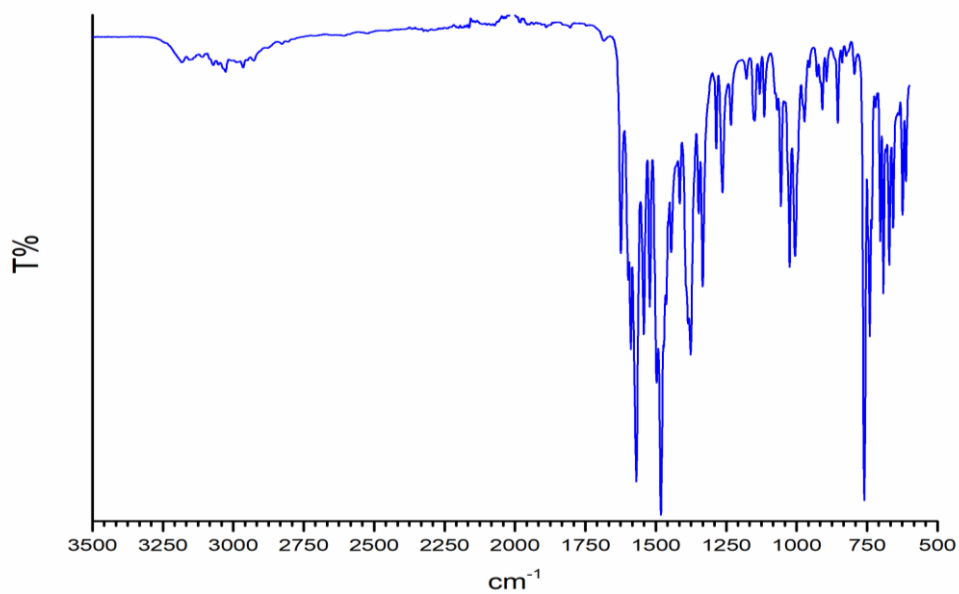


Figure 128. IR spectrum of $[\text{Cu}(\text{HL}^2)_2]$ (**4**).

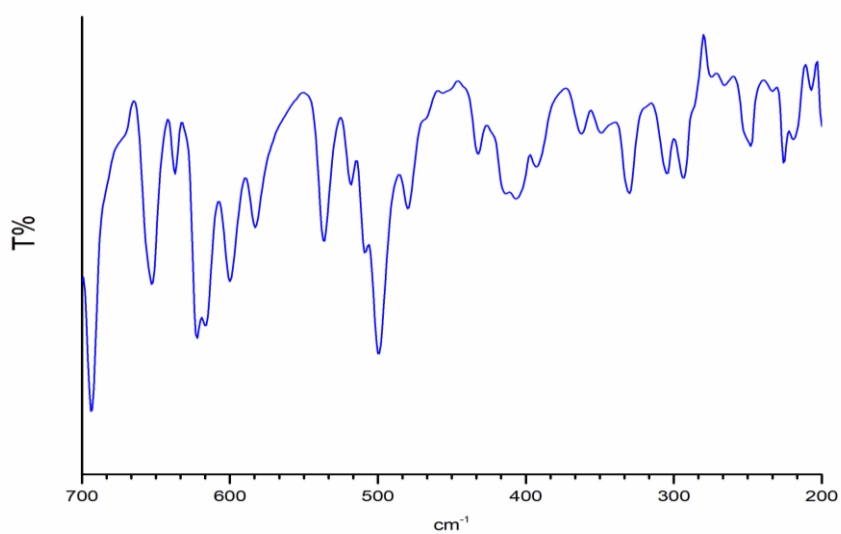


Figure 129. FIR spectrum of H_2L^1 .

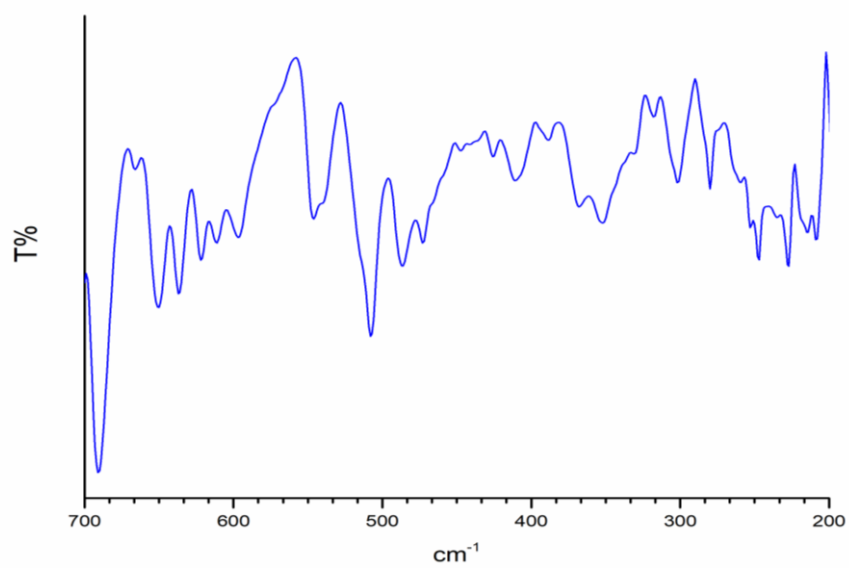


Figure 130. FIR spectrum of H_2L^2 .

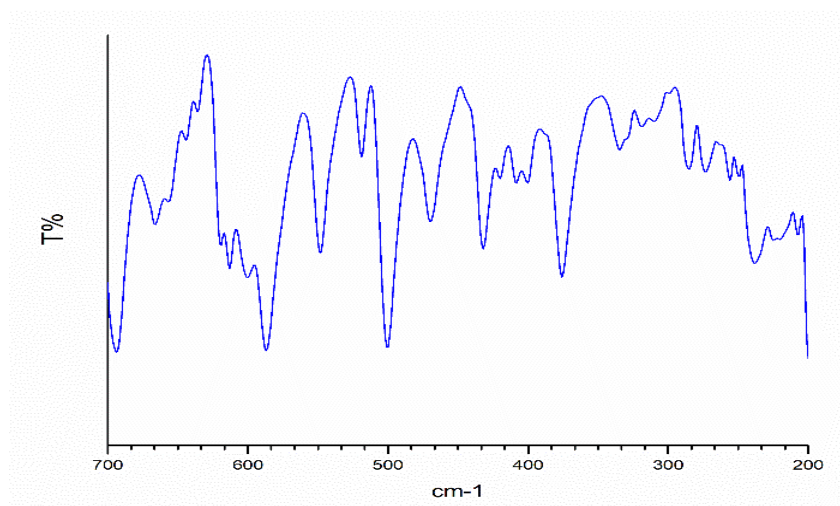


Figure 131. FIR spectrum of $[Zn(HL^1)_2(MeOH)_2]$ (**1**).

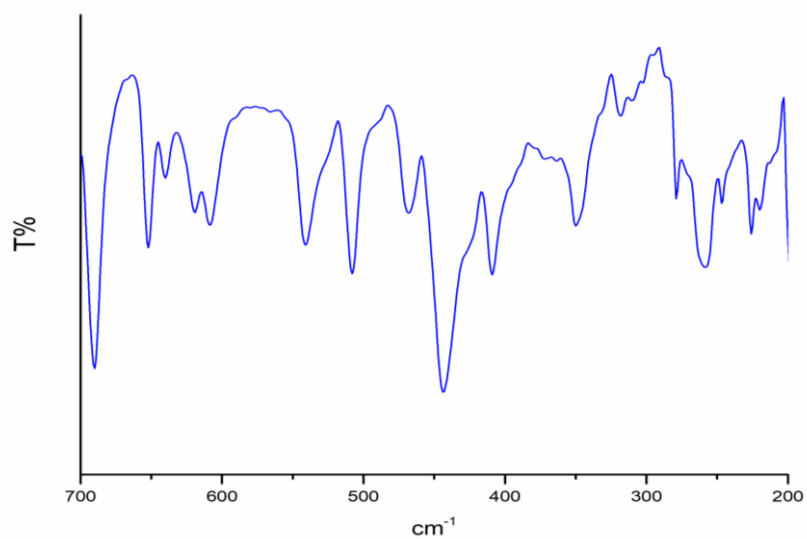


Figure 132. FIR spectrum of $[Zn(HL^2)_2]$ (2).

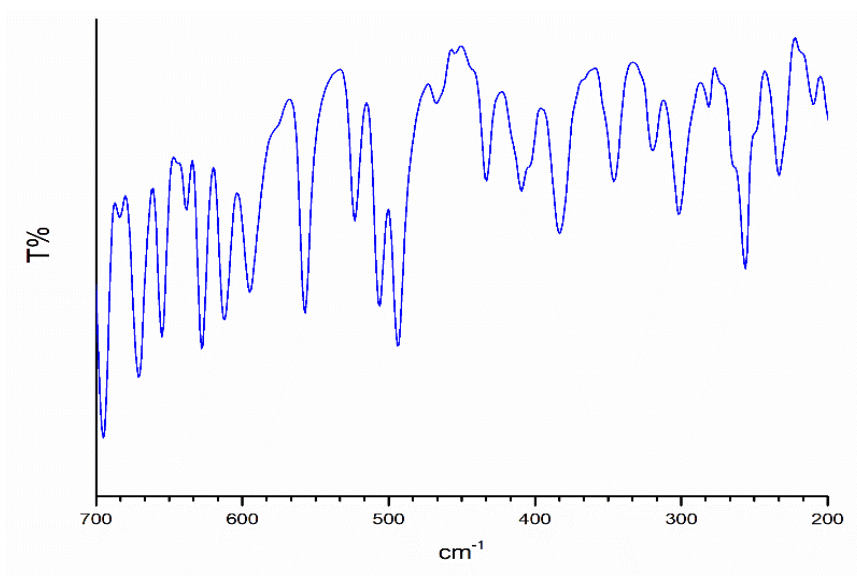


Figure 133. FIR spectrum of $[Cu(HL^1)_2]$ (3).

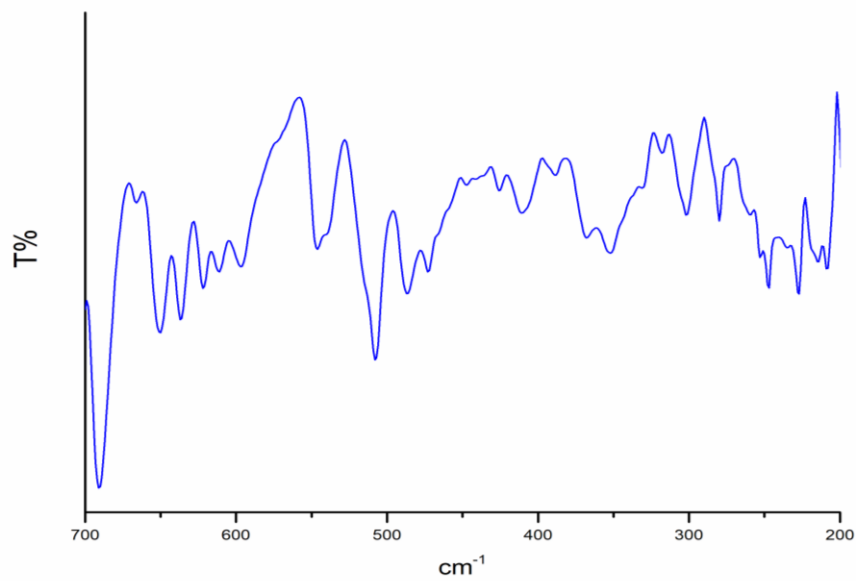


Figure 134. FIR spectrum of $[Cu(HL^2)_2]$ (**4**).

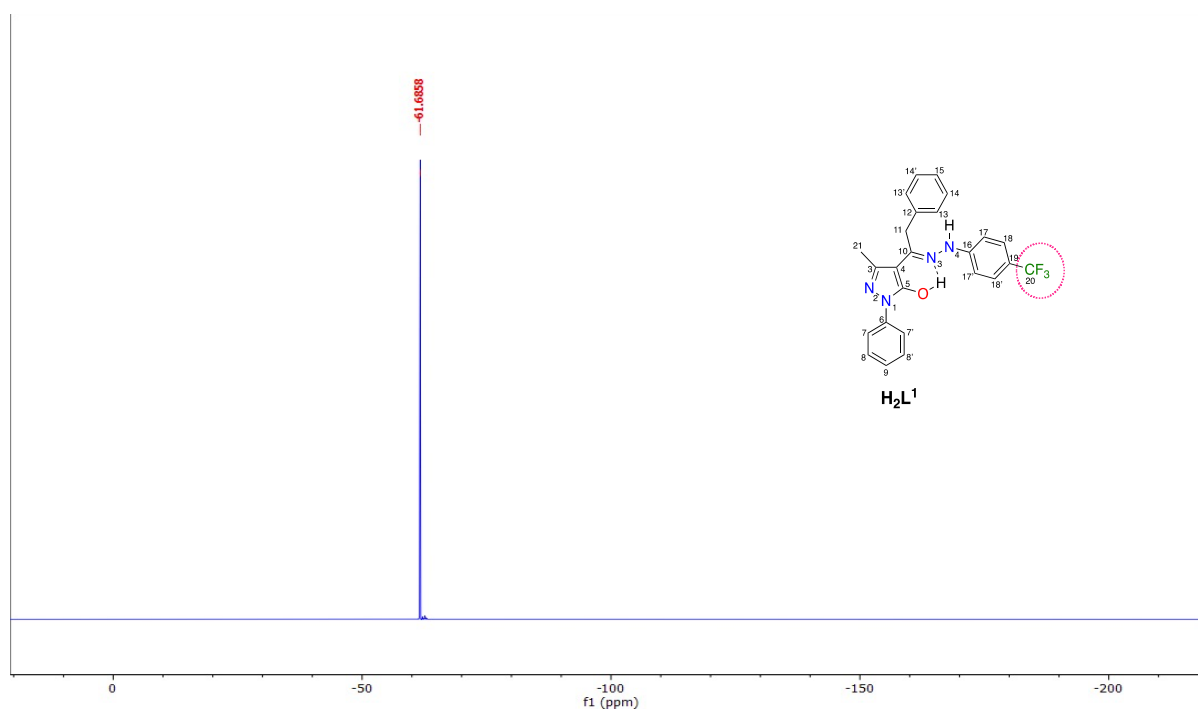


Figure 135. $^{19}F\{^1H\}$ NMR spectrum in $CDCl_3$ at 298 K of H_2L^1 .

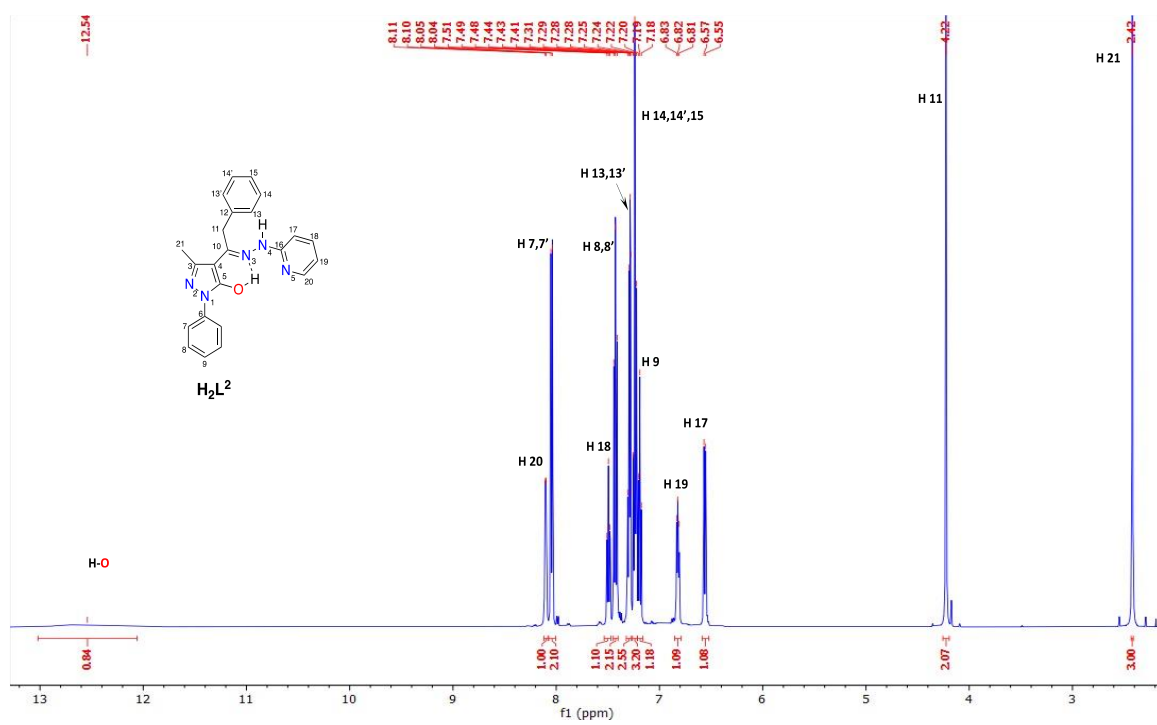


Figure 136. ^1H NMR spectrum in CDCl_3 at 298 K of H_2L^2 .

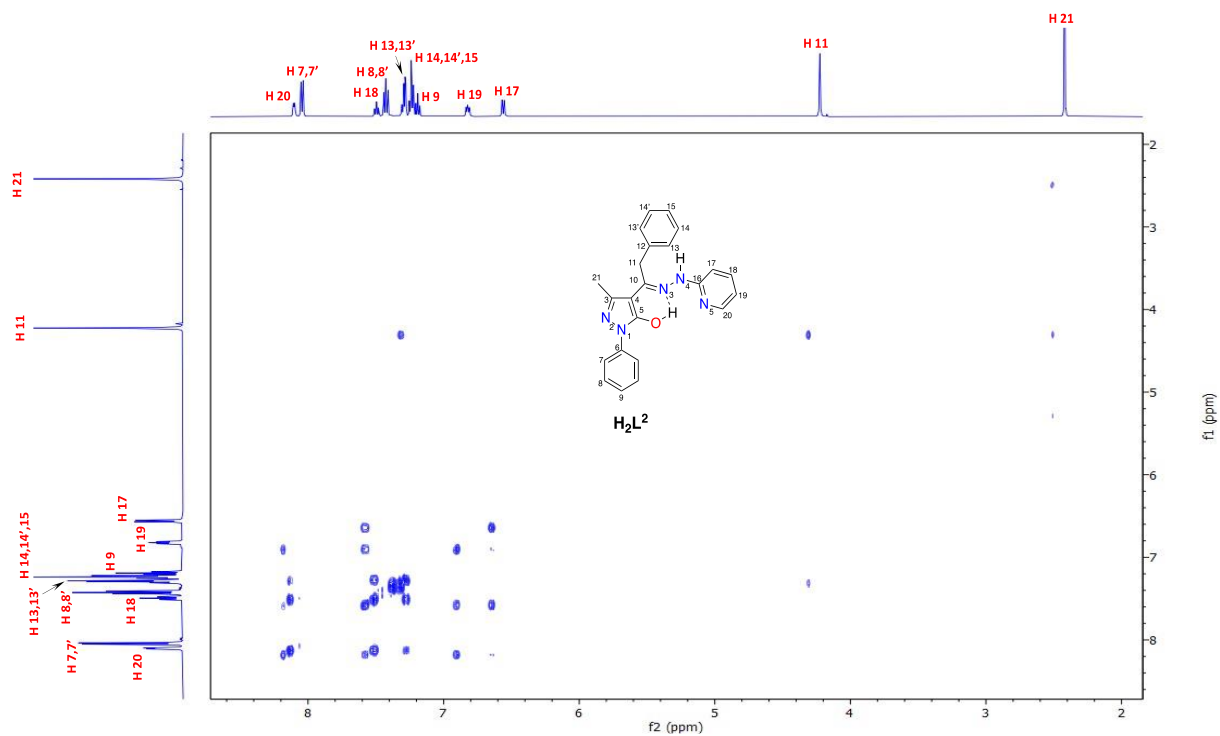


Figure 137. $\{^1\text{H}, ^1\text{H}\}$ -COSY spectrum in CDCl_3 at 298 K of H_2L^2 .

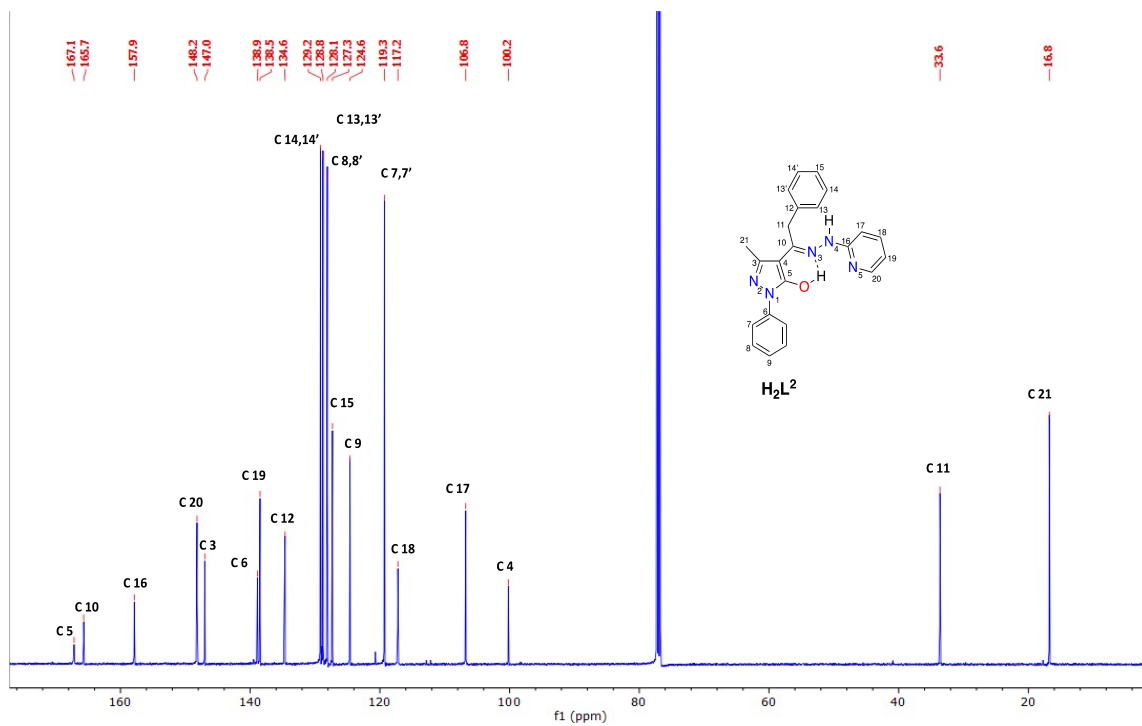


Figure 138. $^{13}\text{C}\{^1\text{H}\}$ NMR spectrum in CDCl_3 at 298 K of H_2L^2 .

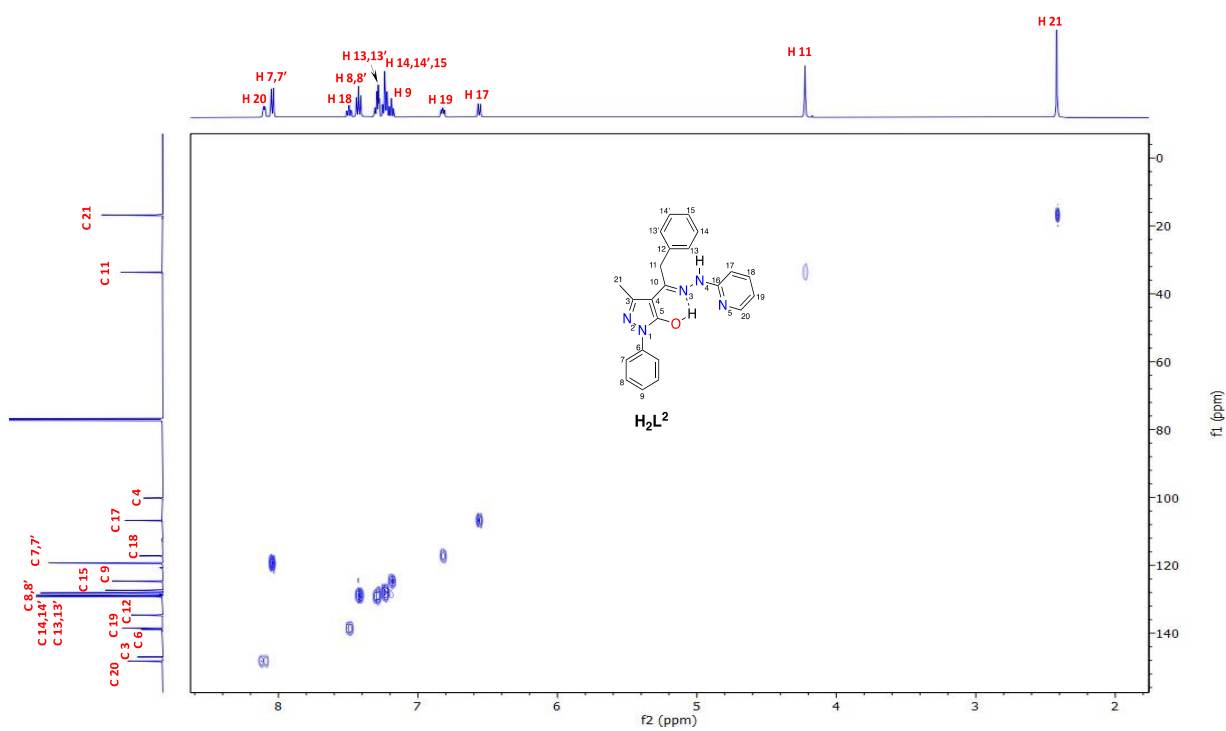


Figure 139. $\{^1\text{H},^{13}\text{C}\}$ -HSQC spectrum in CDCl_3 at 298 K of H_2L^2 .

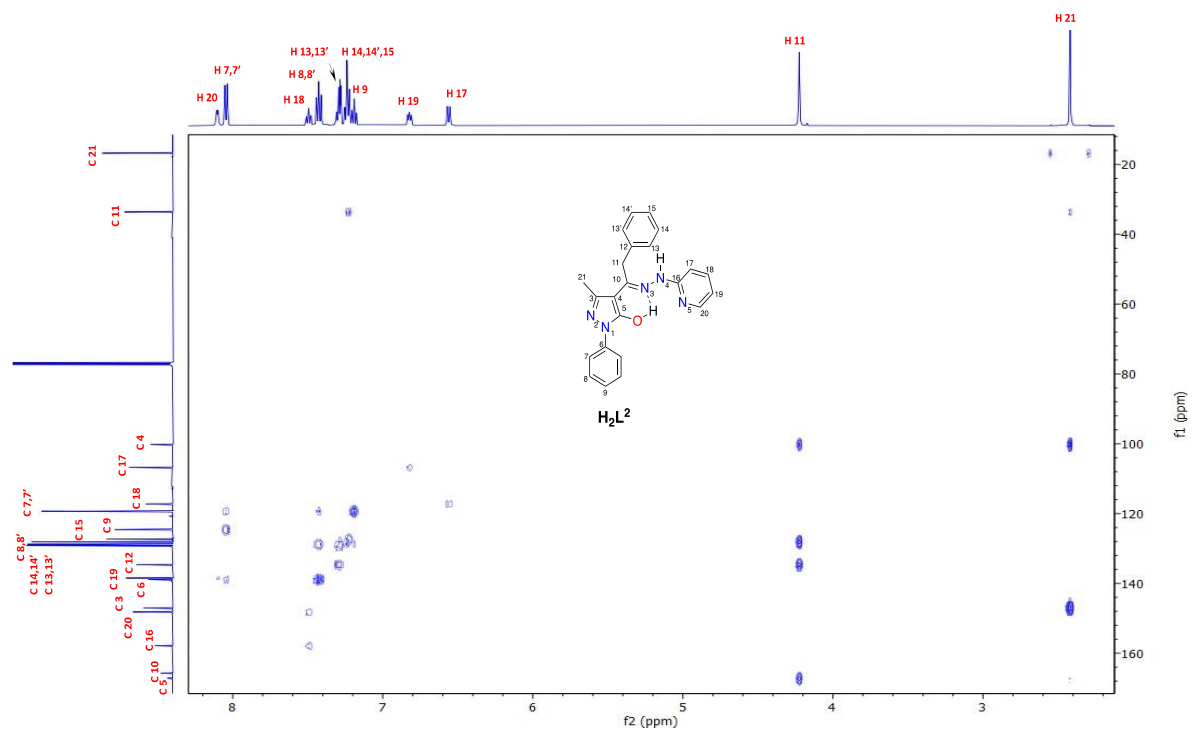


Figure 140. $\{^1\text{H},^{13}\text{C}\}$ -HMBC spectrum in CDCl_3 at 298 K of H_2L^2 .

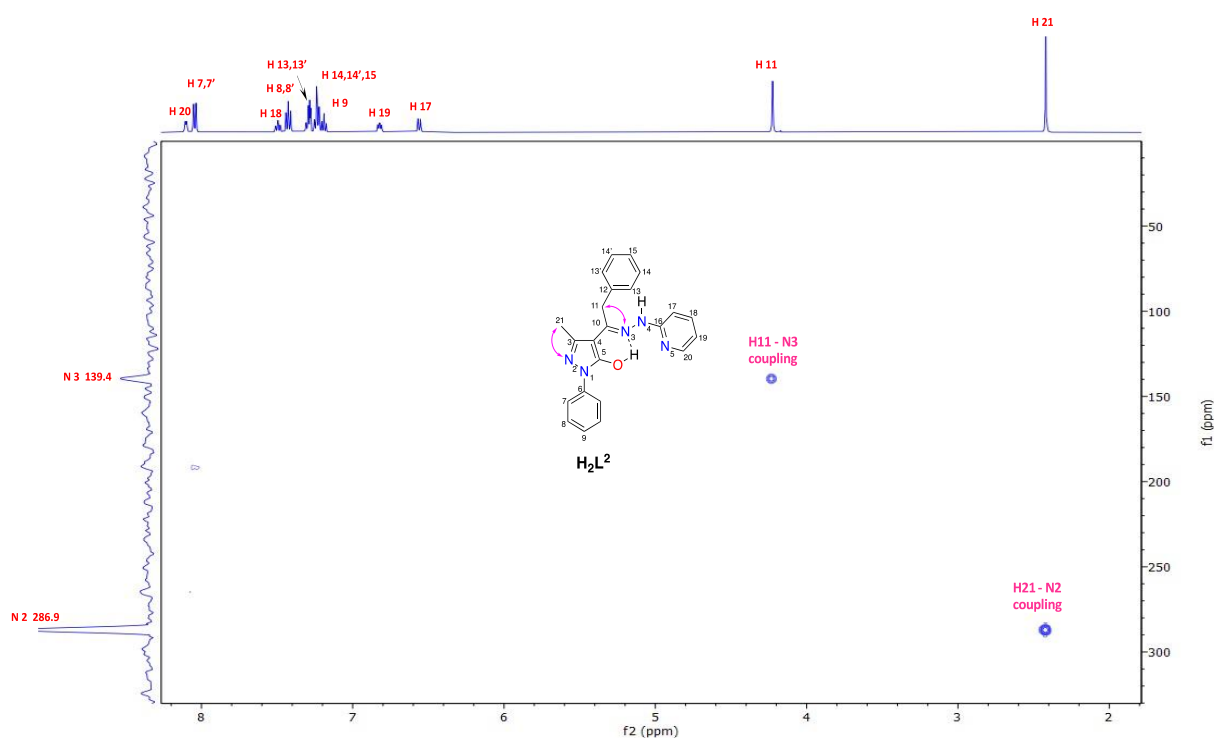


Figure 141. $\{^1\text{H},^{15}\text{N}\}$ -HMBC spectrum in CDCl_3 at 298 K of H_2L^2 .

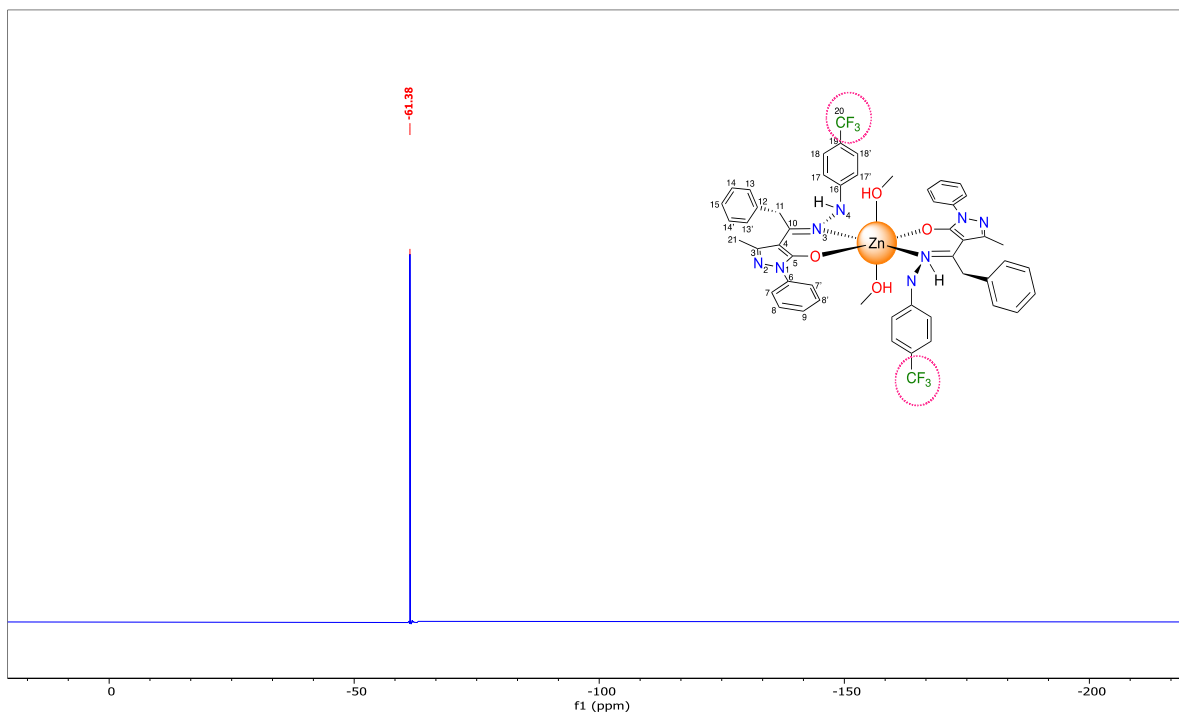


Figure 142. $^{19}\text{F}\{^1\text{H}\}$ NMR spectrum in CDCl_3 at 298 K of $[\text{Zn}(\text{HL}^1)_2(\text{MeOH})_2]$ (1).

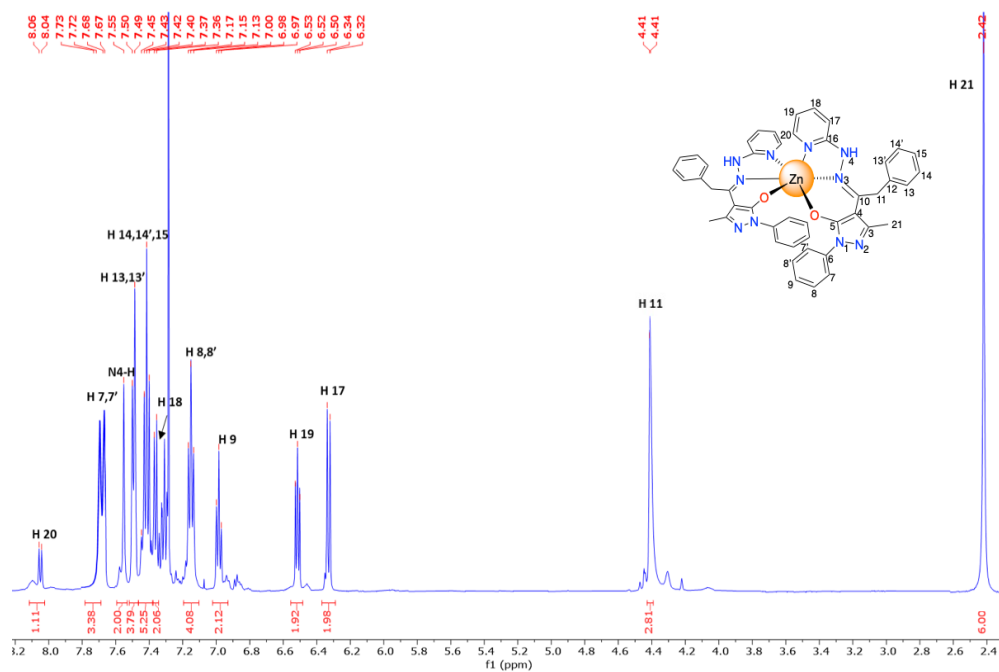


Figure 143. ^1H NMR spectrum in CDCl_3 at 298 K of $[\text{Zn}(\text{HL}^2)_2]$ (2).

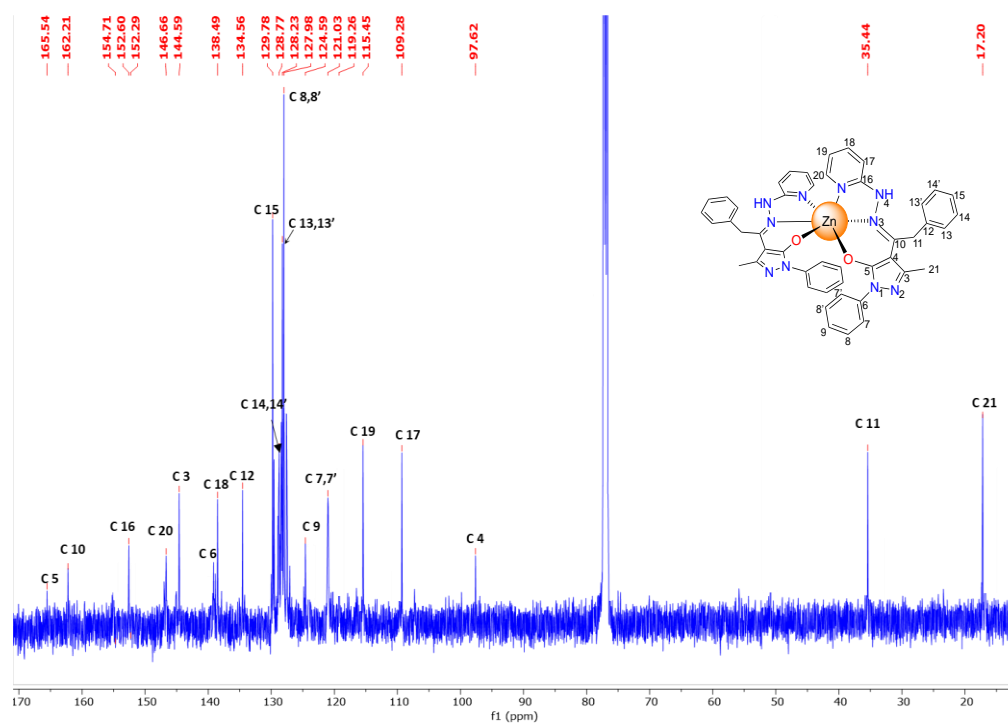


Figure 144. ^{13}C NMR spectrum in CDCl_3 at 298 K of $[\text{Zn}(\text{HL}^2)_2]$ (2).

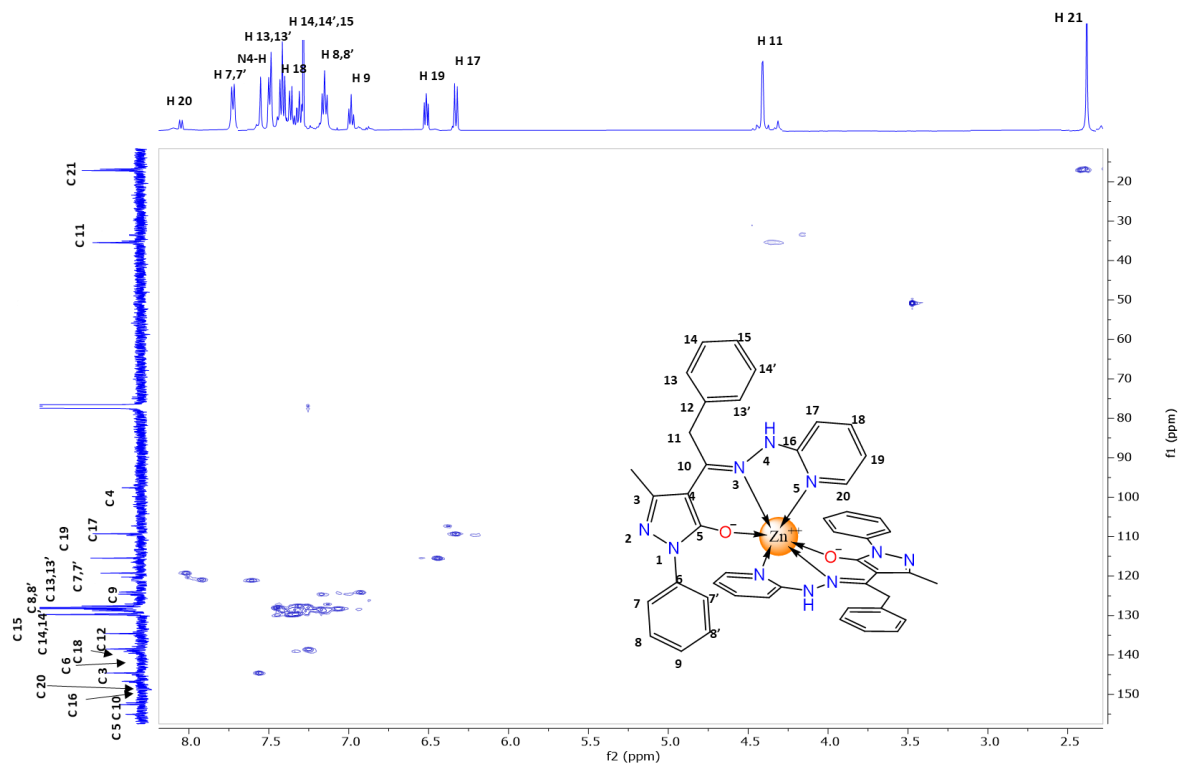


Figure 145. $^1\text{H},^{13}\text{C}$ -HSQC spectrum in CDCl_3 at 298 K of $[\text{Zn}(\text{HL}^2)_2]$ (2).

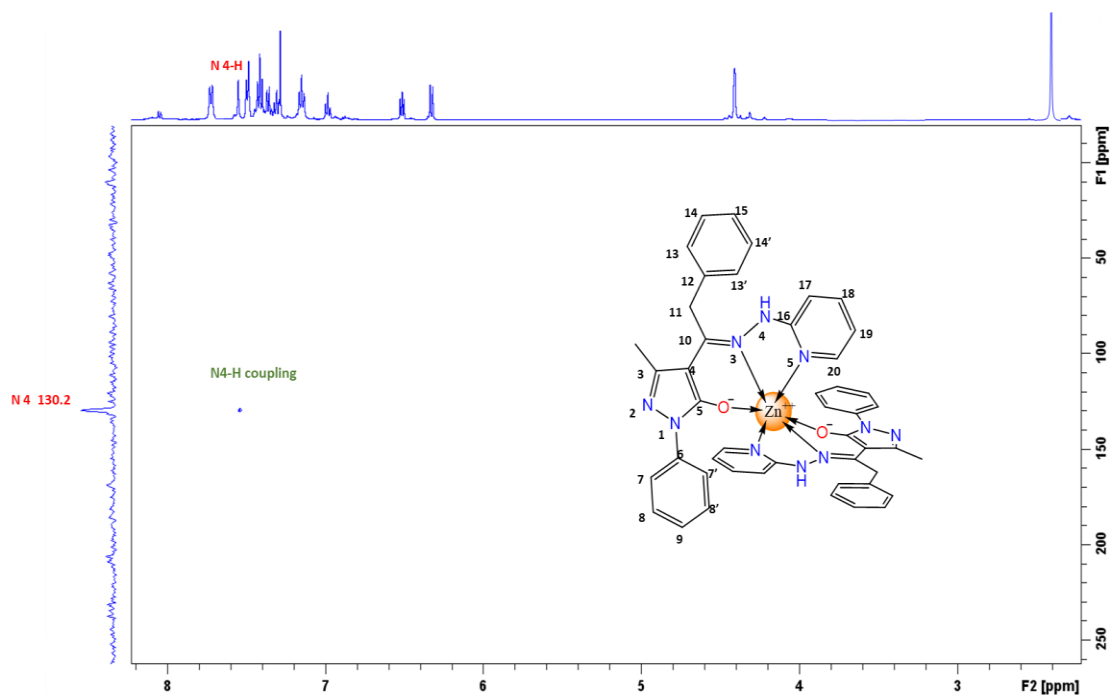


Figure 146. $\{^1\text{H}, ^{15}\text{N}\}$ -HSQC spectrum in CDCl_3 at 298 K of $[\text{Zn}(\text{HL}^2)_2]$ (2).

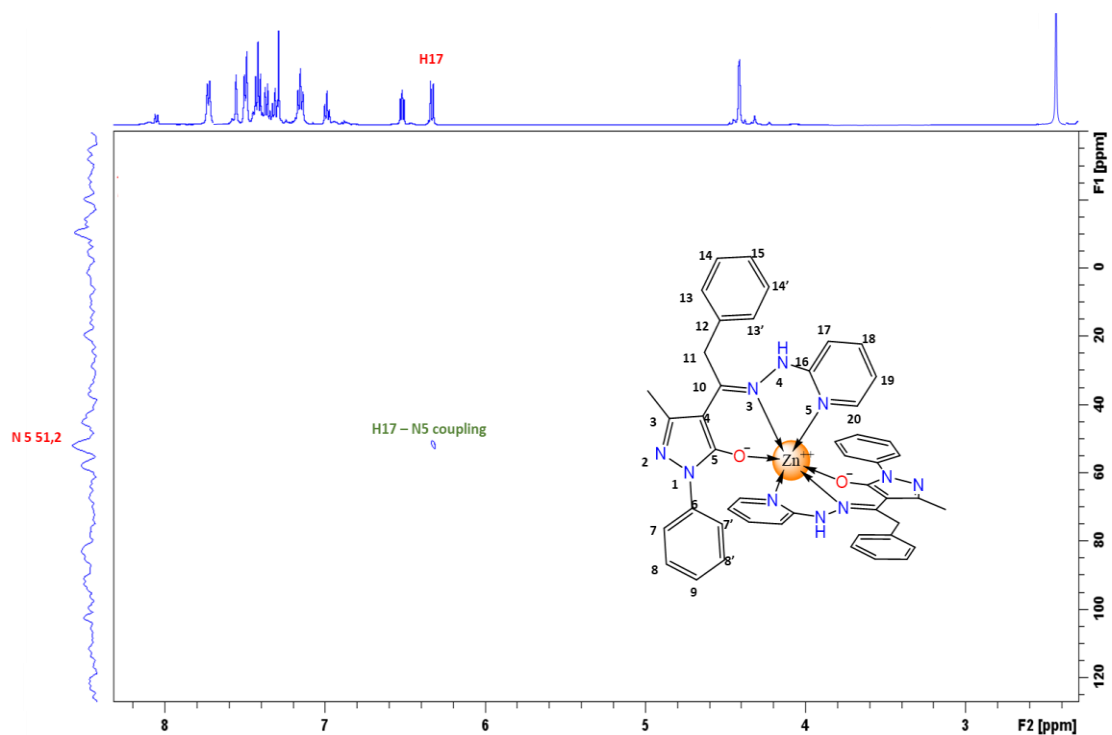


Figure 147. $\{^1\text{H}, ^{15}\text{N}\}$ -HMBC spectrum in CDCl_3 at 298 K of $[\text{Zn}(\text{HL}^2)_2]$ (2).

Table 16. Details of data collection and structure refinements for proligands H_2L^1 and H_2L^2 .

	H₂L₁	H₂L₂
formula	C ₂₅ H ₂₁ N ₄ O F ₃	C ₂₃ H ₂₁ N ₅ O
<i>Mr</i>	450.46	383.45
crystal size [mm]	0.40 x 0.20 x 0.04	0.30 x 0.20 x 0.14
crystal system	Monoclinic	Triclinic
space group	<i>P</i> 2 ₁ / <i>c</i>	<i>P</i> -1
<i>a</i> [Å]	11.153(3)	8.9495(4)
<i>b</i> [Å]	22.940(6)	9.9398(5)
<i>c</i> [Å]	9.084(3)	12.5083(6)
α [°]	90	112.787(2)
β [°]	97.324(16)	91.215(2)
γ [°]	90	102.879(2)
<i>V</i> [Å ³]	2305.1(11)	992.86(8)
<i>Z</i>	4	2
ρ calcd [gcm ⁻³]	1.295	1.283
μ [mm ⁻¹]	0.098	0.082
θ range [°]	2.429 to 24.974	2.269 to 25.016
data collected	33167	10490
unique data, <i>R</i> _{int}	4001, 0.0758	3474, 0.0267
obs. data [<i>I</i> > 2 σ (<i>I</i>)]	2155	2525
no. Parameters	326	271
restraints	0	48
<i>R</i> ₁ [<i>I</i> > 2 σ (<i>I</i>)]	0.0543	0.0478
<i>wR</i> ₂ [all data]	0.1455	0.1496
GOF	1.001	1.026

Table 17. Details of data collection and structure refinements for complexes **1** and **5**.

	1	5
formula	C ₅₄ H ₅₆ F ₆ N ₈ O ₆ Zn	C ₃₆ H ₃₀ N ₄ O ₄ Cu
<i>Mr</i>	1092.43	646.18
crystal size [mm]	0.40 x 0.20 x 0.06	0.40 x 0.20 x 0.10
crystal system	Triclinic	Triclinic
space group	<i>P</i> -1	<i>P</i> -1
<i>a</i> [Å]	9.941(3)	6.4458(2)
<i>b</i> [Å]	11.872(4)	9.3271(4)
<i>c</i> [Å]	12.109(5)	13.4708(5)
α [°]	95.200(17)	110.043(2)
β [°]	101.884(17)	96.231(2)
γ [°]	105.333(16)	95.695(2)
<i>V</i> [Å ³]	1332.6(8)	748.21(5)
<i>Z</i>	1	1
ρ calcd [gcm ⁻³]	1.361	1.434
μ [mm ⁻¹]	0.539	0.778
θ range [°]	2.303 to 25.678	3.258 to 26.372
data collected	11965	15703
unique data, <i>R</i> _{int}	5012, 0.0642	3045, 0.0260
obs. data [<i>I</i> > 2 σ (<i>I</i>)]	2600	2627
no. Parameters	362	206
restraints	0	0
<i>R</i> ₁ [<i>I</i> > 2 σ (<i>I</i>)]	0.0543	0.0341
<i>wR</i> ₂ [all data]	0.1314	0.0931
GOF	0.942	1.057

Acknowledgments

To conclude this thesis, I would like to thank all those who have contributed to its realization and accompanied me on this journey. Firstly, I would like to thank my supervisor Prof. **Riccardo Pettinari** who allowed me to embark on this journey by making me part of his research group. A special thanks also goes to the other professors in the research group, Prof. **Fabio Marchetti**, Prof. **Corrado Di Nicola**, and Prof. **Claudio Pettinari**, for their support in research, invaluable advices, priceless teachings, and assistance in all the various projects undertaken. An immense thanks also goes to Dr. **Alessia Tombesi** who, in the three years we spent together, was able to play the role of colleague, friend, and tutor, sharing her invaluable technical and human experience, allowing me to adapt better to the dynamics of the research world. I would like to particularly thank Dr. **Stefania Scuri** for her patience and availability, whose testimony I hope will also be impressed on these pages. I cannot leave out my fellow colleagues Noemi Pagliaricci, Sara Pagliaricci, and Paolo Montebello with whom I shared the laboratory and who helped and supported me in every way during the most difficult period of this journey. For the same reason, I would like to mention my other fellow doctoral colleagues in my research group and beyond, especially Patrizio Campitelli, Giorgio Mercuri, Sonila Xhafa, Leonardo Sbrascini, Andrea Rossi, Antunes Staffolani, Roberto Giacomantonio, Benedetta Bassetti, Lucia Lenti and Jo' Del Gobbo.

I would like to express my sincere gratitude to Prof. **Agustín Galindo** and all the members of his research group for hosting me in his laboratory at the Departamento de Química Inorgánica de la Universidad de Sevilla, for his commitment to imparting his knowledge of computational chemistry, and for making me feel immediately integrated into the group, making the period spent in Seville one of the most beautiful experiences to remember.

Finally, I conclude by thanking the entire University of Camerino and TechPol srl for the financial support and the opportunity to learn and apply myself in various fields of chemistry.

Bibliography

- 1 L. Claisen and E. F. Ehrhardt, Ueber die Darstellung des Acetylacetons und seiner Homologen, *Ber. Dtsch. Chem. Ges.*, 1889, **22**, 1009–1019.
- 2 S. Fustero, M. Sánchez-Roselló, P. Barrio and A. Simón-Fuentes, From 2000 to mid-2010: A fruitful decade for the synthesis of pyrazoles, *Chem Rev*, 2011, **111**, 6984–7034.
- 3 S. Liu, X. Bao and B. Wang, Pyrazolone: a powerful synthon for asymmetric diverse derivatizations, *Chem. Commun*, 2018, **54**, 11515.
- 4 M. H. Norman, L. Liu, M. Lee, N. Xi, I. Fellows, N. D. D'Angelo, C. Dominguez, K. Rex, S. F. Bellon, T. S. Kim and I. Dussault, Structure-based design of novel class II c-Met inhibitors: 1. Identification of pyrazolone-based derivatives, *J Med Chem*, 2012, **55**, 1858–1867.
- 5 T. Takahashi, T. Nagase, T. Sasaki, A. Nagumo, K. Shimamura, Y. Miyamoto, H. Kitazawa, M. Kanesaka, R. Yoshimoto, K. Aragane, S. Tokita and N. Sato, Synthesis and evaluation of a novel indole-dione class of long chain fatty acid elongase 6 (ELOVL6) inhibitors, *J Med Chem*, 2009, **52**, 3142–3145.
- 6 K. J. Duffy, M. G. Darcy, E. Delorme, S. B. Dillon, D. F. Eppley, C. Erickson-Miller, L. Giampa, C. B. Hopson, Y. Huang, R. M. Keenan, P. Lamb, L. Leong, N. Liu, S. G. Miller, A. T. Price, J. Rosen, R. Shah, T. N. Shaw, H. Smith, K. C. Stark, S. S. Tian, C. Tyree, K. J. Wiggall, L. Zhang and J. I. Luengo, Hydrazinonaphthalene and azonaphthalene thrombopoietin mimics are nonpeptidyl promoters of megakaryocytopoiesis, *J Med Chem*, 2001, **44**, 3730–3745.
- 7 P. Chiba, W. Holzer, M. Landau, G. Bechmann, K. Lorenz, B. Plagens, M. Hitzler, E. Richter and G. Ecker, Substituted 4-Acylpyrazoles and 4-Acylpyrazolones: Synthesis and Multidrug Resistance-Modulating Activity, *J Med Chem*, 1998, **41**, 4001–4011.
- 8 K. L. Kees, J. J. Fitzgerald, K. E. Steiner, J. F. Mattes, B. Mihan, T. Tosi, D. Mondoro and M. L. McCaleb, New Potent Antihyperglycemic Agents in db/db Mice: Synthesis and Structure–Activity Relationship Studies of (4-Substituted benzyl)(trifluoromethyl)pyrazoles and -pyrazolones, *J Med Chem*, 1996, **39**, 3920–3928.

- 9 D. Costa, A. P. Marques, R. L. Reis, J. L. F. C. Lima and E. Fernandes, Inhibition of human neutrophil oxidative burst by pyrazolone derivatives, *Free Radic Biol Med*, 2006, **40**, 632–640.
- 10 M. Himly, B. Jahn-Schmid, K. Pittertschatscher, B. Bohle, K. Grubmayr, F. Ferreira, H. Ebner and C. Ebner, Ig E-mediated immediate-type hypersensitivity to the pyrazolone drug propyphenazone, *J. Allergy Clin. Immunol.*, 2003, **111**, 882–888.
- 11 T. W. Wu, L. H. Zeng, J. Wu and K. P. Fung, Myocardial protection of MCI-186 in rabbit ischemia-reperfusion, *Life Sci*, 2002, **71**, 2249–2255.
- 12 T. Watanabe, S. Yuki, M. Egawa and H. Nishi, Protective effects of MCI-186 on cerebral ischemia: possible involvement of free radical scavenging and antioxidant actions., *J. Pharmacol Exp. Ther.*
- 13 B. S. Jensen, The synthesis of 1-Phenyl-2-methyl-4-acyl-pyrazolone, *Acta Chem. Scand.*, 1959, **13**, 1668.
- 14 P. F. Liguori, A. Valentini, M. Palma, A. Bellusci, S. Bernardini, M. Ghedini, M. L. Panno, C. Pettinari, F. Marchetti, A. Crispini and D. Pucci, Non-classical anticancer agents: synthesis and biological evaluation of zinc(II) heteroleptic complexes, *Dalton Trans.*, 2010, **39**, 4205–4212.
- 15 R. Pettinari, C. Pettinari, F. Marchetti, B. W. Skelton, A. H. White, L. Bonfili, M. Cuccioloni, M. Mozzicafreddo, V. Cecarini, M. Angeletti, M. Nabissi and A. M. Eleuteri, Arene–Ruthenium(II) Acylpyrazolonato Complexes: Apoptosis-Promoting Effects on Human Cancer Cells, *J. Med. Chem*, 2014, **57**, 6.
- 16 B. Ayo Omotowa and M. Adediran Mesubi, Correlation of Coordination Geometries and Stability Factors in Organotin(IV) Derivatives of 4-Acylpyrazol-5-onates with their Fungicidal (Mycelial Control) and Insecticidal (Topical Toxicity, Larvicidal and Ovicidal) Activities, *Appl Organomet Chem*, 1997, **11**, 1–10.
- 17 A. Joshi, S. Vermaa, R. B. Gaurb and R. R. Sharma, Di-n-butyltin(IV) Complexes Derived from Heterocyclic β -diketones and N-Phthaloyl Amino Acids: Preparation, Biological Evaluation, Structural Elucidation Based upon Spectral [IR,NMR(^1H , ^{13}C , ^{19}F and ^{119}Sn)] Studies., *Bioinorg. Chem. Appl.*, 2005, **3**, 3–4.

- 18 T. Filipský, P. Mladěnka, K. MacÁková, R. Hrdina, L. Saso, F. Marchetti and C. Pettinari, In vitro characteristics of 1-phenyl-3-methyl-4-acylpyrazol-5-ones iron chelators, *Biochimie*, 2012, **94**, 125–131.
- 19 F. Caruso, C. Pettinari, F. Marchetti, M. Rossi, C. Opazo, S. Kumar, S. Balwani and B. Ghosh, Inhibitory effect of β -diketones and their metal complexes on TNF- α induced expression of ICAM-1 on human endothelial cells, *Bioorg Med Chem*, 2009, **17**, 6166–6172.
- 20 D. Castagnolo, A. de Logu, M. Radi, B. Bechi, F. Manetti, M. Magnani, S. Supino, R. Meleddu, L. Chisu and M. Botta, Synthesis, biological evaluation and SAR study of novel pyrazole analogues as inhibitors of Mycobacterium tuberculosis, *Bioorg Med Chem*, 2008, **16**, 8587–8591.
- 21 E. C. Okafor, The metal complexes of heterocyclic β -diketones and their derivatives—V. The synthesis, structure and i.r. spectral studies of metal(II) complexes of 1-phenyl-3-methyl-4-acetyl-pyrazolone-5 (HPMAP), *Spectrochim Acta A*, 1981, **37**, 939–944.
- 22 E. C. Okafor, The metal complexes of heterocyclic β -diketones and their derivatives—VI. The synthesis, structure and i.r. spectral studies of some new metal(II) complexes of 1-phenyl-3-methyl-4-benzoyl-pyrazolone-5 (HPMBP), *Spectrochim Acta A*, 1981, **37**, 945–950.
- 23 C. Pettinari, F. Marchetti, A. Cingolani, D. Leonesi, E. Mundorff, M. Rossi and F. Caruso, Tin(IV) and organotin(IV) derivatives of novel β -diketones. III Diorgano- and dihalotin(IV) complexes of 1,3-dimethyl-4-R(C=O)-pyrazol-5-one (R=CH₃, C₆H₅) and the crystal structure of trans-dicyclohexylbis(1,3-dimethyl-4-acetylpyrazolon-5-ato)tin(IV), *J Organomet Chem*, 1998, **557**, 187–205.
- 24 B. Bovio, A. Cingolani, F. Marchetti and C. Pettinari, Tin(IV) and organotin(IV) complexes containing the anion of some substituted-3-methyl-4-acyl-5-pyrazolones. Crystal structure of dimethylbis(1-phenyl-3-methyl-4-benzoyl pyrazolon-5-ato)tin(IV), *J Organomet Chem*, 1993, **458**, 39–48.
- 25 C. Pettinari, F. Marchetti, A. Cingolani, A. Gindulyte, L. Massa, M. Rossi and F. Caruso, syn-anti Conversion in Octahedral Bis(β -diketonato)diorganotin(IV) Derivatives

- Containing Fluorinated 4-Acyl-5-pyrazolonato Donors, *Eur. J. Inorg. Chem.*, 2001, 2171–2180.
- 26 A. Cingolani, Effendy, F. Marchetti, C. Pettinari, R. Pettinari, B. W. Skelton and A. H. White, Silver coordination chemistry of a new versatile ‘Janus’-type N₂O₂-bichelating donor, formation of an unprecedented supramolecular network of binuclear silver building blocks containing a five-coordinate β -diketonate, and isolation of unexpected silver-tin-silver heterotrimetallic complexes from silver metathesis reactions, *Inorg Chem*, 2004, **43**, 4387–4399.
- 27 G. Bombiere, A. Polo, W. Jia-Fu, W. Jinguang and X. Guang-Xian, Synthesis and characterization of a ytterbium complex with diphenylacetylpyrazolone Yb(DPAP)₃·(H₂O)₂·3EtOH, *Inorganica Chim Acta*, 1987, **132**, 263–271.
- 28 F. Marchetti, C. Pettinari, A. Cingolani, R. Pettinari, M. Rossi and F. Caruso, Organotin(IV) derivatives of novel β -diketones: Part V. Synthesis and characterization of di- and triorganotin(IV) derivatives of 4-acyl-5-pyrazolones modified in position 3 of the pyrazole. Crystal structure of (1,3-diphenyl-4-benzoyl-pyrazolon-5-ato)triphenyltin(IV), *J Organomet Chem*, 2002, **645**, 134–145.
- 29 A. Cingolani, Effendy, F. Marchetti, C. Pettinari, R. Pettinari, B. W. Skelton and A. H. White, Silver(I) derivatives with new functionalised acylpyrazolonates, *Inorganica Chim Acta*, 2002, **329**, 100–112.
- 30 C. Pettinari, F. Marchetti, R. Pettinari, A. Pizzabiocca, A. Drozdov, S. I. Troyanov and V. Vertlib, Reactivity of rhodium- β -diketonato cyclooctadiene derivatives with mono- and di-phosphines. Synthesis, structural and spectroscopic characterization of Rh(I) and Rh(III) species containing unsymmetrical β -diketonate and P-donor ligands, *J Organomet Chem*, 2003, **688**, 216–226.
- 31 C. Pettinari, F. Marchetti, A. Gregori, A. Cingolani, J. Tanski, M. Rossi and F. Caruso, Tin(IV) and organotin(IV) derivatives of novel β -diketones I. Dialkyltin(IV) complexes of 1-phenyl-3-methyl-4-R'(C=O)-pyrazol-5-one (R' = CCl₃, O-CH₃, O-C₂H₅, O-i-C₃H₇, O-C₇H₇). Crystal and molecular structure of trans-dimethylbis[1-phenyl-3-methyl-4-i-propoxycarbonyl-pyrazolon-5-ato]tin(IV), *Inorganica Chim. Acta*, 1997, **257**, 37–48.

- 32 C. Pettinari, F. Marchetti, A. Cingolani, A. Lorenzotti, E. Mundorff, M. Rossi and F. Caruso, Tin(IV) and organotin(IV) derivatives of novel β -diketones: II. Mono- and diaryltin(IV) complexes of 1-phenyl-3-methyl-4-R(C \square O)-pyrazol-5-one (R=CCl₃, OCH₃, OC₂H₅). Crystal and molecular structure of trans-dibenzylbis(1-phenyl-3-methyl-4-methoxycarbonyl-pyrazolon-5-ato)tin(IV), (C₇H₇)₂Sn(QOMe)₂, *Inorganica Chim Acta*, 1997, **262**, 33–46.
- 33 S. Mohanty, S. R. P. Sy, S. Rao and M. As, Fungicidal activity & synthesis of 5-thiopyrazolones & compounds having alpha -pyrone attached to pyrazolin nucleus., *Indian J. Chem. B*, 1977, **15**, 1146–1148.
- 34 W. Holzer, K. Mereiter and B. Plagens, 4-acyl-5-methyl-2-phenylpyrazolones: NMR and X-ray structure investigations, *Heterocycles*, 1999, **2**, 799–818.
- 35 S. Gelin, B. Chantegrel and A. I. Nadi, Synthesis of 4-(Acylacetyl)-1-phenyl-2-pyrazolin-5-ones from 3-Acyl-2H-pyran-2,4(3H)-diones. Their Synthetic Applications to Functionalized 4-Oxopyrano[2,3-c]pyrazole Derivatives, *J. Org. Chem.*, 1983, **48**, 4078–4082.
- 36 M. O'Connell, C. Ramsay and P. Steel, Heterocyclic Tautomerism. II. 4-Acylpyrazolones. X-Ray Crystal Structures of 4-Benzoyl-5-methyl-2-phenylpyrazol-3(2H)-one and 4-Acetoacetyl-3-methyl-1-phenylpyrazol-5-ol, *Aust J Chem*, 1985, **38**, 401–409.
- 37 S. Miyazaki, H. Mukai, S. Umetani, S. Kihara and M. Matsui, Steric Effects of Polymethylene Chain Length on the Liquid-Liquid Extraction of Copper(II) with Bis(4-acylpyrazol-5-one) Derivatives, *Inorg Chem*, 1989, **28**, 3014–3017.
- 38 T. Yoshikuni, Cerium complexes with phthaloylbis(pyrazolone) ligands as an efficient catalysts for cresols dioxygenation, *J Mol Catal A Chem*, 1999, **148**, 285–288.
- 39 C. Pettinari, F. Marchetti, R. Pettinari, D. Martini, A. Drozdov and S. Troyanov, The interaction of organotin(IV) acceptors with a benzoic acid containing two pyrazolone groups, *Journal of the Chemical Society, Dalton Trans*, 2001, **0**, 1790–1797.
- 40 C. Pettinari, F. Marchetti, A. Drozdov, V. Vertlib and S. Troyanov, Interaction of Rh(I) with a new polydentate O₄,N-donor pyrazolone able to form mononuclear, dinuclear and heterobimetallic compounds, *Inorg Chem Commun*, 2001, **4**, 290–293.

- 41 D. W. Johnson, J. Xu, R. W. Saalfrank, K. N. Raymond, R. W. Saalfrank, K. N. Raymond, D. W. Johnson, J. Xu and F. J. Hollander, Self-Assembly of a Three-Dimensional [Ga₆(L₂)₆] Metal-Ligand ‘Cylinder’, *Angew. Chem. Int. Ed.*, 1999, **38**, 2882–2885.
- 42 T. N. Parac, M. Scherer and K. N. Raymond, Lord of the Rings: An Octameric Lanthanum Pyrazolonate Cluster, *Angew. Chem. Int. Ed.*, 2000, **39**, 2745–2747.
- 43 S. Yamazaki, M. Kanada, Y. Yanase, C. Fukumori, K. Ogura, T. Saeki and S. Umetani, A simple synthesis of novel extraction reagents. 4-Acyl-5-pyrazolone-substituted crown ethers, *J Chem Soc Perkin 1*, 1999, **0**, 693–696.
- 44 N. Raman, S. Johnson Raja and A. Sakthivel, Transition metal complexes with Schiff-base ligands: 4-aminoantipyrine based derivatives—a review, *J Coord Chem*, 2009, **62**, 691–709.
- 45 Y. Akama, M. Shiro, T. Ueda, M. Kajitani and IUCr, Keto and Enol Tautomers of 4-Benzoyl-3-methyl-1-phenyl-5(2H)-pyrazolone, *Acta Cryst*, 1995, **51**, 1310–1314.
- 46 J. Guard and P. Steel, Heterocyclic Tautomerism. VII. X-Ray Structures of Two Crystalline Tautomers of 4-Cinnamoyl-1,3-dimethylpyrazol-5-one, *Aust J Chem*, 1994, **47**, 1453–1459.
- 47 A. Cingolani, Effendy, F. Marchetti, C. Pettinari, R. Pettinari, B. W. Skelton and A. H. White, First structurally characterized silver(I) derivatives with nonfluorinated β-diketones, *Inorg Chem*, 2002, **41**, 1151–1161.
- 48 A. Cingolani, F. Marchetti, C. Pettinari, R. Pettinari, B. W. Skelton, N. Somers and A. H. White, Copper(I) monophosphine complexes with functionalized acylpyrazolonate ligands: Syntheses of heterobimetallic Cu–Zn and Cu–Ru adducts, *Polyhedron*, 2006, **25**, 124–133.
- 49 P. N. Remya, C. H. Suresh and M. L. P. Reddy, Rapid reduction and complexation of vanadium by 1-phenyl-3-methyl-4-toluoyl-5-pyrazolone: Spectroscopic characterization and structure modelling, *Polyhedron*, 2007, **26**, 5016–5022.
- 50 C. Pettinari, F. Marchetti, R. Pettinari, P. Natanti, A. Drozdov, S. Semenov, S. I. Troyanov and V. Zolin, Syntheses, spectroscopic characterization and X-ray structural studies of lanthanide complexes with adamantyl substituted 4-acylpyrazol-5-one, *Inorganica Chim Acta*, 2006, **359**, 4063–4070.

- 51 M. Shi, F. Li, T. Yi, D. Zhang, H. Hu and C. Huang, Tuning the triplet energy levels of pyrazolone ligands to match the 5D0 level of europium(III), *Inorg Chem*, 2005, **44**, 8929–8936.
- 52 F. Marchetti, J. Palmucci, C. Pettinari, R. Pettinari, F. Condello, S. Ferraro, M. Marangoni, A. Crispini, S. Scuri, I. Grappasonni, M. Cocchioni, M. Nabissi, M. R. Chierotti and R. Gobetto, Novel Composite Plastics Containing Silver(I) Acylpyrazolonato Additives Display Potent Antimicrobial Activity by Contact, *Chem Eur J*, 2015, **21**, 836–850.
- 53 E. Uhlemann, U. Schilde and F. Weller, Calcium- und Bariumkomplexe mit 1-Phenyl-3-methyl-4-benzoylpyrazol-5-on, *Z Naturforsch B*, 1995, **50**, 31–36.
- 54 A. Cingolani, F. Marchetti, C. Pettinari, R. Pettinari, B. W. Skelton and A. H. White, A 4-acyl-5-pyrazolone ligand (HQ) in N-unidentate coordination mode in a Rh(CO)2Cl(HQ)-type complex, *Inorg Chem Commun*, 2004, **7**, 235–237.
- 55 C. Pettinari, F. Marchetti, A. Cingolani, D. Leonesi, E. Mundorff, M. Rossi and F. Caruso, Tin(IV) and organotin(IV) derivatives of novel β -diketones. III Diorgano- and dihalotin(IV) complexes of 1,3-dimethyl-4-R(C=O)-pyrazol-5-one (R=CH₃, C₆H₅) and the crystal structure of trans-dicyclohexylbis(1,3-dimethyl-4-acetylpyrazolon-5-ato)tin(IV), *J Organomet Chem*, 1998, **557**, 187–205.
- 56 E. C. Okafor, A. B. Uzoukwu, P. B. Hitchcock and J. D. Smith, Pyrazolonato complexes of uranium. Crystal structures of bis-oxobis(1-phenyl-3-methyl-4-acetylpyrazol-5-onato)aquouranium(VI) and Bis-oxobis(1-phenyl-3-methyl-4-benzoylpyrazol-5-onato)(propanol)uranium(VI), *Inorganica Chim Acta*, 1990, **172**, 97–103.
- 57 C. Pettinari, F. Marchetti, A. Cingolani, D. Leonesi, S. Troyanov and A. Drozdov, New coordination compounds derived from barium(II) and the anionic 4- tert -butylacetyl-3-methyl-1-phenylpyrazol-5-onate ligand (Q⁻). Crystal and molecular structure of [Ba₂Q₄(H₂O)₄], [Ba₂Q₄(Him)₄], [BaQ₂(tetraglyme)] (tetraglyme = 2,5,8,11,14-pentaoxapentadecane) and [BaQ₂(phen)₂], *J Chem Soc, Dalton Trans*, 1999, **0**, 1555–1562.
- 58 F. Marchetti, C. Pettinari, R. Pettinari, A. Cingolani, A. Drozdov and S. Troyanov, A new family of ionic dinuclear strontium (imH₂)₂[Sr₂(Q)₆] compounds (imH = imidazole; QH = 1-phenyl-3-methyl-4-acylpyrazol-5-one), *J Chem Soc, Dalton Trans*, 2002, 2616–2623.

- 59 M. F. Mahon, K. C. Molloy, B. A. Omotowa and M. A. Mesubi, Organotin(IV) derivatives of acylpyrazol-5-ones, *J Organomet Chem*, 1996, **511**, 227–237.
- 60 B. A. Uzoukwu, P. U. Adiukwu, S. S. Al-Juaid, P. B. Hitchcock and J. D. Smith, Pyrazolonato complexes of lead. Crystal structures of bis(1-phenyl-3-methyl-4-acetyl pyrazolonato)lead(II) and bis(1-phenyl-3-methyl-4-butanoylpyrazolonato)lead(II), *Inorganica Chim Acta*, 1996, **250**, 173–176.
- 61 A. Jain, S. Saxena, A. K. Rai, R. Bohra and H. Wang, Preparation, structural chemistry and spectroscopic (IR, ¹H & ¹³C) characterization of certain lead(II) complexes of sterically demanding heterocyclic β-diketones. X-ray crystal structure of bis[4-acetyl-2,4-dihydro-5-methyl-2-phenyl-3H-pyrazol-3-onato) lead(II), C₂₄H₂₂N₄O₄Pb, *Main Group Met Chem*, 2003, **26**, 1–11.
- 62 A. Cingolani, Effendy, F. Marchetti, C. Pettinari, R. Pettinari, B. W. Skelton and A. H. White, First structurally characterized silver(I) derivatives with nonfluorinated β-diketones, *Inorg Chem*, 2002, **41**, 1151–1161.
- 63 C. Pettinari, F. Marchetti, R. Pettinari, A. Cingolani, E. Rivarola, C. Phillips, J. Tanski, M. Rossi and F. Caruso, Tin(II) and Lead(II) 4-Acyl-5-pyrazolonates: Synthesis, Spectroscopic and X-ray Structural Characterization, *Eur J Inorg Chem*, 2004, **2004**, 3484–3497.
- 64 A. Cingolani, Effendy, F. Marchetti, C. Pettinari, R. Pettinari, B. W. Skelton and A. H. White, Silver coordination chemistry of a new versatile ‘Janus’-type N₂O₂-bichelating donor, formation of an unprecedented supramolecular network of binuclear silver building blocks containing a five-coordinate β-diketonate, and isolation of unexpected silver-tin-silver heterotrimetallic complexes from silver metathesis reactions, *Inorg Chem*, 2004, **43**, 4387–4399.
- 65 T. Watanabe, S. Yuki, M. Egawa and H. Nishi, Protective effects of MCI-186 on cerebral ischemia: possible involvement of free radical scavenging and antioxidant actions, *J Pharmacol Exp Ther.*, 1994, **268**, 1597-1604.
- 66 H. Kawai, H. Nakai, M. Suga, S. Yuki, T. Watanabe and K.-I. Saito, Effects of a Novel Free Radical Scavenger, MCI-186, on Ischemic Brain Damage in the Rat Distal Middle Cerebral Artery Occlusion Model, *J Pharmacol Exp Ther*, 1997, **281**, 921-927.

- 67 T.-W. Wu, L.-H. Zeng, J. Wu and K.-P. Fung, Myocardial protection of MCI-186 in rabbit ischemia–reperfusion, *Life Sci*, 2002, **71**, 2249–2255.
- 68 M. Himly, B. Jahn-Schmid, K. Pittertschatscher, B. Bohle, K. Grubmayr, F. Ferreira, H. Ebner and C. Ebner, IgE-mediated immediate-type hypersensitivity to the pyrazolone drug propyphenazone, *J. Allergy Clin. Immunol.*, 2003, **111**, 882–888.
- 69 D. Costa, A. P. Marques, R. L. Reis, J. L. F. C. Lima and E. Fernandes, Inhibition of human neutrophil oxidative burst by pyrazolone derivatives, *Free Radic Biol Med*, 2006, **40**, 632–640.
- 70 J. B. Field, E. C. Dolendo, A. Mã, • Reles and B. H. Ershoff, Evaluation of the Effect of a Pyrazolone Derivative KB-95 on the Toxicity and Activity of Some Anticancer Drugs¹, *Cancer Res*, 1966, **26**, 1371–1373.
- 71 D. Castagnolo, F. Manetti, M. Radi, B. Bechi, M. Pagano, A. de Logu, R. Meleddu, M. Saddi and M. Botta, Synthesis, biological evaluation, and SAR study of novel pyrazole analogues as inhibitors of Mycobacterium tuberculosis: Part 2. Synthesis of rigid pyrazolones, *Bioorg Med Chem*, 2009, **17**, 5716–5721.
- 72 F. Manetti, M. Magnani, D. Castagnolo, L. Passalacqua, M. Botta, F. Corelli, M. Saddi, D. Deidda and A. de Logu, Ligand-Based Virtual Screening, Parallel Solution-Phase and Microwave-Assisted Synthesis as Tools to Identify and Synthesize New Inhibitors of Mycobacterium tuberculosis, *ChemMedChem*, 2006, **1**, 973–989.
- 73 D. Castagnolo, A. de Logu, M. Radi, B. Bechi, F. Manetti, M. Magnani, S. Supino, R. Meleddu, L. Chisu and M. Botta, Synthesis, biological evaluation and SAR study of novel pyrazole analogues as inhibitors of Mycobacterium tuberculosis, *Bioorg Med Chem*, 2008, **16**, 8587–8591.
- 74 F. Caruso, C. Pettinari, F. Marchetti, M. Rossi, C. Opazo, S. Kumar, S. Balwani and B. Ghosh, Inhibitory effect of β -diketones and their metal complexes on TNF- α induced expression of ICAM-1 on human endothelial cells, *Bioorg Med Chem*, 2009, **17**, 6166–6172.
- 75 T. Filipský, P. Mladěnka, K. MacÁková, R. Hrdina, L. Saso, F. Marchetti and C. Pettinari, In vitro characteristics of 1-phenyl-3-methyl-4-acylpyrazol-5-ones iron chelators, *Biochimie*, 2012, **94**, 125–131.

- 76 L. Y. Xu, N. Li, J. M. Li and W. Dong, Synthesis, Structure, Antibacterial and Spectroscopic Properties of a Zinc(II) Complex with the Ligand 4-Heptanoyl-pyrazol-5-one, *Z Anorg Allg Chem*, 2013, **639**, 1800–1803.
- 77 A. Joshi, S. Verma, R. B. Gaur and R. R. Sharma, Di-n-butyltin(IV) Complexes Derived from Heterocyclic β -diketones and N-Phthaloyl Amino Acids: Preparation, Biological Evaluation, Structural Elucidation Based upon Spectral [IR, NMR (^1H , ^{13}C , ^{19}F and ^{119}Sn)] Studies, *Bioinorg Chem Appl*, 2005, **3**, 201–215.
- 78 B. T. Thaker, K. R. Surati and C. K. Modi, Synthesis, spectral, thermal, and antibacterial investigation of mixed ligand complexes of oxovanadium(IV), *Russ J Coord Chem*, 2011, **34**, 25–33.
- 79 B. Ayo Omotowa and M. Adediran Mesubi, Correlation of Coordination Geometries and Stability Factors in Organotin(IV) Derivatives of 4-Acylpyrazol-5-onates with their Fungicidal (Mycelial Control) and Insecticidal (Topical Toxicity, Larvicidal and Ovicidal) Activities, *Appl Organomet Chem*, 1997, **11**, 1–10.
- 80 P. F. Liguori, A. Valentini, M. Palma, A. Bellusci, S. Bernardini, M. Ghedini, M. L. Panno, C. Pettinari, F. Marchetti, A. Crispini and D. Pucci, Non-classical anticancer agents: synthesis and biological evaluation of zinc(ii) heteroleptic complexes, *Dalton Trans*, 2010, **39**, 4205–4212.
- 81 R. Pettinari, C. Pettinari, F. Marchetti, B. W. Skelton, A. H. White, L. Bonfili, M. Cuccioloni, M. Mozzicafreddo, V. Cecarini, M. Angeletti, M. Nabissi and A. M. Eleuteri, Arene-ruthenium(II) acylpyrazolonato complexes: Apoptosis-promoting effects on human cancer cells, *J Med Chem*, 2014, **57**, 4532–4542.
- 82 C. Deng, S. Abdurehman, L. Liu, D. Wu, D. Jia and R. Zhou, Synthesis, photoisomerization properties and thermal bleaching kinetics of pyrazolones containing 3-cyanobenzal, *Spectrochim Acta A Mol Biomol Spectrosc*, 2015, **148**, 318–323.
- 83 J. Guo, H. Yuan, D. Jia, M. Guo and Y. Li, Synthesis and improved photochromic properties of pyrazolones in the solid state by incorporation of halogen, *Spectrochim Acta A Mol Biomol Spectrosc*, 2017, **171**, 149–154.

- 84 H. Chai, G. Liu, L. Liu and D. Jia, Synthesis and spectroscopic study on photochromism of a new thiosemicarbazone compound containing pyrazolone, *Spectrochim Acta A Mol Biomol Spectrosc*, 2005, **61**, 2590–2594.
- 85 H. Liu, J. Guo, D. Jia, M. Guo, F. Le, L. Liu, D. Wu and F. Li, Modulation of a solid-state reversible fluorescent photoswitching based on a controllable photochromic pyrazolones, *J Solid State Chem*, 2014, **216**, 73–78.
- 86 G. Q. Wang, J. C. Qin, C. R. Li and Z. Y. Yang, A highly selective fluorescent probe for Al³⁺ based on quinoline derivative, *Spectrochim Acta A Mol Biomol Spectrosc*, 2015, **150**, 21–25.
- 87 S. Parihar, V. P. Boricha and R. N. Jadeja, Pyrazolone as a recognition site: Rhodamine 6G-based fluorescent probe for the selective recognition of Fe³⁺ in acetonitrile–aqueous solution, *Luminescence*, 2015, **30**, 168–174.
- 88 I. C. Vasiliu, I. Ionita, A. Matei, M. Elisa, R. Iordanescu, I. Feraru and A. Emandi, Homogenous smooth sol gel films doped with organic compounds for nonlinear optics, *Thin Solid Films*, 2016, **601**, 73–75.
- 89 K. G. Sangeetha, K. K. Aravindakshan and K. P. Safna Hussan, Insight into the theoretical and experimental studies of 1-phenyl-3-methyl-4-benzoyl-5-pyrazolone N(4)-methyl-N(4)-phenylthiosemicarbazone - A potential NLO material, *J Mol Struct*, 2017, **1150**, 135–145.
- 90 O. T. Gunkara, E. Bagdatli and N. Ocal, Synthesis of New Pyrazolone Dyes, *J Chem Res*, 2013, **37**, 227–231.
- 91 E. Abdel-Latif and H. E. Gaffer, Effect of gamma irradiation on the color properties of synthetic fabrics dyed by arylazo-pyrazolone disperse dyes, *Text Inst*, 2016, **108**, 653–656.
- 92 Y. P. Zhang, Y. Li, G. C. Xu, J. Y. Li, H. Y. Luo, J. Y. Li, L. Zhang and D. Z. Jia, Synthesis, crystal structure, DNA/bovine serum albumin binding and antitumor activity of two transition metal complexes with 4-acylpyrazolone derivative, *Appl Organomet Chem*, 2019, **33**, e4668.
- 93 R. Pettinari, C. Pettinari, F. Marchetti, C. M. Clavel, R. Scopelliti and P. J. Dyson, Cytotoxicity of ruthenium-arene complexes containing β -ketoamine ligands, *Organometallics*, 2013, **32**, 309–316.

- 94 R. Pettinari, F. Marchetti, C. Pettinari, A. Petrini, R. Scopelliti, C. M. Clavel and P. J. Dyson, Synthesis, structure, and antiproliferative activity of ruthenium(II) arene complexes with N,O-chelating pyrazolone-based β -ketoamine ligands, *Inorg Chem*, 2014, **53**, 13105–13111.
- 95 E. A. Bakr, G. B. Al-Hefnawy, M. K. Awad, H. H. Abd-Elatty and M. S. Youssef, New Ni(II), Pd(II) and Pt(II) complexes coordinated to azo pyrazolone ligand with a potent anti-tumor activity: Synthesis, characterization, DFT and DNA cleavage studies, *Appl Organomet Chem*, 2018, **32**, e4104.
- 96 M. A. Alhasani, T. A. Farghaly and H. A. El-Ghamry, Mono- and bimetallic complexes of pyrazolone based ligand: Synthesis, characterization, antitumor and molecular docking studies, *J Mol Struct*, 2022, **1249**, 131607.
- 97 E. Pahontu, F. Julea, T. Rosu, V. Purcarea, Y. Chumakov, P. Petrenco and A. Gulea, Antibacterial, antifungal and in vitro antileukaemia activity of metal complexes with thiosemicarbazones, *J Cell Mol Med*, 2015, **19**, 865–878.
- 98 V. A. Joseph, J. H. Pandya and R. N. Jadeja, Syntheses, crystal structure and biological evaluation of Schiff bases and copper complexes derived from 4-formylpyrazolone, *J Mol Struct*, 2015, **1081**, 443–448.
- 99 R. Jayarajan, G. Vasuki and P. S. Rao, Synthesis and Antimicrobial Studies of Tridentate Schiff Base Ligands with Pyrazolone Moiety and Their Metal Complexes, *Org Chem Int*, 2010,
- 100 C. K. Modi, B. G. Gade, J. A. Chudasama, D. K. Parmar, H. D. Nakum and A. L. Patel, Synthesis, spectral investigation and catalytic aspects of entrapped VO(IV) and Cu(II) complexes into the supercages of zeolite-Y, *Spectrochim Acta A Mol Biomol Spectrosc*, 2015, **140**, 174–184.
- 101 D. F. Liu, L. Y. Wu, W. X. Feng, X. M. Zhang, J. Wu, L. Q. Zhu, D. di Fan, X. Q. Lü and Q. Shi, Ring-opening copolymerization of CHO and MA catalyzed by mononuclear [Zn(L2)(H2O)] or trinuclear [Zn3(L2)2(OAc)2] complex based on the asymmetrical bis-Schiff-base ligand precursor, *J Mol Catal A Chem*, 2014, **382**, 136–145.

- 102 D. Liu, Z. Zhang, X. Zhang, X. Lü, D. Liu, Z. Zhang, X. Zhang and X. Lü, Alternating Ring-Opening Copolymerization of Cyclohexene Oxide and Maleic Anhydride with Diallyl-Modified Manganese(III)–Salen Catalysts, *Aust J Chem*, 2015, **69**, 47–55.
- 103 S. A. Abdel-Latif and A. A. Mohamed, Synthesis, spectroscopic characterization, first order nonlinear optical properties and DFT calculations of novel Mn(II), Co(II), Ni(II), Cu(II) and Zn(II) complexes with 1,3-diphenyl-4-phenylazo-5-pyrazolone ligand, *J Mol Struct*, 2018, **1153**, 248–261.
- 104 Y. Wang and Z. Y. Yang, Crystal structure of Ni(II) complex and fluorescence properties of Zn(II) complex with the Schiff base derived from diethenetriamine and PMBP, *J Lumin*, 2008, **128**, 373–376.
- 105 H. Li, G. C. Xu, L. Zhang, J. X. Guo and D. Z. Jia, Structural diversity and properties of four complexes with 4-acyl pyrazolone derivative, *Polyhedron*, 2013, **55**, 209–215.
- 106 D. A. Garnovskii, A. S. Antsyshkina, N. I. Makarova, V. G. Vlasenko, G. G. Sadikov, V. S. Sergienko, Y. v. Zubavichus, S. I. Levchenkov, A. I. Uraev and A. S. Burlov, Electrochemical synthesis, structure, and photoluminescent properties of copper, zinc, and cadmium mixed-ligand complexes, *Russ J Inorg Chem*, 2015, **60**, 1528–1536.
- 107 A. Gusev, V. Shul'gin, E. Braga, E. Zamnius, G. Starova, K. Lyssenko, I. Eremenko and W. Linert, Luminescent properties of zinc complexes of 4-formylpyrazolone based azomethine ligands: Excitation-dependent emission in solution, *J Lumin*, 2018, **202**, 370–376.
- 108 H. Xiao, X. Jiang, D. Li, L. Wu, W. Zhang and D. Guo, Synthesis and luminescence properties of pyrazolone derivatives and their terbium complexes, *Luminescence*, 2015, **30**, 677–685.
- 109 H. F. Qian, J. Geng, D. Xu and W. Huang, Hydrazone to deprotonated azo/azo-enol transformation for isomeric pyrazolone based heterocyclic dyes via metal-ion complexation, *Dyes Pigm*, 2019, **160**, 853–862.
- 110 G. Hussain, N. Abass, G. Shabir, M. Athar, A. Saeed, R. Saleem, F. Ali and M. A. Khan, New acid dyes and their metal complexes based on substituted phenols for leather: Synthesis, characterization and optical studies, *J Appl Res Technol*, 2017, **15**, 346–355.

- 111 M. Ayaz, M. Ayaz, F. Ali, A. Saeed, A. Khurshid, G. Shabir, T. Ahmad, S. A. R. Kazmi and H. A. Khan, Synthesis of Symmetric Bridged Bis-Pyrazolone Based Metal Complex Acid Dyes and their Applications on Leather, *J Fluoresc*, 2018, **28**, 1181–1193.
- 112 J. S. Casas, M. S. García-Tasende, A. Sánchez, J. Sordo and Á. Touceda, Coordination modes of 5-pyrazolones: A solid-state overview, *Coord Chem Rev*, 2007, **251**, 1561–1589.
- 113 M. Formica, G. Favi, V. Fusi, L. Giorgi, F. Mantellini and M. Micheloni, Synthesis and study of three hydroxypyrazole-based ligands: A ratiometric fluorescent sensor for Zn(II), *J Lumin*, 2018, **195**, 193–200.
- 114 P. Elo, A. Pärssinen, S. Rautiainen, M. Nieger, M. Leskelä and T. Repo, Titanium complexes with modifiable pyrazolonato and pyrazolonato-ketimine ligands: Synthesis, characterization and ethylene polymerization behavior, *J Organomet Chem*, 2010, **695**, 11–17.
- 115 L. Zhang, L. Liu, G. F. Liu, G. C. Xu, D. Z. Jia and J. P. Lang, Synthesis and crystal structure of mixed-ligand Cu(II) complex of N-(1-phenyl-3-methyl-4-benzylidene- 5-pyrazolone) p-nitrobenzoylhydrazide and pyridine, *J Chem Cryst*, 2005, **35**, 583–588.
- 116 J. Wang, G. C. Xu, Y. P. Zhang, H. Y. Luo, J. Y. Li, L. Zhang and D. Z. Jia, Copper(ii) complexes with 4-acyl pyrazolone derivatives and diimine coligands: synthesis, structural characterization, DNA binding and antitumor activity, *New J Chem*, 2019, **43**, 2529–2539.
- 117 L. C. Emeleus, D. C. Cupertino, S. G. Harris, S. Owens, S. Parsons, R. M. Swart, P. A. Tasker and D. J. White, Diazopyrazolones as weak solvent extractants for copper from ammonia leach solutions, *J Chem Soc, Dalton Trans*, 2001, **0**, 1239–1245.
- 118 R. Pettinari, F. Marchetti, C. di Nicola, C. Pettinari, A. Galindo, R. Petrelli, L. Cappellacci, M. Cuccioloni, L. Bonfili, A. M. Eleuteri, M. F. C. Guedes Da Silva and A. J. L. Pombeiro, Ligand Design for N, O- or N, N-Pyrazolone-Based Hydrazones Ruthenium(II)-Arene Complexes and Investigation of Their Anticancer Activity, *Inorg Chem*, 2018, **57**, 14123–14133.
- 119 J. Guo, D. Jia, L. Liu, H. Yuan and F. Li, Solid-state photochromism of pyrazolones with highly improved sensitivity, fatigue resistance and reversible fluorescent switching properties, *J Mater Chem*, 2011, **21**, 3210–3215.

- 120 A. S. Amarasekara, O. S. Owereh, K. A. Lyssenko and T. v. Timofeeva, Structural tautomerism of 4-acylpyrazolone schiff bases and crystal structure of 5-methyl-2-phenyl-4-{1-[(pyridin-2-ylmethyl)-amino]-ethylidene}-2,4-dihydro-pyrazol-3-one, *J Struct Chem*, 2010, **50**, 1159–1165.
- 121 E. A. Orabi, Tautomerism and antioxidant activity of some 4-acylpyrazolone-based Schiff bases: a theoretical study, *RSC Adv*, 2018, **8**, 30842–30850.
- 122 L. Liu, D. Jia and Y. Ji, SYNTHESIS AND CHARACTERIZATION OF METAL COMPLEXES OF N-(1-PHENYL-3-METHYL-4-BENZAL-5-PYRAZOLONE)-p-METHOXY-BENZOYLHYDRAZINE, *Synth React Inorg Met Org Chem*, 2007, **32**, 739–751.
- 123 H. Y. Luo, J. Y. Li, Y. Li, L. Zhang, J. Y. Li, D. Z. Jia and G. C. Xu, Cadmium(ii) complexes with a 4-acyl pyrazolone derivative and co-ligands: crystal structures and antitumor activity, *RSC Adv*, 2016, **6**, 114997–115009.
- 124 A. K. Oraby, K. R. A. Abdellatif, M. A. Abdelgawad, K. M. Attia, L. N. Dawe and P. E. Georghiou, 2,4-Disubstituted Phenylhydrazonopyrazolone and Isoxazolone Derivatives as Antibacterial Agents: Synthesis, Preliminary Biological Evaluation and Docking Studies, *ChemistrySelect*, 2018, **3**, 3295–3301.
- 125 L. Zhang, G. C. Xu, L. Liu, G. F. Liu and D. Z. Jia, Synthesis, characterization and crystal structure of 1-phenyl-3-methyl-4- (salicylidene hydrazide)-phenylethylene-pyrazolone-5, *J Chem Crystallogr*, 2008, **38**, 151–155.
- 126 L. Liu, Y. Li, D. Z. Jia, G. F. Liu and K. B. Yu, A novel coordination polymer with helical chain: Synthesis and crystal structure of [Cu 4(PMEP-sal) 4·H 2O] n, *J Inorg Organomet Polym Mater*, 2007, **17**, 535–539.
- 127 G. Xu, L. Liu, L. Zhang, G. Liu, D. Jia and J. Lang, Synthesis and Characterization of Tetra- μ -phenolatotetrazinc(II) Complex with 1-Phenyl-3-Methyl-4-(salicylidene hydrazone)-Phenylethylene-Pyrazolone-5, *Struct Chem*, 2005, **16**, 431–437.
- 128 Y. Zhang, L. Zhang, L. Liu, J. Guo, D. Wu, G. Xu, X. Wang and D. Jia, Anticancer activity, structure, and theoretical calculation of N-(1-phenyl-3-methyl-4-propyl-pyrazolone-5)-salicylidene hydrazone and its copper(II) complex, *Inorganica Chim Acta*, 2010, **363**, 289–293.

- 129 L. Zhang, L. Liu, G. C. Xu and D. Z. Jia, Syntheses, crystal structures and fluorescence properties of Zn(II) complexes with pyrazolone derivatives, *J Chem Crystallogr*, 2008, **38**, 837–843.
- 130 O. G. Idemudia, A. I. Okoh, A. P. Sadimenko, E. C. Hosten and O. O. Okoh, Substituted 4-Acyl-5-methyl-2-phenyl-pyrazol-3-one-phenylhydrazones with antioxidant properties: X-ray crystal and spectroscopic studies, *J Chem*, 2017.
- 131 O. G. Idemudia, A. P. Sadimenko and E. C. Hosten, Metal Complexes of New Bioactive Pyrazolone Phenylhydrazones; Crystal Structure of 4-Acetyl-3-methyl-1-phenyl-2-pyrazoline-5-one phenylhydrazone Amp-Ph, *Int J Mol Sci*, 2016, **17**, 687.
- 132 O. G. Idemudia, A. P. Sadimenko and E. C. Hosten, 4-{[2-(2,4-Dinitrophenyl)hydrazinylidene](phenyl)methyl} -5-methyl-2-phenyl-1H-pyrazol-3(2H)-one ethanol monosolvate, *Acta Crystallogr Sect E Struct Rep Online*, 2012, **68**, o3380–o3380.
- 133 Y. F. Sun and Y. P. Cui, 4-{[(1,3-Benzothiazolium-2-yl)hydra-zono](phen-yl)meth-yl} -3-methyl-1-phenyl-1H-pyrazol-5-olate monohydrate, *Acta Crystallogr Sect E Struct Rep Online*, 2008, **64**, o690–o690.
- 134 L. Liu, D. Z. Jia and K. B. Yu, Synthesis, structure and photochromic properties of 4-acyl pyrazolone derivants, *J Photochem Photobiol A Chem*, 2003, **154**, 117–122.
- 135 Y. Zhong, L. Liu, G. Liu, D. Wu, J. Guo and D. Jia, Crystal structure and photoisomerism of 1-phenyl-3-methyl-4-(4-fluorobenzal)-5-pyrazolone 4-methylthiosemicarbazone in the solid state, *J Mol Struct*, 2008, **889**, 259–264.
- 136 B. H. Peng, G. F. Liu, L. Liu, D. Z. Jia and K. B. Yu, Crystal structure and spectroscopic study on photochromism of 1-phenyl-3-methyl-4-benzal-5-pyrazolone 4-ethylthiosemicarbazone, *J Mol Struct*, 2004, **692**, 217–222.
- 137 J. Guo, D. Jia, L. Liu, H. Yuan, M. Guo, D. Wu and F. Li, Photochromism and mechanism of pyrazolones in crystals: structural variations directly observed by X-ray diffraction, *J Mater Chem*, 2011, **21**, 12202–12205.

- 138 M. Guo, J. Guo, D. Jia, H. Liu, L. Liu, A. Liu and F. Li, Synthesis, properties, and mechanism of two novel photoisomerization pyrazolones in the solid state, *J Mol Struct*, 2013, **1035**, 271–276.
- 139 Y. Li, J. Guo, A. Liu, D. Jia, X. Wu and Y. Chen, Synthesis, mechanism and efficient modulation of a fluorescence dye by photochromic pyrazolone with energy transfer in the crystalline state, *RSC Adv*, 2017, **7**, 9847–9853.
- 140 H. Sun, L. Liu, D. Wu, D. Jia and J. Guo, Synthesis, photochromic properties and thermal bleaching kinetics of pyrazolone phenylsemicarbazones containing a thiophene ring, *New Journal of Chemistry*, 2013, **37**, 2351–2357.
- 141 H. Chai, G. Liu, L. Liu, D. Jia, Z. Guo and J. Lang, Crystal structure and spectroscopic study on photochromism of 1,3-diphenyl-4-(4'-fluoro)benzal-5-pyrazolone N(4)-phenyl semicarba-zone, *J Mol Struct*, 2005, **752**, 124–129.
- 142 F. Marchetti, C. Pettinari and R. Pettinari, Acylpyrazolone ligands: Synthesis, structures, metal coordination chemistry and applications, *Coord Chem Rev*, 2005, 249, 2909–2945.
- 143 F. Marchetti, R. Pettinari and C. Pettinari, Recent advances in acylpyrazolone metal complexes and their potential applications, *Coord Chem Rev*, 2015, **303**, 1–31.
- 144 F. Marchetti, C. Pettinari, C. di Nicola, A. Tombesi and R. Pettinari, Coordination chemistry of pyrazolone-based ligands and applications of their metal complexes, *Coord Chem Rev*, 2019, **401**, 213069.
- 145 R. R. Conry, in *Encyclopedia of Inorganic and Bioinorganic Chemistry*, John Wiley & Sons, Ltd, 2011.
- 146 F. Caruso, L. Massa, A. Gindulyte, C. Pettinari, F. Marchetti, R. Pettinari, M. Ricciutelli, J. Costamagna, J. C. Canales, J. Tanski and M. Rossi, (4-Acyl-5-pyrazolonato)titanium Derivatives: Oligomerization, Hydrolysis, Voltammetry, and DFT Study, *Eur J Inorg Chem*, 2003, **2003**, 3221–3232.
- 147 B. V. Patel and B. T. Thaker, New Azomethyne and Tetradentate Schiff Base Complexes of Transition Metals Containing Heterocyclic β -Diketones as Ligands, *Synth React Inorg Met Org Chem*, 2006, **16**, 1319–1335.

- 148 E. C. Okafor, Observations on 1-phenyl-3-methyl-4-trifluoroacetylpyrazolone-5, a promising extracting agent, *Talanta*, 1982, **29**, 275–278.
- 149 B. A. Uzoukwu, Electronic and vibrational studies of copper(II) complexes of 1-phenyl-3-methyl-4-acylpyrazolones-5, *Spectrochim Acta A*, 1992, **48**, 1021–1022.
- 150 S. K. Dey, B. Bag, D. K. Dey, V. Gramlich, Y. Li and S. Mitra, Synthesis and Characterization of Copper(II) and Zinc(II) Complexes Containing 1-Phenyl-3-methyl-4-benzoyl-5-pyrazolone, *Z Naturforsch*, 2003, **58**, 1009–1014.
- 151 F. Marchetti, C. Pettinari, R. Pettinari, A. Cingolani, M. Camalli and R. Spagna, Influence of sterically demanding groups on the structure and stability in the solid and solution state of (acylpyrazolonate)bis(phosphine)copper(I) derivatives, *Inorganica Chim Acta*, 2000, **299**, 65–79.
- 152 F. Marchetti, C. Pettinari, A. Cingolani, D. Leonesi, M. Camalli and A. Pifferi, Synthesis and characterization of copper(I) and copper(II) coordination compounds containing 4-acylpyrazolon-5-ato ligands. crystal structure of [(4-trifluoroacetyl-1-phenyl-3-methylpyrazolon-5-ato)bis (triphenylphosphine)copper(I)], *Polyhedron*, 1996, **15**, 3835–3849.
- 153 A. A. Drozdov, V. A. Vertlib, I. Timokhin, S. I. Troyanov, C. Pettinari and F. Marchetti, Complexes of Some d and f Elements with New 4-Acylpyrazol-5-ones: Synthesis and Study, *Russ J Coord Chem*, 2002, **28**, 259–263.
- 154 C. Pettinari, F. Marchetti, C. Santini, R. Pettinari, A. Drozdov, S. Troyanov, G. A. Battiston and R. Gerbasi, Structure and volatility of copper complexes containing pyrazolyl-based ligands, *Inorganica Chim Acta*, 2001, **315**, 88–95.
- 155 C. Pettinari, F. Marchetti, R. Pettinari, A. Drozdov, S. Troyanov, A. I. Voloshin and N. M. Shavaleev, Synthesis, structure and luminescence properties of new rare earth metal complexes with 1-phenyl-3-methyl-4-acylpyrazol-5-ones, *J Chem Soc, Dalton Trans*, 2002, **0**, 1409–1415.
- 156 B. A. Uzoukwu, K. Gloe and H. Duddeck, Metal(II) Complexes of 4-Acylbis(Pyrazolone-5): Synthesis and Spectroscopic Studies, *Synth React Inorg Met Org Chem*, 2008, **28**, 207–221.

- 157 R. N. Jadeja, K. M. Vyas, V. K. Gupta, R. G. Joshi and C. Ratna Prabha, Syntheses, characterization and molecular structures of calcium(II) and copper(II) complexes bearing O₂-chelate ligands: DNA binding, DNA cleavage and anti-microbial study, *Polyhedron*, 2012, **31**, 767–778.
- 158 K. M. Vyas, R. N. Jadeja, D. Patel, R. v. Devkar and V. K. Gupta, Effect of ligand substitution in pyrazolone based binary and ternary Cu(II) complexes on DNA binding, protein binding and anti-cancer activity on A549 lung carcinoma cell lines, *Polyhedron*, 2014, **80**, 20–33.
- 159 L. N. Bochkarev, Y. P. Bariniva, A. I. Ilicheva, S. Y. Ketkov, E. v. Baranov, V. A. Ilichev and D. G. Yakhvarov, Synthesis, crystal structures and luminescent properties of the copper(I) pyrazolonate complexes, *Inorganica Chim Acta*, 2015, **425**, 189–197.
- 160 T. U. Sheikh, M. N. Khan, G. Hussain, M. M. Athar, M. Ashraf, F. H. Nasim, S. Arshad, K. Mahmood and M. A. Khan, Synthesis and biological screening of heterocyclic ligands-pyrazole derivatives metal complexes, *Asian J Chem*, 2015, **27**, 257–260.
- 161 K. M. Vyas, R. v. Devkar, A. Prajapati and R. N. Jadeja, Pyrazolone incorporating bipyridyl metallointercalators as effective DNA, protein and lung cancer targets: Synthesis, characterization and in vitro biocidal evaluation, *Chem Biol Interact*, 2015, **240**, 250–266.
- 162 M. Hasanzadeh Esfahani, M. Behzad, M. Dusek and M. Kucerakova, Synthesis and characterization of a series of acylpyrazolone transition metal complexes: Crystal structures and catalytic performance in the epoxidation of cyclooctene, *Inorganica Chim Acta*, 2020, **508**.
- 163 E. Bagdatli, F. Yildirim, G. Ulucay and U. Sayin, Novel copper(II) and palladium(II) complexes with 4-acyl-5-pyrazolone ligands: Synthesis and characterization, *J Organomet Chem*, 2019, **896**, 38–50.
- 164 M. Hasanzadeh Esfahani, F. Boorboor Ajdari, E. B. Poormohammadi, A. Abbasi and M. Behzad, Synthesis, crystal structure and battery-like studies on a new acylpyrazolone-based mixed-ligand Cu(II) complex, *Res Chem Interim*, 2021, **48**, 575–591.
- 165 R. N. Jadeja, K. M. Vyas, K. K. Upadhyay and R. v. Devkar, In vitro apoptosis-inducing effect and gene expression profiles of mixed ligand Cu(II) complexes derived from 4-acyl pyrazolones on human lung cancer cells, *RSC Adv*, 2017, **7**, 17107–17116.

- 166 K. Nakum and R. N. Jadeja, Synthesis, characterization, and electrochemical study of a mononuclear Cu(II) complex with a 4-acyl pyrazolone ligand, *Z Naturforsch*, 2018, **73**, 713–718.
- 167 M. S. Masoud, A. R. Youssef and M. A. Mostafa, Structural studies of 3-amino-4-(substituted arylazo)-5-(1H)pyrazolone compounds, *Transit Met Chem*, 1988, **13**, 253–255.
- 168 O. P. Anderson, J. Becher, H. Frydendahl, L. F. Taylor and H. Toftlund, Characterization of a pseudo-tetrahedral copper(II) complex with two thiolato and two imino donor atoms, *J Chem Soc Chem Commun*, 1986, **0**, 699–701.
- 169 A. I. Uraev, A. L. Nivorozhkin, G. I. Bondarenko, K. A. Lysenko, O. Y. Korshunov, V. G. Vlasenko, A. T. Shuvaev, V. P. Kurbatov, M. Y. Antipin and A. D. Garnovskii, Synthesis, structures, and spectral properties of biomimetic azomethine metal chelates with chromophores CuN₂S₂, CuN₂O₂, and CuN₂Se₂. Crystal structure of bis[4-(benzyl)aldimino-3-methyl-1-phenyl-5-pyrazolothiolato]copper(II), *Russ Chem Bull*, 2000, **49**, 1863–1868.
- 170 J. L. Wang, F. Ding and F. M. Miao, Bis{4-[α -(4-acetylphenylimino)benzyl]-3-methyl-1-phenylpyrazol-5- onato}aquacopper(II), *Acta Crystallogr Sect E Struct Rep Online*, 2003, **59**, m128–m130.
- 171 R. N. Jadeja, J. R. Shah, E. Suresh and P. Paul, Synthesis and structural characterization of some Schiff bases derived from 4-[(arylimino)ethyl]-3-methyl-1-(4'-methylphenyl)-2-pyrazolin-5-one and spectroscopic studies of their Cu(II) complexes, *Polyhedron*, 2004, **23**, 2465–2474.
- 172 Y. Moreno, J. Belmar, F. Brovelli, A. Buljan, O. Peña and L. Moreno, electrochemical and computational study of copper (ii) alkylpyrazolone based enamine complex, *J Chil Chem Soc*, 2008, **53**, 1689–1693.
- 173 P. Hermosilla, Y. Moreno, A. Buljan, J. Belmar, F. Brovelli, O. Peña and R. Baggio, magneto-structural studies of a copper (ii)-alkylpyrazolone enamine complex, *J Chil Chem Soc*, 2006, **51**, 773–774.
- 174 F. R. Pérez, J. Belmar, C. Jiménez, Y. Moreno, P. Hermosilla and R. Baggio, Bis{ 1-n-hexyl-3-methyl-4-[1-(phenylimino)propyl]-1H-pyrazol-5-olato } -copper(II): A new copper(II)

- complex with a chelating alkylpyrazolone-based enamine, *Acta Crystallogr C*, 2005, **61**, m318–m320.
- 175 F. Bao, R. Ma, R. Ma and Y. Jiao, A copper complex with β -ketoamine ligand based on pyrazolone derivative: synthesis, crystal structure and catalysis for norbornene polymerization, *J Coord Chem*, 2007, **60**, 557–566.
- 176 X. Q. Lü, F. Bao, B. S. Kang, Q. Wu, H. Q. Liu and F. M. Zhu, Syntheses, structures and catalytic activity of copper(II) complexes bearing N,O-chelate ligands, *J Organomet Chem*, 2006, **691**, 821–828.
- 177 A. S. Thakar, K. K. Singh, K. T. Joshi, A. M. Pancholi and K. S. Pandya, Synthesis, Characterization and Antibacterial Activity of Schiff Bases and their Metal Complexes Derived from 4-Acyl-1-phenyl-3-methyl-2-pyrazolin-5-ones and 2-Amino-4(4'-methylphenyl)thiazole, *E-J Chem*, 2010, **7**, 1396-1406.
- 178 S. Sunitha and K. K. Aravindakshan, Synthesis, characterization and antimicrobial studies on transition metal complexes of n-[phenyl(methylphenyl-5-pyrazolyl)methylidene]aniline, *Int. J. Pharm. Biomed. Sci.*, 2011, **2**, 108–113.
- 179 N. J. Parmar, H. A. Barad, B. R. Pansuriya and R. A. Patel, Chelation and extraction of copper(II) with 5-pyrazolone-based Schiff bases, *J Coord Chem*, 2011, **64**, 688–698.
- 180 X. Y. Cheng, M. F. Wang, Z. Y. Yang, Y. Li, Z. C. Liu and Q. X. Zhou, Synthesis, Characterization, Crystal Structure, and Biological Activities of Transition Metal Complexes with 1-Phenyl-3-methyl-5-hydroxypyrazole-4-methylene-8'-quinolineimine, *Z Anorg Allg Chem*, 2013, **639**, 832–841.
- 181 R. C. Maurya, S. Jhamb, S. Roy, J. Chourasia, A. K. Sharma and P. Vishwakarma, Synthesis, characterization, and 3D-molecular modeling and analysis of some copper(II) chelates in O, N-donor coordination pattern involving Schiff bases derived from 4-butyryl-3-methyl-1-phenyl-2-pyrazolin-5-one and some sulfa drugs, *Arab J Chem*, 2015, **8**, 143–154.
- 182 O. G. Idemudia, A. P. Sadimenko, A. J. Afolayan and E. C. Hosten, Synthesis and Characterization of Bioactive Acylpyrazolone Sulfanilamides and Their Transition Metal Complexes: Single Crystal Structure of 4-Benzoyl-3-methyl-1-phenyl-2-pyrazolin-5-one Sulfanilamide, *Bioinorg Chem Appl*, , DOI:10.1155/2015/717089.

- 183 X. Hu, L. Zhang, L. Liu, G. Liu, D. Jia and G. Xu, Synthesis and structural characterization of three hydrogen-bonding connected supramolecular complexes of nickel, zinc and copper with 1,3-diphenyl-4-(salicylidene hydrazide)-acetyl-pyrazolone-5 and 2,2'-bipyridine, *Inorganica Chim Acta*, 2006, **359**, 633–641.
- 184 J. N. Asegbeloyin, O. T. Ujam, E. C. Okafor, I. Babahan, E. P. Coban, A. Özmen and H. Biyik, Synthesis, Characterization, and Biological Activity of N' -[(Z)-(3-Methyl-5-oxo-1-phenyl-1,5-dihydro-4 H -pyrazol-4-ylidene)(phenyl)methyl]benzohydrazide and Its Co(II), Ni(II), and Cu(II) Complexes, *Bioinorg Chem Appl*, 2014.
- 185 G. C. Xu, L. Zhang, L. Liu, G. F. Liu and D. Z. Jia, Thermal kinetic TG-analysis of the mixed-ligand copper(II) and nickel(II) complexes of N-(1-phenyl-3-methyl-4-benzylidene-5-pyrazolone) p-nitrobenzoylhydrazide and pyridine, *Thermochim Acta*, 2005, **429**, 31–42.
- 186 S. S. Kandil, Cobalt(II), nickel(II) and copper(II) complexes of 4-(sulfonylazido)phenylazopyrazolones, *Transit Met Chem*, 1998, **23**, 461–465.
- 187 O. v. Kovalchukova, M. A. Ryabov, P. v. Dorovatovskii, Y. v. Zubavichus, A. N. Utenyshev, D. N. Kuznetsov, O. v. Volyansky, V. K. Voronkova and V. N. Khrustalev, Synthesis and characterization of a series of novel metal complexes of N-heterocyclic azo-colorants derived from 4-azo-pyrazol-5-one, *Polyhedron*, 2017, **121**, 41–52.
- 188 O. v. Koval'chukova, S. B. Strashnova, O. v. Avramenko, M. A. Ryabov, P. v. Dorovatovskii, Y. v. Zubavichus and V. N. Khrustalev, Coordination Compounds of Bivalent Metals with (Z)-4-(2-Hydroxy-5-nitrophenyl)hydrazono-3-methyl-1-phenyl-1H-pyrazol-5(4H)-one: Crystal and Molecular Structure of C₁₆H₁₃N₅O₄, *Russ J Inorg Chem*, 2018, **63**, 874–880.
- 189 S. A. Abdel-Latif and A. A. Mohamed, Synthesis, spectroscopic characterization, first order nonlinear optical properties and DFT calculations of novel Mn(II), Co(II), Ni(II), Cu(II) and Zn(II) complexes with 1,3-diphenyl-4-phenylazo-5-pyrazolone ligand, *J Mol Struct*, 2018, **1153**, 248–261.
- 190 S. M. Morgan, M. A. Diab and A. Z. El-Sonbati, Supramolecular assembly of hydrogen bonding, ESR studies and theoretical calculations of Cu(II) complexes, *Appl Organomet Chem*, 2018, **32**, e4504.

- 191 M. Gaber, A. M. Khedr, M. A. Mansour and M. Elsharkawy, Nano-synthesis, characterization, modeling and molecular docking analysis of Mn (II), Co (II), Cr (III) and Cu (II) complexes with azo pyrazolone ligand as new favorable antimicrobial and antitumor agents, *Appl Organomet Chem*, 2018, **32**, e4606.
- 192 S. I. Levchenkov, I. N. Shcherbakov, L. D. Popov, V. v. Lukov, V. v. Minin, Z. A. Starikova, E. v. Ivannikova, A. A. Tsaturyan and V. A. Kogan, The magnetic exchange interaction via N–H···O-bonding in copper(II) complex with 1-phenyl-3-methyl-4-formylpyrazol-5-one 2-quinolyldrazone, *Inorganica Chim Acta*, 2013, **405**, 169–175.
- 193 L. D. Popov, S. I. Levchenkov, I. N. Shcherbakov, V. v. Minin, G. G. Aleksandrov, E. A. Ugolkova, V. v. Lukov and V. A. Kogan, Polymeric copper(II) complexes with 4-formyl-3-methyl-1-phenylpyrazol-5-one hetarylhydrazones: Synthesis and crystal structures, *Russ J Coord Chem*, 2013, **39**, 849–856.
- 194 R. J. Yadav, K. M. Vyas and R. N. Jadeja, Synthesis and spectral characterization of Cu(II) complexes of some thio-Schiff bases of acyl pyrazolone analogues, *J Coord Chem*, 2010, **63**, 1820–1831.
- 195 V. M. Leovac, G. A. Bogdanović, L. S. Jovanović, L. Joksović, V. Marković, M. D. Joksović, S. M. Denčić, A. D. S. Isaković, I. Marković, F. W. Heinemann, S. Trifunović and I. Crossed D Signalović, Synthesis, characterization and antitumor activity of polymeric copper(II) complexes with thiosemicarbazones of 3-methyl-5-oxo-1-phenyl-3-pyrazolin-4-carboxaldehyde and 5-oxo-3-phenyl-3-pyrazolin-4-carboxaldehyde, *J Inorg Biochem*, 2011, **105**, 1413–1421.
- 196 S. Akcha, L. Hammal, S. Triki, L. Lezama, B. Nedjar-Kolli and O. Benali Baitich, Copper(II) and nickel(II) complexes derived from a carbothioamide-5-pyrazolone ligand: synthesis, characterization, crystal structures, electrochemical, potentiometric and DNA-binding studies, *J Coord Chem*, 2015, **68**, 4373–4394.
- 197 S. Parvarinezhad, M. Salehi, R. Eshaghi Malekshah, M. Kubicki and A. Khaleghian, Synthesis, characterization, spectral studies two new transition metal complexes derived from pyrazolone by theoretical studies, and investigate anti-proliferative activity, *Appl Organomet Chem*, 2022, **36**.

- 198 O. G. Idemudia, A. P. Sadimenko, A. J. Afolayan and E. C. Hosten, Synthesis and Characterization of Bioactive Acylpyrazolone Sulfanilamides and Their Transition Metal Complexes: Single Crystal Structure of 4-Benzoyl-3-methyl-1-phenyl-2-pyrazolin-5-one Sulfanilamide, *Bioinorg Chem Appl*, 2015.
- 199 S. N. Lyubchenko, I. N. Shcherbakov, Y. P. Tupolova, L. D. Popov, S. I. Levchenkov, A. N. Morozov, S. A. Borodkin, V. A. Lazarenko, V. N. Khrustalev, Y. v. Zubavichus and V. v. Minin, Anion mediated switching from mono- to polymer structure in copper(II) complexes with 4,6-dimethylpyrimidinylhydrazone 1-phenyl-3-methyl-4-formylpyrazol-5-one, *Inorganica Chim Acta*, 2020, **502**.
- 200 S. Syed Ali Fathima, M. Mohamed Sahul Meeran and E. R. Nagarajan, Design and synthesis of novel pyrazolone based coordination compounds: DNA synergy, biological screening, apoptosis, molecular docking and in-silico ADMET profile, *J Mol Struct*, 2019, **1197**, 292–307.
- 201 E. B. Poormohammadi, M. Behzad, Z. Abbasi and S. D. A. Astaneh, Copper complexes of pyrazolone-based Schiff base ligands: Synthesis, crystal structures and antibacterial properties, *J Mol Struct*, 2020, **1205**.
- 202 M. H. Esfahani, N. Fallah, H. Iranmanesh, J. E. Beves and M. Behzad, Experimental and computational studies on copper(II) Schiff base complex derived from 4-acetyl-3-methyl-1-phenyl-2-pyrazolin-5-one, *J Mol Struct*, 2022, **1257**.
- 203 W. Xi, F. Q. Song, X. L. Xia and X. Q. Song, Tuned structure and DNA binding properties of metal complexes based on a new 4-acylpyrazolone derivative, *New J Chem*, 2020, **44**, 2281–2290.
- 204 A. van Nguyen, A. T. N. Vu, L. v. Bazan, R. T. Galeev, A. N. Utenyshev, E. B. Markova, V. T. Le and O. V. Kovalchukova, Synthesis, characterization, and sorption activity of novel azo-colorants derived from phloroglucinol and antipyrine and their metal complexes, *RSC Adv*, 2022, **12**, 888–898.
- 205 A. S. Burlov, V. G. Vlasenko, T. v. Lifintseva, M. S. Milutka, Y. v. Koshchienko, A. I. Uraev, D. A. Garnovskii, Y. v. Rusalev, V. A. Lazarenko and V. N. Khrustalev, Cu(II) and Co(II) Complexes with (4Z)-4-[(2-Diethylaminoethylamino)methylene]-5-Methyl-2-

- Phenylpyrazol-3-one: Synthesis, Magnetic Properties, and Crystal Structures, *Russ J Coord Chem*, 2020, **46**, 485–492.
- 206 J. Burgess and R. H. Prince, in *Encyclopedia of Inorganic Chemistry*, John Wiley & Sons, Ltd, 2006.
- 207 E. C. Okafor, The metal complexes of heterocyclic β -diketones and their derivatives—VII. The synthesis, structure and i.r. spectral studies of 1-phenyl-3-methyl-4-trifluoroacetylpyrazolone-5 (HPMTEFP) and its divalent metal complexes, *Spectrochim Acta A*, 1981, **37**, 951–955.
- 208 W. Mickler, A. Reich, S. Sawusch, U. Schilde and E. Uhlemann, Aquabis(3-methyl-4-octanoyl-1-phenyl-5-pyrazolonato-O,O')zinc(II) and Bis(ethanol-O)bis(3-methyl-1-phenyl-4-stearoyl-5-pyrazolonato-O,O')cadmium(II), *Metal-Organic Compounds*, 1998, **54**, 776–779.
- 209 J. Wang, Synthesis and Structure of Zinc Complex of 1-Phenyl-3-methyl-4-benzoylpyrazolone-5, *Pol J Chem*, 2001, 1367–1370.
- 210 S. K. Dey, B. Bag, D. K. Dey, V. Gramlich, Y. Li and S. Mitra, Synthesis and Characterization of Copper(II) and Zinc(II) Complexes Containing 1-Phenyl-3-methyl-4-benzoyl-5-pyrazolone, *Z Naturforsch*, 2003, **58**, 1009–1014.
- 211 F. Marchetti, C. Pettinari, R. Pettinari, D. Arriva, S. Troyanov and A. Drozdov, On the interaction of acylpyrazolonates with zinc(II) acceptors: the role of ancillary ligands, *Inorganica Chim Acta*, 2000, **307**, 97–105.
- 212 F. Marchetti, Zinc and cadmium derivatives containing several 4-acyl-5-pyrazolonate donors and additional ancillary ligands, *Main Group Met Chem*, 2001, **24**, 252–266.
- 213 F. Marchetti, C. Pettinari, R. Pettinari, A. Cingolani, D. Leonesi and A. Lorenzotti, Group 12 metal complexes of tetradentate N₂O₂-Schiff-base ligands incorporating pyrazole: Synthesis, characterisation and reactivity toward S-donors, N-donors, copper and tin acceptors, *Polyhedron*, 1999, **18**, 3041–3050.
- 214 H. Q. Zhang, J. Z. Li, S. Gao and Y. Zhang, Diethanolbis[4-(2-furoyl)-3-methyl-1-phenyl-1H-pyrazol-5-onato]zinc(II), *Acta Crystallogr Sect E Struct Rep Online*, 2007, **63**, m165–m166.

- 215 R. N. Jadeja, M. Chhatrola and V. K. Gupta, Zn(II) coordination compounds derived from 4-acyl pyrazolones and 1,10 phenanthroline: Syntheses, crystal structures, spectral analysis and DNA binding studies, *Polyhedron*, 2013, **63**, 117–126.
- 216 L. Y. Xu, N. Li, J. M. Li and W. Dong, Synthesis, Structure, Antibacterial and Spectroscopic Properties of a Zinc(II) Complex with the Ligand 4-Heptanoyl-pyrazol-5-one, *Z Anorg Allg Chem*, 2013, **639**, 1800–1803.
- 217 T. U. Sheikh, M. N. Khan, G. Hussain, M. M. Athar, M. Ashraf, F. H. Nasim, S. Arshad, K. Mahmood and M. A. Khan, Synthesis and biological screening of heterocyclic ligands-pyrazole derivatives metal complexes, *Asian J Chem*, 2015, **27**, 257–260.
- 218 I. U. Shaikh, R. K. Patel, V. A. Mevada, V. K. Gupta and R. N. Jadeja, Binary and Ternary Zinc(II) Complexes of Acyl Pyrazolones: Synthesis, Spectroscopic Analysis, Crystal Structure and Antimalarial Activity, *ChemistrySelect*, 2019, **4**, 8286–8294.
- 219 F. Marchetti, C. di Nicola, R. Pettinari, C. Pettinari, I. Aiello, M. la Deda, A. Candreva, S. Morelli, L. de Bartolo and A. Crispini, Zinc(II) Complexes of Acylpyrazolones Decorated with a Cyclohexyl Group Display Antiproliferative Activity Against Human Breast Cancer Cells, *Eur J Inorg Chem*, 2020, **2020**, 1027–1039.
- 220 A. C. Vamja and K. R. Surati, Photoluminescent properties of novel design heteroleptic Zn(II) complexes, *Luminescence*, 2017, **32**, 1197–1202.
- 221 J. D. Solanki and K. R. Surati, in *Materials Today: Proceedings*, Elsevier Ltd, 2020, vol. 29, pp. 1006–1012.
- 222 I. Shaikh, R. N. Jadeja and R. Patel, Three mixed ligand mononuclear Zn(II) complexes of 4-acyl pyrazolones: Synthesis, characterization, crystal study and anti-malarial activity, *Polyhedron*.
- 223 B. T. Thaker, A. Patel, J. Lekhadia and P. Thaker, Physicochemical studies of symmetrical tetradentate schiff base complexes of chromium(III), cobalt(II), nickel(II), copper(II), zinc(II), oxovanadium(IV) and dioxouranium(VI) derived from 4-acyl pyrazolone and 1,4-diamine, *Indian J Chem*, 1996, **35A**, 483-488.

- 224 H. H. Zhang, W. Dou, W. S. Liu, X. L. Tang and W. W. Qin, A 2-Pyrazoline-Functionalized Zinc Complex: Available N–AgI Interaction Modulating Its Fluorescence Properties, *Eur J Inorg Chem*, 2011, **2011**, 748–753.
- 225 X. Q. Song, Y. Q. Peng, G. Q. Cheng, X. R. Wang, P. P. Liu and W. Y. Xu, Substituted group-directed assembly of Zn(II) coordination complexes based on two new structural related pyrazolone based Salen ligands: Syntheses, structures and fluorescence properties, *Inorganica Chim Acta*, 2015, **427**, 13–21.
- 226 X. Y. Cheng, M. F. Wang, Z. Y. Yang, Y. Li, Z. C. Liu and Q. X. Zhou, Synthesis, Characterization, Crystal Structure, and Biological Activities of Transition Metal Complexes with 1-Phenyl-3-methyl-5-hydroxypyrazole-4-methylene-8'-quinolineimine, *Z Anorg Allg Chem*, 2013, **639**, 832–841.
- 227 A. N. Gusev, V. F. Shul'gin, E. v. Braga, I. Nemeč, B. F. Minaev, G. v. Baryshnikov, Z. Trávníček, H. Ågren, I. L. Eremenko, K. A. Lyssenko and W. Linert, Synthesis and photophysical properties of Zn(II) Schiff base complexes possessing strong solvent-dependent solid-state fluorescence, *Polyhedron*, 2018, **155**, 202–208.
- 228 X. Hu, L. Zhang, L. Liu, G. Liu, D. Jia and G. Xu, Synthesis and structural characterization of three hydrogen-bonding connected supramolecular complexes of nickel, zinc and copper with 1,3-diphenyl-4-(salicylidene hydrazide)-acetyl-pyrazolone-5 and 2,2'-bipyridine, *Inorganica Chim Acta*, 2006, **359**, 633–641.
- 229 L. Zhang, G. C. Xu, Y. Yang, J. X. Guo and D. Z. Jia, Syntheses, structure diversity and properties of complexes with 4-acyl pyrazolone salicylidene hydrazide derivatives, *Dalton Trans*, 2013, **42**, 4248–4257.
- 230 A. L. Nivorozhkin, H. Toftlund, L. E. Nivorozhkin, I. A. Kamenetskaya, A. S. Antsishkina and M. A. Porai-Koshits, Synthesis and structure of tetracoordinated nickel(II) complexes of deprotonated chelated aminoazo ligands: X-ray crystal structure of bis[1-isopropyl-3-methyl-4-(4-methylphenylazo)-5-(4-methoxyphenylamidato)pyrazole] nickel(II), *Trans Met Chem*, 1994, **19**, 319–324.
- 231 G. G. Mohamed and M. A. M. Gad-Elkareem, Synthesis, characterization and thermal studies on metal complexes of new azo compounds derived from sulfa drugs, *Spectrochim Acta A Mol Biomol Spectrosc*, 2007, **68**, 1382–1387.

- 232 S. A. Abdel-Latif and A. A. Mohamed, Novel Zn(II) complexes of 1,3-diphenyl-4-(arylo)pyrazol-5-one derivatives: Synthesis, spectroscopic properties, DFT calculations and first order nonlinear optical properties, *J Mol Struct*, 2018, **1156**, 712–725.
- 233 A. Gusev, V. Shul'gin, E. Braga, E. Zamnius, M. Kryukova and W. Linert, Luminescent properties of Zn complexes based on tetradentate N₂O₂-donor pyrazolone schiff bases, *Dyes Pigm*, 2020, **183**.
- 234 I. Shaikh, M. Travadi, R. N. Jadeja, R. J. Butcher and J. H. Pandya, Crystal feature and spectral characterization of Zn(II) complexes containing Schiff base of Acylpyrazolone ligand with antimalarial action, *J Ind Chem Soc*, 2022, **99**.
- 235 J. A. Antunes, T. A. de Toledo, L. E. da Silva, P. T. C. Freire, A. M. R. Teixeira, H. D. M. Coutinho, J. L. B. Faria, R. J. Ramos and R. R. F. Bento, Characterization of zinc complex with 4-[(1E)-(2 Hydroxyphenyl) methylidene]amino}-1,5-dimethyl-2-phenyl-1,2-dihydro-3H-pyrazol-3-one by FT-IR and FT-Raman spectroscopies and DFT calculations, *J Mol Struct*, 2020, **1202**.
- 236 I. Shaikh, R. N. Jadeja, R. Patel, V. Mevada and V. K. Gupta, 4-Acylhydrazone-5-Pyrazolones and their Zinc(II) Metal Complexes: Synthesis, Characterization, Crystal Feature and Antimalarial Activity, *J Mol Struct*, 2021, **1232**, 130051.
- 237 A. Ramesh, B. Srinivas, R. Pawar and A. Ramachandraiah, Synthesis, characterization, crystal structure determination, computational modelling and biological studies of a new tetrakis-(2-hydroxy-5-methylphenyl)(1H-pyrazol-4-yl)methanonezinc(II) complex, *J Mol Struct*, 2022, **1255**.
- 238 A. Arunadevi, J. Porkodi, L. Ramgeetha and N. Raman, Biological evaluation, molecular docking and DNA interaction studies of coordination compounds gleaned from a pyrazolone incorporated ligand, *Nucleosides Nucleotides Nucleic Acids*, 2019, **38**, 656–679.
- 239 D. A. Garnovskii, V. G. Vlasenko, K. A. Lyssenko, N. I. Makarova, S. I. Levchenkov, A. L. Trigub, T. N. Danilenko, A. I. Uraev, Y. v. Koshchienko and A. S. Burlov, Synthesis, structural, spectral studies, and DFT calculations of a series of mixed ligand complexes of a tridentate N, N, S pyrazole based aldimine and 2,2'-bipyridine. The first example of structurally characterized dimeric cadmium(II) adduct with unusua, *Polyhedron*, 2020, **190**, 114763.

- 240 A. S. Burlov, V. G. Vlasenko, A. v. Dmitriev, V. v. Chesnokov, A. I. Uraev, D. A. Garnovskii, Y. v. Zubavichus, A. L. Trigub, I. S. Vasilchenko, D. A. Lypenko, E. I. Mal'Tsev, T. v. Lifintseva and G. S. Borodkin, Synthesis, structure, photo- and electroluminescent properties of zinc(II) complexes with aminomethylene derivatives of 1-phenyl-3-methyl-4-formylpyrazol-5-one and 3- and 6-aminoquinolines, *Synth Met*, 2015, **203**, 156–163.
- 241 J. A. McCleverty, in *Encyclopedia of Inorganic Chemistry*, John Wiley & Sons, Ltd, 2006.
- 242 R. C. Maurya, V. Pillai and S. Rajput, Synthesis and Structural Investigation of Some Mixed-Ligand Cyanonitrosyl {Mo(NO)}₄ Complexes of Molybdenum(II) Containing Potentially Mono- and Bidentate Biologically Active Organic Ligands, *Synth React Inorg Met Org Chem*, 2007, **33**, 699–716.
- 243 B. A. Uzoukwu, K. Gloe and O. Rademacher, Synthesis and X-Ray Diffraction Studies of Bis(4-propanoyl-2,4-dihydro-5-methyl-2-phenyl-3H-pyrazol-3-onato) Dioxomolybdenum(VI) and [4-(1-trichloro-2-ethoxy)propanoyl-2,4-dihydro-5-methyl-2-phenyl-3H-pyrazol-3-onato][4-trichloroacetyl-2,4-dihydro-5-methyl-2-phenyl-3H-pyrazol-3-onato] Dioxomolybdenum(VI), *Z Anorg Allg Chem*, 2001, **627**, 108–113.
- 244 L. Hills, R. Moyano, F. Montilla, A. Pastor, A. Galindo, E. Álvarez, F. Marchetti and C. Pettinari, Dioxomolybdenum(VI) Complexes with Acylpyrazolonate Ligands: Synthesis, Structures, and Catalytic Properties, *Eur J Inorg Chem*, 2013, **2013**, 3352–3361.
- 245 E. Begines, C. J. Carrasco, F. Montilla, E. Álvarez, F. Marchetti, R. Pettinari, C. Pettinari and A. Galindo, Oxidoperoxidomolybdenum(VI) complexes with acylpyrazolonate ligands: Synthesis, structure and catalytic properties, *Dalton Trans*, 2018, **47**, 197–208.
- 246 J. M. Mir, P. K. Vishwakarma, S. Roy and R. C. Maurya, Quinoline and pyrazolone functionalized cis-dioxomolybdenum(VI) complexes: synthesis, hyphenated experimental-DFT studies and bactericidal implications, *J Coord Chem*, 2018, **71**, 3860–3873.
- 247 N. Sumita Rao, M. N. Jaiswal, D. D. Mishra, R. C. Maurya and N. Nageswara Rao, Synthesis and characterization of cis-dioxomolybdenum(VI) Schiff base complexes derived from 1-phenyl-3-methyl-4-benzoyl-5-pyrazolone, *Polyhedron*, 1993, **12**, 2045–2050.

- 248 N. S. Rao, D. D. Mishra, R. C. Maurya and N. N. Rao, Synthesis and characterisation of Dinitrosylmolybdenum(0) Schiff base complexes derived from 1-phenyl-3-methyl-4-benzoyl-5-pyrazolone, *Polyhedron*, 1994, **13**, 2653–2658.
- 249 R. C. Maurya, D. D. Mishra, M. N. Jayaswal and S. Kovil, Synthesis and Spectral Studies of Novel Dioxomolybdenum(VI) Heterochelates Involving some Schiff Bases Derived from 4-Acetyl-3-Methyl-1-Phenyl-2-Pyrazolin-5-One, *Synth React Inorg Met Org Chem*, 2006, **27**, 77–92.
- 250 R. C. Maurya, B. Shukla and A. Pandey, Synthesis, magnetic and spectral studies of some cis-dioxomolybdenum(VI) complexes derived from N, O- and N2O2- type Schiff bases , *Indian J Chem*, 2002, **41A**, 554–559.
- 251 B. T. Thaker and R. S. Barvalia, Synthesis, spectral, and thermal studies of oxomolybdenum(V) Schiff-base complexes derived from heterocyclic β -diketone, *J Coord Chem*, 2010, **63**, 1597–1610.
- 252 R. C. Maurya, J. Chourasia, M. H. Martin, S. Roy, A. K. Sharma and P. Vishwakarma, Dioxomolybdenum(VI) chelates of bioinorganic, catalytic, and medicinal relevance: Studies on some cis-dioxomolybdenum(VI) complexes involving O, N-donor 4-oximino-2-pyrazoline-5-one derivatives, *Arab J Chem*, 2015, **8**, 293–306.
- 253 M. R. Maurya, N. Saini and F. Avecilla, Study of temperature dependent three component dynamic covalent assembly via Hantzsch reaction catalyzed by dioxido- and oxidoperoxidomolybdenum(vi) complexes under solvent free conditions, *RSC Adv*, 2016, **6**, 12993–13009.
- 254 F. Caruso, M. Rossi, J. Tanski, R. Sartori, R. Sariego, S. Moya, S. Diez, E. Navarrete, A. Cingolani, F. Marchetti and C. Pettinari, Synthesis, structure, and antitumor activity of a novel tetranuclear titanium complex, *J Med Chem*, 2000, **43**, 3665–3670.
- 255 F. Caruso, C. Pettinari, F. Marchetti, P. Natanti, C. Phillips, J. Tanski and M. Rossi, Synthesis, molecular structure (X-ray and DFT), and solution behavior of titanium 4-acyl-5-pyrazolonates. Correlations with related antitumor β -diketonato derivatives, *Inorg Chem*, 2007, **46**, 7553–7560.
- 256 F. Caruso, E. Monti, J. Matthews, M. Rossi, M. B. Gariboldi, C. Pettinari, R. Pettinari and F. Marchetti, Synthesis, characterization, and antitumor activity of water-soluble

- (arene)ruthenium(II) derivatives of 1,3-dimethyl-4-acylpyrazolon-5-ato ligands. First example of Ru(arene)(ligand) antitumor species involving simultaneous Ru-N7(guanine) bonding and ligand intercalation to DNA, *Inorg Chem*, 2014, **53**, 3668–3677.
- 257 R. Pettinari, F. Marchetti, C. Pettinari, A. Petrini, B. W. Skelton, A. H. White, L. Bonfili, M. Cuccioloni and A. M. Eleuteri, Dinuclear (η^6 -arene) ruthenium(II) acylpyrazolone complexes: Synthesis, characterization and cytotoxicity, *J Organomet Chem*, 2015, **791**, 1–5.
- 258 J. Palmucci, F. Marchetti, R. Pettinari, C. Pettinari, R. Scopelliti, T. Riedel, B. Therrien, A. Galindo and P. J. Dyson, Synthesis, structure, and anticancer activity of arene-ruthenium(II) complexes with acylpyrazolones bearing aliphatic groups in the acyl moiety, *Inorg Chem*, 2016, **55**, 11770–11781.
- 259 F. Marchetti, R. Pettinari, C. di Nicola, C. Pettinari, J. Palmucci, R. Scopelliti, T. Riedel, B. Therrien, A. Galindo and P. J. Dyson, Synthesis, characterization and cytotoxicity of arene-ruthenium(ii) complexes with acylpyrazolones functionalized with aromatic groups in the acyl moiety, *Dalton Trans*, 2018, **47**, 868–878.
- 260 S. A. de Pascali, D. Migoni, M. Monari, C. Pettinari, F. Marchetti, A. Muscella and F. P. Fanizzi, Synthesis, Crystal Structure, and Biological Study of PtII Complexes with 4-Acyl-5-pyrazolones, *Eur J Inorg Chem*, 2014, **2014**, 1249–1259.
- 261 C. Pettinari, F. Caruso, N. Zaffaroni, R. Villa, F. Marchetti, R. Pettinari, C. Phillips, J. Tanski and M. Rossi, Synthesis, spectroscopy (IR, multinuclear NMR, ESI-MS), diffraction, density functional study and in vitro antiproliferative activity of pyrazole-beta-diketone dihalotin(IV) compounds on 5 melanoma cell lines, *J Inorg Biochem*, 2006, **100**, 58–69.
- 262 A. Jain, A. K. Rai and P. N. Saxena, Assessment of toxicity of some penta- and hexacoordinated organotin(IV) and tetraordinated tin(II) complexes of heterocyclic β -diketones, *Bioinorg Chem Appl*, 2006, **2006**, 1–4.
- 263 B. Zhao, X. Shang, L. Xu, W. Zhang and G. Xiang, Novel mixed ligand di-n-butyltin(IV) complexes derived from acylpyrazolones and fluorinated benzoic acids: Synthesis, characterization, cytotoxicity and the induction of apoptosis in Hela cancer cells, *Eur J Med Chem*, 2014, **76**, 87–97.

- 264 F. Marchetti, J. Palmucci, C. Pettinari, R. Pettinari, S. Scuri, I. Grappasonni, M. Cocchioni, M. Amati, F. Lelj and A. Crispini, Linkage Isomerism in Silver Acylpyrazolonato Complexes and Correlation with Their Antibacterial Activity, *Inorg Chem*, 2016, **55**, 5453–5466.
- 265 F. Marchetti, J. Palmucci, C. Pettinari, R. Pettinari, M. Marangoni, S. Ferraro, R. Giovannetti, S. Scuri, I. Grappasonni, M. Cocchioni, F. J. Maldonado Hodar and R. Gunnella, Preparation of Polyethylene Composites Containing Silver(I) Acylpyrazolonato Additives and SAR Investigation of their Antibacterial Activity, *ACS Appl Mater Interfaces*, 2016, **8**, 29676–29687.
- 266 M. Cossi, N. Rega, G. Scalmani and V. Barone, Energies, structures, and electronic properties of molecules in solution with the C-PCM solvation model, *J Comput Chem*, 2003, **24**, 669–681.
- 267 M. W. Wong, Vibrational frequency prediction using density functional theory, *Chem Phys Lett*, 1996, **256**, 391–399.
- 268 A. P. Scott and L. Radom, Harmonic vibrational frequencies: An evaluation of Hartree-Fock, Møller-Plesset, quadratic configuration interaction, density functional theory, and semiempirical scale factors, *J Phys Chem*, 1996, **100**, 16502–16513.
- 269 M. J. Frisch, G. W. Trucks, H. B. Schlegel, G. E. Scuseria, M. A. Robb, J. R. Cheeseman, G. Scalmani, V. Barone, G. A. Petersson, H. Nakatsuji, X. Li, M. Caricato, A. v. Marenich, J. Bloino, B. G. Janesko, R. Gomperts, B. Mennucci, H. P. Hratchian, J. v. Ortiz, A. F. Izmaylov, J. L. Sonnenberg, D. Williams-Young, F. Ding, F. Lipparini, F. Egidi, J. Goings, B. Peng, A. Petrone, T. Henderson, D. Ranasinghe, V. G. Zakrzewski, J. Gao, N. Rega, G. Zheng, W. Liang, M. Hada, M. Ehara, K. Toyota, R. Fukuda, J. Hasegawa, M. Ishida, T. Nakajima, Y. Honda, O. Kitao, H. Nakai, T. Vreven, K. Throssell, J. A. , Jr. Montgomery, J. E. Peralta, F. Ogliaro, M. J. Bearpark, J. J. Heyd, E. N. Brothers, K. N. Kudin, V. N. Staroverov, T. A. Keith, R. Kobayashi, J. Normand, K. Raghavachari, A. P. Rendell, J. C. Burant, S. S. Iyengar, J. Tomasi, M. Cossi, J. M. Millam, M. Klene, C. Adamo, R. Cammi, J. W. Ochterski, R. L. Martin, K. Morokuma, O. Farkas, J. B. Foresman and D. J. Fox, 2016.
- 270 A. D. Becke, Density-functional thermochemistry. I. The effect of the exchange-only gradient correction, *J Chem Phys*, 1998, **96**, 2155.

- 271 C. Lee, W. Yang and R. G. Parr, Development of the Colle-Salvetti correlation-energy formula into a functional of the electron density, *Phys Rev B*, 1988, **37**, 785.
- 272 J. H. Jorgensen and M. J. Ferraro, Antimicrobial susceptibility testing: A review of general principles and contemporary practices, *Clin Infect Dis* 2009, **49**, 1749–1755.
- 273 A. W. Bauer, W. M. Kirby, J. C. Sherris and M. Turck, Antibiotic Susceptibility Testing by a Standardized Single Disk Method, *Am J Clin Pathol*, 1966, **45**, 493–496.
- 274 R. Pettinari, F. Marchetti, C. di Nicola, C. Pettinari, A. Galindo, R. Petrelli, L. Cappellacci, M. Cuccioloni, L. Bonfili, A. M. Eleuteri, M. F. C. Guedes Da Silva and A. J. L. Pombeiro, Ligand Design for N,O- or N,N-Pyrazolone-Based Hydrazones Ruthenium(II)-Arene Complexes and Investigation of Their Anticancer Activity., *Inorg. Chem*, 2018, **57**, 14123–14133.
- 275 K. Parimala and V. Balachandran, Vibrational spectroscopic (FTIR and FT Raman) studies, first order hyperpolarizabilities and HOMO, LUMO analysis of p-toluenesulfonyl isocyanate using ab initio HF and DFT methods, *Spectrochim Acta A Mol Biomol Spectrosc*, 2011, **81**, 711–723.
- 276 G. Shanmugam and S. Brahadeeswaran, Spectroscopic, thermal and mechanical studies on 4-methylanilinium p-toluenesulfonate - A new organic NLO single crystal, *Spectrochim Acta A Mol Biomol Spectrosc*, 2012, **95**, 177–183.
- 277 S. Vijayalakshmi and S. Kalyanaraman, Non-linear optical analyses of nitro aniline derived Schiff bases of 9-anthraldehyde, *Opt Mater (Amst)*, 2013, **35**, 440–443.
- 278 J. Clarkson and W. E. Smith, A DFT analysis of the vibrational spectra of nitrobenzene, *J Mol Struct*, 2003, **655**, 413–422.
- 279 M. F. Brana, A. Gradillas, A. G. Ovalles, B. López, N. Acero, F. Llinares and D. M. Mingarro, Synthesis and biological activity of N, N-dialkylaminoalkyl-substituted bisindolyl and diphenyl pyrazolone derivatives, *Bioorg Med Chem*, 2006, **14**, 9–16.
- 280 N. M. Kreienborg and C. Merten, How to treat C-F stretching vibrations? A vibrational CD study on chiral fluorinated molecules, *Phys Chem Chem Phys*, 2019, **21**, 3506–3511.
- 281 Z.-Y. Yang, R.-D. Yang, F.-S. Li and K.-B. Yu, Crystal structure and antitumor activity of some rare earth metal complexes with Schiff base, *Polyhedron*, 2000, **19**, 2599–2604.

- 282 V. G. Vlasenko, D. A. Garnovskii, G. G. Aleksandrov, N. I. Makarova, S. I. Levchenkov, A. L. Trigub, Y. v. Zubavichus, A. I. Uraev, Y. v. Koshchienko and A. S. Burlov, Mixed ligand metal-complexes of tridentate N, N, S pyrazole containing Schiff base and 2-amino-1-ethylbenzimidazole: Synthesis, structure, spectroscopic studies and quantum-chemical calculations, *Polyhedron*, 2017, **133**, 245–256.
- 283 N. M. Hosny, A. Belal, R. Motawea, M. A. Hussien and M. H. Abdel-Rhman, Spectral characterization, DFT, docking and cytotoxicity of N-benzyl-4,5-dihydro-3-methyl-5-oxo-1H-pyrazole-4-carbothioamide and its metal complexes, *J Mol Struct*, 2021, **1232**, 130020.
- 284 P. J. Petersen, C. H. Jones and P. A. Bradford, In vitro antibacterial activities of tigecycline and comparative agents by time-kill kinetic studies in fresh Mueller-Hinton broth, *Diagn Microbiol Infect Dis*, 2007, **59**, 347–349.
- 285 S. v. Kumar, S. O. Scottwell, E. Waugh, C. J. McAdam, L. R. Hanton, H. J. L. Brooks and J. D. Crowley, Antimicrobial Properties of Tris(homoleptic) Ruthenium(II) 2-Pyridyl-1,2,3-triazole ‘click’ Complexes against Pathogenic Bacteria, Including Methicillin-Resistant Staphylococcus aureus (MRSA), *Inorg Chem*, 2016, **55**, 9767–9777.
- 286 H. Kargar, A. A. Ardakani, M. N. Tahir, M. Ashfaq and K. S. Munawar, Synthesis, spectral characterization, crystal structure and antibacterial activity of nickel(II), copper(II) and zinc(II) complexes containing ONNO donor Schiff base ligands, *J Mol Struct*, 2021, **1233**, 130112.
- 287 R. S. Joseyphus and M. S. Nair, Antibacterial and Antifungal Studies on Some Schiff Base Complexes of Zinc(II), *Mycobiology*, 2008, **36**, 93–98.
- 288 Y. Anjaneyulu and R. P. Rao, Preparation, characterization and antimicrobial activity studies on some ternary complexes of Cu(II) with acetylacetone and various salicylic acids, *Synth React Inorg Met Org Chem*, 1986, **16**, 257–272.
- 289 L. Mishra and V. Singh, Synthesis, structural and antifungal studies of Co(II), Ni(II), Cu(II) and Zn(II) complexes with new Schiff bases bearing benzimidazoles, *Indian J Chem*, 1993, **32**, 446–449.
- 290 Neglected tropical diseases: Sleeping sickness (human African trypanosomiasis), [https://www.who.int/news-room/questions-and-answers/item/neglected-topical-diseases-sleeping-sickness-\(human-african-trypanosomiasis\)](https://www.who.int/news-room/questions-and-answers/item/neglected-topical-diseases-sleeping-sickness-(human-african-trypanosomiasis)).

- 291 2019 R&D portfolio in review: Sleeping sickness | DNDi, <https://dndi.org/news/2020/sleepingsickness-rnd-portfolio-update/>.
- 292 E. Torreele, B. B. Trunz, D. Tweats, M. Kaiser, R. Brun, G. Mazué, M. A. Bray and B. Pécoul, Fexinidazole – A New Oral Nitroimidazole Drug Candidate Entering Clinical Development for the Treatment of Sleeping Sickness, *PLoS Negl Trop Dis*, 2010, **4**, e923.
- 293 P. P. Simarro, G. Cecchi, J. R. Franco and M. Paone, Estimating and Mapping the Population at Risk of Sleeping Sickness, *PLoS Negl Trop Dis*, 2012, **6**, e1859.
- 294 F. Chappuis, Oral fexinidazole for human African trypanosomiasis, *The Lancet*, 2018, **391**, 100–102.
- 295 P. Babokhov, A. O. Sanyaolu, W. A. Oyibo, A. F. Fagbenro-Beyioku and N. C. Iriemenam, A current analysis of chemotherapy strategies for the treatment of human African trypanosomiasis, *Pathog. Glob.Health*, 2013, **107**, 242–252.
- 296 P. C. Sharma, D. Sharma, A. Sharma, N. Saini, R. Goyal, M. Ola, R. Chawla and V. K. Thakur, Hydrazone comprising compounds as promising anti-infective agents: chemistry and structure-property relationship, *Mater Today Chem*, 2020, **18**, 100349.
- 297 Z. Zhao, X. Dai, C. Li, X. Wang, J. Tian, Y. Feng, J. Xie, C. Ma, Z. Nie, P. Fan, M. Qian, X. He, S. Wu, Y. Zhang and X. Zheng, Pyrazolone structural motif in medicinal chemistry: Retrospect and prospect, *Eur J Med Chem*, 2020, **186**, 111893.
- 298 F. Marchetti, C. di Nicola, R. Pettinari, C. Pettinari, I. Aiello, M. la Deda, A. Candreva, S. Morelli, L. de Bartolo and A. Crispini, Zinc(II) Complexes of Acylpyrazolones Decorated with a Cyclohexyl Group Display Antiproliferative Activity Against Human Breast Cancer Cells, *Eur J Inorg Chem*, 2020, **2020**, 1027–1039.
- 299 M. Cuccioloni, L. Bonfili, V. Cecarini, M. Nabissi, R. Pettinari, F. Marchetti, R. Petrelli, L. Cappellacci, M. Angeletti and A. M. Eleuteri, Exploring the Molecular Mechanisms Underlying the in vitro Anticancer Effects of Multitarget-Directed Hydrazone Ruthenium(II)–Arene Complexes, *ChemMedChem*, 2020, **15**, 105–113.
- 300 Biochemistry and Molecular Biology of Parasites, J. Marr, M. Muller, 1995.
- 301 D. J. Hammond and W. E. Gutteridge, UMP synthesis in the kinetoplastida, *Biochimica et Biophysica Acta (BBA) - General Subjects*, 1982, **718**, 1–10.

- 302 A. Hofer, D. Steverding, A. Chabes, R. Brun and L. Thelander, Trypanosoma brucei CTP synthetase: a target for the treatment of African sleeping sickness., *Proc Natl Acad Sci*, 2001, **98**, 6412–6416.
- 303 G. Sheldrick, SADABS, 2002.
- 304 A. Bruker, SAINTS, 2005.
- 305 O. V. Dolomanov, L. J. Bourhis, R. J. Gildea, J. A. K. Howard and H. Puschmann, OLEX2: a complete structure solution, refinement and analysis program, *J Appl Cryst*, 2009, **42**, 339–341.
- 306 R. Petrelli, G. Orsomando, L. Sorci, F. Maggi, F. Ranjbarian, P. C. Biapa Nya, D. Petrelli, L. A. Vitali, G. Lupidi, L. Quassinti, M. Bramucci, A. Hofer and L. Cappellacci, Biological Activities of the Essential Oil from Erigeron floribundus, *Molecules*, 2016, **21**, 1065.
- 307 R. Petrelli, F. Ranjbarian, S. Dall’Acqua, F. Papa, R. Iannarelli, S. L. Ngahang Kamte, S. Vittori, G. Benelli, F. Maggi, A. Hofer and L. Cappellacci, An overlooked horticultural crop, Smyrnum olusatrum, as a potential source of compounds effective against African trypanosomiasis, *Parasitol Int*, 2017, **66**, 146–151.
- 308 F. Ranjbarian, S. Sharma, G. Falappa, W. Taruschio, A. Chabes and A. Hofer, Isocratic HPLC analysis for the simultaneous determination of dNTPs, rNTPs and ADP in biological samples, *Nucleic Acids Res*, 2022, **50**, e18–e18.
- 309 N. M. Hosny, N. Y. Hassan, H. M. Mahmoud and M. H. Abdel-Rhman, Synthesis, characterization and cytotoxicity of new 2-isonicotinoyl-N-phenylhydrazine-1-carbothioamide and its metal complexes, *Appl Organomet Chem*, 2019, **33**, e4998.
- 310 N. Morozov, I. N. Shcherbakov, S. I. Levchenkov and L. D. Popov, Structure, Spectral Properties, and Complexing Ability of 1-Phenyl-3-methylpyrazol-5-one Ferrocenoyl Hydrazone, *Russ J Gen Chem*, 2020, **90**, 257–267.
- 311 G. C. Xu, L. Zhang, Y. H. Zhang, J. X. Guo, M. Q. Shi and D. Z. Jia, Syntheses, crystal structures and luminescent properties of four Zn(II) coordination polymers with pyrazolone derivatives and 4,4'-bipyridine, *CrystEngComm*, 2013, **15**, 2873–2880.
- 312 A. N. Gusev, M. A. Kiskin, E. v. Braga, M. Chapran, G. Wiosna-Salyga, G. v. Baryshnikov, V. A. Minaeva, B. F. Minaev, K. Ivaniuk, P. Stakhira, H. Ågren and W. Linert, Novel Zinc

- Complex with an Ethylenediamine Schiff Base for High-Luminance Blue Fluorescent OLED Applications, *J Phys Chem C*, 2019, **123**, 11850–11859.
- 313 Y. Li, Z. Yang, M. Zhou, Y. Li, J. He, X. Wang and Z. Lin, Ni(II) and Co(II) complexes of an asymmetrical aroylhydrazone: synthesis, molecular structures, DNA binding, protein interaction, radical scavenging and cytotoxic activity, *RSC Adv*, 2017, **7**, 41527–41539.
- 314 M. Barwiolek, A. Kaczmarek-Kędziera, T. M. Muziol, D. Jankowska, J. Jezierska and A. Bieńko, Dinuclear Copper(II) Complexes with Schiff Bases Derived from 2-Hydroxy-5-Methylisophthalaldehyde and Histamine or 2-(2-Aminoethyl)pyridine and Their Application as Magnetic and Fluorescent Materials in Thin Film Deposition, *Inter J Mol Sci*, 2020, **21**, 4587.
- 315 I. U. Shaikh, R. K. Patel, V. A. Mevada, V. K. Gupta and R. N. Jadeja, Binary and Ternary Zinc(II) Complexes of Acyl Pyrazolones: Synthesis, Spectroscopic Analysis, Crystal Structure and Antimalarial Activity, *ChemistrySelect*, 2019, **4**, 8286–8294.
- 316 R. D. Shannon and IUCr, Revised effective ionic radii and systematic studies of interatomic distances in halides and chalcogenides, *Acta Cryst*, 1976, **32**, 751–767.
- 317 L. Tamborini, A. Pinto, T. K. Smith, L. L. Major, M. C. Iannuzzi, S. Cosconati, L. Marinelli, E. Novellino, L. lo Presti, P. E. Wong, M. P. Barrett, C. DeMicheli and P. Conti, Synthesis and Biological Evaluation of CTP Synthetase Inhibitors as Potential Agents for the Treatment of African Trypanosomiasis, *ChemMedChem*, 2012, **7**, 1623–1634.
- 318 J. Tendam and U. Hanefeld, Renewable Chemicals: Dehydroxylation of Glycerol and Polyols, *ChemSusChem*, 2011, **4**, 1017–1034.
- 319 C. Boucher-Jacobs and K. M. Nicholas, Deoxydehydration of polyols, *Top Curr Chem*, 2014, **353**, 163–184.
- 320 Sabatier P. and Gaudion G., On the division of glycerin in the presence of diverse catalyses: The formation of ethylic and allylic alcohols, *C. R. Hebd. Seances Acad. Sci.*, 1918, **166**, 1033–1039.
- 321 J. R. Dethlefsen, D. Lupp, A. Teshome, L. B. Nielsen and P. Fristrup, Molybdenum-catalyzed conversion of diols and biomass-derived polyols to alkenes using isopropyl alcohol as reductant and solvent, *ACS Catal*, 2015, **5**, 3638–3647.

- 322 G. Chapman and K. M. Nicholas, Vanadium-catalyzed deoxydehydration of glycols, *Chem Comm*, 2013, **49**, 8199–8201.
- 323 G. K. Cook and M. A. Andrews, Toward nonoxidative routes to oxygenated organics: Stereospecific deoxydehydration of diols and polyols to alkenes and allylic alcohols catalyzed by the metal oxo complex (C₅Me₅)ReO₃, *J Am Chem Soc*, 1996, **118**, 9448–9449.
- 324 A. Galindo, DFT Studies on the Mechanism of the Vanadium-Catalyzed Deoxydehydration of Diols, *Inorg Chem*, 2016, **55**, 2284–2289.
- 325 R. G. Bergman, J. A. Ellman, A. R. Elena and P. C. Marsden, Method of converting a polyol to an olefin, US 8,273,926 B2, 2012.
- 326 C. Lee, W. Yang and R. G. Parr, Development of the Colle-Salvetti correlation-energy formula into a functional of the electron density, *Phys Rev B*, 1988, **37**, 785.
- 327 J. van Slageren, A. Klein, S. Zális and D. J. Stufkens, Resonance Raman spectra of d₆ metal–diimine complexes reflect changes in metal–ligand interaction and character of electronic transition, *Coord Chem Rev*, 2001, **219–221**, 937–955.
- 328 M. A. Pietsch, M. Couty and M. B. Hall, Comparison of Møller-Plesset Perturbation Methods, Complete Active Space Self-Consistent Field Theory, and a New Generalized Molecular Orbital Method for Oxygen Atom Transfer from a Molybdenum Complex to a Phosphine, *J Phys Chem*, 1995, **99**, 16315–16319.
- 329 H. Arzoumanian, Molybdenum-oxo chemistry in various aspects of oxygen atom transfer processes, *Coord Chem Rev*, 1998, **178**, 191–202.
- 330 A. J. Millar, C. J. Doonan, P. D. Smith, V. N. Nemykin, P. Basu and C. G. Young, Oxygen atom transfer in models for molybdenum enzymes: Isolation and structural, spectroscopic, and computational studies of intermediates in oxygen atom transfer from molybdenum(VI) to phosphorus(III), *Chem Eur J* 2005, **11**, 3255–3267.
- 331 K. P. Gable and F. A. Zhuravlev, Kinetic isotope effects in cycloreversion of rhenium (V) diolates, *J Am Chem Soc*, 2002, **124**, 3970–3979.

- 332 L. J. Goossen, D. Koley, H. L. Hermann and W. Thiel, Palladium monophosphine intermediates in catalytic cross-coupling reactions: A DFT study, *Organometallics*, 2006, **25**, 54–67.
- 333 M. Drees, S. A. Hauser, M. Cokoja and F. E. Kühn, DFT studies on the reaction pathway of the catalytic olefin epoxidation with CpMoCF₃ dioxo and oxo-peroxo complexes, *J Organomet Chem*, 2013, **748**, 36–45.
- 334 Y. Yoo, M. W. Spencer and D. R. Paul, Morphology and mechanical properties of glass fiber reinforced Nylon 6 nanocomposites, *Polymer*, 2011, **52**, 180–190.
- 335 N. M. al Andis, A New Method for Synthesis of Poly (2,6-dimethyl-1,4-phenylene oxide) and Poly (2,6-diphenyl-1,4-phenyl oxide), *J Chem*, 2013, **2013**, 0–4.
- 336 H. Wang, B. Shentu and Z. Weng, One-pot synthesis of poly(2,6-dimethyl-1,4-phenylene oxide)/polystyrene alloy with CuCl₂/4-dimethylaminopyridine as a versatile catalyst in water, *RSC Adv*, 2014, **4**, 510–515.
- 337 H. Wang, B. Shentu and Z. Weng, Oxidative coupling copolymerization for synthesis of poly(phenylene oxide) containing allyl groups in water, *RSC Adv*, 2014, **4**, 18317–18322.
- 338 I. S. Bayer, A. Biswas, A. Tripathi, D. K. Avasthi, J. P. Singh and C. M. Megaridis, Composite thin films of poly(phenylene oxide)/poly(styrene) and PPO/silver via vapor phase deposition, *Polym Adv Technol*, 2009, **20**, 775–784.